NONLINEAR STABILITY, BIFURCATION AND MODE INTERACTION IN GRANULAR PLANE COUETTE FLOW

A Thesis

Submitted for the Degree of

Doctor of Philosophy

by

PRIYANKA SHUKLA

$$\frac{dA}{dt} = f(A,t)$$

$$\frac{\partial A}{\partial t} + a_1 \frac{\partial A}{\partial x} + a_2 \nabla^2 A = g(A, t, x, \ldots)$$

ENGINEERING MECHANICS UNIT
JAWAHARLAL NEHRU CENTRE FOR ADVANCED SCIENTIFIC RESEARCH
(A Deemed University)
Bangalore 560 064

AUGUST 2010

The true laboratory is the mind, where behind illusions we uncover the laws of truth.

J.C. Bose

To my parents and brother

DECLARATION

I hereby declare that the matter embodied in the thesis entitled "**Nonlinear Stability, Bifurcation and Mode Interaction in Granular Plane Couette Flow**" is the result of investigations carried out by me at the Engineering Mechanics Unit, Jawaharlal Nehru Centre for Advanced Scientific Research, Bangalore, India under the supervision of **Prof. Meheboob Alam** and that it has not been submitted elsewhere for the award of any degree or diploma.

In keeping with the general practice in reporting scientific observations, due acknowledgment has been made whenever the work described is based on the findings of other investigators.

Priyanka Shukla

CERTIFICATE

I hereby certify that the matter embodied in this thesis entitled "**Nonlinear Stability, Bifurcation and Mode Interaction in Granular Plane Couette Flow**" has been carried out by **Ms. Priyanka Shukla** at the Engineering Mechanics Unit, Jawaharlal Nehru Centre for Advanced Scientific Research, Bangalore, India under my supervision and that it has not been submitted elsewhere for the award of any degree or diploma.

10/2/2011

Prof. Meheboob Alam
(Research Supervisor)

Acknowledgments

I am indebted to all those who made this thesis possible. It is an honor for me to express my deep gratitude to my thesis advisor, Prof. Meheboob Alam. Without his skilful guidance, insightful comments, immense patience and impressive depth of knowledge, this thesis would not have been possible. I highly appreciate him for encouraging me to develop analytical solutions of nonlinear problem during the period of research frustration induced by 'jamming', 'banding' and 'clustering' of numerics. I am very fortunate to have him as my research advisor.

I thank Prof. Roddam Narasimha, Prof. C. N. R. Rao and all the faculty members of *Engineering Mechanics Unit* for their valuable teachings and inspiration. I gratefully thank all my teachers: Prof. Meheboob Alam, Prof. Umesh Waghmare (TSU), Dr. Ganesh Subramanian (EMU), Prof. Peeyush Chandra (IITK), Prof. Prawal Sinha (IITK) and Prof. S. Ghorai (IITK) for teaching me courses which are the basis for my research work.

My special thanks to my friends: Snehalatha, Anjulika, Gargi and Ritika for their valuable advice, motivation and countless discussions on various aspect of science. I would like to thank my labmates: Vinay, Ujjayan, Satya, Reddy, Rohan and Pascal for their immeasurable help and creating a very good friendly working environment in the Lab. I offer my regards to all of those who supported me in any respect during the completion of the project.

I have been fortunate to come across many good friends without whom life at JNC would be bleak. Special thanks go to: Ankana, Moumita, Selvi, Sasmita, Saswati, Surbhi and Sutapa. I am ever grateful to my institute, JNCASR, for providing excellent infrastructure and financial support.

Finally, I would like to thank my grandparents and parents for their unconditional love and blessings which gave me enough courage to face any tough problem. I offer special thanks to my sister-in-law Mamta for her moral support. My deepest gratitude goes to my brother, Prashant, for being my best friend and first teacher, and for his encouragement to pursue interdisciplinary research. Without his constant love, help and care, this thesis would have been impossible. This thesis is dedicated to my parents and brother.

Synopsis

This thesis starts with a brief overview of patterns in rapid granular flows driven by vibration, gravity and shear, e.g. standing wave patterns and convection rolls in a vibrated granular system, density waves in gravity driven granular Poiseuille flow, fingering in chute flow, shearbanding in shear flow, etc. The pattern forming order parameter models such as coupled complex Ginzburg-Landau model, Swift-Hohenberg model and continuous coupled map model have been described in chapter 1.

The continuum theory of granular fluid and Navier Stokes order constitutive models for the inelastic hard-sphere and hard-disk fluids have been detailed in chapter 2. In chapter 3 a general weakly nonlinear stability analysis using amplitude expansion method has been described. A spectral based numerical scheme for solving weakly nonlinear equations and solvability condition have been developed in chapter 3.

In the first problem of present thesis, a weakly nonlinear theory, in terms of the well-known Landau equation, has been developed to describe the nonlinear saturation of shear-banding instability in rapid granular plane Couette flow. The shear-banding instability corresponds to streamwise-independent perturbations ($\partial/\partial x(\cdot) = 0$ and $\partial/\partial y(\cdot) \neq 0$, where x and y refer to flow and gradient directions, respectively) of the underlying steady uniform shear flow which degenerates into alternate layers of dense and dilute regions of low and high shear-rates, respectively, along the gradient direction. The nonlinear stability of this shear-banding instability is analyzed using two perturbation methods, the *center manifold reduction method* (chapter 4) and the *amplitude expansion method* (chapter 5); the resulting nonlinear problem has been reduced to a sequence of linear problems for the fundamental mode, its higher-order harmonics and distortions, and the base-flow distortions of various order. The first Landau coefficient, which is the leading nonlinear correction in the Landau equation at cubic order in the amplitude of perturbation, derived from the present method exactly matches with the same obtained from the center manifold reduction technique. The nonlinear modes are found to follow certain symmetries of the base flow and the fundamental mode. These symmetries helped to identify *analytical* solutions for the base-flow distortion and the second harmonic, leading to an exact calculation of the first Landau coefficient. The present analytical solutions are further used to validate an spectral-based numerical method for nonlinear stability calculation. The regimes of *supercritical* and *subcritical* bifurcations for the shear-banding instability are identified, leading to the prediction that the lower branch of the neutral stability contour in the (H, ϕ^0)-plane, where H is the scaled Couette gap (the ratio between the Couette gap and the particle diameter) and ϕ^0 is the mean density or the volume fraction of particles, is sub-critically unstable. Our results suggest that there is a subcritical finite amplitude instability for dilute flows even though the dilute flow is stable according to the linear theory which agrees with previous numerical simulation. Bifurcation diagrams are presented, and the predicted finite-amplitude solutions, representing shear-localization and density segregation, are discussed in the light of previous molecular dynamics simulations of plane shear flow. Our analysis suggests that there is a sequence of transitions among three types of pitchfork bifurcations with increasing mean density: from (i) the *bifurcation from infinity* in the Boltzmann limit to (ii) *subcritical* bifurcation at moderate densities to (iii) *supercritical* bifurcation at a larger density to (iv) *subcritical* bifurcation in the dense limit and finally again to (v) *supercritical* bifurcation near the close packing density. It is shown that the appearance of

subcritical bifurcation in the dense limit depends on the choice of the contact radial distribution function and the constitutive relations. The critical mean density at any transition from one bifurcation-type to another is exactly calculated from our analytical bifurcation theory. The scalings of the first Landau coefficient, the equilibrium amplitude and the phase diagram, in terms of mode number and inelasticity, are demonstrated. The granular plane Couette flow serves as a paradigm that supports all three possible types of pitchfork bifurcations, with the mean density (ϕ^0) being the single control parameter that dictates the nature of bifurcation.

In chapter 6 the evidence of a variety of non-linear equilibrium states of travelling and stationary waves is provided in a two-dimensional granular plane Couette flow. The relevant order parameter equation, the Landau equation, has been derived for the most unstable two-dimensional perturbation of finite size. Along with the linear eigenvalue problem, the mean-flow distortion, the second harmonic, the distortion to the fundamental mode and the first Landau coefficient are calculated using a spectral-based numerical method. Two types of bifurcations, Hopf and pitchfork, that result from travelling and stationary instabilities, respectively, are analyzed using the first Landau coefficient. The present bifurcation theory shows that the flow is subcritically unstable to stationary finite-amplitude perturbations of long wave-lengths ($k_x \sim 0$, where k_x is the streamwise wavenumber) in the dilute limit that evolve from subcritical shearbanding modes ($k_x = 0$), but at large enough Couette gaps there are stationary instabilities with $k_x = O(1)$ that lead to supercritical pitchfork bifurcations. At moderate-to-large densities, in addition to supercritical shearbanding modes, there are long-wave travelling instabilities that lead to Hopf bifurcations. It is shown that both supercritical and subcritical nonlinear states exist at moderate-to-large densities that originate from the dominant stationary and travelling instabilities for which $k_x = O(1)$. Nonlinear patterns of density, velocity and granular temperature for all types of instabilities are contrasted with their linear eigenfunctions. While the supercritical solutions appear to be modulated forms of the fundamental mode, the structural features of unstable subcritical solutions are found to be significantly different from their linear counterpart. It is shown that the granular plane Couette flow is prone to nonlinear resonances in both stable and unstable regimes, the signature of which is implicated as a discontinuity in the first Landau coefficient. Our analysis identified two types of modal resonances that appear at the quadratic order in perturbation amplitude: (i) a 'mean-flow resonance' which occurs due to the interaction between a streamwise-independent shear-banding mode ($k_x = 0$) and a linear/fundamental mode $k_x \neq 0$, and (ii) an exact '1:2 resonance' that results from the interaction between two waves with their wave-number ratio being 1:2.

In chapter 7 of this thesis the vorticity banding in three-dimensional granular plane Couette flow has been investigated via nonlinear stability analysis. Due to the pure spanwise ($\partial/\partial x(.) = 0, \partial/\partial y(.) = 0, \partial/\partial z(.) \neq 0$) instabilities the uniform shear flow breaks into regions of high and low shear stresses along the mean vorticity direction, this is known as vorticity banding. For such pure spanwise instabilities an *analytical* order parameter theory has been developed. The general solutions of the nonlinear equations (distortions of mean flow and fundamental, and harmonics of fundamental) and Landau coefficients have been derived at any arbitrary order in amplitude. The bifurcation analysis has been carried out for all the flow regimes. Our analysis suggests that the vorticity banding appears via supercritical pitchfork bifurcation for density $\phi^0 < \phi^d$ and via subcritical pitchfork bifurcation for density $\phi^0 > \phi^d$, where ϕ^0 is the mean density and ϕ^d is the critical mean density for the transition from supercritical to subcritical bifurcations. The first and second order transitions at the onset of pure spanwise instabilities have been investigated using cubic and quintic order amplitudes. The subcritical Hopf bifurcation has been found for large spanwise wavenumbers in moderate-to-dense flows. The present analysis suggests that the parameters far away from the neutral stability curve there exist both types of bifurcations, Hopf or pitchfork. The crucial effect of higher order nonlinear terms while calculating higher order Landau coefficients is demonstrated. The variations of perturbation fields, pressure and shear viscosity have been shown.

In chapter 8, the gradient and vorticity bandings in three-dimensional granular plane Couette flow have been probed via analytical solutions of weakly nonlinear analysis. Such instability leads to bands along the gradient and vorticity directions. The analytical expressions for the distortion of mean flow, second harmonic and first Landau coefficient have been derived using trigonometric functions. The bifurcation analysis for these instabilities has been carried out. The finite amplitude patterns for density, temperature, velocity and vorticity have been analyzed.

At the end of this thesis two possible extensions of weakly nonlinear analysis have been studied. The single mode analysis is not valid for the case of resonant and non-resonant mode interactions. One possible extension is to derive coupled Landau equations for such mode interactions. The coupled Landau equations have been derived for mode interactions with or without resonance using center manifold method in chapter 9. Another extension is to allow non-periodic time and space dependent perturbations in the flow. The appropriate order parameter theory in this case contains complex Ginzburg Landau equation. The "complex Ginzburg Landau equation" has been derived for the granular plane Couette flow using multiple scale analysis in chapter 10. The numerical results for coupled equations and complex Ginzburg-Landau equation are left to future work.

Contents

Synopsis vii

1 Introduction 1
1.1 Granular Matter . . . 1
1.2 Pattern Formation and Models for Granular Fluids . . . 3
1.2.1 Vibration Driven Patterns . . . 3
1.2.2 Gravity Driven Flows . . . 9
1.2.3 Shear Driven Flows . . . 10
1.3 Models for Granular Patterns . . . 11
1.4 Patterns in Granular Couette Flow and Present Work . . . 13
1.4.1 Shear-banding in Granular Couette Flow . . . 14
1.4.2 Clustering and Density Waves in Granular Couette Flow . . . 18
1.4.3 Present Work . . . 21
1.4.4 Organization of the Present Thesis . . . 22
Appendix 1A. List of Symbols . . . 24

2 Governing Equation 25
2.1 Introduction . . . 25
2.2 Balance Equations . . . 25
2.3 Navier-Stokes Order Constitutive Model . . . 26
2.4 Model for Smooth Identical Inelastic Spheres (Lun *et al.* 1984) . . . 27
2.5 Model for Inelastic Hard-disks . . . 28
2.6 Model for Dense Fluid Transport of Inelastic Hard Spheres, Garzó & Dufty (1999) 28
2.7 Arbitrary Energy Loss Model, Lutsko (2005) . . . 29
2.8 Present Constitutive Model . . . 31
2.9 Boundary Conditions . . . 33
2.9.1 Boundary Conditions in the Dense Limit using Heuristic Approach by Hui *et al.* (1984) . . . 34
2.9.2 Boundary Conditions of Johnson & Jackson (1987) . . . 35
2.9.3 Boundary Conditions of Jenkins & Richman (1986) . . . 36
2.9.4 Present Choice of Boundary Conditions for the Nonlinear Stability Analysis 37
Appendix 2A. List of Symbols . . . 38

3 Weakly Nonlinear Theory for Granular Shear Flows 39
3.1 Different Approaches to Derive Landau-Stuart Equation . . . 39
3.1.1 Amplitude Expansion Method of Stuart and Watson (1960) . . . 39
3.1.2 Center Manifold Reduction . . . 40
3.1.3 Multiple Scale Analysis . . . 40
3.1.4 Organization of this Chapter . . . 41
3.2 Nonlinear Perturbation Equations for Granular Flows . . . 42

3.3 Amplitude Expansion Method . . . 43
3.3.1 Transformed Nonlinear Equations . . . 44
3.3.2 Fourier Expansion and Transformed Nonlinear Equations . . . 45
3.3.3 Taylor Expansion and Superscript Notation . . . 46
3.3.4 Landau Equation and Modal Equations for $X^{[k;n]}$ . . . 47
3.3.5 Adjoint Problem and Bi-orthogonality Condition . . . 50
3.4 Numerical Method: Spectral Collocation and Gauss Chebyshev Quadrature . . . 51
3.4.1 Type (1): Generalized Eigenvalue Problem, $AX = cBX$ . . . 51
3.4.2 Type (2): $AX = b$ Problem ($k \neq 1, n \geq k$) . . . 56
3.4.3 Type (3): $AX = \lambda X + b$ Problem ($k = 1, n > 1$) . . . 56

4 Landau-type Order Parameter Equation for Shear Banding in Granular Couette Flow 59
4.1 Plane Couette flow: Continuum Equations and Boundary Conditions . . . 59
4.1.1 Streamwise Independent Equations . . . 60
4.1.2 Steady Plane Couette Flow: Base State . . . 61
4.2 Nonlinear Analysis . . . 61
4.2.1 Linear Problem . . . 62
4.2.2 Linear Eigenvalue Problem . . . 63
4.3 Center Manifold Reduction . . . 64
4.3.1 Landau Equation . . . 66
4.3.2 Comparison of $c^{(2)}$ between Center Manifold and Amplitude Expansion Methods . . . 67
4.4 Results and Discussion . . . 68
4.4.1 Numerical Method . . . 68
4.4.2 Phase Diagram and Bifurcation . . . 68
4.5 Conclusion . . . 70

5 Nonlinear Shear Banding Instability in Granular Plane Couette Flow: Analytical Solution, Comparison with Numerics and Bifurcation 71
5.1 Analytical Solutions for Fundamental Mode and its Adjoint . . . 71
5.2 Outline of Weakly Nonlinear Analysis for Stream-wise Independent Flow . . . 73
5.2.1 Linear Disturbance: Fundamental Mode . . . 74
5.2.2 Mean Flow Distortion and Second Harmonic . . . 74
5.2.3 Distortion of Fundamental and the First Landau Coefficient . . . 74
5.3 Symmetries of Linear and Nonlinear Modes . . . 75
5.4 Analytical Solution and Comparison with Numerical (Spectral) Solution . . . 76
5.4.1 Solution for Second Harmonic and Mean Flow Distortion . . . 77
5.4.2 Solution for First Landau Coefficient . . . 78
5.4.3 Resonance at $O(A^2)$: Second Harmonic and Distortion to Mean Flow . . . 83
5.4.4 Solution for Higher-order Harmonics: Distortion to Fundamental . . . 86
5.5 Bifurcation, Phase Diagram and Finite-amplitude Solution . . . 87
5.5.1 Phase Diagram and Critical Parameters for 'Linear' Shear-banding Instability 87
5.5.2 Equilibrium Amplitude and the Nature of Bifurcation . . . 89
5.5.3 Phase Diagram for 'Nonlinear' Shear-banding Instability . . . 90
5.5.4 Finite Amplitude Solutions: Density Segregation and Shear Localization . . 96
5.5.5 Scaling of First Landau Coefficient, Equilibrium Amplitude and Bifurcation Diagram . . . 99
5.6 Discussion . . . 103
5.6.1 Influence of Radial Distribution Function . . . 103

5.6.2 Influence of Constitutive Relations: Disks vs Spheres . . . 106
5.6.3 Granular Plane Couette Flow: a "Microcosm" for Pitchfork Bifurcations . . 107
5.7 Conclusions . . . 108
Appendix 5A. Nonlinear Terms ($\mathcal{N}_2$ and $\mathcal{N}_3$) . . . 111
Appendix 5B. Inhomogeneous Terms G_{13} . . . 112
Appendix 5C. Locus of $a^{(2)} = 0$ . . . 114
Appendix 5D. Dispersion Relation . . . 117

6 Nonlinear Stability and Patterns in Two-dimensional Granular Plane Couette Flow: Hopf and Pitchfork Bifurcation, Evidence for Resonance 119
6.1 Introduction . . . 119
6.2 Governing Equations . . . 119
6.3 Nonlinear Stability: Amplitude Expansion Method . . . 121
6.3.1 $O(A)$: Fundamental Mode . . . 122
6.3.2 $O(A^2)$: Mean Flow Distortion and Second Harmonic . . . 123
6.3.3 $O(A^3)$: Distortion to Fundamental, First Landau Coefficient and Third Harmonic . . . 123
6.4 Nonlinear Resonance: Criteria for Mean-flow and 1:2 Resonances . . . 124
6.5 Analysis of Landau-Stuart Equation, Bifurcation and Disturbance Field . . . 125
6.5.1 Equilibrium Amplitude and Phase Velocity . . . 126
6.5.2 Bifurcations, Limit Cycle and Spirals . . . 126
6.5.3 Nonlinear Disturbance Field . . . 128
6.6 Numerical Method and Control Parameters . . . 128
6.7 Results and Discussion: Hopf and Pitchfork Bifurcations, and Resonances . . . 129
6.7.1 Nonlinear Shear-banding ($k_x = 0$) and Long-Wave ($k_x \sim 0$) Instabilities . . 130
6.7.2 Nonlinear Results on Stationary and Travelling Instabilities: $k_x \sim O(1)$ . . 135
6.7.3 Evidence of Mean-flow Resonance and 1:2 Resonance . . . 139
6.7.4 Dominant Stationary and Travelling Instabilities: Effects of Density and Couette Gap . . . 143
6.7.5 Effect of Restitution Coefficient at Large H . . . 150
6.8 Conclusions . . . 155
Appendix 6A. Elements of Linear and Adjoint Operators . . . 156
Appendix 6B. Nonlinear Terms ($\mathcal{N}_2$ and $\mathcal{N}_3$) . . . 157

7 Vorticity Banding in Three Dimensional Granular Couette Flow 161
7.1 Introduction . . . 161
7.1.1 Previous Work on Linear Stability . . . 163
7.1.2 Organization of Present Chapter . . . 164
7.2 Continuum Equations and Boundary Conditions . . . 165
7.2.1 Uniform Shear Flow . . . 166
7.2.2 Nonlinear Disturbance Equations . . . 167
7.3 Linear Problem . . . 167
7.4 Weakly Nonlinear Analysis . . . 168
7.5 Linear Stability Analysis for Pure Spanwise Flow . . . 169
7.5.1 Asymptotic Analysis and Dispersion Relation . . . 170
7.5.2 Locus of the Neutral Stability Curve . . . 172
7.5.3 Analytical Expression for Eigenvectors . . . 174
7.5.4 Analytical Eigenvectors for Adjoint Operator . . . 175
7.6 Weakly Nonlinear Analysis for Pure Spanwise Flow . . . 176
7.6.1 $O(A)$: Fundamental Mode . . . 176
7.6.2 $O(A^2)$: Second Harmonic . . . 177

7.6.3 $O(A^2)$: Mean Flow Distortion . . . 178
7.6.4 $O(A^3)$: First Landau Coefficient . . . 178
7.6.5 General Solution of Weakly Nonlinear Equations . . . 179
7.6.6 $O(A^n)$: Higher Order Harmonics for $n = 3, 4, 5$ . . . 180
7.7 Numerical Results and Discussion . . . 180
7.7.1 Critical Parameters for Vorticity Banding: Linear Stability . . . 180
7.7.2 Equilibrium Amplitude and the Nature of Bifurcation . . . 181
7.7.3 Phase Diagram for Nonlinear Vorticity-banding Instability . . . 182
7.7.4 Switchover from Supercritical to Subcritical Bifurcation . . . 184
7.7.5 Bifurcation Diagrams using Quintic Landau Equation . . . 185
7.7.6 Variation of Amplitude with Density . . . 190
7.7.7 Scaling with Couette Gap . . . 192
7.7.8 Effect of Higher Order Nonlinear Terms . . . 192
7.7.9 Vorticity Banding as a Subcritical Instabilities . . . 195
7.7.10 Finite Amplitude Solutions . . . 198
7.7.11 Results for Dense Flows at Small Wave Lengths: Linearly Stable Regime . 202
7.8 Conclusions and Outlook . . . 203
Appendix 7A. Elements of Linear and Adjoint Operators . . . 206
Appendix 7B. Nonlinear Terms ($\mathcal{N}_2$ and $\mathcal{N}_3$) . . . 207
Appendix 7C. Nonlinear Terms for Pure Spanwise Flow . . . 210
Appendix 7D. $\mathbf{G}_{04}$, $\mathbf{G}_{24}$ and $\mathbf{G}_{15}$ . . . 212

8 Streamwise Independent Three-dimensional Granular Couette Flow: Patterns and Bifurcations 213
8.1 Linear Stability Analysis: Analytical Solution . . . 213
8.1.1 Asymptotic Analysis: Dispersion Relation . . . 215
8.2 Nonlinear Problem for the Streamwise Independent Flow . . . 216
8.2.1 Symmetries of Linear and Nonlinear Modes . . . 217
8.2.2 Second Harmonic: Analytical Solution . . . 218
8.2.3 Distortion of Mean Flow: Analytical Solution . . . 219
8.2.4 First Landau Coefficient . . . 220
8.2.5 Third Harmonic . . . 221
8.3 Results and Discussions . . . 222
8.3.1 Linear Theory: Locus of Neutral Stability Curve . . . 222
8.3.2 Equilibrium Amplitude and Bifurcation . . . 224
8.3.3 Dilute Flows . . . 225
8.3.4 Moderately Dense Flows . . . 228
8.3.5 Dense Flows . . . 229
8.3.6 Bifurcation Diagrams . . . 231
8.3.7 Finite Amplitude Patterns . . . 234
8.4 Conclusion . . . 239
Appendix 8A. Elements of Linear Stability Matrix $\mathcal{L} = [l_{ij}]$ for $\partial/\partial x = 0$ . . . 240
Appendix 8B. Nonlinear Terms . . . 240
Appendix 8C. Analytical Expressions for Second Harmonic . . . 242
Appendix 8D. Analytical Expressions for Distortion of Mean Flow . . . 243
Appendix 8E. Analytical Expression for $\mathbf{G}_{13}$ . . . 244

9 Theory for Mode Interaction: Coupled Landau Equations **251**
9.1 Introduction . . . 251
9.2 Interaction of Non-resonating Waves . . . 252
9.2.1 Expansion Formalism . . . 252
9.2.2 Coupled Landau Equations . . . 254
9.3 Theory for 1:2 Wave Resonance . . . 255
9.3.1 Resonance Condition for 1:2 Resonance . . . 255
9.3.2 Derivation of Amplitude Equation for 1:2 Resonance . . . 256
9.4 Theory for Mean Flow Resonance . . . 257
9.4.1 Resonance Condition . . . 257
9.4.2 Derivation of Amplitude Equation . . . 258
9.5 Analytical Solution for Non-resonating Mode Interactions: $k_x = 0$ . . . 259
9.5.1 Linear Problems: $O(\mathscr{A}_1)$ and $O(\mathscr{A}_2)$ . . . 260
9.5.2 Second Harmonic: $O(\mathscr{A}_1^2)$, $O(\mathscr{A}_2^2)$ and $O(\mathscr{A}_1\mathscr{A}_2)$ . . . 260
9.5.3 First Landau Coefficients: $O(\mathscr{A}_1|\mathscr{A}_2|^2)$ and $O(\mathscr{A}_2|\mathscr{A}_1|^2)$ . . . 261
9.5.4 Bifurcation Analysis . . . 262
9.5.5 Limit of Single Landau Equation . . . 263
9.5.6 Preliminary Numerical Results . . . 263
9.6 Summary . . . 264
Appendix 9A. Nonlinear Terms of Eqn. (9.47) . . . 265

10 Complex Ginzburg Landau Equation for Granular Couette Flow **267**
10.1 Temporal and Spatial Development of a Linear Wave System . . . 267
10.1.1 Linear Problem for Wave Systems . . . 267
10.1.2 Preliminary Linear Results . . . 271
10.2 Nonlinear Problem: Complex Ginzburg Landau Equation . . . 273
10.2.1 $O(\epsilon)$: Linear Problem . . . 273
10.2.2 $O(\epsilon^2)$: Second Harmonic and Mean Flow Distortion . . . 274
10.2.3 $O(\epsilon^3)$: Solvability Condition and Complex Ginzburg Landau Equation . . . 275
10.3 Summary . . . 276
Appendix 10A. Outline of Derivation . . . 277
Appendix 10B. Adjoint Matrix Elements $\mathbf{L}^\dagger = [l_{ij}^\dagger]$ . . . 279
Appendix 10C. Elements of Matrices . . . 280

11 Summary and Outlook **281**
11.1 Introduction . . . 281
11.2 Development of Nonlinear Theory . . . 282
11.3 Gradient Banding in Granular Couette Flow . . . 282
11.4 Two-dimensional Patterns in Granular Couette Flow . . . 285
11.5 Nonlinear Stability of 3D Granular Couette Flow . . . 286
11.5.1 Vorticity Banding in Granular Couette Flow . . . 286
11.5.2 Gradient and Vorticity Bandings . . . 287
11.6 Order-parameter Theory using Coupled Landau Equations . . . 287
11.7 Complex Ginzburg-Landau Equation . . . 288
11.8 Future Work . . . 288

References **291**

CHAPTER 1

INTRODUCTION

1.1 Granular Matter

Granular materials are a collection of discrete, dissipative, solid particles, which are ubiquitous in nature. They can be seen in our daily life in the form of building materials (e.g. sand, gravel, coal and cement), pharmaceutical products (e.g. pills, powders and capsules), food grains (e.g. sugar, seeds and rice) and chemicals (minerals), as shown in figure 1.1. They occur in various sizes and shapes; a typical macroscopic grain size can vary from 1μm or larger to many meters. The granular particles are non-Brownian particles which interact solely by friction and collision.

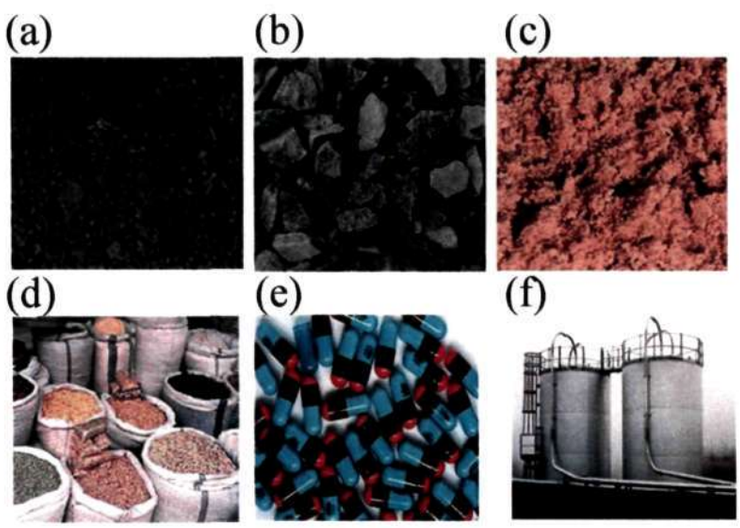

Figure 1.1: Examples of granular matter: (a) soil, (b) crushed stone, (c) sand, (d) food grains, (e) pharmaceutical products and (f) chemicals.

Many industrial processes involve the bulk transport of coal, cereals, food grains, powders and pharmaceuticals through pipes and channels. Rapid flows of granular materials occur in geophysical phenomena and natural hazards such as rock slides, debris flows, snow avalanches (see, figure 1.2), and the motion of the Arctic ice pack. On the other hand, the granular material shows various dynamical phenomena and patterns under different conditions, for example, sand ripples and dunes as shown in figure 1.3, and avalanche formation (figure 1.2), etc. The formation of shearbands and density waves are common in such flowing materials.

Granular materials are strong enough to support building and soft enough to flow like a liquid. Granular materials cut all the boundaries of solid, liquid and gas, and hence should be considered as an additional state of matter in its own right (Jaeger *et al.* 1996). Moreover, two different flow regimes can co-exist in the same system as shown in figure 1.4. For example, an hour-glass where one can see all the flow regimes of granular materials: rapid, quasi-static and dense flow regimes.

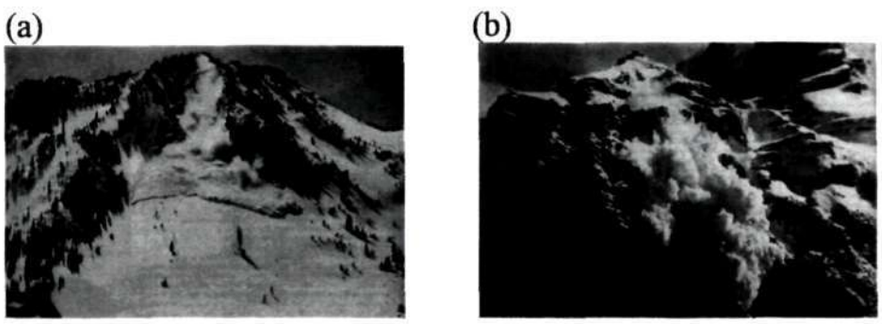

Figure 1.2: (*a*) Slab-snow avalanche occurred at Alta, Utah. (*b*) Loose-snow avalanche occurred at Murren, Switzerland. Images are taken from: http://www.avalanche.org/ moonstone/forecasting/snow avalanches.htm.

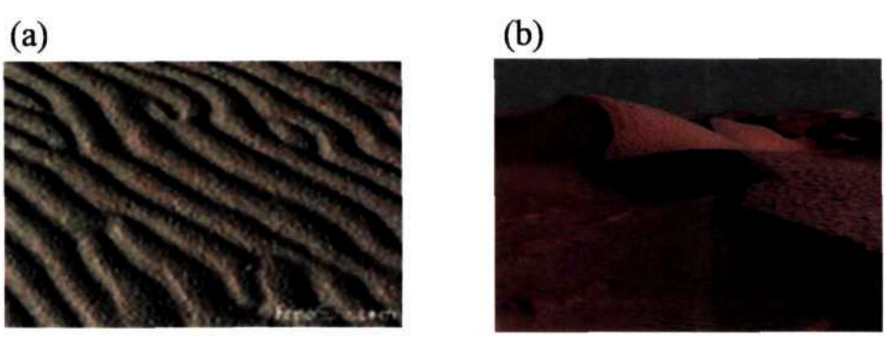

Figure 1.3: (*a*) Sand ripples and (*b*) dunes.

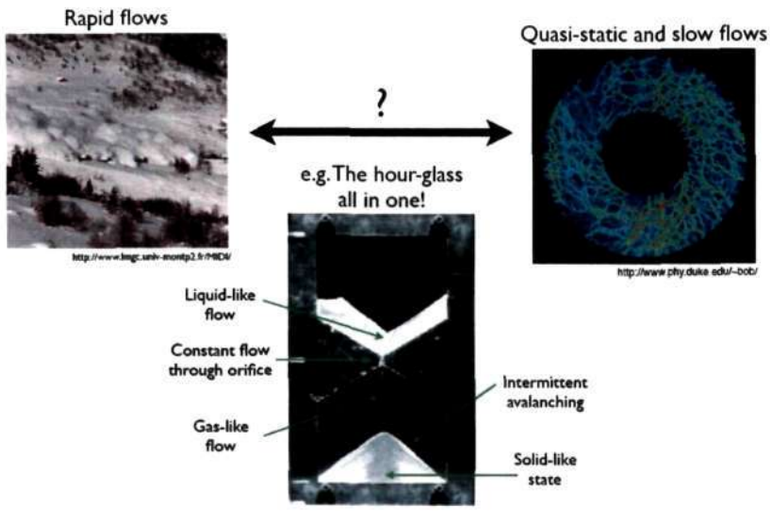

Figure 1.4: Demonstration of all the flow regimes of granular matter. The existence of solid, liquid and gas behavior within hour-glass.

The vast variety of behavior and phenomena in granular flows represents one of the difficulties to understand the physics of such system.

In the following sections we will discuss various patterns in rapid granular flows and the phenomenological models to describe such patterns.

1.2 Pattern Formation and Models for Granular Fluids

In the rapid flow regime (Campbell 1990; Kadanoff 1999; Ottino & Khakhar 2000; Goldhirsch 2003) a collection of particles, when subject to external forcing, show a variety of dynamical patterns, such as Faraday patterns (Faraday 1831) in thin layers of particles under vertical vibration, density waves in gravity driven flows (Ramirez *et al.* 2000), Kelvin-Helmoltz instability (Goldfarb *et al.* 2002) and shear banding in granular Couette flow (Mueth *et al.* 2000; Alam 2005). The pattern forming systems belong to a class of problems where an external control parameter governs the system behavior beyond the critical point. As the control parameter is increased above its critical value, the homogeneous state loses stability and reach some other state, giving rise to a patterned state.

1.2.1 Vibration Driven Patterns

The experiments in which the energy is supplied by a vertically vibrated plate show a plethora of dynamical behavior: heap formation, convection, size segregation, bubbling and standing waves. The most fascinating patterns are the standing wave patterns and localized structures (oscillons) in vertically vibrated granular layers. When a thin multilayer of granular materials is subject to vertical harmonic oscillation, a range of standing wave patterns, squares, stripes, hexagons and interfaces, similar to Faraday waves, can be observed (Melo *et al.* 1995; Umbanhower *et al.* 1996) as shown in figure 1.5. These spontaneous patterns are robust which arise from the correlations

induced by multiple collisions between the grains and by the coherent motion of the particle layers, see figure 1.5(a)-(f).

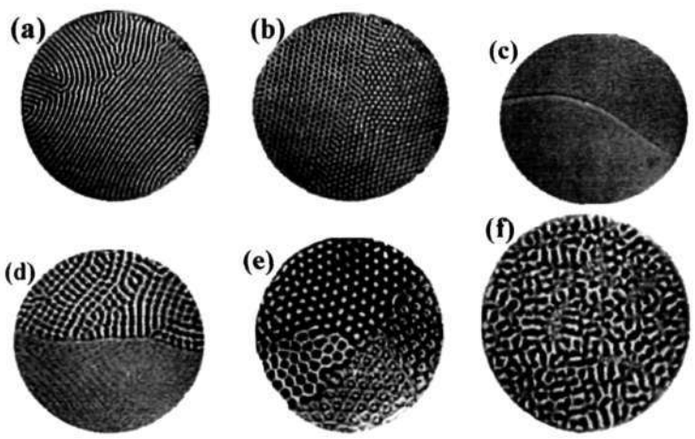

Figure 1.5: Patterns in a 1.2 mm deep layer at $f = 67$ Hz: (a) $f/2$ strips ($\Gamma = 3.3$), (b) $f/2$ hexagons ($\Gamma = 4.0$), (c) flat with kink ($\Gamma = 5.8$), (d) competing $f/4$ squares and stripes ($\Gamma = 6.0$), (e) $f/4$ hexagons ($\Gamma = 7.4$), and (f) disorder ($\Gamma = 8.5$). The particles are bronze spheres of diameter 0.15-0.18 mm. Taken from Melo *et al.* (1995).

In the experiments of Melo *et al.* (1995), 0.15-0.18 mm diameter bronze spheres were placed on a cylindrical container of diameter 127 mm and height 90 mm. The container was evacuated to 0.1 Torr[1], a value at which the volumetric effects of the gas are negligible to prevent heaping (Pak *et al.* 1995). The control parameters which govern patterns are: the frequency (f) of the sinusoidal vibration (produced by an electromagnetic shaker) with displacement $z = Asin(2\pi ft)$, and the dimensionless acceleration amplitude $\Gamma = 4\pi^2 f^2 A/\boldsymbol{g}$, where $\boldsymbol{g}$ is the acceleration due to gravity.

The patterns in figure 1.5(a)-(f) are subharmonic or quarter-harmonic waves which oscillate at either one-half or one-quarter of the driving frequency f, in which the relative phase separated by phase discontinuities (kinks) appears in all patterns except those just beyond the onset of instability. The stability diagram of standing wave patterns in (f, Γ) plane, figure 1.6, shows that the layer remains flat for $\Gamma \leq 2.4$ and beyond that various patterns emerge. The transition from square to stripe pattern occurs at $f = f_c \approx 40$ Hz as indicated by a dashed line above the flat layer in figure 1.6. The transition from flat layer to square pattern is subcritical and to stripe pattern is supercritical (Melo *et al.* 1994). The bifurcation in this case is stationary, i.e. pitchfork bifurcation. At $\Gamma \approx 3.9$, the hexagonal patterns appear spontaneously from the square and strip patterns when the layer undergoes a period doubling bifurcation (see, for period doubling bifurcation, Wiggins 1990; Strogatz 1994). For $\Gamma > 3.9$, the square and stripe patterns disappear and a flat surface with a kink which separates the regions of different phases appears due to period doubling bifurcation. With further increase of Γ (< 7.6), the quarter-harmonic, $f/4$, squares, stripes and hexagons patterns appear and for $\Gamma \approx 7.6$ a disordered state emerges.

A localized structure, "oscillon", which is reminiscent of solitary waves in water (Umbanhower *et al.* 1996), can appear via a hysteretic transition under certain external forcing conditions on frequency and acceleration. An "oscillon" is a small, circularly symmetric excitation which oscillates at a frequency $f/2$; during one cycle of the vibration, it is a peak and on the next cycle it is a crater, as shown in figure 1.7. The modified phase diagram for oscillon for the parameter

[1]A unit of pressure that is equal to approximately 133.3 Pa.

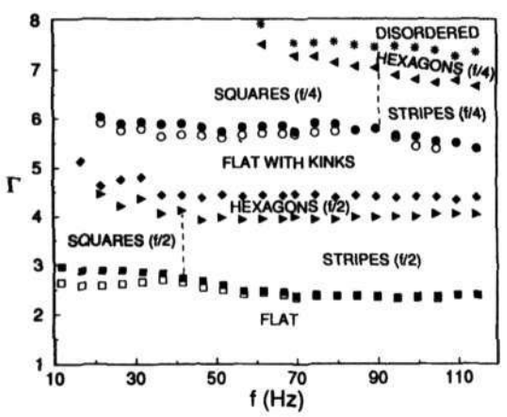

Figure 1.6: Stability diagram showing transition in a 1.2 mm deep layer. The vertical dashed lines indicate the frequencies above which only stripes appears in the square or stripe regime. Closed (open) square and circular symbols denote transitions with increasing (decreasing) Γ. This figure is taken from Melo *et al.* (1995).

range, $\Gamma = (2.3, 2.8)$ and $f = (10, 40)$ Hz, is shown in figure 1.8. The square patterns appear at a frequency $f < 18$ Hz which shows a hysteresis, i.e. the acceleration at which squares appear from a flat surface for increasing Γ is 20% larger than the value of Γ at which they disappear for decreasing acceleration. In a similar manner, the stripes form for $f > 35$ Hz with hysteresis which is about 5%. As shown in figure 1.8 that the hysteresis decreases with increasing frequency. The oscillons are found for a range of frequencies $f = (18, 35)$ Hz, which is the range of frequencies between square and stripe patterns, and for acceleration Γ below the lower stability boundary of standing wave patterns. In general, they do not appear spontaneously from the flat layer which in contrast to other standing wave patterns (squares, stripes, hexagons, etc), rather they appear from perturbing the layer or by decreasing Γ from the patterned state (square and/or stripe pattern). The like-phase oscillons (peak or crater) show a short-range repulsive interaction while the same phase oscillons show attraction and create a dipole-type pattern shown in figure 1.7($d1$)-($d2$). Due to correlations among different oscillons, more and more complicated patterns emerge, such as polymeric chain, triangular tetramer and square ionic lattice as shown in figure 1.7($d3$)-($d6$).

A typical snapshot from a molecular dynamics simulation of inelastic hard disks vibrated in the vertical direction is shown in figure 1.9 which is adopted from Paolotti *et al.* (2004). This figure shows five convection rolls and a wave like horizontal density profile in a large aspect ratio box. Depending on the control parameters and boundary conditions of the problem, we may observe many convection rolls with different dynamical properties. These periodic convective patterns show various types of instabilities similar to Reyleigh Bénard convection, such as skew-varicose and crossroll instability (de Bruyn *et al.* 1998).

Granular convection is driven by a negative granular temperature gradient which arises spontaneously due to inelastic collisions of grains whereas an externally imposed temperature gradient is needed for Rayleigh-Bénard convection of fluid. The convection pattern emerges when the absolute value of granular temperature gradient, which is a function of inelasticity, is large enough. In a granular system, the viscous and thermal diffusions, the buoyancy force and the inelastic dissipation govern convection patterns unlike in a conservative fluid in which there is no role of dissipation because the energy is conserved there. The granular convection pattern can be observed even without vertical vibration as reported by Bizon *et al.* (1998) in which the shear-free

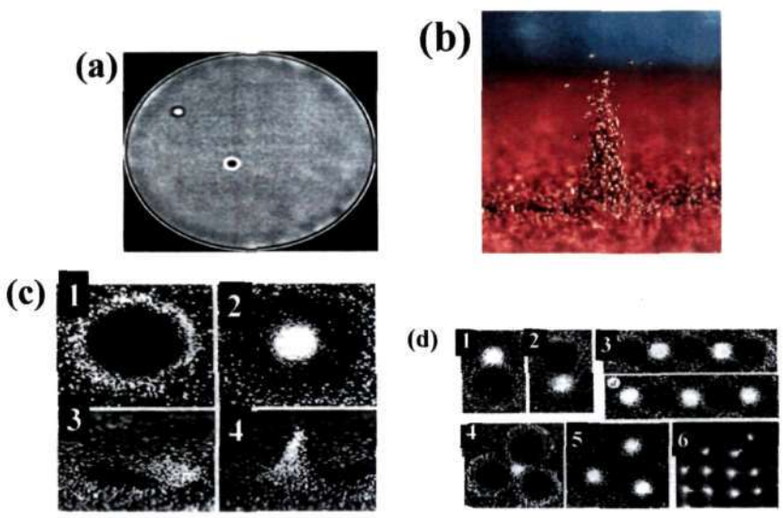

Figure 1.7: (*a*) Two oscillons with opposite phase, (*b*) side view of an oscillon, (*c*) (1)-(2) a single oscillon viewed from above, at times differing by $1/f$; (3) and (4) corresponding side view ($f = 26$ Hz, $\Gamma = 2.45$, layer depth of 17 particles). Oscillon as a molecule and crystal: (*d*) (1)-(2) dipole; (3) polymeric chain; (4)-(5) triangular tetramer and (6) square ionic lattice, the pictures (1) to (5) are separated in time by $1/f$. This figure is adopted from Umbanhower *et al.* (1996)

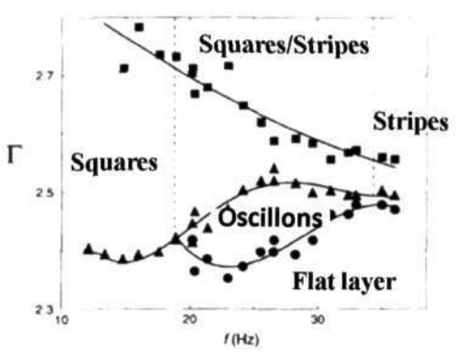

Figure 1.8: Stability diagram for different states, as a function of f and Γ, for increasing Γ (squares) and decreasing Γ (triangles and circles). The transitions from the flat layer to squares and stripes are hysteretic. Ref. Umbanhower *et al.* (1996)

thermal boundary condition on the static base was used to supply energy into the system. This shows that dissipation and gravity are enough for granular convection.

Under strong vertical shaking, a density inversion has been observed recently (Eshuis *et al.* 2005, 2010) in which a high-density cluster of grains is supported by a dilute gas-like layer of fast particles as shown in figure 1.10. This is known as the granular analogue of Leidenfrost effect or granular Leidenfrost effect. As we increase shaking strength, which is a ratio of kinetic energy inserted into the system by vertical vibration and potential energy associated with particle diameter, a transition from Leidenfrost state to convection takes place. The convection rolls

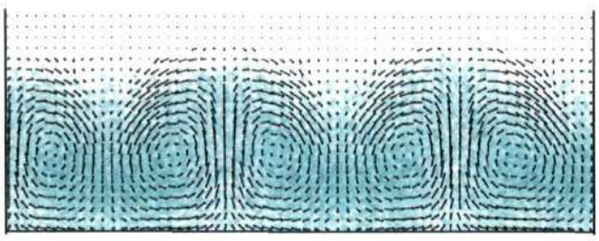

Figure 1.9: Convection in a monodisperse particle system: length of box is 375 cm, number of particles 18000, hard-disk diameter 1 cm, amplitude of vibration 0.5 cm, frequency 50 $\sec^{-1}$ and $\boldsymbol{g} = 28$ cm/sec^2. Taken from Paolotti *et al.* (2004).

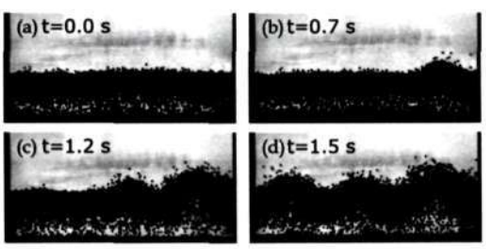

Figure 1.10: Onset of convection in experiment. The number of layers 11 of steal beads of diameter 1.0 mm was vibrated on a container of dimensionless length 101. The frequency was linearly increased from $f = 42$ to 48 Hz at the rate 90 Hz/min. The transition from steady Leidenfrost state to fully developed convection took place at $f = 35$ Hz (between (a) and (b)). Ref. Eshuis *et al.* (2010).

which appear under a strong shaking are different from earlier convection patterns as observed by Ramirez *et al.* (2000) and Paolotti *et al.* (2004) which emerge mainly due to dissipation and boundary effects (Bourzutschky & Miller 1995).

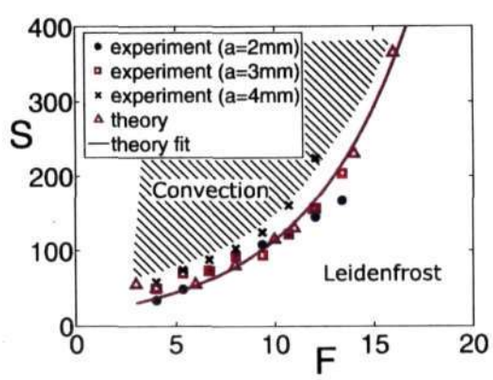

Figure 1.11: Phase diagram in (S, F) plane showing the convection threshold from MD simulation (filled symbols), experiment (open symbol) and theory (solid line). Here S is a shaking strength and F denotes the number of layers. Ref Eshuis *et al.* (2010).

The linear stability analysis of Leidenfrost state shows that the convection patterns form due to an instability of this base state and there is a threshold shaking strength below which there is no convection and above which convection rolls form as shown in the phase diagram in figure 1.11. This is similar to Rayleigh-Bénard convection in which convection occurs above a critical Rayleigh number $Re_c \approx 1708$ for rigid boundaries, i.e. for $Re > Re_c$ the conduction state becomes unstable and convection pattern emerges. As seen in figure 1.11, the theory, experiment and simulation agree with each other.

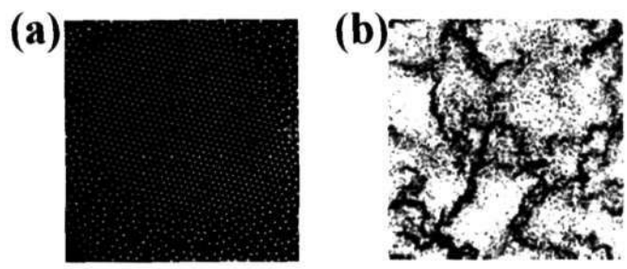

Figure 1.12: (*a*) Top view of a submonolayer of particles on a vibrated plate, adopted from Olafsen & Urbach (1998). Here a dense immobile cluster coexists with a dilute granular gas. (*b*) Numerical simulation of a late phase of a cooling inelastic granular gas at a coefficient of restitution 0.6 and number of particles 40000, adopted from Goldhirsch & Zanetti (1993).

The richness of patterns in a vertically vibrated layer can be realized if we vibrate a quasi-two-dimensional submonolayer of grains that exhibit a bimodal regime of dense and dilute clusters (Olafsen & Urbach 1998) when the vibration frequency decreases, i.e. when the system is cooled down which is reminiscent of the clustering instability of non-driven system of inelastic particles as observed in the simulation of Goldhirsch & Zanetti (1993), see figure 1.12. This is the simplest pattern in a granular system which emerges solely because of inelastic collisions of grains.

The physical interpretation of the above clustering phenomenon is that the local increase in the density of a granular gas increases the collision rate which results in more dissipation of energy that in turn decreases the granular temperature. Since the pressure is directly proportional to temperature, a decrease in granular temperature implies a decrease in pressure which creates a flux of grains towards this low-pressure dense region and this leads to further increase in the density.

Kudrolli *et al.* (1997) observed a phenomenon of particle clustering in a two dimensional wall bounded setup, which appears opposite to the vibrating wall in a horizontally vibrated bed experiment. Figure 1.13 shows an image of a dense cluster in which the maximum density occurs opposite to the hot wall (Kudrolli *et al.* 1997).

Another interesting pattern forming phenomenon is the size-segregation of polydisperse granular mixtures. When we shake a polydisperse granular mixture vertically as shown in figure 1.14(*a*), larger particles come at the top (Brazil nut effect). On the other hand, depending on the physical conditions, larger particles can sink to the bottom, figure 1.14(*b*) (reverse Brazil nut effect). In other cases when a polydisperse granular system is subject to horizontal shaking (Mullin 2000), the system segregates into banded patterns in the orthogonal direction of shaking as shown in figure 1.14(*c*).

1.2.2 Gravity Driven Flows

The gravity driven granular flows such as Poiseuille flow and chute flow often show spectacular spatio-temporal structures. The gravity driven granular Poiseuille flow exhibits density wave

Figure 1.13: A dense cold cluster formed opposite to the driving wall. From Kudrolli *et al.* (1997)

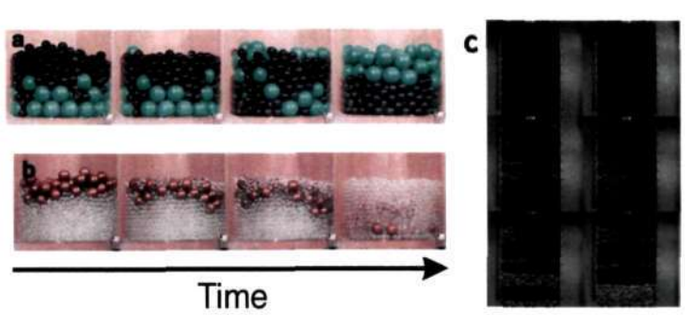

Figure 1.14: Size segregation showing the (*a*) Brazil nut effect and (*b*) reverse Brazil nut effect, adopted from Breu *et al.* (2003). (*c*) segregation in a layer of copper balls and poppy seeds mixture in a horizontally shaken cavity, adopted from Mullin (2000).

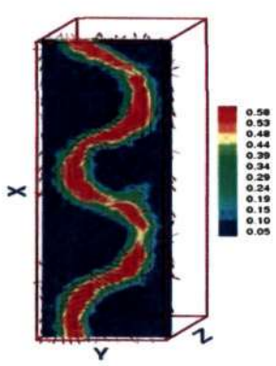

Figure 1.15: A snapshot of density waves in a gravity driven 3D-Poiseuille flow obtained from event-driven MD simulation, Ref. Malik (2008).

patterns (Liss *et al.* 2002; Alam *et al.* 2010), see figure 1.15. It is shown in Alam *et al.* (2010) that the appearance of density wave patterns (plug, slug and sinuous wave) depend on the mean density, wall roughness and inelasticity. For example, the clumps and slugs emerge in dilute flows,

the plugs, sinuous waves and slugs in moderately dense flows and the varicose density waves in dense flows.

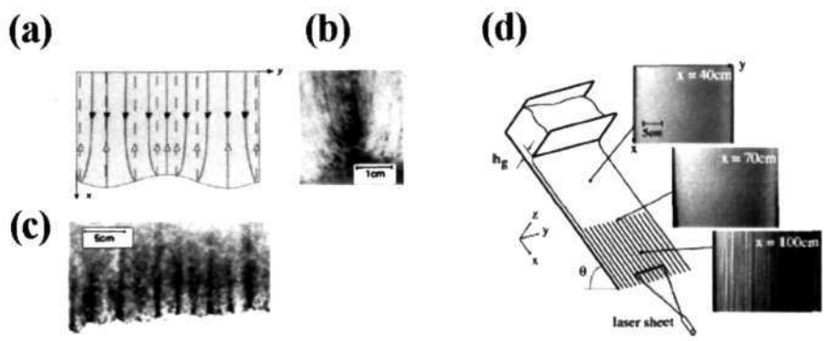

Figure 1.16: Fingering instability in a chute flow. (a) Schematic of the instability mechanism adopted from Pouliquen *et al.* (1997). Images taken from the (b) front, (c) bottom of the layer. (d) Schematic of the experimental setup where three pictures are the top views of the free surface at three different locations (Forterre & Pouliquen 2001).

The fingering (Pouliquen *et al.* 1997) and longitudinal vortices (Forterre & Pouliquen 2001) have been observed in rapid chute flow, see figure 1.16. When a uniform cross-sectioned front of granular material propagates along a rough inclined plane it rapidly breaks up into fingers as shown in figure 1.16(d) leading to fingering instability in the chute flow. The fingering instability of viscous fluid in driven by surface tension, however, in granular fluid there is no role of surface tension. Such fingering instabilities develop size-segregation in the flow. Figure 1.16(a) shows a schematic diagram for instability mechanism where the arrows indicates the coarse particles on the surface of flowing particles. The close look images of fingering instability from front, bottom and top sides of the layer are shown in figure 1.16(b), 1.16(c) and 1.16(d), respectively.

1.2.3 Shear Driven Flows

If we shear granular materials (between two opposite walls or between rotating cylinders), it develops shearbands (Savage & Sayed 1984; Mueth *et al.* 2000; Alam & Luding 2003a; Alam 2005; Alam *et al.* 2008), clusters (Hopkins & Louge 1991; Tan 1995; Tan & Goldhirsch 1997), density waves and coherent structures (Conway & Glasser 2004).

The phenomenon in which the homogeneous flow separates into macroscopic co-existing bands of different shear rates and viscosities is called shearbanding. When a granular material is sheared in shear-cell experiments, shearing remains confined to a narrow zone ('shear-band' where the shear-rate is non-zero) near the walls, leaving rest of the material unsheared (dense 'plug' where the shear rate is almost zero). Depending on whether these bands extend along the flow gradient or vorticity direction, the banding is called as 'gradient banding' or 'vorticity banding'.

The experimental observation of shearbands in dense granular flows was performed by Mueth *et al.* (2000). In their experimental setup, the granular material (mustard seeds) was sheared in a Couette shear cell, consisting of two concentric cylinders, see figure 1.17(a). The shear was applied by rotating the inner cylinder. An image of shearband (taken from a high speed camera) is shown in figure 1.17(b) where the fast particles (yellow colour particles) are near the inner wall and slow particles (orange colour particles) gather around the outer wall of the Couette cell. This is an example of "gradient banding" because the shearband extends along the gradient direction.

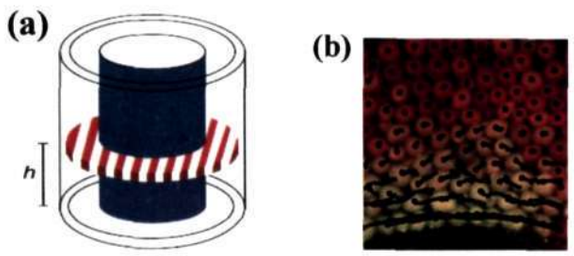

Figure 1.17: Shear-band formation in cylindrical Couette flow, Mueth *et al.* (2000). (*a*) Sketch of the Couette cell, consisting two concentric cylinders, and (*b*) high speed video frame showing mustard seeds observed through the cell's transparent bottom.

Similar evidence of gradient banding has been observed by Alam & Luding (2003*a*), in the molecular dynamics simulations of granular plane Couette flow. More details on shearbanding in granular plane Couette flow has been given in §1.4. Another effect of shearing is the formation of dense clusters (Hopkins & Louge 1991) and density waves (Conway & Glasser 2004).

As discussed above, the collective behavior of grains give rise to a profusion of phenomena (see, for an excellent review on patterns in granular media, Aranson & Tsimring 2006). Granular patterns, as discussed above, employ short range forces which turn to more complex patterns if we include additional features (shape anisotropy, interstitial fluid, magnetization or electrostatic forces charges, etc.) and additional long range forces. Few examples of such complex patterns are: vertically vibrated rods (Blair *et al.* 2003), patterns in submonolayer of magnetic micro-particles subject to magnetic field (Snezhko *et al.* 2005) and patterns in electrostatically driven granular media (Voth *et al.* 2002; Sapozhnikov *et al.* 2003).

Dynamical patterns of granular fluids		
Vibration $\updownarrow$	**Gravity** $\downarrow$	**Shear** $\rightarrow$
Bimodel regime	Avalanches	Shear-banding
Clustering	Clustering	Clustering
Size-segregation	Size-segregation	Size-segregation
Heaping	Density waves	Density waves
Convection	Fingering	
Standing waves	Longitudinal vortices	
Oscillon		

Table 1.1: Summary of dynamical patterns in rapid granular flow when subjected to vibration, gravity and shear (Aranson & Tsimring 2006).

1.3 Models for Granular Patterns

The theoretical description of granular patterns are challenging because there is no unified approach existing for such nontrivial patterns. In general we can divide theoretical study of pattern formation into three classes: (1) microscopic model and molecular-dynamics simulation, (2) statistical mechanics and kinetic theories, and (3) continuum and phenomenological models. In view of the current lack of physical understating of granular media in terms of appropriate governing equations, valid in all regimes, and the lack of scale separation between microscopic and

macroscopic scales, it seems that the third approach, continuum and phenomenological models, is reasonable to study pattern forming phenomenon.

Order parameter equations like Ginzburg-Landau equation, Swift-Hohenberg equation, Kuramoto-Sivashinsky equation and reaction-diffusion equation (Newell *et al.* 1993; Cross & Hohenberg 1993; Aranson & Kramer 2002) are widely used to study pattern-forming systems in many fields (superconductivity, superfluidicity, vacancy diffusion, defect turbulence, convection, surface waves, absolute and convective instabilities, etc). In order to describe cellular patterns and localized structures as observed in vibrated-bed experiments (Melo *et al.* 1995; Umbanhower *et al.* 1996), Tsimring & Aranson (1997), Venkataramani & Ott (1998), Aranson *et al.* (1999) and Crawford & Riecke (1999) adopted this approach of order parameter models which are discussed in the present section.

Tsimring & Aranson (1997) proposed a phenomenological order parameter model, the Ginzburg-Landau equation coupled with an effective mass conservation equation, to theoretically study the patterns in vibrated granular bed (squares, stripes, etc, see figure 1.5):

$$\frac{\partial \psi}{\partial t} = \gamma \psi^* - (1 - i\omega)\psi + (1 + ib)\nabla^2 \psi - |\psi|^2 \psi - \rho\psi \tag{1.1}$$

$$\frac{\partial \rho}{\partial t} = \alpha \nabla . \left(\rho \nabla |\psi|^2\right) + \beta \nabla^2 \rho. \tag{1.2}$$

Equation (1.1) is an evolution equation for a complex quantity ψ, called 'order-parameter' or the 'amplitude function' of the subharmonic patterns at frequency $\omega = f/2$; (1.2) represents an effective equation for the conservation of mass (average mass of granular material per unit area), with $\rho(x,t)$ being the mass-density of granular materials. The last term in (1.1), $\rho\psi$, represents a coupling between order parameter and the local bulk density of material; the cubic nonlinear term $|\psi|^2\psi$ accounts for the nonlinear saturation of oscillations due to dissipation; the term involving Laplacian accounts for any diffusive mechanism, providing a length scale for patterns; $\gamma\psi^*$ accounts for the parametric driving that excites standing waves, with γ being the normalised amplitude of the parametric forcing; parameter b is related to the wavenumber, k, of the pattern as $k = \sqrt{\omega/b}$ where b must be chosen to reproduce the correct wavenumber at given frequency. Two terms in the right hand side of equation (1.2) represent two physical mechanisms contribute to the mass conservation. The first term indicates average particle drift due to the gradient of magnitude of high-frequency oscillations (i.e. flux corresponding to particles escaping from regions of large fluctuation). The second term $\beta\nabla^2\rho$ describes diffusive relaxation of the inhomogeneous mass distribution where $\beta > 0$ is the mass diffusion coefficient which is proportional to the energy of the plate vibration.

The above order parameter model is phenomenological in the sense that it has not been derived from the governing equations of granular fluids, and the coefficients of (1.1-1.2) have to be determined from experiments or simulations as a case-by-case basis. It may be noted that the above model is strictly valid for flows where the mean velocity is zero, such as in a vertically shaken bed under harmonic excitation, for which the momentum equation is identically satisfied. Information about the rheology of flow needs to be supplemented, in addition to (1.1-1.2), via momentum balance equations (Volfson *et al.* 2003). At any rate, the above order-parameter model has been able to interpret the experimental and simulation data in a variety of granular flows (see, for a review, Aranson & Tsimring (2006)). For an application of this model to predict the rheology of surface flows in a rotating drum, see Orpe & Khakhar (2007).

Besides the standing wave pattern, Ginzburg-Landau equation (1.1), without the coupling term $\rho\psi$, gives a model for the parametric instability in an oscillating liquid layer (Zhang & Viñals 1995); in particular, the term $\gamma\psi^*$ accounts for the parametric driving that excites standing waves. As seen in (1.1) the order parameter $\psi(\mathbf{x}, \mathbf{t})$ is a function of space and time, and hence is suitable to describe aperiodic patterns having slow modulations in space and time. For patterns having spatial periodicity, the Ginzburg-Landau equation reduces to an ordinary differential equation for

the temporally varying order parameter $\psi(t) \equiv \psi(\mathbf{x}, t)$ which is the primary focus of the present thesis.

Another model which describes primary pattern-forming bifurcation was given by Crawford & Riecke (1999) using generalized Swift-Hohenberg equation,

$$\begin{aligned} \frac{\partial \psi}{\partial t} &= R\psi - \left(\frac{\partial^2}{\partial x^2} + 1\right)^2 \psi + b_1\psi^3 - b_2\psi^5 + \epsilon\nabla\cdot(\nabla\psi)^3 \\ &\quad -\beta_1\psi(\nabla\psi)^2 - \beta_2\psi^2\nabla^2\psi \end{aligned} \tag{1.3}$$

where ψ is a real amplitude of the oscillating solution; it is assumed that the whole pattern always oscillates in phase. The term proportional to ϵ is added for the description of rolls and additional fifth order terms are incorporated into the standard Swift-Hohenberg equation for subcritical bifurcation. Depending on the magnitude of ϵ, this equation describes squares and stripes patterns; it also gives a stable oscillon type solution for negative control parameter R.

Both models, Ginzburg-Landau model and Swift-Hohenberg model, employ an order parameter equation. Note that the coupled Ginzburg-Landau equation [Eqns. (1.1)-(1.2)] and the generalized Swift-Hohenberg equation [Eqn. (1.3)] are continuous in time and space. The dynamics and behavior of the solution of these models resemble the properties of localized structures like oscillon and standing wave patterns like squares, stripes and hexagons. The extra terms and coupling terms in these models are system dependent and originate due to the characteristics of granular system that need to be taken into account in order to get a correct theoretical interpretation of these patterns.

In contrast to these models (e.g. Ginzburg-Landau model and Swift-Hohenberg model) which contain partial differential equations, Venkataramani & Ott (1998) proposed a 'continuous coupled map' (CCM) model in the framework of discrete time and continuous space map system. The various patterns (e.g. squares, stripes, hexagons, etc.) emerge due to the interaction between a temporal period doubling sequence and an instability that induces standing waves on the surface of the granular layer. This lead Venkataramani & Ott (1998) to use discrete time (for incorporating period doubling sequence) and continuous space (for incorporating surface waves) approach. According to this model, the height of the granular layer at time $t = n$ (discrete) and at position $\mathbf{x} = (x, y)$ (continuous) is given by $\xi_n(\mathbf{x})$ and a one dimensional map is defined at each point in space

$$\xi_n'(\mathbf{x}) = M(\xi_n(\mathbf{x}), r) \tag{1.4}$$

where r is a parameter of the chosen map function and mapping $M(\xi)$ is a Gaussian map

$$M(\xi) = \tilde{r}e^{-(\xi-1)^2/2}. \tag{1.5}$$

To incorporate continuous space dynamics in this model, a linear spatial operator $\mathcal{L}$ is inserted. Thus the model can be written as

$$\xi_{n+1}(\mathbf{x}) = \mathcal{L}(\xi_n'(\mathbf{x})). \tag{1.6}$$

This model predicts various patterns and yields a similar phase diagram as shown in figure 1.6 and 1.8.

1.4 Patterns in Granular Couette Flow and Present Work

The pattern formation in granular plane Couette flow has attracted much attention during the last two decades using both simulation and theory (Hopkins & Louge 1991; Savage 1992; Babic 1993; Schmid & Kytomaa 1994; Tan & Goldhirsch 1997; Alam & Nott 1997, 1998; Sasvári *et al.* 2000; Kumaran 2004; Alam & Luding 2003*a*; Conway & Glasser 2004; Alam *et al.* 2005; Gayen & Alam 2006; Alam 2006; Conway *et al.* 2006; Khain & Meerson 2006; Khain 2007; Saitoh & Hayakawa 2007). Among many other pattern-forming systems (see §1.2) the granular Couette flow is a prototype problem which exhibits various spatio-temporal patterns; for example, patterns induced by clustering inhomogeneities (Alam & Nott 1998; Conway & Glasser 2004; Alam *et al.* 2005; Conway *et al.* 2006) and shear-banded patterns (Alam 2005; Alam *et al.* 2008; Shukla & Alam 2008, 2009). The earliest particle dynamics simulations of Hopkins & Louge (1991) identified travelling-wave patterns in the form of oblique bands, aligned along the compressional axis of the shear flow for a range of densities - most of these simulations were carried with about 5000 particles and hence the observed structures were no so well defined. The "large-scale" particle simulations of Tan & Goldhirsch (1997) at a particle volume fraction of 0.05 identified a variety of two-dimensional patterns, including a "churn-type" flow. That the granular Couette flow supports inhomogeneous patterns, having modulations along both the streamwise and gradient directions, was predicted by Alam & Nott (1998) from a linear stability analysis; they also systematically probed the effect of the boundary conditions on the predicted instabilities (Nott *et al.* 1999).

Recently, Conway & Glasser (2004) have conducted a series of two-dimensional particle simulations of "bounded" plane Couette flow at low-to-moderate densities (particle volume fraction less than 0.4 in two-dimensions), with walls acting as sinks of granular energy which is one of the three cases considered by Alam & Nott (1998). In these simulations, the width and the length of the channel were systematically varied so as to get access to any long-wave instability with streamwise modulations. They reproduced the main features of the full phase diagram of different instabilities as predicted by the linear stability analysis of Alam & Nott (1998). However, some of the long-wave instabilities of Alam & Nott (1998) were not found in simulations (Conway & Glasser 2004). Possibly those very long-wave instabilities are not admitted once the nonlinear terms are taken into account or the channel length of simulations was not long enough to capture structures with very large wavelengths-the former issue can be answered only via a nonlinear stability analysis. More recent dense simulations of Conway *et al.* (2006) identified a two-dimensional antisymmetric stationary wave (i.e. a sinuous-type mode). This structure might be related to the nonlinear saturation of the dominant stationary wave instabilities of Alam & Nott (1998).

In the present thesis, the weakly nonlinear stability analysis will be carried out for the (*i*) shearbanding instability (gradient and vorticity banding) and (*ii*) finite-wave length instabilities in two and three dimensional granular Couette flow. In the following sections, we will show some existing particle simulation results (Tan 1995; Tan & Goldhirsch 1997; Conway & Glasser 2004; Conway *et al.* 2006) and experimental (Conway *et al.* 2006) observations of shearbanding, clustering, and antisymmetric wave patterns in two and three-dimensional granular Couette flow.

1.4.1 Shear-banding in Granular Couette Flow

The phenomenon in which the homogeneous flow separates into macroscopic co-existing bands of different shear rates and viscosities is called *shear-banding*. When a granular material is sheared in shear-cell experiments (Savage & Sayed 1984; Mueth *et al.* 2000; Conway *et al.* 2006), shearing remains confined to a narrow zone ('shear-band' where the shear-rate is non-zero) near the walls leaving rest of the material unsheared (dense 'plug' where the shear rate is almost zero).

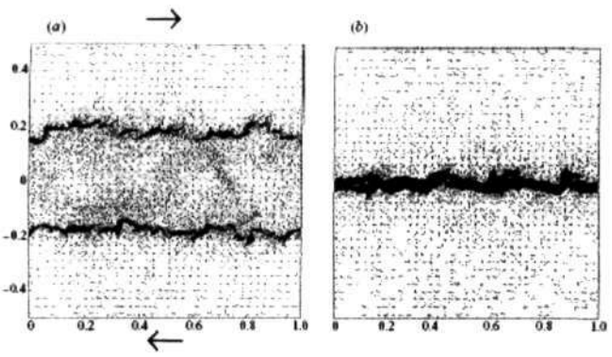

Figure 1.18: Molecular dynamics simulation of shear flow of inelastic disks. (a) Formation of two dense layers of disks which subsequently coalesce to give a single layer as shown in panel, (b), for $e = 0.6$, $\phi = 0.05$ and Couette gap $H = \bar{h}/\bar{d}_p = 1123.5$ with $\bar{h}$ and $\bar{d}_p$ being the distance between moving walls and particle diameter, respectively. Taken from Tan (1995).

Depending on whether these bands extend along the flow gradient or the mean vorticity direction, the banding is called as '*gradient banding*' or '*vorticity banding*', respectively.

Such shear-banding, wherein the flow undergoes an ordering transition into alternate layers of dense and dilute regions of low and high shear rates, respectively, aligned along the gradient direction (i.e. the density-bands are parallel to the flow-direction), has also been realized in the molecular dynamics simulation of granular Couette flow (Tan & Goldhirsch 1997; Alam & Luding 2003a; Conway & Glasser 2004; Khain 2007; Conway *et al.* 2006) for a range of densities from dilute to dense flows (without gravity) in the rapid flow regime.

The MD simulation of inelastic hard disk shear flow in dilute flow regime ($\phi = 0.05$) has been studied by Tan (1995) and Tan & Goldhirsch (1997). Figure 1.18(a), a particle position plot, shows two dense plugs which subsequently coalesce to form a single plug at the center as in figure 1.18(a). Similar MD simulations have been carried out by Alam *et al.* (2005) for moderately dense flows where the mean density has been set to 0.3, see figure 1.19. It is seen that the flow forms a shearband around the channel center-line and two plugs near the walls.

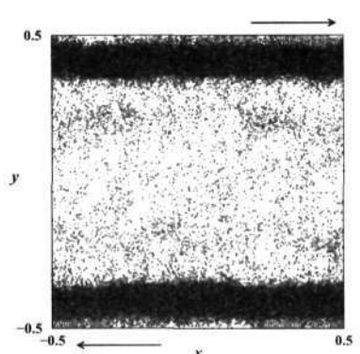

Figure 1.19: Formation of shear-band and plug in MD simulation of a sheared inelastic hard-disk system. The average solid fraction in $\phi = 0.3$, the restitution coefficient $e = 0.8$ and the number of particle 15000. Ref. Alam *et al.* (2005).

The numerical experiments show that the position and the intensity of plugs depend on the system parameters such as mean density, coefficient of restitution, Couette gap, etc., as described below.

Effect of Inelasticity and Couette Gap on Shear-bands

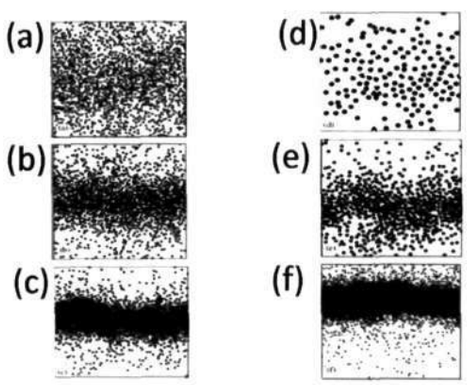

Figure 1.20: Effect of inelasticity $e = (a)$ 0.99, (b) 0.95, (c) 0.85, for mean density $\phi = 0.3$ and Couette gap $H = \bar{h}/\bar{d}_p = 60$. Effect of Couette gap $H = (d)$ 20, (e) 40 and (f) 80, for $e = 0.85$ and other parameters are same as figure (a)-(c). Ref. Conway *et al.* (2006).

The effect of particle-particle coefficient of restitution is shown by the particle position plots from the MD simulation of Conway *et al.* (2006), see figure 1.20(a)-(c); these figures clearly show that the plug is becoming more and more prominent for increasing inelasticity. For nearly elastic particles, the particles are uniformly distributed within the Couette cell, see figure 1.20(a). With increasing inelasticity plugs form around the channel center-line where the density approaches maximum packing density for inelastic particles as shown in figure 1.20(b)-(c).

Figure 1.20(c)-(d) shows the effect of Couette gap on the shearbanding instability. The signature of clustering appears even for small Couette gaps which becomes more and more apparent for larger domain size, see figures 1.20 (d)-(e). It has been predicted by Alam & Nott (1998) that the granular plane Couette flow without gravity is unstable to the streamwise independent disturbances that leads to shearbanding in this flow.

Shear-banding in Polydisperse System

The banding and segregation in 2D-Couette flow of binary mixtures have been observed in the simulation of Conway *et al.* (2006). The pressure and temperature diffusion of individual components in mixtures occur due to inhomogeneities in monodisperse flows which induce large flow property gradients. The local sampling (in streamwise strips) was performed by Conway *et al.* (2006), for a binary mixture of equal density particles of different sizes, to unveil two types of segregation in their simulations which is shown by particle position plots in figures 1.21(a)-(b) for densities $\phi = 0.25$ and 0.3. Figure 1.21(a) shows that the large and small particles form a plug at the center of the flow but the concentration of large particles are about one third greater than the smaller size particles at the center. This clearly shows segregation where the large particles accumulate within the plug region and small particles have larger concentration in the dilute region. However, a contrasting situation arises for a slightly higher density $\phi = 0.3$

for which both types of particles form a plug but the concentration of smaller size particles is larger at the center than the larger particles (reversal of the previous situation) as shown in figure 1.21(b). The gradients in velocity, temperature and stresses are same in both the scenarios but the mechanisms that drive segregations are different; the former is thermally driven whereas the latter is pressure driven. The size segregation for $\phi = 0.25$, figure 1.21(a), is consistent with simplified binary kinetic theory (Willits & Arnarson 1999; Alam *et al.* 2002) which predicts that the flux of heavier particles to low temperature regions is driven by thermal gradients i.e. thermal (or Soret) diffusion. In the reverse situation for $\phi = 0.3$, figure 1.21(b), the diffusion is due to the pressure gradients which dominate over thermal diffusion that results in an accumulation of lighter particles in high-pressure regions (Ottino & Khakhar 2000).

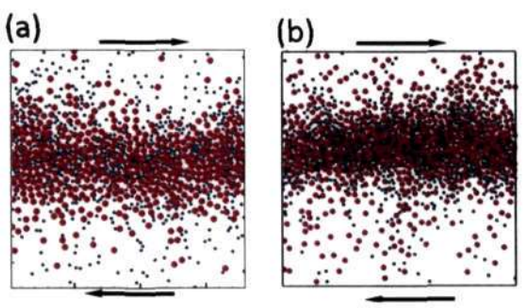

Figure 1.21: Particle position plots showing size segregation for two values of densities $\phi =$ (a) 0.25 and (b) 0.3 for parameters $d_C/d_F = 2$, $n_C/n_F = 1$, $H = \bar{h}/(d_C + d_F) = 80$ and $e = 0.8$. Here d_C and d_F are the diameters of the larger (red dots) and smaller (blue dot) particles, respectively. n_C and n_F are the number densities of larger and smaller particles, respectively. From Conway *et al.* (2006).

The initial conditions are an important factor in mixing and segregation dynamics of granular mixture. Figure 1.22 shows particle position plots of the evolution of fully developed Couette flow from contrasting initial conditions: a homogeneous mixture, see figure 1.22(a), and a complete transverse segregation of fine and coarse particles, see figure 1.22(b). When the initially random, homogeneous binary mixture is sheared, total kinetic energy immediately drops as particles rapidly cluster. This drop in kinetic energy corresponds to a plateau in a graph of energy vs. time. The segregated initial condition has been used in figure 1.22(b) where the particles are segregated by size into upper and lower halves (fine particles are in the upper half position and the course particles are in the lower half). As shown in figure 1.22(b) that the plug is no longer fixed at the center, instead its position oscillates between the walls. However with homogeneous initial condition, the plug does not show any oscillatory behavior rather it is more stable. The particle pressures in the two halves of the segregated initial conditions is not equal and the vertical movement of cluster is an indication of pressure balance (Conway *et al.* 2006).

The effect of inelasticity on shear-bands is shown figure 1.23, adopted from Conway *et al.* (2006). This figure shows the particle positions for equal density particles with varying diameter for increasing inelasticity. It is seen from this figure that the plug appears even for nearly elastic particles ($e = 0.99 \approx 1$) and the plug becomes denser for larger inelasticity.

An Experiment for Shearbanding Instability

A pseudo-2D experiment for shear-banding in granular Couette flow has been performed by Conway *et al.* (2006) to verify the formation of plugs (shear-bands) as predicted by the linear stability theory (Alam & Nott 1998) and the MD simulations (Tan 1995; Tan & Goldhirsch 1997).

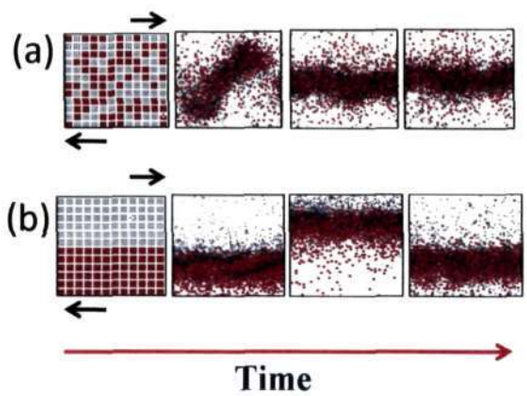

Figure 1.22: Particle position plot of transient development of clustering instability for $d_c/d_F = 2$, $\phi = 0.3$, $H = \bar{h}/(d_C + d_F) = 80$, and $e = 0.85$ from (a) uniform and (b) segregated initial conditions. Ref. Conway *et al.* (2006).

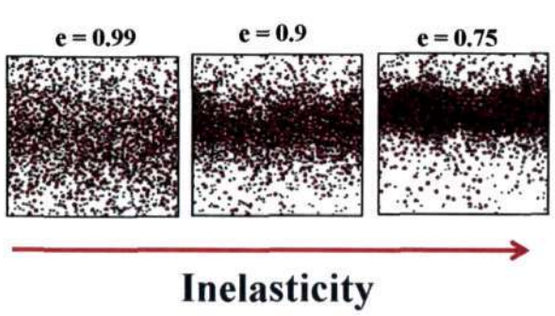

Figure 1.23: Particle position plot with $d_C/d_F = 2$, $m_C/m_F = 4$ i.e. equal density particles with varying diameter as a function of increasing inelasticity. Here m_C and m_F represent masses of the larger (red dot) and smaller (blue dot) particles, respectively. Ref. Conway *et al.* (2006).

The schematic diagram of their setup and observations are shown in figure 1.24.

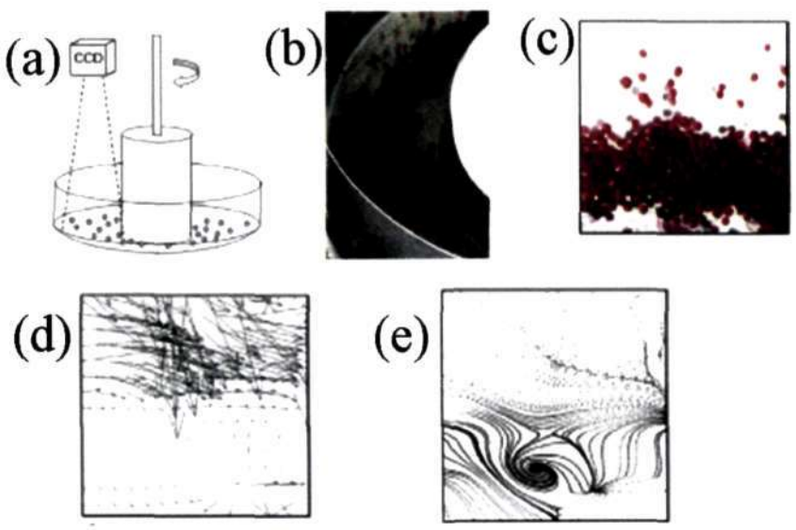

Figure 1.24: A pseudo-2D experiment (a) schematic of Couette cell containing an inner cylinder of diameter 9.5 cm and a outer cylinder of diameter 20 cm, (b) a digital photograph of a shear band in Couette cell, (c) zoomed part of (b). Associated (d) velocity field and (e) vorticity field.

Since the infinite moving walls are not possible in the laboratory, a circular geometry was used in these experiments. To avoid outward normal force, i.e. centrifugal forces, the base slopes slightly towards the inner wall ($< 5^o$); gravity prevents all particles from accumulating at the outer wall. Shearing was given by the moving inner cylinder with high shear-rate. As shown in figure 1.24(b), the particles form a single dense plug of about 16 particle diameters wide near the middle of the Couette gap at a rotation speed of above 400 rpm (a shear rate of 44 s^{-1}). An image of dense and dilute regions of particles and the corresponding velocity field, from PIV (particle image velocimetry), are shown in figure 1.24(c) and 1.24(d), respectively. The particles within dilute regions have higher velocities than the particles within dense regions as shown in figure 1.24(d). The coherent vorticity within dense regions has been observed in experiment, see figure 1.24(e). These experimental results support dense and dilute regions of low and high shear rates, respectively, along the flow gradient direction, which agree with MD-simulation results.

1.4.2 Clustering and Density Waves in Granular Couette Flow

As discussed by Alam & Nott (1998), the granular plane Couette flow supports various types of stationary and traveling wave instabilities. The patterns induced by stationary and traveling wave instabilities in granular Couette flow have been verified by particle simulations of Conway & Glasser (2004). In this section, we discuss particle simulation results of (Conway & Glasser 2004; Conway *et al.* 2006) for such instabilities.

Two-dimensional Plugs and Density Waves

The particle position plots, adopted from Conway & Glasser (2004), for fully developed wave structures are shown in figure 1.25 for varying streamwise length parameter $\bar{l}/\bar{h}$, where $\bar{l}$ and $\bar{h}$ are

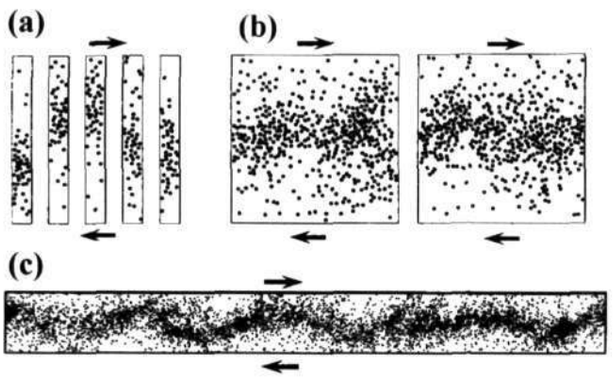

Figure 1.25: Effect of wavelength or streamwise dimension on density waves. Particle position plots for three values of $\bar{l}/\bar{h}$ (length vs height ratio), (a) 0.1, (b) 1.0 and (c) 10. The parameters are $e = 0.8$, $\phi = 0.15$, $H = 50$, $\bar{d}_p = 0.0018$ m, $\rho_p = 2980$ kg/m^3, tangential restitution coefficient $= -1$, particle-wall restitution coefficient $e_w = 1$ and specularity coefficient for wall collision is 0.6. From Conway & Glasser (2004).

the length and height (width) of the Couette cell. The density inhomogeneities are clearly shown in all figures 1.25(a)-(c). The sequential snapshots in figure 1.25(a) were taken at different time intervals, which show a dense plug which floats between the boundaries. Figure 1.25(b) shows that the movement of the cluster is reduced and the particles are less constrained for larger aspect ratio ($\bar{l}/\bar{h} \geq 1$). For increasing $\bar{l}/\bar{h}$ ratio, a two-dimensional wave appears due to the accumulation of particles as shown in figure 1.25(c). These waves, which arise due to density inhomogeneities in the system, are stationary waves as the basic structure of the wave does not vary in space and time (Conway & Glasser 2004).

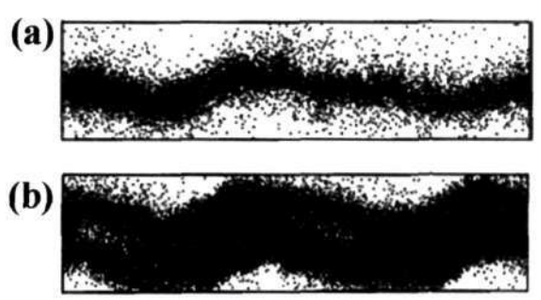

Figure 1.26: Particle position plots of fully developed structures for varying mean densities (ϕ) (a) 0.3 and (b) 0.6. For $\bar{l}/\bar{h} = 4$ and other parameters are same as figure 1.25.

The extent of modulation of the structure (density wave) increases with increasing mean density which gives a large-scale structure. For $\bar{l}/\bar{h} = 4$, the density waves for two values of mean densities, $\phi = 0.3$ and 0.6, are shown in figure 1.26, which clearly shows that the density waves are more apparent at higher volume fractions.

The physical reason of clustering instabilities, which induce plugs and stationary waves, can be interpreted as follows: the inelastic collisions lead to fluctuations that generates regions of

higher densities than the average density. The disturbance or instability spontaneously leads to dense clusters. The density disturbances are thus the cause of clusters to grow which has been verified from the linear eigenfunctions of the equations of motion (Alam & Nott 1998; Conway & Glasser 2004). For higher density and longer domain, these clusters form a large-scale structure in the form of antisymmetric standing wave as shown in figure 1.26.

Antisymmetric Waves in Shallow 3D System

The 1D-plugs and antisymmetric waves as observed in planar Couette flow are also observed in a shallow 3D system as shown in figure 1.27. For the pseudo-1D case of $\bar{l}/\bar{h} = \bar{d}/\bar{h} = 0.1$, see figure 1.27($a$), a similar plug is observed as in the case of 2D simulation domain (see figure 1.25(a)). The observed clusters and antisymmetric waves, similar to figure 1.25(b)-(c), can be seen in a shallow 3D system for $\bar{l}/\bar{h} = 1$ and $\bar{l}/\bar{h} = 3$ with $\bar{d}/\bar{h} = 0.1$ as shown in figure 1.27(b-c).

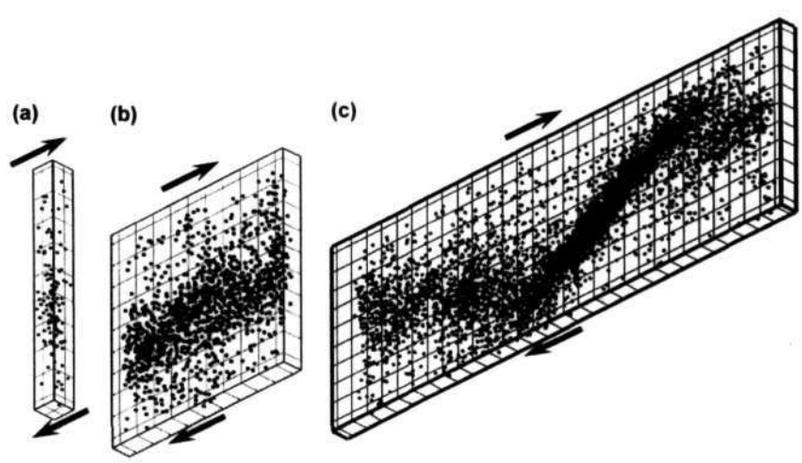

Figure 1.27: Particle position plots for $\phi = 0.05$, $e = 0.6$, $\bar{d}/\bar{h} = 0.1$, where $\bar{d}$ is the depth and $\bar{l}/\bar{h}$ (a) 0.1, (b) 1 ,(c) 3. $1D$ plug and antisymmetric wave in a shallow system. Taken from Conway & Glasser (2004).

Fully 3D-dimensional Plugs and Antisymmetric Density Waves

For a deeper system of 3D-Couette geometries, the clusters are more extended in streamwise, spanwise and cross-stream directions, depending on length, width and height ratios of the system. Such 3D-clusters are shown by isosurface plots in figure 1.28(a)-(d). The isosurfaces are surfaces of higher density than mean density, i.e. the isosurface plot marks the region where the density is higher than mean density. For increasing depth, 1D-plug (see figure 1.27(a)) transforms to a 2D-plug (see figure 1.28(a)). A 2D-antisymmetric wave appears for $\bar{d}/\bar{h} = 3$ and $\bar{l}/\bar{h} = 0.5$, which changes to 3D-antisymmetric wave for increasing domain size. An isosurface for $\bar{l}/\bar{h} = 3$ and $\bar{d}/\bar{h} = 1$ which is depicted in figure 1.28(c) shows simultaneous wave formation in the spanwise (z) and streamwise (x) directions. The intensity of 3D-antisymmetric standing wave and plugs increases with increasing $\bar{d}/\bar{h}$ ratio: three dense plugs with $\bar{d}/\bar{h} = 3$ in the spanwise direction (z) are shown in figure 1.28(d).

The linear stability analysis predicts (Alam & Nott 1998) that the granular plane Couette flow is unstable to traveling and stationary waves which lead to clusters of high and low densities

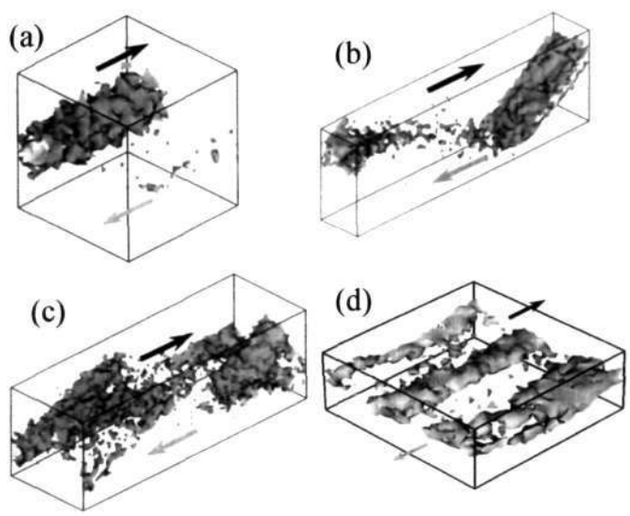

Figure 1.28: Formation of 3D-structures. (*a*) 2D plug ($\frac{\bar{l}}{h} = \frac{\bar{d}}{h} = 1$), (*b*) 2D-antisymmetric wave ($\frac{\bar{l}}{h} = 3$, $\frac{\bar{d}}{h} = 0.5$), (*c*) 3D-antisymmetric wave ($\frac{\bar{l}}{h} = 3$, $\frac{\bar{d}}{h} = 1$), and (*d*) 3D-plugs ($\frac{\bar{l}}{h} = \frac{\bar{d}}{h} = 3$). For $\phi = 0.05$, $e = 0.6$ and other parameters are same as figure 1.25. Ref. Conway & Glasser (2004).

along the flow gradient. The formation of clusters and shear-bands has also been predicted by the linear stability analysis of three-dimensional granular Couette flow (Alam 2006).

1.4.3 Present Work

In the present thesis an order parameter theory for various instabilities in two and three dimensional granular Couette flow has been developed. Starting with granular hydrodynamic equations, the Landau and Ginzburg-Landau equations have been derived for such instabilities (for the first time in granular flows). The amplitude expansion method and center manifold reduction method, for the weakly nonlinear analysis, have been used to derive these amplitude equations.

For the shearbanding instability in granular plane Couette flow, analytical expressions of the fundamental mode, the second harmonic, the distortion to fundamental mode and the first Landau coefficient have been derived. The results from analytical solutions have been compared with those obtained from the spectral based numerical method. The main result of this study is that the granular plane Couette flow is subcritically unstable in dilute limit. The predicted bifurcation scenario for the shearbanding is in qualitative agreement with particle dynamics simulations and the experiment in the rapid shear regime of the granular plane Couette flow.

We further extended order parameter theory to spatially periodic patterns in two dimensional granular plane Couette flow. The stationary and travelling instabilities leading to Pitchfork and Hopf bifurcation are analyzed. The nonlinear patterns of density, velocity and granular temperature for all kinds of instabilities are compared with their linear eigenfunctions. This analysis predicts two types of resonances, mean flow resonance and 1:2 resonance. The analytical weakly nonlinear analysis, similar to the shearbanding instabilities, has been generalized for (*i*) vorticity banding, and (*ii*) gradient and vorticity banding, in three dimensional granular plane Couette flow. Two generalized theories, theory for mode interactions and theory for spatial modulated patterns, in granular plane Couette flow, have been developed, and some prelimary results for both cases have been shown.

1.4.4 Organization of the Present Thesis

Chapter 2

The general hydrodynamic equations, constitutive models and boundary conditions for granular materials are discussed in detail.

Chapter 3

The general weakly nonlinear analysis using amplitude expansion method is explained in detail that will subsequently be used in the later chapters. The spectral-based numerical method for the nonlinear stability calculation is discussed.

Chapter 4

The center manifold method is used to derive Landau equation and its equivalence with amplitude expansion method is shown. The phase diagram for the subcritical instability in plane Couette flow is computed using spectral-based numerical method as given in chapter 3.

Chapter 5

For shearbanding instability, analytical solutions for the fundamental, second harmonic, distortion of mean flow and first Landau coefficient are discussed. The spectral-based numerical results are compared with analytical solutions. The complete bifurcation diagram for shearbanding instability in plane Couette flow is shown.

Chapter 6

This chapter differs from chapters 4 and 5 in that the streamwise wavenumber in non-zero. The weakly nonlinear analysis is performed using the amplitude expansion method to understand the effect of nonlinearities on various linear instability modes as well as to unveil the underlying bifurcation scenario in a two-dimensional granular plane Couette flow. This work is an extension of the previous work on the shear-banding instability (chapters 4 and 5). The subcritical and supercritical patterns, with non-zero wave number, are observed. The possibility of resonant mode interaction is discussed.

Chapter 7

The weakly nonlinear stability analysis for the three dimensional granular Couette flow is discussed using amplitude expansion method. The results for vorticity banding in pure-spanwise granular Couette flow are presented. The bifurcation diagrams for the various values of parameters are studied.

Chapter 8

We extend the analytical weakly nonlinear stability analysis for shear-banding instability in granular plane Couette flow, as given in chapter 5, to the streamwise-independent three dimensional case. The finite amplitude density, vorticity and velocity patterns are observed.

Chapter 9

The coupled Landau equations for two-dimensional granular plane Couette flow is derived for the case of two non-resonating modes which is subsequently extended for the situation of 1 : 2 wave number resonance as well as mean flow resonance.

Chapter 10

The complex Ginzburg Landau equation for two-dimensional granular shear flow is derived.

Chapter 11

The summary of the present thesis along with future directions is discussed.

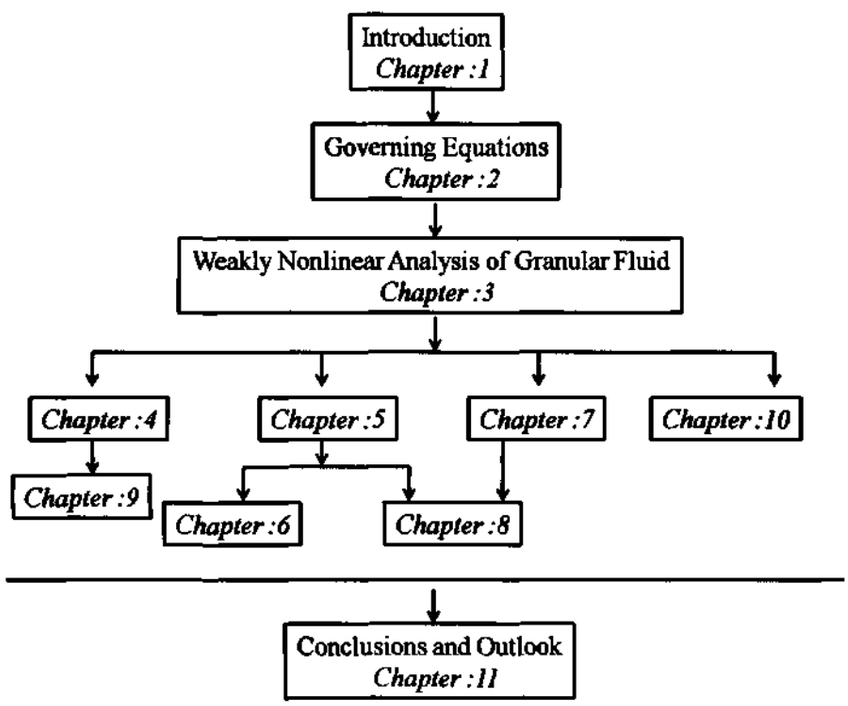

Figure 1.29: Road map of the thesis.

Appendix 1A. List of Symbols

Γ	:	Dimensionless acceleration amplitude
A	:	Amplitude of the sinusoidal vibration
f	:	Frequency of the sinusoidal vibration
z	:	Displacement of vibration
t	:	Time
g	:	Acceleration due to gravity
S	:	Shaking strength
F	:	Number of layers
Re	:	Rayleigh number
Re_c	:	Critical Rayleigh number
ψ	:	Order parameter or amplitude function
ρ	:	Average mass of granular material per unit area
ρ_p	:	Material density
γ	:	Dimensionless forcing amplitude
α	:	Nonlinear coupling coefficient in evolution equation for ρ
β	:	Diffusion coefficient in evolution equation for ρ
ω	:	Frequency of subharmonic pattern
b	:	Positive paramter which related wavenumber with frequency of the pattern
b_1, b_2	:	Coefficient of cubic and quintic nonlinearity in Swift-Hohenberg equation
β_1, β_2	:	Coefficient related to tuning possibilities in Swift-Hohenberg equation
ϵ	:	Parameter in favor of square pattern in Swift-Hohenberg equation
ξ_n	:	Height of the granular layer at time $t = n$
M	:	Mapping function
$\mathbf{x} = (x, y)$	:	Position vector
$\mathcal{L}$	:	Linear spatial operator
R	:	Control parameter
$\bar{d}_p$	:	Particle diameter
$\bar{h}$	:	Height (gap) of the Couette cell
$\bar{l}$	:	Length of the Couette cell
$\bar{d}$	:	Depth of the Couette cell
H	:	Dimensionless Couette gap
ϕ	:	Volume fraction
e	:	Particle-particle restitution coefficient
e_w	:	Particle-wall restitution coefficient
d_C, d_F	:	Diameters of the coarse and fine particles
m_C, m_F	:	Mass of the coarse and fine particles
n_C, n_F	:	Number density of the coarse and fine particles

CHAPTER 2

GOVERNING EQUATION

2.1 Introduction

The flowing of granular materials can be divided into two regimes depending on the interaction between grains (Campbell 1990): "quasi-static" flow and "rapid" flow. In the quasi-static regime of granular flow, the shear stress is shear rate independent and the contact between the particles are long enough to give rise frictional forces, thus the flow is slow in this regime. To study such flows one needs to consider modified plasticity models based on Coulomb friction criterion (Jackson 1983; Savage 1984). Another flow regime is the rapid flow regime (fluid like behavior) (Goldhirsch 2003; Campbell 1990) in which the particles are in continuous fluctuational motion and the momentum transfer occurs through collisions and 'streaming' motion of particles. The collisions of particles in this flow regime are nearly instantaneous and the stress is rate dependent. The granular flow in rapid flow regime is also known as 'granular gas' because of its resemblance with molecular gases.

Despite similarities with molecular gases, there is a fundamental difference: the collisions between granular particles are "inelastic" which is in contrast with the molecular gases where the collisions are "elastic". The rule of equipartition of energy does not hold in granular systems whereas in molecular gases thermal energy is equally divided among each degree of modes (such as translational, rotational and vibration) which contain $\frac{1}{2}k_B\overline{T}$ of thermal energy where k_B is the Boltzmann's constant. In granular systems there is no role of $\frac{1}{2}k_B\overline{T}$. The effective energy scale is the potential energy (Jaeger *et al.* 1996), $\bar{m}\bar{g}\bar{d}_p$, of a particle of mass $\bar{m}$ raised by its own diameter $\bar{d}_p$ in Earth's gravity $\bar{g}$. During particle collisions the translational kinetic energy is lost by inelastic collisions and transformed to thermal energy of molecules comprising granular particles. Since the thermal energy is incoherent, it cannot further transform back to the translational kinetic energy of particles (Brilliantov & Pöschel 2004; Rao & Nott 2008).

This chapter is organized as follows. The general balance equations are given in §2.2. Navier-Stokes order constitutive relations are described in §2.3, and the expressions for the transport coefficients are given in §2.4-§2.8. The boundary conditions are given in §2.9.

2.2 Balance Equations

The granular hydrodynamic field variables can be obtained through the coarse graining of the particle level variables. The bulk density or coarse grained density $\overline{\rho}(\bar{\boldsymbol{x}},\bar{t}) = \overline{m}\overline{n}(\bar{\boldsymbol{x}},\bar{t})$ is defined as

$$\overline{\rho}(\bar{\boldsymbol{x}},\bar{t}) \equiv \overline{mn} = \overline{m}\int f(\bar{\boldsymbol{x}},\bar{\boldsymbol{c}},\bar{t})\,d\bar{\boldsymbol{c}}, \tag{2.1}$$

where $\overline{n}$ is the number density, $f(\bar{\boldsymbol{x}},\bar{\boldsymbol{c}},\bar{t})$ is the single particle velocity distribution function at position $\bar{\boldsymbol{x}}$ and time $\bar{t}$ and the 'overbar' refers a dimensional quantity. The bulk velocity field or coarse grained velocity, $\bar{\boldsymbol{u}}(\bar{\boldsymbol{x}},\bar{t})$, is defined as

$$\bar{\boldsymbol{u}}(\bar{\boldsymbol{x}},\bar{t}) = \langle\bar{\boldsymbol{c}}\rangle = \frac{1}{\bar{n}}\int \bar{\boldsymbol{c}} f(\bar{\boldsymbol{x}},\bar{\boldsymbol{c}},\bar{t})\,d\bar{\boldsymbol{c}}, \tag{2.2}$$

where $\bar{c}$ is the instantaneous velocity (local velocity) of an individual particle. Similarly, the granular temperature, $\overline{T}$, can be defined as

$$\overline{T}(\bar{x},\bar{t}) = \frac{1}{\dim}\langle \bar{C}\cdot\bar{C}\rangle = \frac{1}{\dim}\frac{1}{\bar{n}}\int \bar{C}^2 f(\bar{x},\bar{c},\bar{t})\,d\bar{c}, \tag{2.3}$$

where $\bar{C} = \bar{c} - \bar{u}$ is the fluctuation or peculiar velocity and dim is the dimension of the problem (= 2 for disks and 3 for spheres).

The bulk density $\overline{\rho}$ can be expressed in terms of volume fraction (ϕ) and number density ($\bar{n}$) such that $\overline{\rho} = \overline{m}\bar{n} = \overline{\rho}_p\phi$, where $\overline{\rho}_p$ is the material density and $\overline{m}$ is the mass of a particle:

$$\overline{\rho} = \frac{\overline{m}N}{\overline{V}} = \overline{m}\bar{n} = \overline{\rho}_p\overline{V}_p\bar{n} = \overline{\rho}_p\frac{\overline{V}_pN}{\overline{V}} = \overline{\rho}_p\phi, \tag{2.4}$$

where N is the total number of particles and, $\overline{V}$ and $\overline{V}_p$ are the total volume and the volume occupied by a particle, respectively.

In the present work, we are interested in the rapid flow regime (Campbell 1990; Goldhirsch 2003); as discussed in chapter 1, the most of the fascinating patterns belong to this flow regime. To simplify governing equations, we are assuming that the particles are spherical, monodisperse and smooth such that there is no tangential force exerted by one particle on the other at the contact point. Consequently, the momentum transfer is mainly due to the collision and translation of the particles.

The balance equations for mass, momentum and 'pseudo-thermal' energy are:

$$\overline{\rho}_p\frac{\mathrm{D}\phi}{\mathrm{D}\bar{t}} = -\overline{\rho}_p\phi(\overline{\nabla}\cdot\overline{\boldsymbol{u}}) \tag{2.5}$$

$$\overline{\rho}_p\phi\frac{\mathrm{D}\overline{\boldsymbol{u}}}{\mathrm{D}\bar{t}} = \overline{\rho}_p\phi\overline{\boldsymbol{g}} - \overline{\nabla}\cdot\overline{\boldsymbol{\Sigma}} \tag{2.6}$$

$$\frac{\dim}{2}\overline{\rho}_p\phi\frac{\mathrm{D}\overline{T}}{\mathrm{D}\bar{t}} = -\overline{\nabla}\cdot\overline{\boldsymbol{q}} - \overline{\boldsymbol{\Sigma}}:\overline{\nabla}\overline{\boldsymbol{u}} - \overline{\mathcal{D}} \tag{2.7}$$

where $\mathrm{D}/\mathrm{D}\bar{t} = \partial/\partial\bar{t} + \overline{\nabla}\cdot\bar{\boldsymbol{u}}$ is the material derivative. The first term on the right hand side of (2.7) is the flux of pseudo-thermal energy, the second term is the source term which denotes the shear work, and the last term is the sink term which represents the rate of energy dissipation due to inelastic collisions per unit volume. Here $\overline{\boldsymbol{g}}$ is the acceleration due to gravity.

The balance equations, (2.5)-(2.7), must be augmented by constitutive relations for stress ($\overline{\boldsymbol{\Sigma}}$), granular heat flux ($\overline{\boldsymbol{q}}$) and dissipation rate ($\overline{\mathcal{D}}$) which are discussed in the following section.

2.3 Navier-Stokes Order Constitutive Model

The Navier-Stokes order constitutive model for stress tensor is given below:

$$\overline{\boldsymbol{\Sigma}} = \left(\overline{p} - \overline{\zeta}(\overline{\nabla}\cdot\overline{\boldsymbol{u}})\right)\mathbf{I} - 2\overline{\mu}\overline{\mathbf{S}} \tag{2.8}$$

where $\overline{p}$ is the pressure, $\overline{\mu}$ and ζ are the coefficient of shear and bulk viscosities, respectively, and $\overline{\mathbf{S}}$ denotes the deviotoric strain rate tensor,

$$\overline{\mathbf{S}} = \frac{1}{2}\left(\overline{\nabla}\overline{\boldsymbol{u}} + \overline{\nabla}\overline{\boldsymbol{u}}^{Tr}\right) - \frac{1}{\dim}(\overline{\nabla}\cdot\overline{\boldsymbol{u}})\mathbf{I} \tag{2.9}$$

where $\mathbf{I}$ is an identity tensor. The flux of pseudo-thermal energy is given by

$$\overline{\boldsymbol{q}} = -\overline{\kappa}\overline{\nabla T} - \overline{\kappa}_h\overline{\nabla}\phi \tag{2.10}$$

where $\overline{\kappa}$ is the coefficient of thermal conductivity associated with the gradient of granular temperature and $\overline{\kappa}_h$ is an additional term that arises due to the gradients in volume fraction (Sela & Goldhirsch 1998). One distinguishing feature of the hydrodynamics of the inelastic particles is that the heat flux is not only generated by a non-uniform temperature (temperature gradients) but also from the density inhomogeneities (density gradients). The second term in the expression of $\overline{\boldsymbol{q}}$ is zero for homogeneous density and $\overline{\kappa}_h \to 0$ for elastic particles ($e \to 0$) leading to Fourier's law of heat conduction.

In the following sections we describe a few widely used kinetic theory models for the flow of hard-spheres and disks (Lun *et al.* 1984; Jenkins & Richman 1985; Garzó & Dufty 1999; Lutsko 2005; Alam *et al.* 2008).

2.4 Model for Smooth Identical Inelastic Spheres (Lun *et al.* 1984)

The transport coefficients, pressure ($\overline{p}$), shear viscosity ($\overline{\mu}$), bulk viscosity ($\overline{\zeta}$), coefficient of thermal conductivity ($\overline{\kappa}$) and dissipation of energy ($\overline{\mathcal{D}}$) are given as

$$\left.\begin{aligned}
\overline{p}(\phi,\overline{T}) &= \overline{\rho}_p \overline{T} f_1(\phi), & \overline{\mu}(\phi,\overline{T}) &= \overline{\rho}_p \overline{d}_p \overline{T}^{1/2} f_2(\phi),\\
\overline{\zeta}(\phi,\overline{T}) &= \overline{\rho}_p \overline{d}_p \overline{T}^{1/2} f_3(\phi), & \overline{\kappa}(\phi,\overline{T}) &= \overline{\rho}_p \overline{d}_p \overline{T}^{1/2} f_4(\phi),\\
\overline{\kappa}_h(\phi,\overline{T}) &= \overline{\rho}_p \overline{d}_p \overline{T}^{3/2} f_{4h}(\phi), & \overline{\mathcal{D}}(\phi,\overline{T}) &= \frac{\overline{\rho}_p}{\overline{d}_p} \overline{T}^{3/2} f_5(\phi)
\end{aligned}\right\} \tag{2.11}$$

where $\overline{d}_p$ is the particle diameter and $f_i(.)$'s are non dimensional functions of density which are given in table 2.1.

$f_1(\phi)$	=	$\phi(1+4\eta\phi\chi(\phi))$
$f_2(\phi)$	=	$\frac{1}{\sqrt{\pi}}\left(\frac{5\pi}{96\eta(2-\eta)}\left(1+\frac{8}{5}\eta\phi\chi(\phi)\right)\left(\frac{1}{\chi(\phi)}+\frac{8}{5}\eta(3\eta-2)\phi\right)+\frac{8}{5}\eta\phi^2\chi(\phi)\right)$
$f_3(\phi)$	=	$\frac{8}{3\pi^{1/2}}\eta\phi^2\chi(\phi)$
$f_4(\phi)$	=	$\frac{25\pi^{1/2}}{16\eta(41-33\eta)}\left(1+\frac{12}{5}\eta\phi\chi(\phi)\right)\left(\frac{1}{\chi(\phi)}+\frac{12}{5}\eta^2(4\eta-3)\phi\right)+\frac{4}{\pi^{1/2}}\eta\phi^2\chi(\phi)$
$f_{4h}(\phi)$	=	$\frac{25\pi^{1/2}}{16\eta(41-33\eta)}\left(\frac{1}{\phi\chi(\phi)}+\frac{12}{5}\eta\right)\frac{12}{5}\eta(2\eta-1)(\eta-1)\frac{d}{d\phi}\left(\phi^2\chi(\phi)\right)$
$f_5(\phi)$	=	$\frac{48}{\pi^{1/2}}\eta(1-\eta)\phi^2\chi(\phi)$
$f_6(\phi)$	=	$\frac{\sqrt{3}\pi\phi\chi(\phi)}{2\phi_m f_4(\phi)}$, $f_7(\phi)=\frac{\pi\phi\chi(\phi)}{2\sqrt{3}\phi_m f_2(\phi)}$, $\eta=\frac{1}{2}(1+e)$

Table 2.1: Non-dimensional functions (Lun *et al.* 1984).

The constitutive relations of Lun *et al.* (1984) are strictly valid for elastic limit ($e \approx 1$), i.e. the parameter $\eta = (1+e)/2$ must set to be unity in the above expressions of f_i's.

Ogawa *et al.* (1980) proposed a form for the radial distribution function that diverges at

$\phi \to \phi_m$, where ϕ_m is the maximum packing limit which is 0.65 for the random close packing:

$$\chi(\phi) = \frac{1}{1-(\phi/\phi_m)^{1/3}}. \tag{2.12}$$

The Carnahan-Starling (Carnahan & Starling 1969) form of radial distribution function is given by

$$\chi(\phi) = \frac{(1-\phi/2)}{(1-\phi/\phi_m)^3} \tag{2.13}$$

which diverges at $\phi \to \phi_m$.

2.5 Model for Inelastic Hard-disks

For the nearly elastic limit ($e \to 1$) of an inelastic hard-disks (of diameter $\overline{d}_p$) fluid, the constitutive expressions for $\overline{p}$, $\overline{\mu}$, $\overline{\zeta}$, $\overline{\kappa}$ and $\overline{\mathcal{D}}$ are given by (2.11) where the f_1-f_5 are given below (Gass 1971; Jenkins & Richman 1985):

$$\left.\begin{aligned}
f_1(\phi) &= \phi + 2\phi^2\chi, \\
f_2(\phi) &= \frac{\sqrt{\pi}}{8\chi} + \frac{\sqrt{\pi}}{4}\phi + \frac{\sqrt{\pi}}{8}\left(1+\frac{8}{\pi}\right)\phi^2\chi, \\
f_3(\phi) &= \frac{2}{\sqrt{\pi}}\phi^2\chi, \\
f_4(\phi) &= \frac{\sqrt{\pi}}{2\chi} + \frac{3\sqrt{\pi}}{2}\phi + \sqrt{\pi}\left(\frac{2}{\pi}+\frac{9}{8}\right)\phi^2\chi, \\
f_{4h}(\phi) &= 0 \\
f_5(\phi,e) &= \frac{4}{\sqrt{\pi}}(1-e^2)\phi^2\chi.
\end{aligned}\right\} \tag{2.14}$$

These constitutive expressions give good predictions for transport coefficients of nearly elastic granular fluid up-to a density of $\phi \approx 0.55$ (Alam & Luding 2003*b*). In the above expressions, $\chi(\phi)$ is the contact radial distribution function which is taken to be of the following form (Henderson 1975)

$$\chi(\phi) = \frac{1-7\phi/16}{(1-\phi/\phi_m)^2}, \tag{2.15}$$

which diverges at $\phi = \phi_m$ that is taken to be either (*i*) $\phi_m = \pi/2\sqrt{3} \approx 0.906$ (the maximum packing limit in two-dimensions) or (*ii*) $\phi_m = \phi_r \approx 0.82$ (the random close packing limit in two-dimensions). The above expression (2.15) boils down to that of Henderson for $\phi_m = 1$ that corresponds to point particles. The range of validity of different variants of model radial distribution functions is discussed in Luding (2009). The linear stability of the shear flow of inelastic hard disks has been probed by Alam *et al.* (2008) using above constitutive expressions.

2.6 Model for Dense Fluid Transport of Inelastic Hard Spheres, Garzó & Dufty (1999)

The hydrodynamic description and the transport coefficients for a low density granular gas have been studied by using the Boltzmann kinetic equations with inelastic binary collisions. Brey *et al.* (1998) recently extended Chapman-Enskog solution of the Boltzmann equation for inelastic

particles to obtain the Navier-Stokes equations and the transport coefficients as a function of coefficient of restitution. The problem considered by Brey *et al.* (1998) was an idealized gas of smooth, spherical hard spheres with inelastic binary collisions. Garzó & Dufty (1999) extended the analysis of Brey *et al.* (1998) to revised Enskog kinetic theory (RET) for inelastic particles at higher densities. The RET for elastic gases (Beijeren & Ernst 1973) is an accurate theory which is likely to be valid for the entire range of flow domain as confirmed by both Monte Carlo and molecular dynamics simulations. The RET provides a unified description of fluid, crystal and metastable states for the hard sphere system near and far from equilibrium. The Navier-Stokes level balance equations and associated transport coefficients for dense systems using revised Enskog kinetic theory (Garzó & Dufty 1999) are given below.

The granular temperature is defined as

$$\frac{\dim}{2}\overline{T} = \frac{1}{2}\overline{m}\langle\overline{C}^2\rangle, \tag{2.16}$$

which leads to following energy balance equation

$$\frac{\dim}{2}\bar{n}\frac{\mathrm{D}\overline{T}}{\mathrm{D}\bar{t}} = -\overline{\nabla}\cdot\overline{q} - \overline{\Sigma}:\overline{\nabla}\overline{u} - \overline{\mathcal{D}}, \tag{2.17}$$

where $\bar{n}$ is the number density [viz. (2.4)] and other notations are same as in previous sections. Here the stress tensor, $\overline{\Sigma}$, and heat flux vector, $\overline{q}$, are defined as a sum of kinetic and collisional contributions, i.e. $\overline{\Sigma} = \overline{\Sigma}_k + \overline{\Sigma}_c$ and $\overline{q} = \overline{q}_k + \overline{q}_c$. The transport coefficients, pressure, ($\overline{p}$), shear viscosity, ($\overline{\mu}$), bulk viscosity, ($\overline{\zeta}$), thermal conductivity, ($\overline{\kappa}$), higher order coefficient of heat flux, $\overline{\kappa}_h$, and the granular energy, $\overline{\mathcal{D}}$ using RET are given below:

$$\overline{p}(\phi,\overline{T}) = \frac{6}{\pi\bar{d}_p^3}\phi f_1(\phi,e)\overline{T}, \qquad \overline{\mu}(\phi,\overline{T},e) = \frac{5}{16}\frac{\sqrt{\overline{m}}}{\bar{d}_p^2}f_2(\phi,e)\overline{T}^{1/2},$$

$$\overline{\zeta}(\phi,\overline{T},e) = \frac{5}{16}\frac{\sqrt{\overline{m}}}{\bar{d}_p^2}f_3(\phi,e)\overline{T}^{1/2}, \qquad \overline{\kappa}(\phi,\overline{T},e) = \frac{75}{64}\frac{1}{\bar{d}_p^2\sqrt{\pi\overline{m}}}f_4(\phi,e)\sqrt{\overline{T}},$$

$$\overline{\kappa}_h(\phi,\overline{T},e) = \frac{25}{128}\frac{\bar{d}_p\sqrt{\pi}}{\sqrt{\overline{m}}}f_{4h}(\phi,e)\frac{\overline{T}^{3/2}}{\phi}, \quad \overline{\mathcal{D}}(\phi,\overline{T},e) = \frac{96}{5}\frac{1}{\bar{d}_p\sqrt{\pi\overline{m}}}\phi f_5(\phi,e)\overline{T}^{3/2} + f_6(\phi,e)(\overline{\nabla}\cdot\overline{u})\overline{T},$$

where f_i's are the non-dimensional functions of volume fraction (ϕ) and coefficient of restitution (e) as given in table 2.2. Note that all the coefficients, $\overline{p}$, $\overline{\mu}$, etc, are functions of volume fraction (ϕ), granular temperature ($\overline{T}$) and coefficient of restitution (e). The second term in the expression of $\overline{\mathcal{D}}$ is an extra term which was not included in the constitutive models of Lun *et al.* (1984).

2.7 Arbitrary Energy Loss Model, Lutsko (2005)

Recently, Lutsko (2005) has given a kinetic theory using Chapman-Enskog expansion for the case of a one component fluid in D-dimensions with an arbitrary model for the normal energy loss. The transport coefficients given by Lutsko (2005) have a simple general form which covers the entire class of models. For example, the elastic hard spheres in two and three dimensions (Gass 1971; McLennan 1989), a simple granular gas in three dimension (Garzó & Dufty 1999) and models with velocity-dependent restitution coefficient (Ramirez *et al.* 1999; Pöschel & Brilliantov 2001; McNamara & Falcon 2005) are special cases of the model given by Lutsko (2005).

According to this model, the only scattering law allowing for energy loss which is consistent

$$
\begin{array}{lcl}
f_1(\phi,e) & = & 1+2(1+e)\phi\chi \\
f_2(\phi,e) & = & \left(g_\mu-\frac{1}{2}f_5\right)^{-1}\left[1-\frac{2}{5}(1+e)(1-3e)\phi\chi\right]\left[1+\frac{4}{5}\phi\chi(1+e)\right]+\frac{3}{5}f_3 \\
f_3(\phi,e) & = & \frac{128}{5\pi}\phi^2\chi(1+e)\left(1-\frac{1}{32}c^*\right) \\
f_4(\phi,e) & = & f_4^k\left[1+\frac{6}{5}\phi\chi(1+e)\right]+\frac{256}{25}\phi^2\chi(1+e)\left(1+\frac{7}{32}c^*\right) \\
f_4^k(\phi,e) & = & \frac{2}{3}\left(g_\kappa-2f_5\right)^{-1}\left[1+\frac{1}{2}(1+f_1)c^*\right. \\
 & & \left.+\frac{3}{5}\phi\chi(1+e)^2\left\{2e-1+\left(\frac{1}{2}(1+e)-\frac{5}{3(1+e)}\right)c^*\right\}\right] \\
f_{4h}(\phi,e) & = & f_{4h}^k\left[1+\frac{6}{5}\phi\chi(1+e)\right] \\
f_{4h}^k(\phi,e) & = & 2\left(2g_\kappa-3f_5\right)^{-1}\left[\left(1+\phi\frac{\partial\log\chi}{\partial\phi}\right)f_5f_4^k+\frac{f_1}{3}\left(1+\phi\frac{\partial\log f_1}{\partial\phi}\right)c^*\right. \\
 & & \left.-\frac{4}{5}\phi\chi\left(1+\frac{1}{2}\phi\frac{\partial\log\chi}{\partial\phi}\right)(1+e)\left\{e(1-e)+\frac{1}{4}\left(\frac{4}{3}+e(1-e)\right)c^*\right\}\right] \\
f_5(\phi,e) & = & \frac{5}{12}\chi(1-e^2)\left(1+\frac{3}{32}c^*\right) \\
f_6(\phi,e) & = & \left[-(1-e)(f_1-1)+\frac{5}{32}(1-e^2)\left(1+\frac{3}{64}c^*\right)\chi C_D\right] \\
C_D(\phi,e) & = & \left[\frac{1}{2}f_5+g_\zeta+\frac{5c^*}{64}\left(1+\frac{3}{64}c^*\right)\chi(1-e^2)\right]^{-1}\left[\frac{4}{15}\Lambda\phi\chi+(f_1-1)\left(\frac{2}{3}-e\right)c^*\right] \\
c^*(e) & = & 32(1-e)(1-2e^2)\left(81-17e+30e^2(1-e)\right)^{-1} \\
\Lambda(e) & = & \frac{3}{8}\left[(1-e)(5e^2+4e-1)+\frac{c^*}{12}(159e+3e^2-19e-15e^3)\right](1+e) \\
\chi(\phi) & = & \frac{1-\phi/2}{(1-\phi)^3} \\
g_\mu(\phi,e) & = & \chi\left[1-\frac{1}{4}(1-e)^2\right]\left[1-\frac{1}{64}c^*\right] \\
g_\kappa(\phi,e) & = & \frac{1+e}{3}\chi\left[1+\frac{33}{16}(1-e)+\frac{19-3e}{1024}c^*\right] \\
g_\zeta(\phi,e) & = & \frac{1+e}{48}\chi\left[128-96e+15e^2-15e^3+\frac{c^*}{64}\left(15e^3-15e^2+498e-434\right)\right]
\end{array}
$$

Table 2.2: Non-dimensional functions (Garzó & Dufty 1999).

with conservation of total momentum and angular momentum is

$$\vec{v}'_{12} = \vec{v}_{12} - \vec{k}_{12}\left(\vec{v}_{12}\cdot\vec{k}_{12} + sgn(\vec{v}_{12}\cdot\vec{k}_{12})\sqrt{(\vec{v}_{12}\cdot\vec{k}_{12})^2 - \frac{4}{m}\delta E}\right) \tag{2.18}$$

where $\vec{v}_{12} = \vec{v}_1 - \vec{v}_2$ is the relative velocity before collision, $\vec{k}_{12}$ is a unit vector pointing from the center of first particle to the center of second particle. The energy loss is δE which is a function of normal relative velocity

$$\delta E = \Delta(\vec{v}_{12}\cdot\vec{k}_{12}) \tag{2.19}$$

and the center of mass velocity is $\vec{V}_{12} = \vec{v}_1 + \vec{v}_2$. The change in energy during a collision for simple granular fluid model is

$$-\delta E = \frac{1}{2}\bar{m}\left(\vec{v}_1'^2 + \vec{v}_1'^2 - \vec{v}_1^2 - \vec{v}_1^2\right) = -\frac{1}{4}\bar{m}(1-e^2)(\vec{v}_{12}\cdot\vec{k}_{12})^2. \tag{2.20}$$

For the simple granular fluid the transport coefficients: pressure ($\overline{p}$), shear viscosity ($\overline{\mu}$), bulk viscosity ($\overline{\zeta}$), coefficient of thermal conductivity ($\overline{\kappa}$), higher order coefficient of thermal conductivity ($\overline{\kappa}_h$) and the granular energy ($\overline{\mathcal{D}}$), take the following form:

$$\overline{p}(\phi,\overline{T},e) = \frac{1}{\overline{V}_{dim}}\phi f_1(\phi,e)\overline{T}, \qquad \overline{\mu}(\phi,\overline{T},e) = \overline{m}^{1/2}\bar{d}_p^{1-dim}\left(f_2^k + f_2^c\right)\overline{T}^{1/2},$$

$$\overline{\zeta}(\phi,\overline{T},e) = \overline{m}^{1/2}\bar{d}_p^{1-dim}f_3(\phi,e)\overline{T}^{1/2}, \qquad \overline{\kappa}(\phi,\overline{T},e) = \overline{m}^{(-1/2)}\bar{d}_p^{1-dim}\left(f_4^k + f_4^c\right)T^{1/2},$$

$$\overline{\kappa}_h(\phi,e,\overline{T}) = \overline{m}^{(-1/2)}\bar{d}_p^{1-dim}\overline{V}_{dim}\left(f_{4h}^k + f_{4h}^c\right)\frac{\overline{T}^{3/2}}{\phi}, \quad \overline{\mathcal{D}}(\phi,\overline{T},e) = \frac{\phi f_5\overline{T}^{3/2}}{\sqrt{\overline{m}}\bar{d}_p\overline{V}_{dim}} + \frac{\phi f_6(\overline{\nabla}\cdot\boldsymbol{u})\overline{T}}{\overline{V}_{dim}}$$

where $\overline{V}_{dim}$ is the volume of a particle of diameter $\bar{d}_p$ having dimension 'dim',

$$\overline{V}_{dim}(r) = 2\pi C_{dim-1}\frac{(\bar{d}_p/2)^{dim}}{\text{dim}} \quad \text{with} \quad C_{dim} = \frac{\pi^{dim/2}}{\Gamma(dim/2+1)}.$$

For example for the sphere i.e. dim = 3, $\overline{V}_3(r) = \frac{1}{6}\pi\bar{d}_p^3$. The superscript k and c refer to the kinetic and collision contributions, respectively, and other symbols are same as in §2.6. The transport coefficients are functions of volume fraction (ϕ), granular temperature (T) and the coefficient of restitution (e). Here f_i's are the non-dimensional functions of volume fraction and coefficient of restitution as given in table 2.3. Note that in the three dimension limit (dim=3) we recover transport coefficients for a low density fluid (Brey & Cubero 2000; Garzó & Montanero 2002) and for a dense fluid (Garzó & Dufty 1999) (see §2.6).

2.8 Present Constitutive Model

We have chosen the Navier-Stokes-order constitutive model of Lun *et al.* (1984) which has been used by many authors (Alam & Nott 1998; Forterre & Pouliquen 2002; Mitarai & Nakanishi 2004; Khain 2007; Alam *et al.* 2005) to probe the stability of various types of granular shear flows. The constitutive relations for stress, heat flux and dissipation are given in (2.8)-(2.10), and

$$
\begin{aligned}
f_1(\phi,e) &= \left[1+\frac{(1+e)S_{dim}\bar{d}_p^{dim}}{4\,dim\overline{V}_{dim}}\phi\chi\right], \quad S_{dim}=\frac{2\pi^{dim/2}}{\Gamma(dim/2)}\\
c_2(e) &= \frac{16(1-2e^2)(1-e)}{24\,dim+9-(41-8\,dim)e+30e^2(1-e)}\\
f_2^k(\phi,e) &= \frac{\sqrt{\pi}(dim+2)}{4S_{dim}}\left(h_\mu-\tfrac{1}{2}h_\chi\right)^{-1}\left(1+\frac{S_{dim}\bar{d}_p^{dim}(e+1)(3e-1)}{4\,dim(dim+2)\overline{V}_{dim}}\phi\chi\right)\\
f_2^c(\phi,e) &= \frac{\sqrt{\pi}\bar{d}_p^{dim}(1+e)}{8\,dim\,\overline{V}_{dim}}\phi\chi\left[\left(h_\mu-\tfrac{1}{2}h_\chi\right)^{-1}\left(1+\frac{S_{dim}\bar{d}_p^{dim}(e+1)(3e-1)}{4\,dim(dim+2)\overline{V}_{dim}}\phi\chi\right)\right.\\
&\quad \left.+\frac{4S_{dim}\bar{d}_p^{dim}}{\pi(dim+2)\overline{V}_{dim}}\phi\left(1-\tfrac{c_2}{16}\right)\right]\\
f_3(\phi,e) &= \frac{S_{dim}(1+e)}{2\sqrt{\pi}dim^2}\left(\frac{\bar{d}_p^{dim}}{\overline{V}_{dim}}\right)^2\phi^2\chi\left(1-\tfrac{c_2}{16}\right)\\
f_4^k(\phi,e) &= \frac{\sqrt{\pi}(dim+2)^2}{8S_{dim}}\left(h_T^*-2h_\chi^*\right)^{-1}\\
&\quad \left[1+2c_2+\frac{3\bar{d}_p^{dim}S_{dim}}{8\,dim\,(dim+2)\overline{V}_{dim}}(e+1)^2\left\{2e-1+(e+1)c_2\right\}\phi\chi\right]\\
f_4^c(\phi,e) &= \frac{3(1+e)S_{dim}}{4dim\,(dim+2)}\frac{\bar{d}_p^{dim}}{\overline{V}_{dim}}\phi\chi f_4^k+\frac{(1+e)S_{dim}}{4\sqrt{\pi}\,dim}\left(\frac{\bar{d}_p^{dim}}{\overline{V}_{dim}}\right)^2\left(1-\tfrac{7c_2}{16}\right)\phi^2\chi\\
f_{4h}^k(\phi,e) &= \frac{\sqrt{\pi}dim\,(dim+2)^2}{4S_{dim}(dim-1)}\left(2h_T-3h_\chi\right)^{-1}\\
&\quad \left[\phi\frac{\partial(\log\phi\chi_0)}{\partial\phi}h_\chi\left(1+\tfrac{3c_2}{16}\right)\frac{8S_{dim}(dim-1)}{\sqrt{\pi}dim\,(dim+2)^2}f_4^k+\frac{dim-1}{dim}c_2\right.\\
&\quad +\frac{\bar{d}_p^{dim}}{\overline{V}_{dim}}\left(\frac{\partial(\phi^2\chi)}{\partial\phi}\right)\frac{3(dim-1)S_{dim}(1+e)}{8\,dim^2(dim+2)}\\
&\quad \left.\left\{-e(1-e)+\tfrac{1}{6}(3e^2-3e+10+2\,dim)c_2\right\}\right]\\
f_{4h}^c(\phi,e) &= \frac{3S_{dim}(1+e)\bar{d}_p^{dim}}{4\,dim\,(dim+2)\overline{V}_{dim}}\phi\chi f_{4h}^k\\
f_5(\phi,e) &= \frac{S_{dim}}{2\sqrt{\pi}}\left(1+\tfrac{3c_2}{16}\right)(1-e^2)\frac{\bar{d}_p^{dim}}{\overline{V}_{dim}}\phi\chi\\
f_6(\phi,e) &= \frac{3}{512\,dim}\left(h_\zeta-dim\,h_\chi\right)^{-1}\chi(1-e^2)-\frac{3S_{dim}}{8\,dim}\frac{\bar{d}_p^{dim}}{\overline{V}_{dim}}(1-e^2)\phi\chi\\
h_T(\phi,e) &= \chi\frac{dim-1}{2\,dim}(e+1)\left(1+\frac{3(dim+8)(1-e)}{8(dim-1)}\right)\\
h_\mu(\phi,e) &= \chi\left(1-\frac{(1-e)(2\,dim-3e-3)}{4\,dim}\right)\\
h_\chi(\phi,e) &= \frac{(dim+2)}{4\,dim}\chi(1-e^2)\\
h_\zeta(\phi,e) &= -\tfrac{1}{48}\chi\left(\tfrac{1+e}{2}\right)\left(30e^3-30e^2+105e+24e\,dim-56\,dim-73\right)
\end{aligned}
$$

Table 2.3: Non-dimensional functions (Lutsko 2005).

the transport properties are given by (2.11) and the related non-dimensional functions are:

$$\left.\begin{aligned} f_1(\phi) &= \phi(1+4\phi\chi) \\ f_2(\phi) &= \frac{5\sqrt{\pi}}{96\chi}\left(1+\frac{8}{5}\phi\chi\right)^2 + \frac{8}{5\sqrt{\pi}}\phi^2\chi \\ f_3(\phi) &= \frac{8}{3\sqrt{\pi}}\phi^2\chi \\ f_4(\phi) &= \frac{25\sqrt{\pi}}{128\chi}(1+\frac{12}{5}\phi\chi)^2 + \frac{4}{\sqrt{\pi}}\phi^2\chi \\ f_{4h}(\phi) &= 0 \\ f_5(\phi,e) &= \frac{12}{\sqrt{\pi}}(1-e^2)\phi^2\chi \end{aligned}\right\} \tag{2.21}$$

where χ is the radial distribution function [cf. (2.12)-(2.13)]. We set $\eta = 1$ in the expressions of f_i's as given in §2.4 in order to get relations (2.21) for the case of nearly elastic particles.

In the expression for the collisional dissipation $\overline{\mathcal{D}}$ (which is proportional to $f_5(\phi, e)$ as in Eqn. 2.21), some authors (e.g. Garzó & Dufty 1999; Lutsko 2005, §2.6, §2.7) have found an additional contribution proportional to $\overline{\nabla}\cdot\bar{\boldsymbol{u}}$ that appears as a dense-gas correction; we have checked that this additional term does not affect the onset of linear shear-banding instability and hence omitted in the present work. We have also neglected a 'Dufour-like' term ($\sim \overline{\nabla}\phi$) in the expression for the granular heat flux (see, for example, Lun *et al.* 1984; Sela & Goldhirsch 1998; Garzó & Dufty 1999) even though this is a Navier-Stokes-order term, i.e. of order Knudsen number[1] (Kn), it appears at $O(\epsilon Kn)$, where $\epsilon = (1-e^2)$ is the inelasticity; however, it can be easily verified that the shear rate ($\sim Kn$) and the inelasticity cannot be separated from each other ($Kn \sim \sqrt{\epsilon}$) in uniform shear flow, and therefore the above 'Dufour-like' term is likely to be of higher-order in terms of Knudsen number. In any case, the effect of this additional term on the stability of uniform shear flow was checked by (Gayen & Alam 2006), along with the effects of spin-fields and tangential restitution, who showed that this term does not introduce any new instability in plane shear flow.

It should be pointed out that Gayen & Alam (2006) used more general expressions for f_1-f_4 in (2.21) that also depend on the restitution coefficient e, having a larger range of validity in terms of e; for example, the correct expression for f_1 for inelastic particles is $f_1(\phi, e) = \phi(1+2(1+e)\phi\chi)$, with similar expressions for f_2-f_4. Even with such an elaborate restitution-coefficient-dependent constitutive model, they reported no new instability in plane shear flow. Since the present nonlinear analysis is a finite-amplitude saturation of the underling linearly unstable mode, our contention is that a more complex restitution-coefficient-dependent constitutive model would not qualitatively alter our predictions on "nonlinear" shear-banding instability.

The Navier-Stokes-level constitutive models are strictly valid in the quasi-elastic limit ($e \sim 1$) since certain non-Newtonian effects, like the normal stress differences (Sela & Goldhirsch 1998; Alam & Luding 2003*a*),become prominent at smaller values of the restitution coefficient (i.e. at larger dissipation levels). Such effects can only be incorporated using Burnett- or super-Burnett order constitutive models (Sela & Goldhirsch 1998) which we do not consider here.

2.9 Boundary Conditions

In contrast to Newtonian fluids, the velocity slip has been observed at the boundaries in experiments (Hanes & Inman 1985; Savage & Sayed 1984) and computer simulations (Campbell & Brennen 1985) of granular flows. The slip velocity generates pseudo-thermal energy at the

[1]The ratio of the mean free path length of the molecules of a fluid to a characteristic length.

boundaries and there is a lose of energy due to inelastic collisions between the particle and wall. Therefore the granular temperature at the boundaries cannot be determined independently, rather it involves solutions of flow fields far away from the boundaries. Consequently the walls may act as a source or a sink of pseudo-thermal energy (granular temperature) under different conditions.

Several theoretical studies have implemented boundary conditions in the flow problems using either huristic or kinetic theory approach. The heuristic approach (Hui *et al.* 1984; Johnson & Jackson 1987) for boundary conditions depend on two specific wall properties: coefficient of restitution for the particle-wall collisions e_w and the specularity coefficient β_s. On the other hand, the boundary conditions using kinetic theory approach (Jenkins & Richman 1986; Richman 1988; Jenkins 1992) deal wall properties in a rigorous manner. Hui *et al.* (1984) modeled boundary conditions for dense flow using the phenomenological theory of Haff (1983). In the derivation of temperature boundary condition, Hui *et al.* (1984) neglected the contribution of shear work performed by the boundaries due to slip velocity which was later modified by Johnson & Jackson (1987). They derived a set of boundary conditions in a generalized manner by assuming the frictional contribution of stress at the boundaries. Moreover, Johnson & Jackson (1987) considered the average distance between the wall and the surface of an adjacent particle, and the average boundary area per particle, as a function of number density or volume fraction. The details of generalized boundary conditions of Hui *et al.* (1984) and Johnson & Jackson (1987) are discussed below.

2.9.1 Boundary Conditions in the Dense Limit using Heuristic Approach by Hui *et al.* (1984)

The boundary conditions derived by Hui *et al.* (1984), based on Haff's theory, are valid in the limit where the rheology is dominated by particle collisions. We consider the flow of spherical, non-cohesive, smooth and identical particles of mass $\bar{m}$. It is assumed that mass density $\bar{\rho}$ is large enough so that the average separation, $\bar{s}$, between the neighbors is always less than the particle diameter, $\bar{d}_p$ i.e. $\bar{s} << \bar{d}_p$. Under this assumption the bulk density can be defined as $\bar{\rho} \sim \bar{m}/\bar{d}_p^3$.

Balance of Tangential Momentum

The balance of momentum can be obtained by equating the tangential momentum at the boundary due to bulk flow with the tangential momentum flux due to particle-wall collisions,

$$\left[\boldsymbol{n} \cdot \overline{\overline{\Sigma}} \cdot \boldsymbol{t}\right]_{\text{at the boundary}} = \boldsymbol{t} \cdot S_w \tag{2.22}$$

where $\boldsymbol{n}$ and $\boldsymbol{t}$ are the normal and tangential unit vectors, respectively. The quantity S_w refer to momentum flux (the rate of transfer of momentum across a unit area) which can be defined as

$$\begin{aligned} S_w = \;& \text{average tangential momentum transfer per collision} \\ & \times \text{collision frequency} \\ & \times \text{number of particles adjacent to unit area of the surface.} \end{aligned} \tag{2.23}$$

Thus we can write

$$S_w = \frac{a_1 \beta_s \bar{m} \overline{\boldsymbol{u}}_s}{\bar{d}_p^2} \frac{\sqrt{3\bar{T}}}{\bar{s}_0} \tag{2.24}$$

where a_1 is an order one dimensionless constant, $\overline{\boldsymbol{u}}_s = \overline{\boldsymbol{u}}_0 - \overline{\boldsymbol{u}}_w$ is the slip velocity with $\overline{\boldsymbol{u}}_0$ and $\overline{\boldsymbol{u}}_w$ being the flow and wall velocities, respectively, β_s the specularity coefficient which is zero for the perfectly specular collisions and unit for the perfectly diffusive collisions. Here the subscript '0' denotes the corresponding property being evaluated at the boundary. The quantity β_s reflects the nature of particle-wall collisions which measures the fraction of collisions that transfer a

significant tangential amount of tangential momentum to the wall (Hui *et al.* 1984). The left hand side of (2.22) is the shear stress evaluated at the wall which is equal to

$$\left[\boldsymbol{n}\cdot\overline{\Sigma}\cdot\boldsymbol{t}\right]_{\text{at the boundary}} = \left[\bar{\mu}\frac{\mathrm{d}\bar{\boldsymbol{u}}_{\boldsymbol{t}}}{\mathrm{d}\bar{y}}\right]_{\text{at the boundary}} = \bar{\mu}_0\frac{\mathrm{d}\bar{\boldsymbol{u}}_{\boldsymbol{0t}}}{\mathrm{d}\bar{y}} \tag{2.25}$$

where $\bar{\mu}$ denotes the shear viscosity and the subscript $\boldsymbol{t}$ denotes the tangential component of a vector. From the Haff's theory, shear viscosity at the wall is given by

$$\bar{\mu}_0 = \frac{a_2\bar{m}\sqrt{3\bar{T}}}{\bar{d}_p\bar{s}_0}, \tag{2.26}$$

where a_2 is an order one dimensionless constant. From (2.22), (2.24), (2.25) and (2.26) we get,

$$|\bar{\boldsymbol{u}}_s| = \frac{a_2\bar{d}_p}{a_1\beta_s}\frac{\mathrm{d}\bar{\boldsymbol{u}}_{\boldsymbol{0t}}}{\mathrm{d}\bar{y}}. \tag{2.27}$$

This is the velocity boundary condition to be satisfied at the boundary.

Balance of Pseudo-thermal Energy

The balance of pseudo-thermal energy can be obtained by equating the rate of energy loss to the wall per unit area due to collisions ($\bar{\mathcal{D}}_w$) with the energy flux transmitted to the wall due to bulk flow, i.e.

$$\left[\boldsymbol{n}\cdot\bar{\boldsymbol{q}}\right]_{\text{at the boundary}} = -\bar{\mathcal{D}}_w, \tag{2.28}$$

where $\bar{\mathcal{D}}_w$ can be written as,

$$\begin{aligned}\bar{\mathcal{D}}_w \;=\;& \text{energy loss per particle-wall collision} \times \text{collision frequency} \\ & \times \text{number of particles per unit area of the wall.}\end{aligned} \tag{2.29}$$

Using the Haff's theory we can write

$$\bar{\mathcal{D}}_w \;=\; a_3\frac{1}{2}\bar{m}\bar{v}_0{}^2(1-e_w^2)\frac{\sqrt{3\bar{T}}}{\bar{s}_0}\frac{1}{\bar{d}_p^2}, \tag{2.30}$$

where $\bar{n}$ is the number density; particles per unit area of the wall is equal to $\bar{n}(\bar{d}_p+\bar{s})\approx\bar{n}\bar{d}_p$ and a_3 is an order one dimensionless constant. The energy flux at the wall is given by

$$\left[\boldsymbol{n}\cdot\bar{\boldsymbol{q}}\right]_{\text{at the boundary}} = -\bar{\kappa}_0\frac{\mathrm{d}}{\mathrm{d}\bar{y}}\left(\frac{3}{2}\bar{\rho}\bar{T}\right), \tag{2.31}$$

where $\bar{\kappa}_0$ is the thermal conductivity at the wall. The expression for the coefficient of thermal conductivity (Haff 1983) is given by

$$\bar{\kappa} = a_4\bar{d}_p^2\frac{\sqrt{3\bar{T}}}{\bar{s}}. \tag{2.32}$$

where a_4 is an order one dimensionless constant. From (2.28)-(2.32) we get an expression for thermal velocity at the boundary,

$$\bar{v}_0 = \frac{2a_4\bar{d}_p}{a_3(1-e_w^2)}\frac{\mathrm{d}\bar{v}_0}{\mathrm{d}\bar{y}} \tag{2.33}$$

where $\mathrm{d}\bar{v}_0/\mathrm{d}\bar{y}$ is the normal derivative at the wall and $\bar{v}_0=\sqrt{3\bar{T}}$ is the thermal velocity.

2.9.2 Boundary Conditions of Johnson & Jackson (1987)

Balance of Tangential Momentum

Let us define the frequency of particle-wall collisions for each particle:

$$\bar{f}_c = (3\bar{T})^{1/2}/\bar{s}_w, \tag{2.34}$$

where $\bar{s}_w$ is the average distance between the wall and the surface of an adjacent particle (Bagnold 1954),

$$\bar{s}_w \equiv \bar{s}_w(\phi, \phi_m, \bar{d}_p) = \bar{d}_p \left[\left(\frac{\phi_m}{\phi} \right)^{1/3} - 1 \right], \tag{2.35}$$

and $(3\bar{T})^{1/2}$ denotes the root-mean-square velocity fluctuation. The average boundary area per particle is defined as

$$\bar{a}_w \equiv \bar{a}_w(\phi, \phi_m, \bar{d}_p) = \bar{d}_p^2 \left(\frac{\phi_m}{\phi} \right)^{2/3}, \tag{2.36}$$

and thus the total number of particles adjacent to unit area of the surface is $1/\bar{a}_w$. Here ϕ_m is the maximum volume fraction at closest random packing. The average tangential momentum transfer per collision from particles to the wall is given by

$$S_{av} = \beta_s \overline{m} \overline{\boldsymbol{u}}_s = \frac{1}{6} \beta_s \pi \bar{\rho}_p \bar{d}_p^3 \bar{\boldsymbol{u}}_s \tag{2.37}$$

where $\overline{\boldsymbol{u}}_s$ is the slip velocity, $\bar{\rho}_p$ is the particle density and β_s is the specularity coefficient. The rate of tangential momentum transfer to unit area of the wall due to particle-wall collisions is given by

$$S_w = S_{av} \times \bar{f}_c \times \frac{1}{\bar{a}_w} = \frac{\beta_s \sqrt{3} \pi \bar{\rho}_p \phi \bar{T}^{1/2} \bar{\boldsymbol{u}}_s}{6 \phi_m \left[1 - (\phi/\phi_m)^{1/3} \right]}. \tag{2.38}$$

Equating the component of bulk stress to the collisional rate of momentum transfer along the tangential direction, we get the boundary condition for velocity

$$\left[\boldsymbol{n} \cdot \overline{\Sigma} \cdot \boldsymbol{t} \right]_{\text{at the boundary}} = \boldsymbol{t} \cdot S_w. \tag{2.39}$$

Balance of Pseudo-thermal Energy

To obtain the boundary condition for granular temperature, we equate the normal component of the flux of pseudo-thermal energy to the (i) net generation of pseudo-thermal energy at the wall due to slip velocity and (ii) the rate of dissipation of energy due to inelastic collisions,

$$\boldsymbol{n} \cdot \overline{\boldsymbol{q}} = \overline{\boldsymbol{u}}_s \cdot S_w - \bar{\mathcal{D}}_w, \tag{2.40}$$

where $\overline{\boldsymbol{u}}_s \cdot S_w$ is the shear work term i.e. the generation of pseudo-thermal energy due to slip velocity at the boundary and $\bar{\mathcal{D}}_w$ is the rate of dissipation of pseudo-thermal energy due to inelastic particle-wall collisions per unit area of the surface. The expression of $\bar{\mathcal{D}}_w$ is given by

$$\begin{aligned} \bar{\mathcal{D}}_w &= \text{energy loss per particle-wall collision} \times \text{collision frequency per particle} \\ &\quad \times \text{number of particles adjacent to unit area of the particle} \\ &= \left[\frac{1}{4} \pi \bar{\rho}_p \bar{d}_p^3 \bar{T} (1 - e_w^2) \right] \times \bar{f}_c \times \frac{1}{\bar{a}_w} = \frac{\sqrt{3} \pi \phi \bar{T}^{3/2} (1 - e_w^2)}{4 \phi_m \left[1 - (\phi/\phi_m)^{1/3} \right]}. \end{aligned} \tag{2.41}$$

The first term of (2.40) was omitted by Hui *et al.* (1984). In the limit of $e_w \to 1$ which implies that $\bar{\mathcal{D}}_w \to 0$, the first term of (2.40) dominants over the second term and thus the boundary acts like a source of pseudo-thermal energy. In the other situation, if e_w is small, the second term of (2.40) dominates and therefore the boundary behaves as an energy sink.

2.9.3 Boundary Conditions of Jenkins & Richman (1986)

The formal derivation of boundary conditions using kinetic theory was first given by Jenkins & Richman (1986). They assumed a boundary which was composed of halves of similar disks for the two dimensional flow, and hemispheres for the three dimensional flow. The particle distribution function was assumed to be Maxwellian. These boundary conditions differ from the heuristic boundary conditions of Hui *et al.* (1984) in the following manner:

I measure of the boundary roughness determined in terms of diameters of two types of disks (or spheres) and the spacing between the wall disks (or spheres);

II the energy balance at the boundary contains the rate of working, i.e. shear work term, of the boundary due to slip velocity;

III a boundary condition on pressure is obtained which fixes the density (or area/volume fraction) of the flow at the boundary and leads a unique solution to the boundary value problem for the steady shear flow between the parallel plates.

The boundary conditions of Jenkins & Richman (1985) are same as (2.39) and (2.40). However the explicit forms of $\vec{S}_w$ and $\mathcal{D}_w$ are obtained from dense gas kinetic theory with a defined structure for the wall.

2.9.4 Present Choice of Boundary Conditions for the Nonlinear Stability Analysis

The general forms of boundary condition with non-zero slip velocity and/or non-adiabatic ($d\bar{T}/d\bar{y} \neq 0$) walls (as defined in §2.9.1, §2.9.2 and §2.9.3) be incorporated into the nonlinear stability theory, but the resulting nonlinear analysis (especially the adjoint problem and the higher harmonics) becomes very complicated which is left for future work.

The walls can act as sources or sinks of granular (fluctuation) energy which might affect the nonlinear saturation of shear-banding instability, thereby modifying the structure and the spatial position of shear-bands within the Couette-cell. The effect of such slip boundary conditions with non-adiabatic walls on the 'linear' shear-banding instability has been discussed by Alam & Nott (1998). In this present work, as a first step towards developing an order-parameter theory, we restrict to simpler boundary conditions, no-slip and zero heat flux, that admit analytical solutions even for the nonlinear problem and the related bifurcation scenario remains *perfect* (Alam *et al.* 2005; Alam 2005).

The no-slip condition implies that the flow velocity at the wall is same as the wall velocity, consequently, the balance of momentum and energy at the boundary gives

$$\boxed{\left[\boldsymbol{n}\cdot\overline{\Sigma}\cdot\boldsymbol{t}\right]=0 \quad \text{and} \quad \boldsymbol{n}\cdot\bar{\boldsymbol{q}}=0, \qquad \text{at the boundaries}}$$

where $\boldsymbol{n}$ and $\boldsymbol{t}$ are the unit vectors along the normal and tangential directions, respectively. In the component form, the boundary conditions for the bulk velocity and the granular temperature are

$$\boxed{\begin{array}{rcl} \bar{u} & = & \bar{u}_w, \quad \bar{v} = 0, \quad \bar{w} = 0, \quad \text{(no-slip)} \\ \dfrac{\mathrm{d}\bar{T}}{\mathrm{d}\bar{y}} & = & 0, \quad \text{(adiabatic walls)} \end{array}}$$

where $\bar{u}_w$ is the wall velocity.

Appendix 2A. List of Symbols

ρ	:	Bulk density or coarse grained density
ρ_p	:	Material density
d_p	:	Particle diameter
m	:	Mass of a particle
n	:	Number density
e	:	Restitution coefficient
$\mathbf{c}$	:	Instantaneous velocity of a particle
$\boldsymbol{u}$	:	Bulk velocity or coarse grained velocity
$\boldsymbol{C}$	:	Fluctuation or peculiar velocity
dim	:	Dimension of the system
ϕ	:	Volume fraction or solid fraction
ϕ_{max}	:	Volume fraction at maximum packing
N	:	Total number of particles in the system
V	:	Volume of the system
V_p	:	Volume occupied by a particle
$\boldsymbol{g}$	:	Acceleration due to gravity
T	:	Granular Temperature
$\boldsymbol{q}$	:	Heat flux
$\boldsymbol{\Sigma}$	:	Stress tensor
$\mathcal{D}$	:	Dissipation rate
p	:	Pressure
μ, ζ	:	Coefficients of shear and bulk viscosities
S	:	Deviotoric strain rate tensor
s	:	Average separation between two neighboring particles
$\boldsymbol{n}$	:	normal unit vector
$\boldsymbol{t}$	:	tangential unit vector
S_w	:	Momentum flux
β_s	:	Specularity Coefficient
κ	:	Coefficient of thermal conductivity related to the granular temperature
κ_h	:	Coefficient of thermal conductivity related to the volume fraction
$f_i's$ for $i \geq 1$	:	Dimensionless functions of volume fraction
χ	:	Radial distribution function

CHAPTER 3

WEAKLY NONLINEAR THEORY FOR GRANULAR SHEAR FLOWS

3.1 Different Approaches to Derive Landau-Stuart Equation

A general approach to derive the Stuart-Landau equation

$$\frac{\mathrm{d}\mathscr{A}}{\mathrm{d}t} = c^{(0)}\mathscr{A} + c^{(2)}\mathscr{A}|\mathscr{A}|^2 + \dots \tag{3.1}$$

with $\mathscr{A}$ being the complex amplitude of the disturbance, or its partial differential analog, the Ginzburg-Landau equation

$$\frac{\partial\mathscr{A}}{\partial t} = c^{(0)}\mathscr{A} + a_2\frac{\partial^2\mathscr{A}}{\partial x^2} + c^{(2)}\mathscr{A}\mathscr{A}^2 + \dots, \tag{3.2}$$

is to reduce the dimension of the system by projecting the infinite-dimensional system onto some low-dimensional system, spanned by the slowly decaying modes of the associated linear eigenvalue problem. A variety of seemingly different methods, like the amplitude expansion method (Stuart 1960; Watson 1960; Reynolds & Potter 1967), the multiple scale analysis (Stewartson & Stuart 1971), the Fourier expansion method (Herbert 1980) and the center manifold reduction (Carr 1981) are widely used in the theory of weakly nonlinear analysis of fluid systems (see for reviews, Stuart 1971; Busse 1978; Newell *et al.* 1993).

3.1.1 Amplitude Expansion Method of Stuart and Watson (1960)

A formal weakly nonlinear analysis for fluid system was first rigorously established by Stuart (1960) and Watson (1960). Stuart derived Landau equation in 1958 using an energy balance equation, based on the assumption that the disturbance retain its 'Orr-Sommerfeld' shape as the amplitude grows which is not true in general because the distortion of disturbance plays an important role for the viscous instabilities. Later, Stuart (1960) used the small growth rate as an expansion parameter and derived the Landau equation from the Navier-Stokes equations for the plane Poiseuille flow. Watson extended and modified Stuart's (1960) work and established an amplitude expansion method which is applicable to arbitrary order. The *amplitude expansion method* (Watson 1960), which uses the small amplitude of the most unstable mode as an expansion parameter, is based on the assumptions of (*i*) separable solution and (*ii*) the validity of the Landau equation. This reduces the set of governing equations into a series of ordinary differential equations: (*a*) at order $O(\mathscr{A})$ we recover the linear eigenvalue problem; (*b*) at each even order, $O(\mathscr{A}^{2n})$, with $n = 1, 2, \dots$, we have sets of inhomogeneous differential equations for the harmonics of even order and the mean-flow distortion; and (*c*) at each odd-order, $O(\mathscr{A}^{2n+1})$, with $n = 1, 2, \dots$, we have sets of inhomogeneous differential equations for the harmonics of odd order and an equation for the distortion of the fundamental. The latter equation can be solved using the solvability condition that yields the Landau coefficients. All these equations are solved sequentially along with Landau coefficients. This method is known as Stuart-Watson's amplitude

expansion method or Stuart-Watson theory.

Davey (1962), Davey *et al.* (1968) and Eagles (1971) applied Stuart-Watson theory to study the well-known Taylor-Couette problem. Reynolds & Potter (1967) extended and modified amplitude expansion method for three dimensional flows and developed an elegant simplified formalism which involves few functions, represented by equations of the same kind. For incompressible shear flows, it has been shown that the amplitude expansion method is equivalent to the direct methods of deriving the Landau-Stuart equation such as center manifold method (Carr 1981) and multiple scale analysis (Fujimura 1989, 1991) which are described below.

3.1.2 Center Manifold Reduction

In the center manifold reduction technique, the spectra of the linear operator is decomposed into critical (slow/active) modes and noncritical (fast/slave) modes, and the resulting system is then projected onto the center manifold; the eigenvectors of the center/active modes span the center manifold. The underlying assumption is that the time-scales for the fundamental and the slave modes are well separated in that the fundamental/critical/slow mode remains constant over a time-scale during which the slave modes decay to zeros. When the control parameter is very close to its critical value, the above ansatz is likely to hold and the amplitudes of all the slave modes relax on the center manifold. If $\mathscr{A}$ represents an active mode and S denotes the slave modes, then the center manifold, W, is defined as $W = \{(\mathscr{A}, S)|S = S(\mathscr{A}), |\mathscr{A}| < \delta\}$ where δ is a sufficiently small number. The functional relationship $S = S(\mathscr{A})$ can be used to formulate governing equations for nonlinear harmonics generated by the interaction of active modes. The dynamics of an infinite system can be predicted by studying the dynamics of a low-dimensional system, restricted to the center manifold (Carr 1981; Wiggins 1990). On this center manifold, the amplitude of the disturbance satisfies an amplitude equation

$$\frac{\mathrm{d}\mathscr{A}}{\mathrm{d}t} = f(\mathscr{A}), \tag{3.3}$$

where f is a nonlinear function of an active mode. For example, f can be written in the following form

$$f(\mathscr{A}) = \sum_{i=1}^{\infty} c^{(i-1)}\mathscr{A}^i + \text{constant} \tag{3.4}$$

where the coefficients of f involve integrals which are functions of active modes. For the problems with perfect symmetry (i.e. without any imperfection or unfolding, Golubitsky & Schaeffer 1985), $f(\mathscr{A})$ has a normal form

$$f(\mathscr{A}) = c^{(0)}\mathscr{A} + c^{(2)}\mathscr{A}^3 + ... \tag{3.5}$$

With this form of $f(\mathscr{A})$, equation (3.3) is invariant under the transformation $\mathscr{A} \to -\mathscr{A}$. The bifurcation and the dynamics of the system can be studied from the amplitude equation (3.3) which is much simpler than solving the original set of nonlinear partial differential equations.

3.1.3 Multiple Scale Analysis

The multiple scale analysis is based on the separation of scales. Stewartson & Stuart (1971) used two time and length scales to derive a complex Ginzburg-Landau equation to describe aperiodic patterns in plane Poiseuille flow. Weinstein (1981) extended the work of Stewartson & Stuart (1971) and shown its equivalence with Watson's amplitude expansion method. The timescale at which nonlinear terms become dominant over the growth of the fundamental mode is taken to be the inverse of the linear growth rate as argued by Stuart (1960). Here the fast time scale, $\tau_1 = O(1)$, is related to the exponential growth/decay rate of the fundamental mode, and the

slow time scale, $\tau_2 = O(1/\epsilon)$, where ϵ is proportional to the growth/decay rate, is related to the amplitude function (which is equivalent to the ansatz that the perturbation amplitude $\mathscr{A}$ is a slowly varying function of time). Similarly we can introduce a series of slow time scales, τ_n, such that $t_n = O(1/\epsilon^n)$. Using ϵ as a small expansion parameter we can expand perturbation variables as a power series in ϵ and the Landau-Stuart equation for the slowly varying amplitude can be derived from the solvability condition (Fujimura 1989).

Although there are interesting and unresolved issues regarding the uniqueness of the Landau coefficients, the validity of expansion methods and the convergence of the Landau series (Herbert 1980, 1983; Morozov & Saarloos 2007; Becherer *et al.* 2009), the weakly nonlinear analysis is able to predict the local bifurcation whether the flow is subcritical or supercritical near the critical point. Such theoretical predictions have also been confirmed experimentally for the plane Poiseuille flow (Davies & White 1928; Nishioka *et al.* 1975), Taylor-Couette flow (Davey 1962) and Rayleigh-Bénard convection (Busse 1978).

3.1.4 Organization of this Chapter

In this chapter we will develop a weakly nonlinear theory that takes into account the nonlinear interaction between modes of different wave numbers. We follow the amplitude expansion method of Stuart (1960) and Watson (1960) which was later formalized by Reynolds & Potter (1967). This is an indirect method to arrive at Landau-Stuart amplitude equation and the related Landau coefficients are found by using the Fredholm integral or the solvability condition as detailed here. The nonlinear solutions are determined in terms of the basic wave, its distortions and harmonics at various order. We have recently developed an order-parameter theory for the granular plane Couette flow (Shukla & Alam 2009) using the second approach of center-manifold reduction technique. This method has been briefly discussed in chapter 4.

This chapter is presented as follows (see figure 3.1). The mathematical formulation of the problem is given in §3.2. The methodology of the amplitude expansion technique is discussed in §3.3. An spectral-based numerical scheme has been developed to solve the related nonlinear stability problems as detailed in §3.4.

3.2 Nonlinear Perturbation Equations for Granular Flows

Consider a granular flow of smooth, monodisperse, inelastic particles (for example, hard spheres in three dimensional system or hard disks in two dimensional system), obeying a simple collision model, driven by shear, gravity or vibration; for instance, plane Couette flow between two opposite moving walls or gravity driven Poiseuille flow or convection in bounded and unbounded geometry driven by shaking and/or vibration (see chapter 1). The stability of such systems employs granular hydrodynamic equations originated from the kinetic theory with appropriate models for the rheology of the medium as described in chapter 2. We have a set of five balance equations (one mass, three momentum and an energy equation).

The first step to study any problem is the nondimensionalization of the governing equations (balance equations with constitutive relations). Depending on the physical geometry of the system we can define reference length, time and velocity scales. Using these reference scales we can obtain a set of dimensionless balance equations and constitutive relations. The flow whose stability we wish to determine, i.e. the base flow or mean flow (X^0), can be obtained by solving balance equations along with boundary conditions under some assumptions on the flow.

The next step is to determine the disturbance equations by imposing a small disturbance in the base flow as shown schematically in figure 3.2. Upon substituting the base flow plus perturbation terms into the set of governing equations and subtracting the base flow equations,

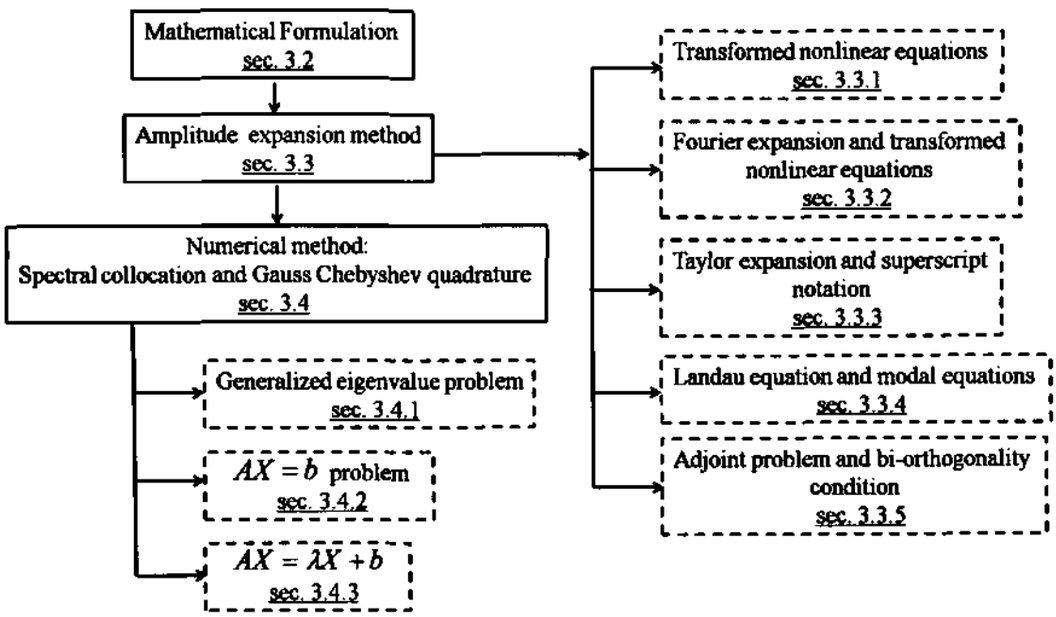

Figure 3.1: Road-map of chapter 3

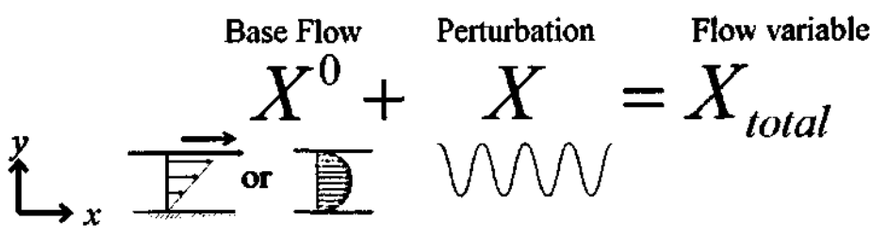

Figure 3.2: Flow decomposition into base flow and finite perturbation, $X^0 + X = X_{total}$.

we get a set of nonlinear disturbance equations. We further assume that the base flow is steady and one-dimensional, i.e. $X^{(0)} \equiv X^{(0)}(y)$. The nonlinear disturbance equations can be expressed in the matrix notation as given below:

$$\left(\frac{\partial}{\partial t} - \mathcal{L}\right) X(x, y, z, t) = \mathcal{N} \tag{3.6}$$

where

$$\mathcal{L} \equiv \mathcal{L}(\partial_x, \partial_y, \partial_z, \partial_x^2, \partial_y^2, \partial_z^2; X^0, \ldots) \tag{3.7}$$

is the linear operator, $X = (\phi', u', v', w', T')$ is the disturbance vector and $\mathcal{N}$ denotes nonlinear terms. Here ϕ', (u', v', w') and T' are the disturbances in volume fraction, velocity components in x-, y- and z-directions, and granular temperature, respectively. Since the granular fluid is compressible, the nonlinearities arise from the inertial terms as well as from the transport coefficients that are nonlinear functions of density and temperature. Note that all the transport coefficients which are the functions of two variables (density and temperature) are expressed in the form of Taylor series around the base state. In most of this thesis, we have considered nonlinear terms up to cubic order

$$\mathcal{N} = \mathcal{N}_2(X, X) + \mathcal{N}_3(X, X), \tag{3.8}$$

where $\mathcal{N}_2$ and $\mathcal{N}_3$ are the vector representations of quadratic and cubic nonlinear terms, respectively. However in chapter 7, we will consider the effect of quartic (N_4) and quintic (N_5) nonlinear terms. The general form of the boundary conditions can be represented as

$$\mathcal{B}X = 0 \quad \text{at} \quad y = \pm 1/2, \tag{3.9}$$

where $\mathcal{B}$ is the boundary operator (for example, no-slip and zero heat flux boundary condition). The explicit forms of $\mathcal{N}$ and $\mathcal{B}$ are not needed to develop the nonlinear theory, but they will be written down explicitly in subsequent chapters (4 to 10) for specific types of perturbations.

In the next section we develop a weakly nonlinear theory of a general granular fluid using amplitude expansion method. All the problems which have been studied in this thesis are particular cases of this general analysis except chapter 4 where we have used another method, namely, the center manifold reduction technique. For a better understanding of the analysis we will give an explicit form of a equation (continuity equation for example) at each step of the procedure.

3.3 Amplitude Expansion Method

Let us consider a flow between two bounded walls (e.g. Couette flow, Poiseuille flow, convection, etc.) as shown in figure 3.3. In this figure x-, y- and z- directions represent the streamwise, gradient and spanwise flow directions, respectively.

In linear theory, we assume infinitesimal disturbances (basic wave) of the form

$$X(x, y, z, t) = X^{[1;1]}(y) e^{i(k_x x + k_z z + \omega t)} e^{at}, \tag{3.10}$$

where X is a disturbance vector as defined in the previous section, $a + i\omega$ is the complex eigenvalue; e^{at} is the amplitude of the basic wave with 'a' denoting its growth rate, and ω is the frequency of the basic wave. Here, k_x and k_z are the streamwise and spanwise wavenumbers, respectively. The superscript notation on the amplitude, $X^{[1;1]}$, of the linear eigenfunction will be clarified later. The flow is linearly unstable or stable or neutrally-stable if a is positive or negative or zero, respectively. In nonlinear stability, the amplitude of the disturbance, $A(t)$, is finite and time dependent which is taken to be the counterpart of the real exponential term in (3.10), i.e. $A(t) = e^{at}$; moreover, the frequency of the basic wave, ω, is allowed to depend on the disturbance amplitude, i.e. $\omega \equiv \omega(A)$. Because of the absence of nonlinear terms in linear theory,

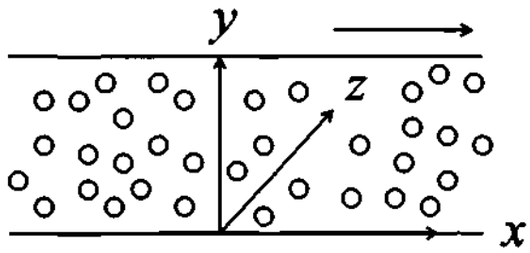

Figure 3.3: Schematic for the coordinate system in the flow

any result, for example eigenfunctions, is independent of the amplitude of the disturbance and hence the amplitude of disturbance is infinitesimally small.

3.3.1 Transformed Nonlinear Equations

Let us use the following transformation (Reynolds & Potter 1967)

$$\theta = k_x x + k_z z + \omega t, \quad \omega = \omega(A) \quad \text{and} \quad A = A(t) \tag{3.11}$$

where $A(t)$ is the "real" amplitude of the disturbance such that $A(t) = e^{\alpha t}$ for infinitesimal disturbances in the linear theory. The following fact is embodied in the above transformation: the growth rate and frequency will change with the *finite* size of the perturbation. Therefore, the partial time derivative can be transformed into

$$\frac{\partial}{\partial t} \rightarrow \frac{\mathrm{d}A}{\mathrm{d}t}\frac{\partial}{\partial A} + \left[\omega + \frac{\mathrm{d}\omega}{\mathrm{d}A}\left(t\frac{\mathrm{d}A}{\mathrm{d}t}\right)\right]\frac{\partial}{\partial \theta}. \tag{3.12}$$

This transformation is equivalent to a two time-scale transformation where the first term in (3.12) represents a slow time-scale (which implies that the perturbation amplitude $A(t)$ is a slowly varying function of time) and the second term represents a fast time-scale. The spatial derivatives are transformed accordingly:

$$\frac{\partial}{\partial x} \rightarrow k_x\frac{\partial}{\partial \theta}, \quad \frac{\partial}{\partial z} \rightarrow k_z\frac{\partial}{\partial \theta}, \tag{3.13}$$

$$\frac{\partial^2}{\partial x^2} \rightarrow k_x^2\frac{\partial^2}{\partial \theta^2}, \quad \frac{\partial^2}{\partial z^2} \rightarrow k_z^2\frac{\partial^2}{\partial \theta^2}. \tag{3.14}$$

The above transformation (3.12)-(3.14) is then inserted into the disturbance equations (3.6). As an illustration, let us consider a disturbance equation for the balance of mass:

$$\frac{\partial \phi'}{\partial t} = -\left[u^0\frac{\partial \phi'}{\partial x} + \phi^0\frac{\partial u'}{\partial x} + \left(\phi_y^0 + \phi^0\frac{\partial}{\partial y}\right)v' + \phi^0\frac{\partial w'}{\partial z}\right] - \left[\frac{\partial(\phi' u')}{\partial x} + \frac{\partial(\phi' v')}{\partial y} + \frac{\partial(\phi' w')}{\partial z}\right] \tag{3.15}$$

where u^0 and ϕ^0 are the base state velocity (streamwise) and density, respectively; and ϕ_y^0 is a derivative of ϕ^0 with respect to y. Equation (3.15) is transformed into:

$$\frac{\mathrm{d}A}{\mathrm{d}t}\frac{\partial \phi'}{\partial A} + \left[\omega + \frac{\mathrm{d}\omega}{\mathrm{d}A}\left(t\frac{\mathrm{d}A}{\mathrm{d}t}\right)\right]\frac{\partial \phi'}{\partial \theta} = -u^0 k_x \frac{\partial \phi'}{\partial \theta} - \phi^0 k_x \frac{\partial u'}{\partial \theta} - \left(\phi_y^0 + \phi^0 \frac{\partial}{\partial y}\right) v' - \phi^0 k_z \frac{\partial w'}{\partial \theta}$$
$$-k_x\left[\phi'\frac{\partial u'}{\partial \theta} + u'\frac{\partial \phi'}{\partial \theta}\right] - \left[\phi'\frac{\partial v'}{\partial y} + v'\frac{\partial \phi'}{\partial y}\right] - k_z\left[\phi'\frac{\partial w'}{\partial \theta} + w'\frac{\partial \phi'}{\partial \theta}\right]. \tag{3.16}$$

The rest of the disturbance equations are transformed accordingly. All disturbance equations can then be written in a compact form:

$$\left[\mathcal{M}(\partial_A, \partial_\theta; \omega) - \mathcal{L}(\partial_y, \partial_y^2, \partial_\theta, \partial_\theta^2; \phi^0, \ldots)\right] X \;=\; \mathcal{N}. \tag{3.17}$$

Here

$$\mathcal{L} \equiv \mathcal{L}(\partial_y, \partial_y^2, \partial_\theta, \partial_\theta^2; \phi^0, \ldots) \tag{3.18}$$

is the linear stability operator and $\mathcal{M}$ is a diagonal operator

$$\mathcal{M} = \left[\frac{\mathrm{d}A}{\mathrm{d}t}\frac{\partial}{\partial A} + \left(\omega + \frac{\mathrm{d}\omega}{\mathrm{d}A}\left(t\frac{\mathrm{d}A}{\mathrm{d}t}\right)\right)\frac{\partial}{\partial \theta}\right]\mathbf{I} \tag{3.19}$$

with $\mathbf{I}$ being the identity operator.

3.3.2 Fourier Expansion and Transformed Nonlinear Equations

To solve (3.17), now we look for solutions $X = X(y, A, \theta)$ in terms of the wall-normal distance (y), the amplitude of perturbation (A) and the instantaneous position in the cycle of the basic wave (θ). It is verified that the coefficients of transformed disturbances equations (3.17) and boundary conditions do not depend explicitly on θ, therefore the transformed equations (3.17) are translational invariant in θ. Consequently, the solution can be expressed in terms of Fourier expansion

$$X(y, A, \theta) \;=\; X^{(k)}(y, A)\, e^{ik\theta} + \tilde{X}^{(k)}(y, A)\, e^{-ik\theta}, \tag{3.20}$$

where the summation is taken over all positive integers $k \geq 0$, and the tilde over any quantity denotes its complex conjugate. This Fourier expansion (3.20) incorporates the fact, as mentioned before, that the finite-size of the perturbation will change both the frequency ($\sim \theta$ as embodied in the exponential term in (3.20)) and the growth rate ($\sim A$ as embodied in the amplitude function in (3.20)) of the perturbation.

Substituting (3.20) into the nonlinear perturbation equations (3.17) and collecting the coefficients of $e^{ik\theta}$, we obtain an infinite set of coupled non-linear partial differential equations for each Fourier coefficient $X^{(k)}$, $k = 0, 1, 2, \ldots$. The matrix representation of these equations for $X^{(k)}(y, A) = (\phi^{(k)}, u^{(k)}, v^{(k)}, w^{(k)}, T^{(k)})^{Tr}$ can be written as:

$$\left(\mathcal{M}^{(k)} - \mathcal{L}(\partial_y, \partial_y^2, ik, -k^2; \phi^0, \ldots)\right) X^{(k)} \;=\; \mathcal{N} \tag{3.21}$$

where $\mathcal{M}^{(k)}$ is

$$\mathcal{M}^{(k)} \equiv \mathcal{M}(\partial_A, ik; \omega) = \left[\frac{\mathrm{d}A}{\mathrm{d}t}\frac{\partial}{\partial A} + \left(\omega + \frac{\mathrm{d}\omega}{\mathrm{d}A}\left(t\frac{\mathrm{d}A}{\mathrm{d}t}\right)\right) ik\right]\mathbf{I}. \tag{3.22}$$

The boundary conditions (3.9) are transformed into

$$\mathcal{B}X^{(k)} = 0 \quad \text{at} \quad y = \pm 1/2. \tag{3.23}$$

Thus equation (3.16) can be written in the following form,

$$\frac{\mathrm{d}A}{\mathrm{d}t}\frac{\partial\phi^{(k)}}{\partial A}+\left[\omega+\frac{\mathrm{d}\omega}{\mathrm{d}A}\left(t\frac{\mathrm{d}A}{\mathrm{d}t}\right)\right]ik\frac{\partial\phi^{(k)}}{\partial\theta}=-u^0ikk_x\phi^{(k)}-\phi^0ikk_xu^{(k)}-\left(\phi^0_y+\phi^0\frac{\partial}{\partial y}\right)v^{(k)}$$
$$-\phi^0ikk_zw^{(k)}-\frac{k_x}{1+\delta_{k0}}\left[\phi^{(k-j)}ijv^{(j)}+\tilde{\phi}^{(j)}i(k+j)u^{(k+j)}-\phi^{(k+j)}ij\tilde{u}^{(j)}\right.$$
$$\left.+u^{(k-j)}ij\phi^{(j)}+\tilde{u}^{(j)}i(k+j)\phi^{(k+j)}-u^{(k+j)}ij\tilde{\phi}^{(j)}\right]$$
$$-\frac{1}{1+\delta_{k0}}\left[\phi^{(k-j)}\frac{\partial v^{(j)}}{\partial y}+\tilde{\phi}^{(j)}\frac{\partial v^{(k+j)}}{\partial y}+\phi^{(k+j)}\frac{\partial\tilde{v}^{(j)}}{\partial y}\right.$$
$$\left.+v^{(k-j)}\frac{\partial\phi^{(j)}}{\partial y}+\tilde{v}^{(j)}\frac{\partial\phi^{(k+j)}}{\partial y}+v^{(k+j)}\frac{\partial\tilde{\phi}^{(j)}}{\partial y}\right]$$
$$-\frac{k_z}{1+\delta_{k0}}\left[\phi^{(k-j)}ijw^{(j)}+\tilde{\phi}^{(j)}i(k+j)w^{(k+j)}-\phi^{(k+j)}ij\tilde{w}^{(j)}\right.$$
$$\left.+w^{(k-j)}ij\phi^{(j)}+\tilde{w}^{(j)}i(k+j)\phi^{(k+j)}-w^{(k+j)}ij\tilde{\phi}^{(j)}\right] \tag{3.24}$$

where $j\geq 0$. Due to the nonlinear interaction/coupling of different Fourier modes, the solution to the infinite set of partial differential equations (3.21) is difficult to ascertain. Focusing on small-amplitude (but finite) waves, a power series solution in the amplitude A can be sought. This procedure amounts to choosing a variable separable solution in terms of a Taylor series in perturbation amplitude which, in turn, helps to decouple the coupled system of nonlinear equations (3.21).

3.3.3 Taylor Expansion and Superscript Notation

When the nonlinearities of governing equations are taken into account, the perturbation interacts (*i*) with itself, (*ii*) its complex conjugate and (*iii*) its higher-order harmonics, leading to the generation of harmonics and the corrections/distortions of various order in the amplitude of perturbation. We require that the nonlinear problem for *infinitesimal* amplitudes ($A\to 0$) should reduce to the linear problem; here $O(A)$ terms denotes the fundamental mode (linear eigenfunction), $O(1)$ denotes the mean flow, $O(A^2)$ consists of the second harmonic ($k=2$) as well as the distortion of the mean flow ($k=0$). The fundamental mode interacting (*i*) with itself and (*ii*) its complex conjugate leads to the generation of (*i*) the second harmonic and (*ii*) a distortion of the mean-flow, respectively, both of $O(A^2)$. Similarly, the interaction of (*ia*) the fundamental mode with the second harmonic and (*ib*) of three fundamental modes generate the third harmonic ($k=3$), and (*ii*) the interaction of the fundamental with the distortion of the mean flow leads to the generation of the distortion of the fundamental mode ($k=1$), all three are of $O(A^3)$. The above physical considerations suggest the following power series expansion for the perturbation vector

$$X^{(k)}(A,y)=A^nX^{[k;n]}(y),\quad \text{with}\quad k\geq 0,\ n\geq 1, \tag{3.25}$$

where $X^{[k;n]}(y)=(\phi^{[k;n]},u^{[k;n]},v^{[k;n]},w^{[k;n]},T^{[k;n]})^{Tr}$ represents the spatially varying amplitude functions. We have followed Reynolds & Potter (1967) to identify the superscript notations and their bounds as indicated below:

$$(n)\ \Rightarrow\ n\geq 0;\quad [n]\ \Rightarrow\ n\geq 1;\quad \{n\}\ \Rightarrow\ n\geq 2;\quad n;m\ \Rightarrow\ n\leq m \tag{3.26}$$

$$[k;n]\ \Rightarrow\ n\geq k,\ k\geq 0,\ n\geq 1 \tag{3.27}$$

$$\{k;n\}\ \Rightarrow\ n\geq k,\ k\geq 1,\ n\geq 2 \tag{3.28}$$

Note that the negative indices are not permitted and the lower bound on any index is greater than or equal to zero, depending on the type of the bracket/delimiter, ( ) or { } or [ ]. The last item in (3.26) asserts that a punctuation (semicolon) puts a limit on the first index which is bounded its second index.

In the dual superscript notation for $X^{[k;n]}$ in (3.25), the first index (k) refers to a particular Fourier mode and the second index (n) indicates the order of a particular term as $O(A^n)$. To clarify this, let us consider the Taylor series expansion of the first three Fourier coefficients:

$$\left.\begin{array}{rcl} X^{(1)}(y,t) & = & A(t)\left(X^{[1;1]}(y) + A(t)^2 X^{[1;3]}(y) + \ldots\right) \\ X^{(0)}(y,t) & = & A(t)^2\left(X^{[0;2]}(y) + A(t)^2 X^{[0;4]}(y) + \ldots\right) \\ X^{(2)}(y,t) & = & A(t)^2\left(X^{[2;2]}(y) + A(t)^2 X^{[2;4]}(y) + \ldots\right) \end{array}\right\}. \tag{3.29}$$

The leading term of the first ($k = 1$) Fourier coefficient $X^{(k=1)}$ is $AX^{[1;1]}$ which is of order $O(A^{n=1})$, representing the fundamental mode; the next-order term in $X^{(k=1)}$, $A^3X^{[1;3]}$, represents the first correction/distortion to the fundamental mode and is of order $O(A^3)$, and $X^{[1;3]}$ is dubbed the distortion of the fundamental. The zeroth ($k = 0$) Fourier coefficient $X^{(k=0)}$ is related to the base/mean flow (which in our double index superscript notation would be $X^{[0;0]}(y) \equiv (\phi^0, u^0, v^0, w^0, T^0)^{Tr}$). Therefore, the leading term in $X^{(0)}$, $A^2X^{[0;2]}$, represents the distortion of the mean flow and the rest being its subsequent higher-order corrections. Similarly, the leading term of the second Fourier coefficients $X^{(k=2)}$ is $A^2X^{[2;2]}$ which is the second harmonic and the rest its subsequent higher-order corrections. It is clear from the arguments in the first paragraph and equation (3.29) that

$$X^{[k;n]} = 0, \quad \text{for odd} \quad (k+n) \tag{3.30}$$

in the power series expansion (3.25).

The above superscript bracket notations (Reynolds & Potter 1967) are extremely useful to simplify the algebra as well as to identify a particular mode (i.e. a fundamental or a harmonic of particular order) and its modal interactions of any order.

3.3.4 Landau Equation and Modal Equations for $X^{[k;n]}$

From the requirement that $A(t)$ be proportional to e^{at} ($a = a^{(0)}$) as $A \to 0$ it follows that

$$\frac{1}{A}\frac{\mathrm{d}A}{\mathrm{d}t} \to a^{(0)} \text{ as } A \to 0. \tag{3.31}$$

This is the well-known limit of infinitesimal disturbances in linear stability theory. Since the amplitude for infinitesimal A must behave as in linear theory (i.e. grow/decay exponentially), we can write $\frac{1}{A}\frac{\mathrm{d}A}{\mathrm{d}t}$ as a power series in A:

$$A^{-1}\frac{\mathrm{d}A}{\mathrm{d}t} = a^{(0)} + Aa^{(1)} + A^2a^{(2)} + \cdots = A^n a^{(n)}, \tag{3.32}$$

where $a^{(0)}$ is an eigenvalue (growth rate) from the linear theory. Similarly, we can write an expression for the terms involving frequency ω,

$$\frac{\partial\theta}{\partial t} = \omega + \frac{\mathrm{d}\omega}{\mathrm{d}A}\left(t\frac{\mathrm{d}A}{\mathrm{d}t}\right) = b^{(0)} + Ab^{(1)} + A^2b^{(2)} + \cdots = A^n b^{(n)}, \tag{3.33}$$

where $b^{(0)}$ is an eigenvalue (frequency) from the linearized theory.

It is clear that the Landau equation is *postulated* to hold in the present formalism of amplitude expansion method (Stuart 1960; Watson 1960; Reynolds & Potter 1967). This is in contrast to the center manifold reduction (Carr 1981) wherein the Landau equation is derived from the evolution

equation of the slow mode by taking its inner product with the adjoint linear eigenfunction (cf. chapter 4, Shukla & Alam 2009). This is one of the main differences between the "direct" method of center manifold reduction and the "indirect" method of amplitude expansion technique. The center manifold reduction is discussed in chapter 4.

Let us insert (3.25), (3.32) and (3.33) into equation (3.24) and equate the coefficients of A^n to obtain:

$$(ma^{(n-m)} + ikb^{(n-m)})\phi^{[k;m]} = -u^0 ikk_x\phi^{[k;n]} - \phi^0 ikk_x u^{[k;n]} - \left(\phi_y^0 + \phi^0\frac{\partial}{\partial y}\right)v^{[k;n]}$$
$$-\phi^0 ikk_z w^{[k;n]} + \mathrm{NL} \tag{3.34}$$

where

$$\mathrm{NL} = -\frac{k_x}{1+\delta_{k0}}\left[\phi^{k-j;n-m]}ijv^{[j;m]} + \tilde{\phi}^{[j;n-m]}i(k+j)u^{[k+j;m]} - \phi^{[k+j;n-m]}ij\tilde{u}^{[j;m]}\right.$$
$$\left.+u^{[k-j;n-m]}ij\phi^{[j;m]} + \tilde{u}^{[j;n-m]}i(k+j)\phi^{[k+j;m]} - u^{[k+j;n-m]}ij\tilde{\phi}^{[j;m]}\right]$$
$$-\frac{1}{1+\delta_{k0}}\left[\phi^{[k-j;n-m]}\frac{\partial v^{[j;m]}}{\partial y} + \tilde{\phi}^{[j;n-m]}\frac{\partial v^{[k+j;m]}}{\partial y} + \phi^{[k+j;n-m]}\frac{\partial \tilde{v}^{[j;m]}}{\partial y}\right.$$
$$\left.+v^{[k-j;n-m]}\frac{\partial \phi^{[j;m]}}{\partial y} + \tilde{v}^{[j;n-m]}\frac{\partial \phi^{[k+j;m]}}{\partial y} + v^{[k+j;n-m]}\frac{\partial \tilde{\phi}^{[j;m]}}{\partial y}\right]$$
$$-\frac{k_z}{1+\delta_{k0}}\left[\phi^{[k-j;n-m]}ijw^{[j;m]} + \tilde{\phi}^{[j;n-m]}i(k+j)w^{[k+j;m]} - \phi^{[k+j;n-m]}ij\tilde{w}^{[j;m]}\right.$$
$$\left.+w^{[k-j;n-m]}ij\phi^{[j;m]} + \tilde{w}^{[j;n-m]}i(k+j)\phi^{[k+j;m]} - w^{[k+j;n-m]}ij\tilde{\phi}^{[j;m]}\right]. \tag{3.35}$$

Equation (3.34) can be reexpressed as

$$(na^{(0)} + ikb^{(0)})\phi^{[k;n]} = -(ma^{[n-m]} + ikb^{[n-m]})\phi^{[k;m]} - u^0 ikk_x\phi^{[k;n]} - \phi^0 ikk_x u^{[k;n]}$$
$$-\left(\phi_y^0 + \phi^0\frac{\partial}{\partial y}\right)v^{[k;n]} - \phi^0 ikk_z w^{[k;n]} + \mathrm{NL}. \tag{3.36}$$

Finally we can write above equation in the following equivalent form

$$(na^{(0)} + ikb^{(0)})\phi^{[k;n]} = -(a^{[n-1]} + ikb^{[n-1]})\phi^{[k;1]} - (ma^{[n-m]} + ikb^{[n-m]})\phi^{\{k;m\}}$$
$$-u^0 ikk_x\phi^{[k;n]} - \phi^0 ikk_x u^{[k;n]} - \left(\phi_y^0 + \phi^0\frac{\partial}{\partial y}\right)v^{[k;n]} - \phi^0 ikk_z w^{[k;n]} + \mathrm{NL}, \tag{3.37}$$

or

$$(na^{(0)} + ikb^{(0)})\phi^{[k;n]} = -(a^{[n-1]} + ib^{[n-1]})\phi^{[1;1]}\delta_{k1} - (ma^{[n-m]} + ikb^{[n-m]})\phi^{\{k;m\}}$$
$$-u^0 ikk_x\phi^{[k;n]} - \phi^0 ikk_x u^{[k;n]} - \left(\phi_y^0 + \phi^0\frac{\partial}{\partial y}\right)v^{[k;n]} - \phi^0 ikk_z w^{[k;n]} + \mathrm{NL}. \tag{3.38}$$

Similarly we reduce all the disturbance equations in this form.

In general, inserting (3.25), (3.32) and (3.33) into equation (3.21) and equating the coefficients of A^n we get an infinite set of inhomogeneous equations [viz. (3.34), (3.36) and (3.37)] for $X^{[k;n]} = [\phi^{[k;n]}, u^{[k;n]}, v^{[k;n]}, w^{[k;n]}, T^{[k;n]}]^{Tr}$:

$$\left.\begin{array}{lcl} \mathbf{L}_{kn}X^{[k;n]} & = & -c^{[n-1]}X^{[1;1]}\delta_{k1} + \mathbf{G}_{kn} \\ c^{[n-1]} & = & a^{[n-1]} + ib^{[n-1]} \\ \mathbf{G}_{kn} & = & -\left(ma^{[n-m]} + ikb^{[n-m]}\right) X^{\{k;m\}} + \mathbf{E}_{kn}/(1+\delta_{k0}) + \mathbf{F}_{kn} \\ \mathbf{L}_{kn} & = & \left(na^{(0)} + ikb^{(0)}\right)\mathbf{I} - \mathbf{L}_k \\ \mathbf{L}_k & = & \mathcal{L}(\partial/\partial x \to ikk_x, \partial/\partial y \to d/dy, \partial/\partial z \to ikk_z) \end{array}\right\}, \tag{3.39}$$

where $\mathbf{L}_{kn}$ and $\mathbf{L}_k$ are the linear operators, $c^{[n-1]}$'s are the Landau coefficients, $\mathbf{G}_{kn}$ represents a sum of linear and nonlinear (quadratic and cubic) terms, and δ_{kj} is the Kronecker delta; for superscript notations on terms in the above equation, see (3.26)-(3.28). In (3.39), the factor $1/(1+\delta_{k0})$ with $\mathbf{E}_{kn}$ arises from the product of two Fourier series in which the zeroth order terms are multiplied by a factor 2; $\mathbf{F}_{kn}$ represents cubic nonlinear terms that arise from the product of three Fourier series. Note that the nonlinear terms $\mathbf{E}_{kn}$ and $\mathbf{F}_{kn}$ are vector valued functions:

$$\mathbf{E}_{kn} = [E^1_{kn}, E^2_{kn}, E^3_{kn}, E^4_{kn}, E^5_{kn}]^{Tr} \quad \text{and} \quad \mathbf{F}_{kn} = [F^1_{kn}, F^2_{kn}, F^3_{kn}, F^4_{kn}, F^5_{kn}]^{Tr}, \tag{3.40}$$

where the superscripts 1, 2, 3, 4 and 5 refer to terms that originate form the continuity, x-momentum, y-momentum, z-momentum and granular energy equations, respectively. Furthermore we can decompose the quadratic nonlinear terms $\mathbf{E}_{kn}$ as

$$\mathbf{E}_{kn} = \mathbf{E}^{\theta}_{kn} + \mathbf{E}^{y}_{kn} \equiv \mathbf{E}^{t}_{kn} + \mathbf{E}^{y}_{kn}, \tag{3.41}$$

where $\mathbf{E}^{\theta}_{kn} = \mathbf{E}^{t}_{kn}$ corresponds to θ-dependent terms that involve time derivatives, and $\mathbf{E}^{y}_{kn}$ corresponds to terms that are y-dependent and their derivatives with respect to y. Note that the term $\mathbf{E}^{t}_{kn}$, corresponding to the time-dependent part of disturbance equations, is the product of a Fourier series and a time-derivative of a Fourier series that involves Landau (3.32). The above system of equations (3.39) is to be solved with following boundary conditions

$$\mathcal{B}X^{[k;n]} = 0 \quad \text{at} \quad y = \pm 1/2. \tag{3.42}$$

Equations (3.39) with boundary conditions (3.42) embody all necessary information for the nonlinear analysis of granular Couette flow as we will discuss in subsequent chapters. We have reduced the nonlinear stability problem, (3.6) and (3.9), into a sequence of linear inhomogeneous differential equations (3.39) for $X^{[k;n]}$ and each of which can be solved sequentially if we know the Landau coefficients $c^{[n-1]}$ along the way. The latter can be obtained using the Fredholm alternative or the solvability condition, which is described below, of inhomogeneous differential equations for the special case when the growth rate is close to zero (weakly nonlinear assumption) as:

$$c^{[n-1]} = a^{[n-1]} + ib^{[n-1]} = \frac{\int_{-1/2}^{1/2} \tilde{X}^{\dagger}\mathbf{G}_{1n}\,\mathrm{d}y}{\int_{-1/2}^{1/2} \tilde{X}^{\dagger}X^{[1;1]}\,\mathrm{d}y}, \tag{3.43}$$

where $X^{\dagger}$ is the adjoint eigenfunction corresponding to the linear problem $\mathbf{L}_{11} = 0$. In the resonance free case, i.e. the weakly nonlinear analysis using a single mode, it is straightforward to verify from (3.30) that $\mathbf{G}_{kn} = 0$ when $(k+n)$ is odd, and hence $c^{(n)}$ vanishes for all *odd* $n = 1, 3, 5, \ldots$.

Table 3.1 shows the nonzero harmonics related to weakly nonlinear analysis. The definition of the Fredholm alternative is given below which we will use frequently in the later chapters.

Fredholm Alternative

A bounded linear operator $L : X \to X$ on a normed linear space X is said to satisfy the Fredholm alternative if L is such that either (1) or (2) holds:

(1) The inhomogeneous equations $Lx = y$ and $L^{\dagger}f = g$ where $L^{\dagger} : X' \to X'$ is the adjoint oper-

	$X^{[0;2]}$		$X^{[0;4]}$	
$X^{[1;1]}$		$X^{[1;3]}$		$X^{[1;5]}$
	$X^{[2;2]}$		$X^{[2;4]}$	
		$X^{[3;3]}$		$X^{[3;5]}$

Table 3.1: Nonzero eigenfunctions

ator of L, have solutions x and f, respectively, for every given $y \in X$ and $g \in X'$, the solutions being unique. The corresponding homogeneous equations $Lx = 0$ and $L^\dagger f = 0$, have only trivial solutions $x = 0$ and $f = 0$, respectively.

(2) The homogeneous equations $Lx = 0$ and $L^\dagger f = 0$ have the same number of linearly independent solutions, $x_1, \ldots x_n$ and $f_1, \ldots f_n$ for $n \geq 1$, respectively. The inhomogeneous equations $Lx = y$ and $L^\dagger f = g$ are not solvable for all y and g, respectively; they have a solution iff y and g are such that

$$\langle f_k, y \rangle = 0 \qquad \text{and} \qquad \langle g, x_k \rangle = 0. \tag{3.44}$$

Note that in the weakly nonlinear analysis we use the second Fredholm alternative that gives an expression for the Landau coefficients (3.43). The condition (3.44) also known as the solvability condition or orthogonality condition. For details, see chapter 8 of Kreyszig (1978).

3.3.5 Adjoint Problem and Bi-orthogonality Condition

At order $O(Ae^{i\theta})$ we get the linear stability problem which can be written as,

$$\mathbf{L}_{11} X^{[1,1]} = 0 \quad \text{or} \quad \mathbf{L}_1 \hat{X} = c^{(0)} \hat{X} \tag{3.45}$$

where $c^{(0)} = a^{(0)} + ib^{(0)}$ is a linear eigenvalue and $\hat{X} = X^{[1,1]}$. The boundary conditions can be represented in matrix form for problem (3.45) as

$$\mathcal{B}\hat{X} = 0 \quad \text{at boundaries.} \tag{3.46}$$

To formulate adjoint eigenvalue problem we need to obtain an adjoint operator corresponding to $\mathbf{L}_1$ and the adjoint boundary conditions related to (3.46). For this we define an inner product such that

$$\langle X^\dagger, \mathbf{L}_1 \hat{X} \rangle = \langle \mathbf{L}^\dagger X^\dagger, \hat{X} \rangle \tag{3.47}$$

where

$$\langle f, g \rangle = \int_{-1/2}^{1/2} [\bar{f}, g] \, dy \tag{3.48}$$

for every complex valued functions $f(y)$ and $g(y)$. The symbol $[x, y]$ means $\sum_j x_j y_j$. For example, we can write $[\hat{X}, \hat{X}] = \hat{\phi}^2 + \hat{u}^2 + \hat{v}^2 + \hat{w}^2 + \hat{T}^2$. Note that the complex conjugation is in the first function of the inner product in (3.48).

Using above inner product (3.48), the adjoint operator $\mathbf{L}_1$ and the adjoint boundary conditions can be derived by using integration by parts. In the matrix notation the adjoint eigenvalue

problem corresponding to (3.45) can be written as

$$\mathbf{L}^{\dagger}X^{\dagger} = c^{(0)}X^{\dagger}, \quad \text{with} \quad B^{\dagger}X^{\dagger} = 0, \quad \text{at boundaries.} \tag{3.49}$$

The eigenvalues of the adjoint problem are complex conjugate of eigenvalues of linear eigenvalue problem. The set of linear eigenvectors are not orthogonal. To solve inhomogeneous set of equations of linear problem we need to find a set which is orthogonal to all the eigenvectors except one (Eckhaus 1965; Schmid & Henningson 2001) and this is called bi-orthogonality condition. Equation (3.47) can be simplified by using (3.45) and (3.49),

$$(c_j^{(0)} - c_k^{(0)})(\hat{X}_k^{\dagger}, \hat{X}_j) = 0. \tag{3.50}$$

The bi-orthogonality condition (see p. 444, Kreyszig 1978) is

$$(\hat{X}_k^{\dagger}, \hat{X}_j) = \begin{cases} 1 & \text{if } j = k \\ 0 & \text{if } j \neq k. \end{cases} \tag{3.51}$$

3.4 Numerical Method: Spectral Collocation and Gauss Chebyshev Quadrature

In the above section we have reduced the nonlinear stability problem to a sequence of system of inhomogeneous linear differential equations for the fundamental mode and its distortions and higher-order harmonics. The general form of this system of equations is

$$\mathbf{L}_{kn}X^{[k;n]} = -c^{[n-1]}X^{[k;n]}\delta_{k1} + \mathbf{G}_{kn}, \quad \text{with} \quad k \geq 0,\ n \geq 1, \tag{3.52}$$

where $\mathbf{L}_{kn}$ is the linear operator, $c^{[n-1]}$ are the Landau coefficients and $\mathbf{G}_{kn}$ denotes the nonlinear terms. We have developed an spectral-based numerical method to solve the above problem and a brief description of this numerical method is given below.

Depending on the particular choice of the index values in (3.52) we can divide numerical method into three categories:

- Type (1) problem: $k = n = 1$,
- Type (2) problem: $k \neq 1$ and $n \geq k$,
- Type (3) problem: $k = 1$, $n > 1$.

Type (1) is an eigenvalue problem, Type (2) and Type (3) are the inhomogeneous problems with or without solvability condition.

3.4.1 Type (1): Generalized Eigenvalue Problem, $AX = cBX$

Substituting $k = n = 1$ into (3.52) we get a generalized eigenvalue problem

$$\mathbf{L}_1 X^{[1;1]} = c^{(0)}X^{[1;1]}. \tag{3.53}$$

For the linear stability problem (3.53), we need to solve the linearized perturbation equations along with homogeneous boundary conditions. All five equations have been discretized along y-direction by implementing the staggered-grid spectral collocation method that uses Chebyshev polynomials (Canuto *et al.* 1988; Mason & Handscomb 2003) as basis set. More specifically, the mass balance equation is collocated at Gauss points and the momentum and energy equations at Gauss-Lobatto points; the interpolation matrices of spectral accuracy are then used to interpolate

between the variables at Gauss (density) and Gauss-Lobatto (velocity and granular temperature) points.

Spectral-Collocation Method using Staggered Grid

Spectral method belongs to the general class of weighted residual methods for which approximations are defined in terms of a truncated series expansion such that error or residual is forced to be zero only in an approximate sense. In the spectral collocation we approximate the unknown variables in terms of the Chebyshev polynomial of degree M:

$$f(\xi) = \sum_{\alpha=0}^{M} a_\alpha T_\alpha(\xi) \tag{3.54}$$

where $T_\alpha(\xi) = \cos(\alpha \cos^{-1}(\xi))$ is the Chebyshev polynomial of degree α. The Chebyshev polynomials are then evaluated at the extrema of the M^{th}-order Chebyshev polynomial, called Gauss-Lobatto points, given by

$$\xi_i = \cos\left(\frac{i\pi}{M}\right) \quad \text{where} \quad i = 0, \ldots, M. \tag{3.55}$$

The coefficients a_α for $\alpha = 1, \ldots, M$, can be determined by imposing the condition that the approximate value of unknown variables, $f(\xi)$, is same as the exact value of the unknown variable at the collocation points (3.55). Therefore the polynomial of degree M defined by (3.54) is same as the Lagrange interpolation polynomial based on the Gauss-Lobatto points (3.55). Hence the unknown variables can be represented as

$$f(\xi) = \sum_{j=0}^{M} \psi_j(\xi) f(\xi_j) \tag{3.56}$$

where the interpolation polynomial is given by

$$\psi_j(\xi) = \frac{(-1)^{j+1}(1-\xi^2)T'_M(\xi)}{c_j M^2(\xi - \xi_j)} \tag{3.57}$$

where $c_0 = c_M = 1$ and $c_j = 2$ for all $0 < j < M$. This expression can be constructed by recalling that the collocation points, ξ_j, are the zeros of the polynomial $(1-\xi^2)T'_M(\xi)$ and by observing that $(1-\xi^2)T'_M(\xi)/(\xi - \xi_j) \to (-1)^{j+1} c_j M^2$ when $\xi \to \xi_j$ for $j = 0, \ldots, M$. Note that $\psi_l(\xi_m) = \delta_{lm}$. The p^{th}-derivative of the unknown variable is

$$f^{(p)}(\xi_i) = \sum_{j=1}^{M} \psi_j^{(p)}(\xi_i) f(\xi_j) = \sum_{j=0}^{M} D_{GL}^{(p)}(i,j) f(\xi_j) \tag{3.58}$$

where $i = 0, \ldots, M$. The explicit expression for the first order derivative (Canuto *et al.* 1988) is

$$D_{GL}^{(1)}(i,j) = \frac{c_i}{c_j} \frac{(-1)^{i+j}}{(\xi_i - \xi_j)}, \quad D_{GL}^{(1)}(i,i) = -\frac{\xi_i}{2(1-\xi_i^2)}, \tag{3.59}$$

$$D_{GL}^{(1)}(0,0) = -D_{GL}^{(1)}(M,M) = (2M^2+1)/6, \tag{3.60}$$

where ξ_i is given by (3.55). The second order derivative can be written as a product of two first

order differentiation matrices,

$$D^{(2)}_{GL}(i,j) = \sum_{k=0}^{M} D^{(1)}_{GL}(i,k) D^{(1)}_{GL}(k,j). \tag{3.61}$$

Here the momentum and energy equations are collocated at the Gauss-Lobatto points. The physical domain in the present problem is $[-1/2, 1/2]$ thus we assume a the transformation $\xi = 2y$ which relates the physical grid variables to computational variables and vice-versa. If the scaling factor for the transformation between physical and computational domains is given as

$$S_i = \left.\frac{d\xi}{dy}\right|_i \quad \text{for} \quad i = 0, \ldots M \tag{3.62}$$

because $\frac{d}{dy} = \frac{d\xi}{dy}\frac{d}{d\xi}$, then the derivative matrix can be written as

$$\overline{\overline{D}}^{(1)}_{GL}(i,j) = S_i D^{(1)}_{GL}(i,j), \tag{3.63}$$

$$\overline{\overline{D}}^{(2)}_{GL}(i,j) = \overline{\overline{D}}^{(1)}_{GL}(i,j)\overline{\overline{D}}^{(1)}_{GL}(i,j). \tag{3.64}$$

In the "staggered-grid" spectral collocation method, the continuity equation is collocated at the Gauss points, $\xi_{i+1/2}$, which are the zeros of the Chebyshev polynomial

$$\xi_{i+1/2} = \cos\left(i + \frac{1}{2}\right)\frac{\pi}{M}, \quad i = 0, \ldots M-1. \tag{3.65}$$

This set of points (3.65) does not contain the boundary points and since we do not have any boundary condition for density (or volume fraction), ϕ, it is appropriate to use staggered grid in which the continuity equation is collocated at the Gauss points (3.65), and the momentum and energy equations at the Gauss-Lobatto points (3.55) as shown in figure 3.4. Following the similar approach we can express density or volume fraction in terms of a interpolation polynomial of degree $M-1$

$$\phi(\xi) = \sum_{j=1}^{M-1} \mathcal{G}_j(\xi)\phi(\xi_{j+1/2}). \tag{3.66}$$

The construction of the interpolation polynomial for Gauss points, $\mathcal{G}_j(\xi)$, is the same as the polynomial for Gauss-Lobatto points ($\psi_j(\xi)$) which is based on the Lagrange polynomial. The expression for $\mathcal{G}_j(\xi)$ is given by

$$\mathcal{G}_j(\xi) = \frac{T_M(\xi)}{(\xi - \xi_j)T'_M(\xi_j)} = \frac{(-1)^j\sqrt{(1-\xi_j^2)}T_M(\xi)}{M(\xi - \xi_j)} \tag{3.67}$$

where we have used $T'_M(\xi_j) = (-1)^j M/\sqrt{(1-\xi_j^2)}$. Note that $\mathcal{G}_j(\xi_{k+1/2}) = \delta_{jk}$.

The p^{th}-derivative of the density is

$$\left.\frac{d^{(p)}\phi(\xi)}{d\xi}\right|_{i+1/2} = \phi^{(p)}(\xi_{i+1/2}) = \sum_{j=0}^{M-1} \mathcal{G}^{(p)}_j(\xi_{i+1/2})\phi(\xi_{j+1/2}) = \sum_{j=0}^{M-1} D^{(p)}_G(i,j)\phi(\xi_{j+1/2}) \tag{3.68}$$

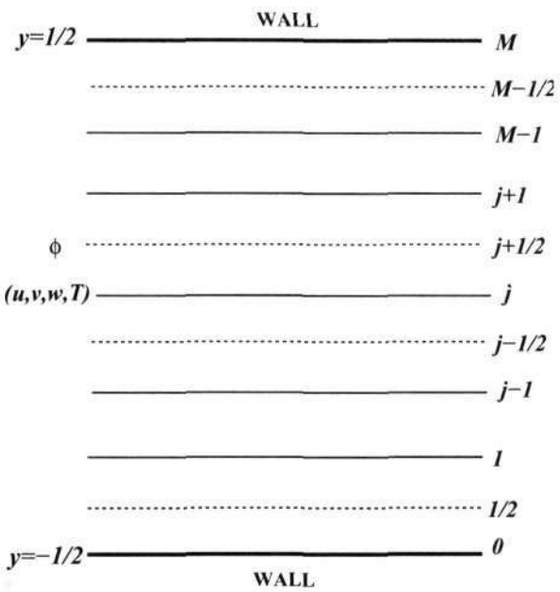

Figure 3.4: Schematic of staggered grid.

where $i = 0, \ldots, M-1$. The explicit expression for the first order derivative is

$$\left.\begin{aligned} D_G^{(1)}(i,j) &= \frac{(-1)^{i+j}}{(\xi_{i+1/2} - \xi_{j+1/2})}\sqrt{\frac{1-\xi_{j+1/2}^2}{1-\xi_{i+1/2}}} \quad \text{for } i \neq j, \\ D_G^{(1)}(i,i) &= \frac{\xi_{i+1/2}}{2(1-\xi_{i+1/2}^2)} \end{aligned}\right\}, \tag{3.69}$$

where $\xi_{i+1/2}$ is given by (3.65). The second order derivative can be obtained by the product of two first order differentiation matrices,

$$D_G^{(2)}(i,j) = \sum_{k=0}^{M-1} D_G^{(1)}(i,k) D_G^{(1)}(k,j). \tag{3.70}$$

The derivative matrix for Gauss points (3.69)-(3.70) in the physical domain can be written as

$$\overline{\overline{D}}_G^{(1)}(i,j) = S_i D_G^{(1)}(i,j), \tag{3.71}$$

$$\overline{\overline{D}}_G^{(2)}(i,j) = \overline{\overline{D}}_G^{(1)}(i,j)\overline{\overline{D}}_G^{(1)}(i,j). \tag{3.72}$$

We know the velocity (u, v, w) and temperature T at Gauss-Lobatto points (3.55) and density at the Gauss points (3.65). While discretizing continuity equation at Gauss points we need to know other variables ((u, v, w) and T) at Gauss points; similarly the discretization of momentum and energy equations at Gauss-Lobatto points requires the density at Gauss-Lobatto points. For this we construct an interpolation polynomial from Gauss variables to Gauss-Lobatto variables

and vice-versa, as given below

$$f(\xi_{i+1/2}) = \sum_{j=0}^{M} \psi_j(\xi_{i+1/2}) f(\xi_j) \quad \text{for } i = 0, \ldots M-1, \tag{3.73}$$

$$\phi(\xi_i) = \sum_{j=0}^{M-1} \mathcal{G}_j(\xi_i) \phi(\xi_{j+1/2}) \quad \text{for } i = 0, \ldots M, \tag{3.74}$$

where $\psi_j(\xi_{i+1/2})$ is the interpolation matrix of order $M-1$ by M, from Gauss-Lobatto point to Gauss point; and $\mathcal{G}_j(\xi_i)$ is the interpolation matrix of order M by $M-1$, from Gauss point to Gauss-Lobatto point. The interpolation matrix can be written as

$$\psi_j(\xi_{i+1/2}) = \frac{(-1)^{j+1}(1-\xi_{i+1/2}^2) T'_M(\xi_{i+1/2})}{c_j M^2 (\xi_{i+1/2} - \xi_j)} = \frac{(-1)^{i+j+1}\sqrt{1-\xi_{i+1/2}^2}}{c_j M (\xi_{i+1/2} - \xi_j)} \tag{3.75}$$

where we have used the following equality

$$T'_M(\xi_{i+1/2}) = \frac{M \sin M(\cos^{-1}\xi_{i+1/2})}{\sin(\cos^{-1}\xi_{i+1/2})} = \frac{M \sin(i+1/2)\pi}{\sqrt{1-\cos^2(\cos^{-1}\xi_{i+1/2})}} = \frac{M(-1)^i}{\sqrt{1-\xi_{i+1/2}^2}}. \tag{3.76}$$

Similarly the interpolation matrix from Gauss points to Gauss-Lobatto points can be written as

$$\mathcal{G}_j(\xi_i) = \frac{(-1)^j \sqrt{(1-\xi_j^2)} T_M(\xi_i)}{M(\xi_i - \xi_j)} = \frac{(-1)^{j+i}\sqrt{(1-\xi_j^2)}}{M(\xi_i - \xi_j)} \tag{3.77}$$

where we have used $T_M(\xi_i) = (-1)^i$.

We replace all the derivatives in the continuity, momentum and energy equations by the spectral derivatives. The continuity equation is collocated at Gauss points (3.65) which uses the interpolated velocity and temperature fields (3.75) from the Gauss-Lobatto points (3.55) to Gauss points (3.65). Similarly, the momentum and energy equations are collocated at Gauss-Lobatto points (3.55) which take interpolated density fields (3.77) from Gauss (3.65) to Gauss-Lobatto points (3.55).

The discretized form of perturbation equations (3.53) are formulated as a generalized matrix eigenvalue problem (Golub & Van-Loan 1983) of the form

$$\mathbf{A} X^{[1;1]} = c \mathbf{B} X^{[1;1]}, \tag{3.78}$$

where $c = c^{(0)}$ is the linear eigenvalue and $X^{[1;1]}$ is the discrete representation of linear eigenfunction; $\mathbf{A}$ and $\mathbf{B}$ are square matrices of order $(5M+4)$ where M denotes the degree of the Chebyshev polynomial.

Implementation of Boundary Conditions

We have chosen 2^{nd} to 5^{th} and $(5M+4)^{th}$ to $(5M-1)^{th}$ rows which corresponds to no-slip $[(u,v,w) = 0$ at $y \pm 1/2]$ and zero heat flux $[dT/dy = 0$ at $y = \pm 1/2]$ boundary conditions. The matrix $\mathbf{B}$ of the generalized eigenvalue problem (3.78) does not contain boundary conditions, thus, this matrix is singular. While computing eigenvalues using QZ-algorithm, we need to avoid the spurious modes associated with the boundary conditions. Below we are describing few methods for removing the singularity of $\mathbf{B}$ and spurious modes.

In the first method, we replace the boundary rows of **A** with the discretized boundary conditions and the same rows of matrix **B** can be replaced by a complex multiple of the corresponding rows of **A**. The spurious modes associated with the boundary conditions can be mapped to an arbitrary location in the complex plane by selecting an appropriate value of a complex multiple. Schmid & Henningson (2001) used a complex multiple, $-200\sqrt{-1}$, for solving the generalized eigenvalue problem for Poiseuille flow (see Appendix A.6, p 492 of Schmid & Henningson (2001)). It is also verified that this works for the present problem too.

Another way is to replace the boundary rows of **A** and the corresponding rows of **B** with discretized boundary conditions. The resulting generalized eigenvalue problem with boundary conditions can be solved by QZ-algorithm of Matlab software. The eigenvalues corresponding to the boundary conditions result into spurious modes with large growth rate (for example $c_r \sim O(10^{16})$), in order to get correct spectrum we need to avoid such modes which can be done by projecting these spurious modes on to the stable regions.

The singularity of matrix **B** can be removed by using row and column operations which reduces the rank of the matrix **A** and **B**. The resultant order of the matrix is $(5M - 4)$. This is the widely used method to remove the singularity associated with the eigenvalue problem (Khorrami *et al.* 1989; Malik 1990; Alam & Nott 1998). The resultant order of the matrix is $(5M - 4)$ which can be solved by QZ-algorithm.

Normalization

The eigenvectors $X^{[1;1]}$ are normalized by dividing it by a component of the vector $X^{[1;1]}$ having maximum absolute value.
Another part of the linear stability problem is to solve the associated adjoint system (3.49). Using the same spectral method, the adjoint system has been discretized and solved for the adjoint eigenfunction $X^\dagger$ and its adjoint eigenvalue $c^\dagger = \tilde{c}$. Recall that the adjoint eigenfunction is used in the solvability condition to calculate the Landau coefficients (3.43).

3.4.2 Type (2): $AX = b$ Problem ($k \neq 1, n \geq k$)

The general form of equation for $k \neq 1, n \geq k$ [viz. (3.52)] is given as

$$\mathbf{L}_{kn} X^{[k;n]} = \mathbf{G}_{kn}. \tag{3.79}$$

Similar to the linear eigenvalue problem, the higher-order inhomogeneous system of differential equations (3.79) are discretized using the same staggered-grid spectral collocation method as explained above where the continuity equation is evaluated at Gauss points and the other equations are at Gauss-Lobatto points. The resulting square matrix A in $AX = b$ turns out to be dense, unstructured, unsymmetric and ill-conditioned; thus the method of Gaussian elimination is not a good choice to solve these algebraic equations. We employed the method of singular value decomposition (Golub & Van-Loan 1983; Press *et al.* 1992; Trefethen & Bau 1997) for solving $AX = b$ system.

3.4.3 Type (3): $AX = \lambda X + b$ Problem ($k = 1, n > 1$)

The general form for the Type (3) problem is

$$\mathbf{L}_{1n} X^{[1;n]} = -c^{[n-1]} X^{[1;1]} + \mathbf{G}_{1n}. \tag{3.80}$$

The first part of nonlinear computations in (3.80) is related to evaluate the solvability condition (3.43) to determine the first Landau coefficient: this is a ratio of two definite integrals, as given

below

$$c^{[n-1]} = a^{[n-1]} + ib^{[n-1]} = \frac{\int_{-1/2}^{1/2} \tilde{X}^{\dagger}\mathbf{G}_{1n}\,\mathrm{d}y}{\int_{-1/2}^{1/2} \tilde{X}^{\dagger}X^{[1;1]}\,\mathrm{d}y}.$$

These integrations are calculated using *Gauss-Chebyshev quadrature*: the Gaussian quadrature using Chebyshev polynomial as a interpolating polynomial is called as Gauss-Chebyshev quadrature. Next we briefly discuss about an accurate quadrature-formula at Gauss-Lobatto points (Hanifi *et al.* 1996) to evaluate the above-mentioned integrals.

Gauss-Chebyshev Quadrature

The general rule for Gaussian quadratures is

$$\int_{-1}^{1} f(\xi)\mathrm{d}\xi = \sum_{\alpha=0}^{M} w(\xi_\alpha) f(\xi_\alpha) \tag{3.81}$$

where $w(\xi_\alpha)$ is the weight function, $f(\xi)$ is given by (3.54) and ξ_α are called nodes. To derive the Gauss-Chebyshev quadrature formula we need to find weight functions on the Chebyshev grid (i.e. on Gauss-Lobatto grid). Now we make use of the discrete orthogonality condition of Chebyshev polynomials which reads as

$$\langle f, g\rangle = \sum_{\alpha=0}^{M} b_\alpha f(\xi_\alpha) g(\xi_\alpha) \tag{3.82}$$

where $b_0 = b_M = \frac{1}{2}, b_\alpha = 1$ for $0 < \alpha < M$, and ξ_α are the Gauss-Lobatto points as defined in (3.55). From this definition it follows that

$$\langle T_\alpha(\xi), T_\gamma(\xi)\rangle = \begin{cases} 0 & \alpha \neq \gamma \\ M & \alpha = \gamma = 0, M \\ M/2 & \alpha = \gamma \neq 0, M \end{cases} \tag{3.83}$$

which can be used to obtain the expansion coefficients a_α in (3.54):

$$a_\alpha = \frac{c_\alpha}{M} \sum_{j=0}^{M} b_j f(\xi_j) T_\alpha(\xi_j) \tag{3.84}$$

where $c_0 = c_M = 1$ and $c_\alpha = 2$ for all $0 < \alpha < M$. Therefore the expansion formula (3.54) simplifies to

$$f(\xi) \;=\; \sum_{\alpha=0}^{M} a_\alpha T_\alpha(\xi) = \sum_{\alpha=0}^{M} c_\alpha T_\alpha(\xi) \sum_{j=0}^{M} \frac{b_j}{M} f(\xi_j) T_\alpha(\xi_j), \tag{3.85}$$

which, upon integration with respect to ξ, leads to

$$\int_{-1}^{1} f(\xi)\mathrm{d}\xi \;=\; \frac{1}{M} \sum_{j=0}^{M} b_j f(\xi_j) \sum_{\alpha=0}^{M} c_\alpha T_\alpha(\xi_j) \int_{-1}^{1} T_\alpha(\xi)\,\mathrm{d}\xi \tag{3.86}$$

where

$$\int_{-1}^{1} T_\alpha(\xi)\,\mathrm{d}\xi = \begin{cases} 0 & \alpha \text{ odd} \\ \frac{2}{1-\alpha^2} & \alpha \text{ even.} \end{cases} \tag{3.87}$$

This immediately yields an expression for the weight function as defined via (3.81):

$$w(\xi_j) = \frac{b_j}{M}\left\{2 + \sum_{\alpha=2}^{M} c_\alpha \frac{1+(-1)^\alpha}{1-\alpha^2}\cos\left(\frac{\alpha j\pi}{M}\right)\right\}. \tag{3.88}$$

If a mapping $\xi = \xi(y)$ is used to transform the physical domain $y \in [a, b]$ into the Chebyshev domain $\xi \in [-1, 1]$, then the expression for the weight function becomes

$$w(\xi_j) \quad = \quad \frac{b_j}{M}\sum_{\alpha=0}^{M} c_\alpha \cos\left(\frac{\alpha j\pi}{M}\right)\int_{-1}^{1} T_\alpha(\xi)\frac{\mathrm{d}y}{\mathrm{d}\xi}\,\mathrm{d}\xi. \tag{3.89}$$

In the present problem the physical domain is $y = [-1/2, 1/2]$ and hence we can assume a mapping $\xi = 2y$ and the Gauss-Chebyshev quadrature formula can be rewritten as

$$\int_{-1/2}^{1/2} f(y)\,\mathrm{d}y = \sum_{j=0}^{M} w(\xi_j) f(y_j) \tag{3.90}$$

where $w(\xi_j)$ is given by (3.89) and $y_j \in [-1/2, 1/2]$.

To numerically evaluate the solvability condition, (3.43), we first calculate each integrand at Gauss-Lobatto points (where the terms related to continuity equation are interpolated from Gauss-points to Gauss-Lobatto points) and then take the weighted summation as in equation (3.90). For the present problem, the above quadrature formula has been compared with two other composite integration methods, namely, Simpson and trapezoidal quadrature rules. It has been verified that the Gauss-Chebyshev quadrature converges with $M = 50$ grid points, while to get the same accuracy using Simpson quadrature we need to use $M > 200$ grid points. The superior convergence of the Gauss-Chebyshev quadrature is presumably due to the spectral accuracy of the underlying scheme (Canuto *et al.* 1988; Hanifi *et al.* 1996).

CHAPTER 4

LANDAU-TYPE ORDER PARAMETER EQUATION FOR SHEAR BANDING IN GRANULAR COUETTE FLOW

In the first part of this chapter we derive Landau equation from center manifold reduction and this complements the analysis of chapter 3 where we used "amplitude expansion method." This proves an equivalence between two methods.

Next we show that a Landau-type 'order-parameter' equation describes the onset of shear-band formation in granular plane Couette flow wherein the flow undergoes an ordering transition into alternate layers of dense and dilute regions of low and high shear rates, respectively, parallel to the flow-direction.

This chapter is organized as follows. The continuum equations and boundary conditions are written down in §4.1. The linear stability analysis and adjoint problem are formulated in §4.2. The 'center manifold reduction' method is explained in §4.3 and the comparison between 'center manifold reduction' and 'amplitude expansion' method is given in §4.3.2. The phase diagram and bifurcation analysis, are shown in §4.4.2. The conclusions are given in §4.5.

4.1 Plane Couette flow: Continuum Equations and Boundary Conditions

Consider a flow of granular particles between two infinite parallel plates at $\overline{y} = \pm\overline{h}/2$, where $\overline{h}$ is the gap between the plates as shown in figure 4.1; both the plates are moving oppositely along the $\overline{x}$-direction with velocity $\overline{U}_w/2$. Here the "overbar" denotes a dimensional quantity. The physical state of the particles of granular system under study is that the particles are mono-disperse, smooth, spherical and inelastic with particle diameter $\overline{d}_p$ and the coefficient of restitution e.

The tensorial form of balance equations in the absence of gravity are:

$$\overline{\rho}_\nu \frac{\mathrm{D}\phi}{\mathrm{D}\overline{t}} = -\overline{\rho}_p(\overline{\nabla}\cdot\overline{\boldsymbol{u}}) \tag{4.1}$$

$$\overline{\rho}_p\phi\frac{\mathrm{D}\overline{\boldsymbol{u}}}{\mathrm{D}\overline{t}} = -\overline{\nabla}\cdot\overline{\boldsymbol{\Sigma}} \tag{4.2}$$

$$\frac{\dim}{2}\,\overline{\rho}_\nu\frac{\mathrm{D}\overline{T}}{\mathrm{D}\overline{t}} = -\overline{\nabla}\cdot\overline{\boldsymbol{q}} - \overline{\boldsymbol{\Sigma}} : \overline{\nabla}\overline{\boldsymbol{u}} - \overline{\mathcal{D}} \tag{4.3}$$

where the stress tensor ($\overline{\boldsymbol{\Sigma}}$) and the granular heat flux ($\overline{\boldsymbol{q}}$) are given by (2.8)-(2.10); 'dim' refers to the dimensionality of the problem (dim = 3 for spheres and 2 for disks).

The boundary conditions are chosen to be no-slip velocity and zero heat flux: $\overline{u}(\overline{y} = \pm\overline{h}/2) = \pm\overline{U}_w/2$, $\overline{v}(\overline{y} = \pm\overline{h}/2) = 0$, and $\mathrm{d}\overline{T}/\mathrm{d}\overline{y}(\overline{y} = \pm\overline{h}/2) = 0$. For the purpose of non-dimensionalization, we use the reference length, velocity and time scales as $\overline{h}$, $\overline{U}_w$ and $\overline{h}/\overline{U}_w$, respectively, see Alam & Nott (1998) and Alam *et al.* (2008) for related details. In the following, all 'unbarred' quantities are dimensionless.

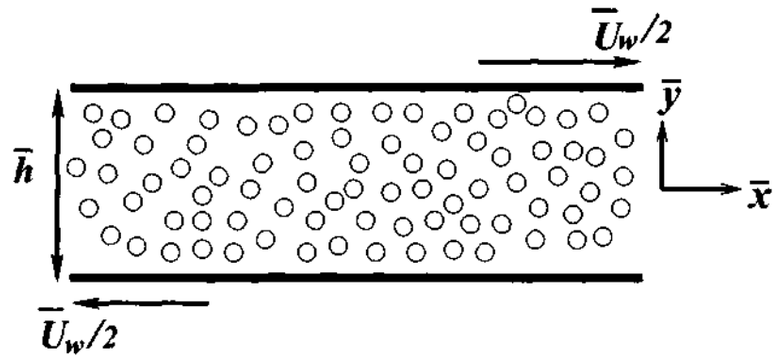

Figure 4.1: Schematic diagram of plane shear flow between parallel plates. The upper plate moves with velocity $\overline{U}_w/2$ along the positive $\overline{x}$-direction and the lower plate moves with the same speed in the opposite direction.

Let us define other non-dimensional quantities,

$$\left.\begin{aligned} (x,y) &= \frac{1}{\overline{h}}(\overline{x},\overline{y}), \qquad (u,v) = \frac{1}{\overline{U}_w}(\overline{u},\overline{v}), \qquad t = \frac{\overline{U}_w}{\overline{h}}\overline{t}, \\ T &= \frac{\overline{T}}{(\overline{d}_p/\overline{h})^2\overline{U}_w^2}, \qquad \Sigma = \frac{\overline{\Sigma}}{\overline{\rho}_p\overline{U}_w^2(\overline{d}_p/\overline{h})^2}, \\ q &= \frac{\overline{q}}{\overline{\rho}_p\overline{U}_w^3(\overline{d}_p/\overline{h})^4}, \qquad \mathcal{D} = \frac{\overline{\mathcal{D}}}{\overline{\rho}_p\overline{U}_w^3(\overline{d}_p/\overline{h})^3/\overline{d}_p} \end{aligned}\right\}. \tag{4.4}$$

The scaling of granular temperature can be derived by balancing the rate of energy dissipation with the stress work. The *Navier-Stokes-order* constitutive relations (Lun *et al.* 1984) for stress tensor, $\overline{\Sigma}$, and thermal energy, $\overline{q}$, are given by (2.8)-(2.10).

4.1.1 Streamwise Independent Equations

Since the focus of the present chapter is the shear-banding instability, that originates from a specific form of perturbations having no variation along the streamwise direction (x), here we start with the simplified form of balance equations that do not depend on the streamwise coordinate. In dimensionless form, the streamwise independent ($\partial/\partial x(.) = 0$) balance equations for mass, momentum and granular energy, respectively, are:

$$\frac{\partial\phi}{\partial t} + \phi\frac{\partial v}{\partial y} + v\frac{\partial\phi}{\partial y} = 0 \tag{4.5}$$

$$\phi\left[\frac{\partial}{\partial t} + v\frac{\partial}{\partial y}\right]u = \frac{1}{H^2}\frac{\partial}{\partial y}\left(\mu\frac{\partial u}{\partial y}\right) \tag{4.6}$$

$$\phi\left[\frac{\partial}{\partial t} + v\frac{\partial}{\partial y}\right]v = \frac{1}{H^2}\left[-\frac{\partial p}{\partial y} + \frac{\partial}{\partial y}\left(2\mu\frac{\partial v}{\partial y} + \lambda\frac{\partial v}{\partial y}\right)\right] \tag{4.7}$$

$$\frac{\dim}{2}\,\phi\left[\frac{\partial}{\partial t}+v\frac{\partial}{\partial y}\right]T = \frac{1}{H^2}\frac{\partial}{\partial y}\left(\kappa\frac{\partial T}{\partial y}\right)-p\frac{\partial v}{\partial y} +2\mu\left[\left(\frac{\partial v}{\partial y}\right)^2+\frac{1}{2}\left(\frac{\partial u}{\partial y}\right)^2+\frac{\lambda}{2\mu}\left(\frac{\partial v}{\partial y}\right)^2\right]-\mathcal{D}. \tag{4.8}$$

Here $H=\overline{h}/\overline{d}_p$ is the ratio between the Couette gap ($\overline{h}$) and the particle diameter ($\overline{d}_p$), called *scaled Couette gap*, which can equivalently be thought of as the inverse of the dimensionless particle diameter i.e. $H=\left(\overline{d}_p/\overline{h}\right)^{-1}$. The dimensionless transport coefficients [cf. (2.11)] are

$$\left.\begin{array}{lll} p(\phi,T) = f_1(\phi)T & \mu(\phi,T)=f_2(\phi)\sqrt{T} \\ \zeta(\phi,T) = f_3(\phi)\sqrt{T} & \kappa(\phi,T)=f_4(\phi)\sqrt{T} \\ \mathcal{D}(\phi,T) = f_5(\phi,e)T^{3/2} & \lambda(\phi,T)=\zeta-\frac{2}{\dim}\mu \end{array}\right\}, \tag{4.9}$$

where $f_i(.)$'s are dimensionless functions as given in (2.21). Note that, as discussed in chapter 2, we have neglected a term in the expression of the collisional dissipation $\mathcal{D}$, proportional to $\nabla\cdot\boldsymbol{u}$ (Garzó & Dufty 1999), that does not affect the onset of shear-banding instability (Alam *et al.* 2008). The contact radial distribution function, $\chi(\phi)$ is given by (2.12). The boundary conditions in dimensionless form are

$$u=\pm\frac{1}{2},\quad v=0,\quad \frac{\mathrm{d}T}{\mathrm{d}y}=0\quad\text{at}\quad y=\pm 1/2, \tag{4.10}$$

that correspond to zero-slip, zero-penetration and zero heat-flux, respectively.

4.1.2 Steady Plane Couette Flow: Base State

The stability of the flow which we want to study is the steady, fully developed, two-dimensional flow between two infinite parallel moving plates. Under these assumptions we can write the base state solution as

$$\phi=\phi^0(y),\quad \boldsymbol{u}=(u^0(y),0),\quad T=T^0(y).$$

With no-slip and adiabatic boundary conditions (4.10), the resulting base flow equations admit the following solution of uniform shear with constant density and granular temperature:

$$u^0(y)=y,\quad v^0=0,\quad \phi^0=\text{constant},\quad T^0(\phi^0)=\text{constant}=\frac{f_2(\phi^0)}{f_5(\phi^0)}. \tag{4.11}$$

Note that the pressure (p^0) and the shear stress [$\mu^0(du^0/dy)$] are also constants for the steady plane Couette flow. In the following, we use density or solid fraction or volume fraction to refer to the same quantity ϕ^0.

4.2 Nonlinear Analysis

The stability of basic flow is examined by decomposing all the flow variables (density, velocity and granular temperature) and transport coefficients into a base flow part, X^0, and a finite-amplitude perturbation, X:

$$X_{total}(y,t)=X^0(y)+X(y,t), \tag{4.12}$$

where the superscript '0' denotes the base state and the prime denotes its perturbation. The transport coefficients are analytic functions of density and temperature, and hence can be written

as a Taylor series around the base state, e.g., pressure can be written as

$$p(\phi,T) = p^0 + p^0_\phi \phi' + p^0_T T' + \frac{1}{2!}\left(p^0_{\phi\phi}\phi'^2 + p^0_{\phi T}\phi' T' + p^0_{TT}T'^2 + p^0_{T\phi}T'\phi'\right) + \ldots, \tag{4.13}$$

where the subscripts denote the respective partial derivatives, and the superscript '0' implies that the quantity being evaluated at the base flow conditions. Inserting the Taylor series expansions of all hydrodynamic variables and transport coefficients into equations (4.5)-(4.8) and subtracting the base flow equations, we obtain nonlinear perturbation equations, correct up-to cubic order, which can be put in the operator form:

$$\left(\frac{\partial}{\partial t} - \mathcal{L}\right) X = \mathcal{N}_2(X,X) + \mathcal{N}_3(X,X,X). \tag{4.14}$$

Here $\mathcal{L}(\frac{\partial}{\partial y}, \frac{\partial^2}{\partial y^2}, \phi^{(0)}, u^{(0)}, T^{(0)} \ldots)$ is the linear operator, $\mathcal{N}_2$ and $\mathcal{N}_3$ are the quadratic and cubic nonlinear terms and $X = (\phi', u', v', T')^{Tr}$ denotes the disturbance vector. The explicit forms of $\mathcal{N}_2$ and $\mathcal{N}_3$ are given in Appendix 5A of chapter 5. The linear operator is given by

$$\mathcal{L} = \begin{pmatrix} 0 & 0 & -\phi^0 \frac{\partial}{\partial y} & 0 \\ \frac{\mu^0_\phi}{\phi^0 H^2}\frac{\partial}{\partial y} & \frac{\mu^0}{\phi^0 H^2}\frac{\partial^2}{\partial y^2} & -1 & \frac{\mu^0_T}{\phi^0 H^2}\frac{\partial}{\partial y} \\ \frac{-p^0_\phi}{H^2\phi^0}\frac{\partial}{\partial y} & 0 & \frac{(2\mu^0+\lambda^0)}{H^2\phi^0}\frac{\partial^2}{\partial y^2} & \frac{-p^0_T}{H^2\phi^0}\frac{\partial}{\partial y} \\ \frac{2(\mu^0_\phi - \mathcal{D}^0_\phi)}{\phi^0 \mathrm{dim}} & \frac{4\mu^0}{\phi^0 \mathrm{dim}}\frac{\partial}{\partial y} & -\frac{2p^0}{\phi^0 \mathrm{dim}}\frac{\partial}{\partial y} & \frac{2}{\phi^0 \mathrm{dim}}\left(\frac{\kappa^0}{H^2}\frac{\partial^2}{\partial y^2} + \mu^0_T - \mathcal{D}^0_T\right) \end{pmatrix}. \tag{4.15}$$

and the quadratic, $\mathcal{N}_2$, and cubic, $\mathcal{N}_3$, nonlinear terms can be expressed in the vector notations,

$$\mathcal{N}_2 = \begin{pmatrix} \mathcal{N}_2^1 \\ \mathcal{N}_2^2 \\ \mathcal{N}_2^3 \\ \mathcal{N}_2^4 \end{pmatrix} \quad \text{and} \quad \mathcal{N}_3 = \begin{pmatrix} \mathcal{N}_3^1 \\ \mathcal{N}_3^2 \\ \mathcal{N}_3^3 \\ \mathcal{N}_3^4 \end{pmatrix}$$

where the superscripts 1, 2, 3 and 4 on nonlinear terms correspond to terms originating from the mass balance, x-momentum, y-momentum and energy balance equations, respectively. The boundary conditions can be written in matrix format

$$\mathcal{B}X(y = \pm 1/2) \equiv \begin{pmatrix} 0 & 0 & 0 & 0 \\ 0 & 1 & 0 & 0 \\ 0 & 0 & 1 & 0 \\ 0 & 0 & 0 & \frac{\partial}{\partial y} \end{pmatrix} \begin{pmatrix} \phi' \\ u' \\ v' \\ T' \end{pmatrix} = 0. \tag{4.16}$$

4.2.1 Linear Problem

Neglecting nonlinearities, we obtain the well-studied linear stability problem (Alam & Nott 1998)

$$\frac{\partial X}{\partial t} = \mathcal{L}X, \quad \text{with} \quad \mathcal{B}X = 0. \tag{4.17}$$

The adjoint problem (cf. chapter 3, §3.3.5) corresponding to linear stability operator ($\mathcal{L}$) is

$$\frac{\partial X^\dagger}{\partial t} = \mathcal{L}^\dagger X^\dagger \tag{4.18}$$

where $X^\dagger = [\phi^\dagger, u^\dagger, v^\dagger, T^\dagger]^{Tr}$ is the adjoint function and $\mathcal{L}^\dagger$ is the adjoint operator which is calculated from the definition of adjoint operator

$$\langle X^\dagger, \mathcal{L}X\rangle = \langle \mathcal{L}^\dagger X^\dagger, X\rangle. \tag{4.19}$$

In the above, the standard inner product has been defined via

$$\langle Y(y), Z(y)\rangle = \int_{-1/2}^{1/2} \tilde{Y}(y)Z(y)\,\mathrm{d}y = \int_{-1/2}^{1/2} \sum_{i=1}^{4} \tilde{y}_i(y)z_i(y)\,\mathrm{d}y, \tag{4.20}$$

for two complex valued vector functions $Y(y) = [y_1, y_2, y_3, y_4]$ and $Z(y) = [z_1, z_2, z_3, z_4]$ on the interval $-1/2 \leq y \leq 1/2$, with the 'tilde' denoting a complex conjugate quantity.

With above definitions, the form of the adjoint operator can be shown to be related to the linear operator via

$$\mathcal{L}^\dagger \equiv \mathcal{L}^{Tr}(\partial/\partial y \rightarrow -\partial/\partial y, \partial^2/\partial y^2; \phi^0, T^0, \ldots) \tag{4.21}$$

and the adjoint boundary conditions are

$$\mathcal{B}X^\dagger = 0, \tag{4.22}$$

with $\mathcal{B}$ being given by (4.16).

4.2.2 Linear Eigenvalue Problem

Since the linear problem is invariant under arbitrary time-translation $t \mapsto t + constant$, the normal mode solutions with complex frequency c are sought

$$X(y,t) = \widehat{X}(y)e^{ct} \tag{4.23}$$

where $\widehat{X}(y) = [\hat{\phi}, \hat{u}, \hat{v}, \hat{T}](y)$ are unknown functions of y. This reduces the linearized system of partial differential equations into a set of ordinary differential equations:

$$c\widehat{X} = \mathbf{L}\widehat{X}, \quad \text{with} \quad \mathcal{B}\widehat{X} = 0, \tag{4.24}$$

where $\mathbf{L} \equiv \mathcal{L}(\mathrm{d}/\mathrm{d}y, \mathrm{d}^2/\mathrm{d}y^2, \ldots)$ is a linear ordinary differential operator, $\widehat{X}$ is a linear eigenfunction and $c = c_r + i\,c_i$ is a complex eigenvalue such that the flow is stable if $c_r > 0$, whereas unstable if $c_r < 0$, and neutrally stable if $c_r = 0$. It can be verified that this system of equations has analytical solutions (Alam & Nott 1998) which will be discussed in the next chapter. In a similar manner we can obtain an adjoint eigenvalue problem:

$$\tilde{c}\widehat{X}^\dagger = \mathbf{L}^\dagger \widehat{X}^\dagger, \quad \text{with} \quad \mathcal{B}\widehat{X} = 0, \tag{4.25}$$

where $\mathbf{L}^\dagger = \mathbf{L}^{Tr}(\frac{d}{dy} \rightarrow -\frac{d}{dy}, \frac{d^2}{dy^2} \rightarrow \frac{d^2}{dy^2}; \phi^{(0)}, u^{(0)}, T^{(0)}, \ldots)$ and $\widehat{X}^\dagger$ is an adjoint eigenfunction Here tilde denotes a complex conjugate. The above eigenvalue problem with boundary conditions form a well posed boundary value problem. The spectral-based numerical scheme (spectral collocation method), as described in chapter 3, has been used to solve eigenvalue problem (see chapter 3).

4.3 Center Manifold Reduction

The spectrum of the linear operator is decomposed into slow, critical or center (i.e. the modes having growth rates close to zero) and fast or non-critical (i.e. the modes having large decay rates) modes. Since the domain of plane Couette flow (see figure 4.2) is bounded, $y \in (-1/2, 1/2)$, the spectrum is discrete which has been verified by computing the eigenvalues of the linear operator $\mathbf{L}$ (Alam & Nott 1998).

For the uniform shear of a granular fluid, a typical spectrum in the complex-plane is displayed in figure 4.2 at a Couette gap $H = 200$ and a density $\phi^0 = \phi_c \approx 0.157$, with $e = 0.95$. There are two branches of propagating modes ($c_i \neq 0$) which are always stable ($c_r < 0$), and the *shearbanding-instability*, that lead to segregated density profiles with alternate layers of dense and dilute regions across the gradient (y) direction, is due to *stationary* ($c_i = 0$) modes for $\phi^0 > \phi_c$.

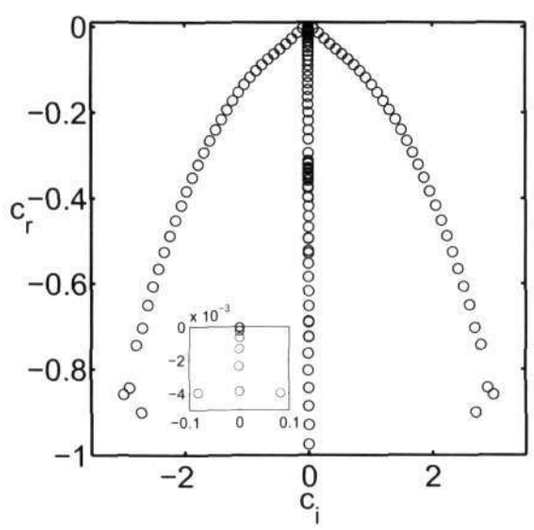

Figure 4.2: Spectra of uniform shear flow in the complex plane for $H = 200$, $\phi^0 = \phi_c \approx 0.157$ and $e = 0.95$. Flow is *neutrally* stable for this parameter set.

The center manifold theorem (Carr 1981) states that the dynamics close to the critical situation is dominated by a finite number of critical modes, resulting in an effective low-dimensional dynamical system. Focusing on a single slow mode, therefore, the disturbance vector field $X(y,t) = \Phi(y,t) + \Psi(y,t)$ is decomposed as a linear combination of the linear critical eigenfunction Φ and an infinite number of non-critical eigenfunctions Ψ.

In our analysis, the most unstable shear-banding mode (Alam & Nott 1998) from the linear theory, (4.24), $X^{[1:1]}(y)$, called the fundamental mode (linear eigenfunction), represents the critical mode:

$$\Phi(y,t) = \mathscr{A}(t)X^{[1:1]}(y) + \tilde{\mathscr{A}}(t)\tilde{X}^{[1:1]}(y). \tag{4.26}$$

In the weakly nonlinear regime, the spatial variation of the critical (or center) mode is taken to be the same as that of the linear theory, but its temporal variation is non-exponential (unlike in linear theory in which $\mathscr{A}(t)$ is taken to be infinitesimally small) having a finite complex amplitude $\mathscr{A}(t)$ whose dynamical equation is of interest here. To proceed further, we follow two steps (Stuart

1960; Newell *et al.* 1993): (i) expend $X(y,t)$ into a generalized Fourier series,

$$X = \sum_{k=0}^{\infty} X^{(k)} + \tilde{X}^{(k)} = \sum_{k=0}^{\infty} \mathscr{A}^k |\mathscr{A}|^{n-k} X^{[k;n]} + c.c, \tag{4.27}$$

and (ii) the Fourier coefficients $X^{(k)}$ are expanded into Taylor series in terms of perturbation amplitude $\mathscr{A}(t)$:

$$X^{(k)} = \mathscr{A}^k |\mathscr{A}|^{n-k} X^{[k;n]}. \tag{4.28}$$

Here the summation convention is such that $0 \leq k \leq n$, $n \geq 1$, and the superscript convention of $X^{[k;n]}$ is defined such that $X^{[k;n]} = 0$ if $(k+n)$ is odd. Substituting (4.28) into (4.27) we get,

$$X = \sum_{k=0}^{\infty} \mathscr{A}^k |\mathscr{A}|^{n-k} X^{[k;n]} + c.c. \tag{4.29}$$

In nonlinear perturbation theory (Stuart 1960; Reynolds & Potter 1967; Carr 1981), one requirement is that the nonlinear problem must reduce to the linear stability problem in the limit of infinitesimal perturbation amplitude ($\mathscr{A} \to 0$). In the present perturbation expansion, $O(\mathscr{A})$ terms denote the linear eigenfunction (i.e. the fundamental mode $X^{[1;1]}$), $O(1)$ terms denote the base-state solution (i.e. $X^{[0;0]}$) and $O(\mathscr{A}^2)$ terms are the nonlinear interactions of two fundamental modes. The fundamental mode interacting with itself is responsible for the generation of the *second harmonic* $X^{[2;2]}$, while its interaction with its complex conjugate generates the *distortion to the mean flow* $X^{[0;2]}$ that appears at order $O(\mathscr{A}\tilde{\mathscr{A}})$. The higher order nonlinear interactions and distortions are defined in a similar fashion. Following the above formalism, the Taylor series expansion of the first three Fourier coefficients can be written as (see (4.29)):

$$\left.\begin{aligned} X^{(1)}(y,t) &= \mathscr{A}(t)\left(X^{[1;1]}(y) + |\mathscr{A}(t)|^2 X^{[1;3]}(y) + \ldots\right) \\ X^{(0)}(y,t) &= |\mathscr{A}(t)|^2\left(X^{[0;2]}(y) + |\mathscr{A}(t)|^2 X^{[0;4]}(y) + \ldots\right) \\ X^{(2)}(y,t) &= \mathscr{A}(t)^2\left(X^{[2;2]}(y) + |\mathscr{A}(t)|^2 X^{[2;4]}(y) + \ldots\right) \end{aligned}\right\}.$$

In the dual superscript notation for $X^{[k;n]}$, the *first index* (k) refers to a particular Fourier mode (e.g. $k=0$ for mean/base flow and its higher order corrections, $k=1$ for the fundamental mode and its higher order corrections, $k=2$ for the second harmonic and its higher order corrections, and so on), and the *second index* (n) indicates the order of a particular term as $O(|\mathscr{A}|^n)$.

Clearly, the leading term of $X^{(1)}$ is $\mathscr{A}X^{[1;1]}$, of order $O(\mathscr{A})$, which represents the *fundamental* mode. The leading term of $X^{(0)}$, is $|\mathscr{A}|^2 X^{[0;2]}$, of $O(|\mathscr{A}|^2)$, which represents the *distortion/correction to the mean flow.* The leading term of $X^{(2)}$ is $\mathscr{A}^2 X^{[2;2]}$ which is the *second harmonic.* The matrix equivalent of the above power-series expressions is given by (4.29). These superscript notations (Stuart 1960; Reynolds & Potter 1967) are extremely useful to simplify the algebra as well as to identify a particular mode and its modal interaction of any order.

Inserting (4.29) into equation (4.14) and using (4.24), and equating the like-order terms, we obtain

$$\left(\frac{d}{dt} - c\right)\mathscr{A}(t)X^{[1;1]} = \text{nonlinear terms}, \tag{4.30}$$

$$\left(\mathbf{I}\frac{\partial}{\partial t} - \mathcal{L}\right)\Psi(y,t) = \text{nonlinear terms}. \tag{4.31}$$

The former (4.30) is the nonlinear evolution equation for the critical mode Φ, and the latter (4.31), representing all noncritical modes Ψ, are called enslaved equations. Note that we have

used (4.17) to obtain the second term on the left hand side.

4.3.1 Landau Equation

Landau equation can be derived from (4.30). For this we rewrite (4.30) with the explicit form of the nonlinear terms as given below,

$$\left(\frac{d}{dt} - c\right) \mathscr{A}(t) X^{[1;1]} = \mathbf{G}_{13} \mathscr{A}|\mathscr{A}|^2 + \mathbf{G}_{15} \mathscr{A}|\mathscr{A}|^4 + \ldots + \mathbf{G}_{11+2n} \mathscr{A}|\mathscr{A}|^{2n} + \ldots . \qquad (*)$$

In the above notation $\mathbf{G}_{11+2n}\mathscr{A}|\mathscr{A}|^{2n}$, the first index, which is one, represents the order of amplitude i.e $O(\mathscr{A})$ and the second index $1+2n$, where n is a positive integer, represents the order of the absolute amplitude term, i.e. $O(|\mathscr{A}|^{2n+1})$. Taking the inner product of (*) with adjoint linear eigenfunction and separating the like-power terms in amplitude, we arrive at the Landau equation for the disturbance amplitude $\mathscr{A}(t)$:

$$\frac{d\mathscr{A}}{dt} = c^{(0)}\mathscr{A} + c^{(2)}\mathscr{A}\,|\mathscr{A}|^2 + ... \qquad (4.32)$$

It is straightforward to verify from (4.32) and (4.24) that $c^{(0)} \equiv c$ is the linear eigenvalue, and the coefficients $c^{(n)}$ $(n = 2, 4\cdots)$ are called the Landau coefficients. Here we have used a normalized adjoint eigenfunction such that

$$\langle X^\dagger, X^{[1;1]} \rangle = 1.$$

Similarly, the expression for the first Landau coefficient, $c^{(2)}$, can be identified as

$$c^{(2)} = \langle X^\dagger, \mathbf{G}_{13} \rangle = \int_{-1/2}^{1/2} \tilde{X}^\dagger \mathbf{G}_{13}\, dy \qquad (4.33)$$

where $X^\dagger$ is the least-stable adjoint eigenfunction of linear stability problem and $\mathbf{G}_{13}$ represents a combination of nonlinear terms as given below,

$$\begin{aligned} \mathbf{G}_{13} \;=\; & N_2(X^{[1;1]}, X^{[0;2]}) + N_2(X^{[0;2]}, X^{[1;1]}) + N_2(\tilde{X}^{[1;1]}, X^{[2;2]}) \\ & + N_2(X^{[2;2]}, \tilde{X}^{[1;1]}) + N_3(X^{[1;1]}, \tilde{X}^{[1;1]}, X^{[1;1]}) \\ & + N_3(\tilde{X}^{[1;1]}, X^{[1;1]}, X^{[1;1]}) + N_3(X^{[1;1]}, X^{[1;1]}, \tilde{X}^{[1;1]}) \end{aligned} \qquad (4.34)$$

where N_2 and N_3 are the quadratic and cubic nonlinear term, respectively.

It is clear from (4.33) that, in addition to knowing the fundamental mode $X^{[1;1]}$ and its adjoint $X^\dagger$, we need to determine second harmonic $X^{[2;2]}$ and the first distortion to fundamental $X^{[0;2]}$ which are described above.

From the enslaved equation (4.31) at quadratic order $O(\mathscr{A}^2)$, we obtain the following equation for the second harmonic

$$(2c\mathbf{I} - \mathbf{L})X^{[2;2]} = N_2(X^{[1;1]}, X^{[1;1]}). \qquad (4.35)$$

This can be solved for $X^{[2;2]}$ since the right-hand side of (4.35) is a known function of the fundamental mode $X^{[1;1]}$. We have verified that the second harmonic and the distortion to the mean flow are equal, $X^{[2;2]} = X^{[0;2]}$, for the shear-banding instability.

Neglecting nonlinear terms in (4.32), we obtain the well-known linear stability result, $\mathscr{A}(t) \sim \exp(ct)$, of exponential growth which is valid at order $O(\mathscr{A})$, in amplitude. In the following discussion, we decompose $c^{(n)}$ into real and imaginary parts: $c^{(n)} = a^{(n)} + \mathrm{i}b^{(n)}$, with $n = 0, 2, 4\cdots$; for example, $a^{(0)}$ and $b^{(0)}$ represent the growth rate and the frequency of the disturbance, respectively. For the present problem of shear-banding instability, it has been verified (Alam & Nott 1998) that $b^{(0)} = 0$; i.e the unstable eigenvalue is always real which implies that the related

bifurcation, if any, must be of pitchfork-type. Moreover the fundamental mode is also real for shear-banding instability leading to real first Landau coefficient i.e. $b^{(2)} = 0$.

The shear-banding is governed by the Landau equation (4.32) which is an order parameter equation. The equilibrium amplitude ($d\mathscr{A}/dt = 0$) of disturbance can be obtained by truncating (4.32) at the cubic order:

$$\mathscr{A}_e = \pm\sqrt{-a^{(0)}/a^{(2)}}, \tag{4.36}$$

with the third solution $\mathscr{A}_e \equiv 0$ representing the base-state of uniform shear and, constant density and granular temperature. It is clear that the finite-amplitude equilibrium solutions (4.36) exist iff $a^{(0)}$ and $a^{(2)}$ are of opposite sign. The sign of the real part of $c^{(2)}$ decides the nature of bifurcation: a positive value for $a^{(2)}$ denotes a subcritical bifurcation and its negative value denotes a supercritical bifurcation.

4.3.2 Comparison of $c^{(2)}$ between Center Manifold and Amplitude Expansion Methods

Recall from the chapter 3 that in amplitude expansion method, we defined amplitude of perturbation A as a real function of time such that

$$\frac{1}{A}\frac{\mathrm{d}A}{\mathrm{d}t} \to a^{(0)} \quad \text{as } A \to 0.$$

In contrast the amplitude $\mathscr{A}$ in center manifold method is defined as a complex function. Substituting $\mathscr{A} = |\mathscr{A}|e^{i\theta}$ into (4.32) and separating the real and imaginary parts, we get

$$\left.\begin{aligned}\frac{1}{|\mathscr{A}|}\frac{\mathrm{d}|\mathscr{A}|}{\mathrm{d}t} &= c_r^{(0)} + c_r^{(2)}|\mathscr{A}|^2 + \dots \\ \frac{\mathrm{d}\theta}{\mathrm{d}t} &= c_i^{(0)} + c_i^{(2)}|\mathscr{A}|^2 + \dots\end{aligned}\right\} \tag{4.37}$$

For $\mathscr{A} \to 0$ (for infinitesimal perturbation), $|\mathscr{A}| \to e^{c_r^{(0)}t}$ and $\theta \to c_i^{(0)}t$. It is straightforward from the comparison between (4.37) with (3.32)-(3.33) that $\mathscr{A} \equiv A$ and

$$\frac{\mathrm{d}\theta}{\mathrm{d}t} \equiv \omega + \frac{\mathrm{d}\omega}{\mathrm{d}A}\left(t\frac{\mathrm{d}A}{\mathrm{d}t}\right). \tag{4.38}$$

Consequently (4.37) is same as (3.32)-(3.33).

Now we compare the expression of $c^{(2)}$ (4.33) with that of (3.43). The form of nonlinear term $\mathbf{G}_{13}$ at cubic order is same in both methods because the fundamental, second harmonic and distortion of mean flow are exactly same. In the definition of $c^{(2)}$, (4.33), derived from the inner product, we have used a normalization condition. In the amplitude expansion method $c^{(2)}$ (see (3.43) for $n = 3$) is derived from the solvability condition. If we use the normalization condition $\langle X^\dagger, X^{[1;1]}\rangle = 1$ in (3.43) we get the same expression as given by (4.33). On the whole, the Landau equation and first Landau coefficient from the center manifold and amplitude expansion methods are same.

4.4 Results and Discussion

4.4.1 Numerical Method

The details of spectral-based numerical techniques are given in chapter 3. Briefly, the differential eigenvalue problem (4.24) and the differential equations (4.35) have been discretized using the Chebyshev spectral method; the resultant matrix eigenvalue problem has been solved using the QR-algorithm and the algebraic equations for (4.35) have been solved using SVD-algorithm of the Matlab-software. The degree of the Chebyshev polynomial was set to 50 which was found to yield accurate results. To calculate the first Landau coefficient (4.33), the integrals have been computed using the Gaussian quadrature with Chebyshev grid that yields spectral accuracy.

4.4.2 Phase Diagram and Bifurcation

The phase diagram, separating the zones of stability and instability by the neutral contour ($a^{(0)} = 0$, thick line), in the (H, ϕ^0)-plane is shown in figure 4.3(a) for a restitution coefficient of $e = 0.95$; the flow is unstable ($a^{(0)} > 0$) inside the neutral line (thick line), and stable ($a^{(0)} < 0$) outside. With decreasing value of e, the neutral contour shifts towards the left (i.e. at lower H) and the growth rate increases Alam & Nott (1998), and hence the size of the unstable region in the (ϕ^0, H) plane increases (and the flow becomes more unstable) with increasing dissipation. It may be noted that the linear stability equations (4.17) admit analytical solution (Alam & Nott 1998):

$$\left(\phi^{[1;1]}, T^{[1;1]}\right)(y) = (\phi_1, T_1)\cos k_\beta(y \pm 1/2) \tag{4.39}$$

where $k_\beta = \beta\pi$ is the "discrete" wavenumber along y, with $\beta = 1, 2, \ldots$ being the mode number that tells us the number of zero-crossing of the density or temperature eigenfunctions along $y \in (-1/2, 1/2)$.

The neutral contour (thick line) in figure 4.3(a) corresponds to mode $\beta = 2$ for which a typical density eigenfunction is displayed in the inset in figure 4.3(a). This suggests that inside the thick neutral contour the unstable shear flow will give birth to new solutions having modulated density profiles along the gradient (y) direction. Interestingly, the uniform shear flow (4.11) is linearly stable for $\phi^0 < \phi_c^l = \min_{\forall H} \phi^0(a^{(0)} = 0) \approx 0.154$ (below the lower branch of the thick neutral contour in figure 4.3(a)). In contrast to this prediction of the linear theory, however, we note that such density-segregated solutions have been found in the molecular dynamic simulations of granular shear flow, see the snapshot of particle positions in figure 4.3(b).

Let us now turn to analyze the results of our nonlinear theory. Figure 4.3(c) shows the variations of the first Landau coefficient, $a^{(2)}$, and the linear growth rate, $a^{(0)}$, with mean density for $H = 200$ and $e = 0.95$. Since $a^{(2)} > 0$ and $a^{(0)} < 0$ for $\phi^0 < \phi_c \equiv \phi^0(a^{(0)} = 0)$, the existence of finite-amplitude subcritical solutions is strongly suggested [viz. (4.36)] in the dilute limit.

The zero-contour of the first Landau coefficient is superimposed in figure 4.3(a) as thin solid lines, and $a^{(2)} > 0$ inside the thin loops. As per (4.36), it is now clear that the finite-amplitude subcritical solutions are possible in the dilute limit, enclosed by the lower thin loop in figure 4.3(a). As in the case of the neutral contour ($a^{(0)} = 0$, the thick contour in figure 4.3(a)), the thin contours for $a^{(2)} = 0$ shift towards the left with decreasing value of e (say, 0.6), and hence the size of the subcritical region (at dilute limit) in the (H, ϕ^0)-plane increases with increasing dissipation. This evidence of subcritical instability for dilute flows is in agreement with the simulations of Tan (1995).

With parameter values as in figure 4.3(c), the bifurcation diagrams in the $(\mathscr{A}_e, \phi^0 - \phi_c)$-plane are shown in figure 4.4(a) for two values of the restitution coefficient: $e = 0.95$ (dash line) and 0.6 (dot-dash line). Here ϕ_c is the critical mean density. Each line in figure 4.4(a) provides the threshold-amplitude, $\mathscr{A}_e(\phi^0, e)$, for nonlinear subcritical instability. This implies that if the

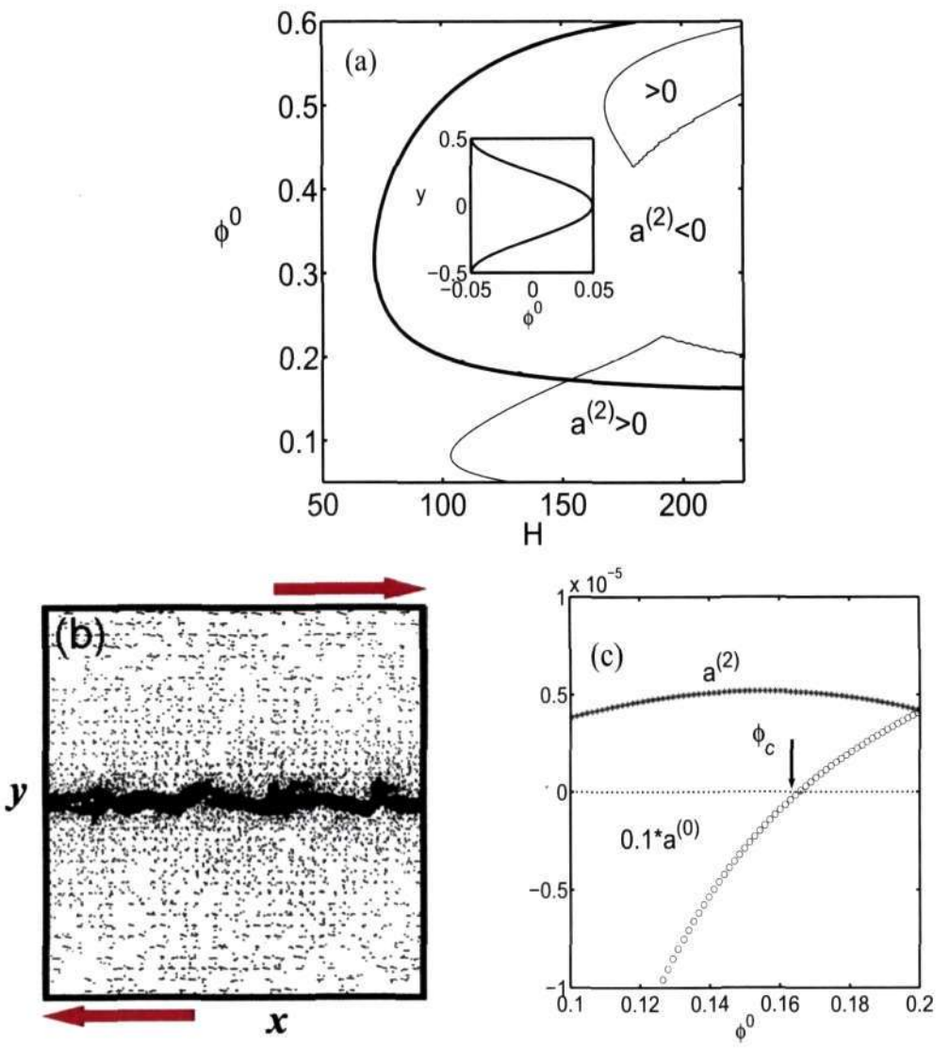

Figure 4.3: (*a*) Phase diagram in the (H, ϕ^0)-plane, showing the neutral stability contour (thick line) and the contours of vanishing first Landau coefficient (thin line) for a restitution coefficient of 0.95. The inset shows a typical density eigenfunction within the "linearly" unstable region. (*b*) Shear-band formation in simulations of dilute granular PCF: $\phi^0 = 0.05$, $e = 0.6$ and $N = 20000$. (adapted from M.-L. Tan's thesis 1995). Lees-Edward boundary condition has been used with the top boundary moving to the right and the bottom boundary to the left with same speed. (*c*) Variations of $a^{(0)}$ and $a^{(2)}$ with density at $H = 200$ for $e = 0.95$. The critical density is defined as the one at which the linear growth rate is zero, $\phi_c = \phi^0(a^{(0)} = 0) \approx 0.157$ at $H = 200$. Ref. Shukla & Alam (2009)

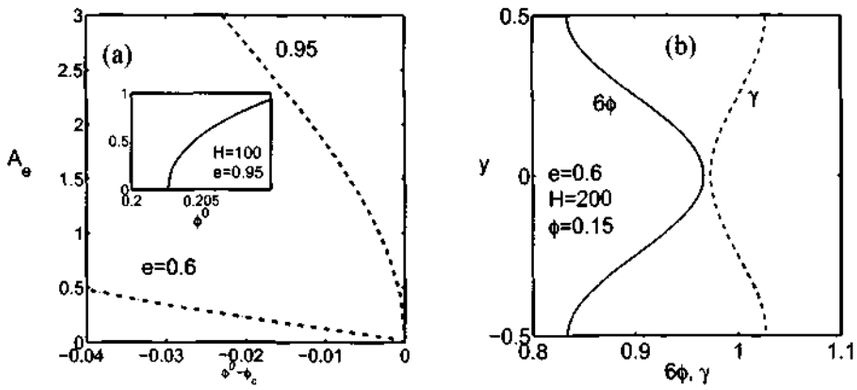

Figure 4.4: (*a*) Bifurcation diagram in the amplitude-vs-density plane for $e = 0.95$ (dash line) and 0.6 (dash-dot line) at $H = 200$. Inset shows a bifurcation diagram at $H = 100$ and $e = 0.95$. (*b*) Finite amplitude solutions for the density and the shear rate at $\phi^0 = 0.15$, $H = 200$ and $e = 0.6$. Note that the density has been multiplied by a factor of 6.

perturbation amplitude $\mathscr{A}$ is larger than its threshold value (i.e., if $\mathscr{A} > \mathscr{A}_c(\phi^0, e)$), then the uniform shear flow will jump into a new state of non-uniform shear and non-uniform density across the gradient direction. Typical sub-critical finite amplitude solutions for the density (solid line), $\phi = \phi^0 + \mathscr{A}_c\phi^{[1;1]}$, and the shear rate (dash line), $\gamma = d/dy(u^0 + \mathscr{A}_c u^{[1;1]})$, are displayed in figure 4.4(*b*), clearly showing density segregation and shear localization across y-direction; these shearbanded solutions have been calculated at the threshold amplitude $\mathscr{A} = \mathscr{A}_c$, with a mean density $\phi^0 = 0.15$, $H = 200$ and $e = 0.6$.

Figure 4.4(*a*) also suggests that the threshold-amplitude for nonlinear instability decreases with increasing dissipation, implying that more dissipative particles are more prone to such sub-critical shearbanding instability. The important point to note is that an appropriate magnitude of finite-amplitude perturbation, $\mathscr{A} > \mathscr{A}_c(\phi^0, e)$, must be imposed in simulations to achieve the shear-banded flow in the dilute limit.

At larger densities, the nature of bifurcation changes from subcritical to supercritical, see the inset of figure 4.4(*a*) for $H = 100$ and $e = 0.95$. The corresponding solutions for $\phi(y)$ and $\gamma(y)$ look similar to those in figure 4.4(*b*). Inside the upper loop of thin contour in figure 4.4(*a*), we have $a^{(0)} > 0$ and $a^{(2)} > 0$, and hence finite-amplitude solutions do not exists (4.36) for some range of ϕ^0 (inside upper thin loop) in the dense limit.

4.5 Conclusion

Starting from the Navier-Stokes level continuum equations of inelastic dense-gas kinetic theory and using the center manifold reduction technique, we showed that a Landau-type order parameter describes the shear-banding transition in granular plane Couette flow. Our results on the first Landau coefficient suggest that there is a subcritical finite-amplitude instability for dilute flows even though the dilute flow is stable according to the linear stability theory. The calculation of higher-order Landau coefficients (required to obtain the associated stable finite amplitude solutions in the dilute limit) is left to a future work. Even though we focused on streamwise-independent flows here, our nonlinear theory can be extended to analyze various nonlinear patterns in a host of granular flow problems as well as to describe shear banding in other complex fluids (Wilson & Fielding 2006; Olmsted 2008).

CHAPTER 5

NONLINEAR SHEAR BANDING INSTABILITY IN GRANULAR PLANE COUETTE FLOW: ANALYTICAL SOLUTION, COMPARISON WITH NUMERICS AND BIFURCATION

Here we develop the analytical solutions for the shear banding instability in granular plane Couette flow. We derive the analytical expression for the first Landau coefficient. The same problem has been solved numerically in chapter 4 (Shukla & Alam 2009) using spectral based numerical method. In this chapter, we compare present analytical solutions with numerical results and therefore this validates our numerical code. The bifurcation analysis for all the flow regimes are detailed. We show that the granular plane Couette flow serve as a microcosm of pitchfork bifurcations since all three possible types of pitchfork bifurcations exists in this flow.

This chapter is organized as follows. The analytical solutions for the fundamental mode and its adjoint are given in §5.1. A brief outline of the amplitude expansion method for the streamwise independent granular plane Couette flow is detailed in §5.2. The symmetries of the linear and nonlinear modes are discussed in §5.3. The symmetries of underlying nonlinear modes have helped us to identify analytical solutions for the second harmonic, the base-flow distortion and the distortion to the fundamental mode, leading to an exact calculation of the first Landau coefficient - these analytical solutions and their comparison with numerical solutions are detailed in §5.4.1, §5.4.2 and §5.4.4. The evidence of meanflow resonance at $O(A^2)$ is discussed in §5.4.3. The predictions of the analytical order-parameter theory are discussed in §5.5.1 (linear shear-banding instability), §5.5.2 (equilibrium amplitude and the nature of bifurcation), §5.5.3 (phase diagram for nonlinear stability), §5.5.4 (finite amplitude solutions) and §5.5.5 (scaling of first Landau coefficient, equilibrium amplitude and phase diagram). The influence of different forms of the contact radial distribution function and the constitutive relations on the nonlinear shearbanding predictions is discussed in §5.6.1 and §5.6.2, respectively, along with a summary of all possible bifurcation scenario for the nonlinear shearbanding instability in granular plane Couette flow in §5.6.3. We summarize the major findings of this chapter in §5.7. Organization map of this chapter is depicted in figure 5.1.

5.1 Analytical Solutions for Fundamental Mode and its Adjoint

The normal mode solution of linear problem and adjoint problem has been discussed in chapter 4 that reduces the linearized system of partial differential equations into a set of ordinary differential equations [viz. (4.24)]. We rewrite linear eigenvalue problem (4.24) as:

$$c\widehat{X} = \mathbf{L}\widehat{X}, \quad \text{with} \quad \mathcal{B}\widehat{X} = 0. \tag{5.1}$$

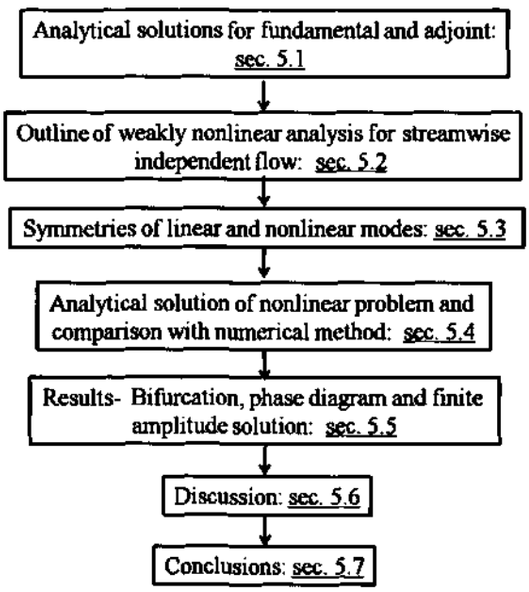

Figure 5.1: Road-map of chapter 5.

It can be verified that this system of equations has analytical solutions (Alam & Nott 1998):

$$\left.\begin{array}{rcl}(\hat{\phi},\hat{T}) &=& (\phi_1,T_1)\cos k_\beta(y\pm 1/2)\\ (\hat{u},\hat{v}) &=& (u_1,v_1)\sin k_\beta(y\pm 1/2)\end{array}\right\} \tag{5.2}$$

where

$$k_\beta = \beta\pi, \text{ with } \beta = 1,2,3,\ldots \tag{5.3}$$

being the mode number. Substituting the above solution in (5.1) we get an algebraic eigenvalue problem for linear stability:

$$cX_1 = \mathcal{Q}X_1$$

where $X_1 = (\phi_1, u_1, v_1, T_1)$ represents the amplitude of the fundamental mode, and the elements of matrix $\mathcal{Q}$ are

$$\mathcal{Q} = \begin{pmatrix} 0 & 0 & -\phi^0 k_\beta & 0 \\ -\frac{\mu^0_\phi}{\phi^0 H^2}k_\beta & -\frac{\mu^0}{\phi^0 H^2}k_\beta^2 & -1 & -\frac{\mu^0_T}{\phi^0 H^2}k_\beta \\ \frac{p^0_\phi}{H^2\phi^0}k_\beta & 0 & -\frac{(2\mu^0+\lambda^0)}{H^2\phi^0}k_\beta^2 & \frac{p^0_T}{H^2\phi^0}k_\beta \\ \frac{2(\mu^0_\phi-\mathcal{D}^0_\phi)}{\phi^0 \mathrm{dim}} & \frac{4\mu^0}{\phi^0 \mathrm{dim}}k_\beta & -\frac{2p^0}{\phi^0 \mathrm{dim}}k_\beta & \frac{2}{\phi^0 \mathrm{dim}}\left(\frac{-\kappa^0}{H^2}k_\beta^2+\mu^0_T-\mathcal{D}^0_T\right) \end{pmatrix}. \tag{5.4}$$

The mode-number β is the number of zero-crossings of the density eigenfunction within $y \in (-1/2, 1/2)$ as shown in figure 5.2 which displays all four eigenfunctions of the first three modes $\beta = 1,2,3$ for $\phi^0 = 0.15$, $H = 100$ and $e = 0.8$. It can be verified that the adjoint system [viz.

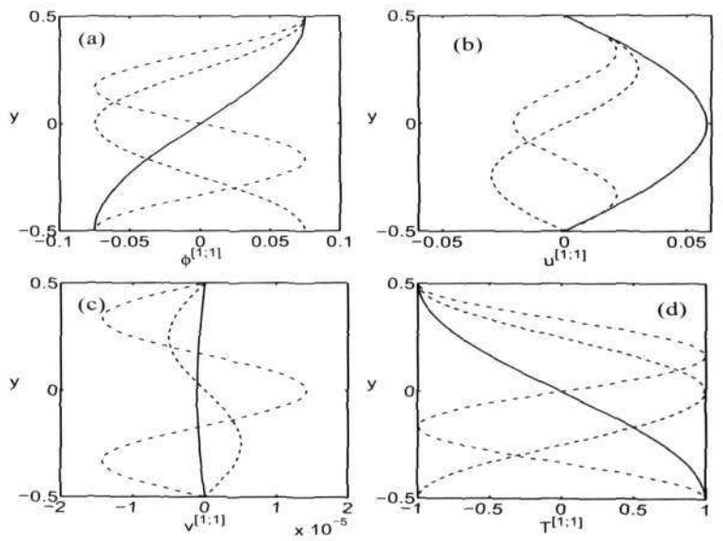

Figure 5.2: Linear eigenfunction profiles across the Couette gap for first three modes $\beta = 1$ (solid line), 2 (dashed line) and 3 (dot-dash line) for $\phi^0 = 0.15$, $H = 100$ and $e = 0.8$; (a) density, (b) streamwise velocity, (c) transverse velocity and (d) granular temperature.

Eqn. (4.25)] satisfies the analytical solution of the linear stability problem, and hence we can write its solution in terms of sine and cosine functions as in (5.2):

$$\left.\begin{array}{llll} \phi^\dagger(y) &= \phi_1^\dagger \cos k_\beta(y \pm 1/2), & u^\dagger(y) &= u_1^\dagger \sin k_\beta(y \pm 1/2), \\ v^\dagger(y) &= v_1^\dagger \sin k_\beta(y \pm 1/2), & T^\dagger(y) &= T_1^\dagger \cos k_\beta(y \pm 1/2) \end{array}\right\} \tag{5.5}$$

Similar to linear eigenfunctions, we found that the adjoint eigenfunctions corresponding to the least-stable shear-banding mode are real.

5.2 Outline of Weakly Nonlinear Analysis for Stream-wise Independent Flow

Below we are summarizing all the related governing equations (up to cubic order) of amplitude expansion method (see chapter 3) for the particular case of streamwise independent granular Couette flow. To formulate the weakly nonlinear analysis, we neglect partial derivatives of x and z from the general nonlinear disturbance equations (3.6) and follow the same procedure as given in §3.2, we obtain the following set of equations [cf. (3.39)]

$$\left.\begin{array}{rcl} \mathbf{L}_{kn} X^{[k;n]} &=& -c^{[n-1]} X^{[1;1]} \delta_{k1} + \mathbf{G}_{kn} \\ c^{[n-1]} &=& a^{[n-1]} + ib^{[n-1]} \\ \mathbf{G}_{kn} &=& -\left(ma^{[n-m]} + ikb^{[n-m]}\right) X^{\{k;m\}} + \mathbf{E}_{kn}/(1+\delta_{k0}) + \mathbf{F}_{kn} \\ \mathbf{L}_{kn} &=& \left(na^{(0)} + ikb^{(0)}\right) \mathbf{I} - \mathbf{L}. \end{array}\right\} \tag{5.6}$$

Note that $\mathbf{L}_k$ in (3.39) is same as $\mathbf{L}$ in (5.6) which is defined as

$$\mathbf{L} = \mathcal{L}(\partial/\partial x \to 0, \partial/\partial y \to d/dy, \ldots). \tag{5.7}$$

5.2.1 Linear Disturbance: Fundamental Mode

At $O(A)$ we get back the linear problem [viz (5.1)] for the fundamental mode $X^{[1;1]}$, by substituting $k = n = 1$ into (5.6):

$$\left.\begin{array}{rcl} \mathbf{L}_{11}X^{[1;1]} & = & 0 \\ \Rightarrow \mathbf{L}X^{[1;1]} & = & c^{(0)}X^{[1;1]} \end{array}\right\}, \tag{5.8}$$

where $\mathbf{L}$ is the linear stability operator. This equation is the same as (5.1) with $c = c^{(0)}$ and $\hat{X} = X^{[1;1]}$.

5.2.2 Mean Flow Distortion and Second Harmonic

At $O(A^2)$, we get equations for the mean flow distortion and the second harmonic. Substituting $k = n = 2$ into equation (5.6), we get

$$\mathbf{L}_{22}X^{[2;2]} \equiv \left[2(a^{(0)} + ib^{(0)})\mathbf{I} - \mathbf{L}\right] X^{[2;2]} = \mathbf{G}_{22} \equiv \mathbf{E}_{22}, \tag{5.9}$$

with the boundary conditions $\mathcal{B}X^{[2;2]} = 0$ at $y = \pm 1/2$. Here, $\mathbf{G}_{22} = N_2(X^{[1;1]}, X^{[1;1]}) = \mathbf{E}_{22}$ is the product of two fundamental modes. Note that there is no cubic nonlinear contribution at second order (i.e. $\mathbf{F}_{22} = 0$).

Substituting $k = 0$ and $n = 2$ into equation (5.6), we get, at $O(A^2)$,

$$\mathbf{L}_{02}X^{[0;2]} \equiv \left[2a^{(0)}\mathbf{I} - \mathbf{L}\right] X^{[0;2]} = \mathbf{G}_{02} \equiv \mathbf{E}_{02}/2 \tag{5.10}$$

where $\mathbf{G}_{02} = \mathbf{G}_{02}(\tilde{X}^{[1;1]}, X^{[1;1]})$, with boundary conditions $\mathcal{B}X^{[0;2]} = 0$ at $y = \pm 1/2$. The explicit functional form of $\mathbf{G}_{02}$ is

$$\mathbf{G}_{02} = 0.5\left[N_2(\tilde{X}^{[1;1]}, X^{[1;1]}) + N_2(X^{[1;1]}, \tilde{X}^{[1;1]})\right]. \tag{5.11}$$

Note that $X^{[0;2]}$ is always real. To verify this, let us write the complex conjugate equation for $X^{[0;2]}$

$$\mathbf{L}_{02}\tilde{X}^{[0;2]} = \tilde{\mathbf{G}}_{02}, \tag{5.12}$$

where $\mathbf{L}_{02} = \tilde{\mathbf{L}}_{02}$, and $\tilde{\mathbf{G}}_{02}$ is given by

$$\tilde{\mathbf{G}}_{02} = 0.5\left[N_2(X^{[1;1]}, \tilde{X}^{[1;1]}) + N_2(\tilde{X}^{[1;1]}, X^{[1;1]})\right] \equiv \mathbf{G}_{02}. \tag{5.13}$$

This immediately implies that $X^{[0;2]}$ is real:

$$X^{[0;2]} = \tilde{X}^{[0;2]}. \tag{5.14}$$

5.2.3 Distortion of Fundamental and the First Landau Coefficient

At $O(A^3)$, we get an equation for the distortion of the fundamental mode $X^{[1;3]}$ by substituting $k = 1$ and $n = 3$ into equation (5.6):

$$\mathbf{L}_{13}X^{[1;3]} \equiv \left[(3a^{(0)} + ib^{(0)})\mathbf{I} - \mathbf{L}\right] X^{[1;3]} = -c^{(2)}X^{[1;1]} + \mathbf{G}_{13}. \tag{5.15}$$

The expression for the inhomogeneous term $\mathbf{G}_{13}$ is given below

$$\begin{aligned}\mathbf{G}_{13} &= N_2(X^{[0,2]}, X^{[1;1]}) + N_2(\tilde{X}^{[0,2]}, X^{[1;1]}) + N_2(X^{[1;1]}, X^{[0,2]}) + N_2(X^{[1;1]}, \tilde{X}^{[0,2]}) \\ &\quad + N_2(\tilde{X}^{[1,1]}, X^{[2;2]}) + N_2(X^{[2;2]}, \tilde{X}^{[1,1]}) + N_3(\tilde{X}^{[1,1]}, X^{[1;1]}, X^{[1;1]}) \\ &\quad + N_3(X^{[1;1]}, \tilde{X}^{[1,1]}, X^{[1;1]}) + N_3(X^{[1;1]}, X^{[1;1]}, \tilde{X}^{[1,1]}) \\ &= 2\left[N_2(X^{[0,2]}, X^{[1;1]}) + N_2(X^{[1;1]}, X^{[0,2]})\right] + N_2(\tilde{X}^{[1,1]}, X^{[2;2]}) + N_2(X^{[2;2]}, \tilde{X}^{[1,1]}) \\ &\quad + N_3(\tilde{X}^{[1,1]}, X^{[1;1]}, X^{[1;1]}) + N_3(X^{[1;1]}, \tilde{X}^{[1,1]}, X^{[1;1]}) + N_3(X^{[1;1]}, X^{[1;1]}, \tilde{X}^{[1,1]})\end{aligned}$$

and the boundary condition is $\mathcal{B}X^{[1;3]} = 0$ at $y = \pm 1/2$. In the above equation, the quadratic and cubic nonlinear terms represent $\mathbf{E}_{kn}$ and $\mathbf{F}_{kn}$, respectively, in (5.6).

In (5.15), the first Landau coefficient $c^{(2)}$ is unknown which can be found by invoking the solvability condition

$$c^{(2)} = a^{(2)} + ib^{(2)} = \frac{\int_{-1/2}^{1/2} \tilde{X}^{\dagger}\mathbf{G}_{13}\,\mathrm{d}y}{\int_{-1/2}^{1/2} \tilde{X}^{\dagger}X^{[1;1]}\,\mathrm{d}y}, \tag{5.16}$$

where $X^{\dagger}$ is the adjoint linear eigenfunction that corresponds to the solution of (4.18) (see chapter 4 for the details of the adjoint problem). The solvability condition or the Fredholm alternative asserts that the inhomogeneous part of differential equations (5.15) must be orthogonal to the adjoint of the associated homogeneous problem this guarantees the uniqueness of the solution of the inhomogeneous differential equations (5.15). For the shearbanding instability, $X^{\dagger}$ is given by (5.5).

5.3 Symmetries of Linear and Nonlinear Modes

Before embarking on the analytical/numerical solution procedure of (5.8), (5.9), (5.10), (5.15) and (5.16), here we analyze certain symmetries of linear ($X^{[1;1]}$) and nonlinear modes ($X^{[2;2]}$, $X^{[0;2]}$ and $X^{[1;3]}$) up-to the cubic order.

First, let us consider the base state solution of uniform shear with constant density and granular temperature. The base state equations remain invariant under the following transformation:

$$\phi^0(-y) = \phi^0(y), \quad u^0(-y) = -u^0(y), \quad T^0(-y) = T^0(y). \tag{5.17}$$

This symmetry about the mid-plane $y = 0$ of the base state solution (4.11) implies that the velocity is antisymmetric about $y = 0$ and the density and granular temperature are symmetric about $y = 0$.

The linear disturbance equations for the fundamental mode and the related boundary conditions satisfy the following two symmetry groups (Alam & Nott 1998)

$$\left.\begin{aligned}\phi^{[1;1]}(y) &= \phi^{[1;1]}(-y), & u^{[1;1]}(y) &= -u^{[1;1]}(-y) \\ v^{[1;1]}(y) &= -v^{[1;1]}(-y), & T^{[1;1]}(y) &= T^{[1;1]}(-y)\end{aligned}\right\} \tag{5.18}$$

and

$$\left.\begin{aligned}\phi^{[1;1]}(y) &= -\phi^{[1;1]}(-y), & u^{[1;1]}(y) &= u^{[1;1]}(-y) \\ v^{[1;1]}(y) &= v^{[1;1]}(-y), & T^{[1;1]}(y) &= -T^{[1;1]}(-y)\end{aligned}\right\}. \tag{5.19}$$

While the former *preserves* the symmetry of the base-state solution (5.17), the latter *breaks* (5.17).

It follows from the symmetries of the fundamental mode that the interaction of two funda-

Symbols	*Definition*
ϕ^0	Mean density or solid fraction (the volume fraction of particles)
$H = h/d$	Ratio between the Couette gap and the particle diameter
e	Restitution coefficient
$\beta = 1, 2, 3, \cdots$	Mode number
$a^{(0)}$	Growth rate of the fundamental mode,
$a^{(2)}$	Real part of first Landau coefficient,
H_c	Critical Couette gap
ϕ_c	Critical mean density
$A = A_e$	Equilibrium amplitude
H^*	$H\beta^{-1}(1-e^2)^{1/2}$

Table 5.1: Control parameters for stability

mentals would give rise to the following symmetry for the second harmonic

$$\left.\begin{array}{llll} \phi^{[2;2]}(y) = \phi^{[2;2]}(-y), & u^{[2;2]}(y) = -u^{[2;2]}(-y) \\ v^{[2;2]}(y) = -v^{[2;2]}(-y), & T^{[2;2]}(y) = T^{[2;2]}(-y) \end{array}\right\}. \tag{5.20}$$

This, of course, preserves the symmetry (5.17) of the base state solution. The distortion to the mean flow, $X^{[0,2]}$, also follows the same symmetry of the base state since $X^{[0,2]}$ appears at the quadratic order $O(A^2)$.

Similarly, the distortion to the fundamental mode, $X^{[1,3]}$, satisfies the following symmetries

$$\left.\begin{array}{llll} \phi^{[1;3]}(y) = \phi^{[1;3]}(-y), & u^{[1;3]}(y) = -u^{[1;3]}(-y) \\ v^{[1;3]}(y) = -v^{[1;3]}(-y), & T^{[1;3]}(y) = T^{[1;3]}(-y) \end{array}\right\} \tag{5.21}$$

and

$$\left.\begin{array}{llll} \phi^{[1;3]}(y) = -\phi^{[1;3]}(-y), & u^{[1;3]}(y) = u^{[1;3]}(-y) \\ v^{[1;3]}(y) = v^{[1;3]}(-y), & T^{[1;3]}(y) = -T^{[1;3]}(-y) \end{array}\right\}. \tag{5.22}$$

The above symmetry groups can be understood from the fact that the fundamental mode is of $O(A)$ and the interaction of two fundamentals gives rise to the terms of order $O(A^2)$, and so forth. Thus the second harmonic $X^{[2;2]}$ admits a symmetry which is the product of symmetries of the fundamental mode. Similarly, the symmetry of the distortion of fundamental at $O(A^3)$ would follow the product of symmetries of the fundamental and the second harmonic.

Table 5.1 summarizes all dimensionless parameters that we will frequently refer to while presenting our results in §5.4-§5.6.

5.4 Analytical Solution and Comparison with Numerical (Spectral) Solution

The underlying symmetries of the fundamental mode and its nonlinear corrections as discussed in §5.3, together with the analytical solution of the fundamental mode (Alam & Nott 1998), helped us to solve the nonlinear problem analytically as we discuss in §5.4.1, §5.4.2 and §5.4.4. As mentioned before this problem was tackled numerically in (Shukla & Alam 2009) which is detailed in chapter 4, even though the order parameter equation was derived there using another method, namely, the center manifold reduction technique. Apart from providing new analytical solutions in this chapter, the spectral-based numerical technique as detailed in chapter 3 is also

validated here against present analytical solutions for harmonics and the first Landau coefficient.

5.4.1 Solution for Second Harmonic and Mean Flow Distortion

It can be verified that there exists analytical solution for the second harmonic:

$$\left.\begin{array}{rclrcl} \phi^{[2;2]}(y) & = & \phi_2 \cos k_{2\beta}(y \pm 1/2), & u^{[2;2]}(y) & = & u_2 \sin k_{2\beta}(y \pm 1/2), \\ v^{[2;2]}(y) & = & v_2 \sin k_{2\beta}(y \pm 1/2), & T^{[2;2]}(y) & = & T_2 \cos k_{2\beta}(y \pm 1/2) + T^{mean}_{k_{2\beta}} \end{array}\right\} \quad (5.23)$$

where

$$k_{2\beta} = 2\beta\pi, \text{ with } \beta = 1, 2, 3 \ldots \quad (5.24)$$

and $X_{22} = [\phi_2, u_2, v_2, T_2]$ is the amplitude of the second harmonic. The mean term in granular temperature is calculated from

$$T^{mean}_{k_{2\beta}} = \frac{f_{nl}}{f_l}, \quad (5.25)$$

where f_{nl} denotes nonlinear terms and f_l are related to linear terms:

$$\begin{aligned} f_{nl} = & -\frac{1}{2\phi^0}\left(-v_1 T_1 k_\beta + c^{(0)}\phi_1 T_1\right) + \frac{1}{\phi^0 dim}\left[-k_\beta\left(p^0_\phi \phi_1 + p^0_T T_1\right) v_1 + 2\mu^0 k^2_\beta\left(v_1^2 + 0.5u_1^2\right)\right. \\ & +0.5\left(\mu^0_{\phi\phi}\phi_1^2 + \mu^0_{TT}T_1^2 + 2\mu^0_{\phi T}\phi_1 T_1\right) + 2k_\beta u_1\left(\mu^0_\phi \phi_1 + \mu^0_T T_1\right) + \lambda^0 k^2_\beta v_1^2 \\ & \left.-0.5\left(\mathcal{D}^0_{\phi\phi}\phi_1^2 + \mathcal{D}^0_{TT}T_1^2 + 2\mathcal{D}^0_{\phi T}\phi_1 T_1\right)\right], \quad (5.26) \\ f_l = & \ 2c^{(0)} - \frac{2}{\phi^0 dim}\left(\mu^0_T - \mathcal{D}^0_T\right). \quad (5.27) \end{aligned}$$

The modal amplitude of the second harmonic, $X_{22} = [\phi_2, u_2, v_2, T_2]$, satisfies the following algebraic matrix-equation:

$$L^\beta_{22} X_{22} = G^\beta_{22} \quad (5.28)$$

where

$$L^\beta_{22} = 2(a^{(0)} + ib^{(0)})I - \hat{L}^\beta \quad (5.29)$$

with

$$\hat{L}^\beta = \begin{pmatrix} 0 & 0 & -\phi^0 k_{2\beta} & 0 \\ -\frac{k_{2\beta}\mu^0_\phi}{\phi^0 H^2} & -\frac{k^2_{2\beta}\mu^0}{\phi^0 H^2} & -1 & -\frac{k_{2\beta}\mu^0_T}{\phi^0 H^2} \\ \frac{k_{2\beta}p^0_\phi}{H^2\phi^0} & 0 & -\frac{k^2_{2\beta}(2\mu^0+\lambda^0)}{H^2\phi^0} & \frac{k_{2\beta}p^0_T}{H^2\phi^0} \\ \frac{2(\mu^0_\phi - \mathcal{D}^0_\phi)}{\phi^0 dim} & \frac{4k_{2\beta}\mu^0}{\phi^0 dim} & -\frac{2k_{2\beta}p^0}{\phi^0 dim} & \frac{2}{\phi^0 dim}\left(-k^2_{2\beta}\frac{\kappa^0}{H^2} + \mu^0_T - \mathcal{D}^0_T\right) \end{pmatrix}, \quad (5.30)$$

and the nonlinear inhomogeneous terms, $G_{22}^{\beta} = (G_{22}^{1\beta}, G_{22}^{2\beta}, G_{22}^{3\beta}, G_{22}^{4\beta})^{Tr}$, are

$$\left.\begin{aligned}
G_{22}^{1\beta} &= -k_\beta \phi_1 v_1, \\
G_{22}^{2\beta} &= \frac{1}{2}\Big[-\frac{1}{\phi^0}\left(\phi^0 v_1 u_1 k_\beta + \phi_1 v_1 + c^{(0)}\phi_1 u_1\right) + \frac{1}{\phi^0 H^2}\left(-2k_\beta^2\left(\mu_\phi^0\phi_1 + \mu_T^0 T_1\right)u_1\right. \\
&\quad \left. -k_\beta\left(\mu_{\phi\phi}^0\phi_1^2 + \mu_{TT}^0 T_1^2 + 2\mu_{\phi T}^0\phi_1 T_1\right)\right)\Big], \\
G_{22}^{3\beta} &= \frac{1}{2}\Big[-\frac{1}{\phi^0}\left(k_\beta\phi^0 v_1^2 + c^{(0)}\phi_1 v_1\right) + \frac{1}{\phi^0 H^2}\left(k_\beta\left(p_{\phi\phi}^0\phi_1^2 + p_{TT}^0 T_1^2 + 2p_{\phi T}^0\phi_1 T_1\right)\right. \\
&\quad \left. -4k_\beta^2\left(\mu_\phi^0\phi_1 + \mu_T^0 T_1\right)v_1 - 2k_\beta^2\left(\lambda_\phi^0\phi_1 + \lambda_T^0 T_1\right)v_1\right)\Big], \\
G_{22}^{4\beta} &= \Big[-\frac{1}{2\phi^0}\left(\phi^0 v_1 T_1 k_\beta + c^{(0)}\phi_1 T_1\right) - \frac{2k_\beta^2 T_1}{\phi^0 H^2 dim}\left(\kappa_\phi^0\phi_1 + \kappa_T^0 T_1\right) \\
&\quad + \frac{1}{\phi^0 dim}\left(-k_\beta\left(p_\phi^0\phi_1 + p_T^0 T_1\right)v_1 + 2\mu^0 k_\beta^2\left(v_1^2 + 0.5u_1^2\right) + 0.5\left(\mu_{\phi\phi}^0\phi_1^2 + \mu_{TT}^0 T_1^2 + 2\mu_{\phi T}^0\phi_1 T\right)\right. \\
&\quad \left. +2k_\beta\left(\mu_\phi^0\phi_1 + \mu_T^0 T_1\right)u_1 + \lambda^0 k_\beta^2 v_1^2 - 0.5\left(\mathcal{D}_{\phi\phi}^0\phi_1^2 + \mathcal{D}_{TT}^0 T_1^2 + 2\mathcal{D}_{\phi T}^0 T_1^2\right)\right)\Big].
\end{aligned}\right\}$$

The matrix equation (5.28) can be easily solved to determine the complete solution for the second harmonic from (5.23) if $2(a^{(0)} + ib^{(0)})$ is not equal to any of the eigenvalues of $\hat{L}^\beta$.

For the shear-banding mode, the eigenvalue is real (Alam & Nott 1998; Alam *et al.* 2008), i.e. $b^{(0)} = 0$. This implies that

$$\mathbf{L}_{22} = \left[2(a^{(0)} + ib^{(0)})\mathbf{I} - \mathbf{L}\right] = \left[2a^{(0)}\mathbf{I} - \mathbf{L}\right] \equiv \mathbf{L}_{02}, \tag{5.31}$$

i.e. the linear operators for the second harmonic and the mean-flow distortion are identical. From (5.9) and (5.10) we have $\mathbf{G}_{22} = N_2(X^{[1:1]}, X^{[1:1]}) = \mathbf{G}_{02}$, and therefore

$$X^{[0,2]} = X^{[2,2]} \tag{5.32}$$

for the shear-banding mode. Therefore, the solution to the mean flow distortion, $X^{[0,2]}$, is the same as in (5.23).

Before moving to the first Landau coefficient, let us compare the analytical solutions for the second harmonic (5.23) with the same calculated numerically by discretizing the differential equations using spectral collocation technique and solving the resulting algebraic equations by the singular value decomposition as detailed in chapter 3. Figures 5.3-5.6 display such comparisons between analytical and numerical solutions for the shape of the fundamental and the second harmonic for mode $\beta = 1$ and $\beta = 2$, respectively, at a mean density of $\phi^0 = 0.15$. A similar comparison for second harmonic with $\beta = 1$ at a lower mean density of $\phi^0 = 0.05$ is displayed in figure 5.7. In each panel, the solid line refers to analytical solution and the circles to numerical solution, and we find excellent agreement between the two.

5.4.2 Solution for First Landau Coefficient

To determine the first Landau coefficient, we consider the equation for the distortion of the fundamental which appears at the cubic order. Recall that the inhomogeneous terms $\mathbf{G}_{13}$ of this equation depend on the fundamental ($X^{[1,1]}$), the second harmonic ($X^{[2,2]}$) and the mean-flow distortion ($X^{[0,2]}$), along with base state solution. Inserting analytical solutions for $X^{[1,1]}$, $X^{[2,2]}$ and $X^{[0,2]}$, the expressions of $\mathbf{G}_{13} = (G_{13}^1, G_{13}^2, G_{13}^3, G_{13}^4)$ are simplified as follows:

$$\begin{aligned}
(G_{13}^1, G_{13}^4) &= 3\left(G_{13}^{1\beta 3}, G_{13}^{4\beta 3}\right)\cos k_{3\beta}(y \pm 1/2) + 3\left(G_{13}^{1\beta 1}, G_{13}^{4\beta 1}\right)\cos k_\beta(y \pm 1/2), \\
(G_{13}^2, G_{13}^3) &= 3\left(G_{13}^{2\beta 3}, G_{13}^{3\beta 3}\right)\sin k_{3\beta}(y \pm 1/2) + 3\left(G_{13}^{2\beta 1}, G_{13}^{3\beta 1}\right)\sin k_\beta(y \pm 1/2).
\end{aligned}$$

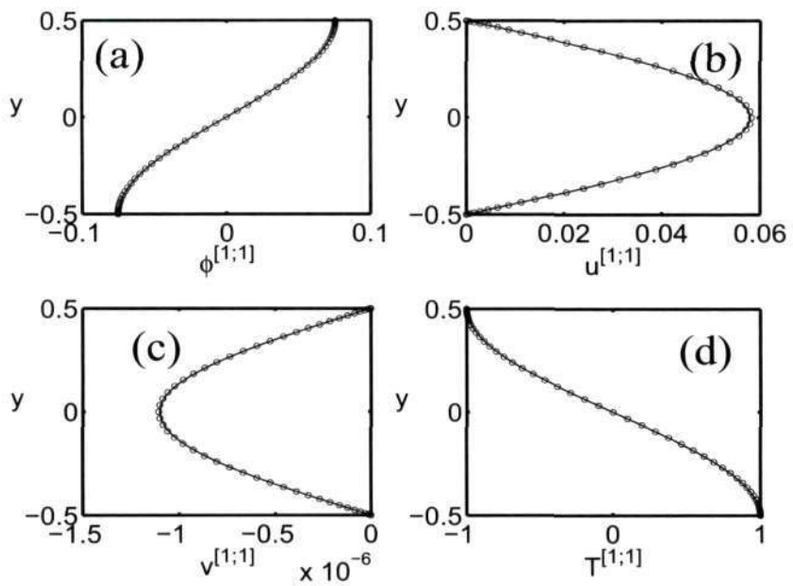

Figure 5.3: Comparison between analytical (solid line) and spectral/numerical (circles) solutions for the fundamental mode (linear eigenfunction) $X^{[1;1]}$ with mode $\beta = 1$: (*a*) $\phi^{[1;1]}$, (*b*) $u^{[1;1]}$, (*c*) $v^{[1;1]}$ and (*d*) $T^{[1;1]}$ for $\phi^0 = 0.15$, $H = 100$ and $e = 0.8$.

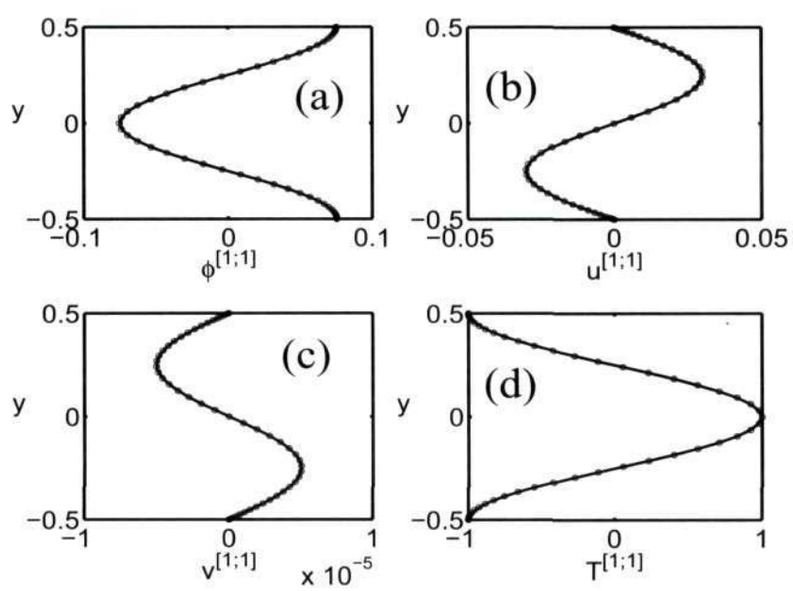

Figure 5.4: Same as figure 5.3 but for mode $\beta = 2$

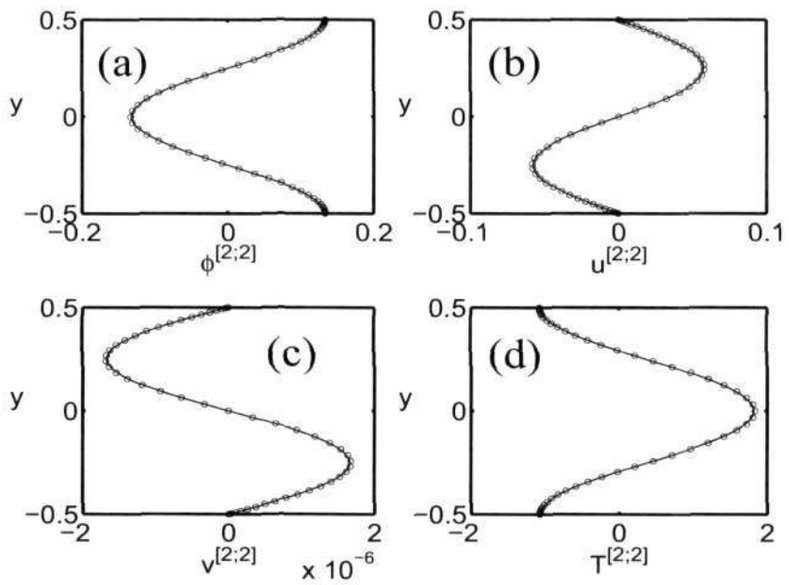

Figure 5.5: Comparison between analytical (solid line) and spectral/numerical (circles) solutions for the second harmonic $X^{[2;2]}$ with mode $\beta = 1$: (a) $\phi^{[2;2]}$, (b) $u^{[2;2]}$, (c) $v^{[2;2]}$ and (d) $T^{[2;2]}$ for $\phi^0 = 0.15$, $H = 100$ and $e = 0.8$.

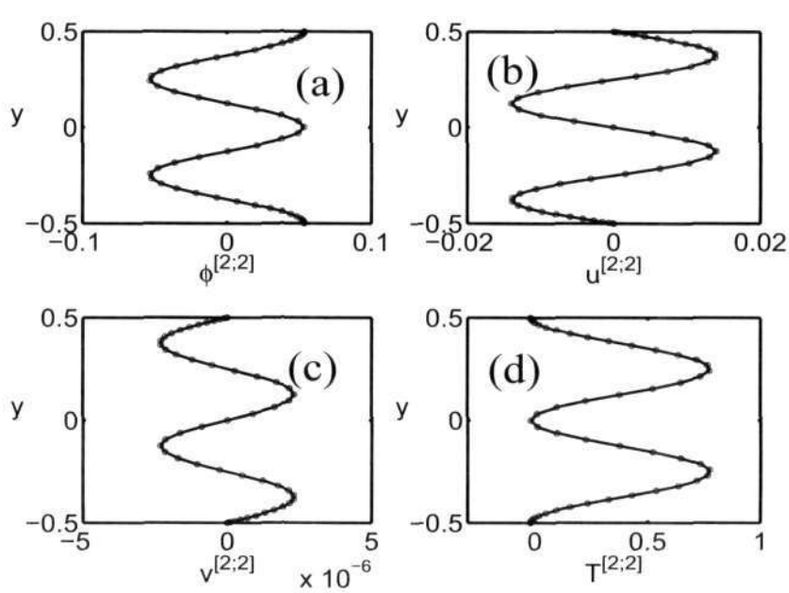

Figure 5.6: Same as figure 5.5 but for mode $\beta = 2$

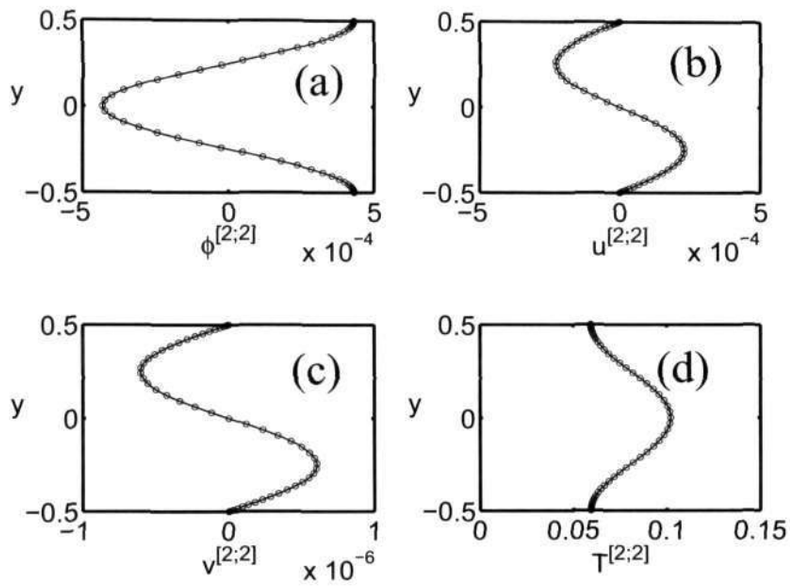

Figure 5.7: Same as figure 5.5, but at a lower density $\phi^0 = 0.05$.

The y-independent terms $G_{13}^{1\beta 3}$, $G_{13}^{4\beta 3}$, $G_{13}^{1\beta 1}$, $G_{13}^{4\beta 1}$, $G_{13}^{2\beta 3}$, $G_{13}^{3\beta 3}$, $G_{13}^{2\beta 1}$ and $G_{13}^{3\beta 1}$ are given in Appendix 5B.

Since we know the analytical form of $\mathbf{G}_{13}$, we can now find *first Landau coefficient* from the solvability condition (5.16) taking the inner product of $\mathbf{G}_{13}$ and the adjoint of the linear problem $X^\dagger$. Inserting the analytical solutions of $X^\dagger$ and $X^{[1;1]}$ and the expressions of $\mathbf{G}_{13}$ in the numerator and denominator of (5.16), we obtain

$$\begin{aligned}
\int_{-1/2}^{1/2} \tilde{X}^\dagger \, \mathbf{G}_{13} \, dy \;=\; & 3\left(\tilde{\phi}_1^\dagger G_{13}^{1\beta 3} + \tilde{T}_1^\dagger G_{13}^{4\beta 3}\right) \int_{-1/2}^{1/2} \cos k_\beta (y \pm 1/2) \cos k_{3\beta} (y \pm 1/2) \, \mathrm{d}y \\
& +3\left(\tilde{u}_1^\dagger G_{13}^{2\beta 3} + \tilde{v}_1^\dagger G_{13}^{3\beta 3}\right) \int_{-1/2}^{1/2} \sin k_\beta (y \pm 1/2) \sin k_{3\beta} (y \pm 1/2) \, \mathrm{d}y \\
& +3\left(\tilde{\phi}_1^\dagger G_{13}^{1\beta 1} + \tilde{T}_1^\dagger G_{13}^{4\beta 1}\right) \int_{-1/2}^{1/2} \cos^2 k_\beta (y \pm 1/2) \, \mathrm{d}y \\
& +3\left(\tilde{u}_1^\dagger G_{13}^{2\beta 1} + \tilde{v}_1^\dagger G_{13}^{3\beta 1}\right) \int_{-1/2}^{1/2} \sin^2 k_\beta (y \pm 1/2) \, \mathrm{d}y \\
= \; & \frac{3}{2}\left(\tilde{\phi}_1^\dagger G_{13}^{1\beta 1} + \tilde{T}_1^\dagger G_{13}^{4\beta 1} + \tilde{u}_1^\dagger G_{13}^{2\beta 1} + \tilde{v}_1^\dagger G_{13}^{3\beta 1}\right) \qquad (5.33)
\end{aligned}$$

and

$$\int_{-1/2}^{1/2} \tilde{X}^\dagger X^{[1;1]}\,\mathrm{d}y = \left(\tilde{\phi}_1^\dagger \phi_1 + \tilde{T}_1^\dagger T_1\right) \int_{-1/2}^{1/2} \cos^2 k_\beta (y \pm 1/2)\,\mathrm{d}y + \left(\tilde{u}_1^\dagger u_1 + \tilde{v}_1^\dagger v_1\right) \int_{-1/2}^{1/2} \sin^2 k_\beta (y \pm 1/2)\,\mathrm{d}y = \frac{1}{2}\left(\tilde{\phi}_1^\dagger \phi_1 + \tilde{T}_1^\dagger T_1 + \tilde{u}_1^\dagger u_1 + \tilde{v}_1^\dagger v_1\right). \tag{5.34}$$

The final expression for the first Landau coefficient (5.16) simplifies to

$$c^{(2)} \equiv a^{(2)} + ib^{(2)} = \frac{3\left(\tilde{\phi}_1^\dagger G_{13}^{1\beta 1} + \tilde{T}_1^\dagger G_{13}^{4\beta 1} + \tilde{u}_1^\dagger G_{13}^{2\beta 1} + \tilde{v}_1^\dagger G_{13}^{3\beta 1}\right)}{\tilde{\phi}_1^\dagger \phi_1 + \tilde{T}_1^\dagger T_1 + \tilde{u}_1^\dagger u_1 + \tilde{v}_1^\dagger v_1}. \tag{5.35}$$

Since for the shear banding mode the linear eigenfunction, its adjoint and the second harmonic are found to be real, the right hand side of the above equation is always real for this mode. This implies that the imaginary part of the first Landau coefficient is identically zero for the shear banding mode:

$$b^{(2)} = 0, \quad \Rightarrow \quad c^{(2)} \equiv a^{(2)}. \tag{5.36}$$

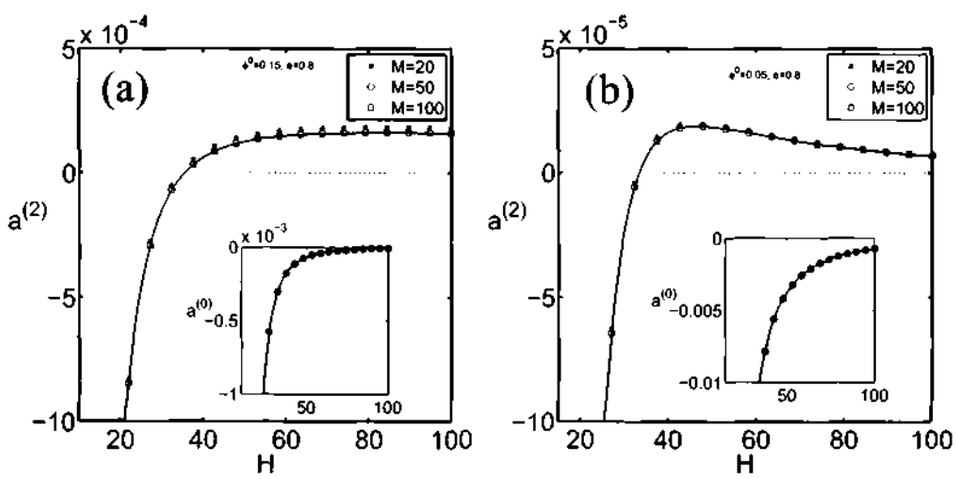

Figure 5.8: Comparison of the first Landau Coefficient between analytical (solid line) and spectral/numerical: stars for $M = 20$, circles for $M = 50$ and squares for $M = 100$, solutions: (a) $\phi^0 = 0.15$ and (b) $\phi^0 = 0.05$, with $e = 0.8$. Inset in each panel shows the variation of growth rate of the least-stable mode (mode number $\beta = 1$) with H.

To compute $a^{(2)}$ analytically, we need to insert the analytical solutions for the fundamental mode (5.2) and the second harmonic (5.23) in (5.35). The solution for the first Landau coefficient $[a^{(2)}]$ from (5.35) is shown in figures 5.8(a) and 5.8(b), marked by solid lines, which display the variations of $a^{(2)}$ with Couette gap at two values of mean density $\phi^0 = 0.15$ and 0.05, respectively.

To further ascertain the accuracy of spectral-based numerical method as given in chapter 3 (more specifically, the Gauss-Chebyshev quadrature as detailed in chapter 3), we also calculated $a^{(2)}$ by using the numerical solutions for the fundamental mode and the second harmonic and

then evaluated the integrals in (5.16) by using the Gauss-Chebyshev quadrature.

The stars, circles and squares in figure 5.8 denote the corresponding numerical solutions for $a^{(2)}$ with $M = 20$, 50 and 100, respectively, which agree well with the analytical solution (solid line in figure). The insets in figures 5.8 (a) and 5.8 (b) show the variation of the growth rate $a^{(0)}$ of the least-stable mode, again calculated both analytically and numerically with excellent agreement between the two. Note that the least-stable mode is stable (i.e. $a^{(0)} < 0$) at both mean densities in figure 5.8, and we will discuss the possibility of subcritical bifurcations in such cases later in §5.5.3.

To know the quantitative accuracy of the numerical method, we show in table 5.2 the spectrally calculated values for the least-stable growth rate $a^{(0)}$ for four set of control parameters (ϕ^0, H) at a restitution coefficient of $e = 0.8$. The second, third and fourth columns in table 5.2 show spectral solutions with collocation points of $M = 10$, 20 and 50, respectively, while the last column shows the corresponding analytical solution. It is clear that with just 10 collocation points the least-stable eigenvalue $a^{(0)}$ agrees with its analytical solution within an error of less than 0.0001%.

Table 5.3 displays a similar comparison between spectral and analytical solutions for the first Landau coefficient $a^{(2)}$, with parameter values as in table 5.2. Note that we have not shown results for $M = 10$ since they are way off from the analytical solution; rather we show spectral solutions with collocation points of $M = 20$, 50 and 80, respectively, in the second, third and fourth columns in table 5.3. Even though the spectral solutions for $a^{(2)}$ with $M = 50$, such as those in figure 5.8, are very close to analytical solutions (solid line), there is an error of up-to 3% with $M = 50$ collocation points; to achieve an accuracy of less than 1% we need to employ more than $M = 75$ collocation points. The same level of accuracy of the spectral solutions for $a^{(2)}$ holds at other values of control parameters (ϕ^0, H, e).

(ϕ^0, H)	$-a^{(0)}$ $(M = 10)$	$-a^{(0)}$ $(M = 20)$	$-a^{(0)}$ $(M = 50)$	$-a^{(0)}$ (Analytical)
$(0.05, 50)$	3.7516040×10^{-3}	3.7516039×10^{-3}	3.7516039×10^{-3}	$3.75160396 \times 10^{-3}$
$(0.05, 100)$	7.4113835×10^{-4}	7.4113835×10^{-4}	7.4113835×10^{-4}	$7.41138354 \times 10^{-4}$
$(0.15, 50)$	6.2902898×10^{-5}	6.2902895×10^{-5}	6.2902895×10^{-5}	$6.29028958 \times 10^{-5}$
$(0.15, 100)$	6.9159585×10^{-6}	6.9159583×10^{-6}	6.9159584×10^{-6}	$6.91595832 \times 10^{-6}$

Table 5.2: Comparison between spectral and analytical solutions for the least-stable growth rate. Spectral solutions with different number of collocation points $M = 10$, 20, 50 are shown in 2nd, 3rd and 4th columns, respectively, and the last column represents analytical solution.

5.4.3 Resonance at $O(A^2)$: Second Harmonic and Distortion to Mean Flow

Figures 5.9(a) and 5.9(b) are same as figure 5.8(a)-5.8(b) but for the higher densities, $\phi^0 = 0.5$ and 0.3, respectively, where the inset shows the variation of growth rate. The insets of figure 5.9(a)-5.9(b) show that $\beta = 1$ mode remains least-stable mode until it crosses the next higher-order mode at $\beta = 2$, after which it becomes least-stable mode which is shown by circles. At some value of H, successive modes cross each other, beyond which the mode with higher β becomes dominant until the next cross over.

Recall that in the numerical method we get eigenvalues in one shot compared to analytical method (Alam & Nott 1998; Alam *et al.* 2008). As shown in the main panel of figure 5.9(a)-(b) that the analytical and numerical values of $a^{(2)}$ are well agreed for the range of Couette gap

(ϕ^0, H)	$a^{(2)}$ $(M = 20)$	$a^{(2)}$ $(M = 50)$	$a^{(2)}$ $(M = 80)$	$a^{(2)}$ (Analytical)
$(0.05, 50)$	1.951184×10^{-5}	1.859661×10^{-5}	1.848715×10^{-5}	$1.84161433 \times 10^{-5}$
$(0.05, 100)$	7.158992×10^{-6}	6.916186×10^{-6}	6.887152×10^{-6}	$6.86830930 \times 10^{-6}$
$(0.15, 50)$	1.477738×10^{-4}	1.289434×10^{-4}	1.266915×10^{-4}	$1.25230414 \times 10^{-4}$
$(0.15, 100)$	1.802382×10^{-4}	1.623106×10^{-4}	1.601668×10^{-4}	$1.58775650 \times 10^{-4}$

Table 5.3: Comparison between spectral and analytical solutions for first Landau coefficient. Spectral solutions with different number of collocation points M = 20, 50, 80 are shown in 2nd, 3rd and 4th columns, respectively, and the last column represents analytical solution.

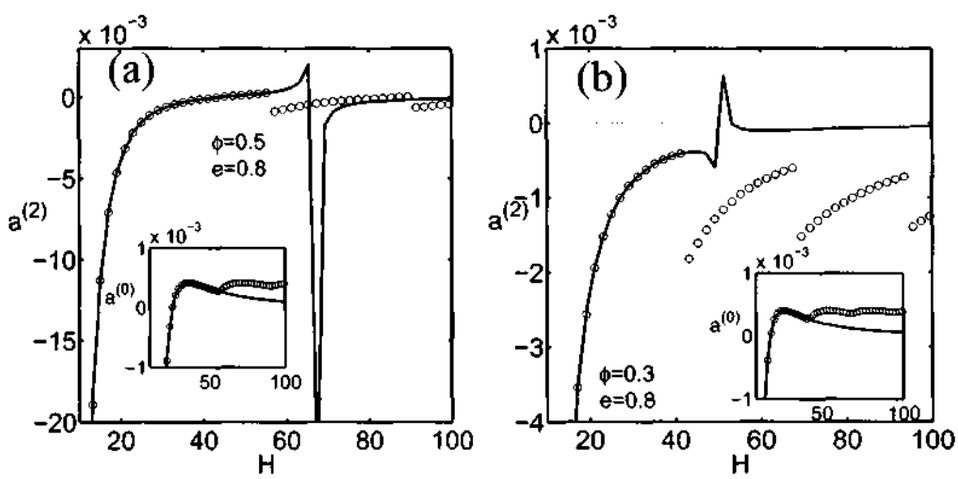

Figure 5.9: Same as figure 5.8 but for ϕ^0: (*a*) 0.5 and (*b*) 0.3. The collocation points are used 50.

before the cross over of modes (see inset). It can be seen from these figures that there is a jump in $a^{(2)}$ for a Couette gap near the cross over of modes $\beta = 1$ and $\beta = 2$. What is the reason of sudden jump or discontinuity in $a^{(2)}$ for a specific value of Couette gap in a well posed 4×4 matrix problem?

To answer this question and to know more about this discontinuity we have magnified figures 5.9(a)-5.9(b), corresponding to analytical solution (represented by a solid lines in figures 5.9(a)-5.9(b)) just beyond the cross over in figures 5.10(a)-5.10(b).

This discontinuity may be explained by looking back to second harmonic equation (5.28). Let us denote the four eigenvalues of $\hat{L}^{\beta}$ operator (5.29) by c_j for $j = 1$ to 4. If $2(a^{(0)} + ib^{(0)})$ is equal to c_j for any $j = 1$ to 4, the homogeneous problem associated to the problem (5.28) admits eigensolution. Thus the condition,

$$2(a^{(0)} + ib^{(0)}) = c_j \tag{5.37}$$

is the "resonance" condition at $O(A^2)$ which arises due to the $1:2$ discrete wave resonant interaction (note that the ratio of wavenumbers is $k_{\beta}/k_{2\beta}$ is $1/2$). Note that c_j is not necessarily the least-stable mode. Therefore, there could be a possibility of mode interactions with fundamental mode for any mode number β with the decaying second harmonic mode at mode number 2β. At resonance points the single mode analysis is not valid. To capture dynamics near these points we need to include these resonating modes in the expansion to derive coupled Landau equation (see chapter 9).

It is verified that the condition for resonance (5.37) exactly satisfies for the parameters at which $a^{(2)}$ diverges which is shown geometrically in inset plots in figures 5.10(a)-5.10(b). In each inset we have plotted the left hand side of (5.37) i.e. $2a^{(0)}$ (since $b^{(0)} = 0$) by a solid line and c_j by a dashed line; their intersection points are shown by arrows. For $\phi^0 = 0.5$ resonance occurs at $H \approx 67$ and consequently $a^{(2)}$ diverges at this point. Similarly for $\phi^0 = 0.3$, figure 5.10(b), $a^{(2)}$ diverges at $H \approx 50.99$ where the resonance condition holds, see inset.

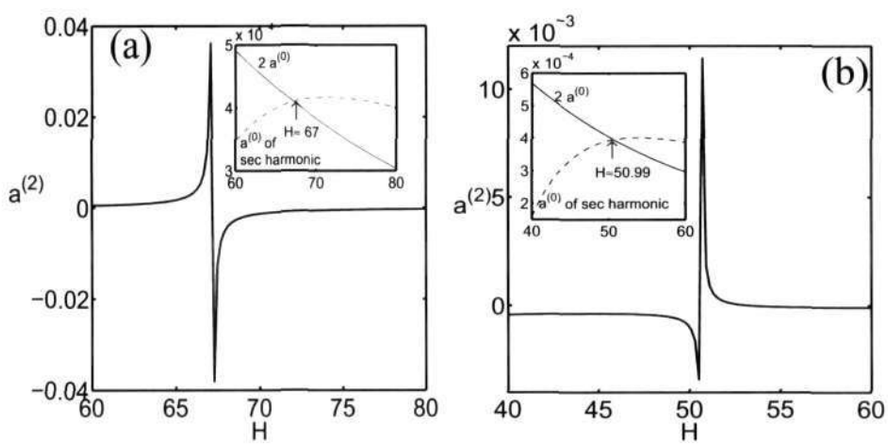

Figure 5.10: Variation of $a^{[2]}$ with Couette gap using analytical solution for ϕ^0: (a) 0.5 and (b) 0.3. The other parameters are same as figure 5.9. The inset shows the mean flow resonance condition for $\beta = 1$ where the solid line is $2a^{(0)}$ and dashed line is the eigenvalue of $\hat{L}^{\beta}$.

As described above that the nonlinear problem encounters resonance, at order two in perturbation amplitude, if we employ fixed mode number throughout the range of Couette gaps, however we know that beyond a certain Couette gap the least-stable mode belongs to a higher value of the mode number. The numerical method does not depend on the mode number rather

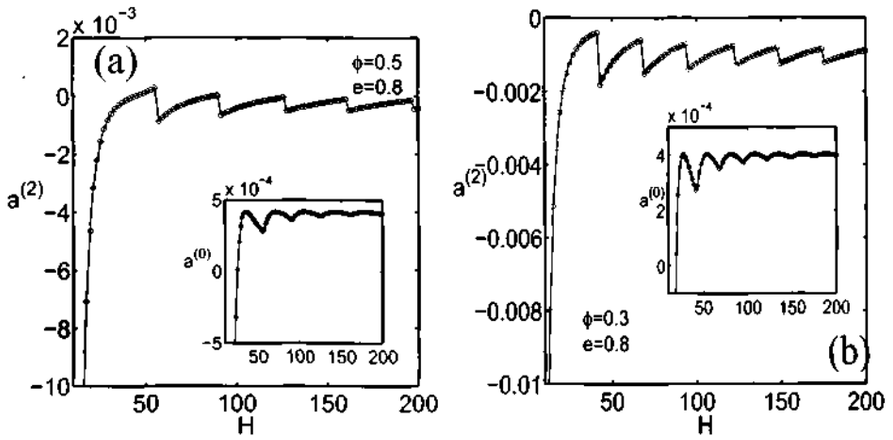

Figure 5.11: Comparison of the first Landau Coefficient between analytical (solid line) and spectral/numerical (circles) solutions: (*a*) $\phi^0 = 0.5$ and (*b*) $\phi^0 = 0.3$ where the selected mode number (β) for the analytical results are a mode number which has maximum growth rate over all the β's.

it provides all leading eigenvalues in one shot (Alam & Nott 1998; Alam *et al.* 2008).

To compare exactly numerical results with those obtained from the analytical method we solve the linear eigenvalue problem for several β and then choose the leading mode such that it has the maximum growth rate over all β which is shown in the inset plots of figures 5.11(*a*)-5.11(*b*) for $\phi^0 = 0.5$ and 0.3, where the circles are the growth rates from the analytical method and the solid lines from the numerical method. In the main panels of figures 5.11(*a*)-5.11(*b*) we have shown the variation of $a^{(2)}$ by using the leading mode which is the maximum over all β. It can be seen from figure 5.11 that the numerical and analytical methods yields the same result.

5.4.4 Solution for Higher-order Harmonics: Distortion to Fundamental

Recall that at cubic order $O(A^3)$ we have two harmonics: the distortion to the fundamental mode $X^{[1;3]}$, and the third harmonic $X^{[3;3]}$. Here we determine analytical solution for $X^{[1;3]}$. The governing equation for the distortion to fundamental is

$$\mathbf{L}_{13}X^{[1;3]} = -c^{(2)}X^{[1;1]} + \mathbf{G}_{13}. \tag{5.38}$$

Having determined the first Landau coefficient $c^{(2)} \equiv a^{(2)}$, the right hand side of (5.38) is now completely known, and hence (5.38) can be solved for $X^{[1;3]}$. The general solution for $X^{[1;3]}$ for any mode number β can be written as

$$\left.\begin{aligned} \phi^{[1;3]} &= \phi^3_{13}\cos k_{3\beta}(y \pm 1/2) + \phi^1_{13}\cos k_\beta(y \pm 1/2) \\ u^{[1;3]} &= u^3_{13}\sin k_{3\beta}(y \pm 1/2) + u^1_{13}\sin k_\beta(y \pm 1/2) \\ v^{[1;3]} &= v^3_{13}\sin k_{3\beta}(y \pm 1/2) + v^1_{13}\sin k_\beta(y \pm 1/2) \\ T^{[1;3]} &= T^3_{13}\cos k_{3\beta}(y \pm 1/2) + T^1_{13}\cos k_\beta(y \pm 1/2) \end{aligned}\right\}, \tag{5.39}$$

where

$$k_{3\beta} = 3\beta\pi \tag{5.40}$$

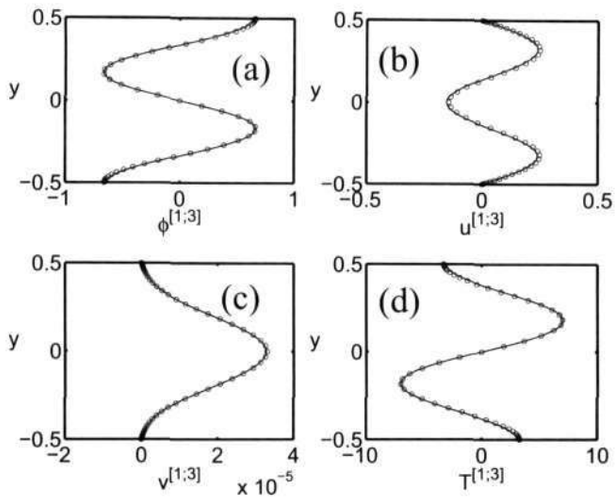

Figure 5.12: Comparison between analytical (solid line) and spectral/numerical (circles) solutions for the distortion to the fundamental $X^{[1;3]}$ with mode number $\beta = 1$: (*a*) $\phi^{[1;3]}$, (*b*) $u^{[1;3]}$, (*c*) $v^{[1;3]}$ and (*d*) $T^{[1;3]}$ for $\phi^0 = 0.15$, $H = 100$ and $e = 0.8$.

with the mode number $\beta = 1, 2, \ldots$, and $[\phi^3_{13}, u^3_{13}, v^3_{13}, T^3_{13}]^{Tr}$ and $[\phi^1_{13}, u^1_{13}, v^1_{13}, T^1_{13}]^{Tr}$ represent unknown amplitudes. Substituting (5.39) into (5.38) and equating *sine* and *cosine* terms, we obtain inhomogeneous algebraic equations for unknown amplitudes that can be easily evaluated.

The analytical solutions (5.39) are compared with the numerical solution of (5.38) using spectral collocation technique (as detailed in chapter 3) in figures 5.12, 5.13 and 5.14 for two values of the mean density $\phi^0 = 0.15$ and 0.05, respectively. We find good quantitative agreement between analytical and numerical solutions for each mode shape of $X^{[1;3]}$.

On the whole, the quantitative agreement in figures 5.3-5.14 between the analytical and the spectral/numerical solutions for the harmonics (of various order) of the fundamental mode as well as for the first Landau coefficient ascertains the accuracy of the spectral-based numerical method for nonlinear stability. One outcome of this chapter is the validation of a numerical technique (based on spectral collocation and Gauss-Chebyshev quadrature) for nonlinear stability calculations: our spectral-based numerical code (cf. chapter 3) can be adapted/extended for a host of granular flow problems for which analytical solutions do not exists.

5.5 Bifurcation, Phase Diagram and Finite-amplitude Solution

5.5.1 Phase Diagram and Critical Parameters for 'Linear' Shear-banding Instability

For linear stability, the dispersion relation is a quartic in $c \equiv c^{(0)} = a^{(0)} + ib^{(0)}$ (Alam & Nott 1998):

$$c^4 + \alpha_3 c^3 + \alpha_2 c^2 + \alpha_1 c + \alpha_0 = 0, \tag{5.41}$$

where α_i are functions of the base state density and temperature, the Couette gap and the restitution coefficient. Previous works on linear stability (Alam & Nott 1998; Alam *et al.* 2008) have

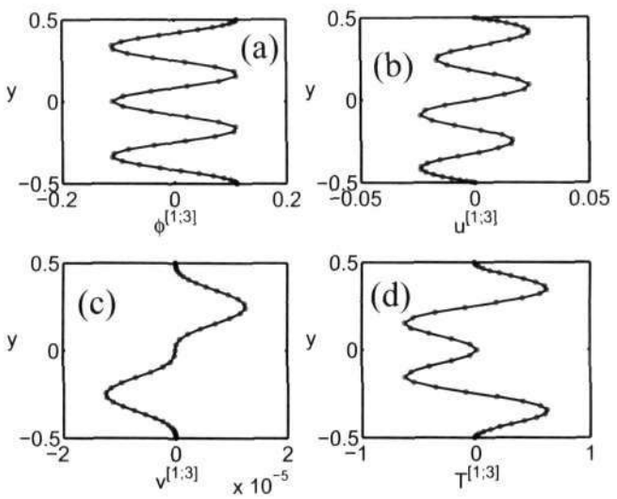

Figure 5.13: Same as figure 5.12, but for mode $\beta = 2$.

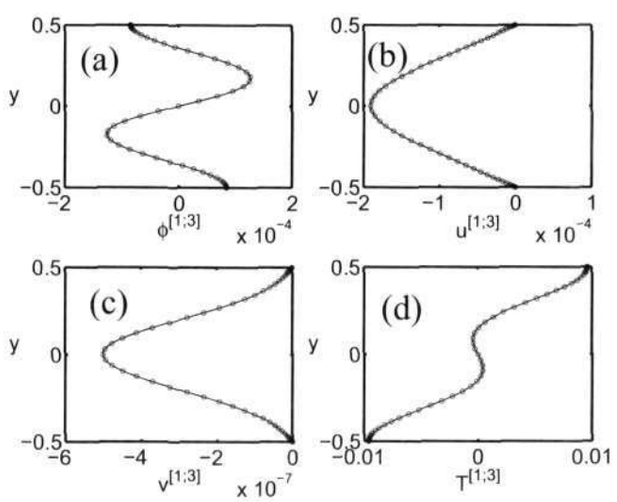

Figure 5.14: Same as figure 5.12, but for $\phi^0 = 0.05$.

established that out of four eigenvalues of (5.41), there is a complex conjugate pair, representing propagating modes, which are always *stable*; one real eigenvalue corresponds to the temperature mode which remains the most stable mode for any values of control parameters, and the remaining real eigenvalue could be *unstable* depending on base state condition. The approximate analytical solutions for these eigenvalues using asymptotic expansion for large Couette gaps (H) are given in Appendix 5D. This real unstable mode has been dubbed *shear-banding* mode (Alam 2005) since the corresponding eigenfunctions represent shear-localization and density segregation along the gradient (y) direction.

Since the shear-banding instability corresponds to a *real* eigenvalue, the locus of neutral stability ($a^{(0)} \equiv \mathrm{Re}(c) = 0$) is given by $\alpha_0 = 0$ which can be simplified to

$$H^2 = \frac{\Psi_1}{\Psi_2} k_\beta^2. \tag{5.42}$$

Here $k_\beta = \beta\pi$, with $\beta = 1, 2, \ldots$ being the *mode number*, and Ψ_1 and Ψ_2 are functions of base-state density

$$\Psi_1 = \frac{f_4^0}{f_5^0} \quad \text{and} \quad \Psi_2 = \left(\frac{f_{5\phi}^0}{f_5^0} + \frac{f_{2\phi}^0}{f_2^0} \right) \frac{f_1^0}{f_{1\phi}^0} - 2. \tag{5.43}$$

The zero growth rate contour $a^{(0)} = 0$ (i.e. the neutral stability curve) for the shear-banding mode is shown in figure 5.15 as a thick solid line; the flow is unstable ($a^{(0)} > 0$) inside the neutral stability contour and stable ($a^{(0)} < 0$) outside. It is seen that, for a given density, there is a minimum/critical value of the Couette gap,

$$H_c = H(\phi^0, e, \beta; a^{(0)} = 0) = k_\beta \sqrt{\Psi_1/\Psi_2}, \tag{5.44}$$

depending on ϕ^0, e and β, below which the shear flow is stable according to linear theory. On the other hand, for a given H, there is a minimum/critical density,

$$\phi_c = \phi^0(H, e, \beta; a^{(0)} = 0), \tag{5.45}$$

below which the shear flow is stable. While this critical density depends on H, e, and β, there is a *global* minimum density, defined as

$$\phi_c^l = \min \phi^0 \left(a^{(0)} = 0 \right) \quad \forall \quad H, \tag{5.46}$$

below which the uniform shear flow is always stable to shear-banding instability, irrespective of the values of e and β. For the present Navier-Stokes's level constitutive model, this global critical density is $\phi_c^l \approx 0.154$.

In the following two sections, we investigate the possibility of *subcritical* shear-banding instability in dilute flows $\phi^0 < \phi_c^l$ from the nonlinear analysis. One goal is to check the feasibility of finite-amplitude segregated solutions that have been observed in molecular dynamics simulations of dilute granular shear flow (Tan & Goldhirsch 1997). This constitutes a stringent test of our order-parameter theory since the same has been predicted from the direct numerical simulation of continuum equations for the same flow configuration (Nott *et al.* 1999). We will also determine finite amplitude solutions for moderately dense flows ($\phi^0 > \phi_c^l$) which are linearly unstable to shear-banding instability, signaling the possibility of *supercritical* bifurcations for $\phi^0 > \phi_c^l$.

5.5.2 Equilibrium Amplitude and the Nature of Bifurcation

First we discuss about the nature of bifurcation for the appearance of finite-amplitude nonlinear solutions that would bifurcate from the uniform shear base state due to the shearbanding insta-

bility as discussed in §5.5.1. This is intimately tied to the concept of equilibrium amplitude (i.e. finite-amplitude equilibrium solution) and the first Landau coefficient $a^{(2)}$ as we show below.

Let us rewrite the amplitude order-parameter or Landau equation (3.32) as

$$S = \frac{\mathrm{d}A}{\mathrm{d}t} = a^{(0)}A + a^{(2)}A^3 + a^{(4)}A^5 + ... \tag{5.47}$$

which is an infinite series where $a^{(0)}$ is the growth rate from the linear theory and $a^{(2)}$, $a^{(4)}$, ... are nonlinear corrections to the linear growth rate, called Landau coefficients. The above series (6.11) is also known as Stuart-Landau series (Stuart 1960; Watson 1960). As mentioned before, in the present work we have stopped at the first nonlinear correction term by calculating only the first Landau coefficient $a^{(2)}$ which was hard enough.

The stationary solution of (6.11) i.e. the value of A for which $S = 0$ is called the equilibrium amplitude $A = A_e$. To determine the equilibrium amplitude, we truncate equation (6.11) at cubic order:

$$\frac{\mathrm{d}A_e}{\mathrm{d}t} = a^{(0)}A_e + a^{(2)}A_e^3 = 0 \tag{5.48}$$

which has three possible solutions:

$$A_e = 0 \quad \text{and} \quad A_e = \pm\sqrt{-\frac{a^{(0)}}{a^{(2)}}}. \tag{5.49}$$

The trivial zero-solution, $A_e = 0$, corresponds to the base state of uniform shear, implying that the uniform shear solution is stable if the two non-zero solutions are unfeasible. It is clear that the finite-amplitude/nonlinear solutions exists if and only if the following condition holds:

$$a^{(0)} \quad \text{and} \quad a^{(2)} \text{ are of opposite sign.}$$

Two situations can arise:

$$(i) \qquad a^{(0)} > 0 \qquad \text{and} \qquad a^{(2)} < 0 \qquad \text{(Supercritical)} \tag{5.50}$$

$$(ii) \qquad a^{(0)} < 0 \qquad \text{and} \qquad a^{(2)} > 0 \qquad \text{(Subcritical)} \tag{5.51}$$

The former/latter condition corresponds to linearly *unstable/stable* flow with *positive/negative* growth rates and *negative/positive* first Landau coefficients, respectively, leading to *supercritical/subcritical* bifurcations. In other words, the subcritical bifurcation arises when the first landau coefficient $a^{(2)}$ has a positive sign and the supercritical bifurcation occurs when $a^{(2)}$ is negative. In either case, there is a new finite-amplitude solution, given by (5.49).

5.5.3 Phase Diagram for 'Nonlinear' Shear-banding Instability

As described in the previous section, the sign of the first Landau coefficient $a^{(2)}$ decides the type of bifurcation: supercritical (5.50) or subcritical (5.51). From the given analytical solution, the condition for vanishing first Landau coefficient (5.35) simplifies to

$$\tilde{\phi}_1^\dagger G_{13}^{1\beta 1} + \tilde{T}_1^\dagger G_{13}^{4\beta 1} + \tilde{u}_1^\dagger G_{13}^{2\beta 1} + \tilde{v}_1^\dagger G_{13}^{3\beta 1} = 0. \tag{5.52}$$

The zero-contour of the first Landau coefficient, $c^{(2)} = a^{(2)} = 0$, is superimposed over the neutral stability contour ($a^{(0)} = 0$) in figure 5.15 as thin solid lines. The restitution coefficient is set to $e = 0.8$, with the mode number being $\beta = 1$. The regions of positive and negative $a^{(2)}$ are marked in this figure. Recall that the thick solid line in figure 5.15 corresponds to the zero growth-rate contour (i.e. the neutral stability contour), to the right of which the uniform shear flow is linearly unstable and is stable in the rest of the (ϕ^0, H)-plane.

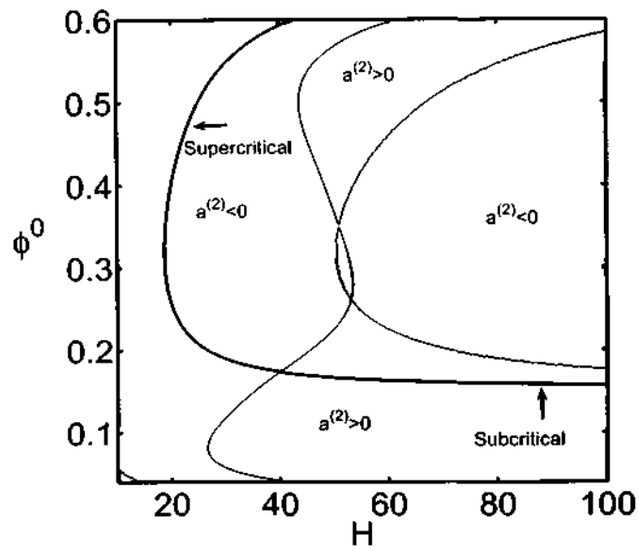

Figure 5.15: Phase diagram in the (H, ϕ) plane: contours of zero first Landau coefficient (thin solid lines) and the zero growth rate (thick solid line) in (H, ϕ^0) plane for $e = 0.8$ and $\beta = 1$. The flow is unstable ($a^{(0)} > 0$) to the right of the thick solid contour.

In the following, we discuss the results on the first Landau coefficient and the related bifurcations for linearly stable ($\phi^0 < \phi_c^l$) and unstable ($\phi^0 > \phi_c^l$) regimes separately. We will establish that the lower part of the neutral contour (enclosed by the zero-line of $a^{(2)} = 0$) in figure 5.15 is subcritically unstable but its upper part is supercritically unstable.

Linearly Stable Regime: $\phi^0 < \phi_c^l$

Focussing on the stable dilute flows ($\phi^0 < \phi_c^l \approx 0.154$) in figure 5.15, we show the variation of the first Landau coefficient with density in figures 5.16(a) and 5.16(b) at two Couette gaps $H = 50$ and 100, respectively. The inset in each plot shows the corresponding variation of the growth rate of the least-stable shear-banding mode ($\beta = 1$); the arrow in each inset marks the critical value of density, ϕ_c, above which the flow is linearly unstable. For both cases, we find that the growth rate, $a^{(0)}$, is negative but the first Landau coefficient, $a^{(2)}$, is positive for a range of densities in the linearly stable region ($\phi^0 < \phi_c$), suggesting the existence of finite-amplitude solutions as per equation (5.51). This is also evident from figures 5.8(a) and 5.8(b) which show the variations of $a^{(2)}$ (main panel) and $a^{(0)}$ (inset) with Couette gap at two values of the mean density $\phi^0 < \phi_c^l$.

The bifurcation diagrams in the $(A, \phi^0 - \phi_c)$-plane, related to figures 5.16(a) and 5.16(b), are shown in figure 5.17 for three values of the Couette gap $H = 50$, 100 and 200. For each case, the horizontal line with $A_e = 0$ represents the base state of uniform shear solution which is stable for $\phi^0 < \phi_c^l$, but we also have new *unstable* finite-amplitude solutions, representing subcritical bifurcations (also known as inverse bifurcation). For subcritical bifurcations, the higher order Landau coefficients (which we have not calculated) are needed to identify *stable* finite-amplitude solution. The important point to note is that the finite-amplitude unstable branch in figure 5.17 provides a *threshold for nonlinear stability*: the uniform shear flow is *non-linearly stable/unstable* for $A < A_e$ or $A > A_e$, respectively. At a given density, this threshold amplitude A_e, to reach

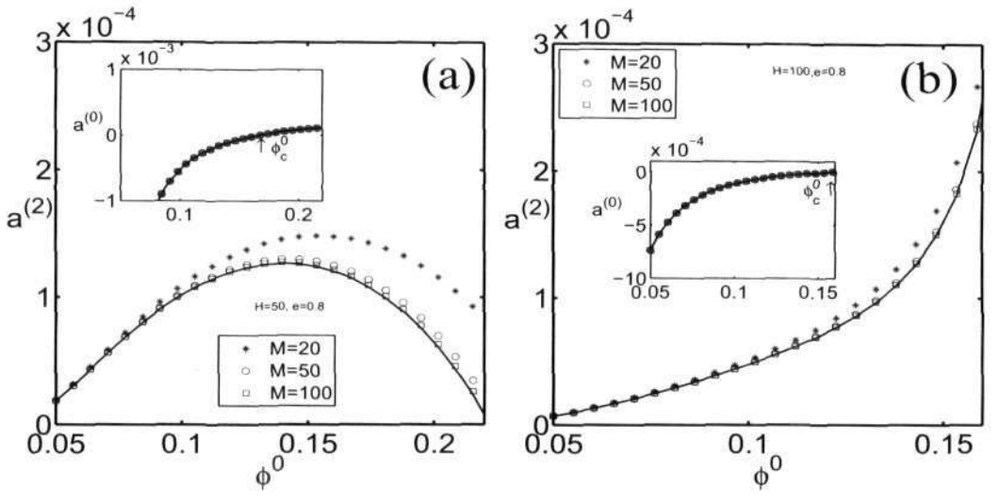

Figure 5.16: Variation of the first Landau Coefficient with density for subcritical flows: (*a*) $H = 50$ and (*b*) $H = 100$, with $e = 0.8$. Inset shows the variation of growth rate of the least-stable mode (mode number $\beta = 1$) with density. The solid line represents analytical solutions. The symbols: stars, circles and squares represent spectral/numerical solutions for collocation points $M = 20$, 50 and 100, respectively. Arrows in insets mark the critical value of density, ϕ_c, above which the flow is linearly unstable.

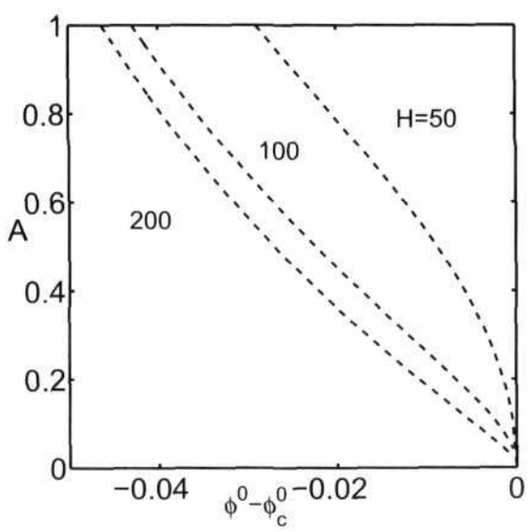

Figure 5.17: Bifurcation diagram in the $(A, \phi^0 - \phi_c)$-plane at three Couette gaps with $e = 0.8$. Note that the bifurcation is subcritical in each case.

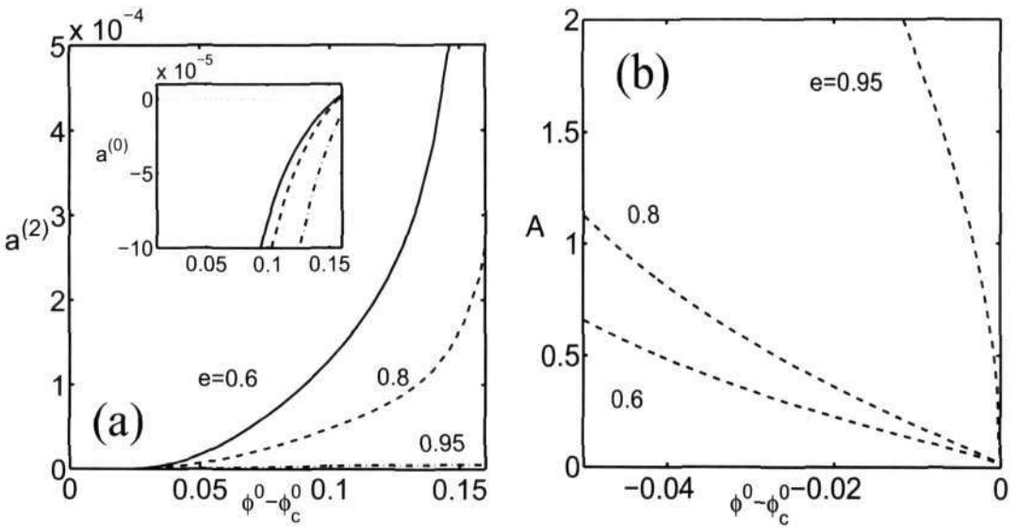

Figure 5.18: Effect of restitution coefficient on (a) the variation of the first Landau coefficient with ϕ^0, and (b) the bifurcation diagram in (A, ϕ^0)-plane for $H = 100$ and $\beta = 1$. The inset in panel *a* shows the related variations of the linear growth rate with ϕ^0 for different e. Note that the bifurcation is subcritical in each case.

a stable nonlinear state, is higher for smaller Couette gaps. Apart from its dependence on the mean density (ϕ^0) and Couette gap (H), A_e also depends on the restitution coefficient (e), i.e. $A_e \equiv A_e(\phi^0, H, e)$. This is evident from figure 5.18 which shows the bifurcation diagrams in the $(A, \phi^0 - \phi_c)$-plane for three values of restitution coefficient at a Couette gap of $H = 100$. Clearly, the threshold amplitude A_e decreases with increasing dissipation (i.e. with decreasing e).

The results presented in figure 5.17 can be replotted as bifurcation diagram in the (A, H)-plane as in figure 5.19. The mean density is set to $\phi^0 < \phi_c^l = 0.154$ ($\phi^0 = 0.15$ and 0.10 in figures 5.19*a* and 5.19*b*, respectively) and the restitution coefficient to $e = 0.8$. The finite-amplitude branch in each panel of figure 5.19 provides a threshold for nonlinear stability, and the magnitude of this nonlinear threshold decreases with increasing Couette gap. In fact, this branch bifurcates from infinity, i.e. from $H = \infty$, as we explain below. Let us consider the leading-order analytical expression for the shear-banding mode (Alam & Nott 1998):

$$a^{(0)} = -H^{-2} \frac{\mu^0 \left[p_\phi^0 (\mathcal{D}_T^0 + \mu_T^0) - p_T^0 (\mathcal{D}_\phi^0 + \mu_\phi^0) \right] k_\beta^2}{2 p_T^0 \mu^0 + \phi^0 \left[p_\phi^0 (\mathcal{D}_T^0 - \mu_T^0) - p_T^0 (\mathcal{D}_\phi^0 - \mu_\phi^0) \right]} + O(H^{-4}). \tag{5.53}$$

It has been verified that $a^{(0)}$ is always negative for $\phi^0 < \phi_c^l$ over which the shear flow is linearly stable. However, it is clear from (5.53) that $a^{(0)} \to 0$ in the limit $H \to \infty$, and hence there is a critical point ($a^{(0)} = 0$) at $H = \infty$. Therefore, the bifurcation point for linearly stable densities ($\phi^0 < \phi_c^l$) originates from $H = \infty$. This is the origin of the nomenclature for the special type of bifurcation as depicted in figure 5.19: *bifurcation from infinity* (Rosenblat & Davis 1979; Alam & Nott 1998). In fact, this belongs to a more general class of subcritical bifurcations.

From the above discussion, we conclude that the region in the (ϕ^0, H)-plane in figure 5.15, below the intersection of the zero-contours of $a^{(2)}$ and $a^{(0)}$, is *subcritically* unstable. More specifically, in this region ($\phi^0 < \phi_c^l$) of *linearly stable* flows, there is a *bifurcation from infinity* in the

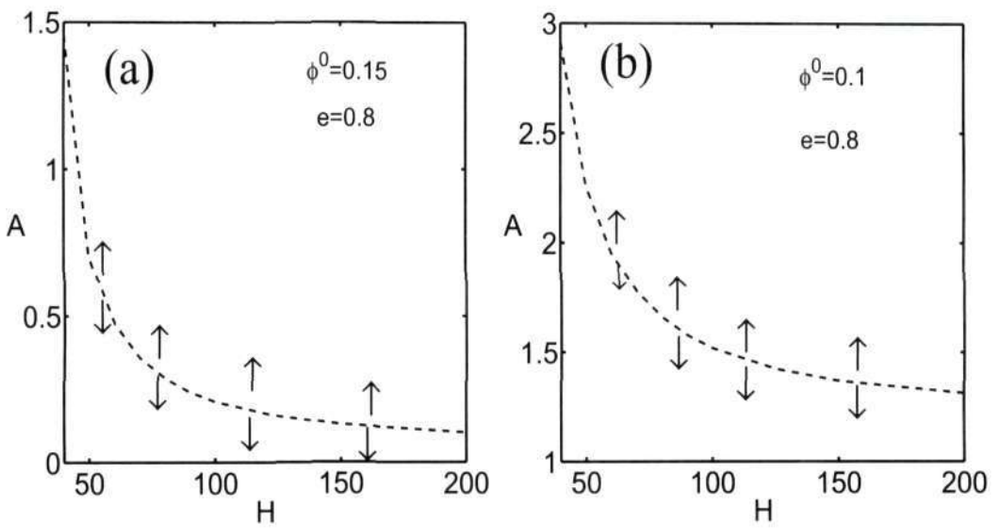

Figure 5.19: Bifurcation from infinity ($H \to \infty$) at (a) $\phi^0 = 0.15$ and (b) $\phi^0 = 0.1$, with $e = 0.8$.

sense that the bifurcation point lies at $H = \infty$. In all cases, there exist finite-amplitude nonlinear solutions, provided the amplitude of perturbation exceeds a *threshold for nonlinear stability*,

$$A > A_e(\phi^0, H, e), \tag{5.54}$$

which depends on various control parameters.

Linearly Unstable Regime: $\phi^0 > \phi_c^l$

Here we consider moderately dense flows with $\phi^0 > \phi_c^l$ for which the linear stability theory predicts that the uniform shear is unstable to shear-banding instability if the Couette gap is sufficiently large; more specifically, we focus on the regime in figure 5.15 which is enclosed by the neutral stability contour ($a^{(0)} = 0$).

Figure 5.20 shows a series of bifurcation diagrams in the $(A, H - H_c)$-plane for six values of the mean density, $\phi^0 = 0.16$, 0.17, 0.173, 0.174, 0.18 and 0.2, just above the critical density for the onset of linear shear-banding instability. The restitution coefficient is set to $e = 0.8$ as in figure 5.15. It is clear that the bifurcation-type is not supercritical immediately, even though we are in the linearly unstable regime ($\phi^0 > \phi_c^l$). Rather, we have a window of mean densities,

$$\phi_c^l \leq \phi^0 \leq \phi_c^s, \tag{5.55}$$

with $\phi_c^s \in (0.173, 0.174)$, over which the bifurcation is *subcritical* and is *supercritical* for larger densities

$$\phi^0 > \phi_c^s. \tag{5.56}$$

From figure 5.20 we find that the critical density at which this *switch-over* between the subcritical and supercritical bifurcations occurs is about $\phi_c^s \approx 0.1735$.

To understand the origin of the above switch-over between two types of bifurcations, we show the variation of the first Landau coefficient with H at $\phi^0 = 0.17$ and 0.18 in figures 5.21(a) and 5.21(b), respectively. In each panel, we have superimposed the corresponding variation of the least-

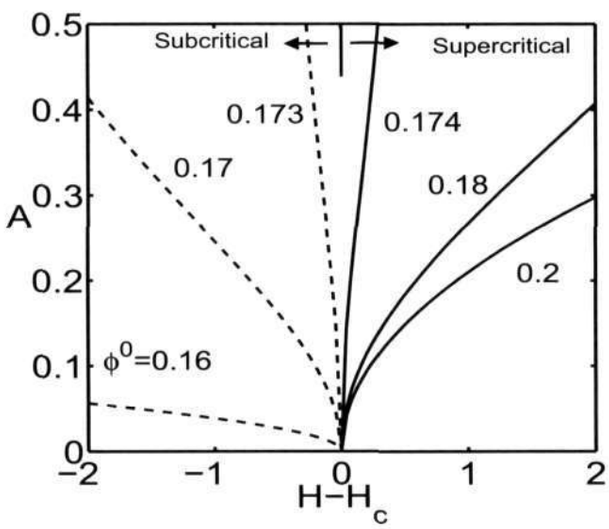

Figure 5.20: Bifurcation diagram in the (A, H)-plane for a range of density with $e = 0.8$. Note that the bifurcation-type changes from supercritical to subcritical below a critical value of the mean density $\phi^0 \in (0.173, 0.174)$.

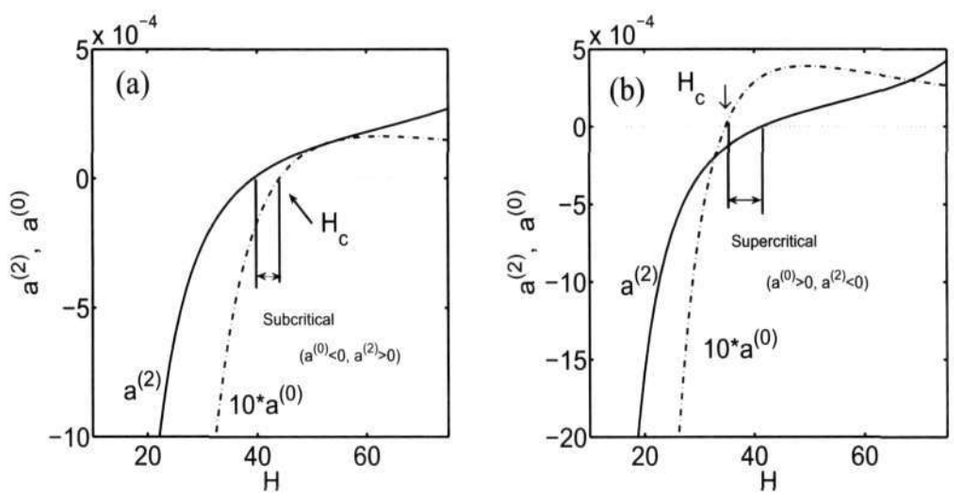

Figure 5.21: Variations of the first Landau Coefficient, $a^{(2)}$, and the growth rate of the least-stable shear-banding mode, $a^{(0)}$, with Couette gap for linearly unstable mean densities $\phi^0 > \phi_c^l \approx 0.154$: (a) $\phi^0 = 0.17$ and (b) 0.18. Arrow in each panel marks the critical Couette gap H_c above which the shear flow is linearly unstable ($a^{(0)} > 0$).

stable mode, $a^{(0)}$, denoted by the dot-dash line, and the critical Couette gap, $H_c = H(a^{(0)} = 0)$, is also marked by an arrow. In the case of $\phi^0 = 0.17 < \phi_c^s$, we find a range Couette gaps (marked by vertical lines in figure 5.21*a*) over which $a^{(0)} < 0$ and $a^{(2)} > 0$, which corresponds to subcritical bifurcations (5.51). On the other hand, for $\phi^0 = 0.18 > \phi_c^s$, we have a range of Couette gaps (marked by vertical lines in figure 5.21*b*) over which $a^{(0)} > 0$ and $a^{(2)} < 0$, signalling the presence of supercritical bifurcations (5.50).

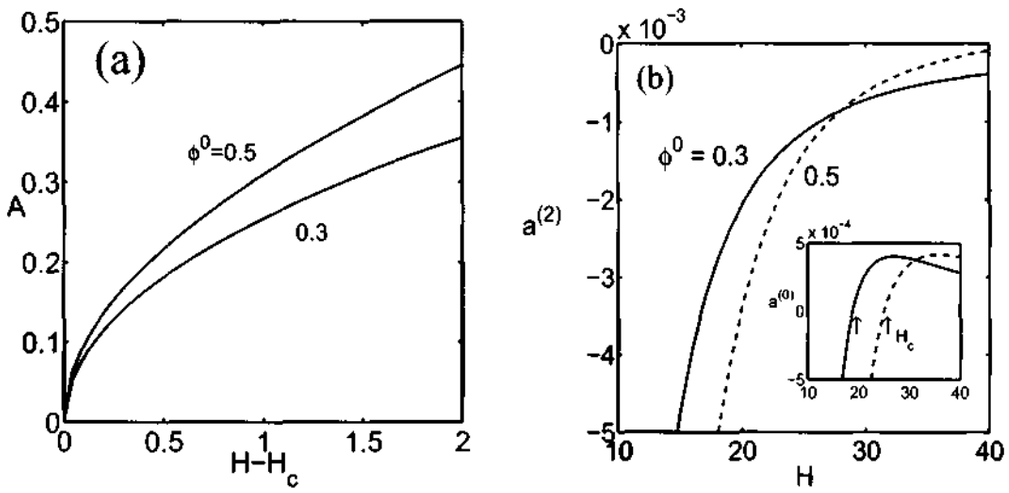

Figure 5.22: (*a*) Bifurcation diagrams in the (A, H)-plane and (*b*) the variations of first Landau coefficients at larger mean densities, $\phi^0 \gg \phi_c^l$, with $e = 0.8$. The inset in panel *b* shows the variations of the linear growth rate with H.

Even at larger mean densities ($\phi^0 \gg \phi_c^s$), the bifurcation remains supercritical as seen in figure 5.22(*a*). The corresponding variations of $a^{(2)}$ and $a^{(0)}$ are displayed in the main panel and the inset of figure 5.22(*b*). At both $\phi^0 = 0.3$ and 0.5, the condition for supercritical bifurcation (5.50), $a^{(0)} > 0$ and $a^{(2)} < 0$, is satisfied. It is seen from figure 5.22(*a*) that the magnitude of A, required to reach the nonlinear finite-amplitude branch, increases with increasing density.

In §5.6, we will discuss the possible influence of different constitutive relations and the contact radial distribution function on the above bifurcation scenario. It may be noted that the direct numerical simulation of continuum equations [cf. (4.5)- (4.8)] for the same problem (**Nott** *et al.* 1999) has also identified the above three types of bifurcations.

5.5.4 Finite Amplitude Solutions: Density Segregation and Shear Localization

Once we know the equilibrium amplitude, the finite amplitude solutions for the density and the shear rate are computed from

$$\phi = \phi^0 \pm A_e \phi^{[1:1]}, \tag{5.57}$$

$$\gamma = \frac{\mathrm{d}}{\mathrm{d}y}\left(u^0 \pm A_e u^{[1:1]}\right), \tag{5.58}$$

with leading-order corrections in amplitude $O(A)$. Typical subcritical finite amplitude solutions for ϕ and γ are shown in figures 5.23(*a*) and 5.23(*b*), respectively, for mode $\beta = 1$, with parameter

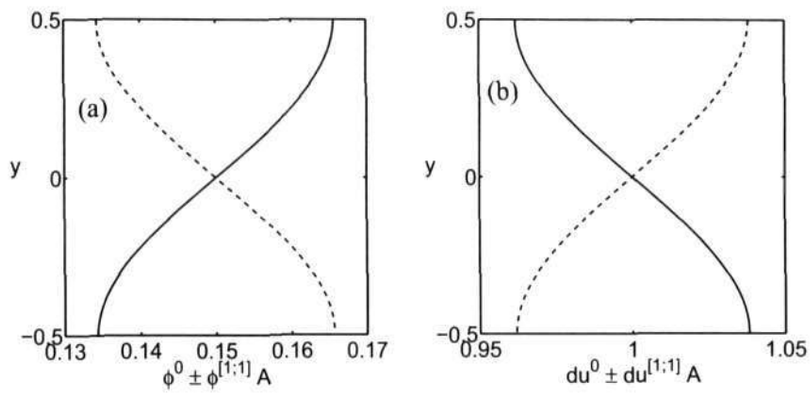

Figure 5.23: Finite amplitude solutions for (a) the density, $\phi^0 + A\phi^{[1;1]}$ and (b) the shear rate, $d/dy(u^0 + Au^{[1;1]})$, for mode $\beta = 1$. Parameter values are $\phi^0 = 0.15$, $H = 100$ and $e = 0.8$

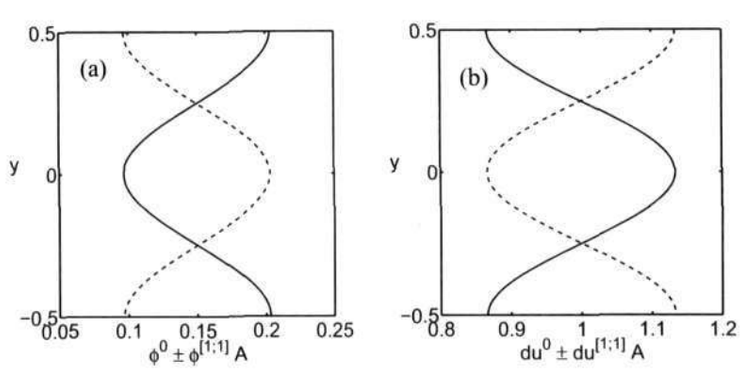

Figure 5.24: Same as figure 5.23, but for mode $\beta = 2$.

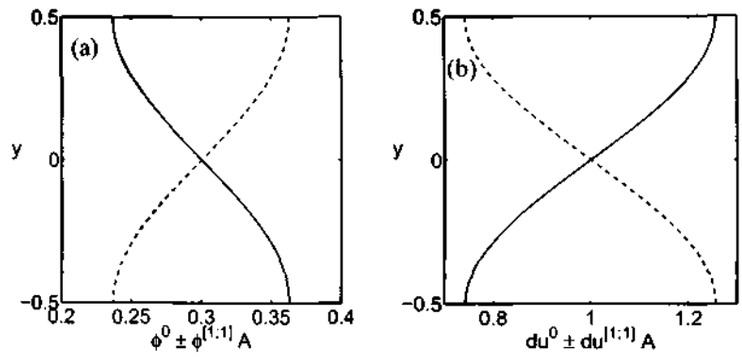

Figure 5.25: Finite amplitude solutions for (a) the density, $\phi^0 + A\phi^{[1;1]}$ and (b) the shear rate, $d/dy(u^0 + Au^{[1;1]})$, for mode $\beta = 1$. Parameter values are $\phi^0 = 0.3$, $H = H_c + 2$ and $e = 0.8$

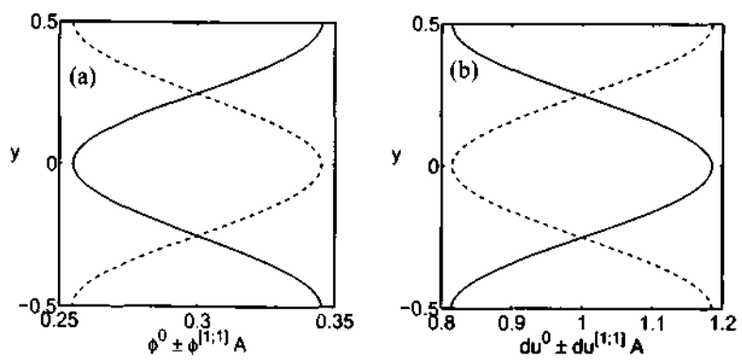

Figure 5.26: Same as figure 5.25, but for mode $\beta = 2$.

values $\phi^0 = 0.15$, $H = 100$ and $e = 0.8$. The analog of these figures for mode $\beta = 2$ are shown in figures 5.24(a) and 5.24(b). For any mode number β, there are two solutions that are mirror-symmetric which is due to the underlying symmetry of the plane Couette flow. It is clear that the density and shear rate are non-uniform across the Couette gap (y), leading to density segregation and shear-localization the shear rate is large/small in the dilute/dense regions, respectively. Note that the solution profiles depicted in figures 5.23 and 5.24 are "unstable" since they belong to the unstable "subcritical" bifurcation branch. For subcritical bifurcation, the higher order Landau coefficients (which we have not calculated) are needed to identify *stable* finite-amplitude solutions.

The 'stable' finite amplitude solutions for the density and the shear rate are displayed in figures 5.25 and 5.26, for mode $\beta = 1$ and 2, respectively. These correspond to *supercritical* bifurcation at $\phi^0 = 0.3$ and $H = H_c + 2$, with $e = 0.8$. Again, the bifurcating solutions show density segregation and shear-localization that correspond to shear-banding.

5.5.5 Scaling of First Landau Coefficient, Equilibrium Amplitude and Bifurcation Diagram

So far we have presented bifurcation diagrams and the first Landau coefficients for mode $\beta = 1$. In this section, we will demonstrate that there exists simple scaling for $a^{(0)}$, $a^{(2)}$ and A in terms of mode number β with respect to the Couette gap H. More specifically we will show that the dependencies of $a^{(0)}$, $a^{(2)}$ and A (at a given density ϕ^0) on β can be absorbed by defining a new length scale: $H \rightarrow H^*(H, \beta)$. In other words, knowing the variations of $a^{(0)}$, $a^{(2)}$ and A with H for any β (at a given density), one can determine these quantities at other values of β at the same mean density. (However, there is no such scaling solutions in terms of mean density.) We will further demonstrate that the phase diagrams in the (H, ϕ^0)-plane, showing zero loci of $a^{(2)}$ and $a^{(0)}$, remain invariant under a composite scaling for the Couette gap: $H \rightarrow H^*(H, \beta, e)$, i.e. in terms of both β and the inelasticity $(1 - e^2)$.

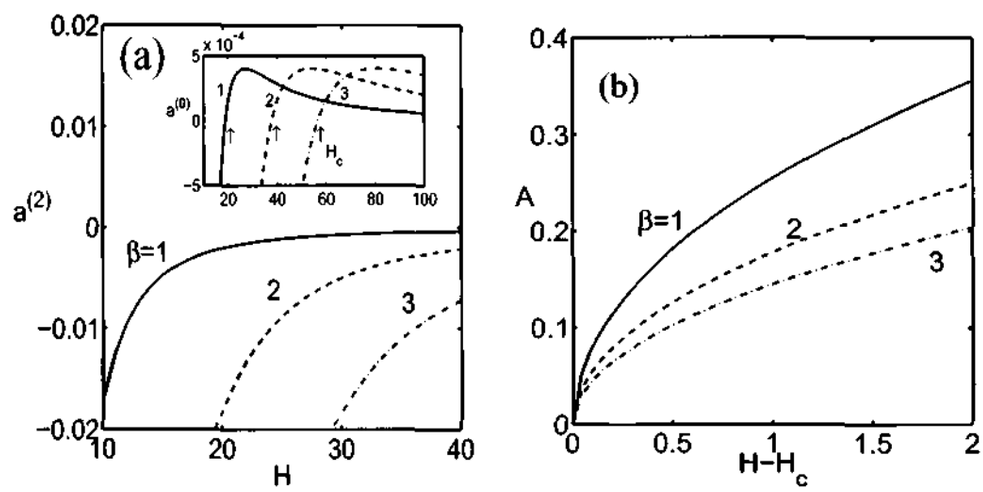

Figure 5.27: Effects of mode number β on the (a) variation of $a^{(2)}$ and $a^{(0)}$, and (b) the bifurcation diagram in the (A, H)-plane. Parameter values are $\phi^0 = 0.3$ and $e = 0.8$.

Figure 5.27(a) shows the effect of mode number β on the first Landau coefficient $a^{(2)}$ (main panel) and the linear mode $a^{(0)}$ (inset) for parameter values of $\phi^0 = 0.3$ and $e = 0.8$. The flow becomes unstable to higher-order mode at larger values of Couette gap, see the inset of figure 5.27(a). The corresponding supercritical bifurcation diagrams for $\beta = 1$, 2 and 3 are shown in figure 5.27(b) – note that the abscissa has been normalized via $H - H_c$, where $H_c = H_c(\beta)$ is the critical Couette gap as denoted by vertical arrows in the inset of figure 5.27(a). When the Couette gap is rescaled via $H \rightarrow H/\beta$, the results for various β do collapse on a single curve for each case of $a^{(2)}$ (main panel of figure 5.28a), $a^{(0)}$ (inset of figure 5.28a) and A (figure 5.28b).

The above scaling of equilibrium amplitude with β holds also for subcritical values of mean density, see figures 5.29(a) and 5.29(b) for $\phi^0 = 0.15$ and 0.1, respectively. The inset in each panel displays the variations of A with H for three values of $\beta = 1, 2, 3$. Such scaling of A with H/β holds at any value of restitution coefficient, see rescaled subcritical bifurcation diagrams in figure 5.30 at $e = 0.95$.

Next we proceed to analyze the phase diagram in figure 5.31(a) which displays the zero contours of the first Landau coefficient $a^{(2)} = 0$ in the (H, ϕ^0)-plane for $\beta = 1$, 2 and 3. All

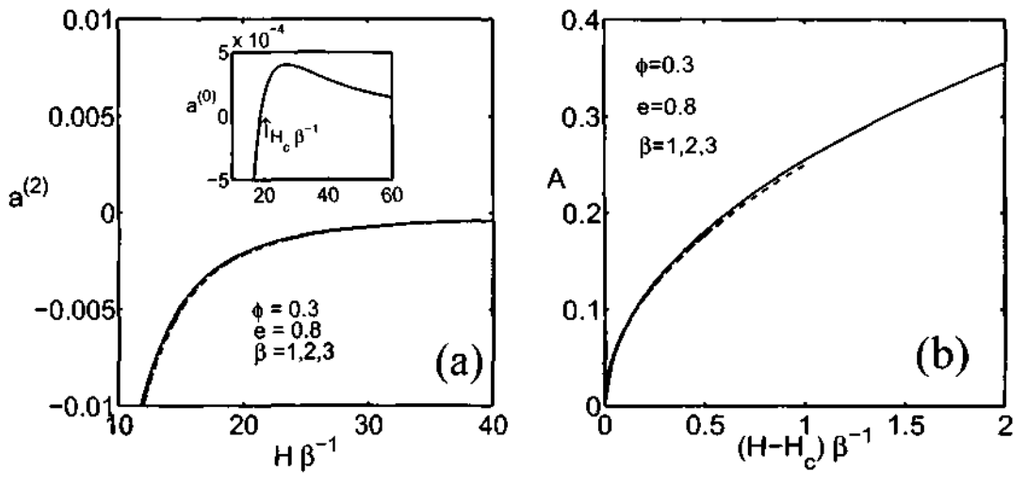

Figure 5.28: Universal scaling with β of the variations of (a) $a^{(2)}$ and $a^{(0)}$ and (b) A with H. Parameter values are $\phi^0 = 0.3$ and $e = 0.8$.

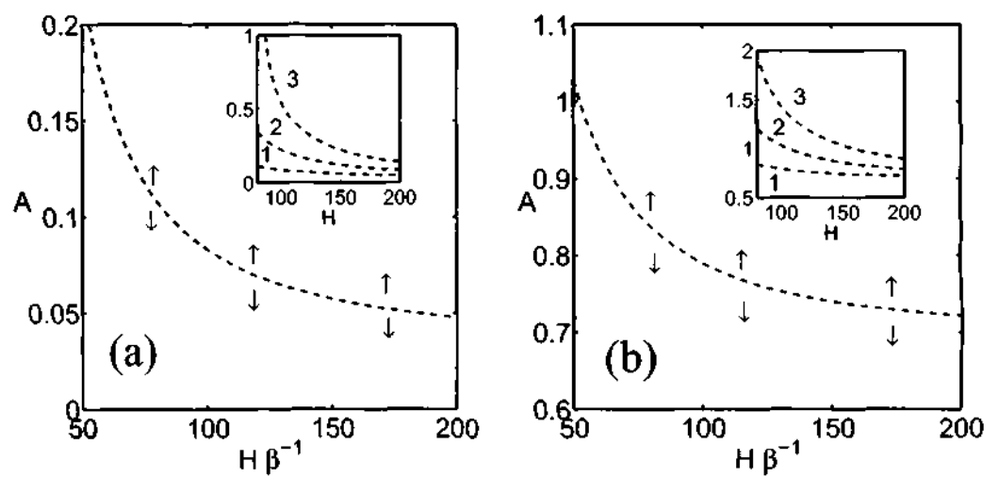

Figure 5.29: Bifurcation from infinity: (*a*) $\phi^0 = 0.15$ and (*b*) $\phi^0 = 0.1$ at $e = 0.6$.

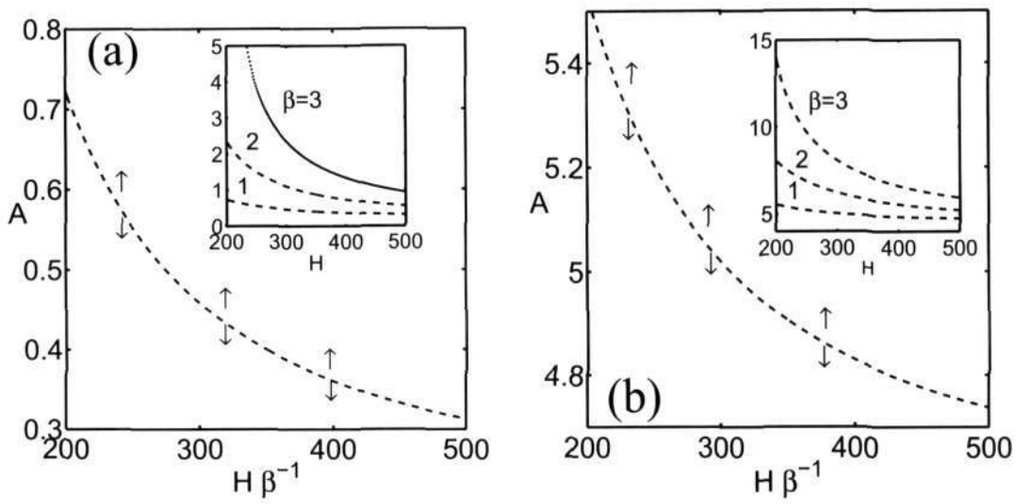

Figure 5.30: Same as figure 5.29, but at $e = 0.95$.

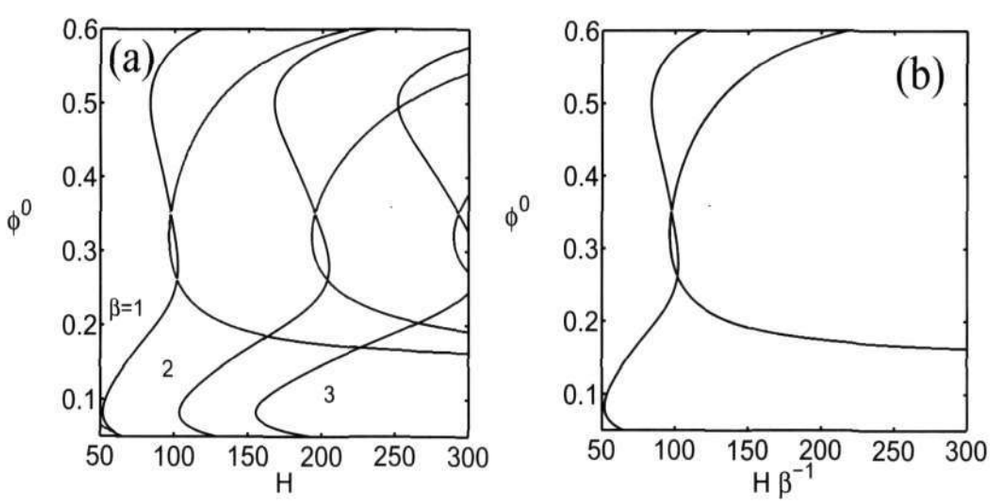

Figure 5.31: Scaling for the zero-contour of the first Landau coefficient, $a^{(2)} = 0$, in terms of mode number β for $e = 0.95$.

these contours collapse into a single contour as seen in figure 5.31(b) under the following scaling of the Couette gap: $H \to H/\beta$. Interestingly, these phase diagrams also remain invariant under a simple transformation in terms of *inelasticity*: $H \to H\sqrt{1-e^2}$, see figures 5.32(a) and 5.32(b).

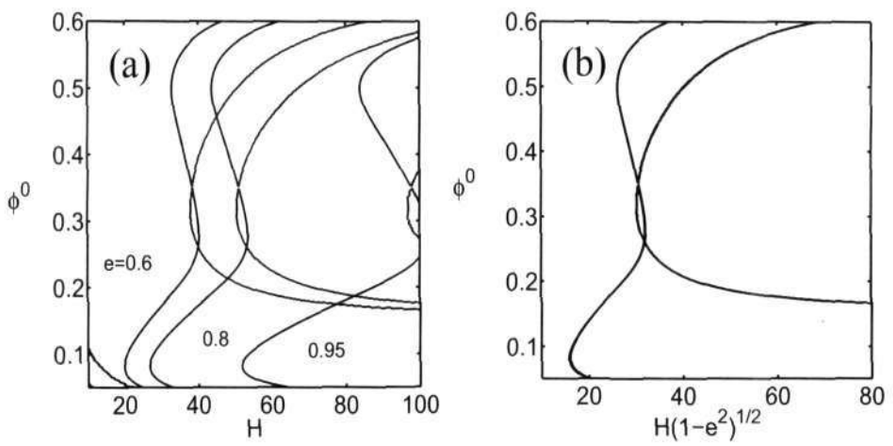

Figure 5.32: Scaling for the zero-contour of the first Landau coefficient, $a^{(2)} = 0$, in terms of restitution coefficient for mode $\beta = 1$.

At least for the neutral stability contour [$a^{(0)} = 0$], the above mentioned composite length scale, $H^*(H, e, \beta)$, directly comes out from the analysis of linear stability results. From equation (5.44) we find that the locus of the neutral stability contour ($a^{(0)} = 0$) is given by $H \sim \beta\sqrt{\psi_1} \sim \beta(1-e^2)^{-1/2}$ since $\psi_1 \sim 1/f_5^0 \sim (1-e^2)^{-1}$, see equation (5.43). Therefore, the neutral stability contour, $a^{(0)} = 0$, would remain invariant under the following scaling of the Couette gap:

$$H \to H\beta^{-1}\sqrt{(1-e^2)} \equiv H^*. \tag{5.59}$$

It is not clear why the above composite scaling (5.59) should hold for the zero-contour of the first Landau coefficient $a^{(2)} = 0$. The expression for $a^{(2)} = 0$ in (5.52) can be simplified to (see Appendix 5C):

$$H^2 = \frac{-\left(k_\beta^4 K_1 + k_\beta^3 K_2 + k_\beta^2 K_3 + k_\beta K_4\right)}{\left(k_\beta^3 K_5 + k_\beta^2 K_6 + k_\beta K_7 + K_0\right)} \tag{5.60}$$

where $k_\beta = \pi\beta$ and the expressions for $K_1, K_2, K_3 \ldots$, which depend on base state variables (and hence on restitution coefficient e) as well as on the modal amplitudes of fundamental and second harmonic, are given in Appendix 5C. The dependence of K_i on β comes via the *implicit* dependence of modal amplitudes on β and hence not known *a priori*. Nevertheless, it appears that the same composite scaling for the Couette gap (5.59) holds for the zero-loci of the first Landau coefficient too as demonstrated in figures 5.31 and 5.32.

Lastly, figure 5.33 displays the scaled phase diagram in the (H^*, ϕ^0)-plane, where $H^* = H\beta^{-1}\sqrt{(1-e^2)}$ is a new length scale or an instability length scale, delineating the regions of supercritical and subcritical bifurcations. The gray-shaded region in figure 5.33 corresponds to $a^{(2)} > 0$ and $a^{(0)} > 0$, and therefore no finite amplitude solution is possible, according to equation (5.49), in the shaded region. There is subcritical bifurcation in the dilute limit (below the lower

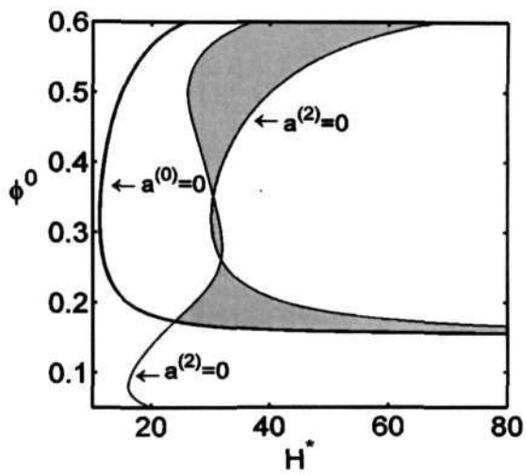

Figure 5.33: Scaled phase diagrams in the (H^*, ϕ^0)-plane, where $H^* = H\beta^{-1}\sqrt{(1-e^2)}$, showing the zero-contours of the first Landau coefficient, $a^{(2)} = 0$, and the linear growth rate $a^{(0)} = 0$. The shaded region in each plot corresponds to $a^{(2))} > 0$ and $a^{(0)} > 0$.

branch of the neutral contour and to the right of $a^{(2)} = 0$ contour), and supercritical bifurcation at moderate-to-large densities.

5.6 Discussion

5.6.1 Influence of Radial Distribution Function

So far we have presented results for a specific choice of the contact radial distribution function, $\chi(\phi)$, as defined in (2.12) i.e.

$$\chi(\phi) = \frac{1}{1-(\phi/\phi_{max})^{1/3}}, \tag{5.61}$$

which was chosen following the previous linear stability analysis of Alam & Nott (1998). Here we consider a modified form of the well-known Carnahan-Starling radial distribution function, $\chi(\phi)$, as given in (2.13):

$$\chi(\phi) = \frac{(1-\phi/2)}{(1-\phi/\phi_m)^3} \tag{5.62}$$

where ϕ_m corresponds to the maximum solid fraction at random close packing which is taken to be 0.65 in the present work. Note that with $\phi_m = 1$ (5.62) boils down to the well-known Carnahan-Starling form with its singularity being at $\phi_m = 1$ that corresponds to point particles.

With constitutive relations as in (4.9) and the Carnahan-Starling radial distribution function (5.62), we show the scaled phase diagrams in the (H^*, ϕ^0)-plane, where $H^* = H\beta^{-1}\sqrt{(1-e^2)}$ and ϕ^0 is the mean density, in figures 5.34(a) and 5.34(b), respectively, for $\phi_m = 0.65$ and 1.0. Note that the thick solid line in each panel is the neutral stability contour ($a^{(0)} = 0$), to the right of which the flow is linearly unstable and is stable in the rest of the (H, ϕ^0)-plane; the

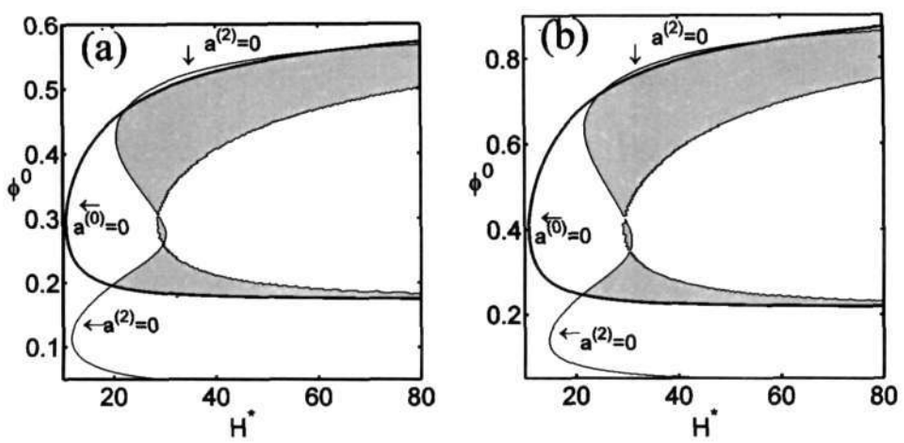

Figure 5.34: Scaled phase diagram in the (H^*, ϕ^0)-plane, where $H^* = H\beta^{-1}\sqrt{(1-e^2)}$, showing the zero-contours of the first Landau coefficient, $a^{(2)} = 0$, and the linear growth rate $a^{(0)} = 0$; the shaded region in each plot corresponds to $a^{(2)} > 0$ and $a^{(0)} > 0$. Constitutive relations for each plot are the same as in figure 5.33 (as given in 4.9), except that we used Carnahan-Starling radial distribution (5.62) with (a) $\phi_m = 0.65$ and (b) $\phi_m = 1$.

thin lines correspond to the zeros of the first Landau coefficient $a^{(2)} = 0$. The overall features of both phase diagrams look similar. A contrasting feature of each phase diagram in figure 5.34 with that in figure 5.33 (for which we had used (5.61) as the radial distribution function) is that the zero-contour of the first Landau coefficient $a^{(2)} = 0$ crosses the neutral stability curve $a^{(0)} = 0$ at two additional points at large densities. Recall that a crossing of $a^{(2)} = 0$ and $a^{(0)} = 0$ signals a switch-over from one type of bifurcation to another. This is clearly depicted in the bifurcation diagrams in the (H^*, A)-plane in figures 5.35$(a-c)$ where we have employed the Carnahan-Starling-type radial distribution function (5.62) with $\phi_m = 0.65$ with other parameters as in figure 5.34(a). In each panel in figure 5.35, a series of finite-amplitude bifurcating solutions are displayed against some control parameter, $\triangle H^* = H^* - H_c^*$ (i.e. a renormalized Couette gap), that measures a distance from its respective neutral/critical point ($H^* = H_c^*$). It is clear that the nature of bifurcation changes (from subcritical to supercritical or vice versa) with increasing mean density in each panel. We find three critical densities at which the nature of bifurcation changes: (1) from subcritical to supercritical bifurcations at $\phi_c^s \approx 0.196$, in figure 5.35(a), (2) from supercritical to subcritical bifurcations at $\phi_c^s \approx 0.467$ in figure 5.35(b), and finally (3) from subcritical to supercritical bifurcations at $\phi_c^s \approx 0.559$ in figure 5.35(c). While the first transition from subcritical to supercritical bifurcation was also found for the radial distribution function (5.61), the latter two transitions in the dense limit, supercritical $\rightarrow$ subcritical $\rightarrow$ supercritical, are specific to the choice of the Carnahan-Starling-type radial distribution function (5.62).

We conclude that both the radial distribution functions, (5.61) and (5.62), predict similar bifurcation scenario (bifurcation-from-infinity $\rightarrow$ subcritical $\rightarrow$ supercritical) at dilute-to-moderate densities; however, the Carnahan-Starling-type radial distribution function (5.62) is responsible for the onset of subcritical bifurcations in the dense limit. Clearly, the exact form of the radial distribution function is needed to correctly predict the bifurcation-type (sub or supercritical) and the corresponding critical density for the onset of nonlinear shear-banding instability.

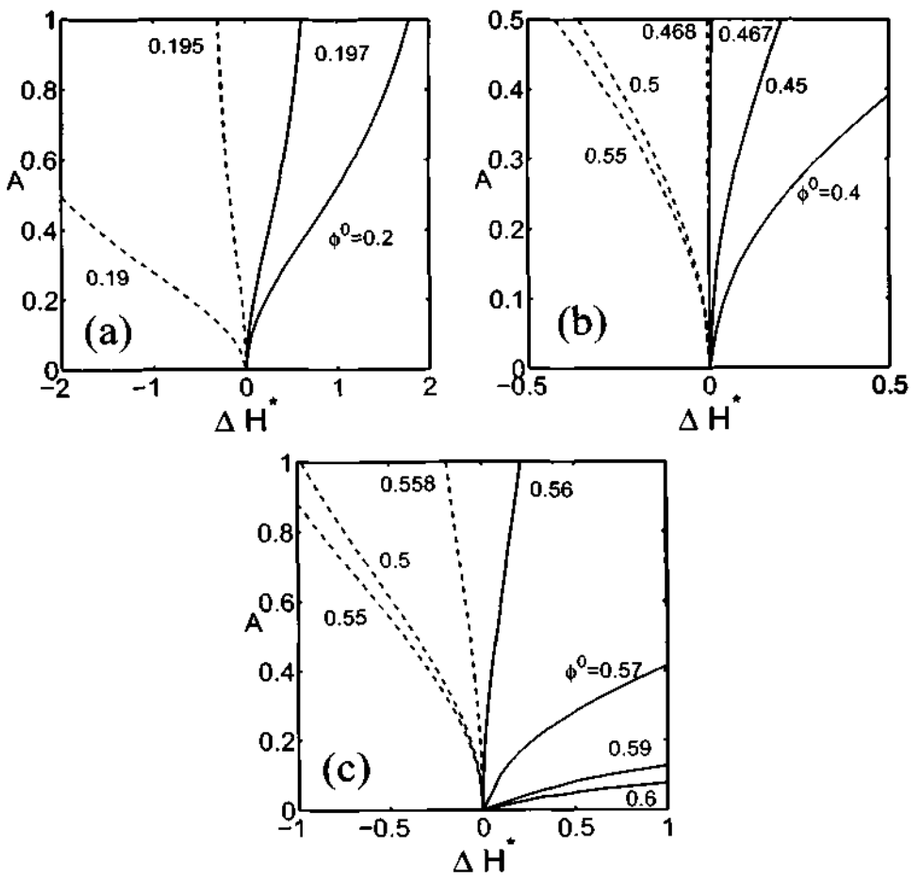

Figure 5.35: Bifurcation diagrams in the $(A, \Delta H^*)$-plane, where $\Delta H^* = H^* - H_c^*$, showing a sequence of transitions from *subcritical* to supercritical bifurcations and vice versa with increasing density. The Carnahan-Starling radial distribution function (5.62) with $\phi_m = 0.65$ has been used, with other parameters as in figure 5.34(*a*). (*a*) $\phi_c^s \approx 0.196$, subcritical to supercritical bifurcations; (*b*) $\phi_c^s \approx 0.467$, supercritical to subcritical bifurcations; (*c*) $\phi_c^s \approx 0.559$, subcritical to supercritical bifurcations.

5.6.2 Influence of Constitutive Relations: Disks vs Spheres

Recall that the constitutive expressions for $f_i(.)'s$ (dimensionless functions of solid fraction, ϕ) in (2.21), that were used in all calculations, are valid only for spheres. Therefore, the present results pertain to the granular plane Couette flow in two-dimensions, having a mono-layer of spheres along the spanwise direction. It is interesting to ascertain whether these predictions about the onset of nonlinear shear-banding instability and the corresponding bifurcation scenario in different density regimes still hold if we use constitutive relations for hard-disks.

For hard-disks in two-dimensions (dim = 2), the balance equations and the form of constitutive relations remain unaltered; however, the expressions for $f_i(.)'s$ as defined in (2.21) are different for disks as define by (2.14) (see chapter 2). In two-dimensions, the contact radial distribution function, $\chi(\phi)$, is chosen to be of the forms as given by (2.15) (see chapter 2).

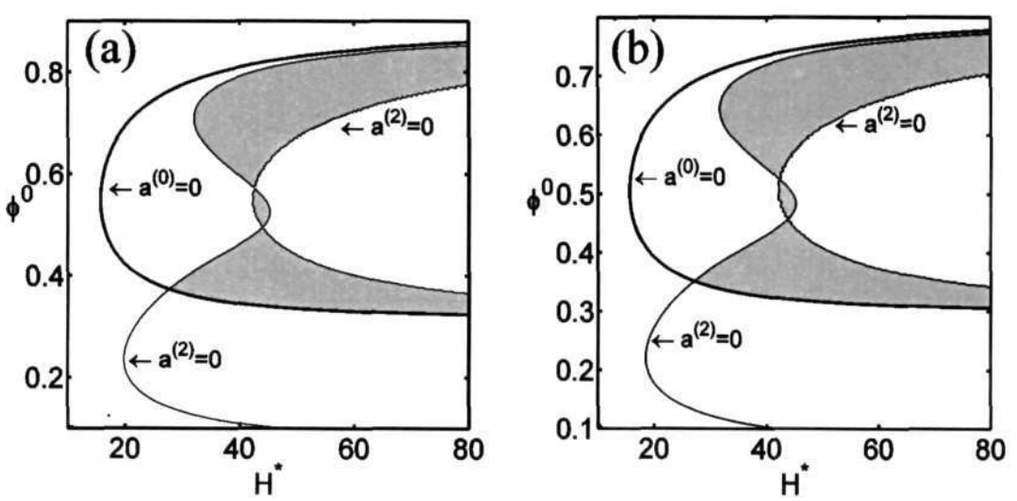

Figure 5.36: Scaled phase diagram in the (H^*, ϕ^0)-plane, where $H^* = H\beta^{-1}\sqrt{(1-e^2)}$, for constitutive relations for hard-disks (two-dimensions) as in (2.14)-(2.15) with (a) $\phi_m = \pi/2\sqrt{3} \approx 0.906$ and (b) $\phi_m = 0.82$.

Recall that changing the explicit forms of constitutive relations amounts to changing only the forms of the linear and nonlinear operators, $\mathbf{L}_{kn}$ and $\mathbf{G}_{kn}$, respectively, in (5.6) since the governing equations (4.5)-(4.8) and the boundary conditions (4.10) are the same for both spheres and disks. With constitutive relations for hard-disks as in (2.14)-(2.15), we have repeated some of the nonlinear stability calculations that we briefly discuss here. The scaled phase diagrams in the (H^*, ϕ^0)-plane, where $H^* = H\beta^{-1}\sqrt{(1-e^2)}$ and ϕ^0 is the mean density, are displayed in figures 5.36(a) and 5.36(b) for $\phi_m = 0.906$ and 0.82, respectively. Both phase diagrams look similar; at closer look at the zero contour of the first Landau coefficient $a^{(2)} = 0$ and the neutral contour $a^{(0)} = 0$ near the dense limit (at much larger values of $H^* \sim 500$) ascertains that there is no cross-over between $a^{(2)} = 0$ and $a^{(0)} = 0$, except the one at a moderate density $\phi^0 \sim 0.37$. With parameter values as in figures 5.36(a), a series of bifurcation diagrams in the $(A, \triangle H^*)$-plane are shown in figure 5.37 for a range of mean densities. For this case, the nature of bifurcation changes from subcritical to supercritical at $\phi_c^s \approx 0.373$. Note in figure 5.36 that the flow is linearly stable in the dilute limit, and the shear-banding occurs via a 'bifurcation-from-infinity' for $\phi_c^l \leq 0.338$ (with $\phi_m = 0.906$) and $\phi_c^l \leq 0.339$ (with $\phi_m = 0.82$). A comparison of figure 5.36 with that for spheres (figure 5.33) reveals that the region of 'bifurcations-from-infinity' is much larger for

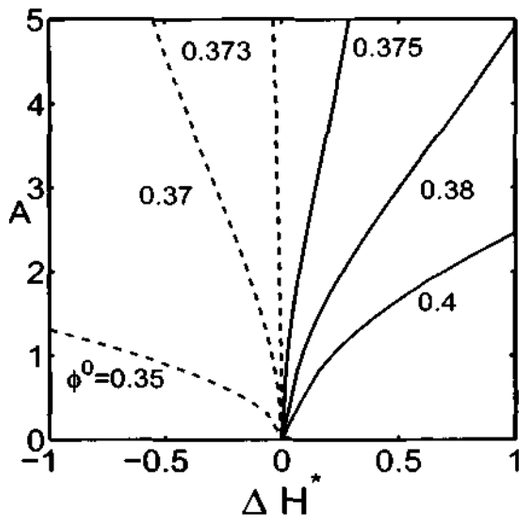

Figure 5.37: Bifurcation diagrams in the $(A, \Delta H^*)$-plane, where $\Delta H^* = H^* - H_c^*$, showing a transition from *subcritical* to supercritical bifurcation for constitutive relations of hard-disks (2.14)-(2.15) with $\phi_m = 0.906$.

hard-disks.

With constitutive expressions for hard-disks as in (2.14)-(2.15), the following sequence of pitchfork bifurcations, leading to nonlinear shear-banded solutions, holds as we increase the mean density from the Boltzmann limit: bifurcation-from-infinity → subcritical → supercritical. In contrast to results for spheres, we do not find subcritical bifurcations in the dense limit for hard-disks with (2.14)-(2.15). We have verified that the same sequence of bifurcations also holds even if we allow the shear viscosity to diverge at a faster rate than other transport coefficients.

5.6.3 Granular Plane Couette Flow: a "Microcosm" for Pitchfork Bifurcations

Let us now summarize results on different types of pitchfork bifurcations in granular plane Couette flow that result from the nonlinear saturation of shear-banding instability. With (5.61) as the contact radial distribution function and the constitutive relations as in (4.9), the sequence of pitchfork bifurcations in the present flow configuration, with increasing mean density, reads as:

$$\left.\begin{array}{rl} \text{Bifurcation from Infinity :} & \phi^0 < \phi_c^l \approx 0.154 \\ \text{Subcritical Bifurcation :} & \phi_c^l < \phi^0 < \phi_c^s \\ \text{Supercritical Bifurcation :} & \phi^0 > \phi_c^s \approx 0.1735 \end{array}\right\}. \tag{5.63}$$

This prediction is the same as in given in chapter 4 and our previous paper Shukla & Alam (2009), note that the direct numerical simulation of continuum equations (4.5)-(4.8) (along with (2.21)) for the same problem (Nott *et al.* 1999) has also identified the above three types of bifurcations. By changing the contact radial distribution function to the Carnahan-Starling-type (5.62), with $\phi_m = 0.65$, and the constitutive relations as in (2.21), the sequence of pitchfork

bifurcations reads as

$$\left.\begin{array}{rl} \text{Bifurcation from Infinity :} & \phi^0 < \phi_c^l \approx 0.174 \\ \text{Subcritical Bifurcation :} & \phi_c^l < \phi^0 < \phi_c^s \approx 0.196 \\ \text{Supercritical Bifurcation :} & \phi_c^s < \phi^0 < \phi_c^{s1} \approx 0.467 \\ \text{Subcritical Bifurcation :} & \phi_c^{s1} < \phi^0 < \phi_c^{s2} \approx 0.559 \\ \text{Subpercritical Bifurcation :} & \phi^0 > \phi_c^{s2} \end{array}\right\}. \tag{5.64}$$

This bifurcation sequence remains intact even when the singularity of the Carnahan-Starling radial distribution function (5.62) is moved to $\phi_m = 1$; only the critical densities at which each transition occurs are quantitatively different: $\phi_c^l \approx 0.218$, $\phi_c^s \approx 0.246$, $\phi_c^{s1} \approx 0.717$ and $\phi_c^{s2} \approx 0.842$.

It is clear from the above discussion that the sequence of bifurcations (the first three in (5.63) and (5.64)) remains same in the regime of dilute to moderate densities, irrespective of explicit forms of constitutive relations for different transport coefficients, however, the nature of bifurcations at larger densities (especially the appearance of subcritical bifurcations in the dense limit) crucially depends on constitutive relations and the contact radial distribution function. It is recommended to employ the exact forms of constitutive relations that are likely to be valid in the whole range of densities (which can be obtained from particle simulations) so as to make a fair conclusion about the bifurcation-type and the corresponding critical density for the onset of nonlinear shear-banding instability in granular plane Couette flow. Such a detailed parametric study is beyond the scope of the present work and is left to the future.

Figure 5.38 summarizes all possible bifurcation scenario for the nonlinear shear-banding instability in granular plane Couette flow; note that a single control parameter, the mean density (ϕ^0), needs to varied to obtain any type of pitchfork bifurcations in this flow. Therefore the granular plane Couette flow serves as a *microcosm* of pitchfork bifurcations since all three possible types of pitchfork bifurcations, as shown schematically in figure 5.38, can be realized by just varying the mean density.

Moving to the well-researched field of Newtonian fluids, we note that a similar type of bifurcation from infinity occurs in the plane Couette flow (Nagata 1990); note, however, that there is no supercritical or subcritical bifurcations in this flow since the Newtonian plane Couette flow is known to be *stable* according to the linear stability theory (Romanov 1973). For Newtonian fluids, the examples of subcritical and supercritical bifurcations can be found in plane Poiseuille flow (Stuart 1960; Reynolds & Potter 1967) and Rayleigh-Benard convection (Busse 1978), respectively, see figure 5.39. We are not aware of any flow which admits all three types of pitchfork bifurcations, and therefore the granular plane Couette flow is truly a *paradigm* for pitchfork bifurcations.

5.7 Conclusions

In this chapter we have studied the weakly nonlinear analysis of granular plane Couette flow for the shearbanding instability which leads to shearbands along the flow gradient direction. The shearbanding instabilities arise due to perturbations which do not depend on streamwise direction. We have employed amplitude expansion method (Stuart 1960; Watson 1960; Reynolds & Potter 1967) for reducing the system of ordinary differential equations to partial differential equations. The first Landau coefficient has been calculated from the solvability condition.

We have developed analytical solutions for the second harmonic, the distortion of mean flow and the first Landau coefficient. The comparison between numerical and analytical solutions constitutes a validation of the spectral-based numerical scheme which is another outcome of the present chapter. These analytical solutions yield an universal scaling between inelasticity $(1-e^2)^{1/2}$ and the mode number β. Further we have analyzed the bifurcations (pitchfork) for the

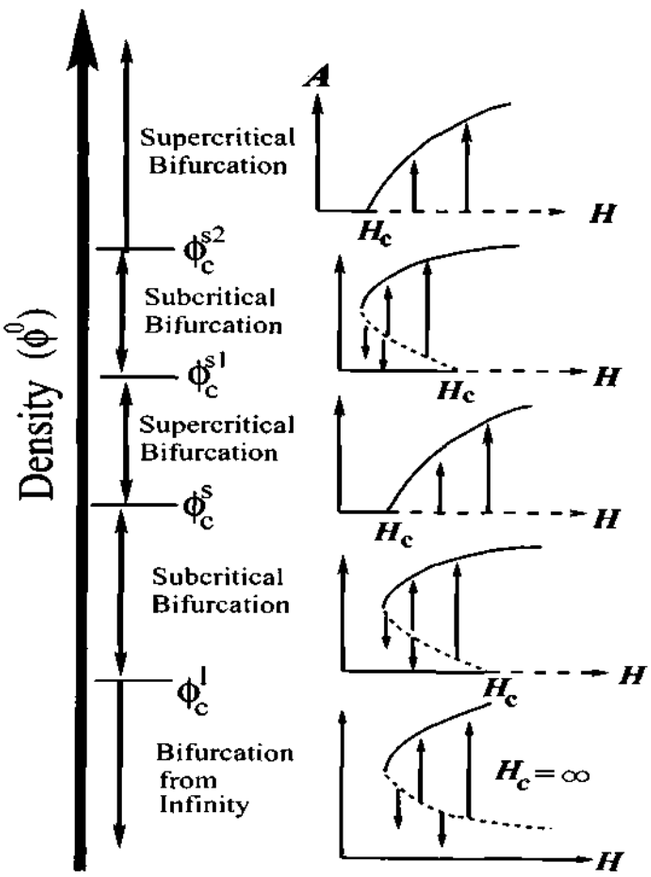

Figure 5.38: A schematic of different types of pitchfork bifurcations, depicting the whole paradigm, in granular plane Couette flow. The dashed lines in subcritical bifurcation diagrams represent *threshold-amplitude* for nonlinear stability.

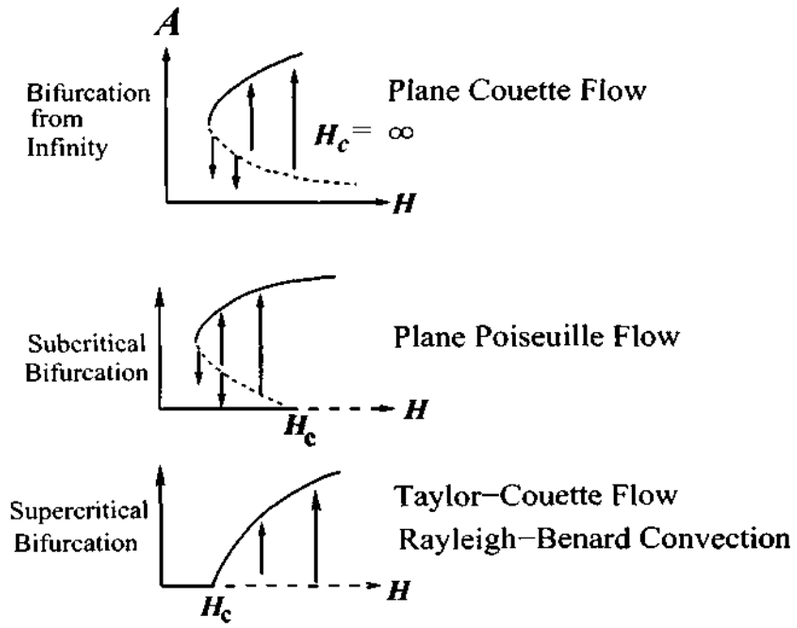

Figure 5.39: A schematic of three types of pitchfork bifurcations in Newtonian fluids.

shearbanding instability. From the zero contour of the first Landau coefficient in (H, ϕ^0)-plane, calculated using analytical solution, we have verified the previous result of Shukla & Alam (2009) that the lower branch of the neutral stability curve is subcritically unstable and the upper branch is supercritically stable.

The transition between the bifurcations from subcritical-to-supercritical and supercritical-to-subcritical depends on the choice of the radial distribution function. From the analysis of the present chapter we can conclude that the granular plane Couette flow serves as a microcosm of pitchfork bifurcations as all the three types of pitchfork bifurcations (subcritical, supercritical, bifurcation from infinity) exist in the flow.

Appendix 5A. Nonlinear Terms ($\mathcal{N}_2$ and $\mathcal{N}_3$)

Here $\mathcal{N}_j = \left(\mathcal{N}_j^1, \mathcal{N}_j^2, \mathcal{N}_j^3, \mathcal{N}_j^4\right)^{Tr}$ correspond to mass balance, x-momentum, y-momentum and energy balance equations, respectively.

$$\mathcal{N}_2^1 = -\frac{\partial(\phi' v')}{\partial y} \quad \text{and} \quad \mathcal{N}_3^1 = 0$$

$$\begin{aligned}
\mathcal{N}_2^2 &= -\frac{1}{\phi^0}\left[\phi^0 v'\frac{\partial u'}{\partial y} + \phi'\left(\frac{\partial u'}{\partial t} + v'\right)\right] + \frac{1}{\phi^0 H^2}\left[(\mu_\phi^0\phi' + \mu_T^0 T')\frac{\partial^2 u'}{\partial y^2}\right. \\
&\left. + \frac{1}{2}\left(\mu_{\phi\phi}^0\frac{\partial \phi'^2}{\partial y} + \mu_{TT}^0\frac{\partial T'^2}{\partial y} + 2\mu_{\phi T}^0\frac{\partial \phi' T'}{\partial y}\right) + \left(\mu_\phi^0\frac{\partial \phi'}{\partial y} + \mu_T^0\frac{\partial T'}{\partial y}\right)\frac{\partial u'}{\partial y}\right] \\
\mathcal{N}_3^2 &= -\frac{1}{\phi^0}\phi' v'\frac{\partial u'}{\partial y} + \frac{1}{\phi^0 H^2}\left[\frac{1}{2}\left(\mu_{\phi\phi}^0\phi'^2 + \mu_{TT}^0 T'^2 + 2\mu_{\phi T}^0\phi' T'\right)\frac{\partial^2 u'}{\partial y^2}\right. \\
&+ \frac{1}{6}\left(\mu_{\phi\phi\phi}^0\frac{\partial \phi'^3}{\partial y} + \mu_{TTT}^0\frac{\partial T'^3}{\partial y} + 3\mu_{\phi\phi T}^0\frac{\partial \phi'^2 T'}{\partial y} + 3\mu_{\phi TT}^0\frac{\partial \phi' T'^2}{\partial y}\right) \\
&\left. + \frac{1}{2}\left(\mu_{\phi\phi}^0\frac{\partial \phi'^2}{\partial y} + \mu_{TT}^0\frac{\partial T'^2}{\partial y} + 2\mu_{\phi T}^0\frac{\partial \phi' T'}{\partial y}\right)\frac{\partial u'}{\partial y}\right] \\
\mathcal{N}_2^3 &= -\frac{1}{\phi^0}\left(\phi^0 v'\frac{\partial v'}{\partial y} + \phi'\frac{\partial v'}{\partial t}\right) + \frac{1}{\phi^0 H^2}\left[-\frac{1}{2}\left(p_{\phi\phi}^0\frac{\partial \phi'^2}{\partial y} + p_{TT}^0\frac{\partial T'^2}{\partial y} + 2p_{\phi T}^0\frac{\partial \phi' T'}{\partial y}\right)\right. \\
&\left. + 2\left(\mu_\phi^0\phi' + \mu_T^0 T'\right)\frac{\partial^2 v'}{\partial y^2} + \left((2\mu_\phi^0 + \lambda_\phi^0)\frac{\partial \phi'}{\partial y} + (2\mu_T^0 + \lambda_T^0)\frac{\partial T'}{\partial y}\right)\frac{\partial v'}{\partial y} + \left(\lambda_\phi^0\phi' + \lambda_T^0 T'\right)\frac{\partial^2 v'}{\partial y^2}\right] \\
\mathcal{N}_3^3 &= -\frac{1}{\phi^0}\phi' v'\frac{\partial v'}{\partial y} + \frac{1}{\phi^0 H^2}\left[-\frac{1}{6}\left(p_{\phi\phi\phi}^0\frac{\partial \phi'^3}{\partial y} + p_{TTT}^0\frac{\partial T'^3}{\partial y} + 3p_{\phi\phi T}^0\frac{\partial \phi'^2 T'}{\partial y} + 3p_{\phi TT}^0\frac{\partial \phi' T'^2}{\partial y}\right)\right. \\
&+ \left(\mu_{\phi\phi}^0\phi'^2 + \mu_{TT}^0 T'^2 + 2\mu_{\phi T}^0\phi' T'\right)\frac{\partial^2 v'}{\partial y^2} + \left(\mu_{\phi\phi}^0\frac{\partial \phi'^2}{\partial y} + \mu_{TT}^0\frac{\partial T'^2}{\partial y} + 2\mu_{\phi T}^0\frac{\partial \phi' T'}{\partial y}\right)\frac{\partial v'}{\partial y} \\
&\left. + \frac{1}{2}\left(\lambda_{\phi\phi}^0\frac{\partial \phi'^2}{\partial y} + \lambda_{TT}^0\frac{\partial T'^2}{\partial y} + 2\lambda_{\phi T}^0\frac{\partial \phi' T'}{\partial y}\right)\frac{\partial v'}{\partial y} + \frac{1}{2}\left(\lambda_{\phi\phi}^0\phi'^2 + \lambda_{TT}^0 T'^2 + 2\lambda_{\phi T}^0\phi' T'\right)\frac{\partial^2 v'}{\partial y^2}\right] \\
\mathcal{N}_2^4 &= -\frac{1}{\phi^0}\left(\phi^0 v'\frac{\partial T'}{\partial y} + \phi'\frac{\partial T'}{\partial t}\right) + \left[\frac{1}{H^2}\left[\frac{\partial T'}{\partial y}\left(\kappa_\phi^0\frac{\partial \phi'}{\partial y} + \kappa_T^0\frac{\partial T'}{\partial y}\right) + \frac{\partial^2 T'}{\partial y^2}\left(\kappa_\phi^0\phi' + \kappa_T^0 T'\right)\right]\right. \\
&- (p_\phi^0\phi' + p_T^0 T')\frac{\partial v'}{\partial y} + 2\mu^0\left[\left(\frac{\partial v'}{\partial y}\right)^2 + \frac{1}{2}\left(\frac{\partial u'}{\partial y}\right)^2\right] + 2(\mu_\phi^0\phi' + \mu_T^0 T')\left(\frac{\partial u'}{\partial y}\right) \\
&\left. + \left(\frac{1}{2}\mu_{\phi\phi}^0\phi'^2 + \frac{1}{2}\mu_{TT}^0 T'^2 + \mu_{\phi T}^0\phi' T'\right) + \lambda^0\left(\frac{\partial v'}{\partial y}\right)^2 - \left(\frac{1}{2}\mathcal{D}_{\phi\phi}^0\phi'^2 + \frac{1}{2}\mathcal{D}_{TT}^0 T'^2 + \mathcal{D}_{\phi T}^0\phi' T'\right)\right]\left(\frac{2}{\phi^0 dim}\right) \\
\mathcal{N}_3^4 &= -\frac{1}{\phi^0}\left(\phi' v'\frac{\partial T'}{\partial y}\right) + \left[\frac{1}{H^2}\left[\frac{\partial T'}{\partial y}\left(\frac{1}{2}\kappa_{\phi\phi}^0\frac{\partial \phi'^2}{\partial y} + \frac{1}{2}\kappa_{TT}^0\frac{\partial T'^2}{\partial y} + \kappa_{\phi T}^0\frac{\partial \phi' T'}{\partial y}\right)\right.\right. \\
&\left. + \frac{\partial^2 T'}{\partial y^2}\left(\frac{1}{2}\kappa_{\phi\phi}^0\phi'^2 + \frac{1}{2}\kappa_{TT}^0 T'^2 + \kappa_{\phi T}^0\phi' T'\right)\right] \\
&- \left(\frac{1}{2}p_{\phi\phi}^0\phi'^2 + \frac{1}{2}p_{TT}^0 T'^2 + p_{\phi T}^0\phi' T'\right)\frac{\partial v'}{\partial y} + 2(\mu_\phi^0\phi' + \mu_T^0 T')\left[\left(\frac{\partial v'}{\partial y}\right)^2 + \frac{1}{2}\left(\frac{\partial u'}{\partial y}\right)^2\right] \\
&+ \left(\frac{1}{6}\mu_{\phi\phi\phi}^0\phi'^3 + \frac{1}{6}\mu_{TTT}^0 T'^3 + \frac{1}{2}\mu_{\phi\phi T}^0\phi'^2 T' + \frac{1}{2}\mu_{\phi TT}^0\phi' T'^2\right) \\
&+ \left(\mu_{\phi\phi}^0\phi'^2 + \mu_{TT}^0 T'^2 + 2\mu_{\phi T}^0\phi' T'\right)\left(\frac{\partial u'}{\partial y}\right) + \left(\lambda_\phi^0\phi' + \lambda_T^0 T'\right)\left(\frac{\partial v'}{\partial y}\right)^2 \\
&\left. - \left(\frac{1}{6}\mathcal{D}_{\phi\phi\phi}^0\phi'^3 + + \frac{1}{6}\mathcal{D}_{TTT}^0 T'^3 + \frac{1}{2}\mathcal{D}_{\phi\phi T}^0\phi'^2 T' + \frac{1}{2}\mathcal{D}_{\phi TT}^0\phi' T'^2\right)\right]\left(\frac{2}{\phi^0 dim}\right)
\end{aligned}$$

Appendix 5B. Inhomogeneous Terms G_{13}

The y-independent terms of G_{13} (cf. §5.4.2) are:

$$
\begin{aligned}
G_{13}^{1\beta 3} &= -\frac{1}{2}\left[(k_{2\beta}+k_\beta)(\phi_1 v_2+\phi_2 v_1)\right] \quad and \quad G_{13}^{1\beta 1}=-\frac{1}{2}\left[(k_{2\beta}-k_\beta)(\phi_1 v_2-\phi_2 v_1)\right]\\
G_{13}^{2\beta 3} &= -\frac{1}{2}v_1u_2k_{2\beta}+\frac{1}{2}\Big[-\frac{1}{\phi^0}\phi_1v_2-2c^{(0)}\frac{\phi_1u_2}{\phi^0}\\
&\quad +\frac{1}{\phi^0H^2}\left(-k_{2\beta}^2(\mu_\phi^0\phi_1+\mu_T^0T_1)u_2-k_{2\beta}\left(\mu_{\phi\phi}^0\phi_1\phi_2+\mu_{TT}^0T_1T_2+\mu_{\phi T}^0\phi_1T_2+\mu_{\phi T}^0T_1\phi_2\right)\right.\\
&\quad \left.-k_\beta k_{2\beta}u_1\left(\mu_\phi^0\phi_2+\mu_T^0T_2\right)\right)\Big]-\frac{1}{2}v_2u_1k_\beta+\frac{1}{2}\Big[-\frac{1}{\phi^0}\phi_2v_1-c^{(0)}\frac{\phi_2u_1}{\phi^0}\\
&\quad +\frac{1}{\phi^0H^2}\left(-k_\beta^2(\mu_\phi^0\phi_2+\mu_T^0T_2)u_1-k_\beta\left(\mu_{\phi\phi}^0\phi_2\phi_1+\mu_{TT}^0T_2T_1+\mu_{\phi T}^0\phi_2T_1+\mu_{\phi T}^0T_2\phi_1\right)\right.\\
&\quad \left.-k_\beta k_{2\beta}u_2(\mu_\phi^0\phi_1+\mu_T^0T_1)\right)\Big]\\
&\quad +\frac{1}{4}\left[-\frac{1}{\phi^0}k_\beta\phi_1v_1u_1\right]+\frac{1}{4\phi^0H^2}\left[-k_\beta^2\left(\frac{1}{2}\mu_{\phi\phi}^0\phi_1^2+\frac{1}{2}\mu_{TT}^0T_1^2+\mu_{\phi T}^0\phi_1T_1\right)u_1\right.\\
&\quad -k_\beta\left(\frac{1}{2}\mu_{\phi\phi\phi}^0\phi_1^3+\frac{1}{2}\mu_{TTT}^0T_1^3+\frac{3}{2}\mu_{\phi\phi T}^0\phi_1^2T_1+\frac{3}{2}\mu_{TT\phi}^0T_1^2\phi_1\right)\\
&\quad \left.-k_\beta^2u_1\left(\mu_{\phi\phi}^0\phi_1^2+\mu_{TT}^0T_1^2+2\mu_{\phi T}^0\phi_1T_1\right)\right]\\
G_{13}^{2\beta 1} &= \frac{1}{2}v_1u_2k_{2\beta}+\frac{1}{2}\Big[-\frac{1}{\phi^0}\phi_1v_2-2c^{(0)}\frac{\phi_1u_2}{\phi^0}\\
&\quad +\frac{1}{\phi^0H^2}\left(-k_{2\beta}^2(\mu_\phi^0\phi_1+\mu_T^0T_1)u_2-k_{2\beta}\left(\mu_{\phi\phi}^0\phi_1\phi_2+\mu_{TT}^0T_1T_2+\mu_{\phi T}^0\phi_1T_2+\mu_{\phi T}^0T_1\phi_2\right)\right.\\
&\quad \left.-k_\beta k_{2\beta}u_1\left(\mu_\phi^0\phi_2+\mu_T^0T_2\right)\right)\Big]-\frac{1}{2}v_2u_1k_\beta-\frac{1}{2}\Big[-\frac{1}{\phi^0}\phi_2v_1-c^{(0)}\frac{\phi_2u_1}{\phi^0}\\
&\quad +\frac{1}{\phi^0H^2}\left(-k_\beta^2(\mu_\phi^0\phi_2+\mu_T^0T_2)u_1-k_\beta\left(\mu_{\phi\phi}^0\phi_2\phi_1+\mu_{TT}^0T_2T_1+\mu_{\phi T}^0\phi_2T_1+\mu_{\phi T}^0T_2\phi_1\right)\right.\\
&\quad \left.-k_\beta k_{2\beta}u_2(\mu_\phi^0\phi_1+\mu_T^0T_1)\right)\Big]+T_{k_{2\beta}}^{mean}\frac{1}{\phi^0H^2}\left[-k_\beta\left(\mu_{TT}^0T_1+\mu_{\phi T}^0\phi_1\right)-k_\beta^2\mu_T^0u_1\right]\\
&\quad +\frac{1}{4}\left[-\frac{1}{\phi^0}k_\beta\phi_1v_1u_1\right]+\frac{1}{4\phi^0H^2}\left[-k_\beta^2\left(\frac{1}{2}\mu_{\phi\phi}^0\phi_1^2+\frac{1}{2}\mu_{TT}^0T_1^2+\mu_{\phi T}^0\phi_1T_1\right)u_1\right.\\
&\quad -k_\beta\left(\frac{1}{2}\mu_{\phi\phi\phi}^0\phi_1^3+\frac{1}{2}\mu_{TTT}^0T_1^3+\frac{3}{2}\mu_{\phi\phi T}^0\phi_1^2T_1+\frac{3}{2}\mu_{TT\phi}^0T_1^2\phi_1\right)\\
&\quad \left.-k_\beta^2u_1\left(\mu_{\phi\phi}^0\phi_1^2+\mu_{TT}^0T_1^2+2\mu_{\phi T}^0\phi_1T_1\right)\right]\\
G_{13}^{3\beta 3} &= \frac{1}{2}\left[-k_{2\beta}v_1v_2-\frac{k_\beta k_{2\beta}v_2}{\phi^0H^2}\left(2(\mu_\phi^0\phi_1+\mu_T^0T_1)+(\lambda_\phi^0\phi_1+\lambda_T^0T_1)\right)\right]-\frac{1}{\phi^0}c^{(0)}\phi_1v_2\\
&\quad +\frac{1}{2\phi^0H^2}\left[k_{2\beta}\left(p_{\phi\phi}^0\phi_1\phi_2+p_{TT}^0T_1T_2+p_{\phi T}^0\phi_1T_2+p_{\phi T}^0T_1\phi_2\right)\right.\\
&\quad \left.-k_{2\beta}^2 2\left(\mu_\phi^0\phi_1+\mu_T^0T_1\right)v_2-k_{2\beta}^2\left(\lambda_\phi^0\phi_1+\lambda_T^0T_1\right)v_2\right]\\
&\quad +\frac{1}{2}\left[-k_\beta v_1v_2-\frac{k_\beta k_{2\beta}v_1}{\phi^0H^2}\left(2(\mu_\phi^0\phi_2+\mu_T^0T_2)+(\lambda_\phi^0\phi_2+\lambda_T^0T_2)\right)\right]-\frac{1}{2\phi^0}c^{(0)}\phi_2v_1\\
&\quad +\frac{1}{2\phi^0H^2}\left[k_\beta\left(p_{\phi\phi}^0\phi_2\phi_1+p_{TT}^0T_2T_1+p_{\phi T}^0\phi_2T_1+p_{\phi T}^0T_2\phi_1\right)\right.\\
&\quad \left.-k_\beta^2 2\left(\mu_\phi^0\phi_2+\mu_T^0T_2\right)v_1-k_\beta^2\left(\lambda_\phi^0\phi_2+\lambda_T^0T_2\right)v_1\right]\\
&\quad +\frac{1}{4}\left[-\frac{1}{\phi^0}k_\beta\phi_1v_1^2\right]+\frac{1}{4\phi^0H^2}\left[k_\beta\left(\frac{1}{2}p_{\phi\phi\phi}^0\phi_1^3+\frac{1}{2}p_{TTT}^0T_1^3+\frac{3}{2}p_{\phi\phi T}^0\phi_1^2T_1+\frac{3}{2}p_{\phi TT}^0T_1^2\phi_1\right)\right.\\
&\quad \left.-2k_\beta^2\left(\frac{3}{2}\mu_{\phi\phi}^0\phi_1^2+\frac{3}{2}\mu_{TT}^0T_1^2+3\mu_{\phi T}^0\phi_1T_1\right)v_1-k_\beta^2\left(\frac{3}{2}\lambda_{\phi\phi}^0\phi_1^2+\frac{3}{2}\lambda_{TT}^0T_1^2+3\lambda_{\phi T}^0\phi_1T_1\right)v_1\right]
\end{aligned}
$$

$$
\begin{aligned}
G_{13}^{3\beta 1} &= -\frac{1}{2}\left[-k_{2\beta}v_1v_2-\frac{k_\beta k_{2\beta}v_2}{\phi^0H^2}\left(2(\mu_\phi^0\phi_1+\mu_T^0T_1)+(\lambda_\phi^0\phi_1+\lambda_T^0T_1)\right)\right]-\frac{1}{\phi^0}c^{(0)}\phi_1v_2\\
&+\frac{1}{2\phi^0H^2}\left[k_{2\beta}\left(p_{\phi\phi}^0\phi_1\phi_2+p_{TT}^0T_1T_2+p_{\phi T}^0\phi_1T_2+p_{\phi T}^0T_1\phi_2\right)\right.\\
&\left.-2k_{2\beta}^2\left(\mu_\phi^0\phi_1+\mu_T^0T_1\right)v_2-k_{2\beta}^2\left(\lambda_\phi^0\phi_1+\lambda_T^0T_1\right)v_2\right]\\
&+\frac{1}{2}\left[-k_\beta v_1v_2-\frac{k_\beta k_{2\beta}v_1}{\phi^0H^2}\left(2(\mu_\phi^0\phi_2+\mu_T^0T_2)+(\lambda_\phi^0\phi_2+\lambda_T^0T_2)\right)\right]+\frac{1}{2\phi^0}c^{(0)}\phi_2v_1\\
&-\frac{1}{2\phi^0H^2}\left[k_\beta\left(p_{\phi\phi}^0\phi_2\phi_1+p_{TT}^0T_2T_1+p_{\phi T}^0\phi_2T_1+p_{\phi T}^0T_2\phi_1\right)\right.\\
&\left.-2k_\beta^2\left(\mu_\phi^0\phi_2+\mu_T^0T_2\right)v_1-k_\beta^2\left(\lambda_\phi^0\phi_2+\lambda_T^0T_2\right)v_1\right]\\
&+\frac{1}{\phi^0H^2}T_{k_{2\beta}}^{mean}\left[k_\beta\left(p_{TT}^0T_1+p_{\phi T}^0\phi_1\right)-2\mu_T^0k_\beta^2v_1-\lambda_T^0k_\beta^2v_1\right]\\
&+\frac{1}{4}\left[-\frac{1}{\phi^0}k_\beta\phi_1v_1^2\right]+\frac{1}{4\phi^0H^2}\left[k_\beta\left(\frac{1}{2}p_{\phi\phi\phi}^0\phi_1^3+\frac{1}{2}p_{TTT}^0T_1^3+\frac{3}{2}p_{\phi\phi T}^0\phi_1^2T_1+\frac{3}{2}p_{\phi TT}^0T_1^2\phi_1\right)\right.\\
&\left.-2k_\beta^2\left(\frac{3}{2}\mu_{\phi\phi}^0\phi_1^2+\frac{3}{2}\mu_{TT}^0T_1^2+3\mu_{\phi T}^0\phi_1T_1\right)v_1-k_\beta^2\left(\frac{3}{2}\lambda_{\phi\phi}^0\phi_1^2+\frac{3}{2}\lambda_{TT}^0T_1^2+3\lambda_{\phi T}^0\phi_1T_1\right)v_1\right]\\
G_{13}^{4\beta 3} &= -\frac{1}{2}\left[k_{2\beta}v_1T_2+\frac{2}{\phi^0H^2dim}k_\beta k_{2\beta}T_1\left(\kappa_\phi^0\phi_2+\kappa_T^0T_2\right)\right]\\
&+\frac{1}{2}\left[-\frac{2}{\phi^0}c^{(0)}\phi_1T_2+\frac{2}{\phi^0dim}\left(-\frac{1}{H^2}k_\beta^2T_1\left(\kappa_\phi^0\phi_2+\kappa_T^0T_2\right)-k_{2\beta}\left(p_\phi^0\phi_1+p_T^0T_1\right)v_2\right.\right.\\
&+2\mu^0k_\beta k_{2\beta}\left(v_1v_2+\frac{1}{2}u_1u_2\right)+\left(\frac{1}{2}\mu_{\phi\phi}^0\phi_1\phi_2+\frac{1}{2}\mu_{TT}^0T_1T_2+\mu_{\phi T}^0\phi_1T_2\right)\\
&\left.\left.+2k_{2\beta}\left(\mu_\phi^0\phi_1+\mu_T^0T_1\right)u_2+\lambda^0k_\beta k_{2\beta}v_1v_2-\left(\frac{1}{2}\mathcal{D}_{\phi\phi}^0\phi_1\phi_2+\frac{1}{2}\mathcal{D}_{TT}^0T_1T_2+\mathcal{D}_{\phi T}^0\phi_1T_2\right)\right)\right]\\
&-\frac{1}{2}\left[k_\beta v_2T_1+\frac{2}{\phi^0H^2dim}k_\beta k_{2\beta}T_2\left(\kappa_\phi^0\phi_1+\kappa_T^0T_1\right)\right]\\
&+\frac{1}{2}\left[-\frac{1}{\phi^0}c^{(0)}\phi_2T_1+\frac{2}{\phi^0dim}\left(-\frac{1}{H^2}k_{2\beta}^2T_2\left(\kappa_\phi^0\phi_1+\kappa_T^0T_1\right)-k_\beta\left(p_\phi^0\phi_2+p_T^0T_2\right)v_1\right.\right.\\
&+2\mu^0k_\beta k_{2\beta}\left(v_2v_1+\frac{1}{2}u_2u_1\right)+\left(\frac{1}{2}\mu_{\phi\phi}^0\phi_2\phi_1+\frac{1}{2}\mu_{TT}^0T_2T_1+\mu_{\phi T}^0\phi_2T_1\right)\\
&\left.\left.+2k_\beta\left(\mu_\phi^0\phi_2+\mu_T^0T_2\right)u_1+\lambda^0k_\beta k_{2\beta}v_2v_1-\left(\frac{1}{2}\mathcal{D}_{\phi\phi}^0\phi_2\phi_1+\frac{1}{2}\mathcal{D}_{TT}^0T_2T_1+\mathcal{D}_{\phi T}^0\phi_2T_1\right)\right)\right]\\
&+\frac{1}{4}\left[\frac{k_\beta}{\phi^0}\phi_1v_1T_1+\frac{2}{\phi^0dim}\left(\frac{k_\beta^2}{H^2}T_1\left(\kappa_{\phi\phi}^0\phi_1^2+\kappa_{TT}^0T_1^2+2\kappa_{\phi T}^0\phi_1T_1\right)\right)\right]\\
&+\left(\frac{1}{2\phi^0dim}\right)\left[-\frac{k_\beta^2}{H^2}T_1\left(\frac{1}{2}\kappa_{\phi\phi}^0\phi_1^2+\frac{1}{2}\kappa_{TT}^0T_1^2+\kappa_{\phi T}^0\phi_1T_1\right)\right.\\
&-k_\beta\left(\frac{1}{2}p_{\phi\phi}^0\phi_1^2+\frac{1}{2}p_{TT}^0T_1^2+p_{\phi T}^0\phi_1T_1\right)v_1+2k_\beta^2\left(\mu_\phi^0\phi_1+\mu_T^0T_1\right)\left(v_1^2+\frac{1}{2}u_1^2\right)\\
&+\left(\frac{1}{6}\mu_{\phi\phi\phi}^0\phi_1^3+\frac{1}{6}\mu_{TTT}^0T_1^3+\frac{1}{2}\mu_{\phi\phi T}^0\phi_1^2T_1+\frac{1}{2}\mu_{\phi TT}^0\phi_1T_1^2\right)\\
&+2k_\beta\left(\frac{1}{2}\mu_{\phi\phi}^0\phi_1^2+\frac{1}{2}\mu_{TT}^0T_1^2+\mu_{\phi T}^0\phi_1T_1\right)u_1+k_\beta^2\left(\lambda_\phi^0\phi_1+\lambda_T^0T_1\right)v_1^2\\
&\left.-\left(\frac{1}{6}\mathcal{D}_{\phi\phi\phi}^0\phi_1^3+\frac{1}{6}\mathcal{D}_{TTT}^0T_1^3+\frac{1}{2}\mathcal{D}_{\phi\phi T}^0\phi_1^2T_1+\frac{1}{2}\mathcal{D}_{\phi TT}^0\phi_1T_1^2\right)\right]
\end{aligned}
$$

$$
\begin{aligned}
G_{13}^{4\beta 1} &= \frac{1}{2}\left[k_{2\beta}v_1T_2+\frac{2}{\phi^0H^2dim}k_\beta k_{2\beta}T_1\left(\kappa_\phi^0\phi_2+\kappa_T^0T_2\right)\right]\\
&+\frac{1}{2}\left[-\frac{2}{\phi^0}c^{(0)}\phi_1T_2+\frac{2}{\phi^0dim}\left(-\frac{1}{H^2}k_\beta^2T_1\left(\kappa_\phi^0\phi_2+\kappa_T^0T_2\right)-k_{2\beta}\left(p_\phi^0\phi_1+p_T^0T_1\right)v_2\right.\right.\\
&+2\mu^0k_\beta k_{2\beta}\left(v_1v_2+\frac{1}{2}u_1u_2\right)+\left(\frac{1}{2}\mu_{\phi\phi}^0\phi_1\phi_2+\frac{1}{2}\mu_{TT}^0T_1T_2+\mu_{\phi T}^0\phi_1T_2\right)\\
&\left.\left.+2k_{2\beta}\left(\mu_\phi^0\phi_1+\mu_T^0T_1\right)u_2+\lambda^0k_\beta k_{2\beta}v_1v_2-\left(\frac{1}{2}\mathcal{D}_{\phi\phi}^0\phi_1\phi_2+\frac{1}{2}\mathcal{D}_{TT}^0T_1T_2+\mathcal{D}_{\phi T}^0\phi_1T_2\right)\right)\right]\\
&+T_{k_{2\beta}}^{mean}\left[-\frac{2c^{(0)}}{\phi^0}\phi_1+\frac{2}{\phi^0dim}\left(-\frac{k_\beta^2}{H^2}T_1\kappa_T^0+\left(\frac{1}{2}\mu_{TT}^0T_1+\mu_{\phi T}^0\phi_1\right)-\left(\frac{1}{2}\mathcal{D}_{TT}^0T_1+\mathcal{D}_{\phi T}^0\phi_1\right)\right)\right]\\
&+\frac{1}{2}\left[k_\beta v_2T_1+\frac{2}{\phi^0H^2dim}k_\beta k_{2\beta}T_2\left(\kappa_\phi^0\phi_1+\kappa_T^0T_1\right)\right]\\
&+\frac{1}{2}\left[-\frac{1}{\phi^0}c^{(0)}\phi_2T_1+\frac{2}{\phi^0dim}\left(-\frac{1}{H^2}k_{2\beta}^2T_2\left(\kappa_\phi^0\phi_1+\kappa_T^0T_1\right)-k_\beta\left(p_\phi^0\phi_2+p_T^0T_2\right)v_1\right.\right.\\
&+2\mu^0k_\beta k_{2\beta}\left(v_2v_1+\frac{1}{2}u_2u_1\right)+\left(\frac{1}{2}\mu_{\phi\phi}^0\phi_2\phi_1+\frac{1}{2}\mu_{TT}^0T_2T_1+\mu_{\phi T}^0\phi_2T_1\right)\\
&\left.\left.+2k_\beta\left(\mu_\phi^0\phi_2+\mu_T^0T_2\right)u_1+\lambda^0k_\beta k_{2\beta}v_2v_1-\left(\frac{1}{2}\mathcal{D}_{\phi\phi}^0\phi_2\phi_1+\frac{1}{2}\mathcal{D}_{TT}^0T_2T_1+\mathcal{D}_{\phi T}^0\phi_2T_1\right)\right)\right]\\
&+T_{k_{2\beta}}^{mean}\frac{2}{\phi^0dim}\left[-k_\beta p_T^0v_1+\frac{1}{2}\mu_{TT}^0T_1+2\mu_T^0k_\beta u_1-\frac{1}{2}\mathcal{D}_{TT}^0T_1\right]\\
&+\frac{1}{4}\left[\frac{k_\beta}{\phi^0}\phi_1v_1T_1+\frac{2}{\phi^0dim}\left(\frac{k_\beta^2}{H^2}T_1\left(\kappa_{\phi\phi}^0\phi_1^2+\kappa_{TT}^0T_1^2+2\kappa_{\phi T}^0\phi_1T_1\right)\right)\right]\\
&+\left(\frac{3}{2\phi^0dim}\right)\left[-\frac{k_\beta^2}{H^2}T_1\left(\frac{1}{2}\kappa_{\phi\phi}^0\phi_1^2+\frac{1}{2}\kappa_{TT}^0T_1^2+\kappa_{\phi T}^0\phi_1T_1\right)\right.\\
&-k_\beta\left(\frac{1}{2}p_{\phi\phi}^0\phi_1^2+\frac{1}{2}p_{TT}^0T_1^2+p_{\phi T}^0\phi_1T_1\right)v_1+2k_\beta^2\left(\mu_\phi^0\phi_1+\mu_T^0T_1\right)\left(v_1^2+\frac{1}{2}u_1^2\right)\\
&+\left(\frac{1}{6}\mu_{\phi\phi\phi}^0\phi_1^3+\frac{1}{6}\mu_{TTT}^0T_1^3+\frac{1}{2}\mu_{\phi\phi T}^0\phi_1^2T_1+\frac{1}{2}\mu_{\phi TT}^0\phi_1T_1^2\right)\\
&+2k_\beta\left(\frac{1}{2}\mu_{\phi\phi}^0\phi_1^2+\frac{1}{2}\mu_{TT}^0T_1^2+\mu_{\phi T}^0\phi_1T_1\right)u_1+k_\beta^2\left(\lambda_\phi^0\phi_1+\lambda_T^0T_1\right)v_1^2\\
&\left.-\left(\frac{1}{6}\mathcal{D}_{\phi\phi\phi}^0\phi_1^3+\frac{1}{6}\mathcal{D}_{TTT}^0T_1^3+\frac{1}{2}\mathcal{D}_{\phi\phi T}^0\phi_1^2T_1+\frac{1}{2}\mathcal{D}_{\phi TT}^0\phi_1T_1^2\right)\right]
\end{aligned}
$$

Appendix 5C. Locus of $a^{(2)}=0$

The condition for 'zero' first Landau coefficient, $a^{(2)}=0$, is

$$\phi_1^\dagger G_{13}^{1\beta 1}+T_1^\dagger G_{13}^{4\beta 1}+u_1^\dagger G_{13}^{2\beta 1}+v_1^\dagger G_{13}^{3\beta 1}=0,$$

where $G_{13}^{1\beta 1}, G_{13}^{4\beta 1},\ldots$ can be written as

$$
\begin{array}{llll}
G_{13}^{1\beta 1} &= \frac{1}{H^2}C_{12}+C_{10}, & G_{13}^{2\beta 1} &= \frac{1}{H^2}C_{22}+C_{20}\\
G_{13}^{3\beta 1} &= \frac{1}{H^2}C_{32}+C_{30}, & G_{13}^{4\beta 1} &= \frac{1}{H^2}C_{42}+C_{40}.
\end{array}
\tag{5.65}
$$

In terms of $C_{12}, C_{22},\ldots$ the zero-loci of the first Landau coefficient can be written as

$$H^2=\frac{-\left(\phi_1^\dagger C_{12}+u_1^\dagger C_{22}+v_1^\dagger C_{32}+T_1^\dagger C_{42}\right)}{\left(\phi_1^\dagger C_{10}+u_1^\dagger C_{20}+v_1^\dagger C_{30}+T_1^\dagger C_{40}\right)}.\tag{5C.1}$$

$C_{12}, C_{22}, \ldots$ can be represented in powers of k_β, if we write the mean-terms of second harmonic in terms of a series in k_β as

$$\begin{aligned}
T^{mean}_{k_{2\beta}} &= \frac{f_{nl}}{f_l} = \frac{k_\beta^2 f_{nl}^{(2)} + k_\beta f_{nl}^{(1)} + f_{nl}^{(0)}}{f_l^0} \\
f_{nl}^{(2)} &= \frac{1}{\phi^0\, dim}\left[2\mu^0\left(v_1^2 + \frac{u_1^2}{2}\right) + \lambda^0 v_1^2\right] \\
f_{nl}^{(1)} &= \frac{v_1 T_1}{2\phi^0} + \frac{1}{\phi^0\, dim}\left[-\left(p_\phi^0\phi_1 + p_T^0 T_1\right)v_1 + 2u_1\left(\mu_\phi^0\phi_1 + \mu_T^0 T_1\right)\right] \\
f_{nl}^{(0)} &= \frac{-c^{(0)}}{2\phi^0}\phi_1 T_1 + \frac{1}{\phi^0\, dim}\left[\tfrac{1}{2}\mu_{\phi\phi}^0\phi_1^2 + \tfrac{1}{2}\mu_{TT}^0 T_1^2 + \mu_{\phi T}^0\phi_1 T_1\right. \\
&\quad \left. -\left(\tfrac{1}{2}\mathcal{D}_{\phi\phi}^0\phi_1^2 + \tfrac{1}{2}\mathcal{D}_{TT}^0 T_1^2 + \mathcal{D}_{\phi T}^0\phi_1 T_1\right)\right] \\
f_l &= f_l^{(0)}.
\end{aligned}$$

Hence the expressions for C_{ij} become

$$\left.\begin{aligned}
C_{12} &= 0, & C_{10} &= k_\beta C_{10}^{(1)} \\
C_{22} &= k_\beta^4 C_{22}^{(4)} + k_\beta^3 C_{22}^{(3)} + k_\beta^2 C_{22}^{(2)} + k_\beta C_{22}^{(1)}, & C_{20} &= k_\beta C_{20}^{(1)} + C_{20}^{(0)} \\
C_{32} &= k_\beta^4 C_{32}^{(4)} + k_\beta^3 C_{32}^{(3)} + k_\beta^2 C_{32}^{(2)} + k_\beta C_{32}^{(1)}, & C_{30} &= k_\beta C_{30}^{(1)} + C_{30}^{(0)} \\
C_{42} &= k_\beta^4 C_{42}^{(4)} + k_\beta^3 C_{42}^{(3)} + k_\beta^2 C_{42}^{(2)}, & & \\
C_{40} &= k_\beta^3 C_{40}^{(3)} + k_\beta^2 C_{40}^{(2)} + k_\beta C_{40}^{(1)} + C_{40}^{(0)} & &
\end{aligned}\right\}$$

Inserting these expressions of C_{ij} into (5C.1), we can further simplify (5C.1) as

$$H^2 = \frac{-\left(k_\beta^4 K_1 + k_\beta^3 K_2 + k_\beta^2 K_3 + k_\beta K_4\right)}{\left(k_\beta^3 K_5 + k_\beta^2 K_6 + k_\beta K_7 + K_0\right)}$$

where $K_1, K_2, K_3 \ldots$ are

$$\left.\begin{aligned}
K_1 &= u_1^\dagger C_{22}^{(4)} + v_1^\dagger C_{32}^{(4)} + T_1^\dagger C_{42}^{(4)}, & K_2 &= u_1^\dagger C_{22}^{(3)} + v_1^\dagger C_{32}^{(3)} + T_1^\dagger C_{42}^{(3)}, \\
K_3 &= u_1^\dagger C_{22}^{(2)} + v_1^\dagger C_{32}^{(2)} + T_1^\dagger C_{42}^{(2)}, & K_4 &= u_1^\dagger C_{22}^{(1)} + v_1^\dagger C_{32}^{(1)}, \\
K_5 &= T_1^\dagger C_{40}^{(3)}, & K_6 &= T_1^\dagger C_{40}^{(2)}, \\
K_7 &= \phi_1^\dagger C_{10}^{(1)} + u_1^\dagger C_{20}^{(1)} + v_1^\dagger C_{30}^{(1)} + T_1^\dagger C_{40}^{(1)}, & K_0 &= u_1^\dagger C_{20}^{(0)} + v_1^\dagger C_{30}^{(0)} + T_1^\dagger C_{40}^{(0)}
\end{aligned}\right\}$$

and the expressions for $C_{ij}^{(k)}$ are

$$
\begin{aligned}
C_{10}^{(1)} &= \frac{1}{2}\left(\phi_2 v_1 - \phi_1 v_2\right) \\
C_{22}^{(4)} &= \frac{-\mu_T^0 u_1 f_{nl}^{(2)}}{\phi^0 f_l^{(0)}}, \qquad C_{22}^{(3)} = \frac{-\mu_T^0 u_1 f_{nl}^{(1)}}{\phi^0 f_l^{(0)}} - \left(\mu_{TT}^0 T_1 + \mu_{\phi T}^0 \phi_1\right) \frac{f_{nl}^{(2)}}{\phi^0 f_l^{(0)}} \\
C_{22}^{(2)} &= -\frac{1}{2\phi^0}\left[2u_2\left(\mu_\phi^0\phi_1 + \mu_T^0 T_1\right) + u_1\left(\mu_\phi^0\phi_2 + \mu_T^0 T_2\right)\right] - \frac{u_1}{4\phi^0}\left(\frac{3}{2}\mu_{\phi\phi}^0\phi_1^2 + \frac{3}{2}\mu_{TT}^0 T_1^2 + 3\mu_{\phi T}^0\phi_1 T_1\right) \\
&\quad \frac{-\mu_T^0 u_1 f_{nl}^{(0)}}{\phi^0 f_l^{(0)}} - \left(\mu_{TT}^0 T_1 + \mu_{\phi T}^0\phi_1\right)\frac{f_{nl}^{(1)}}{\phi^0 f_l^{(0)}} \\
C_{22}^{(1)} &= -\frac{1}{2\phi^0}\left(\mu_{\phi\phi}^0\phi_1\phi_2 + \mu_{TT}^0 T_1 T_2 + \mu_{\phi T}^0\phi_1 T_2 + \mu_{\phi T}^0 T_1\phi_2\right) \\
&\quad -\frac{1}{4\phi^0}\left(\frac{1}{2}\mu_{\phi\phi\phi}^0\phi_1^3 + \frac{1}{2}\mu_{TTT}^0 T_1^3 + \frac{3}{2}\mu_{\phi\phi T}^0\phi_1^2 T_1 + \frac{3}{2}\mu_{\phi TT}^0 T_1^2\phi_1\right) - \left(\mu_{TT}^0 T_1 + \mu_{\phi T}^0\phi_1\right)\frac{f_{nl}^{(0)}}{\phi^0 f_l^{(0)}} \\
C_{20}^{(1)} &= \frac{1}{4}\left(4u_2 v_1 - 2u_1 v_2\right) - \frac{u_1 v_1 \phi_1}{4\phi^0} \\
C_{20}^{(0)} &= \frac{1}{2\phi^0}\left[c^{(0)}\left(-2u_2\phi_1 + u_1\phi_2\right) + \left(-v_2\phi_1 + v_1\phi_2\right)\right] \\
C_{32}^{(4)} &= -\left(2\mu_T^0 + \lambda_T^0\right)\frac{v_1 f_{nl}^{(2)}}{\phi^0 f_l^{(0)}}, \quad C_{32}^{(3)} = -\left(2\mu_T^0 + \lambda_T^0\right)\frac{v_1 f_{nl}^{(1)}}{\phi^0 f_l^{(0)}} + \left(p_{TT}^0 T_1 + p_{\phi T}^0\phi_1\right)\frac{f_{nl}^{(2)}}{\phi^0 f_l^{(0)}} \\
C_{32}^{(2)} &= -\frac{1}{\phi^0}\left[2\left(\mu_\phi^0\phi_1 + \mu_T^0 T_1\right)v_2 + \left(\lambda_\phi^0\phi_1 + \lambda_T^0 T_1\right)v_2 + \left(\mu_\phi^0\phi_2 + \mu_T^0 T_2\right)v_1 + \frac{1}{2}\left(\lambda_\phi^0\phi_1 + \lambda_T^0 T_2\right)v_1\right] \\
&\quad -\frac{1}{4\phi^0}\left[2\left(\frac{3}{2}\mu_{\phi\phi}^0\phi_1^2 + \frac{3}{2}\mu_{TT}^0 T_1^2 + 3\mu_{\phi T}^0\phi_1 T_1\right)v_1 + \left(\frac{3}{2}\lambda_{\phi\phi}^0\phi_1^2 + \frac{3}{2}\lambda_{TT}^0 T_1^2 + 3\lambda_{\phi T}^0\phi_1 T_1\right)v_1\right] \\
&\quad -\left(2\mu_T^0 + \lambda_T^0\right)\frac{v_1 f_{nl}^{(0)}}{\phi^0 f_l^{(0)}} + \left(p_{TT}^0 T_1 + p_{\phi T}^0\phi_1\right)\frac{f_{nl}^{(1)}}{\phi^0 f_l^{(0)}} \\
C_{32}^{(1)} &= \frac{1}{2\phi^0}\left(p_{\phi\phi}^0\phi_1\phi_2 + p_{TT}^0 T_1 T_2 + p_{\phi T}^0\phi_1 T_2 + p_{\phi T}^0 T_1\phi_2\right) + \left(p_{TT}^0 T_1 + p_{\phi T}^0\phi_1\right)\frac{f_{nl}^{(0)}}{\phi^0 f_l^{(0)}} \\
&\quad +\frac{1}{4\phi^0}\left(\frac{1}{2}p_{\phi\phi\phi}^0\phi_1^3 + \frac{1}{2}p_{TTT}^0 T_1^3 + \frac{3}{2}p_{\phi\phi T}^0\phi_1^2 T_1 + \frac{3}{2}p_{\phi TT}^0 T_1^2\phi_1\right) \\
C_{30}^{(1)} &= \frac{v_1}{4\phi^0}\left(2v_2\phi^0 - v_1\phi_1\right), \quad C_{30}^{(0)} = \frac{c^{(0)}}{2\phi^0}\left(-2v_2\phi_1 + v_1\phi_2\right) \\
C_{42}^{(4)} &= \frac{-2T_1\kappa_T^0 f_{nl}^{(2)}}{\phi^0 f_l^{(0)} dim}, \quad C_{42}^{(3)} = \frac{-2T_1\kappa_T^0 f_{nl}^{(1)}}{\phi^0 f_l^{(0)} dim} \\
C_{42}^{(2)} &= \frac{1}{\phi^0 dim}\left[\kappa_\phi^0(T_1\phi_2 - 2\phi_1 T_2) - \kappa_T^0 T_1\left(T_2 + \frac{2f_{nl}^{(0)}}{f_l^{(0)}}\right) - \frac{T_1}{2}\left(\frac{1}{2}\kappa_{\phi\phi}^0\phi_1^2 + \frac{1}{2}\kappa_{TT}^0 T_1^2 + \kappa_{\phi T}^0\phi_1 T_1\right)\right] \\
C_{40}^{(3)} &= \left(-p_T^0 v_1 + 2\mu_T^0 u_1\right)\frac{2f_{nl}^{(2)}}{\phi^0 f_l^{(0)} dim} \\
C_{40}^{(2)} &= \frac{1}{\phi^0 dim}\left[8\mu^0\left(v_1 v_2 + \frac{1}{2}u_1 u_2\right) + 4\lambda^0 v_2 v_1\right] + \frac{3}{2\phi^0 dim}\left[2\left(\mu_\phi^0\phi_1 + \mu_T^0 T_1\right)\left(v_1^2 + \frac{1}{2}u_1^2\right)\right. \\
&\quad \left. + \left(\lambda_\phi^0\phi_1 + \lambda_T^0 T_1\right)v_1^2\right] + \left(-p_T^0 v_1 + 2\mu_T^0 u_1\right)\frac{2f_{nl}^{(1)}}{\phi^0 f_l^{(0)} dim} - \frac{2c^{(0)} f_{nl}^{(2)}}{\phi^0 f_l^{(0)}} \\
&\quad + \left(\mu_{TT}^0 T_1 - \mathcal{D}_{TT}^0 T_1 + \mu_{\phi T}^0\phi_1 - \mathcal{D}_{\phi T}^0\right)\frac{2f_{nl}^{(2)}}{\phi^0 f_l^{(0)} dim}
\end{aligned}
$$

$$
\begin{aligned}
C_{40}^{(1)} &= \left(v_1T_2+\frac{1}{2}v_2T_1\right)+\frac{1}{\phi^0 dim}\left[-2(p_\phi^0\phi_1+p_T^0T_1)v_2-(p_\phi^0\phi_2+p_T^0T_2)v_1\right.\\
&\left.+4(\mu_\phi^0\phi_1+\mu_T^0T_1)u_2+2(\mu_\phi^0\phi_2+\mu_T^0T_2)u_1\right]+\frac{1}{4\phi^0}\phi_1v_1T_1\\
&+\frac{3}{2\phi^0 dim}\left[-\left(\frac{1}{2}p_{\phi\phi}^0\phi_1^2+\frac{1}{2}p_{TT}^0T_1^2+p_{\phi T}^0\phi_1T_1\right)v_1+2\left(\frac{1}{2}\mu_{\phi\phi}^0\phi_1^2+\frac{1}{2}\mu_{TT}^0T_1^2+\mu_{\phi T}^0\phi_1T_1\right)u_1\right]\\
&+\left(-p_T^0v_1+2\mu_T^0u_1\right)\frac{2f_{nl}^{(0)}}{\phi^0f_l^{(0)}dim}-\frac{2c^{(0)}f_{nl}^{(1)}}{\phi^0f_l^{(0)}}+\left(\mu_{TT}^0T_1+\mu_{\phi T}^0\phi_1-\mathcal{D}_{TT}^0T_1-\mathcal{D}_{\phi T}^0\phi_1\right)\frac{2f_{nl}^{(1)}}{\phi^0f_l^{(0)}dim}\\
C_{40}^{(0)} &= -\frac{c^{(0)}}{\phi^0}\left(\phi_1T_2+\frac{1}{2}\phi_2T_1\right)+\frac{2f_{nl}^{(0)}}{\phi^0f_l^{(0)}dim}(\mu_{TT}^0T_1+\mu_{\phi T}^0\phi_1-\mathcal{D}_{TT}^0T_1-\mathcal{D}_{\phi T}^0\phi_1)\\
&-\frac{2c^{(0)}f_{nl}^{(0)}}{\phi^0f_l^{(0)}}+\frac{1}{\phi^0dim}\left[\left(\mu_{\phi\phi}^0\phi_1\phi_2+\mu_{TT}^0T_1T_2+\mu_{\phi T}^0\phi_1T_2+\mu_{\phi T}^0\phi_2T_1\right)\right.\\
&\left.-\left(\mathcal{D}_{\phi\phi}^0\phi_1\phi_2+\mathcal{D}_{TT}^0T_1T_2+\mathcal{D}_{\phi T}^0\phi_1T_2+\mathcal{D}_{\phi T}^0\phi_2T_1\right)\right]\\
&+\frac{3}{2\phi^0dim}\left[\left(\frac{1}{6}\mu_{\phi\phi\phi}^0\phi_1^3++\frac{1}{6}\mu_{TTT}^0T_1^3+\frac{1}{2}\mu_{\phi\phi T}^0\phi_1^2T_1+\frac{1}{2}\mu_{\phi TT}^0\phi_1T_1^2\right)\right.\\
&\left.-\left(\frac{1}{6}\mathcal{D}_{\phi\phi\phi}^0\phi_1^3++\frac{1}{6}\mathcal{D}_{TTT}^0T_1^3+\frac{1}{2}\mathcal{D}_{\phi\phi T}^0\phi_1^2T_1+\frac{1}{2}\mathcal{D}_{\phi TT}^0\phi_1T_1^2\right)\right]
\end{aligned}
$$

Appendix 5D. Dispersion Relation

As describe in §5.5 the dispersion relation can be written as,

$$c^4+\alpha_3c^3+\alpha_2c^2+\alpha_1c+\alpha_0=0,$$

where $\alpha_3=\alpha_{30}+\alpha_{32}/H^2$, $\alpha_2=\alpha_{22}/H^2+\alpha_{24}/H^4$,
$\alpha_1=\alpha_{12}/H^2+\alpha_{14}/H^4+\alpha_{16}/H^6$, $\alpha_0=\alpha_{04}/H^4+\alpha_{06}/H^6$.

$$
\begin{aligned}
\alpha_{04} &= \frac{2\mu^0}{dim\,\phi^{0^2}}\left[-p_T^0(\mathcal{D}_\phi^0+u_y^{0^2}\mu_\phi^0)+p_\phi^0(\mathcal{D}_T^0+u_y^{0^2}\mu_T^0)\right]k_\beta^4,\quad \alpha_{06}=\frac{2\kappa^0\mu^0p_\phi^0}{dim\,\phi^{0^2}}k_\beta^6\\
\alpha_{12} &= \frac{4u_y^{0^2}\mu^0p_T^0}{dim\,\phi^{0^2}}k_\beta^2+\frac{2}{dim\,\phi^0}\left[p_\phi^0(\mathcal{D}_T^0-u_y^{0^2}\mu_T^0)-p_T^0(\mathcal{D}_\phi^0-u_y^{0^2}\mu_\phi^0)\right]k_\beta^2\\
\alpha_{14} &= \frac{2\mu^0}{dim\,\phi^{0^3}}\left[(2\mu^0+\lambda^0)(\mathcal{D}_T^0+u_y^{0^2}\mu_T^0)+p^0p_T^0\right]k_\beta^4+\frac{p_\phi^0}{\phi^0}\left(\mu^0+\frac{2\kappa^0}{dim}\right)k_\beta^4\\
\alpha_{16} &= \frac{2\kappa^0\mu^0}{dim\,\phi^{0^3}}(2\mu^0+\lambda^0)k_\beta^6,\\
\alpha_{22} &= \frac{k_\beta^2}{\phi^{0^2}}\left[\frac{4}{dim}\mu^0\mu_T^0u_y^{0^2}+\frac{2}{dim}p^0p_T^0+\phi^{0^2}p_\phi^0\right]+\frac{2}{dim\,\phi^{0^2}}(3\mu^0+\lambda^0)(\mathcal{D}_T^0-u_y^{0^2}\mu_T^0)k_\beta^2\\
\alpha_{24} &= \frac{1}{\phi^{0^2}}\left[\frac{2\kappa^0}{dim}(3\mu^0+\lambda^0)+\mu^0(2\mu^0+\lambda^0)\right]k_\beta^4\\
\alpha_{30} &= \frac{2}{dim\,\phi^0}(\mathcal{D}_T^0-u_y^{0^2}\mu_T^0),\quad \alpha_{32}=\frac{1}{\phi^0}\left[\frac{2\kappa^0}{dim}+3\mu^0+\lambda^0\right]k_\beta^2
\end{aligned}
$$

From the asymptotic analysis for large Couette gap (H) we get two real roots and a complex conjugate pair as given below,

$$c^{(1)} = c_0^{(1)}-\frac{1}{H^2}\frac{(\alpha_{12}+c_0^{(1)}\alpha_{22}+c_0^{(1)^2}\alpha_{32})}{c_0^{(1)}(4c_0^{(1)}+3\alpha_{30})}+O(H^{-4}),\quad c^{(2)}=-\frac{1}{H^2}\left(\frac{\alpha_{04}}{\alpha_{12}}\right)+O(H^{-4})$$

where $c_0^{(1)}$ is

$$c_0^{(1)}=-\frac{2}{3\phi^0}f_5^0T^{0^{1/2}}<0$$

A complex conjugate pair $c^{(3,4)}=c_r^{(3,4)}+ic_i^{(3,4)}$ is

$$
\begin{aligned}
c_r^{(3,4)} &= \frac{1}{H^2}\left[\frac{\left(\frac{\alpha_{12}}{\alpha_{30}}\right)^2-\frac{\alpha_{12}\alpha_{22}}{\alpha_{30}}+\alpha_{04}}{2\alpha_{12}}\right]+O(H^{-4})\\
\left(c_i^{(3,4)}\right)^2 &= \frac{1}{H^2}\left(\frac{\alpha_{12}}{\alpha_{30}}\right)+O(H^{-4})
\end{aligned}
$$

CHAPTER 6

NONLINEAR STABILITY AND PATTERNS IN TWO-DIMENSIONAL GRANULAR PLANE COUETTE FLOW: HOPF AND PITCHFORK BIFURCATION, EVIDENCE FOR RESONANCE

6.1 Introduction

In this chapter we develop the order parameter theory of two-dimensional patterns that emerge due to the travelling and stationary instabilities in granular Couette flow using Landau-Stuart order parameter equation. Following the Stuart-Watson theory (Stuart 1960; Watson 1960; Reynolds & Potter 1967) and our previous work (Shukla & Alam 2011) as given in chapter 5, we develop the order parameter theory for spatially inhomogeneous patterns in two-dimensional granular Couette flow. Note that in chapter 5 we considered only streamwise independent flow which is equivalent to the zero-wavenumber ($k_x = 0$) limit of the present problem. The two-dimensional ($k_x \neq 0$) nonlinear patterns that arise from a variety of linear instability modes in granular plane Couette flow is probed in this chapter.

This chapter is organized as follows. The Navier-Stokes' level hydrodynamics equations and constitutive relations are described in §6.2, along with the steady mean flow of plane Couette flow. The amplitude expansion method and the modal equations at different orders are briefly discussed in §6.3; we have identified two types of resonances that are discussed in §6.4, along with their numerical evidence in §6.7.3. Different measures of nonlinear stability in terms of the first Landau coefficient as well as the signatures of Hopf bifurcations are discussed in §6.5. A detailed numerical analysis of various stationary and travelling wave instabilities, their nonlinear saturation, possible occurrences of nonlinear resonances, effects of mean density, Couette gap and restitution coefficients are discussed in §6.7. The conclusions are given in §6.8. The organization map of this chapter is depicted in figure 6.1.

6.2 Governing Equations

We consider a plane Couette flow of granular materials between two parallel moving walls with speed $\bar{U}_w/2$ in opposite directions, see figure 4.1. For non-dimensionlization we are using the gap between two walls as the reference length, the difference between the wall velocities as the reference velocity and the inverse of the overall shear rate as the time scale and the material density of the particle as the density scale [cf. §4.1 and (4.1)-(4.4)]. The dimensionless balance

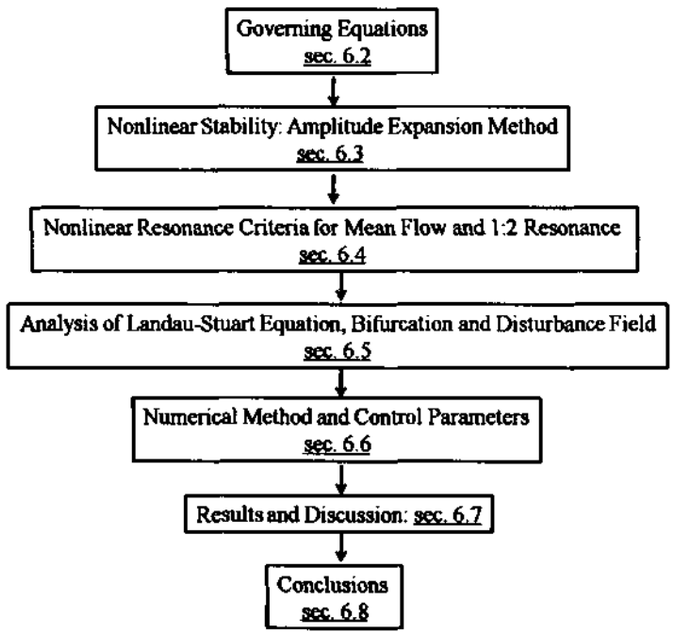

Figure 6.1: Road-map of chapter 6.

equations are

$$\frac{\partial \phi}{\partial t} + \frac{\partial}{\partial x}(\phi u) + \frac{\partial}{\partial y}(\phi v) = 0 \tag{6.1}$$

$$\phi\left[\frac{\partial}{\partial t} + u\frac{\partial}{\partial x} + v\frac{\partial}{\partial y}\right]u = -\frac{1}{H^2}\frac{\partial p}{\partial x} + \frac{1}{H^2}\frac{\partial}{\partial x}\left[2\mu\frac{\partial u}{\partial x} + \lambda\left(\frac{\partial u}{\partial x} + \frac{\partial v}{\partial y}\right)\right] + \frac{1}{H^2}\frac{\partial}{\partial y}\left[\mu\left(\frac{\partial u}{\partial y} + \frac{\partial v}{\partial x}\right)\right] \tag{6.2}$$

$$\phi\left[\frac{\partial}{\partial t} + u\frac{\partial}{\partial x} + v\frac{\partial}{\partial y}\right]v = -\frac{1}{H^2}\frac{\partial p}{\partial y} + \frac{1}{H^2}\frac{\partial}{\partial y}\left[2\mu\frac{\partial v}{\partial y} + \lambda\left(\frac{\partial u}{\partial x} + \frac{\partial v}{\partial y}\right)\right] + \frac{1}{H^2}\frac{\partial}{\partial x}\left[\mu\left(\frac{\partial u}{\partial y} + \frac{\partial v}{\partial x}\right)\right] \tag{6.3}$$

$$\frac{\dim}{2}\,\phi\left[\frac{\partial}{\partial t} + u\frac{\partial}{\partial x} + v\frac{\partial}{\partial y}\right]T = \frac{1}{H^2}\left[\frac{\partial}{\partial x}\left(\kappa\frac{\partial T}{\partial x}\right) + \frac{\partial}{\partial y}\left(\kappa\frac{\partial T}{\partial y}\right)\right] - p(\nabla.\vec{u}) + 2\mu\left[\left(\frac{\partial u}{\partial x}\right)^2 + \left(\frac{\partial v}{\partial y}\right)^2 + \frac{1}{2}\left(\frac{\partial u}{\partial y} + \frac{\partial v}{\partial x}\right)^2 + \frac{\lambda}{2\mu}(\nabla.\vec{u})^2\right] - \mathcal{D}, \tag{6.4}$$

with dimensionless constitutive relations as [cf. (4.9)]

$$\left.\begin{array}{llllll} p(\phi,T) = f_1 T, & \mu(\phi,T) = f_2\sqrt{T}, & \zeta(\phi,T) = f_3\sqrt{T}, \\ \lambda(\phi,T) = \left(\zeta - \frac{2}{\dim}\mu\right), & \kappa(\phi,T) = f_4\sqrt{T}, & \mathcal{D}(\phi,T) = f_5 T^{3/2} \end{array}\right\}. \tag{6.5}$$

where f_i's are the functions of the mean density and the radial distribution function as given in (2.21). The radial distribution function is defined in (2.12). In the above, $H = \bar{h}/\bar{d}$ is the dimensionless Couette gap (ratio between the wall separation and the particle diameter).

In chapters 4 and 5, we considered one-dimensional streamwise-independent equations which can be obtained by putting $\partial/\partial x(\cdot) = 0$ in (6.1-6.4) since our focus was on the shear-banding instability for which the associated patterns have no variations along the streamwise direction.

We are imposing no-slip and zero heat-flux conditions at walls

$$u = \pm 1/2, \quad v = 0, \quad \frac{\mathrm{d}T}{\mathrm{d}y} = 0, \quad \text{at} \quad y = \pm 1/2, \tag{6.6}$$

which is of course an idealization of the reality. Nevertheless probing instability with such ideal boundary conditions helps to make a bridge with instabilities in a plane Couette flow with slip-velocity and non-zero heat flux boundary conditions as established previously by Alam & Nott (1998) in the context of linear stability analysis.

The steady, fully developed equations with boundary conditions (6.6) admit the uniform shear solution:

$$u^0(y) = y, \quad v^0(y) = 0, \quad \phi^0 = \text{const.}, \quad T^0 = \frac{f_2(\phi^0)}{f_5(\phi^0, e)}, \tag{6.7}$$

for which the shear rate ($\mathrm{d}u^0/\mathrm{d}y = 1$) is uniform/constant, with density and granular temperature being constants. The linear stability of (6.7) against two-dimensional perturbations has been investigated in detail by Alam & Nott (1998). In this chapter we focus on nonlinear saturation of various linear instability modes using Landau-Stuart equation which is briefly discussed in the following section for spatially periodic patterns.

6.3 Nonlinear Stability: Amplitude Expansion Method

In chapter 5 we used the Stuart-Watson theory to develop an order parameter theory for the nonlinear shear-banding instability ($k_x = 0$) of granular plane Couette flow. The same order parameter theory is extended to two-dimensional disturbances ($k_x \neq 0$) in this chapter.

Here we provide a brief account of the nonlinear theory, mainly pointing out the essential differences with previous chapter 5 (Shukla & Alam 2011) as well as deriving the criteria for possible nonlinear resonances at quadratic order in amplitude. It may be noted that the present nonlinear equations boil down to those in chapter 5 (Shukla & Alam 2011) for the special case of streamwise-independent perturbations ($k_x = 0$).

We start with the nonlinear disturbance equations which can be represented in matrix form

$$\left(\mathrm{I}\frac{\partial}{\partial t} - \mathcal{L}\right) X = \mathcal{N}_2(X, X; \partial_t) + \mathcal{N}_3(X, X, X) \tag{6.8}$$

where

$$\mathcal{L} \equiv \mathcal{L}\left(\frac{\partial}{\partial x}, \frac{\partial^2}{\partial x^2}, \frac{\partial}{\partial y}, \frac{\partial^2}{\partial y^2}; \phi^0, \ldots\right) \tag{6.9}$$

is the linear stability operator, $X = (\phi', u', v', T')$ is the disturbance variables, $\mathcal{N}_2$ and $\mathcal{N}_3$ are the quadratic and cubic nonlinear terms, respectively. The explicit expressions of $\mathcal{L}$ and the nonlinear terms $\mathcal{N}_2$ and $\mathcal{N}_3$ are given in Appendix 6A and 6B, respectively.

The argument ∂_t in $\mathcal{N}_2(X, X; \partial_t)$ refers to the fact that there are quadratic nonlinearities that involve time-derivatives of the form $\phi'\partial(u', v', T')/\partial t$ (in momentum and granular energy equations) and this is a consequence of the fact that the granular fluid is compressible.

The details of the amplitude expansion method are given in chapter 3. The final matrix form of reduced modal equations for the nonlinear stability analysis is given as

$$\left.\begin{array}{rcl} \mathbf{L}_{kn} X^{[k;n]} &=& -\, c^{[n-1]} X^{[1;1]} \delta_{k1} + G_{kn} \\ c^{[n-1]} &=& a^{[n-1]} + ib^{[n-1]} \\ G_{kn} &=& -\left(ma^{[n-m]} + ikb^{[n-m]}\right) X^{\{k;m\}} + E_{kn}/(1+\delta_{0k}) + F_{kn} \\ \mathbf{L}_{kn} &=& \left(na^{(0)} + ikb^{(0)}\right)\mathbf{I} - \mathbf{L}_k \\ \mathbf{L}_k &=& \mathcal{L}(ikk_x, (ikk_x)^2, d/dy, d^2/dy^2; \phi^0, \ldots) \end{array}\right\} \tag{6.10}$$

where $X^{[k;n]} = (\phi^{[k;n]}, u^{[k;n]}, v^{[k;n]}, T^{[k;n]})^T$ is disturbance vector, $c^{[n-1]}$'s are Landau coefficients, $\mathbf{L}_k$ is a linear operator with $\mathbf{L}_{k=1}$ being the well-known linear stability operator (see (6.15)), and $\mathbf{I}$ is an identity operator. It can be verified that $X^{[k;n]} = 0$ when $k+n$ is odd and hence $c^{[n]}$ vanishes for odd n. Note that the nonlinear terms $E_{kn} \equiv E_{kn}(X, X)$ and $F_{kn} \equiv F_{kn}(X, X, X)$ have quadratic and cubic nonlinearities, respectively. It is worth pointing out that the inclusion of cubic nonlinearities in disturbance equations is a must for *correct* computation of first Landau coefficient $c^{(2)}$. The Landau equation is terms of real amplitude and frequency is given as [cf. (3.32)-(3.33)]

$$A^{-1}\frac{\mathrm{d}A}{\mathrm{d}t} = a^{(0)} + Aa^{(1)} + A^2a^{(2)} + \ldots = a^{(n)}A^n, \tag{6.11}$$

$$\omega + \frac{\mathrm{d}\omega}{\mathrm{d}A}\left(t\frac{\mathrm{d}A}{\mathrm{d}t}\right) = b^{(0)} + Ab^{(1)} + A^2b^{(2)} + \ldots = b^{(n)}A^n. \tag{6.12}$$

The above system (6.10) needs to be solved at each order of amplitude along with boundary conditions:

$$u^{[k;n]} = 0, \quad v^{[k;n]} = 0, \quad \frac{\mathrm{d}T^{[k;n]}}{\mathrm{d}y} = 0. \tag{6.13}$$

In the following sections we detail a sequence of governing equations up to cubic order in amplitude.

6.3.1 $O(A)$: Fundamental Mode

Substituting $k = n = 1$ into (6.10) we recover the linear eigenvalue problem at $O(A)$:

$$\mathbf{L}_{11}X^{[1;1]} \equiv \left[(a^{(0)} + ib^{(0)})\mathbf{I} - \mathbf{L}_1\right] X^{[1;1]} = 0, \tag{6.14}$$

where

$$\mathbf{L}_1 \equiv \mathcal{L}\left(ik_x, (ik_x)^2, \frac{\mathrm{d}}{\mathrm{d}y}, \frac{\mathrm{d}^2}{\mathrm{d}y^2}\right), \tag{6.15}$$

is the linear stability operator, $a^{(0)} + ib^{(0)}$ is its eigenvalue and $X^{[1;1]}$ is the corresponding eigenvector or the fundamental mode. The above eigenvalue problem (6.14) along with boundary conditions can be solved numerically. We are using a normalization such that

$$\max_y |T^{[1;1]}(y)| = T^0 \tag{6.16}$$

where T^0 is the base state temperature as defined in (6.7).

6.3.2 $O(A^2)$: Mean Flow Distortion and Second Harmonic

At $O(A^2)$, we have two sets of equations: one for the mean flow distortion ($k = 0$) and the other for the second harmonic ($k = 2$). Substituting $k = 0$ and $n = 2$ into equation (6.10), we get equations for the distortion to the mean flow

$$\mathbf{L}_{02}X^{[0;2]} \equiv \left[2a^{(0)}\mathbf{I} - \mathbf{L}_0\right] X^{[0;2]} \quad = \quad E_{02}, \tag{6.17}$$

where the linear operator $\mathbf{L}_0$ is given by

$$\mathbf{L}_0 \equiv \mathbf{L}_k(k_x = 0) = \mathcal{L}\left(k_x = 0, \frac{\mathrm{d}}{\mathrm{d}y}, \frac{\mathrm{d}^2}{\mathrm{d}y^2}\right). \tag{6.18}$$

*It is worth pointing out that $\mathbf{L}_0$ is nothing but the linear stability operator for streamwise-*independent or shear-banding ($k_x = 0$) modes. The explicit functional form of nonlinear terms E_{02} in (6.17) is

$$E_{02} = N_2(\tilde{X}^{[1;1]}, X^{[1;1]}) + N_2(X^{[1;1]}, \tilde{X}^{[1;1]}) \tag{6.19}$$

which is a real function.

Substituting $k = n = 2$ into equation (6.10), we obtain equations for the second harmonic $X^{[2;2]}$:

$$\mathbf{L}_{22}X^{[2;2]} \equiv \left[2(a^{(0)} + ib^{(0)})\mathbf{I} - \mathbf{L}_2\right] X^{[2;2]} = E_{22} \tag{6.20}$$

where the linear operator $\mathbf{L}_2$ is given by

$$\mathbf{L}_2 \equiv \mathcal{L}\left(i2k_x, (i2k_x)^2, \frac{\mathrm{d}}{\mathrm{d}y}, \frac{\mathrm{d}^2}{\mathrm{d}y^2}\right), \tag{6.21}$$

and the nonlinear term $E_{22} \equiv N_2(X^{[1;1]}, X^{[1;1]})$ is the product of two fundamentals.

While the second harmonic $X^{[2;2]}$ is, in general, a complex quantity, the mean-flow distortion $X^{[0;2]}$ is always a real harmonic. For the special case of shear-banding modes ($k_x = 0$), it has been shown Shukla & Alam (2011) that the second harmonic $X^{[2;2]}$ is real and $X^{[2;2]} = \tilde{X}^{[2;2]} = X^{[0;2]}$.

6.3.3 $O(A^3)$: Distortion to Fundamental, First Landau Coefficient and Third Harmonic

At $O(A^3)$, we get equations for the distortion to the fundamental mode $X^{[1;3]}$ and the third harmonic $X^{[3;3]}$. Substituting $k = 1$ and $n = 3$ into (6.10) yields:

$$\mathbf{L}_{13}X^{[1;3]} \equiv \left[(3a^{(0)} + ib^{(0)})\mathbf{I} - \mathbf{L}_1\right] X^{[1;3]} = -c^{[2]}X^{[1;1]} + G_{13}. \tag{6.22}$$

The dependence of G_{13} on modal amplitudes $X^{[i;j]}$ is given below

$$\begin{aligned} G_{13} \quad = \quad & N_2(X^{[0,2]}, X^{[1;1]}) + N_2(X^{[1;1]}, X^{[0,2]}) + N_2(\tilde{X}^{[1,1]}, X^{[2;2]}) \\ & + N_2(X^{[2;2]}, \tilde{X}^{[1,1]}) + N_3(\tilde{X}^{[1,1]}, X^{[1;1]}, X^{[1;1]}) \\ & + N_3(X^{[1;1]}, \tilde{X}^{[1,1]}, X^{[1;1]}) + N_3(X^{[1;1]}, X^{[1;1]}, \tilde{X}^{[1,1]}). \end{aligned} \tag{6.23}$$

Note that when $a^{(0)} = 0$, $\mathbf{L}_{13}$ is identical to $\mathbf{L}_{11}$ for which the associated homogeneous problem and its adjoint (see below) have eigensolutions and hence the problem (6.22) is solvable if and only if the inhomogeneous part is orthogonal to the adjoint eigenfunction. This is called the

solvability condition which simplifies to yield the expression for the first Landau coefficient:

$$c^{[2]} = a^{[2]} + ib^{[2]} = \frac{\langle X^\dagger, G_{13} \rangle}{\langle X^\dagger, X^{[1;1]} \rangle}, \tag{6.24}$$

with the inner product $\langle \cdot, \cdot \rangle$ being defined by

$$\langle f(y), g(y) \rangle = \int_{-1/2}^{1/2} \tilde{f}(y) g(y) \mathrm{d}y. \tag{6.25}$$

Here $f(y)$ and $g(y)$ are two complex-valued functions, and a 'tilde' denotes a complex conjugate quantity. The adjoint eigenfunction $X^\dagger$ in (6.24) is obtained by solving the adjoint eigenvalue problem

$$\frac{\partial X^\dagger}{\partial t} = \mathcal{L}^\dagger X^\dagger, \tag{6.26}$$

with the adjoint operator $\mathcal{L}^\dagger$ being obtained from the following definition:

$$\langle X^\dagger, \mathcal{L} X \rangle = \langle \mathcal{L}^\dagger X^\dagger, X \rangle. \tag{6.27}$$

The explicit form of $\mathcal{L}^\dagger$ is given in Appendix 6A.

Once $c^{[2]}$ is determined from (6.24), the right-hand side of (6.22) is completely known since G_{13} is a function of $X^{[1;1]}$, $X^{[0;2]}$ and $X^{[2;2]}$ only as defined in (6.23), and hence we can solve (6.22) to yield the distortion to the fundamental mode $X^{[1;3]}$.

The equation for the third harmonic is obtained from (6.10) by substituting $k = 3$ and $n = 3$:

$$\mathbf{L}_{33} X^{[3;3]} \equiv \left[3(a^{(0)} + ib^{(0)})\mathbf{I} - \mathbf{L}_3 \right] X^{[1;3]} = G_{33} \tag{6.28}$$

where

$$\mathbf{L}_3 \equiv \mathcal{L}\left(i3k_x, (i3k_x)^2, \frac{\mathrm{d}}{\mathrm{d}y}, \frac{\mathrm{d}^2}{\mathrm{d}y^2} \right) \tag{6.29}$$

and the nonlinear terms are

$$G_{33} = N_2(X^{[1;1]}, X^{[2;2]}) + N_2(X^{[2;2]}, X^{[1;1]}) + N_3(X^{[1;1]}, X^{[1;1]}, X^{[1;1]}). \tag{6.30}$$

6.4 Nonlinear Resonance: Criteria for Mean-flow and 1:2 Resonances

The modal equations at quadratic order (6.17) and (6.20) admit two types of resonances: (i) mean-flow resonance and (ii) $1:2$ resonance, which are analysed below. Since both appear at $O(A^2)$ we call them 'nonlinear' resonances, and this nomenclature distinguishes them from linear resonance that occurs when two eigenvalues of the linear stability operator (6.14) are identical.

The system of equations for mean-flow distortion (6.17) is solvable, i.e.,

$$X^{[0;2]} = \left[2a^{(0)}\mathbf{I} - \mathbf{L}_0 \right]^{-1} E_{02} = \text{finite}, \tag{6.31}$$

if the operator $(2a^{(0)}\mathbf{I} - \mathbf{L}_0)$ is non-singular; this is possible if and only if $2a^{(0)}$ is not equal to any of the eigenvalues of $\mathbf{L}_0$ (which is the linear stability operator for shear-banding modes $k_x = 0$). The violation of this condition is responsible for the resonance between a linear mode of the operator $\mathbf{L}_0$ (which is a shear-banding mode) and the mean-flow distortion $X^{[0;2]}$ at k_x, dubbed

mean flow resonance. Therefore, the criterion for the mean flow resonance can be written as

$$2a_{j_1}^{(0)}(k_x) = a_{j_2}^{(0)}(k_x = 0) \qquad \text{and} \qquad b_{j_2}^{(0)}(k_x = 0) = 0, \tag{6.32}$$

for two modes j_1 and j_2. Here $a_{j_1}^{(0)} = \mathrm{Re}\{c_{j_1}^{(0)}\}$ is an eigenvalue of the linear stability operator $\mathbf{L}_1$ and $a_{j_2}^{(0)} \equiv c_{j_2}^{(0)}$ is an eigenvalue of the shear-banding operator $\mathbf{L}_0$. Therefore, the interaction of a linear mode with a shear-banding mode, obeying (6.32), is responsible for the genesis of 'mean-flow' resonance. We will show evidence of such resonance in §6.7.3.

The system of inhomogeneous equations for second harmonic (6.20) has a solution, i.e.

$$X^{[2;2]} = \left[2c^{(0)}\mathbf{I} - \mathbf{L}_2\right]^{-1} E_{22} = \text{finite} \tag{6.33}$$

if and only if $2c^{(0)}$ is not equal to any of the eigenvalues of $\mathbf{L}_2$. Recall from (6.21) that the second harmonic operator $\mathbf{L}_2$ is nothing but the linear stability operator with wavenumber $2k_x$. Therefore, the solution for the second harmonic (6.33) becomes indeterminate when $2c^{(0)}$ (with $c^{(0)}$ being an eigenvalue of $\mathbf{L}_1$) is an eigenvalue of $\mathbf{L}_2$, leading to a resonance between two modes with their wavenumber ratio being $1:2$. This is referred to as '$1:2$ resonance', the criterion for which can be written as

$$\begin{aligned} & 2c_{j_1}^{(0)}(k_x) = c_{j_2}^{(0)}(2k_x) \\ \Rightarrow\ & 2a_{j_1}^{(0)}(k_x) = a_{j_2}^{(0)}(2k_x) \qquad \text{and} \qquad 2b_{j_1}^{(0)}(k_x) = b_{j_2}^{(0)}(2k_x). \end{aligned} \tag{6.34}$$

for any positive integers j_1 and j_2 that correspond to two different modes. Note that while $c_{j_1}^{(0)}(k_x)$ is an eigenvalue of $\mathbf{L}_1$ (see 6.15), $c_{j_2}^{(0)}(2k_x)$ is an eigenvalue of $\mathbf{L}_2$ (see 6.21). Therefore, the interaction of a fundamental mode with a second harmonic, obeying (6.34), is responsible for the genesis of $1:2$ resonance. We will discuss the possible occurrence of such resonance in §6.7.3.

In either type of resonances since $X^{[0;2]}$ or $X^{[2;2]}$ diverges, the first Landau coefficient (6.24), which is given in terms of an inner product of a nonlinear function G_{13}, would also diverge since G_{13} in (6.23) is a linear function of $X^{[0;2]}$ and $X^{[2;2]}$. Therefore, the signature of above resonances would appear as a discontinuity in the first Landau coefficient as we shall demonstrate in §6.7.3. It is worth pointing out that the mean-flow and $1:n$ resonances have been uncovered and are known to play an important role on dynamical transition and pattern formation, via mode-interactions, for both Newtonian and non-Newtonian fluids in a variety of flows (Mizushima & Gotoh 1985; Proctor & Jones 1988; Manneville 1990; Suslov & Paolucci 1997; Fujimura & Kelly 1997).

6.5 Analysis of Landau-Stuart Equation, Bifurcation and Disturbance Field

From the viewpoint of nonlinear stability, the pertinent question is: do the unstable/stable 'linear' modes become stable/unstable if we disturb the flow with finite amplitude disturbances? Do we have supercritical or subcritical bifurcation in each case? The nonlinear terms may saturate the exponential growth of the disturbance for the bands of wavenumbers where the flow is linearly unstable due to travelling and stationary instabilities. What is the nature of nonlinear solutions? The above issues are systematically probed in §6.7 using the weakly nonlinear theory developed in §6.3. In the following we briefly discuss about different measures of nonlinear stability in terms of the equilibrium amplitude, the types of bifurcations (pitchfork or Hopf), and the nonlinear disturbance field.

6.5.1 Equilibrium Amplitude and Phase Velocity

Similar to chapter 4 and 5 (Shukla & Alam 2009, 2011), we will restrict our attention to the leading nonlinear correction in the order-parameter theory, namely, the computation of the first Landau coefficient $c^{(2)} = a^{(2)} + \mathrm{i}b^{(2)}$ from (6.24). Knowing the growth rate $a^{(0)}$ and the real part of the first Landau coefficient $a^{(2)}$, the equilibrium amplitude ($\mathrm{dA/dt} = 0$) is calculated from (6.11) as

$$A_e = \pm\sqrt{-\frac{a^{(0)}}{a^{(2)}}}. \tag{6.35}$$

Clearly, the equilibrium solution exists if and only if $a^{(0)}$ and $a^{(2)}$ are of opposite signs. For linearly unstable flows $a^{(0)} > 0$ and therefore $a^{(2)}$ must be negative for the existence of any equilibrium solution- the new stable solution bifurcates from the critical point, leading to supercritical bifurcations. On the other hand, the existence of any equilibrium solution for linearly stable $[a^{(0)} < 0]$ flows requires a positive value of $a^{(2)}$, leading to subcritical bifurcations.

As explained in §6.3, the nonlinearities also affect the propagation speed of the disturbance, see (6.12). More specifically, the imaginary part of the first Landau coefficient, $b^{(2)}$, changes the equilibrium phase velocity c^e_{ph} whose expression follows from (6.12):

$$c^e_{ph} = -\frac{\omega}{k_x} = c_{ph} - \frac{b^{(2)}A_e^2}{k_x}, \tag{6.36}$$

where A_e is given by (6.35), and c_{ph} represents the linear phase velocity

$$c_{ph} = -\frac{b^{(0)}}{k_x}, \tag{6.37}$$

with $b^{(0)}$ being the imaginary part of the complex frequency $c^{(0)} = a^{(0)} + \mathrm{i}b^{(0)}$. Note that $b^{(2)} = 0$ for a stationary instability for which $c^e_{ph} = c_{ph} = 0$.

6.5.2 Bifurcations, Limit Cycle and Spirals

Up-to the cubic order in amplitude, the Landau-Stuart equations (6.11-6.12) boil down to

$$\frac{\mathrm{d}A}{\mathrm{d}t} = a^{(0)}A + a^{(2)}A^3, \tag{6.38}$$

$$\frac{\mathrm{d}\theta}{\mathrm{d}t} = b^{(0)} + b^{(2)}A^2, \tag{6.39}$$

where θ is the phase of the perturbation and A is its amplitude. For stationary disturbances, $b^{(n)} = 0$ for $n \geq 0$ and the phase equation (6.39) is identically satisfied, $\theta \equiv 0$. Hence the normal form for pitchfork bifurcations is (6.38) for which the fixed points are simple as given by 0 and A_e in (6.35). In contrast to pitchfork bifurcations for which the linear eigenvalue is real, a complex eigenvalue $c^{(0)} = a^{(0)} + ib^{(0)}$, representing an oscillatory mode, leads to oscillatory or Hopf bifurcation (Wiggins 1990) for which the normal form equations are (6.38)-(6.39) that we discuss below.

Case I: $a^{(2)} < 0$

For negative values of the first Landau coefficient ($a^{(2)} < 0$), we have three situations when (i) $a^{(0)} < 0$: the origin $A = 0$ is a stable spiral; (ii) $a^{(0)} = 0$: the origin is a stable spiral with algebraically fast decay; and (iii) $a^{(0)} > 0$ yields an unstable spiral at the origin and a stable limit cycle solution at $A = \sqrt{-a^{(0)}/a^{(2)}}$ via a supercritical Hopf bifurcation. All the above situations are schematically shown in figure 6.2(a-c). Figure 6.2(a) shows a state of a stable spiral at the

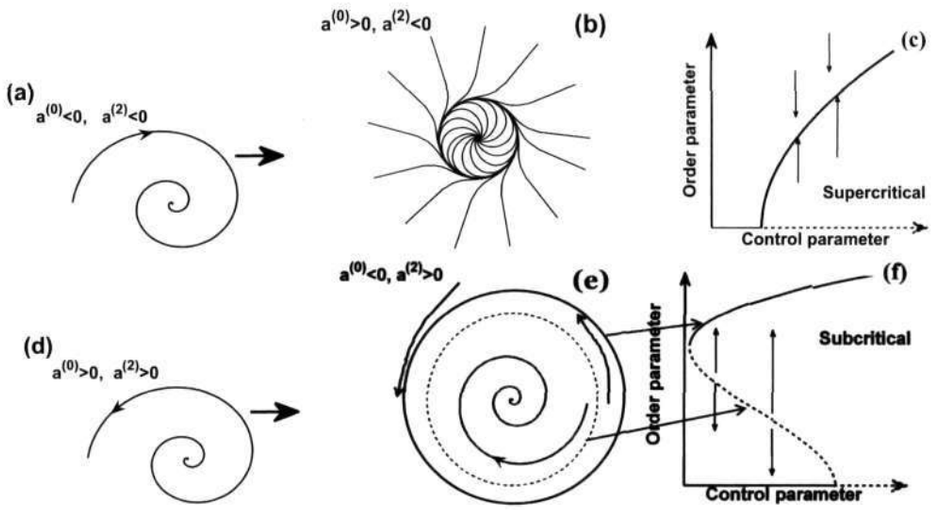

Figure 6.2: Hopf bifurcation and solution trajectories: (*a*) $a^{(0)} < 0$ and $a^{(2)} < 0$, stable spiral; (*b*) $a^{(0)} > 0$ and $a^{(2)} < 0$, stable limit cycle; (*c*) supercritical bifurcation; (*d*) $a^{(0)} > 0$ and $a^{(2)} > 0$, unstable spiral; (*e*) $a^{(0)} < 0$ and $a^{(2)} > 0$, unstable limit cycle; (*f*) subcritical bifurcation.

origin for $a^{(0)} < 0$, which losses stability as the control parameter increases from its critical value (when $a^{(0)} = 0$) and gives a stable limit cycle solution which is shown in figure 6.2(*b*). The supercritical bifurcation is shown in figure 6.2(*c*) where the stable (indicated by arrows) and unstable solutions are shown by solid and dashed lines, respectively.

Case II: $a^{(2)} > 0$

Similarly for $a^{(2)} > 0$ we have two situations, $a^{(0)} > 0$ or $a^{(0)} < 0$. In the former case we have an unstable spiral at the origin (see figure 1*d*). If $a^{(0)} < 0$, three solutions exist: a stable spiral at the origin, an unstable limit cycle at a distance $A = \sqrt{-a^{(0)}/a^{(2)}}$ and a stable limit cycle corresponding to the higher amplitude branch. This higher-amplitude branch can be obtained by adding a stabilizing 'quintic' nonlinear term to the Landau-Stuart equation:

$$\frac{\mathrm{d}A}{\mathrm{d}t} = a^{(0)}A + a^{(2)}A^3 + a^{(4)}A^5. \tag{6.40}$$

This equation has five equilibrium solutions, a zero solution (base state or mean flow) and four non-trivial solutions, as defined by

$$|A_e| = \pm\sqrt{\frac{-a^{(2)} \pm \sqrt{(a^{(2)})^2 - 4a^{(0)}a^{(4)}}}{2a^{(4)}}}. \tag{6.41}$$

Among these four solutions two are stable equilibrium solutions and the remaining two are unstable. Figure 6.2(*f*) shows the bifurcation diagram for subcritical instabilities where the dotted line represents an unstable solution which corresponds to an 'unstable' limit cycle (dashed circle in figure 1*e*). The solid line in figure 6.2(*f*) corresponds to the higher-order solution that represents a 'stable' limit cycle with a larger amplitude as shown by the outer circle in figure 6.2(*e*) – this solution corresponds to $a^{(0)} < 0$, $a^{(2)} > 0$ and $a^{(4)} < 0$ in (6.40). A disturbance with an amplitude

greater than the amplitude of the stable limit cycle (outer circle in figure 6.2e) or an amplitude in between the outer limit cycle and the inner limit cycle will converge to the 'stable' outer limit cycle as shown by curved arrows in figure 6.2(e). If the amplitude of the disturbance is less than the amplitude of the inner (unstable) limit cycle in figure 6.2(e), the amplitude converges to the origin that gives a stable spiral at the origin.

6.5.3 Nonlinear Disturbance Field

The nonlinear disturbance flow field $X(x,y,t) = (\phi', u', v', T')(x,y,t)$, correct up-to the cubic order in perturbation amplitude $O(A^3)$, can be written as

$$\begin{aligned} X(x,y,t) &= A^2 X^{[0;2]} + \left[\left(AX^{[1;1]}e^{i\theta} + A^3 X^{[1;3]}e^{i\theta} + A^2 X^{[2;2]}e^{2i\theta} + A^3 X^{[3;3]}e^{3i\theta}\right) + c.c\right] \\ &= A^2 X^{[0;2]} + 2A\left[X_r^{[1;1]}\cos(\theta) - \mathrm{X}_\mathrm{i}^{[1;1]}\sin(\theta)\right] \\ &\quad +2A^3\left[X_r^{[1;3]}\cos(\theta) - \mathrm{X}_\mathrm{i}^{[1;3]}\sin(\theta)\right] + 2A^2\left[X_r^{[2;2]}\cos(2\theta) - \mathrm{X}_\mathrm{i}^{[2;2]}\sin(2\theta)\right] \\ &\quad +2A^3\left[X_r^{[3;3]}\cos(3\theta) - \mathrm{X}_\mathrm{i}^{[3;3]}\sin(3\theta)\right]. \end{aligned} \tag{6.42}$$

Here the subscripts r and i refer to the real and imaginary parts of the complex vector $X^{[i;j]}$, and $\theta = (k_x x + \omega t)$ [cf. (3.11)]. Note that $X^{[0;2]}$ is the distortion of the mean flow (that appears at $O(A^2)$) which is always real. At equilibrium (dA/dt = 0), (6.11) leads to $\omega = (b^{(0)} + b^{(2)}A^2)$, and hence the expression for θ is

$$\theta = k_x x + \left(b^{(0)} + b^{(2)}A^2\right)t = k_x\left(x - c_{ph}^e t\right), \tag{6.43}$$

with c_{ph}^e being given by (6.36).

Knowing the equilibrium amplitude (6.35) and the phase velocity (6.36), now we can calculate the nonlinear disturbance flow field from (6.42) and (6.43) by using the numerical solutions for $X^{[1;1]}$, $X^{[0;2]}$, $X^{[2;2]}$, $X^{[1;3]}$ and $X^{[3;3]}$ that are obtained from (6.14), (6.17), (6.20), (6.22) and (6.28), respectively. In §6, we will a make comparison between the linear ($O(A)$) and nonlinear ($O(A^3)$) disturbance fields in the (x,y)-plane.

6.6 Numerical Method and Control Parameters

The details of the spectral-based numerical method are given in chapter 3. For the present case with $k_x \neq 0$, it has been verified that about 30 collocation points are enough to obtain converged eigenvalues (with an error less than 1 %). For an accurate computation of the first Landau coefficient, we needed $M \sim 50$ if the Couette gap is $H \leq 100$; for larger Couette gaps $H > 100$, we have used $M = 100$ or more collocation points.

There are four control parameters to describe the granular plane Couette flow: (i) the mean density or the volume fraction of particles ϕ^0, (ii) the Couette gap $H = \overline{h}/\overline{d}$ (i.e. the gap between two walls in terms of particle diameter) and (iii) the restitution coefficient e. For stability, we have an additional parameter: (iv) the dimensionless streamwise wavenumber

$$k_x = \frac{2\pi}{\lambda_x}, \quad \text{with} \quad \lambda_x = \frac{\overline{\lambda}_x}{\overline{h}} \tag{6.44}$$

being the dimensionless wavelength of perturbation. Note that λ_x sets the streamwise length ($L_x = \overline{l}_x/\overline{h}$, where $\overline{l}_x$ is the dimensional length of the Couette cell and $\overline{h}$ is its height) of the

Couette cell in the sense that for any perturbation with wavelength λ_x to grow, the system must be large enough (i.e. $L_x > \lambda_x$) to accommodate it.

6.7 Results and Discussion: Hopf and Pitchfork Bifurcations, and Resonances

It is known (Alam & Nott 1998) that the plane Couette flow is unstable to shear-banding ($k_x = 0$), stationary and travelling instabilities with $k_x \neq 0$ for a range of particle volume fractions (ϕ^0) and Couette gaps (H) at any restitution coefficient $e < 1$. Let us focus on the specific case of $H = 100$, $\phi^0 = 0.2$ and $e = 0.8$ for which all the above instabilities coexist. For these parameters the variations of the growth rate of the least-stable mode, $a_l^{(0)}$, and its phase velocity c_{ph} (see, equation 6.37) are shown in figure 6.3 by the solid and dot-dashed lines, respectively.

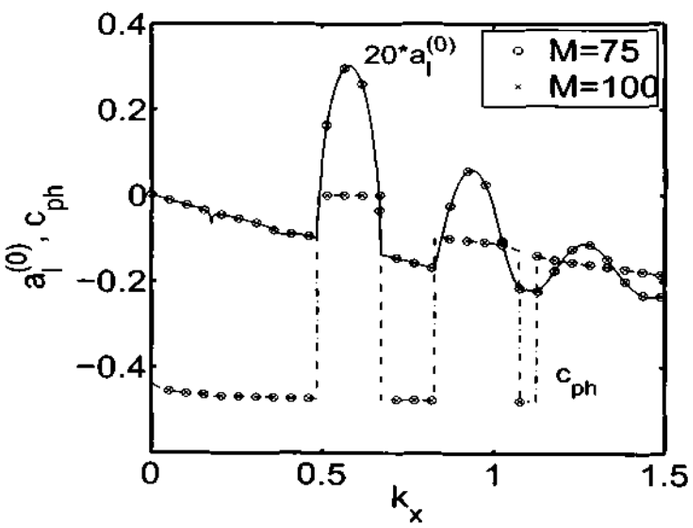

Figure 6.3: Variations of the growth rate (solid line) and the phase velocity (dot-dash line) of the least-stable mode for $\phi^0 = 0.2$, $H = 100$ and $e = 0.8$, with $M = 50$ collocation points. The circles and crosses refer to results with $M = 75$ and 100, respectively.

We define the least-stable mode (or, the leading eigenvalue) as the eigenvalue having the maximum real part for a given wavenumber k_x:

$$a_l^{(0)} = \max a^{(0)}, \tag{6.45}$$

out of all $(4M + 3)$ eigenvalues of discritized linear operator, where $(M + 1)$ is the number of Gauss-Lobatto collocation points (momentum and energy equations) and M is the number of Gauss collocation points (continuity equation). While the solid and dot-dashed lines in figure 6.3 correspond to results with $M = 50$, the circles and crosses refer to results with $M = 75$ and 100 collocation points, respectively. This validates the convergence of our numerical results with $M = 50$ collocation points; for most computations about $M = 75$ collocation points have been used.

In figure 6.3, the phase velocity corresponding to the first peak of the growth rate curve is zero, which represents a *stationary* instability. Similarly, the phase velocity for the second peak

is *non-zero* and thus the flow is unstable due to *travelling* waves there. For parameter values of figure 6.3, the flow is also unstable to the shear-banding mode ($k_x = 0$); moreover, there are other stationary and travelling wave instabilities at very long wavelengths ($k_x = 2\pi/\lambda_x \sim 0$) that we discuss next in §6.7.1.

6.7.1 Nonlinear Shear-banding ($k_x = 0$) and Long-Wave ($k_x \sim 0$) Instabilities

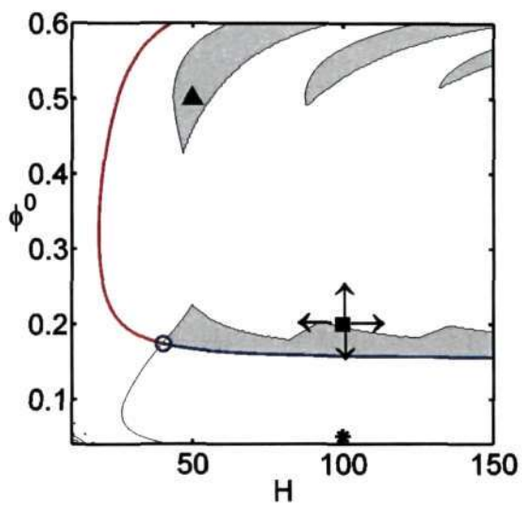

Figure 6.4: Phase diagram for the nonlinear instability of shear-banding modes ($k_x = 0$); the restitution coefficient is $e = 0.8$. The thick red-blue contour represents 'critical line' at which the linear growth rate is zero, i.e. $a^{(0)} = 0$, and the thin black contours represent zeros of the first Landau coefficient $a^{(2)} = 0$; the grey-shaded region corresponds to $a^{(0)} > 0$ and $a^{(2)} > 0$. The square, star and triangle symbols refer to points at which most of the nonlinear results with $k_x \neq 0$ will be presented. The blue-circle is the degenerate point.

Before presenting results for $k_x \neq 0$, let us briefly recall nonlinear results for shear-banding modes ($k_x = 0$) since they eventually give birth to long-wave instabilities. Figure 6.4 presents a phase diagram in the (ϕ^0, H)-plane for a restitution coefficient of $e = 0.8$, delineating the regimes of supercritical and subcritical flows.

The thick contour in figure 6.4 corresponds to the zero growth rate $[a^{(0)} = 0]$, representing the *critical line*, and the thin contours represent the zeros of the first Landau coefficient $[a^{(2)} = 0]$. In figure 6.4, $a^{(2)}$ has been calculated that corresponds to the shear-banding mode ($k_x = 0$) having the maximum growth rate over all possible gradient wavenumbers ($k_\beta = \beta\pi$, with $\beta = 1, 2, 3, \ldots$, being mode-number; the value of the mode number β corresponds to the number of zero crossings, along y, of the density eigenfunction, see chapter 5 and Shukla & Alam (2011)). The grey-shaded regions in figure 6.4 correspond to $a^{(0)} > 0$ and $a^{(2)} > 0$, in which there are 'growing' nonlinear solutions at cubic-order, and this calls for higher-order Landau coefficients (not calculated here) to locate the related stable, if any, solutions. The point at which the growth rate and the first Landau coefficient are simultaneously zero $[a^{(0)} = 0 = a^{(2)}]$ is known as the *degenerate* point, shown by the blue circle in figure 6.4 at $\phi_s \approx 0.1735$. The red upper branch of the critical line above the degenerate-point in figure 6.4 is *supercritically* stable, and the blue lower branch is

subcritically unstable. The nonlinear equilibrium solutions of shear-banding-type appear via a super-critical bifurcation for $\phi^0 > \phi_s$ and via a subcritical bifurcation for $\phi^0 < \phi_s$ below it (see, chapter 5 and Shukla & Alam 2011).

In addition to the shear-banding instability, there are long-wave ($k_x \sim 0$) stationary and travelling instabilities whose origin can be tied to the shear-banding modes (Alam & Nott 1998) - these long-wave modes might be unstable/stable and might be responsible for supercritical and subcritical nonlinear solutions as we discuss next.

Long-wave Modes ($k_x \sim 0$)

The variations of the growth rate of the least-stable mode $a_l^{(0)}$ and its phase velocity (inset plot) with wavenumber k_x are shown in figure 6.5(a). The parameter values are $\phi^0 = 0.2$, $H = 100$ and $e = 0.8$, which correspond to the 'square' symbol in figure 6.4. The shear-banding mode corresponds to $k_x = 0$ which is unstable [$a^{(0)} > 0$ and $a^{(2)} < 0$]. It is seen that the flow remains unstable to *stationary* disturbances with long wavelengths (i.e. $k_x = 2\pi/\lambda_x \sim 0$) up to a wavenumber of $k_x \sim 2.1 \times 10^{-5}$, and thereafter to *travelling* waves (see the inset for phase velocity). In fact, two stationary modes merge together at $k_x \sim 2.1 \times 10^{-5}$ to yield a pair of forward- and backward-propagating travelling waves which remain unstable for a range of k_x. It can be verified (Alam & Nott 1998) that the linear eigenvalue problem (6.14) is invariant under the transformation

$$(x, y, t) \rightarrow (-x, -y, t), \quad [\phi', u', v', T'] \rightarrow [\phi', -u', -v', T'] \tag{6.46}$$

$$\Rightarrow \quad [\hat{\phi}, \hat{u}, \hat{v}, \hat{T}](y) \exp\left(c^{(0)}t + ik_x x\right) \rightarrow [\hat{\phi}, -\hat{u}, -\hat{v}, \hat{T}](-y) \exp\left(c^{(0)}t - ik_x x\right) \tag{6.47}$$

This implies that a forward-propagating wave ($c_{ph} \equiv -b^{(0)}/k_x > 0$, see eqn. 6.37) always coexists with a backward-propagating wave ($c_{ph} < 0$) in the plane Couette flow.

In figure 6.5(b), we show the variations of the real, $a^{(2)}$, and the imaginary, $b^{(2)}$, parts of the first Landau coefficient for small k_x. The sharp jump in each curve of figure 6.5(b) at $k_x \sim 2.1 \times 10^{-5}$ indicates a mode-switching between stationary and travelling waves. The variations of the equilibrium amplitude A_e and the equilibrium phase velocity c_{ph}^e are shown in figures 6.5(c) and 6.5(d), respectively. Note that the bifurcation-type changes from *pitchfork* (static/stationary) to *Hopf* (dynamic/oscillatory) at $k_x \sim 2.1 \times 10^{-5}$ due to the above-mentioned switch-over from stationary to travelling waves. For the range of k_x in figure 6.5, $a^{(0)} > 0$ and $a^{(2)} < 0$ for both stationary and travelling waves, and hence the bifurcations are supercritical in nature for both cases.

Fixing the Couette gap at $H = 100$, we now move to the dilute regime of $\phi^0 = 0.05$ (the 'star' symbol in figure 6.4), where the plane Couette flow is subcritically unstable to shear-banding instability. Figure 6.6(a) shows the variation of the growth rate of the least-stable mode for small k_x, with the corresponding variation of the phase velocity being displayed as an inset. The growth rates remain negative for both stationary and travelling waves, and hence the flow is linearly stable at long waves $k_x \sim 0$ (and we have verified that the flow is stable at any k_x for this parameter set). However, the variations of the first Landau coefficient in figure 6.6(b) clearly show that $a^{(2)} > 0$ for a range of $k_x \sim 0$ that represents only stationary waves. Therefore, the finite-amplitude nonlinear solutions exist for stationary instabilities at long waves, as shown in the inset of figure 6.6(b). Note that the corresponding nonlinear solutions are unstable since the underlying bifurcation is *subcritical* [$a^{(0)} < 0$ and $a^{(2)} > 0$]; therefore A_e in figure 6.6(b) provides a *threshold* for nonlinear stability in the sense that for any finite-amplitude perturbation with $A < A_e$ the uniform shear flow will be recovered, however, with $A > A_e$ the flow will reach a new stable equilibrium solution. To locate this stable finite-amplitude solution we need to calculate

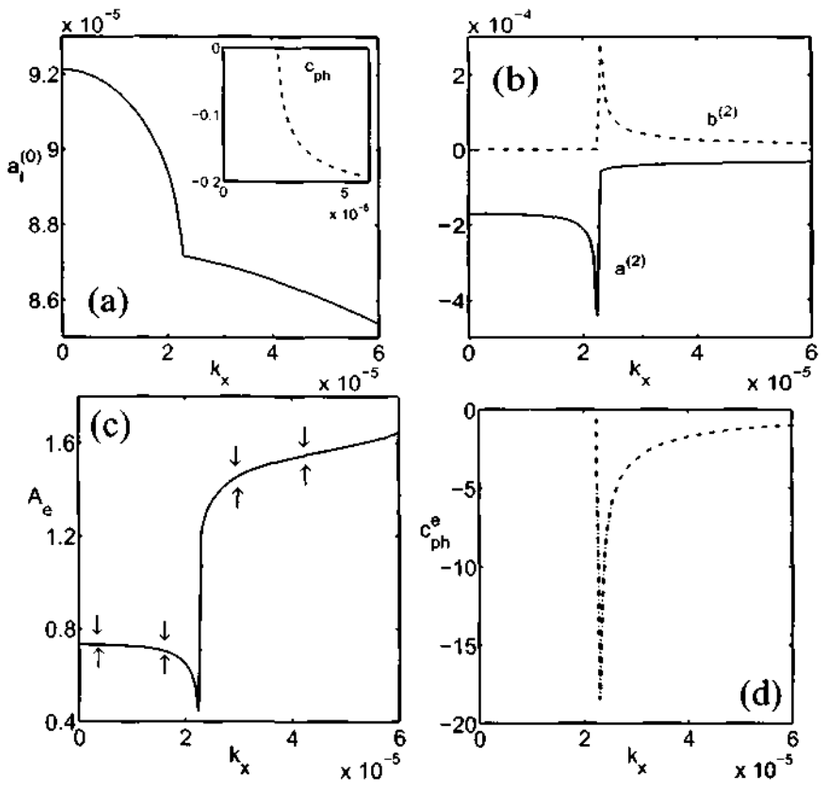

Figure 6.5: Long wavelength variations at $\phi^0 = 0.2$, $H = 100$ and $e = 0.8$: (a) linear growth rate and phase velocity (inset) of the least-stable mode, (b) $a^{(2)}$ (solid line) and $b^{(2)}$ (dot-dash line) with k_x, (c) equilibrium amplitude with k_x, (d) equilibrium phase velocity.

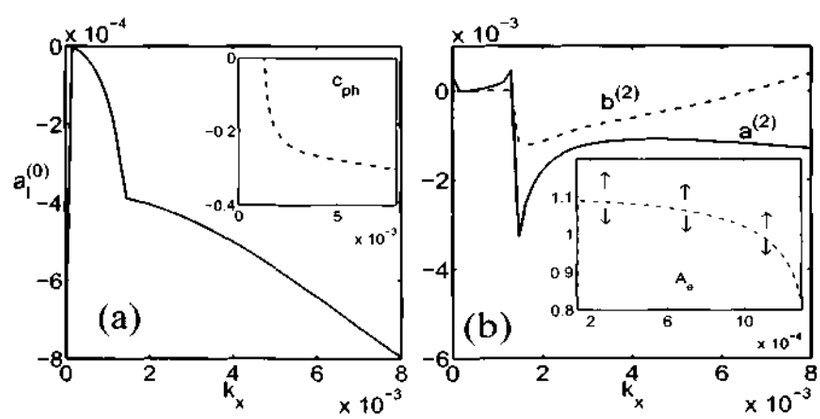

Figure 6.6: Long wavelength variations in the dilute limit ($\phi^0 = 0.05$): (a) $a_l^{(0)}$ (main panel) and c_{ph} (inset); (b) $a^{(2)}$ and $b^{(2)}$ (main panel), and equilibrium amplitude A_e (inset). Other parameters as are the same as in figure 6.5.

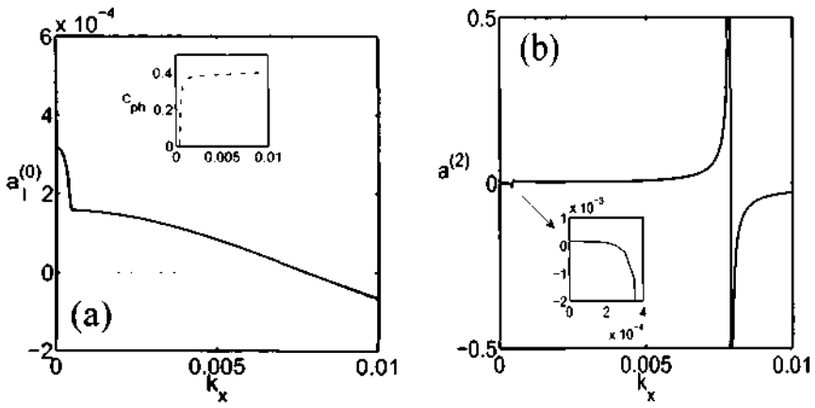

Figure 6.7: Long wavelength variations for dense flows at $\phi^0 = 0.5$ (corresponding to the 'triangle'-symbol in figure 6.4 at $H = 50$): (a) $a_l^{(0)}$ (main panel) and c_{ph} (inset); (b) $a^{(2)}$.

the second Landau coefficient which has not been pursued in this thesis.

Lastly, we consider the parameter values corresponding to the 'triangle' symbol in figure 6.4 ($\phi^0 = 0.5$ and $H = 50$) at which the nonlinear shear-banding solutions ($k_x = 0$) are growing since $a^{(0)} > 0$ and $a^{(2)} > 0$. The long-wave variations of $a^{(0)}$ and c_{ph} are shown in the main panel and the inset of figure 6.7(a). It is seen that the flow is unstable to stationary and travelling waves up to a wavenumber $k_x \sim 0.008$, and stable thereafter. The corresponding variation of $a^{(2)}$ with k_x is shown in figure 6.7(b). Note that $a^{(2)}$ diverges and changes its sign at $k_x \sim 0.008$ - the divergence of $a^{(2)}$ is in fact tied to the onset of nonlinear resonance which will be discussed in §6.7.3. Within the wavenumber band $k_x \sim (0, 0.008)$, $a_l^{(0)} > 0$ but $a^{(2)}$ also remains positive except over an extremely small range of k_x (see the inset of figure 6.7b) just below the mode-switching point, located at $k_x \approx 3.8 \times 10^{-4}$, at which two unstable stationary modes merge to yield a pair of unstable travelling waves. Therefore, at $\phi^0 = 0.5$ and $H = 50$, the flow remains nonlinearly stable except near $k_x \approx 3.8 \times 10^{-4}$.

Figures 6.8 and 6.9 show a comparison between nonlinear and linear disturbance patterns for long-wave stationary and travelling instabilities, respectively, of figure 6.5 - the wavenumbers are $k_x = 10^{-5}$ and 4×10^{-5}, respectively. The nonlinear disturbance pattern is calculated using (6.42) which is correct up to cubic order $O(A^3)$, and the linear disturbance field is calculated by setting $O(A^2)$- and $O(A^3)$-terms to zeros in (6.42). Figures 6.8(a-f) and 6.9(a-f) corresponds to nonlinear and linear patterns, respectively; while figures 6.8(a-f) and 6.9(a-f) show the grey-scale maps of the perturbation density ϕ' and granular temperature T', those in figures 6.8(e, f) and 6.9(e, f) display the vector plots of the perturbation velocity field (u', v').

On the grey-scale, the black and white represent minimum and maximum values, respectively. The linear eigenfunction of the stationary instability in figure 6.8(b, d, f) contains two rows of particle clusters (density maxima) across the gradient direction y (see also the temperature eigenfunction in figure 6.8d) this is because the parental origin of this long-wave stationary instability at $H = 100$ (refer to 'square' symbol in figure 6.4) is the 'mode 2' shear-banding instability whose density eigenfunction has two zero-crossings across y (Shukla & Alam 2011). The corresponding nonlinear equilibrium solution in figure 6.8(a,c,e) is a modulated version of the linear eigenfunction in figure 6.8(b,d,f). Note that the temperature is maximum at the location of minimum density, and the velocity field is seen to be changing its direction at the location of density maxima.

The long-wave travelling solution displayed in figure 6.9 corresponds to a backward-propagating

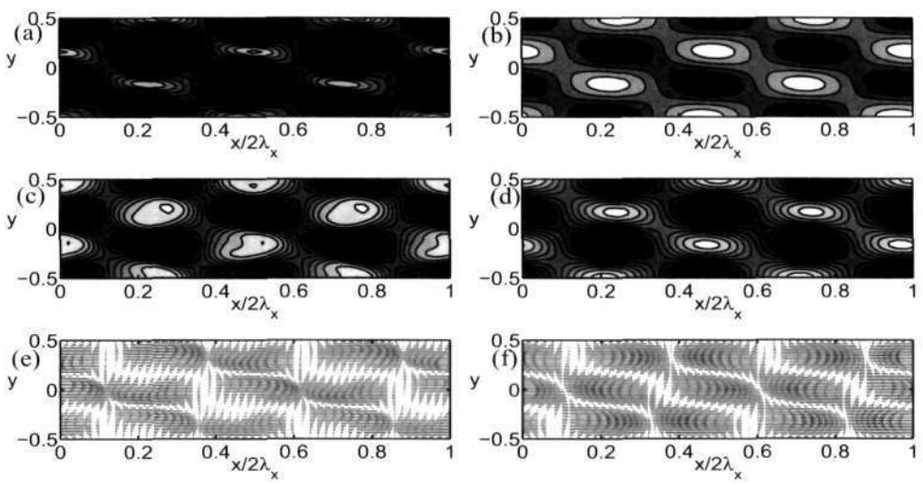

Figure 6.8: Long-wave patterns of (*a-b*) density, (*c-d*) granular temperature and (*e-f*) velocity field with $k_x = 10^{-5}$. Parameter values as in figure 6.5.

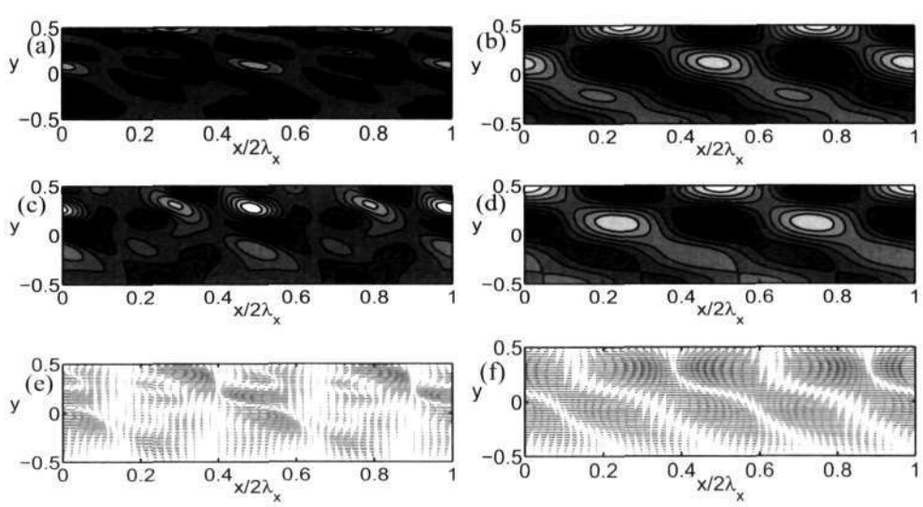

Figure 6.9: Same as figure 6.8, but for long-wave travelling instability at $t = 0$ with $k_x = 4 \times 10^{-5}$.

mode. For this instability, the nonlinear fields in figure 6.9(a,c,e) appear to be much more distorted from their linear counterparts in figure 6.9(b,d,f). Other features look similar to those for the stationary mode in figure 6.8.

6.7.2 Nonlinear Results on Stationary and Travelling Instabilities: $k_x \sim O(1)$

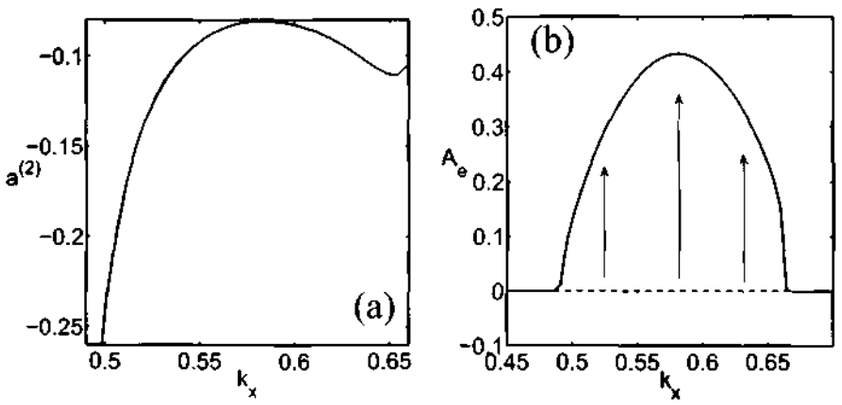

Figure 6.10: Variations of (a) the first Landau coefficient $a^{(2)}$ and (b) the equilibrium amplitude A_e with wavenumber k_x. Parameter values are as in figure 6.3.

We now focus on the instabilities due to the first peak of figure 6.3 for the wavenumber band $k_x \sim (0.5, 0.65)$ in figure 6.3, the phase velocity is zero and the growth rate is positive, and hence the flow is linearly unstable to stationary waves. The corresponding variation of the real part of the first Landau coefficient, $a^{(2)}$, with k_x is shown in figure 6.10(a); the imaginary part, $b^{(2)}$, is not shown since it remains zero for stationary waves. It is clear that $a^{(2)}$ is negative for $k_x \sim (0.5, 0.65)$ but $a^{(0)}$ is positive there, and hence there are *stable* nonlinear solutions, with the equilibrium amplitudes as displayed in figure 6.10(b). Because of the stationary nature of the underlying instability, we have supercritical *pitchfork/static* bifurcations within the wavenumber band $k_x \sim (0.5, 0.65)$ in figure 6.3.

Note that varying k_x is equivalent to varying the channel length since the channel length in terms of particle diameter is given by $L_x = \lambda_x = (2\pi/k_x)H$, and therefore the range of channel lengths in figure 6.10 corresponds to $L_x \in (12.56 - 9.75)H$ at a fixed Couette gap of $H = 100$.

A comparison between the nonlinear and linear patterns of density, granular temperature and velocity is shown respectively in figures 6.11(a, c, e) and 6.11(b, d, f). On the grey scale in figure 6.11(a-d) the white represents maximum and the black represents minimum; the vector plot of the velocity field (u, v) is displayed in figure 6.11(e, f). The nonlinear density and temperature fields are seen to be highly distorted from their linear counterparts - the location of the density maxima for the nonlinear case (compare figures 6.11a and 6.11b) shifts away from the walls into the bulk. With nonlinear corrections, the pockets of dilute and dense zones in figures 6.11(a) and 6.11(c) are seen to be tenuously distributed in the (x, y)-plane. To ascertain the true aspect ratio of the plots in figure 6.11, we must stretch the x-axis by a factor of about $2\pi/k_x \approx 10.72$, since $k_x = 0.5858$ for these plots. A comparison of the linear eigenfunctions in figure 6.11(b,d,f) with those in figure 6.8(b,d,f) suggests that the structural features of the 'dominant' stationary instability (at $k_x \sim O(1)$) are significantly different from those for 'long waves' (at $k_x \sim 0$)

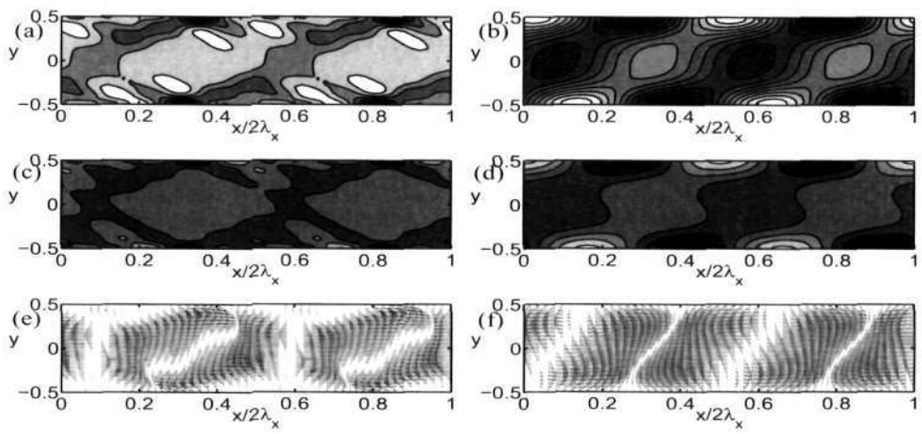

Figure 6.11: Patterns of (a, b) perturbation density $\phi'(x,y)$, (c, d) granular temperature $T'(x,y)$ and (e, f) velocity (u',v'), for the dominant stationary mode in figure 6.10 at $k_x = 0.5858$. Panels (a, c, e) represent nonlinear patterns, while (b, d, f) represent linear eigenfunction. Other parameter values are $H = 100$, $e = 0.8$ and $\phi = 0.2$, as in figure 6.3.

stationary instability.

For the wavenumber band around the second peak in figure 6.3, we show the variations of growth rate (solid line) and the phase velocity (dot-dashed line) in figure 6.12(a) clearly, the flow is unstable to travelling waves. (It may be noted that the growth rates of these travelling waves at $k_x = O(1)$ are an order of magnitude larger that those at long waves $k_x \sim 0$, see figure 6.5.) The corresponding variations of the real (solid line) and the imaginary (dot-dashed line) parts of the first Landau coefficient are shown in figure 6.12(b). The real part of the first Landau coefficient ($a^{(2)}$) changes its sign from positive to negative at $k_x \approx 0.926$, shown by an arrow in figure 6.12(b). Since the underlying instability is oscillatory, we have supercritical *Hopf/oscillatory* bifurcations within the wavenumber band $k_x \in (0.926, 0.99)$. The corresponding equilibrium amplitude (solid line) and the equilibrium phase velocity (dot-dashed line) are shown in figure 6.12(c). Note that even though the flow is unstable to travelling waves (i.e. $a^{(0)} > 0$, see figure 6.12a) over $k_x \in (0.88, 0.926)$, the nonlinear equilibrium solutions do not exist over $k_x \in (0.88, 0.926)$ since $a^{(2)} > 0$ there.

The cubic Landau-Stuart equations (6.38)-(6.39) have exact analytical solutions:

$$A^2(t) = \frac{a^{(0)} A_0^2}{\left[a^{(0)} + a^{(2)} A_0^2\right] \exp(-2a^{(0)}t) - a^{(2)} A_0^2}, \tag{6.48}$$

$$\theta(t) = \theta_0 + b^{(0)}t - \frac{b^{(2)} a^{(0)}}{a^{(2)}} \ln\left[\frac{a^{(0)} + a^{(2)} A_0^2 (1 - \exp(-2a^{(0)}t))}{a^{(0)}}\right], \tag{6.49}$$

with $a^{(0)} \neq 0$, where $A_0 \equiv A(t=0)$ and $\theta_0 \equiv \theta(t=0)$ are initial conditions. At $k_x = 0.93$ and other parameters of figure 6.12(c), the coefficients of (6.38)-(6.39) are $a^{(0)} \approx 2.9711 \times 10^{-3}$, $b^{(0)} \approx 9.7524 \times 10^{-2}$, $a^{(2)} \approx -1.5185 \times 10^{-2}$ and $b^{(2)} \approx 7.7618 \times 10^{-1}$. For these parameters, the equilibrium amplitude is $A_e = \sqrt{-a^{(0)}/a^{(2)}} \approx 0.4423$. We have evaluated the exact solution trajectories (6.48)-(6.49) for two initial conditions: one with $A_0 > A_e$ and other with $A_0 < A_e$, with $\theta_0 = 0$. These solutions are indicated by solid lines in figure 6.12(d) in the (A_x, A_y)-plane, where $A_x = A\cos\theta$ and $A_y = A\sin\theta$. Both spiralling orbits asymptotically approach a limiting circle of radius $A = A_e$ as $t \to \infty$ - this is the *limit cycle* which is stable for the present case.

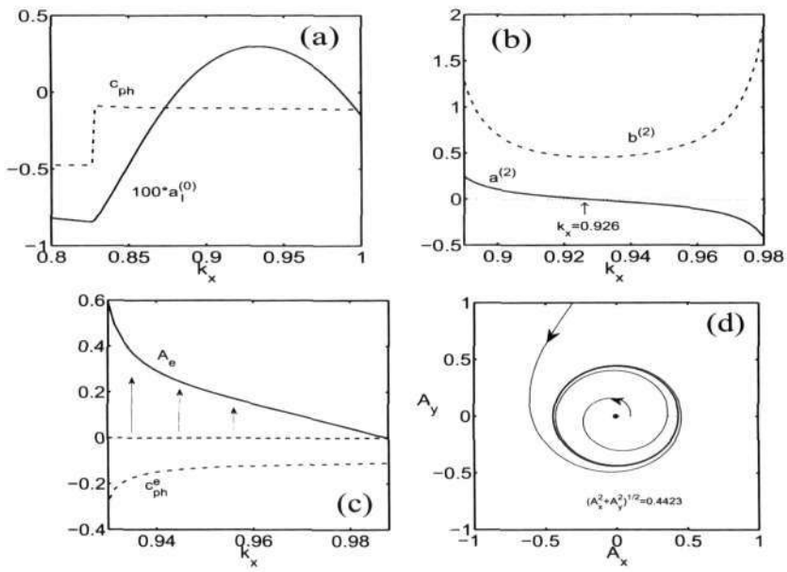

Figure 6.12: Variations with k_x of (a) the growth rate, $100a_l^{(0)}$, (solid line) and c_{ph}, (dot-dashed line) of the least-stable travelling mode, (b) the first Landau coefficient: $a^{(2)}$ (solid line), $b^{(2)}$ (dot-dashed line), and (c) A_e (solid line) and c_{ph}^e (dot-dashed line); parameter values are as in figure 6.3. (d) Stable limit cycle and two spiralling orbits in the (A_x, A_y)-plane at $k_x = 0.93$.

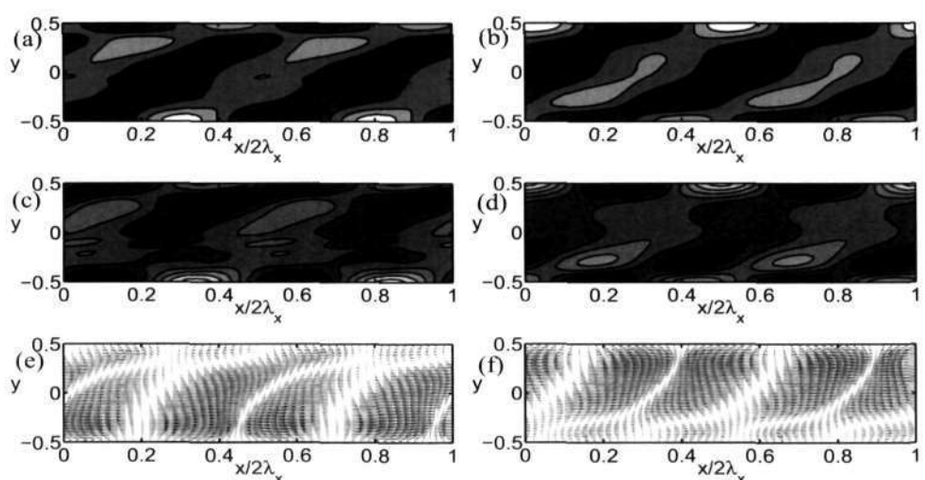

Figure 6.13: Same as figure 6.11, but for the dominant travelling wave at $t = 0$ with $k_x = 0.93$.

For the dominant travelling wave instability of figure 6.12 that occurs at $k_x \approx 0.93$, the nonlinear and linear perturbation fields of density, granular temperature and velocity are compared in figure 6.13 - this is a backward-propagating mode. To visualise the true aspect ratio of these plots, we need to stretch the x-axis by a factor of about $2\pi/k_x \approx 6.75$, and therefore the density bands, for example in figure 6.12(a), are much more elongated than what is seen here. In contrast to the case of stationary instability in figure 6.11, the nonlinear corrections induce a significant change in the velocity field (compare figures 6.13e and 6.13f); the nonlinear density and temperature fields have some resemblance to their linear counterparts, even though they are also similarly distorted like the velocity field. In particular, the nonlinear velocity field clearly shows vortical-type motions (not shown for brevity) if we analyse the total velocity $(u, v) = (u^0 + u', v + v')$.

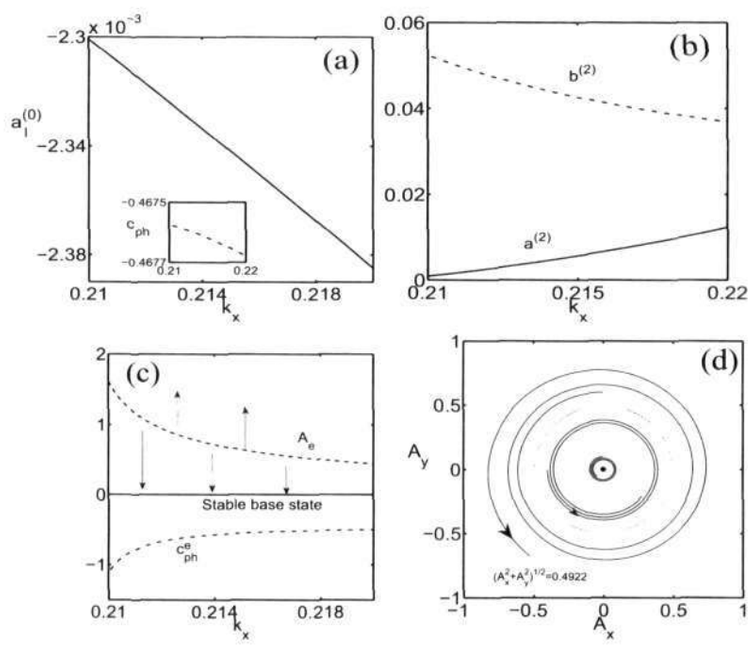

Figure 6.14: Variations of (a) $a_l^{(0)}$ (main panel) and c_{ph} (inset), (b) $a^{(2)}$ (solid line) and $b^{(2)}$ (dot-dashed line), and (c) A_e (dashed line) and c_{ph}^e (dot-dashed line) with k_x; other parameters are the same as in figure 6.3. (d) Unstable limit cycle and two spiraling orbits at $k_x = 0.215$.

The evidence of subcritical instability at moderate values of k_x is shown in figure 6.14 for a range of wavenumbers $k_x \in (0.21, 0.22)$; other parameters are as in figure 6.3. While the variations of the growth rate of the least-stable mode and the phase velocity (inset) are shown in figure 6.14(a), the first Landau coefficient is shown figure 6.14(b). These are 'stable' $[a^{(0)} < 0]$ travelling waves as seen in figure 6.14(a). Since $a^{(2)}$ and $a^{(0)}$ are of opposite signs over $k_x \in (0.21, 0.22)$, this leads to 'subcritical' Hopf bifurcations, with oscillatory nonlinear solutions. The corresponding variations of the equilibrium amplitude A_e and the equilibrium phase velocity c_{ph}^e are shown in figure 6.14(c) by dashed and dot-dashed lines, respectively. As discussed in §6.5.2, the equilibrium amplitude in figure 6.14(c) provides a measure for the 'threshold' amplitude for nonlinear stability since we have calculated only the first Landau coefficient. Figure 6.14(d) shows the limit cycle (dashed circle) at $k_x = 0.215$ with other parameters as in figure 6.14(c). For these parameters, the coefficients of the Landau-Stuart equations (6.38)-(6.39) are $a^{(0)} \approx -2.3418 \times 10^{-3}$, $b^{(0)} \approx 1.0053 \times 10^{-1}$, $a^{(2)} \approx 9.6679 \times 10^{-3}$ and $b^{(2)} \approx 7.2967 \times 10^{-2}$; the

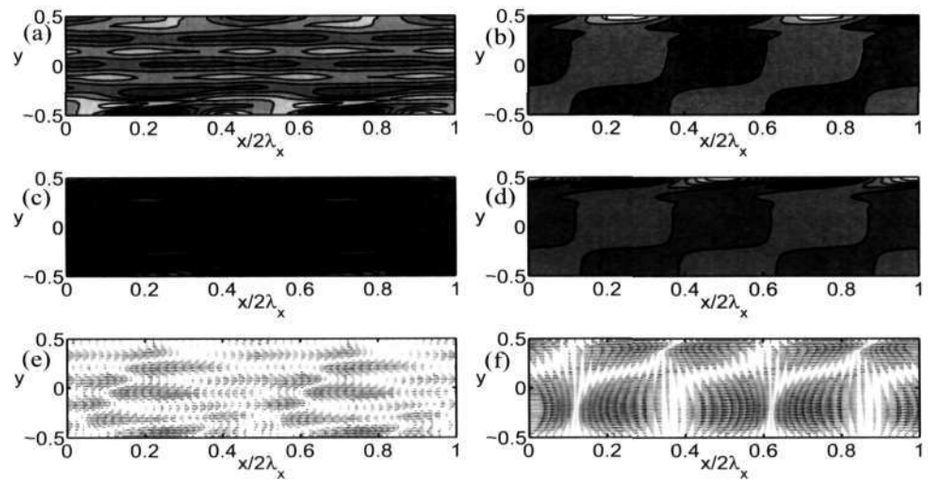

Figure 6.15: Same as figure 6.13, but for the subcritical travelling wave at $t = 0$ with $k_x = 0.215$ with parameter values as in figure 6.14(d).

corresponding equilibrium amplitude is $A_e = \sqrt{-a^{(0)}/a^{(2)}} \approx 0.4922$. The solution trajectories (6.48)-(6.49) for two initial conditions (one inside the limit cycle and the other outside) are plotted by solid lines in figure 6.14(d) – both orbits spiral away from the limit cycle (dashed circle) as $t \to \infty$, confirming that this represents an 'unstable' limit cycle.

With parameter values as in figure 6.14(d), the nonlinear and linear patterns are compared in figure 6.15(a-f). Recall that this is an 'unstable' subcritical travelling wave. Unlike the supercritical solutions in figure 6.13, the nonlinear subcritical patterns in figure 6.15(a,c,e) have little resemblance with their linear eigenfunctions in figure 6.15(b,d,f). The structural features of all perturbation fields in figure 6.15(a,c,e) appears to be elongated and aligned along the streamwise direction, and the pockets of dilute and dense regions are tenuously distributed in the (x, y)-plane.

6.7.3 Evidence of Mean-flow Resonance and 1:2 Resonance

We first consider the *mean-flow resonance* condition (6.32) which represents a resonant interaction between a linear mode at some value of k_x and a shear-banding mode (i.e. a disturbance at zero wavenumber $k_x = 0$). Focussing on the wavenumber band $k_x = (0.26, 0.38)$ with other parameters as in figure 6.3, we have plotted the variations of the least-stable growth rate and its phase velocity in figure 6.16(a) and that of $a^{(2)}$ (solid line) and $b^{(2)}$ (dot-dashed line) with wavenumber in figure 6.16(b). Note in figure 6.16(b), that $a^{(2)}$ has a kink near $k_x \sim 0.37$ which is consequence of the mean-flow resonance condition being satisfied, there as we show below.

Recall from (6.32) that the condition for the mean-flow resonance is $2a^{(0)}_{j1}(k_x) = a^{(0)}_{j2}(k_x = 0)$ with $b^{(0)}_{j2}(k_x = 0) = 0$ for any two modes $j1$ and $j2$. In figure 6.16(c), the line with open circles represents the variation of $2a^{(0)}$ with k_x (where $a^{(0)}$ corresponds to the least-stable mode as displayed in figure 6.16a), and the dashed horizontal line represents a real eigenvalue of the streamwise independent flow (which is not the least-stable eigenvalue at $k_x = 0$ for this parameter set). Both the growth rate curves intersect at $k_x \approx 0.3677$, as shown by an arrow in figure 6.16(c),

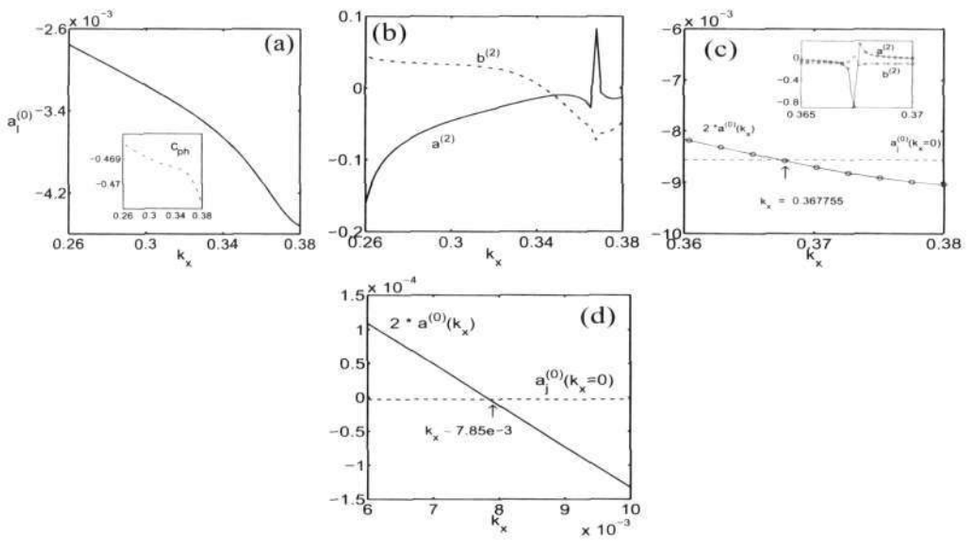

Figure 6.16: Variations of (a) $a_l^{(0)}$ (main panel) and c_{ph} (inset plot) and (b) $a^{(2)}$ (solid line) and $b^{(2)}$ (dot-dashed line). Evidence of mean flow resonance at (c) $k_x \approx 0.3677$ and (d) $k_x \approx 0.00785$. Parameter values are $(a\text{-}c)$ $\phi^0 = 0.2$ and $H = 100$ (same as figure 6.3), and (d) $\phi^0 = 0.5$ and $H = 50$ (same as figure 6.7).

and this is the point at which the mean-flow resonance condition,

$$2a^{(0)}(k_x = 0.3677) = a_j^{(0)}(k_x = 0) \approx -8.56434 \times 10^{-3}, \tag{6.50}$$

is exactly satisfied. In (6.50), $j = 11$, implying that the 11th mode (the ordering of modes is done by arranging them in descending-order of their growth rates) of the streamwise independent flow ($k_x = 0$) is responsible for the above mean-flow resonance, resulting in a kink on the $a^{(2)}$-curve in figure 6.16(b). The inset of figure 6.16(c) shows a zoomed variation of the first Landau coefficient that diverges and undergoes a sign-change at the resonant wavenumber ($k_x \approx 0.3677$).

We now explain the divergence of $a^{(2)}$ at long-waves in figure 6.7(b), for which the parameter values are $\phi^0 = 0.5$, $H = 50$ and $e = 0.8$. The corresponding variations of $2a^{(0)}(k_x)$ and $a^{(0)}(k_x = 0)$ are displayed in figure 6.16(d) by solid and dashed lines, respectively, which are seen to intersect at $k_x \approx 0.00785$. (The dashed line in figure 6.16d corresponds to the second shear-banding mode, $a_{j=2}^{(0)}(k_x = 0) \approx -2.97079 \times 10^{-6}$, which is stable; note that the 'leading' shear-banding mode is unstable at $\phi^0 = 0.5$ and $H = 50$, see figure 6.4.) Hence, there is a mean-flow resonance at $k_x \approx 0.00785$, which is responsible for the divergence of $a^{(2)}$ in figure 6.7(b).

In fact, such a mean-flow resonance (6.32) can occur at multiple locations at various values of k_x for a given set of parameters (ϕ^0, H, e). To demonstrate this, we replotted the growth rate curve of figure 6.3 in figure 6.17(a) by a solid line - recall that this corresponds to the parameter values ($\phi^0 = 0.2$, $H = 100$ and $e = 0.8$) of the square symbol in figure 6.4. We have also plotted five real eigenvalues of shear-banding modes (i.e. at $k_x = 0$) whose growth-rates can be parametrized by wavenumber such that

$$2a^{(0)}(k_x) = a_j^{(0)}(0), \quad \forall \quad j = 1, 2, 3, \ldots, \tag{6.51}$$

shown by dashed horizontal lines in figure 6.17. In fact, the upper (thick) dashed line in figure 6.17

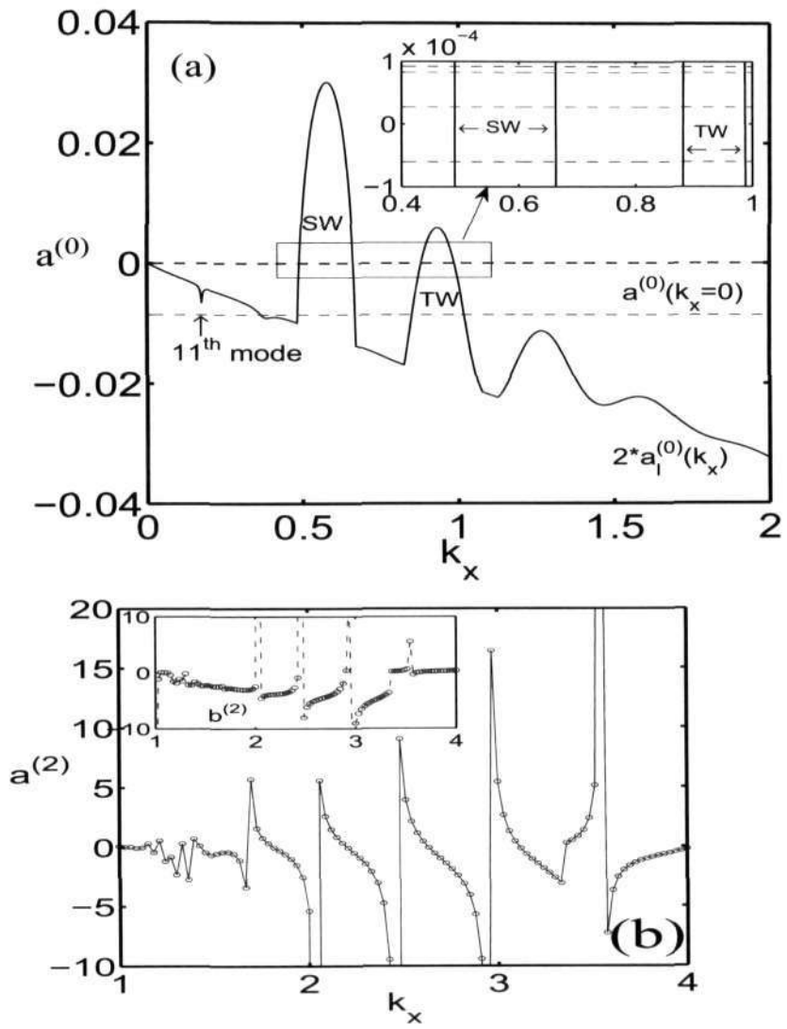

Figure 6.17: (*a*) Evidence of mean-flow resonance: variation of the real part of the least-stable mode $[2a^{(0)}(k_x)]$ with k_x at $\phi^0 = 0.2$, $H = 100$ and $e = 0.8$. The dashed horizontal lines refer to different shear-banding modes $k_x = 0$. The intersection points of dashed lines with the solid line denote the locations of k_x at which mean-flow resonance occurs as explained in the text. (*b*) Divergence of $a^{(2)}(k_x)$ for $k_x > 1$.

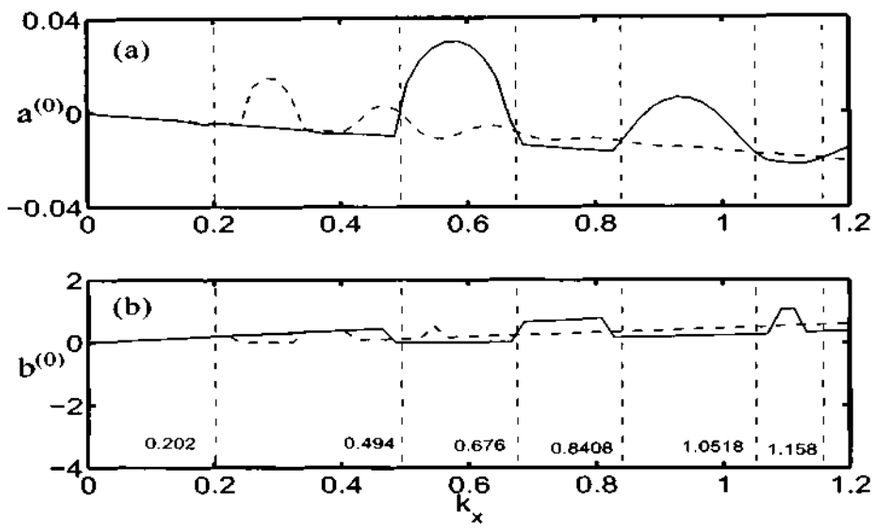

Figure 6.18: Possible onset of the 1:2 resonance at $\phi^0 = 0.2$, $H = 100$ and $\epsilon = 0.8$: (a) the real part, $a^{(0)}$, (b) the imaginary part, $b^{(0)}$, of the least-stable mode with k_x.

corresponds to the first four modes, $a^{(0)}_{j=1,2,3,4}(0) = 9.2125 \times 10^{-5}$, 8.28485×10^{-5}, 2.72077×10^{-5} and -5.99651×10^{-5}, which are very close to each other, as clarified in the zoomed inset. The first two (almost) vertical solid lines in the inset correspond to the zoomed version of the dominant stationary wave (SW) of figure 6.17 and the next two vertical lines correspond to travelling waves (TW). It is clear from this inset that the growth rates of these four shear-banding modes ($a^{(0)}(k_x = 0)$) coincide with the growth rates ($2a^{(0)}(k_x)$) of the dominant stationary and travelling waves, satisfying the mean-flow resonance condition (6.32) exactly at 16 different values of k_x (which are, of course, very close to each other). Consequently, there are multiple resonance points at various values of k_x, near the zero crossings of SW and TW. That the first Landau coefficient diverges at such resonance points can be ascertained from figures 6.10(a) and 6.12(b). The lower dashed line in figure 6.17 corresponds to the 11th shear-banding mode [$a^{(0)}_{j=11}(k_x = 0) = -8.56434 \times 10^{-3}$] which is responsible for the mean-flow resonance in figure 6.16(c). Note that in figure 6.17(a) the flow is linearly stable for large values of $k_x > 1$. However, there are multiple resonance points in this stable regime too, as implicated by the discontinuities on the curves of $a^{(2)}$ and $b^{(2)}$ at various values of k_x, see figure 6.17(b), where the mean-flow resonance condition (6.32) is satisfied.

Now we discuss about the possible occurrence of the 1 : 2 resonance condition (6.34) in the present flow. While the solid line in figure 6.18(a) represents the variation twice of the growth rate of the least-stable mode, $2a^{(0)}_l(k_x)$, that in figure 6.18(b) represents the corresponding variation of frequency, $2b^{(0)}_l(k_x)$. The dashed lines in figure 6.18(a,b) represent the growth rate and frequency curves, parametrized by $a^{(0)}(k_x) = a^{(0)}_l(2k_x)$ and $b^{(0)}(k_x) = b^{(0)}_l(2k_x)$, respectively. The points of intersection of the solid and dashed lines in figure 6.18(a) are marked by vertical dotted lines where the growth rates are equal. However, the 1:2 resonance condition (6.34) is not satisfied at these points because while the condition on the growth rate,

$$2a^{(0)}_l(k_x) = a^{(0)}_l(2k_x),$$

is satisfied, the equality of frequencies does not hold, i.e.

$$2b_l^{(0)}(k_x) \neq b_l^{(0)}(2k_x)$$

at these points. We have checked a few other parameter combinations, but could not find the occurrence of a 1 : 2 resonance in this flow. We note in passing that the 1 : 2 resonance between two travelling waves corresponds to a codimension-3 bifurcation point (Golubitsky & Schaeffer 1985; Proctor & Jones 1988; Fujimura & Kelly 1997) and therefore requires an exhaustive search in the parameter space which was not pursued further in this thesis.

Irrespective of the types of resonance (i.e. mean flow or 1 : 2), the first Landau coefficient is divergent at the resonance point. In the following sections, we will present results for $a^{(2)}$ and $b^{(2)}$, which contain such resonance points as implicated by discontinuities in the first Landau coefficient.

6.7.4 Dominant Stationary and Travelling Instabilities: Effects of Density and Couette Gap

We define the *dominant* eigenvalue as the one having the maximum growth rate over all wavenumbers for a specified control parameter combination of (H, ϕ^0, e) - in other words it is the supremum of all leading eigenvalues, as defined in (6.45), over all k_x:

$$a_l^d = \sup_{k_x} a_l^{(0)}. \tag{6.52}$$

The wavenumber corresponding to this dominant mode is referred to as the dominant wavenumber:

$$k_x^d = k_x(a^{(0)} = a_l^d). \tag{6.53}$$

For example, in figure 6.3, we have plotted the growth rate of the leading eigenvalue, $a_l^{(0)}$, with k_x at $(H, \phi^0) = (100, 0.2)$ and $e = 0.8$. The dominant mode for this parameter combination comes from the maximum of the growth rate curve that occurs at the first peak at $k_x \approx 0.5858$, which is a stationary wave; the second dominant mode corresponds to the maximum of the second peak at $k_x \approx 0.9349$ in figure 6.3, which is a travelling wave. Recall that the growth rates of these stationary and travelling instabilities, which appear at $k_x = O(1)$, are an order of magnitude larger than those appearing at long waves ($k_x \sim 0$, see §6.7.1). So far, we have presented results on these dominant instabilities at a mean density of $\phi^0 = 0.2$ and a Couette gap of $H = 100$ in §6.7.2 and §6.7.3. In this section, we probe the effects of varying mean density and Couette gap on the nonlinear saturation of these dominant stationary and travelling instabilities.

Effect of Mean Density

In figure 6.19, we show the variations of $a_l^{(0)}$ with k_x for 24 different mean densities ranging from $\phi^0 = 0.1$ to 0.3, with parameter values as in figure 6.3. The dashed and thick solid lines correspond to $\phi^0 = 0.1$ and 0.3, respectively, and the thin solid lines refer to the remaining equally spaced densities. For each density, the first dominant peak refers to stationary waves, and the next one to travelling waves. Note that the locations of both the dominant stationary and travelling wave peaks move to larger values of k_x with increasing density from $\phi^0 = 0.1$ to 0.3.

The variation of the growth rate of the above-discussed dominant stationary instability, a_l^d, with mean density is shown in figure 6.20(a), and the corresponding variation of the dominant wavenumber, k_x^d, is shown in its inset. It is seen that the dominant growth rate is maximum at

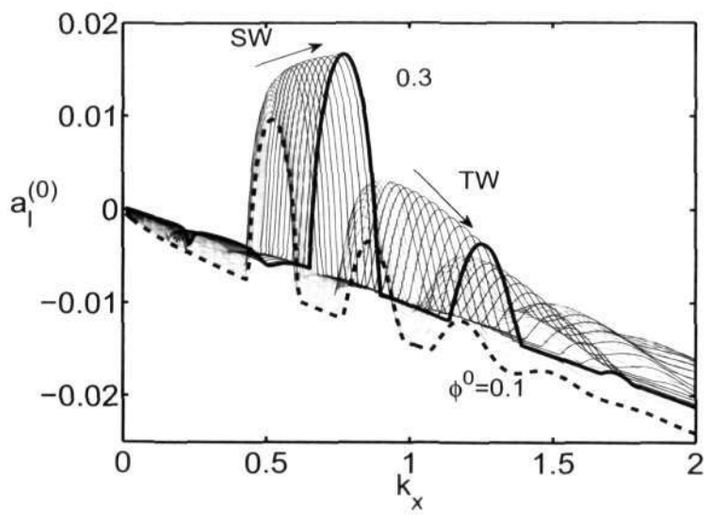

Figure 6.19: Effect of mean density on the growth rate of least-stable mode at $H = 100$ and $e = 0.8$.

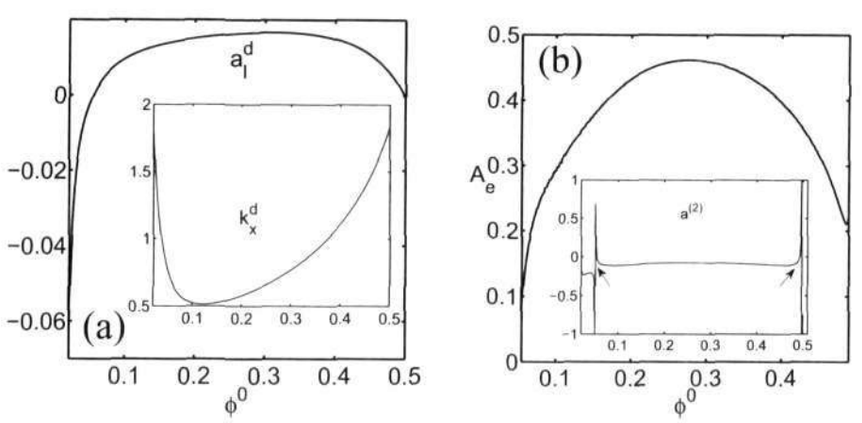

Figure 6.20: Effect of mean density on the dominant stationary instability, corresponding to the first peak in figure 6.19. (*a*) a_l^d (main panel) and k_x^d (inset); (*b*) supercritical/stable A_e (main panel) and $a^{(2)}$ (inset).

an intermediate value of $\phi^0 \sim 0.3$ and decreases in both the dilute and dense limits. Also, the dominant wavenumber is minimum at $\phi^0 \sim 0.1$ and increases in both the dilute and dense limits, implying that the wavelength ($\lambda_x = 2\pi/k_x$) of the dominant instability is maximum at some intermediate density but decreases sharply in both dilute and dense limits. Within the density range over which the dominant stationary instability is unstable ($a_l^d > 0$), the first Landau coefficient $a^{(2)}$ is negative as seen in the inset of figure 6.20(b); the imaginary part of the first Landau coefficient $b^{(2)}$ is zero for stationary waves and hence not shown. (Note that the jumps in $a^{(2)}$, marked by arrows in the inset of figure 6.20b, correspond to the mean-flow resonance condition (6.32) being satisfied at those locations.) Therefore, at $H = 100$ (refer to the square symbol in figure 6.4), the supercritical (and hence stable) stationary solutions exist for a range of mean densities as shown in the main panel of figure 6.20(b). It has been verified that this range of ϕ^0, over which such nonlinear equilibrium states exist becomes larger in wider Couette gaps (i.e. with increasing H).

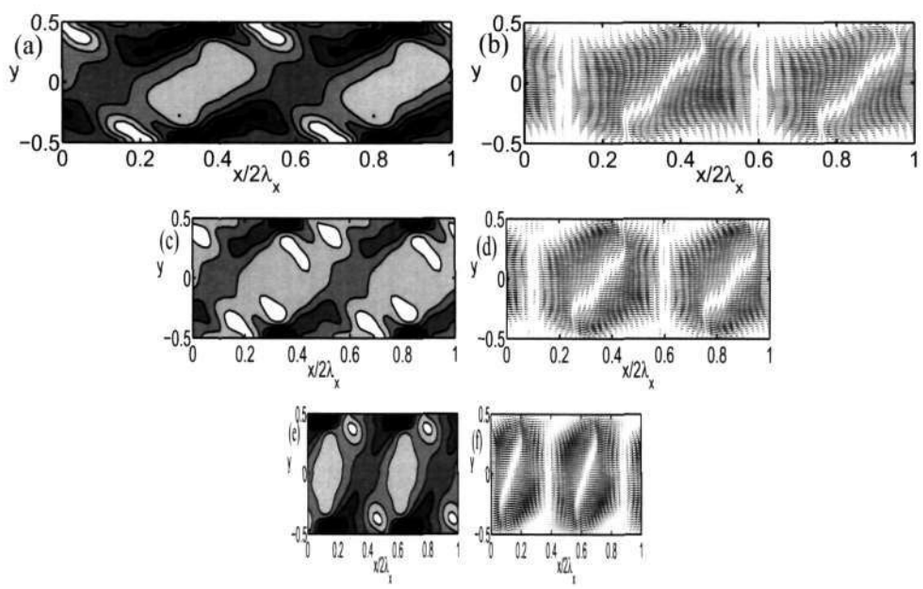

Figure 6.21: Effect of the mean density on nonlinear patterns of density (a, c, e) and velocity (b, d, f) for the dominant stationary instability in figure 6.20: (a,b) $\phi^0 = 0.1$ ($k_x = 0.52$), (c,d) $\phi^0 = 0.3$ ($k_x = 0.77$) and (e,f) $\phi^0 = 0.45$ ($k_x = 1.39$).

With the finite amplitudes as in figure 6.20(b), the corresponding nonlinear stationary patterns of the perturbation density and velocity fields are displayed in figures 6.21(a, c, e) and 6.21(b, d, f), respectively, for three values of mean density: figures 6.21(a, b), 6.21(c, d) and 6.21(e, f correspond to $\phi^0 = 0.1$, 0.3 and 0.45, respectively, with dominant wavenumbers $k_x^d = 0.52$, 0.77 and 1.39. These plots should also be compared with figure 6.11(a,e) for $\phi^0 = 0.2$. It is seen that the overall features of density and velocity fields look similar at any mean density. Note further that the related plots of linear perturbations at $\phi^0 = 0.1$, 0.3 and 0.45 (not shown) look strikingly similar to those at $\phi^0 = 0.2$ as in figure 6.11(b,f). Therefore, the overall structural features of both linear and nonlinear perturbation fields for the dominant stationary instability remain relatively unaffected by variations in mean density, i.e. whether the flow is dilute ($\phi^0 = 0.1$) or dense ($\phi^0 = 0.45$).

For the dominant travelling wave, corresponding to the second peak in figure 6.19, the variations of a_l^d and c_{ph} with mean density ϕ^0 are shown by solid and dot-dashed lines, respectively, in figure 6.22(a). The phase velocity, c_{ph}, of the dominant travelling mode remains relatively unaffected with changes in mean density, however, its growth rate a_l^d is maximum at some intermediate density $\phi^0 \sim 0.2$ and decreases in both dilute and dense limits. The corresponding dominant wavenumber k_x^d, shown in the inset of figure 6.22(a), varies non-monotonically with ϕ^0 and is minimum at $\phi^0 \sim 0.1$ and increases in both dilute and dense limits. Comparing figure 6.22(a) with figure 6.20(a) we find that the growth rate and the unstable range of densities are much smaller for the dominant travelling wave than its stationary counterpart and so is its wavelength (since $\lambda_x \sim 1/k_x^d$).

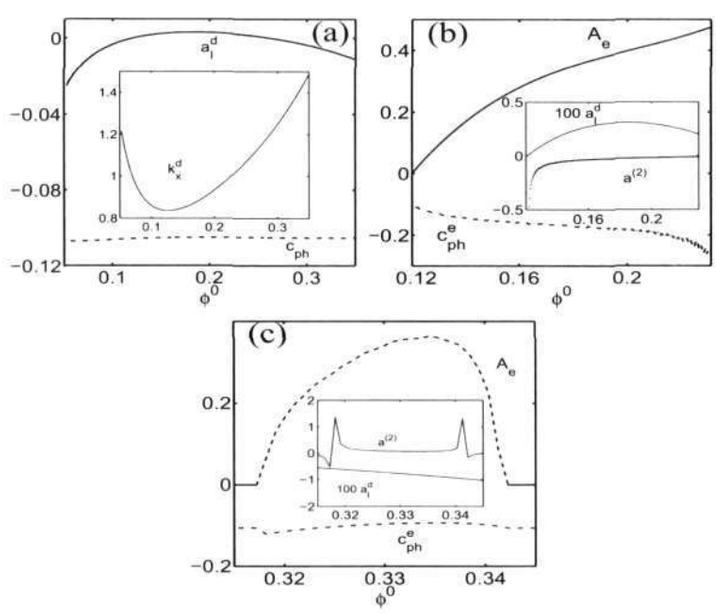

Figure 6.22: Effect of the mean density on the dominant travelling wave, corresponding to the second peak in figure 6.19. (a) a_l^d (solid line), its phase velocity (dot-dashed line) and k_x^d (inset); (b) supercritical/stable A_e, c_{ph}^e (main panel) and $a^{(0)}$ and $a^{(2)}$ (inset); (c) subcritical/unstable A_e, c_{ph}^e (main panel) and $a^{(0)}$ and $a^{(2)}$ (inset).

The dominant travelling waves in figure 6.22(a) undergo 'supercritical' and 'subcritical' Hopf bifurcations over the density range of $\phi^0 \sim (0.12, 0.25)$ and $\phi^0 \sim (0.317, 0.343)$, respectively, see figures 6.22(b) and 6.22(c). The variations of the real part of the first Landau coefficient, $a^{(2)}$, and the growth rates are displayed in the insets of figures 6.22(b) and 6.22(c), and those of the equilibrium amplitude A_e and the equilibrium phase velocity c_{ph}^e in their respective main panels. The nonlinear solution branches in figures 6.22(b) and 6.22(c) are responsible for 'stable' and 'unstable' limit cycles, respectively, similar to those in figures 6.12(d) and 6.14(d). Corresponding to an unstable limit cycle such as in figure 6.14(d), there exists a stable limit cycle of larger amplitude that requires the knowledge of the second Landau coefficient $c^{(4)}$ (which is not calculated here).

The nonlinear travelling patterns (at $t = 0$) of the perturbation density, granular temperature and velocity fields are shown in figure 6.23 - figures 6.23(a, c, e) and 6.23(b, d, f) correspond to *stable* and *unstable* solutions at $\phi^0 = 0.15$ and 0.33, respectively, with other parameters as in

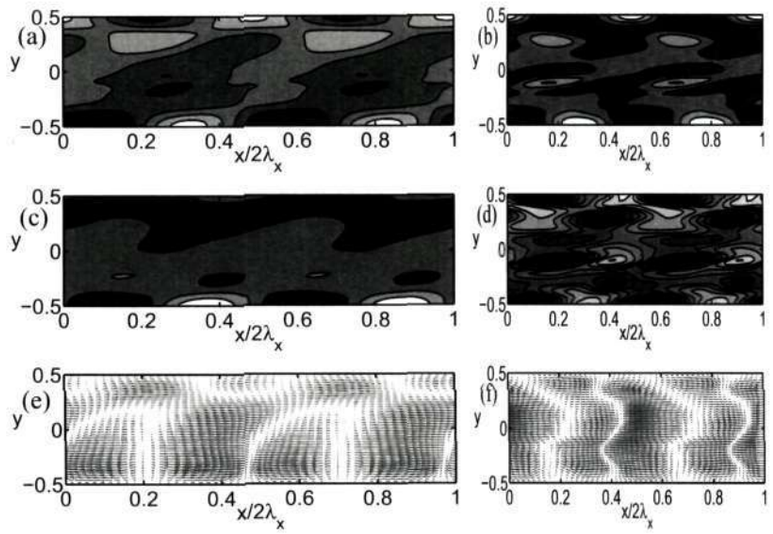

Figure 6.23: Nonlinear patterns of (a, b) density, (c, d) temperature and (e,f) velocity fields for the dominant travelling instability in figure 6.22 at two mean densities: (a, c, e) $\phi^0 = 0.15$ and $k_x = 0.84$ (stable); (b, d, f) $\phi^0 = 0.33$ and $k_x = 1.3$ (unstable).

figure 6.22. It must be noted that the structural features of stable travelling solutions at any density over $\phi^0 \sim (0.12, 0.23)$ resemble those in figure 6.23(a,c,e) and the unstable solutions at any $\phi^0 \sim (0.317, 0.342)$ look similar to those in figure 6.23(b, d, f). It is clear from figure 6.23 that the stable and unstable nonlinear solutions for all three fields are markedly different from each other. More specifically, the unstable patterns support larger fluctuations in the (x, y)-plane in all fields than the stable patterns. This may be contrasted with the fact that the underlying linear fields for either case of supercritical and subcritical Hopf bifurcations look similar, such as those in figure 6.13(b, d, f).

Effect of Couette Gap

The above results, figures 6.19 - 6.23, pertain to a fixed Couette gap of $H = 100$ over a range of mean densities $\phi^0 \in (0.05, 0.5)$. Here, we fix the mean density at $\phi^0 = 0.2$ and probe the effect of varying Couette gaps on dominant instabilities, along the horizontal arrows in figure 6.4. Figure 6.24 shows the variation of the growth of the least-stable mode with k_x for few values of $H \in (25, 100)$. It is seen that the dominant stationary instability at $H = 100$ (the first peak on thick solid line) becomes stable for narrower Couette gaps (say, at $H = 25$, indicated by the dashed line in figure 6.24). Therefore, there is a minimum Couette gap ($H = H_c^{SW}$) below which the stationary instability with $k_x \sim O(1)$ becomes stable.

For the dominant instability, corresponding to the first peak in figure 6.24, we have shown the variations of its growth rate a_l^d with H and the corresponding first Landau coefficient $a^{(2)} = 0$ (with $b^{(2)} = 0$) in figures 6.25(a) and 6.25(b), respectively. The flow is unstable to this instability for $H > 35.8$; the growth rate a_l^d reaches a maximum at some value of H (~ 70) and decreases slowly thereafter. The dominant wavenumber k_x^d decreases monotonically with increasing H, see the inset in figure 6.25(a), and hence the corresponding wavelength increases. In fact, the dominant wavelength λ_x^d/d (in terms of particle diameter) increases from 20π to 1000π at $H = 25$ and 200, respectively, and $\lambda_x^d/\overline{h}$ from 0.8π to 5π in terms of the Couette gap. The inset in figure 6.25(b) displays a zoomed version of $a^{(2)}$ over a smaller range of H, and the two

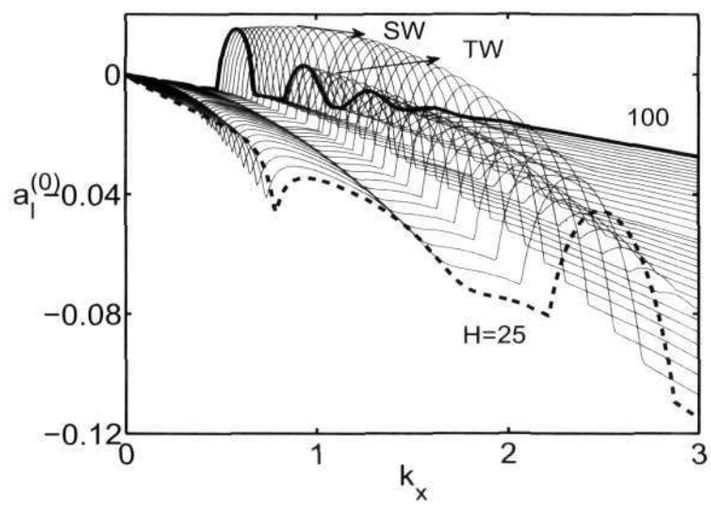

Figure 6.24: Effect of the Couette gap on the growth rate of the least-stable mode at $\phi^0 = 0.2$ and $e = 0.8$.

discontinuities in $a^{(2)}$ at $H \sim 29$ and $H \sim 36$ correspond to the mean-flow resonance condition (6.32) being satisfied there.

For the dominant stationary instability in figure 6.25(a), the nonlinear solutions appear via 'super-critical' pitchfork bifurcations for a large range of Couette gaps $H \in (36, 100)$ as shown in the main panel of figure 6.25(c). However, the 'subcritical' solutions also exist but for a very narrow range of Couette gaps $H \in (29, 30)$ as in the inset of figure 6.25(c). Note that in the inset of figure 6.25(b), $a^{(2)}$ is positive for $H \in (29, 30)$, leading to subcritical bifurcations.

For parameter values of figure 6.25, the stable/supercritical nonlinear solutions at any $H \in (36, 100)$ look similar. This can be verified by comparing a representative stationary-wave solution for the patterns of density, granular temperature and velocity as displayed in figure 6.26(a,c,e) at a Couette gap of $H = 50$ (with other parameters as in figure 6.25) with figure 6.11(a,c,e) at $H = 100$. However, the unstable/subcritical solution at $H = 30$ looks completely different as shown in figure 6.26(b,d,f). (Note that the height and length ratios between two sets of images in figures 6.26(a, c, e) and 6.26(b, d, f) in the first and second column of figure 6.26 have been set proportional to $H_1/H_2 = 5/3$ and $L_{x1}/L_{x2} = k_{x2}/k_{x1} \approx 1.75$, respectively.) In the latter case the particle bands/clusters are wavy and aligned primarily along the streamwise direction, which is in contrast to oblique clusters observed for stable/supercritical solutions in figure 6.26(a,c,e). The density field in figure 6.26(b) has some resemblance to the sinuous stationary mode found in particle simulations of Conway *et al.* (2006). (The solution for the corresponding stable branch, which requires the second Landau coefficient, is expected to remain similar since it represents a continuation of the unstable branch, see figure 6.2f.)

The effect of the Couette gap on the dominant travelling instability, corresponding to the second peak on thick solid line in figure 6.24, has been studied at $\phi^0 = 0.2$ for a range of $H \in (25, 200)$, but we do not show these results for the sake of brevity. We found that the flow is linearly unstable to the dominant travelling instability (i.e. $a_l^d > 0$) beyond $H = H_c^{TW} \sim 85.5$. Here too we have subcritical and supercritical Hopf bifurcations over $H \in (78.5, 85.5)$ and $H > 85.5$, respectively. Over the subcritical range $H \in (78.5, 85.5)$, the flow is found to be susceptible to the mean-flow resonance (since this range of H belongs to the stable regime where

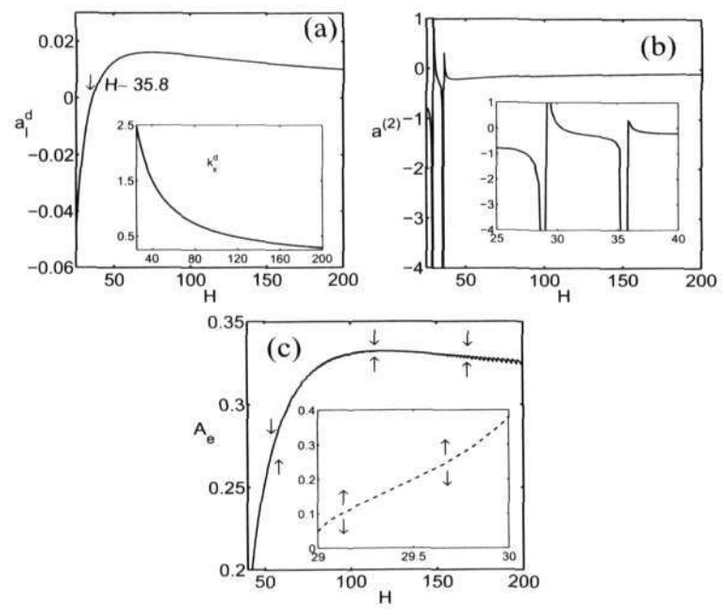

Figure 6.25: Effect of the Couette gap on the dominant stationary instability at $\phi^0 = 0.2$ and $e = 0.8$: (*a*) a_l^d (main panel) and k_x^d (inset); (*b*) $a^{(2)}$; (*c*) 'supercritical' equilibrium amplitude (main panel) for $H > 36$ and 'subcritical' amplitude (inset) for $H \in (29, 30)$.

the shear-banding modes, which participate in creating the mean-flow resonance, exists, see §6.7.3 at different values of H. The patterns of stable/supercritical nonlinear travelling-wave solutions at $H > 85.5$ (not shown) look similar to those for $H = 100$i, as displayed in figure 6.13. In contrast, the unstable/subcritical nonlinear solution at $H = 80$, shown in figure 6.27 (compare with figure 6.13(*a*,*c*,*e*)), looks markedly different from supercritical solution, even though the underlying linear perturbation fields (i.e. the eigenfunction or the fundamental mode) are similar in both cases. From the density and temperature contours in figure 6.27(*a*, *b*), we find that there are two additional rows of clusters in the bulk along with wall clusters, and the density bands are aligned along the streamwise direction.

Effect of Restitution Coefficient on Dominant Stationary Instability

From figures 6.19 - 6.27 we have seen the effect of density and the Couette gap on the dominant stationary instability for a fixed restitution coefficient of $e = 0.8$. Figure 6.28 shows the variation of the growth rate of the least-stable mode, a_l^d with k_x for few values of $e \in [0.5, 0.99]$ for $\phi^0 = 0.2$ and $H = 100$. The dashed and thick solid lines correspond to $e = 0.5$ and 0.99, respectively. The flow is unstable due to stationary waves for the full range of restitution coefficients $e \in [0.5, 0.99]$. It is clear from this figure that the range of unstable wavenumbers increases with increasing restitution coefficient. The flow is always stable in the elastic limit and becomes unstable for decreasing restitution coefficient.

The variations of dominant growth rate a_d^l and corresponding wavenumber k_x^d are shown in the main panel and in the inset of figure 6.29(*a*). The growth rate of the dominant stationary instability and the corresponding wavenumber increases with the restitution coefficient. Since $a^{(2)} > 0$, see inset of figure 6.29(*b*), thus the bifurcation is supercritical pitchfork bifurcation. The

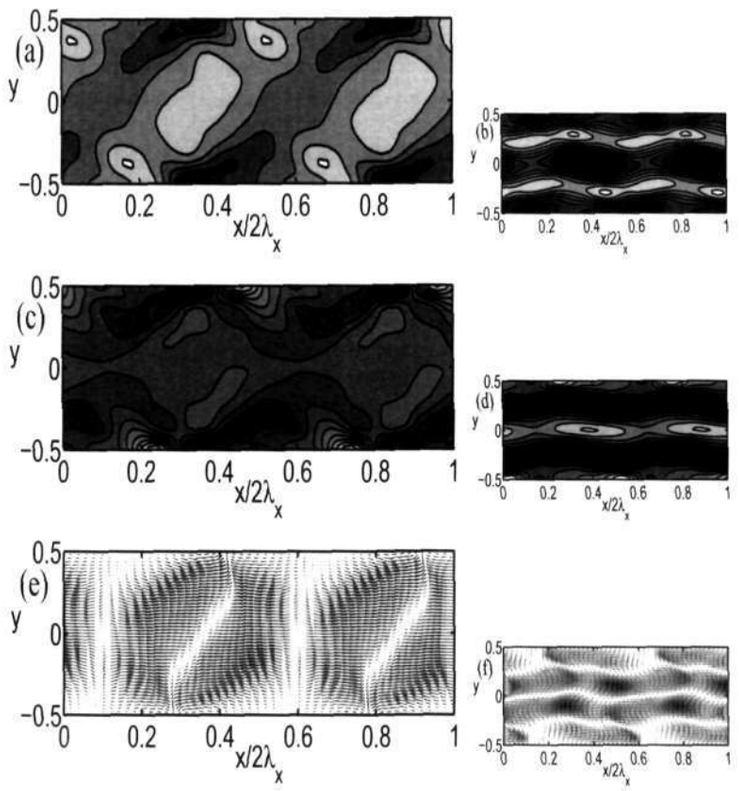

Figure 6.26: Effects of the Couette gap on the nonlinear patterns of density (a, b), granular temperature (c, d) and velocity (e, f) for the dominant stationary instability in figure 6.25: (a, c, e) $H = 50$ and $k_x = 1.18$ (stable solution) and (b, d, f) $H = 30$ and $k_x = 2.05$ (unstable solution).

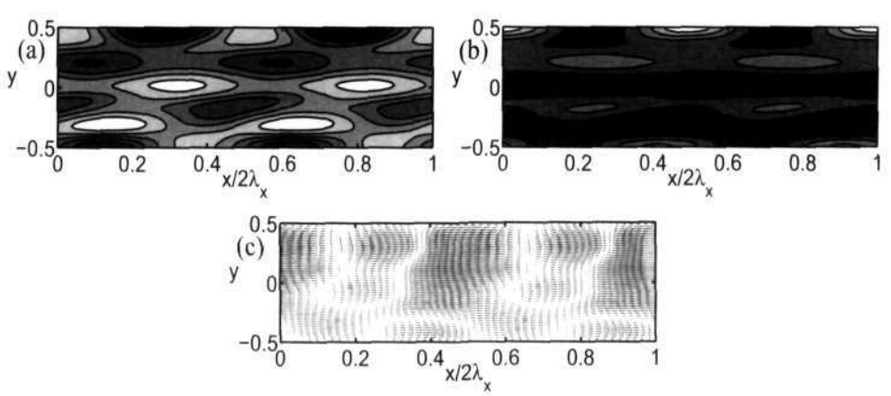

Figure 6.27: Nonlinear travelling patterns ($t = 0$) of (a) density, (b) temperature and (c) velocity field for the subcritical solution at $H = 80$, $\phi = 0.2$, $e = 0.8$ and $k_x = 1.1$.

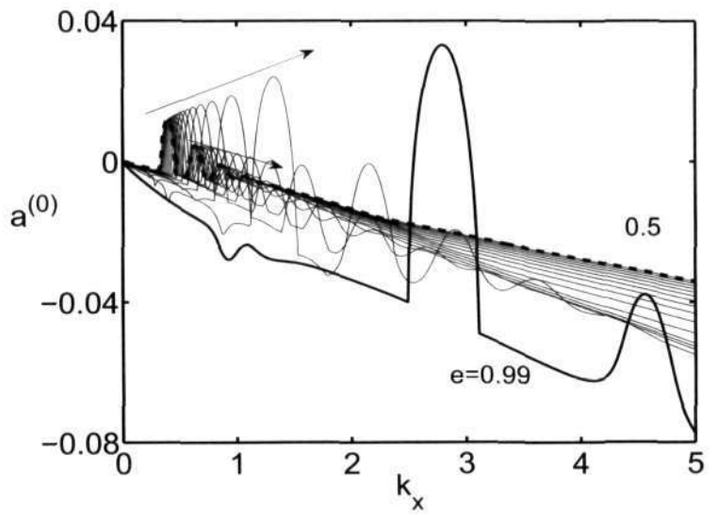

Figure 6.28: Effect of the restitution coefficient on the growth rate of the least-stable mode at $\phi^0 = 0.2$ and $H = 100$.

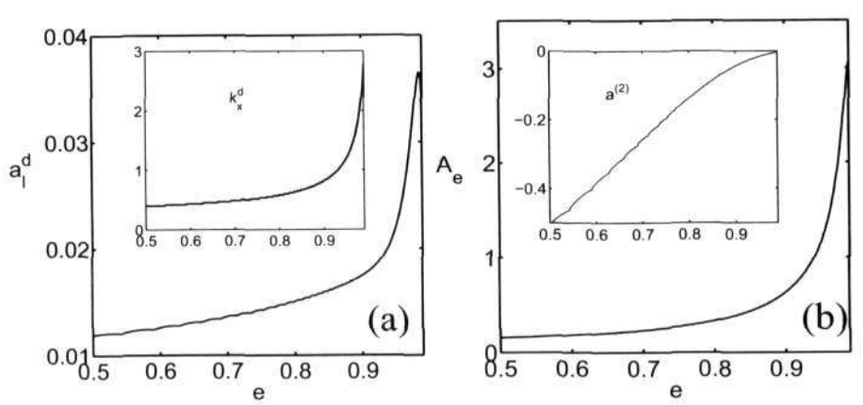

Figure 6.29: Effect of the restitution on the dominant stationary instability, corresponding to the first peak in figure 6.28. (*a*) a_l^d (main panel) and k_x^d (inset); (*b*) supercritical/stable A_e (main panel) and $a^{(2)}$ (inset).

variation of the equilibrium amplitude with the restitution coefficient is shown in the main panel of figure 6.29(b).

6.7.5 Effect of Restitution Coefficient at Large H

So far, we have presented most of the results for a single restitution coefficient of $e = 0.8$ (except those figures 6.28 and 6.29), and this was done in continuation of previous linear stability results (Alam & Nott 1998) and nonlinear shear-banding results (Shukla & Alam 2011) of the same problem. It is of interest to know how the values of e, which is a measure of inelastic dissipation in a granular fluid, would affect the nonlinear saturation of dominant stationary and travelling wave instabilities at very large Couette gaps. Here we present brief results at a mean density of $\phi^0 = 0.2$ and a Couette gap of $H = 500$, focussing on a restitution coefficient of $e = 0.95$ that belongs to the quasi-elastic limit ($e \sim 1$).

For $e = 0.95$, $\phi^0 = 0.2$ and $H = 500$, figures 6.30(a) and 6.30(b) show the variations with k_x of the least-stable growth rate $a_l^{(0)}$ and its phase velocity c_{ph}, and the real part of the first Landau coefficient $a^{(2)}$, respectively. As explained in §6.7.3, the discontinuities on the $a^{(2)}$-curve in figure 6.30(b) signal the onset of mean-flow resonance (6.32). The first peak on the growth rate curve in figure 6.30(a) corresponds to the dominant stationary ($c_{ph} = 0$, see dot-dashed line) instability since the global maximum of $a_l^{(0)}$ over all k_x belongs to this peak; see, the upper inset in figure 6.30(c) for a zoomed-view of this peak which is located at $k_x \sim 0.22$. The second peak of the $a_l^{(0)}$-curve belongs to the dominant travelling ($c_{ph} \neq 0$) instability. The rest of the growth rate curve in figure 6.30(a) for even larger values of k_x belongs to travelling waves too, except for a small window of $k_x \sim (0.51, 0.535)$ over which the least-stable mode is stationary; see the corresponding variation of $a_l^{(0)}$ in the upper inset of figure 6.30(d).

The variations of $a^{(2)}$ and the equilibrium amplitudes A_e for the above two stationary instabilities are displayed in the main panel and the lower inset, respectively, of figures 6.30(c) and 6.30(d). For both cases, we have supercritical pitchfork bifurcations since $a^{(0)} > 0$ and $a^{(2)} < 0$. The vertical double arrows in figures 6.30(c) and 6.30(d) correspond to k_x-values at which $a^{(2)}$ suffers a jump discontinuity due to the mean-flow resonance. From the lower insets of figures 6.30(c) and 6.30(d), we find that $A_e(k_x \approx 0.22)$ is about five times larger than $A_e(k_x \approx 0.517)$ – therefore, the nonlinear saturation of the 'second-type' stationary instability (at larger k_x) is more likely to occur than the dominant stationary instability (at smaller k_x) even though the growth rate of the former is smaller than that of the latter by about an order of magnitude (compare upper insets in figures 6.30c and 6.30d).

The nonlinear and linear disturbance patterns for the dominant stationary instability, corresponding to the first peak in figure 6.30(a), resemble those in figure 6.11 at $e = 0.8$ and $H = 100$, and hence we do not show them here. However, we focus on patterns for the new stationary waves in figure 6.30(d) at $k_x = 0.517$ (with maximum growth rate). The corresponding nonlinear and linear patterns of perturbation density, granular temperature and velocity field are displayed in figures 6.31(a, c, e) and 6.31(b, d, f), respectively. A comparison between the linear density eigenfunctions in figures 6.11(b) and 6.31(b) suggests that the latter mode has two additional rows of particle clusters near two walls, the signature of which is also evident in the temperature and velocity maps as in figure 6.31(d, f). Therefore, this is a 'new' stationary instability which is structurally different (from that in figure 6.11) and that appears only in wider Couette cells of large H. The corresponding nonlinear patterns also look different as seen in figures 6.31(a, c, e) and 6.11(a, c, e).

We have checked that this new stationary mode persists at other values of e as long as the Couette gap H is large enough. More Specifically, reducing the restitution coefficient e leads to the appearance of this new stationary instability in a system with a smaller Couette gap ($H < 500$), with other parameters being fixed as in figure 6.30.

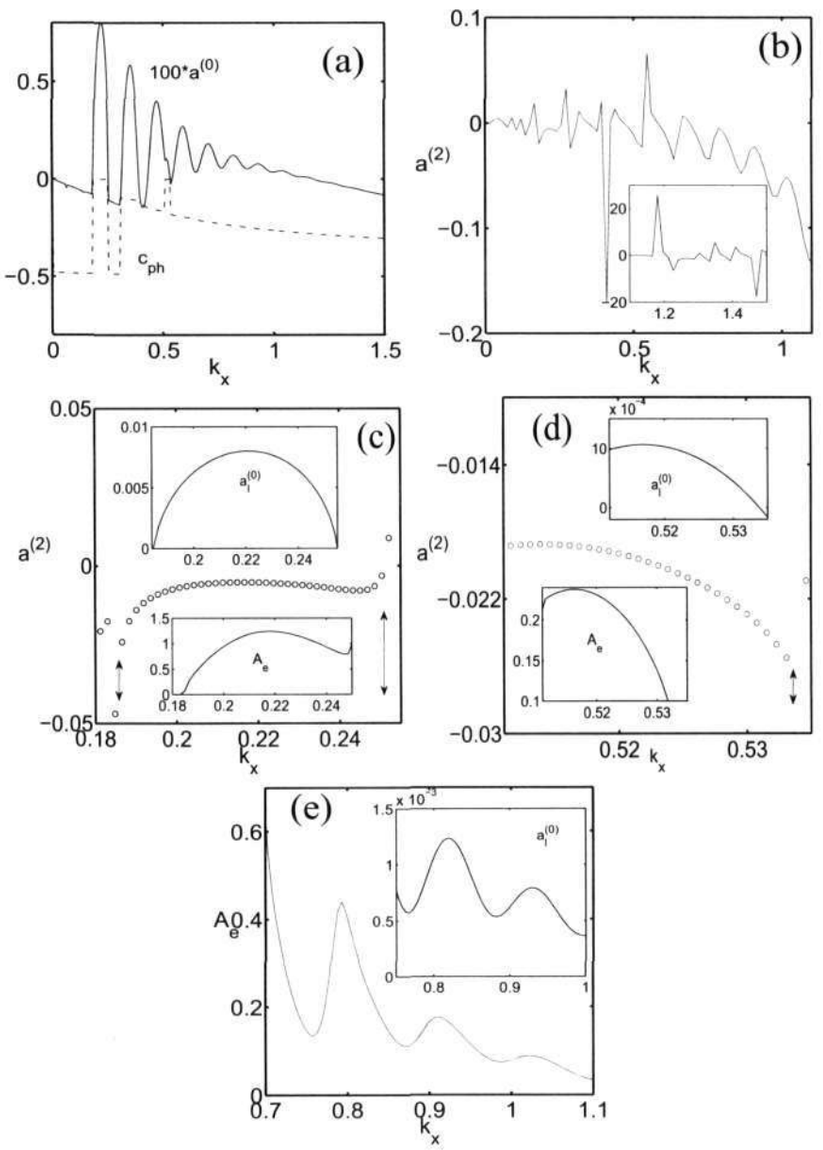

Figure 6.30: (*a-e*) Results in the quasi-elastic limit ($e = 0.95$) for a very large Couette gap $H = 500$ at $\phi^0 = 0.2$. See text for details.

With parameters as in figure 6.30(a), the variations of A_e for larger values of k_x are shown in figure 6.30(e) over which supercritical Hopf bifurcations occur, see the corresponding zoomed variation of $a^{(0)} > 0$ in the inset of figure 6.30(e) and that of $a^{(2)} < 0$ in the main panel of figure 6.30(b). For these travelling waves too, A_e decreases with increasing k_x. We show a comparison between the nonlinear patterns at $k_x = 0.75$ and 1.0 in the first and second columns in figure 6.32, respectively. Both represent backward travelling waves - note that the lengths of images in both columns are proportional to ratio of their wavelengths ($\lambda_{x1}/\lambda_{x2} = k_{x2}/k_{x1} = 4/3$). The patterns of density, temperature and velocity at $k_x = 1$ are more stretched and tenuous around the centreline compared with those at $k_x = 0.75$, but their structures near two walls look similar. The overall structural features of the pattern at $k_x = 1$ have some resemblance to the corresponding dominant travelling wave pattern, see figure 6.13(a,c,e).

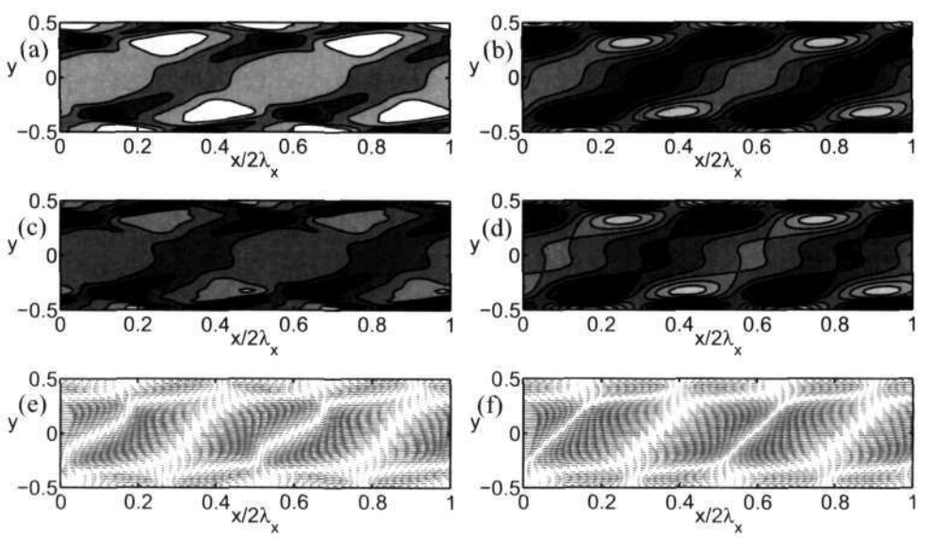

Figure 6.31: Nonlinear (a, c, e) and linear (b, d, f) 'stationary' patterns of (a, b) density, (c, d) temperature and (e, f) velocity fields in the (x, y)-plane. Parameter values are $H = 500$, $e = 0.95$, $\phi = 0.2$ and $k_x = 0.517$ as in figure 6.30(d).

6.8 Conclusions

In this chapter, we have probed nonlinear stability of two-dimensional granular plane Couette flow which is known to be unstable due to a variety of traveling and stationary waves (Alam & Nott 1998), having modulations in both streamwise (x) and gradient (y) directions. The amplitude expansion method (Stuart 1960; Watson 1960; Reynolds & Potter 1967) has been used to derive Landau equation. Along with the linear eigenvalue problem, the mean-flow distortion, the second harmonic, the distortion to the fundamental mode and the first Landau coefficient has been calculated using a spectral-based numerical method.

We have studied the nonlinear equilibrium states and patterns for various bands of wavenumbers ranging from long waves to short waves. The bifurcation analysis for travelling and stationary wave instabilities has been detailed in this chapter. We found that the two-dimensional granular plane Couette flow admits both Hopf and pitchfork bifurcations, that result from travelling and stationary instabilities, respectively.

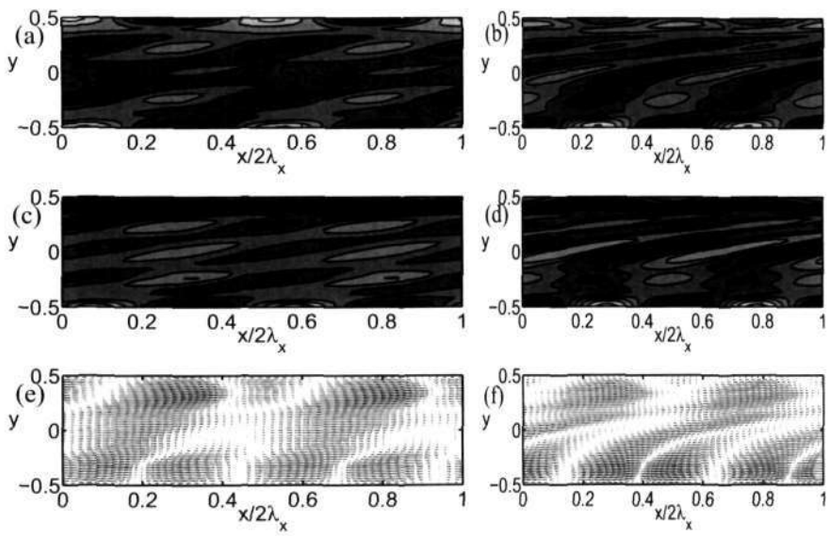

Figure 6.32: Nonlinear patterns of the travelling instability at (a,c,e) $k_x = 0.75$ (first column) and (b,d,f) $k_x = 1.0$ (second column). Parameter values are the same as in figure 6.30.

Our results show that the flow is subcritically unstable to stationary finite amplitude perturbations of long wavelengths ($k_x \sim 0$, where k_x is the streamwise wavenumber) in the dilute limit that evolve from subcritical shearbanding modes ($k_x = 0$), but at large enough Couette gaps there are stationary instabilities with $k_x = O(1)$ that lead to supercritical pitchfork bifurcations. At moderate-to-large densities, in addition to supercritical shearbanding modes, there are long-wave travelling instabilities that lead to Hopf bifurcations. It is shown that both supercritical and subcritical nonlinear states exist at moderate-to-large densities that originate from the dominant stationary and travelling instabilities for which $k_x = O(1)$. Nonlinear patterns of density, velocity and granular temperature for all types of instabilities are contrasted with their linear eigenfunctions. While the supercritical solutions appear to be modulated forms of the fundamental mode, the structural features of unstable subcritical solutions are found to be significantly different from their linear counterparts.

It is shown that the granular plane Couette flow is prone to nonlinear resonances in both stable and unstable regimes. The signature of such resonances is implicated as a discontinuity in the first Landau coefficient. Our analysis identified two types of modal resonances that appear at the quadratic order in perturbation amplitude: (i) a 'mean-flow resonance' which occurs due to the interaction between a streamwise-independent shear-banding mode ($k_x = 0$) and a linear/fundamental mode $k_x \neq 0$, and (ii) an exact '1:2 resonance' that results from the interaction between two waves with their wavenumber ratio being 1:2.

Appendix 6A. Elements of linear and adjoint operators

Elements of linear operator $\mathcal{L} = [l_{ij}]$

$$
\left.\begin{aligned}
l_{11} &= -u^0\tfrac{\partial}{\partial x}, \quad l_{12} = -\phi^0\tfrac{\partial}{\partial x}, \quad l_{13} = -\left(\phi^0_y + \phi^0\tfrac{\partial}{\partial y}\right), \quad l_{14} = 0,\\
l_{21} &= \tfrac{1}{\phi^0 H^2}\left[-p^0_{\phi x} - p^0_\phi\tfrac{\partial}{\partial x} + u^0_y\left(\mu^0_{\phi y} + \mu^0_\phi\tfrac{\partial}{\partial y}\right) + u^0_{yy}\mu^0_\phi\right],\\
l_{22} &= -u^0\tfrac{\partial}{\partial x} + \tfrac{1}{\phi^0 H^2}\left((2\mu^0+\lambda^0)\tfrac{\partial^2}{\partial x^2} + \mu^0_y\tfrac{\partial}{\partial y} + \mu^0\tfrac{\partial^2}{\partial y^2}\right),\\
l_{23} &= -u^0_y + \tfrac{1}{\phi^0 H^2}\left(\mu^0_y\tfrac{\partial}{\partial x} + (\mu^0+\lambda^0)\tfrac{\partial^2}{\partial x\partial y}\right),\\
l_{24} &= \tfrac{1}{\phi^0 H^2}\left[-p^0_{Tx} - p^0_T\tfrac{\partial}{\partial x} + u^0_y\left(\mu^0_{Ty} + \mu^0_T\tfrac{\partial}{\partial y}\right) + u^0_{yy}\mu^0_T\right],\\
l_{31} &= \tfrac{1}{\phi^0 H^2}\left(u^0_y\mu^0_\phi\tfrac{\partial}{\partial x} - p^0_{\phi y} - p^0_\phi\tfrac{\partial}{\partial y}\right),\\
l_{32} &= \tfrac{1}{\phi^0 H^2}\left(\lambda^0_y\tfrac{\partial}{\partial x} + (\lambda^0+\mu^0)\tfrac{\partial^2}{\partial x\partial y}\right),\\
l_{33} &= -u^0\tfrac{\partial}{\partial x} + \tfrac{1}{\phi^0 H^2}\left(\mu^0\tfrac{\partial^2}{\partial x^2} + (2\mu^0_y + \lambda^0_y)\tfrac{\partial}{\partial y} + (2\mu^0+\lambda^0)\tfrac{\partial^2}{\partial y^2}\right),\\
l_{34} &= \tfrac{1}{\phi^0 H^2}\left(u^0_y\mu^0_T\tfrac{\partial}{\partial x} - p^0_{Ty} - p^0_T\tfrac{\partial}{\partial y}\right),\\
l_{41} &= \tfrac{2}{\phi^0 d}\left[\tfrac{1}{H^2}\left(T^0_y\kappa^0_{\phi y} + T^0_y\kappa^0_\phi\tfrac{\partial}{\partial y} + \kappa^0_\phi T^0_{yy}\right) + \mu^0_\phi(u^0_y)^2 - \mathcal{D}^0_\phi\right],\\
l_{42} &= \tfrac{2}{\phi^0 d}\left[-p^0\tfrac{\partial}{\partial x} + 2\mu^0 u^0_y\tfrac{\partial}{\partial y}\right],\\
l_{43} &= -T^0_y + \tfrac{2}{\phi^0 d}\left[-p^0\tfrac{\partial}{\partial y} + 2\mu^0 u^0_y\tfrac{\partial}{\partial x}\right],\\
l_{44} &= -u^0\tfrac{\partial}{\partial x} + \tfrac{2}{\phi^0 d}\left[\tfrac{1}{H^2}\left(\kappa^0\tfrac{\partial^2}{\partial x^2} + \left(T^0_y\kappa^0_{Ty} + \kappa^0_T T^0_{yy}\right)\right.\right.\\
&\quad \left.\left. + \left(\kappa^0_y + T^0_y\kappa^0_T\right)\tfrac{\partial}{\partial y} + \kappa^0\tfrac{\partial^2}{\partial y^2}\right) + \mu^0_T(u^0_y)^2 - \mathcal{D}^0_T\right]
\end{aligned}\right\}
$$

Adjoint matrix elements $\mathbf{L}^\dagger = [l^\dagger_{ij}]$

$$
\left.\begin{aligned}
l^\dagger_{11} &= ik_x u^0 \qquad l^\dagger_{12} = \tfrac{ik_x p^0_\phi}{\phi^0 H^2} + \tfrac{\mu^0_\phi u^0_y}{(\phi^0 H)^2}\left(\phi^0_y - \phi^0 D\right)\\
l^\dagger_{13} &= -\tfrac{ik_x u^0_y \mu^0_\phi}{\phi^0 H^2} + \tfrac{p^0_\phi}{(\phi^0 H)^2}\left(\phi^0 D - \phi^0_y\right) \quad l^\dagger_{14} = \tfrac{2(\mu^0_\phi {u^0_y}^2 - \mathcal{D}^0_\phi)}{\phi^0\, dim} + \tfrac{2\kappa^0_\phi T^0_y}{(\phi^0 H)^2\, dim}(\phi^0_y - \phi^0 D)\\
l^\dagger_{21} &= ik_x\phi^0\\
l^\dagger_{22} &= ik_x u^0 - \tfrac{k_x^2(2\mu^0+\lambda^0)}{\phi^0 H^2} + \tfrac{1}{(\phi^0 H)^2}\left[-\mu^0_y\phi^0_y - \mu^0\phi^0_{yy}\right.\\
&\quad \left. + (\phi^0\mu^0_y - 2\phi^0_y\mu^0)D + \phi^0\mu^0 D^2 + \tfrac{2{\phi^0_y}^2\mu^0}{\phi^0}\right]\\
l^\dagger_{23} &= \tfrac{ik_x}{(\phi^0 H)^2}\left[(\mu^0+\lambda^0)(\phi^0 D - \phi^0_y) + \phi^0\mu^0_y\right]\\
l^\dagger_{24} &= \tfrac{2ik_x p^0}{\phi^0\, dim} - \tfrac{4}{(\phi^0)^2\, dim}\left[\phi^0\left(\mu^0 u^0_y D + \mu^0_y u^0_y + \mu^0 u^0_{yy}\right) - \phi^0_y\mu^0 u^0_y\right]\\
l^\dagger_{31} &= \phi^0 D\\
l^\dagger_{32} &= -u^0_y + \tfrac{ik_x}{(\phi^0 H)^2}\left[(\mu^0+\lambda^0)(\phi^0 D - \phi^0_y) + \phi^0\lambda^0_y\right]\\
l^\dagger_{33} &= ik_x u^0 - \tfrac{k_x^2\mu^0}{\phi^0 H^2} + \tfrac{1}{(\phi^0)^2 H^2}\left[-(2\mu^0_y + \lambda^0_y)\phi^0_y - (2\mu^0+\lambda^0)\phi^0_{yy}\right.\\
&\quad \left. + \left(\phi^0(2\mu^0_y + \lambda^0_y) - 2\phi^0_y(2\mu^0+\lambda^0)\right)D + \phi^0(2\mu^0+\lambda^0)D^2 + \tfrac{2{\phi^0_y}^2(2\mu^0+\lambda^0)}{\phi^0}\right]\\
l^\dagger_{34} &= -T^0_y - \tfrac{4ik_x\mu^0 u^0_y}{\phi^0\, dim} + \tfrac{2}{(\phi^0)^2\, dim}\left[p^0(\phi^0 D - \phi^0_y) + \phi^0 p^0_y\right]\\
l^\dagger_{41} &= 0, \qquad l^\dagger_{42} = \tfrac{ik_x p^0_T}{\phi^0 H^2} + \tfrac{\mu^0_T u^0_y}{(\phi^0 H)^2}\left(\phi^0_y - \phi^0 D\right) \quad l^\dagger_{43} = \tfrac{-ik_x u^0_y \mu^0_T}{\phi^0 H^2} + \tfrac{p^0_T}{(\phi^0 H)^2}\left(\phi^0 D - \phi^0_y\right)\\
l^\dagger_{44} &= ik_x u^0 + \tfrac{2}{\phi^0\, dim}\left[-\tfrac{k_x^2\kappa^0}{H^2} + \mu^0_T(u^0_y)^2 - \mathcal{D}^0_T\right] + \tfrac{2}{(\phi^0 H)^2\, dim}\left[\phi^0\kappa_y D\right.\\
&\quad \left. - \phi^0 T^0_y\kappa^0_T D + \phi^0_y T^0_y\kappa^0_T + \phi^0\kappa^0 D^2 - 2\phi^0_y\kappa^0 D - \phi^0_{yy}\kappa^0 - \phi^0_y\kappa^0_y + \tfrac{2({\phi^0_y})^2\kappa^0}{\phi^0}\right]
\end{aligned}\right\}
$$

Appendix 6B. Nonlinear Terms ($\mathcal{N}_2$ and $\mathcal{N}_3$)

In the following, the subscript ϕ, T, x and y indicate partial derivative with respect to ϕ, T, x and y, respectively, and superscript 0 indicates the values being calculated at the base state. For example

$$\left.\begin{array}{lll} \mu^0_{\phi y} & = & \mu^0_{\phi\phi}\phi^0_y + \mu^0_{\phi T}T^0_y, \qquad \mu^0_{Ty} = \mu^0_{T\phi}\phi^0_y + \mu^0_{TT}T^0_y, \\ \mu^0_{\phi\phi y} & = & \mu^0_{\phi\phi\phi}\phi^0_y + \mu^0_{\phi\phi T}T^0_y, \qquad \mu^0_{TTy} = \mu^0_{TT\phi}\phi^0_y + \mu^0_{TTT}T^0_y \end{array}\right\}$$

The quadratic and cubic nonlinear terms of disturbance equation can be written in vector forms: $\mathcal{N}_2 = (\mathcal{N}_2^1, \mathcal{N}_2^2, \mathcal{N}_2^3, \mathcal{N}_2^4)^{Tr}$ and $\mathcal{N}_3 = (\mathcal{N}_3^1, \mathcal{N}_3^2, \mathcal{N}_3^3, \mathcal{N}_3^4)$ where the superscript 1, 2, 3 and 4 correspond to terms from mass, x-momentum, y-momentum and energy equations, respectively, as given below.

$$\mathcal{N}_2^1 = -\frac{\partial(\phi' u')}{\partial x} - \frac{\partial(\phi' v')}{\partial y} \quad \text{and} \quad \mathcal{N}_3^1 = 0.$$

$$\begin{aligned}
\mathcal{N}_2^2 = & -\frac{1}{\phi^0}\left[\phi^0(\mathbf{u}'.\nabla)u' + \phi'\left(\frac{\partial u'}{\partial t} + u^0\frac{\partial u'}{\partial x} + u^0_y v'\right)\right] \\
& + \frac{1}{\phi^0 H^2}\left[-\left(p^0_{\phi\phi}\phi'\frac{\partial\phi'}{\partial x} + p^0_{TT}T'\frac{\partial T'}{\partial x} + p^0_{\phi T}\phi'\frac{\partial T'}{\partial x} + p^0_{\phi T}T'\frac{\partial\phi'}{\partial x}\right)\right. \\
& + 2\left(\mu^0_\phi\phi' + \mu^0_T T'\right)\frac{\partial^2 u'}{\partial x^2} + 2\left(\mu^0_\phi\frac{\partial\phi'}{\partial x} + \mu^0_T\frac{\partial T'}{\partial x}\right)\frac{\partial u'}{\partial x} + (\lambda^0_\phi\phi' + \lambda^0_T T')\frac{\partial(\nabla.\mathbf{u}')}{\partial x} \\
& + \left(\lambda^0_\phi\frac{\partial\phi'}{\partial x} + \lambda^0_T\frac{\partial T'}{\partial x}\right)(\nabla.\mathbf{u}') + \left(\frac{1}{2}\mu^0_{\phi\phi}\phi'^2 + \frac{1}{2}\mu^0_{TT}T'^2 + \mu^0_{\phi T}T'^2\right) \\
& + (\mu^0_\phi\phi' + \mu^0_T T')\frac{\partial}{\partial y}\left(\frac{\partial u'}{\partial y} + \frac{\partial v'}{\partial x}\right) + \left(\frac{\partial u'}{\partial y} + \frac{\partial v'}{\partial x}\right)\left(\mu^0_{\phi y}\phi' + \mu^0_\phi\frac{\partial\phi'}{\partial y} + \mu^0_{Ty}T' + \mu^0_T\frac{\partial T'}{\partial y}\right) \\
& \left. + \left(\frac{1}{2}\mu^0_{\phi\phi y}\phi'^2 + \mu^0_{\phi\phi}\phi'\frac{\partial\phi'}{\partial y} + \frac{1}{2}\mu^0_{TTy}T'^2 + \mu^0_{TT}T'\frac{\partial T'}{\partial y} + \mu^0_{\phi Ty}\phi'T' + \mu^0_{\phi T}\frac{\partial\phi' T'}{\partial y}\right)\right] \\
\mathcal{N}_3^2 = & -\frac{1}{\phi^0}\phi'(\mathbf{u}'.\nabla)u' + \frac{1}{\phi^0 H^2}\left[-\frac{\partial}{\partial x}\left(\frac{1}{6}p^0_{\phi\phi\phi}\phi'^3 + \frac{1}{6}p^0_{TTT}T'^3 + \frac{1}{2}p^0_{\phi\phi T}\phi'^2 T' + \frac{1}{2}p^0_{\phi TT}\phi' T'^2\right)\right. \\
& + 2\left(\frac{1}{2}\mu^0_{\phi\phi}\phi'^2 + \frac{1}{2}\mu^0_{TT}T'^2 + \mu^0_{\phi T}\phi'T'\right)\frac{\partial^2 u'}{\partial x^2} + 2\frac{\partial}{\partial x}\left(\frac{1}{2}\mu^0_{\phi\phi}\phi'^2 + \frac{1}{2}\mu^0_{TT}T'^2 + \mu^0_{\phi T}\phi'T'\right)\frac{\partial u'}{\partial x} \\
& + \left(\frac{1}{2}\lambda^0_{\phi\phi}\phi'^2 + \frac{1}{2}\lambda^0_{TT}T'^2 + \lambda^0_{\phi T}\phi'T'\right)\frac{\partial(\nabla.\mathbf{u}')}{\partial x} + \frac{\partial}{\partial x}\left(\frac{1}{2}\lambda^0_{\phi\phi}\phi'^2 + + \frac{1}{2}\lambda^0_{TT}T'^2 + \lambda^0_{\phi T}\phi'T'\right)(\nabla.\mathbf{u}') \\
& + u^0_{yy}\left(\frac{1}{6}\mu^0_{\phi\phi\phi}\phi'^3 + \frac{1}{6}\mu^0_{TTT}T'^3 + \frac{1}{2}\mu^0_{\phi\phi T}\phi'^2 T' + \frac{1}{2}\mu^0_{\phi TT}\phi' T'^2\right) \\
& + \left(\frac{1}{2}\mu^0_{\phi\phi}\phi'^2 + \frac{1}{2}\mu^0_{TT}T'^2 + \mu^0_{\phi T}\phi'T'\right)\frac{\partial}{\partial y}\left(\frac{\partial u'}{\partial y} + \frac{\partial v'}{\partial x}\right) \\
& + u^0_y\left(\frac{1}{6}\mu^0_{\phi\phi\phi y}\phi'^3 + \frac{1}{6}\mu^0_{\phi\phi\phi}\frac{\partial\phi'^3}{\partial y} + \frac{1}{6}\mu^0_{TTTy}T'^3 + \frac{1}{6}\mu^0_{TTT}\frac{\partial T'^3}{\partial y}\right. \\
& \left. + \frac{1}{2}\mu^0_{\phi\phi Ty}\phi'^2 T' + \frac{1}{2}\mu^0_{\phi\phi T}\frac{\partial\phi'^2 T'}{\partial y} + \frac{1}{2}\mu^0_{\phi TTy}\phi' T'^2 + \frac{1}{2}\mu^0_{\phi TT}\frac{\partial\phi' T'^2}{\partial y}\right) \\
& \left. + \left(\frac{\partial u'}{\partial y} + \frac{\partial v'}{\partial x}\right)\left(\frac{1}{2}\mu^0_{\phi\phi y}\phi'^2 + \frac{1}{2}\mu^0_{\phi\phi}\frac{\partial\phi'^2}{\partial y} + \frac{1}{2}\mu^0_{TTy}T'^2 + \frac{1}{2}\mu^0_{TT}\frac{\partial T'^2}{\partial y} + \mu^0_{\phi Ty}\phi'T' + \mu^0_{\phi T}\frac{\partial\phi' T'}{\partial y}\right)\right]
\end{aligned}$$

$$
\begin{aligned}
\mathcal{N}_2^3 &= -\frac{1}{\phi^0}\left[\phi^0(\mathbf{u}'.\nabla)v' + \phi'\left(\frac{\partial v'}{\partial t} + u^0\frac{\partial v'}{\partial x}\right)\right] \\
&+\frac{1}{\phi^0 H^2}\left[-\left(\frac{1}{2}p^0_{\phi\phi y}\phi'^2 + \frac{1}{2}p^0_{\phi\phi}\frac{\partial \phi'^2}{\partial y} + \frac{1}{2}p^0_{TTy}T'^2 + \frac{1}{2}p^0_{TT}\frac{\partial T'^2}{\partial y} + p^0_{\phi Ty}\phi'T' + p^0_{\phi T}\frac{\partial \phi' T'}{\partial y}\right)\right. \\
&+2\left(\mu^0_\phi\phi' + \mu^0_T T'\right)\frac{\partial^2 v'}{\partial y^2} + 2\left(\mu^0_{\phi y}\phi' + \mu^0_\phi\frac{\partial \phi'}{\partial y} + \mu^0_{Ty}T' + \mu^0_T\frac{\partial T'}{\partial y}\right)\frac{\partial v'}{\partial y} \\
&+\left(\lambda^0_\phi\phi' + \lambda^0_T T'\right)\frac{\partial(\nabla.\mathbf{u}')}{\partial y} + \left(\lambda^0_{\phi y}\phi' + \lambda^0_\phi\frac{\partial \phi'}{\partial y} + \lambda^0_{Ty}T' + \lambda^0_T\frac{\partial T'}{\partial y}\right)(\nabla.\mathbf{u}') \\
&+(\mu^0_\phi\phi' + \mu^0_T T')\frac{\partial}{\partial x}\left(\frac{\partial u'}{\partial y} + \frac{\partial v'}{\partial x}\right) + u^0_y\frac{\partial}{\partial x}\left(\frac{1}{2}\mu^0_{\phi\phi}\phi'^2 + \frac{1}{2}\mu^0_{TT}T'^2 + \mu^0_{\phi T}\phi'T'\right) \\
&\left.+\left(\mu^0_\phi\frac{\partial \phi'}{\partial x} + \mu^0_T\frac{\partial T'}{\partial x}\right)\left(\frac{\partial u'}{\partial y} + \frac{\partial v'}{\partial x}\right)\right] \\
\mathcal{N}_3^3 &= -\frac{1}{\phi^0}\phi'(\mathbf{u}'.\nabla)v' + \frac{1}{\phi^0 H^2}\left[-\left(\frac{1}{6}p^0_{\phi\phi\phi y}\phi'^3 + \frac{1}{6}p^0_{\phi\phi\phi}\frac{\partial \phi'^3}{\partial y} + \frac{1}{6}p^0_{TTTy}T'^3 + \frac{1}{6}p^0_{TTT}\frac{\partial T'^3}{\partial y}\right.\right. \\
&+\frac{1}{2}p^0_{\phi\phi Ty}\phi'^2 T' + \frac{1}{2}p^0_{\phi\phi T}\frac{\partial \phi'^2 T'}{\partial y} + \frac{1}{2}p^0_{\phi TTy}\phi' T'^2 + \frac{1}{2}p^0_{\phi TT}\frac{\partial \phi' T'^2}{\partial y}\Big) \\
&+2\left(\frac{1}{2}\mu^0_{\phi\phi}\phi'^2 + \frac{1}{2}\mu^0_{TT}T'^2 + \mu^0_{\phi T}\phi'T'\right)\frac{\partial^2 v'}{\partial y^2} \\
&+2\frac{\partial v'}{\partial y}\left(\frac{1}{2}\mu^0_{\phi\phi y}\phi'^2 + \frac{1}{2}\mu^0_{\phi\phi}\frac{\partial \phi'^2}{\partial y} + +\frac{1}{2}\mu^0_{TTy}\phi'^2 + \frac{1}{2}\mu^0_{TT}\frac{\partial T'^2}{\partial y} + \mu^0_{\phi Ty}\phi'T' + \mu^0_{\phi T}\frac{\partial \phi' T'}{\partial y}\right) \\
&+\left(\frac{1}{2}\lambda^0_{\phi\phi}\phi'^2 + \frac{1}{2}\lambda^0_{TT}T'^2 + \lambda^0_{\phi T}\phi'T'\right)\frac{\partial(\nabla.\mathbf{u}')}{\partial y} \\
&+(\nabla.\mathbf{u}')\left(\frac{1}{2}\lambda^0_{\phi\phi y}\phi'^2 + \frac{1}{2}\lambda^0_{\phi\phi}\frac{\partial \phi'^2}{\partial y} + \frac{1}{2}\lambda^0_{TTy}T'^2 + \frac{1}{2}\lambda^0_{TT}\frac{\partial T'^2}{\partial y} + \lambda^0_{\phi Ty}\phi'T' + \lambda^0_{\phi T}\frac{\partial \phi' T'}{\partial y}\right) \\
&+\left(\frac{1}{2}\mu^0_{\phi\phi}\phi'^2 + \frac{1}{2}\mu^0_{TT}T'^2 + \mu^0_{\phi T}\phi'T'\right)\frac{\partial}{\partial x}\left(\frac{\partial u'}{\partial y} + \frac{\partial v'}{\partial x}\right) \\
&+u^0_y\frac{\partial}{\partial x}\left(\frac{1}{6}\mu^0_{\phi\phi\phi}\phi'^3 + \frac{1}{6}\mu^0_{TTT}T'^3 + \frac{1}{2}\mu^0_{\phi\phi T}\phi'^2 T' + \frac{1}{2}\mu^0_{\phi TT}\phi' T'^2\right) \\
&\left.+\frac{\partial}{\partial x}\left(\frac{1}{2}\mu^0_{\phi\phi}\phi'^2 + \frac{1}{2}\mu^0_{TT}T'^2 + \mu^0_{\phi T}\phi'T'\right)\left(\frac{\partial u'}{\partial y} + \frac{\partial v'}{\partial x}\right)\right]
\end{aligned}
$$

$$
\begin{aligned}
\mathcal{N}_2^4 &= -\frac{1}{\phi^0}\left[\phi^0(\mathbf{u}'.\nabla)T' + \phi'\left(\frac{\partial T'}{\partial t} + u^0\frac{\partial T'}{\partial x} + T_y^0 v'\right)\right] \\
&+\frac{2}{\phi^0\, dim}\left[\frac{1}{H^2}\left\{\frac{\partial T'}{\partial x}\left(\kappa_\phi^0\frac{\partial \phi'}{\partial x} + \kappa_T^0\frac{\partial T'}{\partial x}\right) + \frac{\partial^2 T'}{\partial x^2}\left(\kappa_\phi^0\phi' + \kappa_T^0 T'\right)\right.\right. \\
&+T_y^0\left(\frac{1}{2}\kappa_{\phi\phi y}^0\phi'^2 + \frac{1}{2}\kappa_{\phi\phi}^0\frac{\partial \phi'^2}{\partial y} + \frac{1}{2}\kappa_{TTy}^0 T'^2 + \frac{1}{2}\kappa_{TT}^0\frac{\partial T'^2}{\partial y}\right. \\
&\left.+\kappa_{\phi Ty}^0\phi' T' + \kappa_{\phi T}^0\frac{\partial \phi' T'}{\partial y}\right) + T_{yy}^0\left(\frac{1}{2}\kappa_{\phi\phi}^0\phi'^2 + \frac{1}{2}\kappa_{TT}^0 T'^2 + \kappa_{\phi T}^0\phi' T'\right) \\
&\left.\left.+\frac{\partial T'}{\partial y}\left(\kappa_{\phi y}^0\phi' + \kappa_\phi^0\frac{\partial \phi'}{\partial y} + \kappa_{Ty}^0 T' + \kappa_T^0\frac{\partial T'}{\partial y}\right) + \frac{\partial^2 T'}{\partial y^2}\left(\kappa_\phi^0\phi' + \kappa_T^0 T'\right)\right\}\right. \\
&-(p_\phi^0\phi' + p_T^0 T')(\nabla.\mathbf{u}') + 2\mu^0\left\{\left(\frac{\partial u'}{\partial x}\right)^2 + \left(\frac{\partial v'}{\partial y}\right)^2 + \frac{1}{2}\left(\frac{\partial u'}{\partial y} + \frac{\partial v'}{\partial x}\right)^2\right\} \\
&+(u_y^0)^2\left(\frac{1}{2}\mu_{\phi\phi}^0\phi'^2 + \frac{1}{2}\mu_{TT}^0 T'^2 + \mu_{\phi T}^0\phi' T'\right) + 2\,u_y^0\left(\mu_\phi^0\phi' + \mu_T^0 T'\right)\left(\frac{\partial u'}{\partial y} + \frac{\partial v'}{\partial x}\right) \\
&\left.+\lambda^0(\nabla.\mathbf{u}')^2 - \left(\frac{1}{2}\mathcal{D}_{\phi\phi}^0\phi'^2 + \frac{1}{2}\mathcal{D}_{TT}^0 T'^2 + \mathcal{D}_{\phi T}^0\phi' T'\right)\right] \\
\mathcal{N}_3^4 &= -\frac{1}{\phi^0}\,\phi'(\mathbf{u}'.\nabla)T' \\
&+\frac{2}{\phi^0\, dim}\left[\frac{1}{H^2}\left\{\frac{\partial T'}{\partial x}\frac{\partial}{\partial x}\left(\frac{1}{2}\kappa_{\phi\phi}^0\phi'^2 + \frac{1}{2}\kappa_{TT}^0 T'^2 + \kappa_{\phi T}^0\phi' T'\right)\right. \\
&+\frac{\partial^2 T'}{\partial x^2}\left(\frac{1}{2}\kappa_{\phi\phi}^0\phi'^2 + \frac{1}{2}\kappa_{TT}^0 T'^2 + \kappa_{\phi T}^0\phi' T'\right) \\
&+T_y^0\left(\frac{1}{6}\kappa_{\phi\phi\phi y}^0\phi'^3 + \frac{1}{6}\kappa_{\phi\phi\phi}^0\frac{\partial \phi'^3}{\partial y} + \frac{1}{6}\kappa_{TTTy}^0 T'^3 + \frac{1}{6}\kappa_{TTT}^0\frac{\partial T'^3}{\partial y}\right. \\
&\left.+\frac{1}{2}\kappa_{\phi\phi Ty}^0\phi'^2 T' + \frac{1}{2}\kappa_{\phi\phi T}^0\frac{\partial \phi'^2 T'}{\partial y} + \frac{1}{2}\kappa_{\phi TTy}^0\phi' T'^2 + \frac{1}{2}\kappa_{\phi TT}^0\frac{\partial \phi T'^2}{\partial y}\right) \\
&+T_{yy}^0\left(\frac{1}{6}\kappa_{\phi\phi\phi}^0\phi'^3 + +\frac{1}{6}\kappa_{\phi TT}^0 T'^3 + \frac{1}{2}\kappa_{\phi\phi T}^0\phi'^2 T' + \frac{1}{2}\kappa_{\phi TT}^0\phi' T'^2\right) \\
&+\frac{\partial T'}{\partial y}\left(\frac{1}{2}\kappa_{\phi\phi y}^0\phi'^2 + \frac{1}{2}\kappa_{\phi\phi}^0\frac{\partial \phi'^2}{\partial y} + \frac{1}{2}\kappa_{TTy}^0 T'^2 + \frac{1}{2}\kappa_{TT}^0\frac{\partial T'^2}{\partial y}\right. \\
&\left.\left.+\kappa_{\phi Ty}^0\phi' T' + \kappa_{\phi T}^0\frac{\partial \phi' T'}{\partial y}\right) + \frac{\partial^2 T'}{\partial y^2}\left(\frac{1}{2}\kappa_{\phi\phi}^0\phi'^2 + \frac{1}{2}\kappa_{TT}^0 T'^2 + \kappa_{\phi T}^0\phi' T'\right)\right\} \\
&-\left(\frac{1}{2}p_{\phi\phi}^0\phi'^2 + \frac{1}{2}p_{TT}^0 T'^2 + p_{\phi T}^0\phi' T'\right)(\nabla.\mathbf{u}') \\
&+2(\mu_\phi^0\phi' + \mu_T^0 T')\left\{\left(\frac{\partial u'}{\partial x}\right)^2 + \left(\frac{\partial v'}{\partial y}\right)^2 + \frac{1}{2}\left(\frac{\partial u'}{\partial y} + \frac{\partial v'}{\partial x}\right)^2\right\} \\
&+(u_y^0)^2\left(\frac{1}{6}\mu_{\phi\phi\phi}^0\phi'^3 + \frac{1}{6}\mu_{TTT}^0 T'^3 + \frac{1}{2}\mu_{\phi\phi T}^0\phi'^2 T' + \frac{1}{2}\mu_{\phi TT}^0\phi' T'^2\right) \\
&+2u_y^0\left(\frac{1}{2}\mu_{\phi\phi}^0\phi'^2 + \frac{1}{2}\mu_{TT}^0 T'^2 + \mu_{\phi T}^0\phi' T'\right)\left(\frac{\partial u'}{\partial y} + \frac{\partial v'}{\partial x}\right) \\
&+\left(\lambda_\phi^0\phi' + \lambda_T^0 T'\right)(\nabla.\mathbf{u}')^2 \\
&\left.-\left(\frac{1}{6}\mathcal{D}_{\phi\phi\phi}^0\phi'^3 + +\frac{1}{6}\mathcal{D}_{TTT}^0 T'^3 + \frac{1}{2}\mathcal{D}_{\phi\phi T}^0\phi'^2 T' + \frac{1}{2}\mathcal{D}_{\phi TT}^0\phi' T'^2\right)\right]
\end{aligned}
$$

CHAPTER 7

VORTICITY BANDING IN THREE DIMENSIONAL GRANULAR COUETTE FLOW

7.1 Introduction

The rapid granular Couette flow undergoes many ordering transitions due to banding instabilities. The pure spanwise instability leads to segregation of particles, in the form of bands of dense and dilute regions, along the vorticity (spanwise) direction. Recently, density waves, coherent structures and vorticity banding have been observed in large-scale MD simulations of granular Couette flow by (Hopkins *et al.* 1992; Conway & Glasser 2004; Conway *et al.* 2006). Figure 7.1 shows a snapshot from MD simulation of three dimensional granular Couette flow (Conway & Glasser 2004). Three plugs with different mesoscopic structures in the vorticity direction, leading to *vorticity* banding, are shown in figure 7.1.

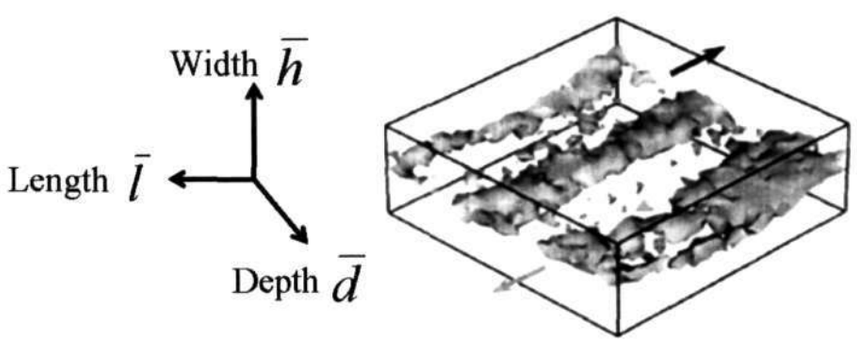

Figure 7.1: Variations of particle densities in sheared granular Couette flow between moving walls. Three plugs are shown. The parameters are: $\bar{l}/\bar{h} = \bar{d}/\bar{h} = 3$, $\phi = 0.05$, $e = 0.6$ and $H = \bar{h}/\bar{d}_p = 50$ where $\bar{l}$, $\bar{h}$ and $\bar{d}$ are the length, width and depth of the system, respectively; $\bar{d}_p$ is the diameter of a particle (see figure 1.28*d* in chapter 1). From Conway & Glasser (2004).

In many complex fluids including granular systems, the homogeneous flow is unstable above a critical applied shear rate or shear stress. The flow then separates into coexisting bands of different internal structures and rheological properties. This phenomenon is known as *shear banding*. Such type of banding is known to occur in many complex fluids having structures that relax on slow time scales, e.g. colloidal suspensions (Hoffman 1972), worm-like micelles (Berret *et al.* 1997), lyotropic liquid crystals (Bonn *et al.* 1998), suspensions of rod-like viruses (Lettinga & Dhont 2004), liquid-liquid biphasic system (Caserta *et al.* 2008), nano-tube suspensions (Lin-Gibson *et al.* 2004), soft glasses (Coussot *et al.* 2002; Holmes *et al.* 2004), wormlike (Britton & Callaghan 1997) and lamellar (Salmon *et al.* 2003) surfactants, side-chain liquid crystalline polymers (Pöschel & Brilliantov 2001). See, for reviews on shearbanding in complex fluids, Fielding (2007), Dhont & Briels (2008), Olmsted (2008) and Schall & van Hecke (2010).

Depending on the direction of banding, two types of banding instability can be classified: gradient banding and vorticity banding. When an applied shear rate exceeds a critical shear rate

the flow breaks into alternate regions of low and high shear rates, respectively, and this is known as gradient banding. In this case the flow separates into bands of different shear rates, connected by sharp interfaces, along the flow gradient direction, as shown in figures 7.2(a) and 7.2(b). The regions of high and low shear rates are shown by a top view of banded state in a cylindrical geometry in figure 7.2(c).

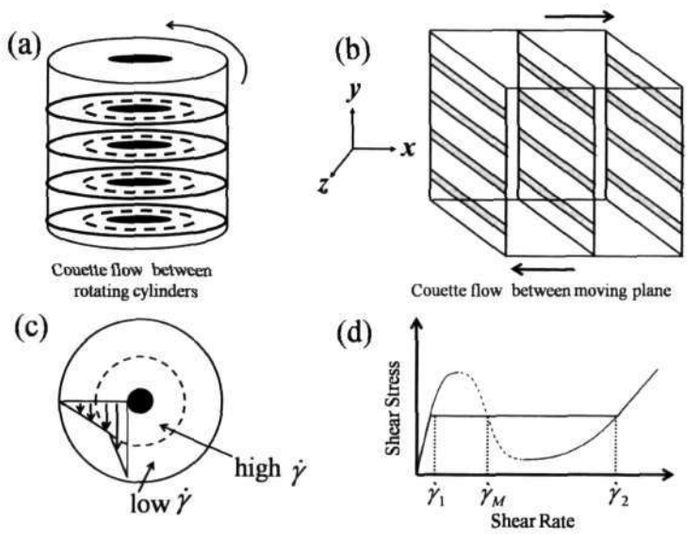

Figure 7.2: Schematic diagram of gradient banding in (a) cylindrical geometry, (b) channel geometry. (c) Cross section of flow in gradient direction showing high and low shear-rate regions and (d) constitutive curve in shear-stress vs. shear-rate plane.

Similarly if the applied shear stress exceed a critical shear stress, the homogeneous flow separates into bands of different shear stresses having the same shear rate along the vorticity (spanwise) direction. The side view of vorticity banding in cylindrical Couette geometry and three-dimensional Couette geometry are illustrated by schematic diagrams 7.3(a) and 7.3(b), with a closure view of a slice of banding being displayed in figure 7.3(c). In this case the regular bands are formed (because shear rates are same in each band) which are stacked along the vorticity direction.

Both types of bandings, gradient and vorticity, originate from the multiple branches of the underlying constitutive curve which is defined as the steady state relation between total applied shear stress and shear rate (or, the shear-stress vs. shear-rate curve when the system was homogeneous). In other words the variation of shear stress with shear rate is "non-monotonic". The constitutive curves for the gradient and vorticity bandings are shown in figures 7.2(c) and 7.2(d), respectively. In each figure the solid and dashed lines represent the stable and unstable branches, respectively. In gradient banding, if the imposed shear rate belongs to the unstable region, for example $\dot{\gamma} = \dot{\gamma}_M$ (see figure 7.2(d)), the homogeneous flow breaks into two bands of shear rates $\dot{\gamma} = \dot{\gamma}_1$ and $\dot{\gamma} = \dot{\gamma}_2$ with same shear stress. Therefore the unstable shear rate demixes the homogeneous flow into a heterogeneous flow with bands of different rheological properties. A similar situation occurs in the vorticity banding, if the imposed shear stress lies within unstable region (dashed line in figure 7.3d), say $\Sigma = \Sigma_M$, the homogeneous flow breaks into two bands having shear stresses $\Sigma = \Sigma_1$ and $\Sigma = \Sigma_2$ with the same shear rate.

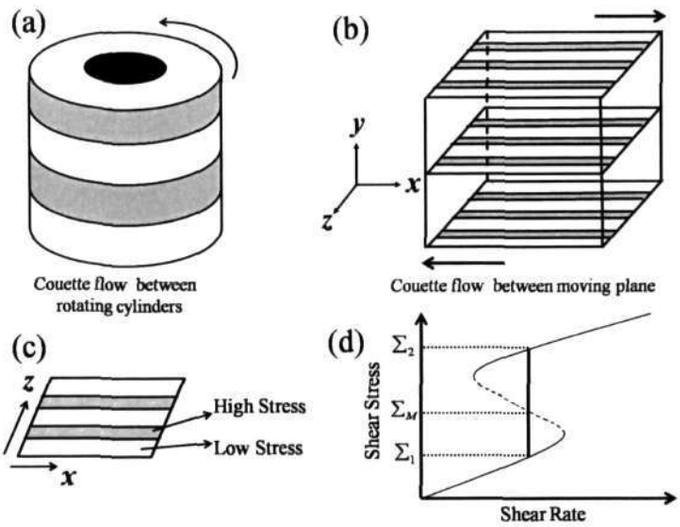

Figure 7.3: Schematic diagram of vorticity banding in (a) cylindrical geometry, (b) channel geometry. (c) Cross section of flow in vorticity direction showing high and low shear-stress regions and (d) constitutive curve in shear-stress vs. shear-rate plane.

7.1.1 Previous Work on Linear Stability

The linear stability analysis (Alam 2006; Gayen & Alam 2006) of three dimensional granular Couette flow shows that the uniform shear flow is unstable due to pure spanwise stationary perturbations for $\phi^0 < \phi^0_{3d}$. The growth rates of pure spanwise instabilities are much larger than the two dimensional streamwise independent instabilities ($k_x = 0$, $k_z = 0$ and $\partial/\partial y \neq 0$, which has been discussed in chapters 4 and 5) for densities $\phi^0 > \phi^0_{2d}$. Recall that the critical density, for two dimensional streamwise independent instabilities leading to shearbanding along the gradient direction, is $\phi^0_{2d} \sim 0.154 > \phi^0_{3d}$. Three dimensional granular Couette flow is unstable due to streamwise-independent instabilities for moderate densities and due to pure spanwise instabilities in the dilute limit. While the two dimensional streamwise independent instabilities lead to shearbanding along the gradient direction in granular plane Couette flow, the pure spanwise instabilities are responsible for banding of particles along vorticity direction in three dimensional granular Couette flow. Many patterns in the form of streamwise structures, density patterns and vortices have been predicted from the linear stability analysis (Alam 2006) for dilute and moderate-to-dense flows. Such patterns have also been observed in three-dimensional molecular dynamics simulations of granular Couette flow (Conway & Glasser 2004). One observation, adopted from Conway & Glasser (2004), of three modulated streamwise rolls parallel to the spanwise direction, which also corresponds to one density band along the gradient direction, is shown in figure 7.1 for $\phi^0 = 0.05$. Although the sink walls have been used in their simulation, the existing linear theory (Alam 2006) with adiabatic walls also supports such banding in dilute limit, originated from pure spanwise instabilities. Irrespective of source or sink or adiabatic walls, the pure-spanwise instability gives rise to vorticity banding in dilute three dimensional granular Couette flow.

Now the question is: are these instability-induced spanwise banding patterns stable/unstable for the finite amplitude perturbations? Can we obtain any equilibrium state for vorticity banding in granular Couette flow, similar to shearbanding in granular plane Couette flow (Shukla &

Alam 2009)? In this chapter, we are trying to answer these questions using an analytical order parameter theory for vorticity banding via Landau equation.

7.1.2 Organization of Present Chapter

This chapter is organized as follows. The non-dimensional form of governing equations (balance of mass, momentum and energy), boundary conditions, base flow and disturbance equations are given in §7.2. The linear stability problem and its adjoint problem are discussed in §7.3. The brief outline of the weakly nonlinear analysis using amplitude expansion method, as explained in chapter 3, is presented in §7.4. In this chapter, §7.2-§7.4 deal with the general three-dimensional granular flow equations ($\frac{\partial}{\partial x} \neq 0$, $\frac{\partial}{\partial y} \neq 0$ and $\frac{\partial}{\partial z} \neq 0$), whereas later sections are specific to the pure spanwise flow equations ($\frac{\partial}{\partial z} \neq 0$, $\frac{\partial}{\partial x} = 0$ and $\frac{\partial}{\partial y} = 0$). Instability in this flow leads to banding of particles along the mean vorticity direction.

The analytical linear stability theory for the pure spanwise instability, asymptotic analysis for finding the eigenvalues, analytical expressions for the linear and adjoint eigenvectors and the locus of neutral stability curve are discussed in §7.5. The analytical weakly nonlinear theory, the analytical expressions for the second harmonic, the distortion of mean flow, the higher order harmonics and the first two Landau coefficients are detailed in §7.6. The phase diagram for nonlinear vorticity banding instability, bifurcation diagrams for subcritical and supercritical bifurcations and the finite amplitude solutions are shown in §7.7. The organization map of this chapter is depicted in figure 7.4 where the dashed arrow indicates that §7.5-§7.7 can be read independently after §7.2.

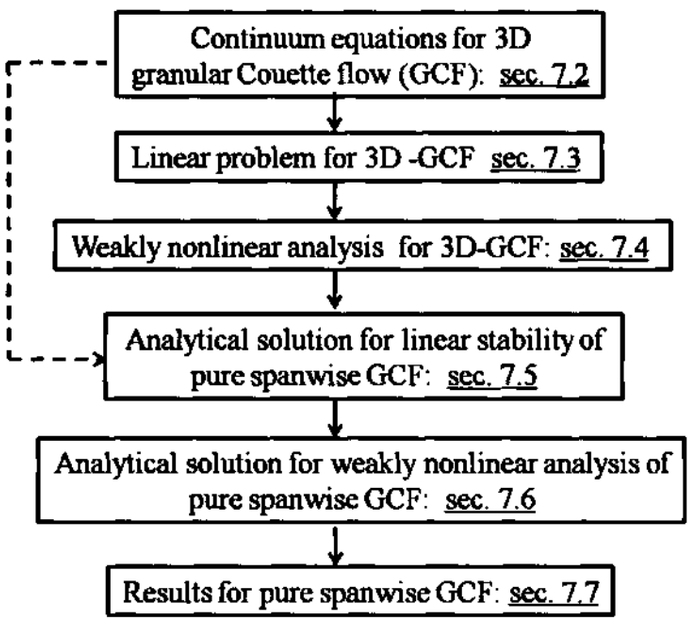

Figure 7.4: Road-map of chapter 7.

7.2 Continuum Equations and Boundary Conditions

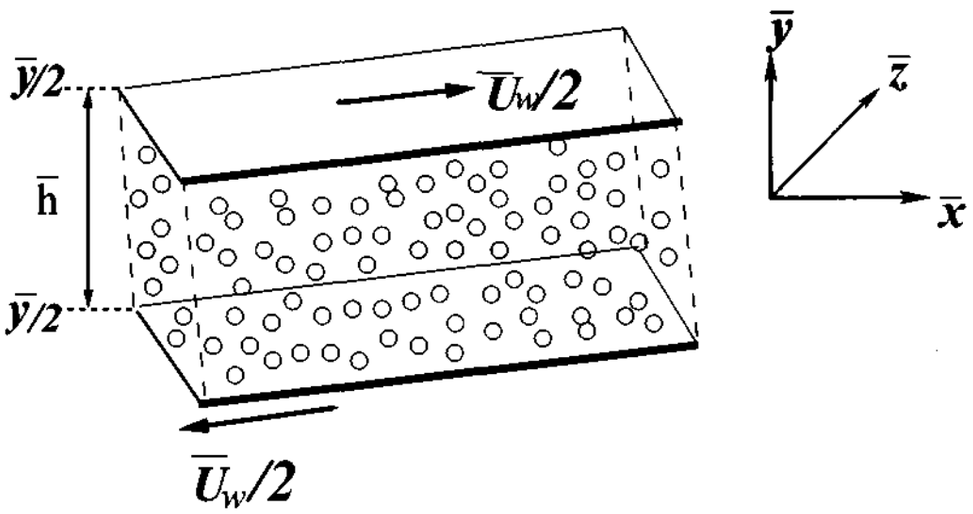

Figure 7.5: Schematic diagram of 3D-granular Couette flow between parallel plates. The upper plate moves with velocity $\overline{U}_w/2$ along the positive $\bar{x}$-direction and the lower plate moves with the same speed in the opposite direction.

We consider a plane Couette flow of granular materials, consisting of monodisperse inelastic particles of diameter $\bar{d}_p$ and material density $\bar{\rho}_p$, between two parallel walls at a distance $\bar{y} = \pm\bar{h}/2$ with $\bar{h}$ being the gap between the walls which move in opposite directions with $\pm\bar{U}_w/2$ velocity in $\pm\bar{x}$-direction. A schematic diagram of 3D Couette flow geometry is shown in figure 7.5. In the co-ordinate system $\bar{x}$, $\bar{y}$ and $\bar{z}$ refer to the streamwise, transverse (gradient) and spanwise directions, respectively. We use wall-to-wall gap ($\bar{h}$) as the reference length scale, the velocity difference between two walls ($\bar{U}_w$) as the reference velocity scale and the inverse of overall shear rate ($\bar{h}/\bar{U}_w$) as the reference time scale (see §4.1 for other related reference scales). The component form of non-dimensional balance of mass, momentum and energy equations without gravity are:

$$\frac{\mathrm{D}\phi}{\mathrm{D}t} = -\phi\nabla\cdot\boldsymbol{u}, \tag{7.1}$$

$$\begin{aligned}\phi\frac{\mathrm{D}u}{\mathrm{D}t} &= -\frac{1}{H^2}\frac{\partial p}{\partial x}+\frac{1}{H^2}\frac{\partial}{\partial x}\left[2\mu\frac{\partial u}{\partial x}+\lambda(\nabla.\boldsymbol{u})\right]\\ &\quad+\frac{1}{H^2}\frac{\partial}{\partial y}\left[\mu\left(\frac{\partial u}{\partial y}+\frac{\partial v}{\partial x}\right)\right]+\frac{1}{H^2}\frac{\partial}{\partial z}\left[\mu\left(\frac{\partial u}{\partial z}+\frac{\partial w}{\partial x}\right)\right],\end{aligned} \tag{7.2}$$

$$\begin{aligned}\phi\frac{\mathrm{D}v}{\mathrm{D}t} &= -\frac{1}{H^2}\frac{\partial p}{\partial y}+\frac{1}{H^2}\frac{\partial}{\partial y}\left[2\mu\frac{\partial v}{\partial y}+\lambda(\nabla\cdot\boldsymbol{u})\right]\\ &\quad+\frac{1}{H^2}\frac{\partial}{\partial z}\left[\mu\left(\frac{\partial v}{\partial z}+\frac{\partial w}{\partial y}\right)\right]+\frac{1}{H^2}\frac{\partial}{\partial x}\left[\mu\left(\frac{\partial u}{\partial y}+\frac{\partial v}{\partial x}\right)\right],\end{aligned} \tag{7.3}$$

$$\begin{aligned}\phi\frac{\mathrm{D}w}{\mathrm{D}t} &= -\frac{1}{H^2}\frac{\partial p}{\partial z}+\frac{1}{H^2}\frac{\partial}{\partial z}\left[2\mu\frac{\partial w}{\partial z}+\lambda(\nabla\cdot\boldsymbol{u})\right]\\ &\quad+\frac{1}{H^2}\frac{\partial}{\partial x}\left[\mu\left(\frac{\partial u}{\partial z}+\frac{\partial w}{\partial x}\right)\right]+\frac{1}{H^2}\frac{\partial}{\partial y}\left[\mu\left(\frac{\partial v}{\partial z}+\frac{\partial w}{\partial y}\right)\right],\end{aligned} \tag{7.4}$$

$$\begin{aligned}\frac{\dim}{2}\phi\frac{\mathrm{D}T}{\mathrm{D}t} &= \frac{1}{H^2}\nabla\cdot\kappa\nabla T-p(\nabla\cdot\boldsymbol{u})\\ &\quad+2\mu\left[\left(\frac{\partial u}{\partial x}\right)^2+\left(\frac{\partial v}{\partial y}\right)^2+\left(\frac{\partial w}{\partial z}\right)^2+\frac{1}{2}\left(\frac{\partial u}{\partial y}+\frac{\partial v}{\partial x}\right)^2\right.\\ &\quad\left.\frac{1}{2}\left(\frac{\partial v}{\partial z}+\frac{\partial w}{\partial y}\right)^2+\frac{1}{2}\left(\frac{\partial w}{\partial x}+\frac{\partial u}{\partial z}\right)^2+\frac{\lambda}{2\mu}(\nabla\cdot\boldsymbol{u})^2\right]-\mathcal{D},\end{aligned} \tag{7.5}$$

where $\mathrm{D}/\mathrm{D}t=\partial/\partial t+\nabla\cdot\boldsymbol{u}$ is the material derivative, $\boldsymbol{u}=(u,v,w)$ is the bulk (coarse-grained) velocity, T is the granular temperature and $H=\overline{h}/\overline{d}_p$ is the dimensionless Couette gap. Here "dim" refers to the dimensionality of the system: for two-dimensions dim = 2 and for three-dimensions dim = 3. In (7.1)-(7.5), p, μ, κ and $\mathcal{D}$ are the pressure, coefficient of shear viscosity, thermal conductivity and the rate of granular energy dissipation, respectively, and $\lambda=\zeta-\frac{2}{\dim}\mu$ with ζ being the bulk viscosity. The dimensionless forms of constitutive relations and the radial distribution function are given by (4.9) and (2.12), respectively.

7.2.1 Uniform Shear Flow

We seek a solution of (7.1)-(7.5) which is steady ($\partial/\partial t=0$), fully developed ($\partial/\partial x=0$) and having no variation in spanwise direction ($\partial/\partial z=0$). Thus we can assume a solution of the form

$$(\phi,u,v,w,T)=(\phi^0(y),u^0(y),0,0,T^0(y)). \tag{7.6}$$

Substituting (7.6) into (7.1)-(7.5), we observe that the mass and z-momentum balance equations are identically satisfied, and other three equations are,

$$\left.\begin{aligned}\tfrac{\mathrm{d}}{\mathrm{d}y}\left(\mu^0\tfrac{\mathrm{d}u^0}{\mathrm{d}y}\right) &= 0\\ \tfrac{\mathrm{d}p^0}{\mathrm{d}y} &= 0\\ \tfrac{1}{H^2}\tfrac{\mathrm{d}}{\mathrm{d}y}\left(\kappa^0\tfrac{\mathrm{d}T^0}{\mathrm{d}y}\right)+\mu^0\left(\tfrac{\mathrm{d}u^0}{\mathrm{d}y}\right)^2-\mathcal{D}^0 &= 0.\end{aligned}\right\} \tag{7.7}$$

With boundary conditions $u^0(y) = v^0(y) = \frac{\mathrm{d}T^0}{\mathrm{d}y} = 0$ at $y \pm 1/2$, the base flow system (7.7) has an analytical solution:

$$\phi^0(y) = \text{const.}, \quad u^0(y) = y \quad \text{and} \quad T^0(y) = \text{const.} = f_2(\phi^0)/f_5(\phi^0, e), \tag{7.8}$$

where f_2 and f_5 are given by (2.21). This solution is a *uniform shear solution* because the shear rate, $\dot{\gamma} = \mathrm{d}u/\mathrm{d}y = \bar{U}_w/\bar{h}$, is uniform (i.e. shear rate is constant) and the volume fraction and granular temperature are constants along transverse direction (y). The base flow equations (7.7) are invariant under the co-ordinate rotation by 180 degree:

$$y \to -y, \qquad (\phi^0, u^0(y), T^0) \to (\phi^0, -u^0(-y), T^0). \tag{7.9}$$

We would like to investigate the weakly nonlinear analysis of *uniform shear flow* under three-dimensional perturbations.

7.2.2 Nonlinear Disturbance Equations

To study the stability of uniform shear flow (7.8) we perturb the flow with small perturbation. We then write each of the flow variables as a sum of base flow and a small perturbation:

$$\left.\begin{aligned} &\phi(x,y,z,t) = \phi^0(y) + \phi'(x,y,z,t) && u(x,y,z,t) = u^0(y) + u'(x,y,z,t) \\ &v(x,y,z,t) = v'(x,y,z,t) && w(x,y,z,t) = w'(x,y,z,t) \\ &T(x,y,z,t) = T^0(y) + T'(x,y,z,t) \end{aligned}\right\}, \tag{7.10}$$

where the superscript '0' denotes the base state variables and primes are perturbations.

Substituting (7.10) into governing equations, (7.1)-(7.5), and subtracting base flow equations (7.7), we obtain the perturbation equations which can be put into matrix form

$$\left(\frac{\partial}{\partial t} - \mathcal{L}\right) X(t,x,y,z) = \mathcal{N} \tag{7.11}$$

where $\mathcal{L}$ is the linear operator,

$$\mathcal{L} \equiv \mathcal{L}\left(\frac{\partial}{\partial x}, \frac{\partial^2}{\partial x^2}, \frac{\partial}{\partial y}, \frac{\partial^2}{\partial y^2}, \frac{\partial}{\partial z}, \frac{\partial^2}{\partial z^2}, \cdots\right), \tag{7.12}$$

$\mathcal{N}$ represents nonlinear terms and $X = (\phi', u', v', w', T)$ is the perturbation vector. The elements of linear operator $\mathcal{L}$ and nonlinear terms up-to cubic order are given in the Appendices 7A and 7B, respectively. The boundary conditions are applied at both walls which have the following matrix form,

$$\mathcal{B}X(t,x,y,z) \equiv \left(1, 1, \frac{\partial}{\partial y}, \frac{\partial}{\partial y}\right)(u', v', w', T') = 0, \quad \text{at } y = \pm 1/2. \tag{7.13}$$

7.3 Linear Problem

In order to formulate linear stability problem, we neglect nonlinear terms of (7.11), i.e.

$$\left(\frac{\partial}{\partial t} - \mathcal{L}\right) X = 0, \quad \text{with} \quad \mathcal{B}X \equiv \left(1, 1, \frac{\partial}{\partial y}, \frac{\partial}{\partial y}\right)(u', v', w', T') = 0, \tag{7.14}$$

where the elements of the linear operator $\mathcal{L}$ are given in Appendix 7A. The coefficients of the linear operator ($\mathcal{L}$) and the boundary operator ($\mathcal{B}$) do not depend explicitly on the streamwise

(x) and spanwise (z) coordinates, this makes (7.14) translational invariant in x and z directions. In fact, we can seek a normal mode solution of (7.14),

$$X(x,y,z,t) = \hat{X}(y)e^{i(k_x x + k_z z)+ct}, \tag{7.15}$$

where k_x and k_z are the streamwise and spanwise wavenumbers, respectively; $c = c_r + ic_i$ is the complex eigenvalue with c_r and c_i being the growth rate and frequency of the perturbation, respectively, and $\hat{X} = (\hat{\phi}, \hat{u}, \hat{v}, \hat{w}, \hat{T})$ is the linear eigenfunction or the fundamental mode. The linear stability of the flow is decided by the real part of c: for negative c_r the flow is stable and unstable for $c_r > 0$. The phase velocity of the perturbation is defined as

$$c_{ph} = -\frac{c_i}{\sqrt{k_x^2 + k_z^2}}. \tag{7.16}$$

Substituting (7.15) into (7.14) and equating the exponential terms we obtain:

$$(c\mathbf{I} - \mathbf{L})\hat{X} = 0 \quad \text{with} \quad \mathcal{B}\hat{X} = 0, \tag{7.17}$$

where

$$\mathbf{L} \equiv \mathcal{L}\left(ik_x, (ik_x)^2, \frac{\mathrm{d}}{\mathrm{d}y}, \frac{\mathrm{d}^2}{\mathrm{d}y^2}, ik_z, (ik_z)^2, \ldots\right). \tag{7.18}$$

It can be verified that the linear eigenvalue problem (7.17) is invariant under the co-ordinate rotation,

$$x \to -x, \quad y \to -y, \quad z \to -z, \quad \omega \to \omega, \quad (\hat{\phi}, \hat{u}, \hat{v}, \hat{w}, \hat{T}) \to (\hat{\phi}, -\hat{u}, -\hat{v}, -\hat{w}, \hat{T}).$$

This implies that for every forward propagating mode there is a backward propagating mode with the same growth rate but having equal and opposite phase speed.

Adjoint Problem

In order to analyze weakly nonlinear stability of the uniform shear flow, we require an adjoint eigenfunction corresponding to the fundamental mode of linear operator $\mathbf{L}$. As discussed in previous chapters, the adjoint problem can be defined as

$$\mathbf{L}^\dagger X^\dagger = \tilde{c} X^\dagger \quad \text{with} \quad \mathcal{B}^\dagger X^\dagger = 0 \tag{7.19}$$

where $\hat{X}^\dagger$ is an adjoint eigenvector, $\mathbf{L}^\dagger$ is the adjoint operator associated with the $\mathbf{L}$ and $\mathcal{B}^\dagger$ is the adjoint boundary operator (see chapter 3 for details on the adjoint problem). It has been verified that the adjoint boundary conditions are same as the boundary conditions of linear problem,

$$\mathcal{B} = \mathcal{B}^\dagger \tag{7.20}$$

The elements of adjoint operator $\mathbf{L}^\dagger$ are given in Appendix 7A.

7.4 Weakly Nonlinear Analysis

The details of the weakly nonlinear analysis using amplitude expansion method have been given in chapter 3 (see §3.3) and therefore we are not showing full analysis for the sake of brevity. However we are rewriting few important equations for the completeness of this chapter.

We employ the following transformation from the (t, x, y, z)-plane to the (θ, A, y)-plane as

suggested by Reynolds & Potter (1967)

$$\theta = k_x x + k_z z + \omega t, \quad \omega = \omega(A) \quad \text{and} \quad A = A(t). \tag{7.21}$$

If we consider a two dimensional system, this transformation would leave the number of independent variables unchanged but for the three dimensional motions, this transformation reduces the dimensionality of the system from four to three. The final reduced form of governing equations as derived in chapter 3 is

$$\left.\begin{array}{rcl} \mathbf{L}_{kn} X^{[k;n]} & = & -c^{[n-1]} X^{[1;1]} \delta_{k1} + \mathbf{G}_{kn} \\ c^{[n-1]} & = & a^{[n-1]} + i b^{[n-1]} \\ \mathbf{G}_{kn} & = & -\left(m a^{[n-m]} + i k b^{[n-m]}\right) X^{\{k;m\}} + \mathbf{E}_{kn}/(1+\delta_{k0}) + \mathbf{F}_{kn} \\ \mathbf{L}_{kn} & = & \left(n a^{(0)} + i k b^{(0)}\right) \mathbf{I} - \mathbf{L}_k \\ \mathbf{L}_k & = & \mathcal{L}(\partial/\partial x \to i k k_x, \partial/\partial x \to d/dy, \partial/\partial z \to i k k_z) \end{array}\right\}, \tag{7.22}$$

where $\mathbf{L}_{kn}$ is a linear operator, $c^{[n-1]}$'s are Landau coefficients, $\mathbf{G}_{kn}$ represents a sum of linear and nonlinear (quadratic and cubic) terms, $\mathbf{I}$ is the identity operator and δ_{kj} is the Kronecker delta; for superscript notations see (3.26)-(3.28). The Landau coefficients can be obtained from the solvability condition (rewriting (3.43)),

$$c^{(n)} = a^{(n)} + i b^{(n)} = \frac{\int_{-1/2}^{1/2} \tilde{X}^\dagger \mathbf{G}_{1n} \, \mathrm{d}y}{\int_{-1/2}^{1/2} \tilde{X}^\dagger X^{[1;1]} \, \mathrm{d}y}. \tag{7.23}$$

Recall from (3.32) and (3.33) that the coefficient $c^{[n-1]}$'s are related to the Landau equation via

$$A^{-1} \frac{\mathrm{d}A}{\mathrm{d}t} = a^{(0)} + A a^{(1)} + A^2 a^{(2)} + \cdots = A^n a^{(n)} \tag{7.24}$$

$$\omega + \frac{\mathrm{d}\omega}{\mathrm{d}A}\left(t \frac{\mathrm{d}A}{\mathrm{d}t}\right) = b^{(0)} + A b^{(1)} + A^2 b^{(2)} + \cdots = A^n b^{(n)}. \tag{7.25}$$

Pure Spanwise Flow: Vorticity Banding

In the rest of this chapter (§7.5-§7.8), we study pure spanwise problem for which the perturbations are independent of x and y directions. Note that such pure spanwise perturbations lead to vorticity banding (i.e. banding of particles along the vorticity direction) in granular Couette flow.

7.5 Linear Stability Analysis for Pure Spanwise Flow

The pure spanwise flow is independent of streamwise (x) and gradient (y) directions and thus we can simplify the linear and nonlinear problems by substituting $\frac{\partial}{\partial x}(.) = \frac{\partial}{\partial y}(.) = 0$ into the governing equations. The explicit form of linear problem (7.14) for the pure spanwise flow is

$$c\hat{X} = \mathbf{L}\hat{X}, \tag{7.26}$$

where $\mathbf{L}$ is given by

$$\mathbf{L} = \begin{pmatrix} 0 & 0 & 0 & -ik_z\phi^0 & 0 \\ 0 & \frac{-\mu^0 k_z^2}{H^2\phi^0} & -u_y^0 & 0 & 0 \\ 0 & 0 & \frac{-\mu^0 k_z^2}{H^2\phi^0} & 0 & 0 \\ \frac{-ik_z p_\phi^0}{H^2\phi^0} & 0 & 0 & \frac{-k_z^2(2\mu^0+\lambda^0)}{H^2\phi^0} & \frac{-ik_z p_T^0}{H^2\phi^0} \\ \frac{2(\mu_\phi^0 - \mathcal{D}_\phi^0)}{\dim\phi^0} & 0 & 0 & \frac{-2ik_z p^0}{\dim\phi^0} & \frac{-2\kappa^0 k_z^2}{\dim H^2\phi^0} + \frac{2(\mu_T^0 - \mathcal{D}_T^0)}{\dim\phi^0} \end{pmatrix}. \tag{7.27}$$

The matrix form of the associated adjoint problem is

$$\tilde{c}X^\dagger = \mathbf{L}^\dagger X^\dagger \tag{7.28}$$

where $\mathbf{L}^\dagger$ is the conjugate transpose of $\mathbf{L}$ and $X^\dagger$ is the related adjoint eigenfunction. Both problems (7.26)-(7.28) can be solved analytically as discussed in following sections.

7.5.1 Asymptotic Analysis and Dispersion Relation

The eigenvalues of (7.27) can be obtained by solving $det(c\,\mathbf{I} - \mathbf{L}) = 0$. In fact, the second and third rows of $\mathbf{L}$, corresponding to x- and y-momentum equations, respectively, are decoupled from the other three rows, and, therefore, these two equations of (7.26)-(7.27) can be solved independently. Thus, from x- and y-momentum equations, we obtain a real eigenvalue with multiplicity two,

$$c = -\mu^0 k_z^2/\phi^0 H^2,$$

which is negative and hence stable. The other three equations (continuity, z-momentum and energy equations) give rise to a cubic dispersion relation,

$$(c^3 + a_2c^2 + a_1c + a_0) = 0, \tag{7.29}$$

where coefficients a_0-a_2 are real which can be expressed in terms of inverse of Couette gap, as defined below:

$$a_0 = a_{02}/H^2 + a_{04}/H^4, \quad a_1 = a_{12}/H^2 + a_{14}/H^4 \quad \text{and} \quad a_2 = a_{20} + a_{22}/H^2,$$

with a_{ij}'s being the functions of the base state variables:

$$\left.\begin{aligned} a_{02} &= \tfrac{2}{3\phi^0}\left(p_\phi^0(\mathcal{D}_T^0 - u_y^{0^2}\mu_T^0) + p_T^0(-\mathcal{D}_\phi^0 + u_y^{0^2}\mu_\phi^0)\right)k_z^2, \\ a_{04} &= \tfrac{2p_\phi^0\kappa^0}{3\phi^0}k_z^4, \\ a_{12} &= \tfrac{2}{3\phi^{0^2}}(2\mu^0+\lambda^0)(\mathcal{D}_T^0 - u_y^{0^2}\mu_T^0)k_z^2 + \tfrac{2p^0p_T^0}{3\phi^{0^2}}k_z^2 + p_\phi^0 k_z^2, \\ a_{14} &= \tfrac{2\kappa^0(2\mu^0+\lambda^0)}{3\phi^{0^2}}k_z^4, \\ a_{20} &= \tfrac{2}{3\phi^0}(\mathcal{D}_T^0 - u_y^{0^2}\mu_T^0), \\ a_{22} &= \tfrac{1}{\phi^0}\left(\tfrac{2\kappa^0}{3} + (2\mu^0+\lambda^0)\right)k_z^2 \end{aligned}\right\}. \tag{7.30}$$

There are two possibilities for three roots of cubic dispersion relation (7.29): (i) all roots are real, and (ii) one is real and a pair of complex conjugate. It can be verified from the asymptotic analysis for large Couette gaps (H), using the inverse of Couette gap as a small expansion parameter, that one eigenvalue is always real and other two can form a complex conjugate pair. The real

eigenvalue has the following approximation for large H:

$$c^{(1)} = c_0^{(1)} - \frac{1}{H^2}\frac{\left(a_{12} + a_{02} + c_0^{(1)} a_{22}\right)}{c_0^{(1)}(3c_0^{(1)} + 2a_{20})} + O\left(\frac{1}{H^4}\right), \text{ with } c_0^{(1)} = -\frac{2}{3\phi^0} f_5^0 T^{0^{1/2}} < 0, \tag{7.31}$$

where $c_0^{(1)}$ is the zeroth order approximation. The complex conjugate pair has the form $c^{(2,3)} = c_r^{(2,3)} \pm i c_i^{(2,3)}$, where

$$c_r^{(2,3)} = \frac{1}{H^2}\frac{\left(\frac{a_{02}}{a_{20}} - a_{12}\right)}{2a_{20}} + O\left(\frac{1}{H^4}\right) \quad \text{and} \quad c_i^{(2,3)} = \frac{1}{H}\sqrt{\frac{a_{02}}{a_{20}}} + O\left(\frac{1}{H^2}\right). \tag{7.32}$$

In the limiting case of $H \to \infty$, $c^{(1)} \to c_0^{(1)}$ and $c^{(2,3)} \to 0$, therefore the flow is neutrally stable for large Couette gaps. In tables 7.1 and 7.2 we compare three eigenvalues for three values of H, which are the roots of (7.29), obtained from the exact cubic solutions and from the asymptotic analysis [cf. (7.31)-(7.32)]. In the limit of large Couette gaps the eigenvalues calculated from the asymptotic analysis are close to those obtained from the exact solutions as shown in tables 7.1 and 7.2.

H	$k_z^* = k_z/H$	Asymptotic analysis	Exact solution of (7.29)
100	0.01	-8.760×10^{-1}	-8.737×10^{-1}
		$-5.895 \times 10^{-4} \pm 1.872 \times 10^{-2}\, i$	$-5.897 \times 10^{-4} \pm 1.872 \times 10^{-2}\, i$
1000	0.001	-8.744×10^{-1}	-8.743×10^{-1}
		$-5.895 \times 10^{-6} \pm 1.872 \times 10^{-3}\, i$	$-5.895 \times 10^{-6} \pm 1.872 \times 10^{-3}\, i$
10000	0.0001	-8.743×10^{-1}	-8.743×10^{-1}
		$-5.895 \times 10^{-8} \pm 1.872 \times 10^{-4} i$	$-5.895 \times 10^{-8} \pm 1.872 \times 10^{-4} i$

Table 7.1: Comparison of eigenvalues between asymptotic analysis and exact values for $\phi^0 = 0.2$, $e = 0.8$ and $k_z = 1$.

H	$k_z^* = k_z/H$	Asymptotic analysis	Exact solution of (7.29)
100	0.01	-3.806503×10^{-1}	-3.638395×10^{-1}
		-3.030242×10^{-2}	-3.086597×10^{-2}
		2.234135×10^{-2}	2.273576×10^{-2}
1000	0.001	-3.704798×10^{-1}	-3.703134×10^{-1}
		-2.671994×10^{-3}	-2.672464×10^{-3}
		2.592383×10^{-3}	2.592837×10^{-3}
10000	0.0001	-3.703781×10^{-1}	-3.703765×10^{-1}
		-2.636169×10^{-4}	-2.636174×10^{-4}
		2.628208×10^{-4}	2.628213×10^{-4}

Table 7.2: Comparison of eigenvalues between asymptotic analysis and exact values for $\phi^0 = 0.05$, $e = 0.8$ and $k_z = 1$.

Figures 7.6(a) and 7.6(b) show the real and imaginary parts of three eigenvalues of (7.29) with ϕ^0, (circles, stars and triangles) for $k_z^* = k_z/H = 0.05$ and $e = 0.8$. It is seen in figure 7.6 that the growth rate, c_r, of one of the eigenvalues (stars) is real ($c_i = 0$) and positive for $\phi^0 < 0.1$

and hence unstable. The origin of the vorticity banding instability can be traced to the complex-conjugate modes (Gayen & Alam 2006) which merge at $\phi^0 \sim 0.1$ and give rise to two stationary modes in dilute regime as shown in figure 7.6. Figures 7.7 and 7.8 are same as figure 7.6 but for

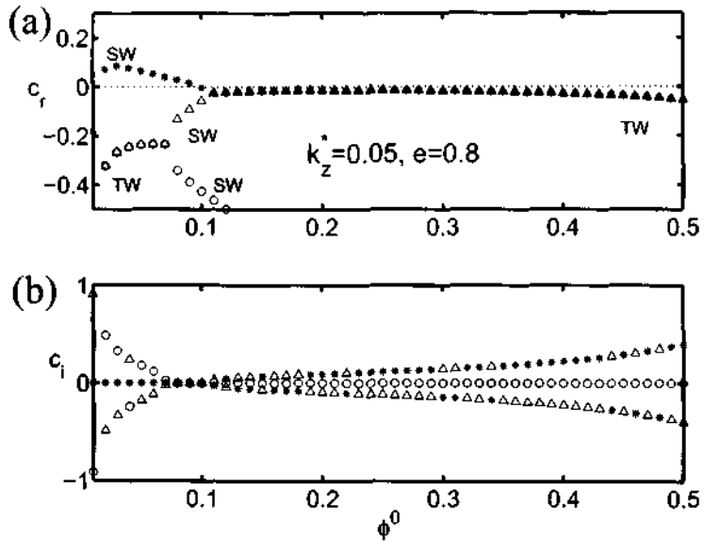

Figure 7.6: Variations of three eigenvalues of cubic dispersion relation (7.29) with ϕ^0, (a) real part and (b) imaginary part, for $k_z^* = 0.05$ and $e = 0.8$.

$k_z^* = 0.1$ and 0.2, respectively. It is observed that a narrower band of densities is unstable at $k_z^* = 0.1$, but the flow is stable at all densities for $k_z^* = 0.2$.

7.5.2 Locus of the Neutral Stability Curve

We have established in §7.5.1 that spanwise instability is due to a "stationary" mode. Hence the locus of neutral stability curve is given by $a_0 = 0$, i.e. $H^2 = -a_{04}/a_{02}$ [cf. (7.29)-(7.30)] which can be represented by the following relation:

$$k_z^2 = H^2 \frac{\Psi_3(\phi^0, e)}{\Psi_1(\phi^0, e)} \sim (1 - e^2), \tag{7.33}$$

where

$$\Psi_1(\phi^0, e) = \frac{f_1^0}{f_5^0} \quad \text{and} \quad \Psi_3(\phi^0, e) = \frac{f_1^0}{f_{1\phi}^0}\left(\frac{f_{5\phi}^0}{f_5^0} - \frac{f_{2\phi}^0}{f_2^0}\right) - 1. \tag{7.34}$$

Here the superscript '0' indicates that the functions, f_1-f_5 (2.21), are evaluated at base state and the subscript ϕ denotes the derivative of these functions with respect to ϕ. Note that Ψ_1 remains positive for all ϕ^0 and Ψ_3 becomes negative beyond a moderate value of ϕ^0. The critical density above which spanwise instability disappears can be obtained by solving $\Psi_3 = 0$, which gives $\phi_{3d}^0 = 0.1$. This critical density ϕ_{3d}^0 does not vary much with restitution coefficient because Ψ_3 is a weak function of e. The values of ϕ^0, for which Ψ_3 is negative, refer to inadmissible solutions. The variation of Ψ_3 with ϕ^0 is shown in figure 7.9(a) where the arrow indicates the

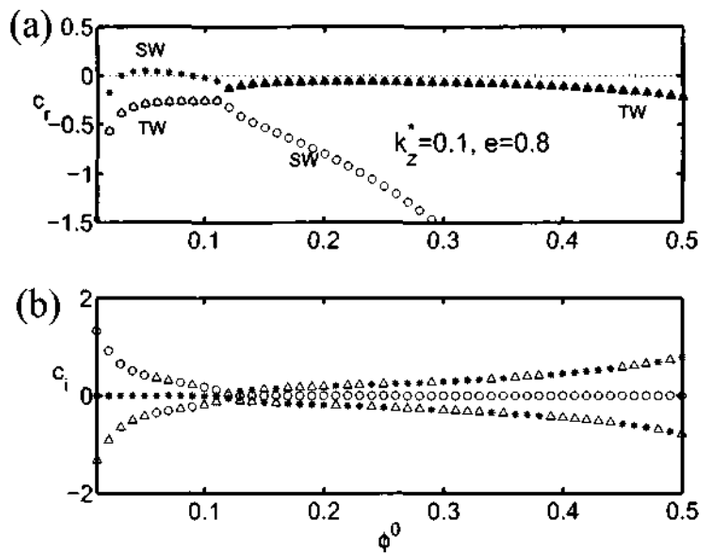

Figure 7.7: Same as figure 7.6(a)-(b) but for $k_z^* = 0.1$.

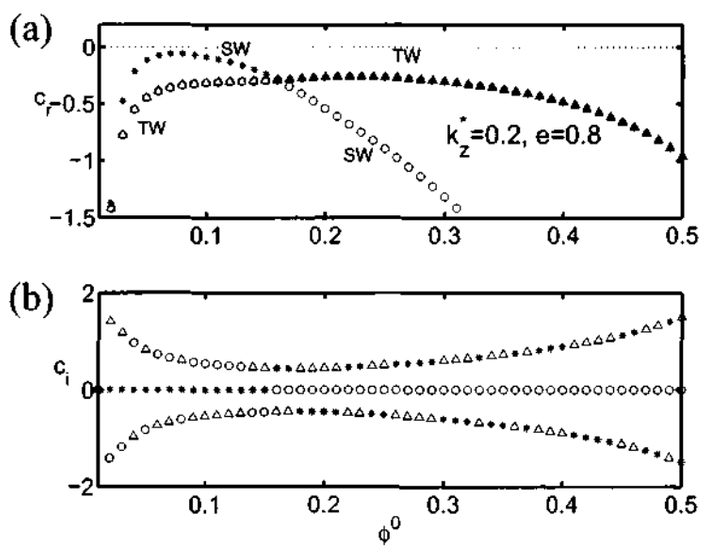

Figure 7.8: Same as figure 7.6(a)-(b) but for $k_z^* = 0.2$.

point ϕ^0_{3d} above which instability vanishes. The contours of zero and positive growth rates in the $(\phi^0, k_z/H)$-plane are shown in figure 7.9(b). The flow is unstable inside the zero contour and stable outside. For densities $\phi^0 > \phi^0_{3d}$, the flow is always stable for any value of k_z/H to pure spanwise perturbations. It is clear from (7.33) that $k_z \to 0$ for $e \to 1$, i.e., the spanwise

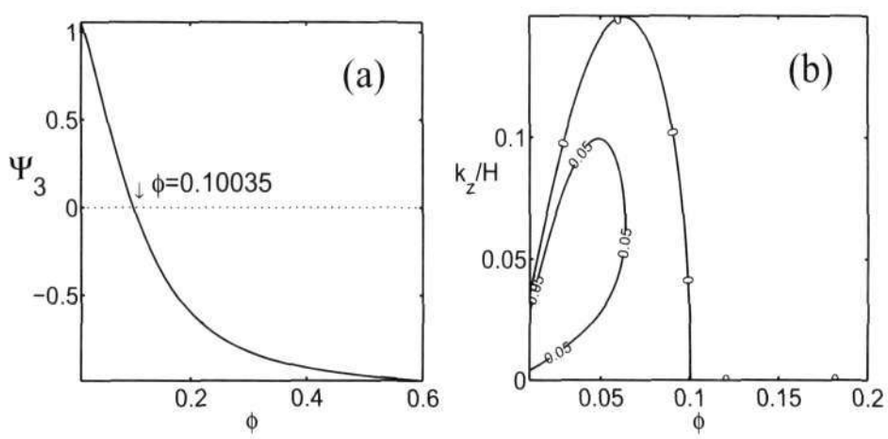

Figure 7.9: (a) Variation of Ψ_3 with volume fraction. (b) Growth rate contours in (ϕ, k_z/H)-plane for $e = 0.8$. Flow is unstable inside the zero contour (since the growth rate is positive) and stable elsewhere.

wavenumber, for which the flow is unstable, vanishes in the elastic limit. Thus the flow is always stable to the pure spanwise perturbations for the perfectly elastic particles.

7.5.3 Analytical Expression for Eigenvectors

Next we proceed to analyze eigenvectors for each eigenvalue. As mentioned before, the eigenvalues associated with the x- and y-momentum equations are equal which make the eigensystem of linear problem (7.26) incomplete. In other words the stability matrix (7.27) associated with (7.26) is a defective matrix because it has only one linearly independent eigenfunction for the double eigenvalue $c = -\mu^0 k_z^2/\phi^0 H^2$. Therefore the system (7.26) has an eigenvalue of algebraic multiplicity two and geometric multiplicity one.

The eigenvector for the double eigenvalue $c = -\mu^0 k_z^2/\phi^0 H^2$ is $(0, 1, 0, 0, 0)$, and the eigenvectors for other three eigenvalues are:

$$\hat{X}^{(1,2,3)} = \left(1, 0, 0, \frac{c^{(1,2,3)}}{l_{14}}, \frac{l_{51} + \frac{l_{54} c^{(1,2,3)}}{l_{14}}}{c^{(1,2,3)} - l_{55}}\right) \tag{7.35}$$

where l_{ij} are the elements of matrix $\mathbf{L}$ (see (7.27)). The superscript $(1, 2, 3)$ in $\hat{X}$ refers to the three eigenvectors corresponding to three eigenvalues $c^{(1,2,3)}$. Substituting l_{14}, l_{51}, l_{54} and l_{55} into (7.35) we get

$$\hat{X}^{(1,2,3)} = \left(1, 0, 0, \frac{ic^{(1,2,3)}}{k_z \phi^0}, \frac{2H^2\left[\mu^0_\phi - \mathcal{D}^0_\phi + p^0 c^{(1,2,3)}\right]}{\mathrm{dim}\phi^0 H^2 c^{(1,2,3)} - 2\kappa^0 k_z^2 + 2(\mu^0_T - \mathcal{D}^0_T)H^2}\right). \tag{7.36}$$

It is clear from the above expression that for real eigenvalue $\hat{w}^{(1,2,3)}$ (4^{th}-element of $\hat{X}^{(1,2,3)}$) is

purely imaginary and $\hat{T}^{(1,2,3)}$ (5^{th}-element of $\hat{X}^{(1,2,3)}$) is real.

After some algebra, it can be easily verified that the eigenvector (7.35) is same as

$$\hat{X}^{(1,2,3)} = \left(1, 0, 0, \frac{c^{(1,2,3)}}{l_{14}}, -\frac{l_{41} + \frac{(l_{44}-c^{(1,2,3)})c^{(1,2,3)}}{l_{14}}}{l_{45}}\right) \tag{7.37}$$

which can be further simplified by substituting l_{14}, l_{41}, l_{44} and l_{45} from (7.27):

$$\hat{X}^{(1,2,3)} = \left(1, 0, 0, \frac{ic^{(1,2,3)}}{k_z\phi^0}, \frac{-p_\phi^0}{p_T^0} + \frac{c^{(1,2,3)}[-k_z^2(2\mu^0+\lambda^0) - c^{(1,2,3)}H^2\phi^0]}{k_z^2 p_T^0 \phi^0}\right). \tag{7.38}$$

Again it can be noted from above equation that for the real eigenvalue $\hat{w}^{(1,2,3)}$ is purely imaginary and $\hat{T}^{(1,2,3)}$ is real.

7.5.4 Analytical Eigenvectors for Adjoint Operator

It is known from the definition of the adjoint that the eigenvalues of the adjoint problem (7.28) are complex conjugate of the eigenvalues of the linear problem (7.26), although the eigenfunctions are different. Recall that the adjoint operator $\mathbf{L}^\dagger$ is defined as

$$\mathbf{L}^\dagger = \mathbf{L}^H \tag{7.39}$$

where superscript H denotes the conjugate transpose. In a similar fashion, as we discussed in §7.5.3, we can classify the eigenvalues of adjoint problem and related eigenvectors. Following §7.5.3, the adjoint eigenvalues are: (i) a double real eigenvalue, (ii) a real eigenvalue, and (iii) a complex conjugate pair. The adjoint eigenfunction for the double eigenvalue is $(0,0,1,0,0)$ and for other three eigenvalues are:

$$X^{\dagger(1,2,3)} = \left(\frac{\frac{\tilde{l}_{54}\tilde{l}_{45}}{(\tilde{l}_{55}-\tilde{c}^{(1,2,3)})} - (\tilde{l}_{44} - \tilde{c}^{(1,2,3)})}{\tilde{l}_{14}}, 0, 0, 1, \frac{\tilde{l}_{45}}{(\tilde{c}^{(1,2,3)} - \tilde{l}_{55})}\right). \tag{7.40}$$

It can be observed that $\phi^{\dagger(1,2,3)}$ (1^{st} element of $X^{\dagger(1,2,3)}$) and $T^{\dagger(1,2,3)}$ (5^{th} element of $X^{\dagger(1,2,3)}$) are purely imaginary for the real eigenvalue. Another form of adjoint eigenfunction can be written as

$$X^{\dagger(1,2,3)} = \left(\frac{\tilde{l}_{41} - \frac{\tilde{l}_{51}\tilde{l}_{45}}{(\tilde{l}_{55}-\tilde{c}^{(1,2,3)})}}{\tilde{c}^{(1,2,3)}}, 0, 0, 1, \frac{\tilde{l}_{45}}{(\tilde{c}^{(1,2,3)} - \tilde{l}_{55})}\right). \tag{7.41}$$

At this point, we know the analytical forms of eigenfunctions of the linear (7.26) and the adjoint (7.28) problems. Subsequently we can evaluate the inner product of linear eigenfunction with its adjoint, which will be used in later sections for calculating the solvability condition, as

$$\left.\begin{aligned}\langle X^{\dagger(1,2,3)}, \hat{X}^{(1,2,3)}\rangle &= \sum \mathrm{conj}\left(X^{\dagger(1,2,3)}\right)\hat{X}^{(1,2,3)} = \tilde{\phi}^\dagger + w^{[1;1]} + \tilde{T}^\dagger T^{[1;1]} \\ &= \frac{1}{l_{14}}\left[\frac{l_{54}l_{45}}{(l_{55}-c^{(1,2,3)})} - (l_{44} - c^{(1,2,3)})\right] + \frac{c^{(1,2,3)}}{l_{14}} + \frac{l_{45}\left(l_{51}+\frac{l_{54}c^{(1,2,3)}}{l_{14}}\right)}{(c^{(1,2,3)}-l_{55})^2}\end{aligned}\right\}. \tag{7.42}$$

Note that $\langle X^{\dagger(1,2,3)}, \hat{X}^{(1,2,3)}\rangle$ is purely imaginary. While the bi-orthogonality condition (see §3.3.5) for the eigenvalues $c^{(1,2,3)}$ is

$$\langle X_j^{\dagger(1,2,3)}, \hat{X}_i^{(1,2,3)}\rangle = \delta_{ij}, \quad \text{where} \quad \delta_{ij} \text{ is the Kronecker delta,} \tag{7.43}$$

for the double eigenvalue this condition is $\langle X^\dagger, \hat{X} \rangle = 0$ which implies that the linear and adjoint eigenvectors are orthogonal to each other.

7.6 Weakly Nonlinear Analysis for Pure Spanwise Flow

In chapter 5 we have studied the weakly nonlinear stability of the streamwise independent 2D-granular Couette flow, which leads to gradient banding, using analytical solutions of weakly nonlinear equations in terms of sine and cosine waves. The pure spanwise granular Couette flow, which leads to vorticity banding, differs from the streamwise independent 2D-granular Couette flow in the following manner.

- The streamwise independent 2D-granular Couette flow (i.e. $k_x = 0$, $\frac{\partial}{\partial y}(.) \neq 0$ and $k_z = 0$) depends only on the gradient ($-1/2 < y < 1/2$) direction and thus the instability due to streamwise independent 2D-perturbations leads to bands of high and low shear rates in the gradient direction. Such instabilities are, thus, called gradient or shear banding instabilities. The gradient direction y is wall bounded and hence the solution has to be found by satisfying the boundary conditions. Apart from the analytical solution of the above problem we can also find the numerical solution as well. The comparison between analytical and numerical solutions has been detailed in chapter 5.

- Likewise, the pure spanwise granular Couette flow (i.e. $k_x = 0$, $\frac{\partial}{\partial y}(.) = 0$ and $k_z \neq 0$) depends only on the spanwise or vorticity (z) direction ($-\infty < z < \infty$) and thus the instability due to pure spanwise perturbations leads to bands of high and low shear stresses in the vorticity direction. Such instabilities are, thus, called vorticity banding instabilities. In this case we have exact expressions of the eigenvalues and eigenvectors of linear and its adjoint problem as explained in the previous section. With the help of these analytical solutions of eigenfunctions we can simplify all the weakly nonlinear equations. Moreover we can give a general solution of these equations at any order of amplitude. In this case we do not require any numerical method as the full weakly nonlinear problem is analytically solvable.

The analytical weakly nonlinear analysis for the pure spanwise granular Couette flow is given below. The form of disturbance equations for pure spanwise flow is given by

$$\left(\frac{\partial}{\partial t} - \mathcal{L}\right) X(t,z) = \mathcal{N} = \mathcal{N}_2 + \mathcal{N}_3 + \mathcal{N}_4 + \mathcal{N}_5 \tag{7.44}$$

where $\mathcal{N}_j = (\mathcal{N}_j^{(1)}, \mathcal{N}_j^{(2)}, \mathcal{N}_j^{(3)}, \mathcal{N}_j^{(3)}, \mathcal{N}_j^{(5)})^{Tr}$ is j^{th} order nonlinear term where the superscripts (1) to (5) denote the continuity, x, y, z-momentum and energy equations, respectively. The explicit expressions for $\mathcal{N}_j$ for $j = 1$ to 5 are given in Appendix 7C.

7.6.1 $O(A)$: Fundamental Mode

Substituting $k = n = 1$ into (7.22) we get back the linear problem (7.26) with $\mathbf{L}_{11} = c^{(0)} - \mathbf{L}_1$ where $\mathbf{L}_1 = \mathbf{L}$ (see Eqn. (7.27)). The analytical expressions for the eigenvalues and the corresponding eigenfunctions (linear and adjoint) (Eqns (7.35)-(7.41)) are given in §7.5. The eigenfunction of the linear problem corresponding to the least-stable eigenvalue is the fundamental mode which generates its harmonics when the disturbance has finite amplitude. The fundamental mode is normalized such that

$$X^{[1;1]} = \hat{X} = T^0 \left(X^{[1;1]} / T^{[1;1]} \right). \tag{7.45}$$

7.6.2 $O(A^2)$: Second Harmonic

Substituting $k = n = 2$ into (7.22), we get the equation for second harmonic

$$\mathbf{L}_{22} X^{[2;2]} = N_2(X^{[1;1]}, X^{[1;1]}) = \mathbf{G}_{22}, \tag{7.46}$$

where $\mathbf{L}_{22} = 2c^{(0)}\mathbf{I} - \mathbf{L}_2$ is a linear operator with $\mathbf{L}_2 = \mathbf{L}(k_z \to 2k_z)$ (cf. Eqn. (7.27)) and $\mathbf{G}_{22} = (G^1_{22}, 0, 0, G^4_{22}, G^5_{22})^{Tr}$ is the vector form of nonlinear terms as defined below:

$$\left.\begin{aligned}
G^1_{22} &= -2ik_z\phi^{[1;1]}w^{[1;1]}, \\
G^4_{22} &= -\tfrac{1}{\phi^0}\left[ik_z\phi^0(w^{[1;1]})^2 + c^{(0)}\phi^{[1;1]}w^{[1;1]}\right] \\
&\quad -\tfrac{1}{\phi^0 H^2}\left[ik_z\left(p^0_{\phi\phi}(\phi^{[1;1]})^2 + p^0_{TT}(T^{[1;1]})^2 + 2p^0_{\phi T}\phi^{[1;1]}T^{[1;1]}\right)\right. \\
&\quad \left. +4k_z^2\left(\mu^0_\phi\phi^{[1;1]} + \mu^0_T T^{[1;1]}\right)w^{[1;1]} + 2k_z^2\left(\lambda^0_\phi\phi^{[1;1]} + \lambda^0_T T^{[1;1]}\right)w^{[1;1]}\right], \\
G^5_{22} &= -\tfrac{1}{\phi^0}\left[ik_z\phi^0 w^{[1;1]}T^{[1;1]} + c^{(0)}\phi^{[1;1]}T^{[1;1]}\right] \\
&\quad +\tfrac{2}{3\phi^0}\left[-\tfrac{2k_z^2}{H^2}T^{[1;1]}(\kappa^0_\phi\phi^{[1;1]} + \kappa^0_T T^{[1;1]}) - ik_z(p^0_\phi\phi^{[1;1]} + p^0_T T^{[1;1]})w^{[1;1]}\right. \\
&\quad + \left(\tfrac{1}{2}\mu^0_{\phi\phi}(\phi^{[1;1]})^2 + \tfrac{1}{2}\mu^0_{TT}(T^{[1;1]})^2 + \mu^0_{\phi T}\phi^{[1;1]}T^{[1;]}\right) - k_z^2(2\mu^0 + \lambda^0)(w^{[1;1]})^2 \\
&\quad \left. - \left(\tfrac{1}{2}\mathcal{D}^0_{\phi\phi}(\phi^{[1;1]})^2 + \tfrac{1}{2}\mathcal{D}^0_{TT}(T^{[1;1]})^2 + \mathcal{D}^0_{\phi T}\phi^{[1;1]}T^{[1;]}\right)\right]
\end{aligned}\right\}. \tag{7.47}$$

Note that $\mathbf{G}_{22}$ is known since we know the analytical expression of fundamental mode [(7.35) or (7.37)]. The second and third equations of the system (7.46) which correspond to x- and y-momentum equations are decoupled from the other three equations. Hence we can reduce (7.46) to a system of order three by removing second and third rows and the corresponding columns, and a system of order two corresponding to the removed rows and columns.

Let us write this reduced system of order two as

$$\boxed{\left[2c^{(0)} + \frac{\mu^0 k_{2z}^2}{H^2\phi^0}\right]u^{[2;2]} + v^{[2;2]} = 0 \qquad \text{and} \qquad \left[2c^{(0)} + \frac{\mu^0 k_{2z}^2}{H^2\phi^0}\right]v^{[2;2]} = 0,} \tag{7.48}$$

which yields $u^{[2;2]} = v^{[2;2]} = 0$. Similarly, the system of order three, which consists of continuity, z-momentum and energy balance equations, can be written as

$$\left.\begin{aligned}
2c^{(0)}\phi^{[2;2]} + ik_{2z}\phi^0 w^{[2;2]} &= G^1_{22} \\
\frac{ik_{2z}p^0_\phi}{H^2\phi^0}\phi^{[2;2]} + \left[2c^{(0)} + \frac{k_{2z}^2(2\mu^0 + \lambda^0)}{H^2\phi^0}\right]w^{[2;2]} + \frac{ik_{2z}p^0_T}{H^2\phi^0}T^{[2;2]} &= G^4_{22} \\
\frac{-2(\mu^0_\phi - \mathcal{D}^0_\phi)}{3\phi^0}\phi^{[2;2]} + \frac{2ik_{2z}p^0}{3\phi^0}w^{[2;2]} + \left[2c^{(0)} + \frac{2\kappa^0 k_{2z}^2}{3H^2\phi^0} - \frac{2(\mu^0_T - \mathcal{D}^0_T)}{3\phi^0}\right]T^{[2;2]} &= G^5_{22}.
\end{aligned}\right\} \tag{7.49}$$

The matrix equivalent of (7.48) is

$$\mathbf{A}_{22}Y^{[2;2]} = \mathbf{B}_{22}, \quad \text{or} \quad \begin{pmatrix} \mathbf{L}^{11}_{22} & \mathbf{L}^{14}_{22} & 0 \\ \mathbf{L}^{41}_{22} & \mathbf{L}^{44}_{22} & \mathbf{L}^{45}_{22} \\ \mathbf{L}^{51}_{22} & \mathbf{L}^{54}_{22} & \mathbf{L}^{55}_{22} \end{pmatrix}\begin{pmatrix} \phi^{[2;2]} \\ w^{[2;2]} \\ T^{[2;2]} \end{pmatrix} = \begin{pmatrix} G^1_{22} \\ G^4_{22} \\ G^5_{22} \end{pmatrix}, \tag{7.50}$$

where $\mathbf{L}^{ij}_{22}$ is the ij^{th} element of matrix $\mathbf{L}_{22}$. The solution of Eqn. (7.49) can be obtained by using the Cramer's rule of basic algebra:

$$Y^{[2;2]} = (\phi^{[2;2]}, w^{[2;2]}, T^{[2;2]}) = \det(\mathbf{A}^j_{22})/\det(\mathbf{A}_{22}), \tag{7.51}$$

where $\mathbf{A}^j_{22}$ is the matrix formed by replacing the j^{th}-column of $\mathbf{A}_{22}$ by the column vector $\mathbf{B}_{22}$.

7.6.3 $O(A^2)$: Mean Flow Distortion

Substituting $k = 0$ and $n = 2$ into (7.22), we arrive at the mean flow distortion equation

$$\mathbf{L}_{02}X^{[0;2]} = N_2(\tilde{X}^{[1;1]}, X^{[1;1]}) + N_2(X^{[1;1]}, \tilde{X}^{[1;1]}) = \mathbf{G}_{02} \tag{7.51}$$

where $\mathbf{L}_{02} = 2a^{(0)}\mathbf{I} - \mathbf{L}_0$ is a linear operator with $\mathbf{L}_0 = \mathbf{L}(k_z = 0)$ and $\mathbf{G}_{02} = (0, 0, 0, 0, G_{02}^5)^{Tr}$ denotes the nonlinear term where G_{02}^5 is given by

$$\begin{aligned} G_{02}^5 \;=\; & -\frac{1}{\phi^0}\left[-ik_z\phi^0 T^{[1;1]}(-2iw_i^{[1;1]}) + 2c^{(0)}\phi^{[1;1]}T^{[1;1]}\right] + \frac{2}{3\phi^0}\Big[\\ & ik_z(p_\phi^0\phi_1 + p_T^0 T_1)\left(-2iw_i^{[1;1]}\right) + \left(\mu_{\phi\phi}^0(\phi^{[1;1]})^2 + \mu_{TT}^0(T^{[1;1]})^2 + 2\mu_{\phi T}^0\phi^{[1;1]}T^{[1;1]}\right) \\ & +2k_z^2(2\mu^0 + \lambda^0)w^{[1;1]}\tilde{w}^{[1;1]} - (\mathcal{D}_{\phi\phi}^0(\phi^{[1;1]})^2 + \mathcal{D}_{TT}^0(T^{[1;1]})^2 + 2\mathcal{D}_{\phi T}^0\phi^{[1;1]}T^{[1;1]})\Big]. \end{aligned} \tag{7.52}$$

Note that G_{02}^5 is always real which verifies that the distortion of mean flow $X^{[0;2]}$ is a real harmonic. The solution of the above system (7.51) yields mean flow distortion:

$$\phi^{[0;2]} = u^{[0;2]} = v^{[0;2]} = w^{[0;2]} = 0 \quad \text{and} \quad T^{[0;2]} = \frac{G_{02}^5}{\left[2a^{(0)} - \frac{2(\mu_T^0 - \mathcal{D}_T^0)}{3\phi^0}\right]} \tag{7.53}$$

where G_{02}^5 is given by (7.52). Note from (7.53) that $T^{[0;2]}$ is independent of Couette gap.

7.6.4 $O(A^3)$: First Landau Coefficient

At this point we know all the analytical solutions up-to second order in amplitude, i.e., the fundamental mode ($X^{[1;1]}$), second harmonic ($X^{[2;2]}$) and distortion to mean flow ($X^{[0;2]}$). Now substituting $k = 1$ and $n = 3$ into (7.22), we obtain the following equation for the distortion to fundamental:

$$\left.\begin{aligned} \mathbf{L}_{13}X^{[1;3]} &= -c^{(2)}X^{[1;1]} + \mathbf{G}_{13} \\ \mathbf{G}_{13} &= N_2(X^{[1;1]}, X^{[0;2]}) + N_2(X^{[0;2]}, X^{[1;1]}) + N_2(X^{[1;1]}, \tilde{X}^{[2;2]}) \\ &\quad + N_2(\tilde{X}^{[2;2]}, X^{[1;1]}) + N_3(\tilde{X}^{[1;1]}, X^{[1;1]}, X^{[1;1]}) \\ &\quad + N_3(X^{[1;1]}, \tilde{X}^{[1;1]}, X^{[1;1]}) + N_3(X^{[1;1]}, X^{[1;1]}, \tilde{X}^{[1;1]}) \end{aligned}\right\} \tag{7.54}$$

where $\mathbf{L}_{13} = (3a^{(0)} + ib^{(0)})\mathbf{I} - \mathbf{L}_1$ is a linear operator with $\mathbf{L}_1 = \mathbf{L}$ (see (7.27)). When the absolute value of growth rate $|a^{(0)}| = 0$ or small, the linear operator $\mathbf{L}_{13} = \mathbf{L}_{11}$ and hence the first Landau coefficient $c^{(2)}$ can be obtained from the solvability condition of (7.54) (see chapter 3). The problem of purely spanwise flow is a special problem because the flow is independent of gradient direction (y) and this simplifies the solvability condition (cf. (7.23)) to a ratio of algebraic terms:

$$c^{(2)} \;=\; \frac{\tilde{\phi}^\dagger G_{13}^1 + \tilde{u}^\dagger G_{13}^2 + \tilde{v}^\dagger G_{13}^3 + \tilde{w}^\dagger G_{13}^4 + \tilde{T}^\dagger G_{13}^5}{\tilde{\phi}^\dagger\phi^{[1;1]} + \tilde{u}^\dagger u^{[1;1]} + \tilde{v}^\dagger v^{[1;1]} + \tilde{w}^\dagger w^{[1;1]} + \tilde{T}^\dagger T^{[1;1]}}, \tag{7.55}$$

where $X^\dagger = (\phi^\dagger, u^\dagger, v^\dagger, w^\dagger, T^\dagger)$ is the adjoint eigenfunction. The condition for vanishing first Landau coefficient can be written as

$$\tilde{\phi}^\dagger G_{13}^1 + \tilde{u}^\dagger G_{13}^2 + \tilde{v}^\dagger G_{13}^3 + \tilde{w}^\dagger G_{13}^4 + \tilde{T}^\dagger G_{13}^5 = 0. \tag{7.56}$$

We know that the x and y velocity components of the fundamental and its adjoint eigenfunction are zeros, i.e. $u^{[1;1]} = v^{[1;1]} = 0$ and $u^\dagger = v^\dagger = 0$ and furthermore $\phi^{[1;1]} = w^\dagger = 1$ which simplify

(7.55) to

$$c^{(2)} = \frac{\tilde{\phi}^\dagger G^1_{13} + \tilde{w}^\dagger G^4_{13} + \tilde{T}^\dagger G^5_{13}}{\tilde{\phi}^\dagger \phi^{[1;1]} + \tilde{w}^\dagger w^{[1;1]} + \tilde{T}^\dagger T^{[1;1]}} = \frac{\tilde{\phi}^\dagger G^1_{13} + G^4_{13} + \tilde{T}^\dagger G^5_{13}}{\tilde{\phi}^\dagger + w^{[1;1]} + \tilde{T}^\dagger T^{[1;1]}} \tag{7.57}$$

and the locus of zeros of the first Landau coefficient (7.56) can be written as $\tilde{\phi}^\dagger G^1_{13} + \tilde{w}^\dagger G^4_{13} + \tilde{T}^\dagger G^5_{13} = 0$. It has been verified that for the real eigenvalue G^1_{13} and G^5_{13} are real and G^4_{13} is purely imaginary and hence $c^{(2)}$ is always real for the real eigenvalue. Recall that for real eigenvalue (i) $T^{[1;1]}$ is real and (ii) $\phi^\dagger$, $T^\dagger$ and $w^{[1;1]}$ are purely imaginary.

Distortion of Fundamental

Substituting $c^{(2)}$ from (7.57) into (7.54), we get an inhomogeneous system. The x- and y-momentum equations, which correspond to the second and third rows of (7.54) are decoupled from other three equations, give $u^{[1;3]} = v^{[1;3]} = 0$. The reduced system of order three can be written as

$$\mathbf{A}_{13} Y^{[1;3]} = \mathbf{B}_{13}, \text{ or } \begin{pmatrix} \mathbf{L}^{11}_{13} & \mathbf{L}^{14}_{13} & 0 \\ \mathbf{L}^{41}_{13} & \mathbf{L}^{44}_{13} & \mathbf{L}^{45}_{13} \\ \mathbf{L}^{51}_{13} & \mathbf{L}^{54}_{13} & \mathbf{L}^{55}_{13} \end{pmatrix} \begin{pmatrix} \phi^{[1;3]} \\ w^{[1;3]} \\ T^{[1;3]} \end{pmatrix} = \begin{pmatrix} -c^{(2)}\phi^{[1;1]} + G^1_{13} \\ -c^{(2)} w^{[1;1]} + G^4_{13} \\ -c^{(2)} T^{[1;1]} + G^5_{13} \end{pmatrix}. \tag{7.58}$$

The solution of (7.58) is

$$Y^{[1;3]} = (\phi^{[1;3]}, w^{[1;3]}, T^{[1;3]}) = \det(\mathbf{A}^j_{13})/\det(\mathbf{A}_{13}) \tag{7.59}$$

where $\mathbf{A}^j_{13}$ is the matrix formed by replacing the j^{th}-column of $\mathbf{A}_{13}$ by the column vector $\mathbf{B}_{13}$.

7.6.5 General Solution of Weakly Nonlinear Equations

So far we have looked at analytical solutions of second harmonic, distortion to mean flow and distortion to fundamental at cubic order along with the first Landau coefficient. We can generalize these solutions at any arbitrary order in amplitude which lead to a general analytical solution of weakly nonlinear theory (see (7.22)).

Depending on the index k of Eqn (7.22), its solutions can be divided into two parts (i) $k \neq 0$ and (ii) $k = 0$. For $k \neq 0$, we have $u^{[k;n]} = v^{[k;n]} = 0$ because x- and y-momentum equations are decoupled from the other three balance equations. We can represent the remaining equations (continuity, z-momentum and energy equations) in the following matrix form,

$$\mathbf{A}_{kn} Y^{[k;n]} = \mathbf{B}_{kn}, \text{ or } \begin{pmatrix} \mathbf{L}^{11}_{kn} & \mathbf{L}^{14}_{kn} & 0 \\ \mathbf{L}^{41}_{kn} & \mathbf{L}^{44}_{kn} & \mathbf{L}^{45}_{kn} \\ \mathbf{L}^{51}_{kn} & \mathbf{L}^{54}_{kn} & \mathbf{L}^{55}_{kn} \end{pmatrix} \begin{pmatrix} \phi^{[k;n]} \\ w^{[k;n]} \\ T^{[k;n]} \end{pmatrix} = \begin{pmatrix} -c^{[n-1]}\phi^{[1;1]}\delta_{k1} + H^1_{kn} \\ -c^{[n-1]} w^{[1;1]}\delta_{k1} + H^4_{kn} \\ -c^{[n-1]} T^{[1;1]}\delta_{k1} + H^5_{kn} \end{pmatrix}. \tag{7.60}$$

The solution of above system (7.60) can be written as

$$Y^{[k;n]} = (\phi^{[k;n]}, w^{[k;n]}, T^{[k;n]}) = \det(\mathbf{A}^j_{kn})/\det(\mathbf{A}_{kn}) \tag{7.61}$$

where $\mathbf{A}^j_{kn}$ is the matrix formed by replacing the j^{th}-column of $\mathbf{A}_{kn}$ by the column vector $\mathbf{B}_{kn}$. For $k = 1$ the inhomogeneous term $\mathbf{B}_{kn}$ involves Landau coefficient $c^{[n-1]}$ which is given by

$$c^{[n-1]} = \frac{\tilde{\phi}^\dagger G^1_{1n} + \tilde{w}^\dagger G^4_{1n} + \tilde{T}^\dagger G^5_{1n}}{\tilde{\phi}^\dagger \phi^{[1;1]} + \tilde{w}^\dagger w^{[1;1]} + \tilde{T}^\dagger T^{[1;1]}}. \tag{7.62}$$

Similarly, for the case of $k = 0$, we get the mean flow distortion equation which has the following

solution:

$$\phi^{[0;n]} = u^{[0;n]} = v^{[0;n]} = w^{[0;n]} = 0 \text{ and } T^{[0;k]} = \frac{G_{02}^5}{\left[ka^{(0)} - \frac{2(\mu_T^0 - \mathcal{D}_T^0)}{3\phi^0}\right]}. \tag{7.63}$$

7.6.6 $O(A^n)$: Higher Order Harmonics for $n = 3, 4, 5$

Let us now turn to the explicit solutions of some of the higher order harmonics which are required for the calculation of second Landau coefficient. The product of three fundamental modes gives a third harmonic of fundamental which can be determined by solving the following inhomogeneous equation

$$\mathbf{L}_{33}X^{[3;3]} = \mathbf{G}_{33} = N_2(X^{[1;1]}, X^{[2;2]}) + N_2(X^{[2;2]}, X^{[1;1]}) + N_3(X^{[1;1]}, X^{[1;1]}, X^{[1;1]}) \tag{7.64}$$

where $\mathbf{L}_{33} = 3c^{(0)}\mathbf{I} - \mathbf{L}_3$ is a linear operator with $\mathbf{L}_3 = \mathbf{L}(k_z \to 3k_z)$.

At quartic order $O(A^4)$, we have harmonics $X^{[0;4]}$ and $X^{[2;4]}$ which represent the mean flow distortion and a correction to the second harmonic at order four, respectively. The governing equations for $X^{[0;4]}$ and $X^{[2;4]}$ are

$$\mathbf{L}_{04}X^{[0;4]} = -2a^{(2)}X^{[0;2]} + \mathbf{G}_{04} \tag{7.65}$$

$$\mathbf{L}_{24}X^{[2;4]} = -2c^{(2)}X^{[2;2]} + \mathbf{G}_{24} \tag{7.66}$$

where $\mathbf{L}_{04} = 4a^{(0)}\mathbf{I} - \mathbf{L}_0$ and $\mathbf{L}_{24} = (4a^{(0)} + 2ib^{(0)})\mathbf{I} - \mathbf{L}_2$ with $\mathbf{L}_2 = \mathbf{L}(k_z \to 2k_z)$. The second Landau coefficient can be obtained at quintic order in amplitude. The equation related to second Landau coefficient can be written as

$$\mathbf{L}_{15}X^{[1;5]} = -c^{(4)}X^{[1;1]} + \mathbf{G}_{15}, \tag{7.67}$$

where the second Landau coefficient can be found from the solvability condition as

$$c^{(4)} = \frac{\tilde{\phi}^\dagger G_{15}^1 + \tilde{u}^\dagger G_{15}^2 + \tilde{v}^\dagger G_{15}^3 + \tilde{w}^\dagger G_{15}^4 + \tilde{T}^\dagger G_{15}^5}{\tilde{\phi}^\dagger \phi^{[1;1]} + \tilde{u}^\dagger u^{[1;1]} + \tilde{v}^\dagger v^{[1;1]} + \tilde{w}^\dagger w^{[1;1]} + \tilde{T}^\dagger T^{[1;1]}} \tag{7.68}$$

which can be further simplified to

$$c^{(4)} = \frac{\tilde{\phi}^\dagger G_{15}^1 + \tilde{w}^\dagger G_{15}^4 + \tilde{T}^\dagger G_{15}^5}{\tilde{\phi}^\dagger \phi^{[1;1]} + \tilde{w}^\dagger w^{[1;1]} + \tilde{T}^\dagger T^{[1;1]}} \tag{7.69}$$

because $\tilde{u}^\dagger = \tilde{v}^\dagger = u^{[1;1]} = v^{[1;1]} = 0$. The solutions of (7.64), (7.65), (7.66) and (7.67) can be obtained by using the general method of solution as given in §7.6.5 for a particular value of k and n depending on harmonics. The explicit forms of $\mathbf{G}_{04}$, $\mathbf{G}_{24}$ and $\mathbf{G}_{15}$ are given in Appendix 7D.

7.7 Numerical Results and Discussion

7.7.1 Critical Parameters for Vorticity Banding: Linear Stability

Recall from §7.5.1 that the form of the quintic dispersion relation for the vorticity banding (cf. Eqn. (7.29)) is

$$\left(c + \frac{\mu^0 k_z^2}{\phi^0 H^2}\right)^2 (c^3 + a_2 c^2 + a_1 c + a_0) = 0$$

where a_i's are functions of the base state density (ϕ^0) and temperature (T^0), the Couette gap (H), the restitution coefficient (e) and the spanwise wavenumber (k_z).

Out of five eigenvalues, there are two real eigenvalues which are always negative and hence stable, a complex conjugate pair representing propagating modes and one real eigenvalue. Two propagating modes can join together to become stationary modes (Gayen & Alam 2006) below a threshold density (ϕ^0_{3d}), leading to the onset of pure spanwise instability. This real eigenmode is referred to as *vorticity-banding* mode (Alam *et al.* 2005; Gayen & Alam 2006) because this leads to banding of particles in the *vorticity* direction which segregates the uniform shear flow into alternate layers of dense and dilute regions of high and low shear-stresses, respectively, along the vorticity direction. In this chapter, we are focusing on this vorticity-banding mode.

Since the vorticity banding instability corresponds to a real eigenvalue, the locus of the neutral stability curve ($a^{(0)} = c_r = 0$) is given by $a_0 = 0$ [viz. (7.29)]. The zero growth rate contour $a^{(0)} = 0$ *(i.e. neutral stability curve) for the vorticity-banding is shown in figure 7.10 by a thick* solid line (red and green); the flow is unstable ($a^{(0)} > 0$) inside the neutral stability contour and stable ($a^{(0)} < 0$) outside. It is seen that there is a minimum/critical value of the normalized spanwise wavenumber $k_z^* = k_z/H$,

$$k^*_{zc} = k^*_z(\phi^0, e; a^{(0)} = 0) = \sqrt{\Psi_3/\Psi_1}, \tag{7.70}$$

depending on ϕ^0, e and H, below which the uniform shear flow is unstable according to linear theory. On the other hand, for a given k_z^*, there is a pair of critical densities,

$$(\phi_{c_1}, \phi_{c_2}) = (\phi_{c_1}, \phi_{c_2})(H, e; a^{(0)} = 0), \tag{7.71}$$

between which the uniform shear flow is unstable.

Although this pair of critical densities depends on k_z^* and e, there is a global maximum density, defined as

$$\phi^u_c = \max\, \phi^0(a^{(0)} = 0) = \phi^0_{3d} \qquad \forall\, k_z^*, \tag{7.72}$$

above which the uniform shear flow is always stable to vorticity banding instability, irrespective of the value of k_z^* and e. For our Navier-Stokes's level constitutive model, this global critical density is $\phi^u_c = \phi^0_{3d} \sim 0.1$. Similarly, a global maximum scaled spanwise wavenumber can be defined as

$$k^u_{zc} = \max\, k^*_z(a^{(0)} = 0) \qquad \forall\, \phi^0, \tag{7.73}$$

above which the flow is always stable.

In the following sections, we investigate the possibility of subcritical and supercritical bifurcations from the uniform shear base flow around the linear vorticity-banding instability.

7.7.2 Equilibrium Amplitude and the Nature of Bifurcation

Let us first discuss about the nature of the equilibrium solutions that would bifurcate from the uniform shear flow due to vorticity banding instability as discussed in §7.7.1. Similar to shearbanding instability of granular plane Couette flow as discussed in chapters 4 and 5, the bifurcation is pitchfork (stationary) and hence the Landau coefficients are real. (It may be noted that there could be Hopf/oscillatory bifurcations in the stable subcritical regime as discussed in §7.7.5.) The equilibrium solutions ($dA/dt = 0$) which give information about the finite amplitude state of bifurcated nonlinear patterns are explained below.

Let us rewrite the Landau equation (7.24) up-to quintic order as

$$\frac{\mathrm{d}A}{\mathrm{d}t} = a^{(0)}A + a^{(2)}A^3 + a^{(4)}A^5, \tag{7.74}$$

where $a^{(0)}$ is the growth rate, and $a^{(2)}$ and $a^{(4)}$ are the first and second Landau coefficients, respectively. Note that the vorticity banding mode is real and the bifurcation is stationary and hence (7.25) is identically satisfied.

In the present work, we have calculated two Landau coefficients which is in contrast to our previous work (Shukla & Alam 2009, 2011) where only the first Landau coefficient was calculated. The present analysis differs from the previous analysis only in terms of second Landau coefficient which uses nonlinear disturbance equations which are correct up-to quintic order. We shall discuss this again in §7.7.8.

The equilibrium amplitude (or, fixed point[1]) $A = A_e$ is given by $\mathrm{d}A/\mathrm{d}t = 0$ which can be determined by solving

$$a^{(0)}A_e + a^{(2)}A_e^3 + a^{(4)}A_e^5 = 0. \tag{7.75}$$

At cubic order, we have two nontrivial finite amplitude solutions (cf. §5.5.2)

$$A_e = \pm\sqrt{-\frac{a^{(0)}}{a^{(2)}}} \tag{7.76}$$

and a trivial solution corresponding to the uniform base state. The bifurcation is *subcritical* if $a^{(2)} > 0$ and $a^{(0)} < 0$, and *supercritical* if $a^{(2)} < 0$ and $a^{(0)} > 0$, which has been explained in §5.5.2. At quintic order, we have four non-trivial finite amplitude solutions

$$A_e = \pm\sqrt{\frac{1}{2a^{(4)}}(-a^{(2)} \pm \sqrt{d})}, \quad \text{where } d = (a^{(2)})^2 - 4a^{(4)}a^{(0)}. \tag{7.77}$$

The stability of these solutions (7.77) can be determined from the linear stability analysis of (7.74) around these steady solutions.

In fact, the sign of the first Landau coefficient decides the bifurcation type, *subcritical* or *supercritical*, and the second Landau coefficient limits the range of these bifurcations. For the case of subcritical bifurcations, the cubic Landau equation does not provide any stable finite amplitude solution. In order to get stable finite amplitude solutions we need to consider higher order Landau coefficients.

7.7.3 Phase Diagram for Nonlinear Vorticity-banding Instability

As described in §7.6.4 and §7.6.6, the conditions for vanishing first and second Landau coefficients are

$$\tilde{\phi}^\dagger G_{13}^1 + \tilde{w}^\dagger G_{13}^4 + \tilde{T}^\dagger G_{13}^5 = 0 \quad \text{and} \quad \tilde{\phi}^\dagger G_{15}^1 + \tilde{w}^\dagger G_{15}^4 + \tilde{T}^\dagger G_{15}^5 = 0, \tag{7.78}$$

respectively, which we have plotted in figure 7.10. The zero contours of the first Landau coefficient, $c^{(2)} = a^{(2)} = 0$ (blue line), and the second Landau coefficient, $c^{(4)} = a^{(4)} = 0$ (black line), in the (ϕ^0, k_z^*) plane are superimposed over the neutral stability contour ($a^{(0)} = 0$, red and green line) in figure 7.10. The restitution coefficient is set to $e = 0.8$. In figure 7.10, the red and green solid lines represent the neutral stability contour ($a^{(0)} = 0$) inside which the uniform shear flow is linearly unstable and stable elsewhere in the (ϕ^0, k_z^*)-plane (cf. figures 7.9(a)-7.9(b)). The regions of positive and negative $a^{(0)}$, $a^{(2)}$ and $a^{(4)}$ are marked in this figure. The zero contour of the first Landau coefficient (blue line) crosses the neutral stability contour at $\phi^0 = \phi^d \sim 0.085001$. The parts of neutral stability contour which lie below and above ϕ^d are shown by red and green lines, respectively.

Depending on the bifurcation type, the density range can be divided into two parts: (i) supercritical for $\phi^0 < \phi^d$ and (ii) subcritical for $\phi^0 > \phi^d$, as depicted in figure 7.10. The

[1] For a general vector field $\dot{x} = f(x)$, the fixed point x^* can be obtained by solving $f(x^*) = 0$.

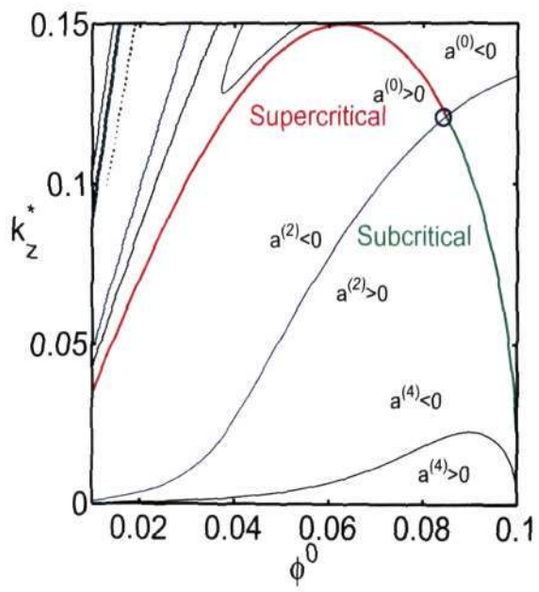

Figure 7.10: Phase diagram for the vorticity banding instability $[\partial/\partial y(.) = 0,\ \partial/\partial x(.) = 0$ and $k_z \neq 0]$ in (k_z^*, ϕ^0)-plane where $k_z^* = k_z/H$. Contours of $a^{(0)} = 0$ (red and green line), $a^{(2)} = 0$ (blue line) and $a^{(4)} = 0$ (black line) are shown.

uniform shear flow for the parameter values inside the neutral stability curve, corresponding to the regions between red and blue lines, is supercritically stable $[a^{(0)} > 0$ and $a^{(2)} < 0]$, as shown in figure 7.10. The rest of the neutral stability curve, shown by green line, is subcritically unstable because $a^{(2)} > 0$ within this region. The black line in figure 7.10 represents the zero contour of the second Landau coefficient which is positive inside the contour. There are various parameters in (ϕ^0, k_z^*)-plane for which $a^{(2)}$ and $a^{(4)}$ are zeros which is a consequence of (7.78) being satisfied there, as shown in the upper left portion (left part of red line) of figure 7.10. The extended phase diagram, showing zeros of growth rate and first Landau coefficient, is discussed later in §7.7.9.

The vorticity banding mode is real for $\phi^0 \leq \phi_{3d}^0$ (see §7.7.1) which leads to pitchfork bifurcations. It has been verified that the first and second Landau coefficients are also real for $\phi^0 \leq \phi_{3d}^0$ (which have been derived analytically in §7.6.4 and §7.6.5), therefore the non-linearity does not change the character of the stationary bifurcation which is similar to the previous work on shear-banding instability (Shukla & Alam 2009, 2011) of granular plane Couette flow. There are "oscillatory" finite amplitude solutions for $\phi^0 > \phi_{3d}^0$ which will be discussed in §7.7.5 and §7.7.10.

The sign of the first Landau coefficient changes from negative to positive if we trace the neutral stability curve from the lower branch with lower density (red line) to the upper branch with higher density (green line). The point where $a^{(0)}$ and $a^{(2)}$ are simultaneously zero is known as a degenerate point (Fujimura & Kelly 1997). In figure 7.10, a point at the intersection of red, green and blue lines is a degenerate point, marked by the blue circle, which occurs at $(\phi^d, k_z^{*d}) \approx (0.085001, 0.121027)$ on the neutral stability curve.

In §7.7.4, we discuss the underlying bifurcations of the uniform shear flow at the onset of linear vorticity banding instability. We focus mainly on cubic amplitude solutions in §7.7.4 and the higher order bifurcation diagrams are shown in §7.7.5.

7.7.4 Switchover from Supercritical to Subcritical Bifurcation

The possible switchover from supercritical to subcritical and vice versa, using cubic Landau equation, near the onset of instability is shown in figures 7.11(a) and 7.11(b).

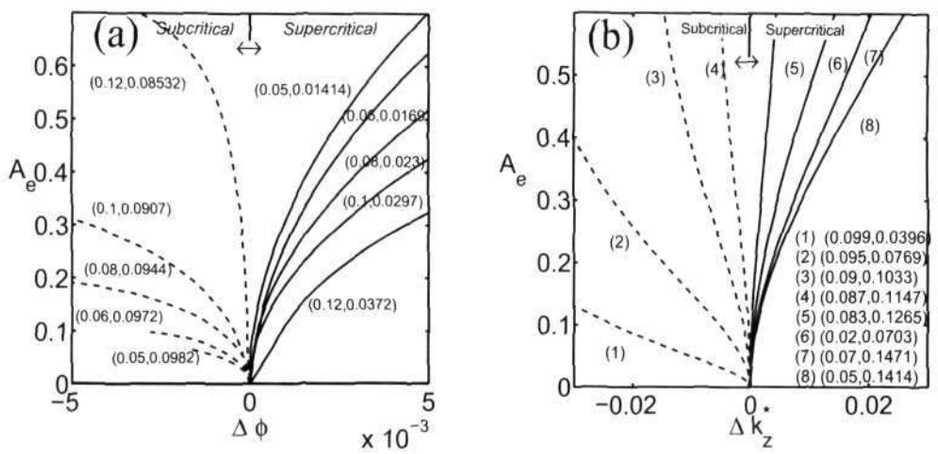

Figure 7.11: Variation of equilibrium amplitude, (a) with scaled density, $\Delta\phi$, in which the quantities in bracket denote (k_z^*, ϕ_c); (b) with scaled spanwise wavenumber Δk_z^* in which the quantities in bracket denote (ϕ^0, k_{zc}^*), for lines (1) to (8). The restitution coefficient is set to $e = 0.8$.

Figure 7.11(a) shows a series of bifurcation diagrams in the $(A_e, \Delta\phi)$-plane for five values of the spanwise wavenumber, $k_z^* = 0.05$, 0.06, 0.08, 0.1 and 0.12, just above the critical density for the onset of linear vorticity banding instability. The restitution coefficient is set to $e = 0.8$ as in figure 7.10. The subcritical and supercritical bifurcations are shown by dashed and solid lines, respectively. The regions of subcritical and supercritical bifurcations are separated by a double headed arrow. In figure 7.11(a), the negative and positive horizontal axes are scaled with critical densities ϕ_{c_1} and ϕ_{c_2} (see Eqn. (7.71)), respectively, so that the negative and the positive $\Delta\phi$-axes represent the stable and unstable uniform shear flow due to vorticity banding instability, respectively. In figure 7.11(a), the bracket represents: (i) (k_z^*, ϕ_{c_1}) for $\Delta\phi > 0$ where $\Delta\phi = \phi^0 - \phi_{c_1}$ (supercritical), and (ii) (k_z^*, ϕ_{c_2}) for $\Delta\phi < 0$ where $\Delta\phi = \phi_{c_2} - \phi^0$ (subcritical). From figure 7.10, the onset of supercritical and subcritical bifurcations are represented by the red and green lines, respectively. Consequently, the bifurcation diagrams as shown in figure 7.11(a) for $\Delta\phi < 0$ and $\Delta\phi > 0$, correspond to the onset of the linear instability shown by red and green lines, respectively.

Similar to figure 7.11(a), the bifurcation diagrams for eight values of the mean density $\phi^0 = 0.02$, 0.05, 0.07, 0.083, 0.087, 0.09, 0.095 and 0.099 in the $(A_e, \Delta k_z^*)$-plane for $e = 0.8$ are shown in figure 7.11(b). In figure 7.11(b), the horizontal axis is scaled with the critical spanwise wavenumber k_{zc}^* (see Eqn. (7.70)), i.e. $\Delta k_z^* = k_{zc}^* - k_z^*$. It is clear that the bifurcation is not subcritical immediately, rather we have a band of mean densities, $\phi^0 \in [0.083, 0.087)$, over which the bifurcation is supercritical which changes to subcritical for larger densities $\phi^0 \geq 0.087$. The supercritical bifurcation gives a stable finite amplitude solution (solid lines in figures 7.11(a) and 7.11(b)), and the subcritical bifurcation gives a threshold amplitude for the finite amplitude vorticity banding (nonlinear) instability, below which the flow is stable and above which it is unstable (shown by dashed lines in figures 7.11(a) and 7.11(b)).

In this section, we have discussed bifurcation diagrams just above the onset of instability in

$(A_e, \Delta\phi)$ and $(A_e, \Delta k_z^*)$-planes, using the cubic Landau equation. While the cubic theory gives the stable equilibrium solution for the supercritical case, it does not give any stable equilibrium solution for the subcritical bifurcation. Therefore, we need to know higher order Landau coefficients in order to get stable equilibrium solutions. The bifurcation diagrams which include quintic term of Landau equation (7.74) are discussed in the next section.

7.7.5 Bifurcation Diagrams using Quintic Landau Equation

Supercritical Bifurcation: $\phi^0 < \phi^d$

The bifurcation diagrams in $(A_e, \Delta\phi = \phi^0 - \phi_c)$-plane for two values of spanwise wavenum-

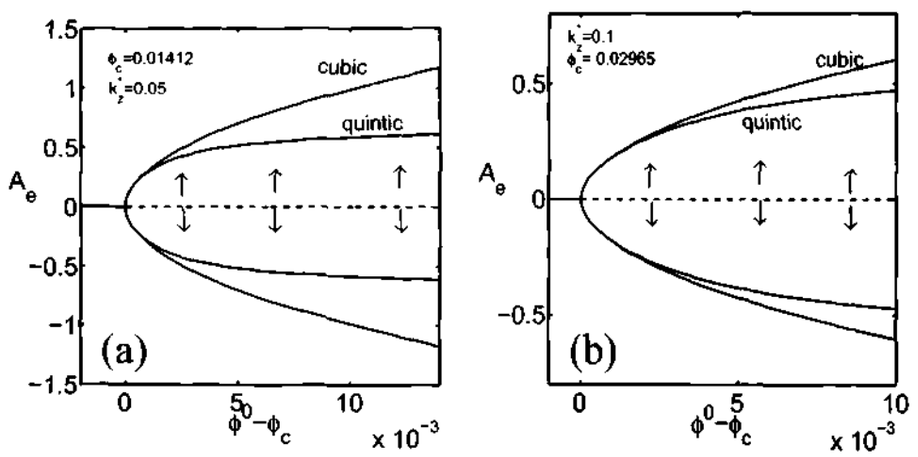

Figure 7.12: The supercritical bifurcation diagram in $(A_e, \phi^0 - \phi_c)$ plane for (a) $k_z^* = 0.05$ and (b) $k_z^* = 0.1$. The cubic and quintic solutions are marked in each figure. The solid and dashed lines above and below zero line denotes the stable and the unstable equilibrium solutions.

bers $k_z^* = 0.05$ and 0.1, using cubic and quintic Landau theory, are shown in figures 7.12(a) and 7.12(b). In these figures, the abscissas have been scaled by the critical density $\phi_c = \phi_{c_1}$, with ϕ_{c_1} being the critical density (see §7.7.1) above which the flow is linearly unstable due to vorticity-banding instability. The cubic and quintic order equilibrium solutions are calculated from (7.76) and (7.77), respectively. While the solid and dashed zero lines represent the stable and unstable base flow, respectively, the non-zero solid and dashed lines denote the stable and unstable equilibrium solutions, respectively. The cubic bifurcation diagrams for $k_z^* = 0.05$ and 0.1 have already been shown in figure 7.11(a). For small values of $\Delta\phi = \phi^0 - \phi_c$ or just above the onset of vorticity banding instability, the amplitudes from cubic and quintic Landau theory are exactly same, but they deviate from each other beyond moderate values of $\Delta\phi$. This deviation in the amplitude is because of the quintic nonlinear term which plays an important role when the parameters are slightly away from critical conditions. It is clear from this figure that the absolute value of quintic equilibrium amplitude is smaller than the cubic amplitude. For the case of supercritical bifurcations, the quintic theory gives more accurate stable amplitudes for the parameters which are away from the critical condition. In any case, the cubic theory is able to predict the correct picture of primary bifurcation near the onset of instability.

Subcritical Bifurcation: $\phi^0 > \phi^d$

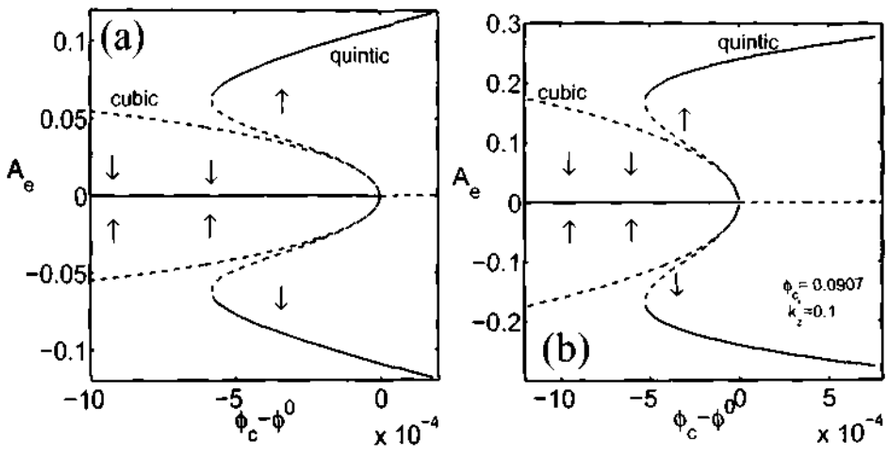

Figure 7.13: The subcritical bifurcation diagram in the $(A_e, \phi_c - \phi^0)$-plane for (a) $k_z^* = 0.05$ and (b) $k_z^* = 0.1$. The cubic and quintic solutions are marked in each figure. The solid and dashed lines above and below zero line denotes the stable and the unstable equilibrium solutions.

Similarly for the subcritical case ($\phi^0 > \phi^d$) the bifurcation diagrams for $k_z^* = 0.05$ and 0.1 are shown in figures 7.13(a) and 7.13(b) in the $(A_e, \phi_c - \phi^0)$-plane. All the four quintic order non-zero equilibrium solutions, (7.77), and two cubic order non-zero solutions, (7.76), are shown in these figures. Here the abscissas are scaled with ϕ_{c_2}, a critical density below which the uniform shear flow is unstable due to vorticity-banding instability.

Figures 7.13(a)-(b) show two backward bending branches of unstable equilibrium solutions which bifurcate from the origin (from the uniform shear flow, $A_e = 0$) when $\Delta\phi = 0$. While the two cubic unstable branches (dashed lines) spread along the negative $\Delta\phi$-axis, the quintic branches turn around, towards positive $\Delta\phi$-axis, and become stable at some $\Delta\phi = \Delta\phi_s$ where $\Delta\phi_s < 0$. The followings are a few notable comments about this subcritical/inverted/backward bifurcation scenario (Strogatz 1994):

- In the range $\Delta\phi_s < \Delta\phi < 0$, two qualitatively different stable states coexist, namely the origin and the large-amplitude equilibrium solutions. The initial condition A_0 determines which equilibrium solution is approached as $t \to \infty$. The origin is stable to small perturbations but unstable to large ones, i.e. the origin is locally stable but globally unstable.

- The existence of different stable states allows for the possibility of *jumps* and *hysteresis* (associated with "memory" of the system) as $\Delta\phi$ is varied. For an illustration we are again showing the quintic diagram of figure 7.13(b) in figure 7.14. If we start from the stable uniform shear state and then slowly increase the parameter $\Delta\phi$ (indicated by an arrow along the $\Delta\phi$-axis), the flow remains stable until $\Delta\phi = 0$, or, $\phi^0 = \phi_{c_2}$, at which the flow loses stability. A slight change in the initial condition will cause the uniform shear state to jump to one of the large-amplitude branches. If we further increases $\Delta\phi$, the flow remain stable with some amplitude. If $\Delta\phi$ is decreased, the state remains stable (on the large amplitude branch) even when $\Delta\phi$ is decreased below zero. We have to lower $\Delta\phi$ even further (below $\Delta\phi_s$) to get the state to jump back to origin, i.e. to get back stable uniform shear flow. This lack of reversibility as a parameter is varied is called hysteresis.

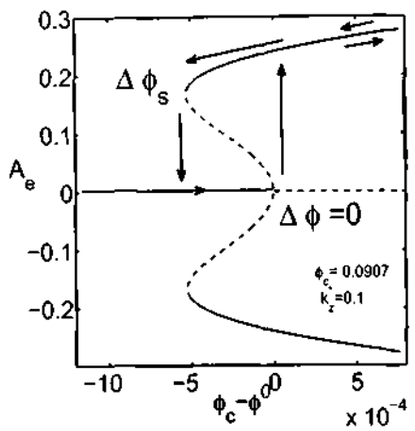

Figure 7.14: Same as figure 7.13(b) but only showing quintic bifurcation solutions.

- The bifurcation at $\Delta\phi_s$ is a saddle node bifurcation (limit point) at which the stable and unstable solutions are simultaneously born as $\Delta\phi$ is increased.
- The "subcritical" pitchfork (inverted or backward) bifurcation is related to discontinuous or first-order phase transitions, and the "supercritical" pitchfork bifurcation is related to continuous or second-order phase transition.

From figures 7.13(a) and 7.13(b), we can conclude that the calculation of second Landau coefficient is necessary for subcritical bifurcations because it provides the corresponding stable equilibrium solutions. Similar situations have been studied by Morozov & van Saarloos (2005) for the plane Couette flow of viscoelastic fluids.

Supercritical Bifurcation for Dilute Flows: Cubic and Quintic Theory

Next we show two more examples of supercritical bifurcation in the $(A_e, k^*_{zc} - k^*_z)$-plane. Figures 7.15(a) and 7.15(b) show the supercritical bifurcation diagrams for two values of mean density $\phi^0 = 0.01$ and 0.05 in the $(A_e, (k^*_{zc} - k^*_z))$-plane, with k^*_{zc} being the critical wavenumber below which the flow is linearly unstable. The qualitative features of these bifurcation diagrams are same as those in figures 7.12(a) and 7.12(b). The quintic solutions give better approximation of equilibrium amplitudes, for away from critical points.

Subcritical Regime ($\phi^0 > \phi^u_c$): Hopf Bifurcation

In this section we show the behavior of the flow in the subcritical regime $\phi^0 > \phi^u_c$ which is associated with Hopf bifurcation since the least-stable mode is a propagating mode at $\phi^0 > \phi^u_c \sim 0.1$.

The variations of $a^{(0)}$ (main panel) and $b^{(0)}$ (inset) for $\phi^0 = 0.15$ and $e = 0.8$ with k^*_z are shown in figure 7.16(a). It is seen in figure 7.16(a) that $a^{(0)}$ is negative and $b^{(0)}$ is non-zero which lead to Hopf (oscillatory) bifurcation. The corresponding $a^{(2)}$, figure 7.16(b), is positive throughout the range $k^*_z \in [0.12, 0.15]$ and, $a^{(4)}$, figure 7.16(c), varies from negative to positive. There is a kink at $k^*_z \approx 0.1339$ in figure 7.16(c) where $a^{(4)}$ (main panel) and $b^{(4)}$ (inset) diverge, and change their signs thereafter. From figure 7.16(c), $a^{(4)} < 0$ for $k^*_z \in [0.12, 0.1339)$ and $a^{(4)} > 0$

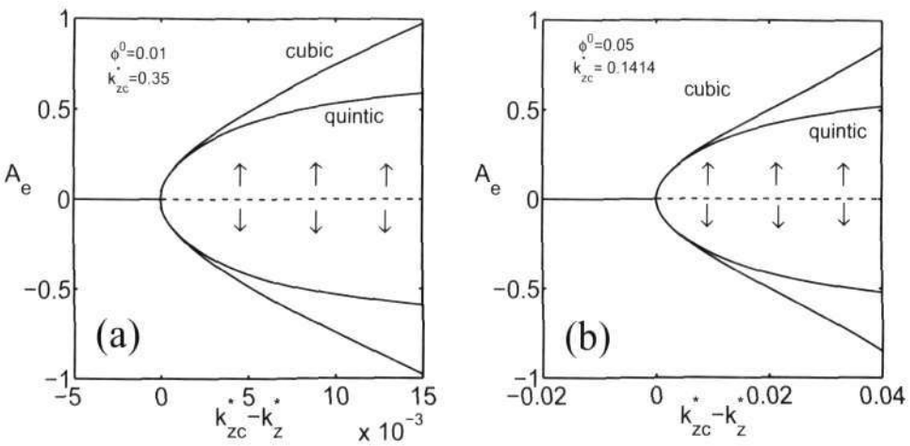

Figure 7.15: Bifurcation diagrams showing the supercritical bifurcation in $(A_e, k^*_{zc} - k^*_z)$-plane for ϕ^0 (a) 0.01 and (b) 0.05.

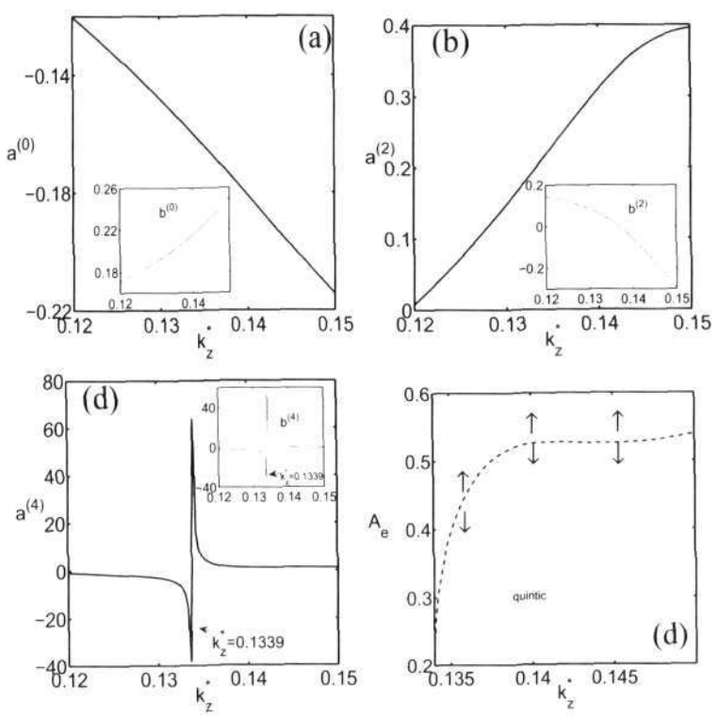

Figure 7.16: The variations of (a) $a^{(0)}$ and $b^{(0)}$ (inset), (b) $a^{(2)}$ and $b^{(2)}$ (inset), (c) $a^{(4)}$ and $b^{(4)}$ (inset), (d) quintic amplitudes, with k^*_z for $\phi^0 = 0.15$.

for $k_z^* \in [0.1339, 0.15]$; note from figure 7.16(b), $a^{(2)}$ is positive for $k_z^* \in [0.12, 0.15]$. Therefore, there exists a band of wavenumbers $k_z^* \in [0.12, 0.1339]$ between which the flow is always stable in quintic approximation which is in contrast to the cubic approximation which leads to subcritical instability in the flow. The quintic amplitude solution exists for $k_z^* \in [0.1339, 0.15]$ as shown in figure 7.16(d).

Next we show results for a fixed $k_z^* = 0.1$ over the density range $\phi^0 \in [0.12, 0.15] > \phi_c^u$. The variations of $a^{(0)}$ (main panel) and $b^{(0)}$ (inset) with density are shown in figure 7.17(a). It is observed in figure 7.17(a) that $a^{(0)} < 0$ and $b^{(0)} \neq 0$, leading to Hopf bifurcation. For this range of densities we show the corresponding variations of $a^{(2)}$ (main panel) and $b^{(2)}$ (inset) in figure 7.17(b) and of $a^{(4)}$ (main panel) and $b^{(4)}$ (inset) in figure 7.17(c). In figure 7.17(b) an arrow at $\phi^0 = 0.1337$ indicates the zero crossing of $a^{(2)}$; similarly an arrow at $\phi^0 = 0.1407$ in figure 7.17(c) represents the zero crossing of $a^{(4)}$. Depending on the sign of $a^{(0)}$, $a^{(2)}$ and $a^{(4)}$, the density range can be divided into three regions as marked in figure 7.17(d): (i) $\phi^0 = [0.12, 0.1337]$ for $a^{(2)} > 0$ and $a^{(4)} < 0$, (ii) $\phi^0 = [0.1337, 0.1407]$ for $a^{(2)} < 0$ and $a^{(4)} < 0$, and (iii) $\phi^0 = [0.1407, 0.15]$ for $a^{(2)} < 0$ and $a^{(4)} > 0$. For the first case, (i), the cubic subcritical amplitude exists but the higher order Landau coefficient $a^{(4)}$ stabilizes the flow which makes the flow stable and, therefore, the quintic amplitude solution does not exist. In the second case, (ii), the flow is always stable because $a^{(2)}$ and $a^{(4)}$ both are negative. The last case (iii) gives the quintic order subcritical instability because the quintic order Landau coefficient $a^{(4)}$ is positive and hence it destabilizes the flow. The cubic (dashed line) and quintic (dot-dashed line) order amplitudes are shown in figure 7.17(d).

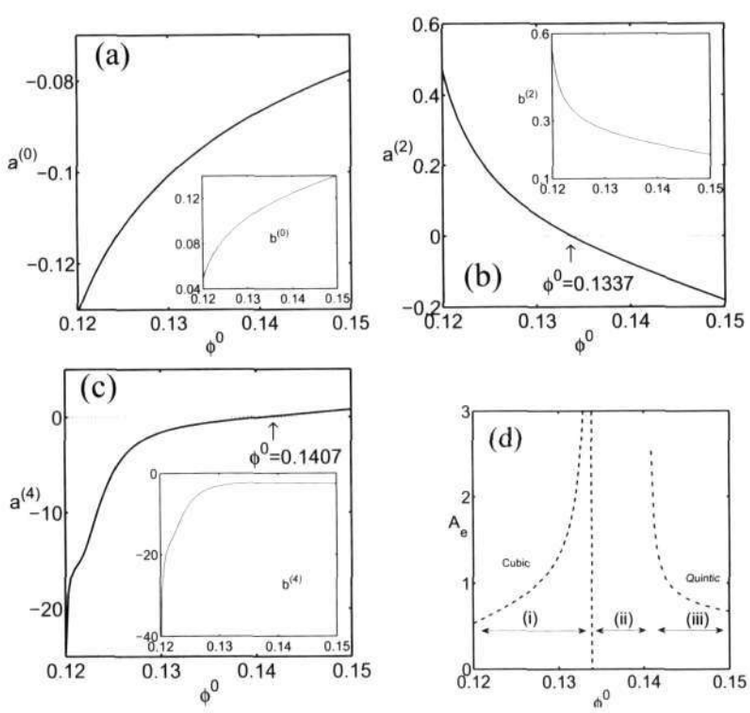

Figure 7.17: The variations of (a) $a^{(0)}$ and $b^{(0)}$ (inset), (b) $a^{(2)}$ and $b^{(2)}$ (inset), (c) $a^{(4)}$ and $b^{(4)}$ (inset), (d) cubic (dashed line) and quintic (dot-dashed line) amplitudes, with ϕ^0 for $k_z^* = 0.1$.

7.7.6 Variation of Amplitude with Density

A similar situation arises for the supercritical case at $\phi^0 < \phi^d$ and $k_z^* = 0.14$ as shown in figure 7.18. The corresponding variations of $a^{(0)}$ (solid line) and $a^{(2)}$ (dash-dot line) are shown in the inset plot. In this case, $a^{(0)}$ changes sign from negative to positive and positive to negative at $\phi^0 = 0.0489$ and $\phi^0 = 0.0765$, respectively. The densities where $a^{(0)} = 0$ are shown by arrows in the inset. Hence the equilibrium amplitude (supercritical pitchfork bifurcation), as shown in the main panel, exists for the range $\phi^0 \approx (0.0489, 0.0765)$.

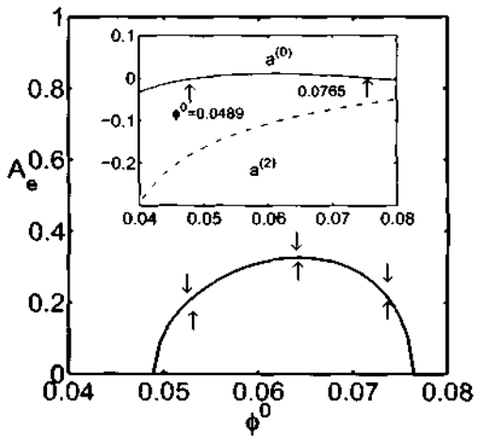

Figure 7.18: Variation of A_e with ϕ^0 for $\phi^0 < \phi^d$ and $k_z^* = 0.14$. The inset of shows the corresponding variations of $a^{(0)}$ (solid line) and $a^{(2)}$ (dash-dot line) where arrows indicate the location of $a^{(2)} = 0$. The restitution coefficient is $e = 0.8$.

The variations of equilibrium amplitude in the (A_e, ϕ^0)-plane, for four values of $k_z^* = 0.05$, 0.08, 0.1 and 0.12, are shown in figure 7.19(a) for the density range $\phi^0 > \phi^d$ where ϕ^d is the degenerate density which is marked by a blue circle in figure 7.10. In this region $a^{(2)} < 0$ and $a^{(2)}$ changes sign from positive to negative. As shown in this figure the bifurcation is subcritical for all values of k_z^* and the threshold amplitude for the instability increases with increasing k_z^*. In all cases, the amplitude first increases till some density beyond which it decreases and finally attains a zero value at the density where $a^{(2)}$ changes its sign. The bifurcation is pitchfork for all values of k_z^* in figure 7.19(a) which is shown next.

For $k_z^* = 0.12$, corresponding to the outer most curve in figure 7.19(a), variations of $a^{(2)}$ (solid line) and $b^{(2)}$ (dashed line) with densities are shown in the main panel and the corresponding $a^{(0)}$ (solid line) and $b^{(0)}$ (dashed line) are shown in the inset of figure 7.19(b). It is clearly shown in figure 7.19(b) that $b^{(0)} = b^{(2)} = 0$, hence the bifurcation is stationary, i.e. pitchfork. It has been verified that the bifurcation is pitchfork for all wavenumbers corresponding to figure 7.19(a).

So far we have discussed results for $\phi^0 > \phi^d$ (subcritical) and $\phi^0 < \phi^d$ (supercritical) for various values of $k_z^* \neq k_z^{*d}$. At $k_z^{*d} = 0.121027$ (see the blue circle in figure 7.10), the variation of A_e for the density range containing ϕ^d is shown in figure 7.20. Both $a^{(0)}$ (solid line) and $a^{(2)}$ (dot-dash line) change their signs at ϕ^d as shown by an arrow in the inset of figure 7.20. Therefore, the bifurcation type also changes from supercritical pitchfork to subcritical pitchfork (note that $b^{(0)} = b^{(2)} = 0$) at ϕ^d which is shown by solid and dashed lines, respectively, in the main panel. The degenerate point $\phi^0 = \phi^d$, separating the regions of supercritical and subcritical bifurcation, is shown by an arrow in the main panel.

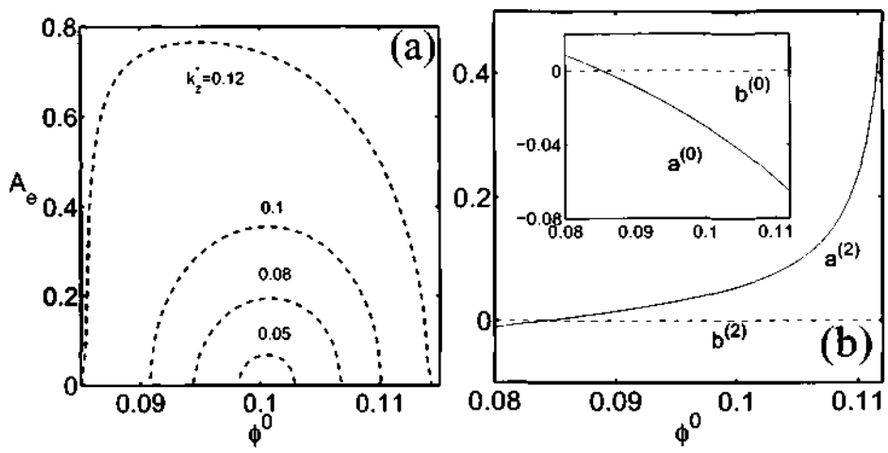

Figure 7.19: (*a*) Variation of A_e with $\phi^0 > \phi^d$, for $k_z^* = 0.05$, 0.08, 0.1 and 0.12. (*b*) Variations of $a^{(2)}$ (solid line) and $b^{(2)}$ (dashed line) and corresponding $a^{(0)}$ (solid line) and $b^{(0)}$ (dashed line) (in inset) with ϕ^0 for $k_z = 0.12$. The restitution coefficient is $e = 0.8$.

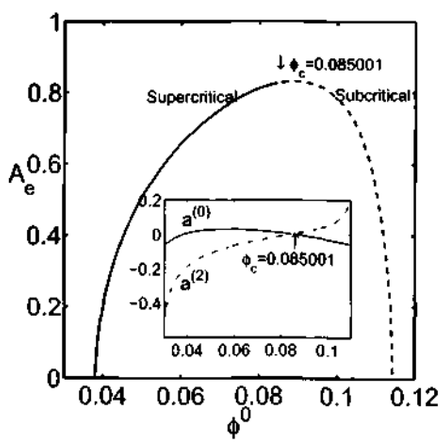

Figure 7.20: Same as figure 7.19 but for $k_z^* = k_z^{*d} = 0.121027$. The inset shows the corresponding variations of growth rate (solid line) and $a^{(2)}$ (dashed-dot line) and the arrow indicates the point where $a^{(0)} = a^{(2)} = 0$ at $\phi^0 = \phi^d = 0.085001$.

7.7.7 Scaling with Couette Gap

As discussed in §7.7.1, the neutral stability contour can be represented in terms of scaled span-wise wavenumber $k_z^* = k_z/H$, see Eqn. 7.70.

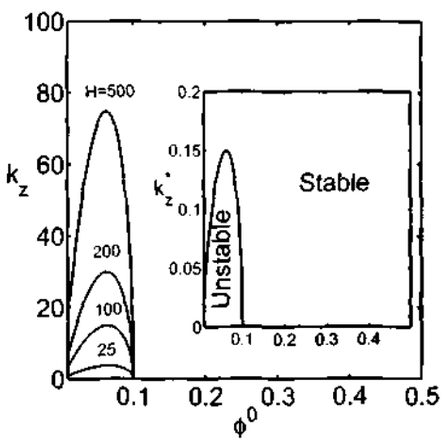

Figure 7.21: Stability diagram in (ϕ^0, k_z)-plane for $H = 25$, 100, 200 and 500 and the inset shows the scaled stability diagram in (ϕ^0, k_z^*)-plane. The restitution coefficient is set to $e = 0.8$.

Figure 7.21 shows the neutral stability curves for four values of Couette gap, $H = 25$, 100, 200 and 500, in the (ϕ^0, k_z)-plane. The flow is unstable inside each contours and stable outside for each H. It is clear from this figure that the neutral stability contour in (ϕ^0, k_z)-plane shifts towards higher values of spanwise wavenumber, k_z, with increasing H, and hence the flow becomes more unstable for larger k_z. This dependence of the neutral stability curve on H can be removed if we define a normalized wavenumber as

$$k_z^* = k_z/H. \tag{7.79}$$

Again all the neutral stability contours (for $H = 25$, 100, 200 and 500) are shown in the inset of figure 7.21 in (ϕ^0, k_z^*)-plane. We get a single neutral stability contour which is same as shown in figures 7.9(b) and 7.10. Thus the dependence of the linear vorticity-banding instability on the Couette gap can be removed using a normalized spanwise wavenumber.

The zero contours of the first Landau coefficient for $H = 25$, 100, 200 and 500 in (ϕ^0, k_z)-plane are shown in figures 7.22(a), 7.22(b), 7.22(c) and 7.22(d), respectively. The zero contour of the first Landau coefficient in (ϕ^0, k_z^*)-plane is shown in figure 7.22(e) where we have superimposed all four figures 7.22(a)-7.22(d) in the (ϕ^0, k_z^*)-plane. Note that this figure is the same as figure 7.10 but for an extended range of density and wavenumber: $\phi^0 \in (0, 0.5)$ and $k_z^* \in (0, 0.5)$. This clearly shows that the dependence of H on the first Landau coefficient can be removed with the scaling (7.79). Therefore, this wavenumber scaling, $k_z^* = k_z/H$, holds for the onset of nonlinear instability similar to the case of neutral stability contour.

7.7.8 Effect of Higher Order Nonlinear Terms

The nonlinear terms at fourth and fifth orders have to be considered to determine the harmonics of fourth and fifth orders that are subsequently used to calculate the second Landau coefficient. However, the first Landau coefficient involves nonlinear terms up-to cubic order, and hence the

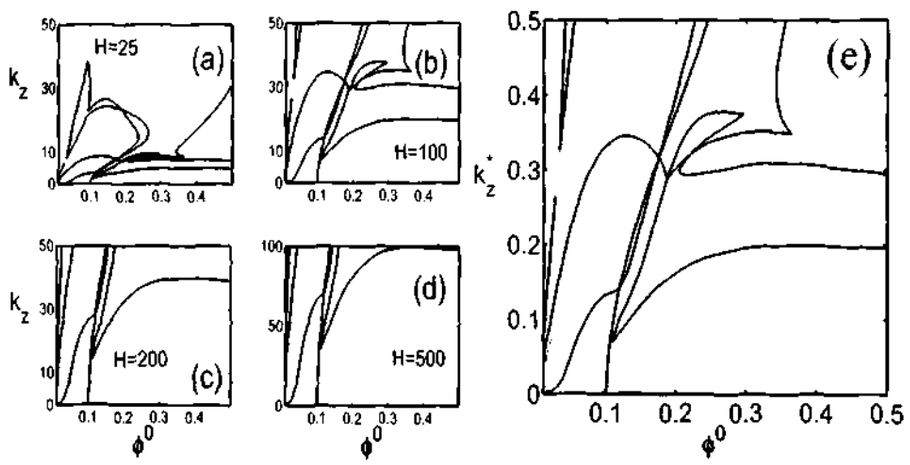

Figure 7.22: Contours of $a^{(2)} = 0$ in (ϕ^0, k_z)-plane for $e = 0.8$, (a) $H = 25$, (b) 100, (c) 200 and (d) 500. (e) Contours of $a^{(2)} = 0$ in (ϕ^0, k_z^*)-plane.

higher order nonlinear terms can be neglected to calculate $c^{(2)}$. We establish these assertions in the following.

Recall that the form of nonlinear disturbance equations is

$$\left(\frac{\partial}{\partial t} - \mathcal{L}\right) X = \mathcal{N} = \mathcal{N}_2 + \mathcal{N}_3 + \mathcal{N}_4 + \ldots. \qquad (*)$$

where $\mathcal{N}_j$ for $j \geq 2$ represents nonlinear terms at order j. The first and second Landau coefficients correct up-to cubic and quintic orders, respectively, can be written in the following functional forms:

$$c^{(2)} = f(\mathcal{N}_2, \mathcal{N}_3) \quad \text{and} \quad c^{(4)} = f(\mathcal{N}_2, \mathcal{N}_3, \mathcal{N}_4, \mathcal{N}_5), \qquad (7.80)$$

where f denotes a function. To check the effect of quartic (fourth) and quintic (fifth) order nonlinear terms, we define $\hat{c}^{(4)}$ as

$$\hat{c}^{(4)} = f(\mathcal{N}_2, \mathcal{N}_3, \boxed{\mathcal{N}_4}, \boxed{\mathcal{N}_5}), \qquad (7.81)$$

where the boxed quantities, i.e., $\mathcal{N}_4$ and $\mathcal{N}_5$ are neglected while calculating $\hat{c}^{(4)}$.

Now we show the variations of $a^{(4)}$ (7.80) and $\hat{a}^{(4)}$ (7.81) with k_z^* and ϕ^0 to demonstrate the effect and importance of incorporating higher nonlinear terms in (*). Figure 7.23 shows the variations of $\hat{a}^{(4)}$ (circles) and $a^{(4)}$ (stars) with k_z^* using cubic and quintic nonlinear terms for four values of $\phi^0 = 0.05$, 0.08, 0.1 and 0.15, with the corresponding variations of the growth rate and the first Landau coefficient being displayed as insets in each plot. It is observed that $\hat{a}^{(4)}$ and $a^{(4)}$ are very different. In fact, in the supercritical regime ($\phi^0 < \phi^d$) for $\phi^0 = 0.05$ and 0.08, $\hat{a}^{(4)}$ and $a^{(4)}$ have different signs as shown in figures 7.23(a) and 7.23(b). Although in the subcritical regime for $\phi^0 = 0.1$ and 0.15, both $\hat{a}^{(4)}$ and $a^{(4)}$ have same signs but their numerical values are vastly different (see figures 7.23c and 7.23d).

The variations of $\hat{a}^{(4)}$ and $a^{(4)}$ with density for two values of $k_z^* = 0.05$ and 0.1 are shown in figures 7.24(a) and 7.24(b), respectively. Again it is observed that the cubic approximation of second Landau coefficient (by neglecting $\mathcal{N}_4$ and $\mathcal{N}_5$) gives incorrect interpretation of underlying

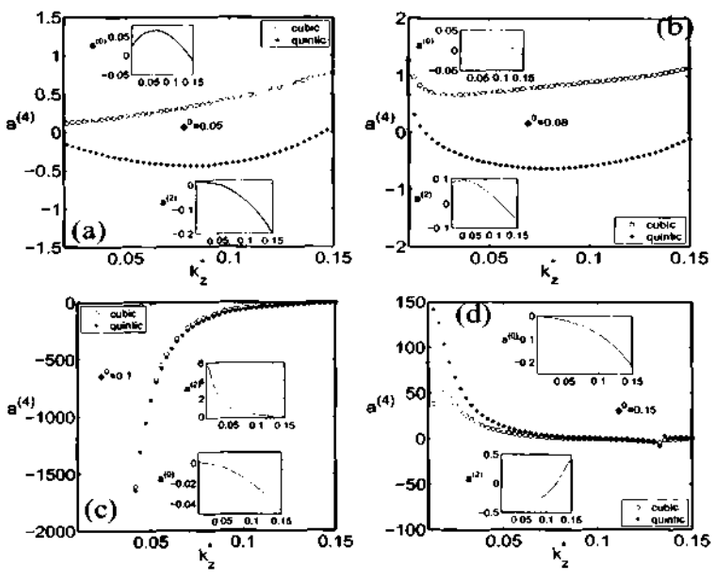

Figure 7.23: Variation of $a^{(4)}$ with k_z^* for (*a*) $\phi^0 = 0.05$, (*b*) $\phi^0 = 0.08$, (*c*) $\phi^0 = 0.1$ and (*d*) $\phi^0 = 0.15$. Circles and stars denote the cubic and quintic approximations, respectively. The insets of each plot show the corresponding variations of $a^{(0)}$ and $a^{(2)}$. Here $e = 0.8$.

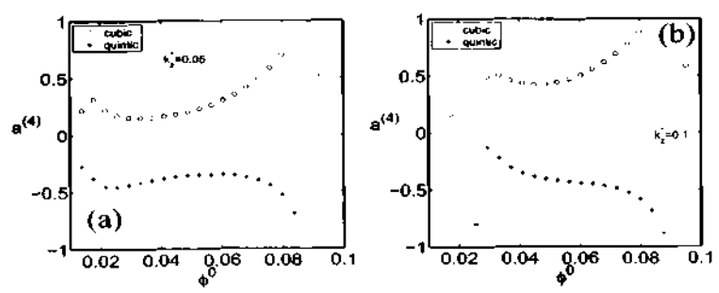

Figure 7.24: Variation of $a^{(4)}$ with ϕ^0 for (*a*) $k_z^* = 0.15$ and (*b*) $k_z^* = 0.1$. Other parameters are same as in figure 7.23.

bifurcation.

From figures 7.23-7.24, we can conclude that the second Landau coefficient at the quintic order cannot be determined by retaining only cubic nonlinear terms in (*). Therefore, for calculating the n^{th}-order Landau coefficient we need to consider nonlinear terms up-to n^{th}-order in (*), i.e., the correct functional form of n^{th}-order Landau coefficient is given by

$$c^{(n)} = f(\mathcal{N}_2, \mathcal{N}_3, \ldots, \mathcal{N}_n). \tag{7.82}$$

Therefore n^{th}-order nonlinearities $\mathcal{N}_n$ must be retained in (*) to correctly calculate $c^{(n)}$.

7.7.9 Vorticity Banding as a Subcritical Instabilities

Figure 7.25 shows regions of subcritical and supercritical bifurcations indicated by cyan and purple colors, respectively. The signs of $a^{(0)}$ and $a^{(2)}$ are marked in this figure. Depending on the sign of $a^{(0)}$ and $a^{(2)}$, we can classify the bifurcation as described below:

(a)	$a^{(0)}$	$>$	0	and $a^{(2)} < 0$,	supercritical bifurcation (purple color),
(b)	$a^{(0)}$	$<$	0	and $a^{(2)} > 0$,	subcritical bifurcation (region ①-ⅳ, cyan color),
(c)	$a^{(0)}$	$>$	0	and $a^{(2)} > 0$,	white region between $\phi \in (0, 0.1)$ and $k_z^* \in (0, 0.15)$,
(d)	$a^{(0)}$	$<$	0	and $a^{(2)} < 0$,	white regions for $\phi > 0.1$ and $k_z^* > 0.15$.

For cases when $a^{(0)}$ and $a^{(2)}$ have same signs (c and d), the equilibrium solution does not exist

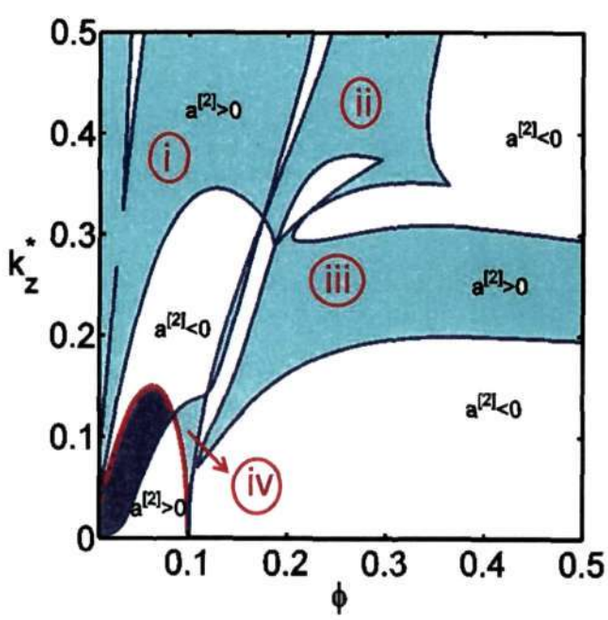

Figure 7.25: Phase diagram showing the subcritical (cyan color) and supercritical (purple color) regions. The amplitude from cubic LE does not exits in the white region.

at cubic order. For the situation as given in (d), the flow is non-linearly stable whereas for the regions described by (c) we need to calculate higher order Landau coefficients. The supercritical

solution is possible for the regions described under condition (a). The regions indicated by (i)-(iv), which satisfy condition (b), have subcritical bifurcations. In this case the cubic Landau equation does not give "stable" equilibrium solution and therefore we need to calculate second Landau coefficient to track the "stable" equilibrium solution. In the following we show that the subcritical instabilities can occur via Hopf and pitchfork bifurcations.

The bifurcation around the neutral stability curve for densities $\phi^0 \leq \phi^0_{3d}$ and $k_z^* \leq k^u_{zc}$ (cf. 7.73) is always pitchfork (stationary), i.e. $b^{(n)} = 0$ for $n = 0, 2, 4, \ldots$. However, for parameters far away from the neutral stability curve the bifurcation may not be pitchfork. It is verified that there exists subcritical Hopf bifurcation for higher densities. In the following we show the evidence of subcritical Hopf bifurcation for two fixed values of $k_z^* \geq k^u_{zc}$.

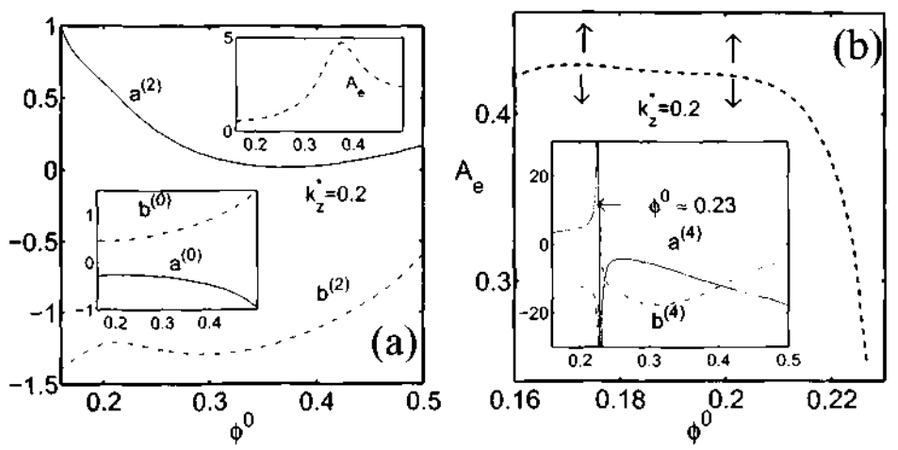

Figure 7.26: Variations with density (a) main panel: $a^{(2)}$ (solid line) and $b^{(2)}$ (dot-dashed line), lower inset: $a^{(0)}$ (solid line) and $b^{(0)}$ (dot-dashed line), upper inset: cubic amplitude A_e. (b) Variations of quintic amplitude A_e (main panel), $a^{(4)}$ (solid line in inset) and $b^{(4)}$ (dot-dashed line in inset) with ϕ^0. Parameters are $k_z^* = 0.2$ and $e = 0.8$.

Figure 7.26(a) shows the variations of $a^{(2)}$ (solid line) and $b^{(2)}$ (dot-dashed line) in main panel for $k_z^* = 0.2$ with densities corresponding to the region (iii) of figure 7.25. In this range of densities, $a^{(0)} < 0$ (solid line in inset) and $a^{(2)} > 0$ and the corresponding imaginary parts are non-zero, i.e. $b^{(0)} \neq 0$ (dot-dashed line in lower inset) and $b^{(2)} \neq 0$ (dot-dashed line), therefore there exists subcritical Hopf bifurcation. The corresponding cubic amplitude solution is shown in the upper inset of figure 7.26(a). In figure 7.26(b) we show the threshold quintic amplitude solution for the nonlinear stability and the corresponding variations of $a^{(4)}$ (solid line) and $b^{(4)}$ (dot-dashed line) are shown in its inset. While $a^{(2)}$ is positive for full range of densities (see figure 7.26a), $a^{(4)}$ changes sign from positive to negative at $\phi^0 \approx 0.23$ as indicated by an arrow in the inset of figure 7.26(b). It is seen in figure 7.26(b) that the amplitude is almost constant for $0.16 < \phi^0 < 0.2$ and then decreases rapidly which implies that the flow is more stable for $0.16 < \phi^0 < 0.2$ (because the threshold amplitude is larger in this region). For this range of densities, the cubic amplitude solution is not valid because the cubic Landau equation is strictly valid near the neutral stability curve and therefore the amplitude, as shown in inset of figure 7.26(a), is not the correct approximation of nonlinear solution. A jump in the second Landau coefficient at $\phi^0 \approx 0.23$ which is shown by an arrow in the inset of figure 7.26(b) is due to the higher-order resonances; for such cases the single mode analysis is not valid and we need to consider coupled Landau equations (see chapter 10).

Figure 7.27 is same as figure 7.26 but for $k_z^* = 0.27$. In this case, the quintic amplitude

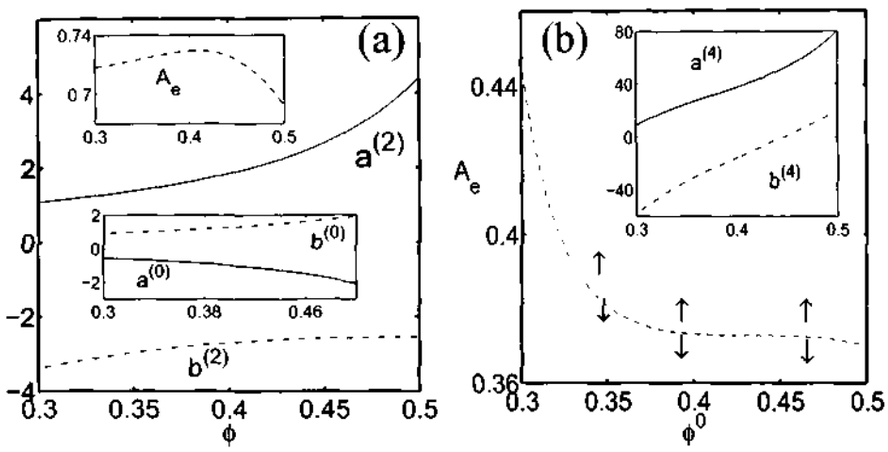

Figure 7.27: Same as figure 7.26 but for $k_z^* = 0.27$.

solution, see figure 7.27(b), exists for $\phi^0 = (0.3, 0.5)$ and the bifurcation is Hopf (subcritical). The threshold amplitude decreases with increasing densities. Similar observations can be made from figure 7.28 which is same as figure 7.26 but for $k_z^* = 0.14$.

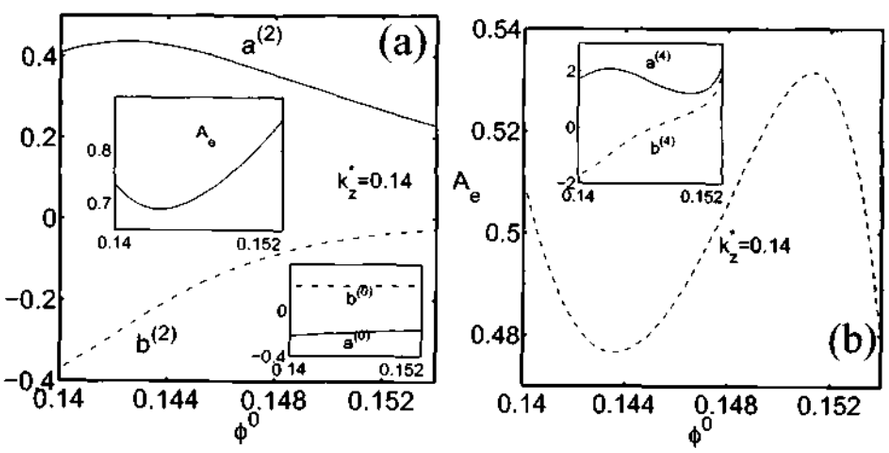

Figure 7.28: Same as figure 7.26 but for $k_z^* = 0.14$.

At this point we can compare bifurcations of vorticity banding and gradient banding (cf. chapter 5) in granular plane Couette flow. As discussed in chapter 5 that the granular plane Couette flow supports all kinds of pitchfork bifurcations with increasing density from Boltzmann limit, which lead to banding of particles in the gradient direction, see figure 5.38. All the bifurcations in the case of gradient banding are pitchfork (stationary) which is in contrast to the vorticity banding. Depending on the spanwise wavenumber the bifurcations which lead to vorticity banding can be classified into two parts: (i) $k_z^* < k_{zc}^u$ and (ii) $k_z^* > k_{zc}^u$ (cf. 7.73).

For $k_z^* < k_{zc}^u$ (cf. 7.73), the vorticity banding occurs via pitchfork, subcritical or supercritical, bifurcation for the densities below some critical density, i.e. $\phi^0 < \phi_c$, and via subcritical Hopf

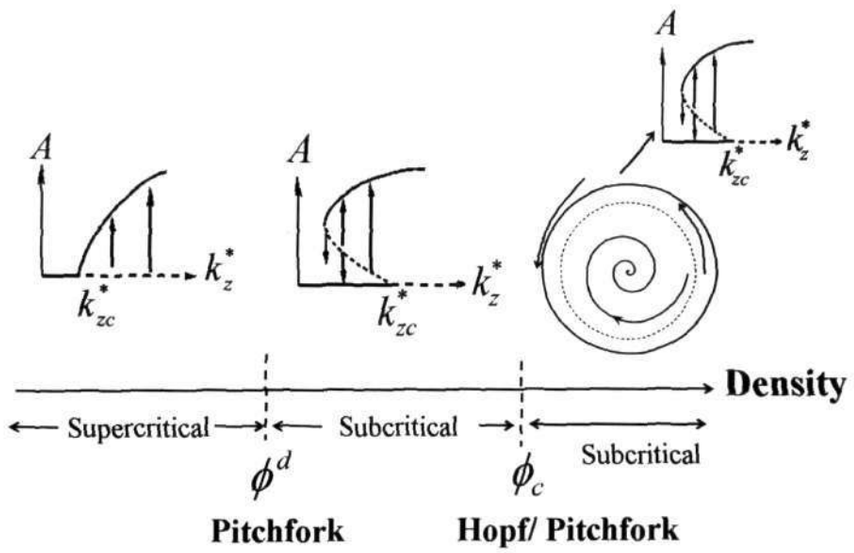

Figure 7.29: A schematic of bifurcation scenario in pure-spanwise flow for $k_z^* < k_{zc}^u$.

bifurcation for densities $\phi^0 > \phi_c$ as shown schematically in figure 7.29. The transition from supercritical (purple color region of figure 7.25) to subcritical (region (iv) of figure 7.25) occurs at $\phi^d < \phi_c$, see figure 7.29. For densities $\phi^0 > \phi_c$ the bifurcation is Hopf bifurcation which is always subcritical. An example of subcritical Hopf bifurcation for $\phi^0 > \phi_c$ is shown in figure 7.28 for $k_z^* = 0.14 < k_{zc}^u$ which belongs to the region (iii) of figure 7.25 corresponding to $k_z^* < k_{zc}^*$.

However, for $k_z^* > k_{zc}^u$ the bifurcation is always subcritical which can be pitchfork (stationary) or Hopf (oscillatory). Examples of Hopf bifurcation for moderate-to-large densities for two values of wavenumbers $k_z^* = 0.2 > k_{zc}^u$ and $k_z^* = 0.27 > k_{zc}^u$ are shown in figures 7.26 and 7.27, respectively, .

For large enough wavenumbers (or smaller wavelength), there exists a range of densities in the dilute limit where the flow admits Hopf bifurcation as shown in figure 7.30(a)-(b) which verifies the existence of Hopf bifurcation in dilute flows, see region (i) of figure 7.25. However, for moderate densities, at large values of k_z^*, the flow admits pitchfork bifurcation, an example of which is shown in figure 7.30(c)-(d).

7.7.10 Finite Amplitude Solutions

The finite amplitude disturbances in density (ϕ'), spanwise velocity (w') and granular temperature (T') [cf. (3.20), (3.29)] up-to quintic order in amplitude are calculated from

$$\begin{aligned}\phi'(z,t) &= A^2\phi^{[0:2]} + A^4\phi^{[0:4]} + \Big[\Big(A\phi^{[1:1]}e^{i\theta} + A^2\phi^{[2:2]}e^{2i\theta} + A^3\phi^{[1:3]}e^{i\theta} \\ &\quad + A^3\phi^{[3:3]}e^{3i\theta} + A^2\phi^{[2:4]}e^{2i\theta} + A^4\phi^{[4:4]}e^{4i\theta}\Big) + \text{c.c.}\Big], \end{aligned} \tag{7.83a}$$

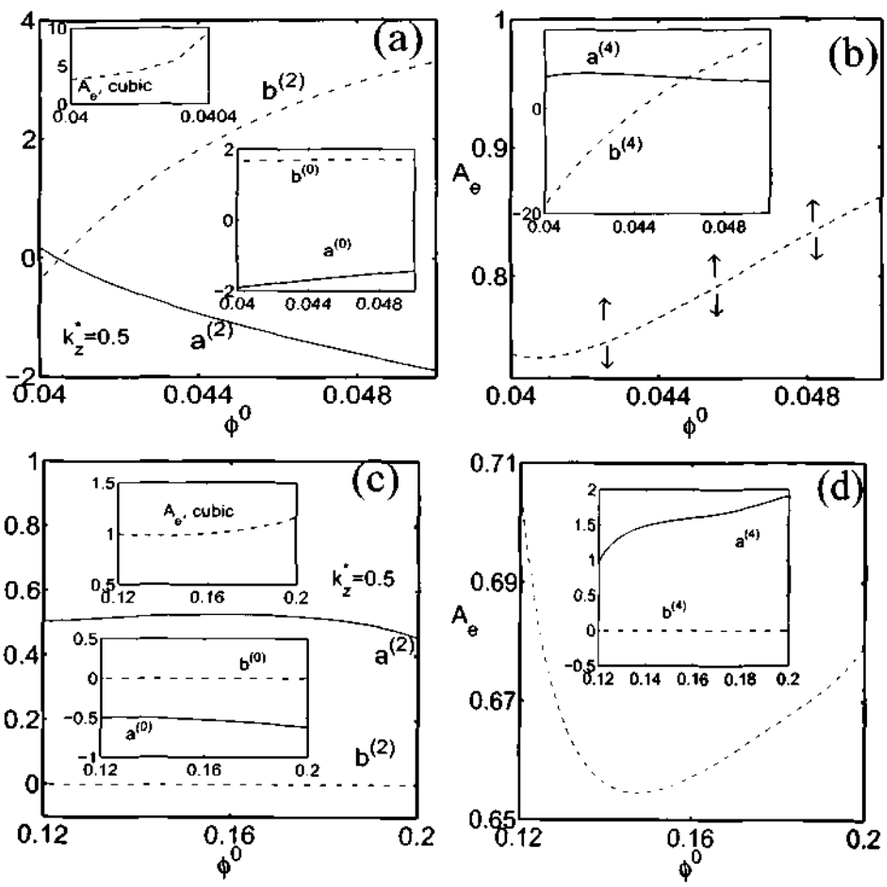

Figure 7.30: Same as figure 7.26 but for $k_z^* = 0.5$.

$$w'(z,t) = A^2 w^{[0;2]} + A^4 w^{[0;4]} + \Big[\Big(A w^{[1;1]} e^{i\theta} + A^2 w^{[2;2]} e^{2i\theta} + A^3 w^{[1;3]} e^{i\theta} + A^3 w^{[3;3]} e^{3i\theta} + A^2 w^{[2;4]} e^{2i\theta} + A^4 w^{[4;4]} e^{4i\theta}\Big) + \text{c.c.}\Big], \tag{7.83b}$$

$$T'(z,t) = A^2 T^{[0;2]} + A^4 T^{[0;4]} + \Big[\Big(A T^{[1;1]} e^{i\theta} + A^2 T^{[2;2]} e^{2i\theta} + A^3 T^{[1;3]} e^{i\theta} + A^3 T^{[3;3]} e^{3i\theta} + A^2 T^{[2;4]} e^{2i\theta} + A^4 T^{[4;4]} e^{4i\theta}\Big) + \text{c.c.}\Big] \tag{7.83c}$$

where $\theta = k_z z + (b^{(0)} + b^{(2)} A^2)t = k_z(z - c^e_{ph} t)$ and c^e_{ph} is the equilibrium phase velocity which is defined as

$$c^e_{ph} = -\frac{\omega}{k_z} = -\frac{b^{(0)}}{k_z} - \frac{b^{(2)} A^2}{k_z} = c_{ph} - \frac{b^{(2)} A^2}{k_z}. \tag{7.84}$$

Here c_{ph} is the linear phase velocity. At $t = 0$, or, for the stationary instability, we can simplify (7.83a) as

$$\begin{aligned}\phi'(z, t=0) = {} & A^2 \phi^{[0;2]} + A^4 \phi^{[0;4]} + 2A \left[\phi_r^{[1;1]} \cos(2\pi z/\lambda_z) - \phi_i^{[1;1]} \sin(2\pi z/\lambda_z)\right] \\ & + 2A^2 \left[\phi_r^{[2;2]} \cos(4\pi z/\lambda_z) - \phi_i^{[2;2]} \sin(4\pi z/\lambda_z)\right] \\ & + 2A \left[\phi_r^{[1;3]} \cos(2\pi z/\lambda_z) - \phi_i^{[1;3]} \sin(2\pi z/\lambda_z)\right] \\ & + 2A^3 \left[\phi_r^{[3;3]} \cos(6\pi z/\lambda_z) - \phi_i^{[3;3]} \sin(6\pi z/\lambda_z)\right] \\ & + 2A^4 \left[\phi_r^{[2;4]} \cos(4\pi z/\lambda_z) - \phi_i^{[2;4]} \sin(4\pi z/\lambda_z)\right],\end{aligned} \tag{7.85}$$

where $\lambda_z = 2\pi/k_z$ is the spanwise wavelength. Similarly, we can simplify spanwise velocity (7.83b) and granular temperature (7.83c) disturbances.

The shear stress τ is defined as:

$$\tau = \mu \frac{\mathrm{d}u}{\mathrm{d}y} = \mu, \quad \text{because} \quad \frac{\mathrm{d}u}{\mathrm{d}y} = 1 \quad \text{(for the linear velocity profile)}, \tag{7.86}$$

where μ is the coefficient of shear viscosity. Similar to above expansions (7.83a)-(7.83c), we can expand stress (τ) and pressure (p) as follows:

$$\tau = \mu = \mu^0 + \mu^0_\phi \phi' + \mu^0_T T' \quad \text{and} \quad p = p^0 + p^0_\phi \phi' + p^0_T T', \tag{7.87}$$

where μ^0 and p^0 are the base state shear viscosity and pressure, respectively, and, ϕ' and T' are the disturbances as defined by (7.83a) and (7.83c), respectively.

Next we are showing variations of stationary and oscillatory finite amplitude solutions as defined by (7.83a)-(7.83c) and (7.87) along the scaled spanwise direction i.e. z/λ_z. We will plot instantaneous disturbance fields (ϕ', w', T'), shear stress (μ) and pressure (p) at equilibrium using the quintic amplitude solution.

Stationary Solutions

The variations of disturbance density (ϕ'), spanwise velocity (w'), temperature (T'), total stress (μ) and pressure (p) with scaled spanwise coordinate (z/λ_z) are shown in figures 7.31(a)-(e) for $\phi^0 = 0.05$, $k_z^* = 0.12$ and $e = 0.8$. In this case the flow is linearly unstable and the bifurcation type is supercritical, see figure 7.15(b). These patterns are stationary because the underlying bifurcation is pitchfork; in other words, the imaginary parts of the least-stable mode

and the Landau coefficients are zeros.

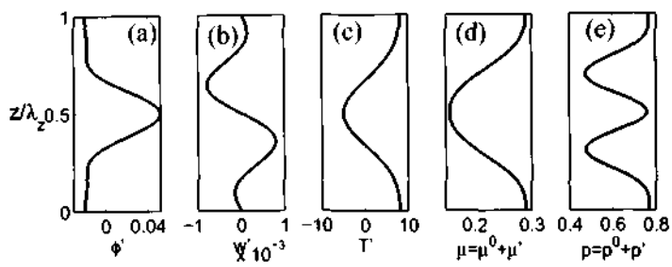

Figure 7.31: Variations of (ϕ', w', T'), $\mu = \mu^0 + \mu'$ and $p = p^0 + p'$ with z/λ_z, for parameters: $\phi^0 = 0.05$, $k_z^* = 0.12$ and $e = 0.8$. (a) Density, (b) spanwise velocity, (c) granular temperature, (d) shear stress and (e) pressure. See the quintic amplitude branch in figure 7.15(b).

The stationary disturbance fields, shear stress and pressure corresponding to the unstable solution at $\phi^0 = 0.091$, $k_z^* = 0.1$ and $e = 0.8$, associated with the lower quintic branch (unstable solution) in figure 7.13(b), are shown in figure 7.32(a)-(e). Figures 7.32(f) to 7.32(j) are same as figures 7.32(a) to 7.32(e) but for the stable solution (corresponding to upper or stable branch of bifurcation diagram 7.13(b)).

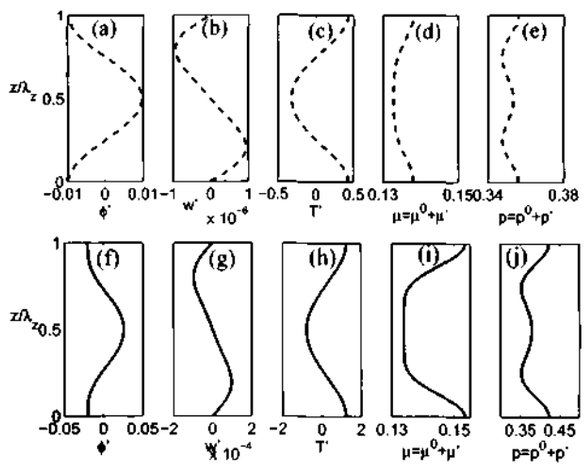

Figure 7.32: For $\phi^0 = 0.091$, $k_z^* = 0.1$ and $e = 0.8$, variations of unstable solutions: (a) ϕ', (b) w', (c) T', (d) $\mu = \mu^0 + \mu'$, and (e) $p = p^0 + p'$. The flow is linearly stable and the bifurcation is subcritical. See the dashed line of quintic amplitude in figure 7.13(b). Figures $(f$-$j)$ are same as $(a$-$e)$ but the amplitude belongs to the stable quintic branch in figure 7.13(b).

It is clear that the density in each of figures 7.31(a), 7.32(a) and 7.32(f) is maximum at the center of the domain, and the corresponding granular temperature, in each of figures 7.31(c), 7.32(c) and 7.32(h) is minimum at the center of the domain. The total shear stress ($\tau = \mu$) and pressure (p) vary significantly along the spanwise direction. Therefore, the vorticity banding leads to localization in shear stress and pressure along the vorticity direction.

Oscillatory Solutions

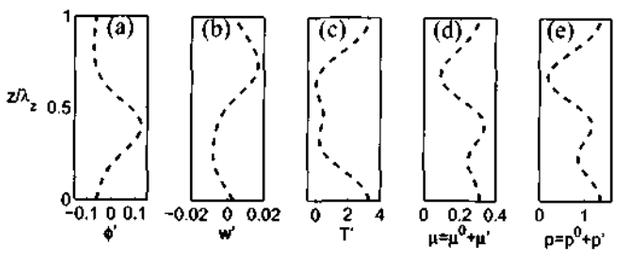

Figure 7.33: Same as figure 7.32 but for $k_z^* = 0.14$ and $\phi^0 = 0.15$, see figure 7.16. Here $a^{(0)} < 0$, $a^{(2)} > 0$ and $a^{(2)} > 0$.

Figures 7.33 and 7.34 represent oscillatory finite amplitude solutions (quintic order) for $\phi^0 = 0.15$ at $k_z^* = 0.14$ and 0.135, respectively. For these parameters the flow has subcritical finite amplitude instability. It is clear that these solutions which originated from oscillatory bifurcations are markedly different from the stationary solutions as depicted in figures 7.31-7.32. The bifurcation diagram related to these solutions in figures 7.33 and 7.34 has been shown in figures 7.16.

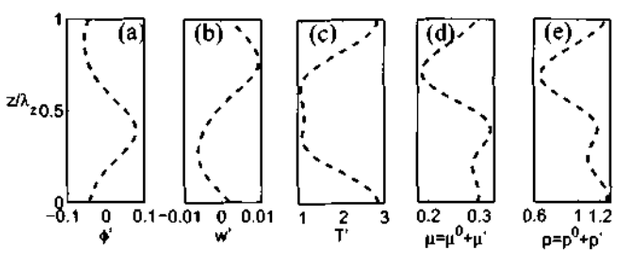

Figure 7.34: Same as figure 7.33 but for $k_z^* = 0.135$.

7.7.11 Results for Dense Flows at Small Wave Lengths: Linearly Stable Regime

The variations of $a^{(2)}$ (solid line in main panel), $b^{(2)}$ (dot-dash line in main panel), $a^{(0)}$ (sold line in inset) and $b^{(0)}$ (dot-dash line in inset) are shown in figure 7.35(a). A kink at $k_z^* \sim 0.3$ in the growth rate curve (solid line), see inset of figure 7.35(a), represents a mode-crossing where two traveling modes merge together to give birth to two stationary modes. Due to this mode crossing, $a^{(2)}$ (solid line) and $b^{(2)}$ (dot-dash line) in figure 7.35(a) and $a^{(4)}$ (solid line) and $b^{(4)}$ (dot-dash line) in figure 7.35(b) diverge at $k_z^* \sim 0.3$. As shown in figure 7.35(b), $a^{(4)}$ and $b^{(4)}$ also diverge at $k_z^* \sim 0.25$ which is due to nonlinear resonances (mean flow resonance, $1:2$ resonance, etc., as discussed in chapter 6 for the two-dimensional granular Couette flow). The quintic (stars) order amplitudes are shown in figure 7.35(c). It is clear from this figure that there is a range of $k_z^* \sim [0.25, 0.5]$ where the quintic amplitude solutions exist.

Similar to figure 7.32, figures 7.36 and 7.37 show the finite amplitude quintic order solutions at $\phi^0 = 0.5$ for two values of spanwise wavenumbers $k_z^* = 0.4$ and 0.285, respectively. The finite

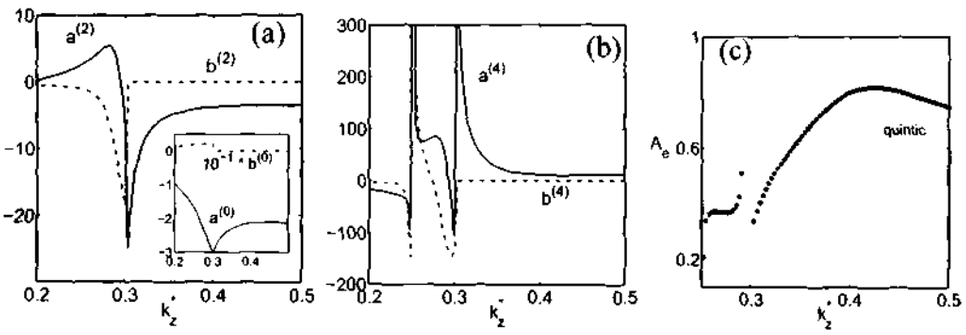

Figure 7.35: Variations with k_z^* for $\phi^0 = 0.5$ and $e = 0.8$: (*a*) $a^{(2)}$ (solid line), $b^{(2)}$ (dot-dash line), $a^{(0)}$ (solid line in inset) and $b^{(0)}$ (dot-dash line in inset), (*b*) $a^{(4)}$ (solid line) and $b^{(4)}$ (dot-dash line), (*c*) quintic solution.

amplitude solutions in figure 7.36 are stationary and those in figure 7.37 are oscillatory, see the bifurcation diagram 7.35(c). Again, it is observed that the oscillatory solutions are different from the stationary solutions.

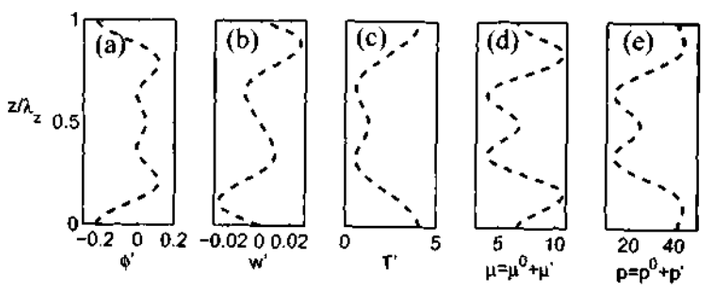

Figure 7.36: Stationary solutions. Same as figure 7.32 but for $\phi^0 = 0.5$ and $k_z^* = 0.4$. Here $a^{(0)} < 0$, $a^{(2)} < 0$ and $a^{(4)} > 0$.

Figure 7.38 shows the variations of cubic and quintic amplitudes with k_z^* for $\phi^0 = 0.12$ and $e = 0.8$. The bifurcation is subcritical. The corresponding variations of $a^{(0)}$ (dot-dash line), $a^{(2)}$ (dash line) and $a^{(4)}$ (solid line) are shown in the inset which shows that both $a^{(2)}$ and $a^{(4)}$ are positive and hence the flow is unstable. The finite amplitude solutions corresponding to the stationary quintic amplitude at $k_z^* = 0.4$, see figure 7.38, are shown in figure 7.39

7.8 Conclusions and Outlook

We have analyzed the nonlinear stability of three dimensional granular plane Couette flow, focusing on the pure spanwise instability (Gayen & Alam 2006; Alam 2006) for which the uniform shear flow degenerates into an ordered state with shear-stress-localization which further induces density segregation in the form of spanwise rolls along the vorticity (spanwise) direction. The amplitude expansion method (Stuart 1960; Watson 1960; Reynolds & Potter 1967; Shukla & Alam 2011) has been used to the present nonlinear problem of pure spanwise granular plane Couette flow. The amplitude expansion method reduces the nonlinear stability problem into a series of linear

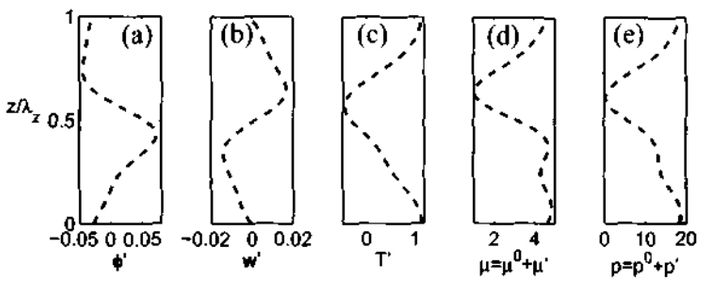

Figure 7.37: Oscillatory solutions.. Same as figure 7.32 but for $\phi^0 = 0.5$ and $k_z^* = 0.285$. Here $a^{(0)} < 0$, $a^{(2)} > 0$ and $a^{(4)} > 0$.

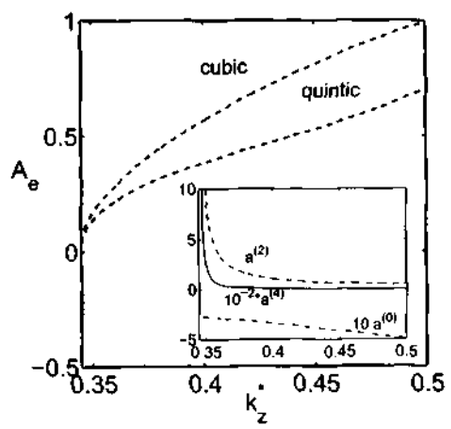

Figure 7.38: Variations of cubic and quintic amplitudes with k_z^* for $\phi^0 = 0.12$ and $e = 0.8$; in inset, $a^{(0)}$ (dot-dash line), $a^{(2)}$ (dash line) and $a^{(4)}$ (solid line).

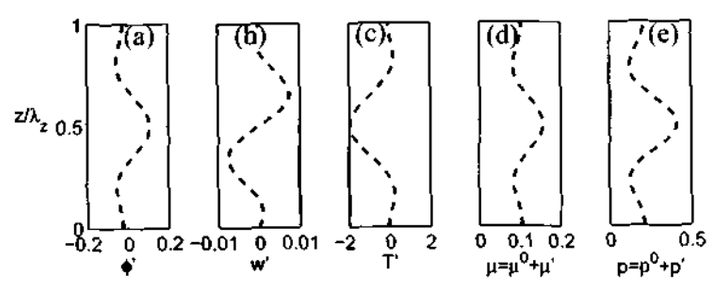

Figure 7.39: Same as figure 7.32 but for $k_z^* = 0.4$ and other parameters are same as figure 7.38.

problems: second harmonic, distortion of mean flow, distortion of fundamental and higher order harmonics. As we have discussed in chapter 5, this is an indirect method to derive Landau equation as compared to the direct method of 'center manifold reduction' which has been discussed in chapter 4.

The pure spanwise granular Couette flow is blessed by a simplified set of balance equations since $\partial/\partial x(.) = 0$ and $\partial/\partial y(.) = 0$. Moreover, two equations of this simplified set, corresponding to streamwise (x) and transverse (y) momentum equations, are decoupled from the other three equations. Therefore, the system of order five can be divided into two parts: the 'first' is related to the x and y-momentum equations which are decoupled from the rest of the equations and the 'second' is related to other three coupled equations. Furthermore, the two components of the higher harmonics which are related to the 'first' system eventually vanish because the corresponding components of the fundamental are zeros. Therefore, we are left with a system of equations of order three which in turn has a general solution. The first and second Landau coefficients also have analytical forms. We have shown in this chapter that all nonlinear equations along with Landau coefficients of the amplitude expansion method for pure spanwise granular Couette flow are analytically solvable. The general analytical order parameter theory has been developed for the pure spanwise granular Couette flow.

Our analytical order parameter theory predicts that for $k_z^* < k_{zc}^u$ there exists a critical density $\phi^d = \phi_{3d}^0 \sim 0.1$ such that (i) for densities $\phi^0 < \phi^d$ the uniform shear flow bifurcates supercritically and gives stable vorticity-bands via a second-order transition, and (ii) for densities $\phi^0 > \phi^d$ the uniform shear flow bifurcates subcritically and gives unstable vorticity-bands. These unstable bands which are formed by the subcritical bifurcation of the uniform shear flow could be stabilized by higher order nonlinear terms. Consequence of this is a first order transition at $\phi^0 > \phi_{3d}^0$ in the linearly stable region.

We have shown that there is a window of densities over which the vorticity bands are supercritically stable via a second-order phase transition; similarly, there exists a window of densities over which the bands are subcritically unstable but can be stable via a first-order phase transition. For the moderate-to-dense flows, i.e. $\phi^0 > \phi_{3d}^0$, we found subcritical instabilities for some range of densities that might cause vorticity banding in moderate-to-dense flows. Not much MD-simulations have been done for this limit.

In regions away from the neutral stability curve there can be either pitchfork or Hopf bifurcation which occurs always via subcritical bifurcation. For sufficiently large wavenumbers there are transitions from pitchfork-to-Hopf for dilute flows and Hopf-to-pitchfork for moderate-to-dense flows. However, for moderate wavenumbers there are transitions from pitchfork-to-Hopf for moderate-to-dense flows. Therefore, vorticity banding changes from stationary to oscillatory bifurcations as a function density and spanwise wavenumber which is in contrast to the gradient banding which occurs only via stationary (pitchfork) bifurcation.

It has been verified that the scaling between spanwise wavenumber and Couette gap hold for the zeros of the Landau coefficients. The crucial effect of higher order nonlinear terms (quartic and quintic) for calculating higher order Landau coefficients (more specifically, the second Landau coefficient) is demonstrated. The variations of disturbance fields along z-direction are also shown, leading to variations in shear stress and viscosity along the vorticity direction for pure spanwise perturbations.

Appendix 7A. Elements of linear and adjoint operators

Elements of Linear Operator $\mathcal{L} = [l_{ij}]$ (cf. Eqn. (7.11))

$$
\left.\begin{aligned}
l_{11} &= -u^0\tfrac{\partial}{\partial x}, \quad l_{12} = -\phi^0\tfrac{\partial}{\partial x}, \quad l_{13} = -\left[\phi^0_y + \phi^0\tfrac{\partial}{\partial y}\right], \quad l_{14} = -\phi^0\tfrac{\partial}{\partial z}, \quad l_{15} = 0\\
l_{21} &= \tfrac{1}{H^2\phi^0}\left[-p^0_\phi\tfrac{\partial}{\partial x} + u^0_y\left(\mu^0_{\phi y} + \mu^0_\phi\tfrac{\partial}{\partial y}\right) + u^0_{yy}\mu^0_\phi\right]\\
l_{22} &= -u^0\tfrac{\partial}{\partial x} + \tfrac{1}{H^2\phi^0}\left[(2\mu^0+\lambda^0)\tfrac{\partial^2}{\partial x^2} + \mu^0\left(\tfrac{\partial^2}{\partial y^2} + \tfrac{\partial^2}{\partial z^2}\right) + \mu^0_y\tfrac{\partial}{\partial y}\right]\\
l_{23} &= -u^0_y + \tfrac{1}{H^2\phi^0}\left[(\mu^0+\lambda^0)\tfrac{\partial^2}{\partial x\partial y} + \mu^0_y\tfrac{\partial}{\partial x}\right], \quad l_{24} = \tfrac{(\mu^0+\lambda^0)}{H^2\phi^0}\tfrac{\partial^2}{\partial x\partial z}\\
l_{25} &= \tfrac{1}{H^2\phi^0}\left[-p^0_T\tfrac{\partial}{\partial x} + u^0_y\left(\mu^0_{Ty} + \mu^0_T\tfrac{\partial}{\partial y}\right) + u^0_{yy}\mu^0_T\right]\\
l_{31} &= \tfrac{1}{H^2\phi^0}\left[-\left(p^0_{\phi y} + p^0_\phi\tfrac{\partial}{\partial y}\right) + u^0_y\mu^0_\phi\tfrac{\partial}{\partial x}\right], \quad l_{32} = \tfrac{1}{H^2\phi^0}\left[\lambda^0_y\tfrac{\partial}{\partial x} + (\lambda^0+\mu^0)\tfrac{\partial^2}{\partial x\partial y}\right]\\
l_{33} &= -u^0\tfrac{\partial}{\partial x} + \tfrac{1}{H^2\phi^0}\left[(2\mu^0_y + \lambda^0_y)\tfrac{\partial}{\partial y} + (2\mu^0+\lambda^0)\tfrac{\partial^2}{\partial y^2} + \mu^0\left(\tfrac{\partial^2}{\partial z^2} + \tfrac{\partial^2}{\partial x^2}\right)\right]\\
l_{34} &= \tfrac{1}{H^2\phi^0}\left[\lambda^0_y\tfrac{\partial}{\partial z} + (\lambda^0+\mu^0)\tfrac{\partial^2}{\partial z\partial y}\right], \quad l_{35} = \tfrac{1}{H^2\phi^0}\left[-\left(p^0_{Ty} + p^0_T\tfrac{\partial}{\partial y}\right) + u^0_y\mu^0_T\tfrac{\partial}{\partial x}\right]\\
l_{41} &= \tfrac{-p^0_\phi}{H^2\phi^0}\tfrac{\partial}{\partial z}, \quad l_{42} = \tfrac{(\mu^0+\lambda^0)}{H^2\phi^0}\tfrac{\partial^2}{\partial x\partial z}, \quad l_{43} = \tfrac{1}{H^2\phi^0}\left[(\mu^0+\lambda^0)\tfrac{\partial^2}{\partial y\partial z} + \mu^0_y\tfrac{\partial}{\partial z}\right]\\
l_{44} &= -u^0\tfrac{\partial}{\partial x} + \tfrac{1}{H^2\phi^0}\left[(2\mu^0+\lambda^0)\tfrac{\partial^2}{\partial z^2} + \mu^0\left(\tfrac{\partial^2}{\partial x^2} + \tfrac{\partial^2}{\partial y^2}\right) + \mu^0_y\tfrac{\partial}{\partial y}\right], \quad l_{45} = \tfrac{-p^0_T}{H^2\phi^0}\tfrac{\partial}{\partial z}\\
l_{51} &= \tfrac{2}{dim\,\phi^0 H^2}\left[T^0_{yy}\kappa^0_\phi + T^0_y\left(\kappa^0_\phi\tfrac{\partial}{\partial y} + \kappa^0_{\phi y}\right)\right] + \tfrac{2(u^{0^2}_y\mu^0_\phi - \mathcal{D}^0_\phi)}{dim\,\phi^0}\\
l_{52} &= \tfrac{2}{dim\,\phi^0}\left[-p^0\tfrac{\partial}{\partial x} + 2\mu^0 u^0_y\tfrac{\partial}{\partial y}\right], \quad l_{53} = -T^0_y + \tfrac{2}{dim\,\phi^0}\left[-p^0\tfrac{\partial}{\partial y} + 2\mu^0 u^0_y\tfrac{\partial}{\partial x}\right]\\
l_{54} &= -\tfrac{2p^0}{dim\,\phi^0}\tfrac{\partial}{\partial z}\\
l_{55} &= -u^0\tfrac{\partial}{\partial x} + \tfrac{2}{dim\,\phi^0 H^2}\left[\kappa^0\left(\tfrac{\partial^2}{\partial x^2} + \tfrac{\partial^2}{\partial y^2} + \tfrac{\partial^2}{\partial z^2}\right) + \kappa^0_y\tfrac{\partial}{\partial y} + \kappa^0_T T^0_{yy} + T^0_y\left(\kappa^0_T\tfrac{\partial}{\partial y} + \kappa^0_{Ty}\right)\right]\\
&\quad + \tfrac{2(\mu^0_T u^{0^2}_y - \mathcal{D}^0_T)}{dim\,\phi^0}
\end{aligned}\right\}
$$

Adjoint Matrix Elements $\mathbf{L}^\dagger = [l^\dagger_{ij}]$ (cf. Eqn. (7.19)) (In the following $D \equiv \frac{d}{dy}$)

$$
\left.\begin{aligned}
l^\dagger_{11} &= ik_x u^0, \quad l^\dagger_{12} = \tfrac{ik_x p^0_\phi}{\phi^0 H^2} - \tfrac{u^0_y\mu^0_\phi\left(\phi^0 D - \phi^0_y\right)}{(\phi^0 H)^2}, \quad l^\dagger_{13} = \tfrac{-ik_x u^0_y\mu^0_\phi}{\phi^0 H^2} + \tfrac{p^0_\phi\left(\phi^0 D - \phi^0_y\right)}{(\phi^0 H)^2}, \quad l^\dagger_{14} = \tfrac{ip^0_\phi k_z}{\phi^0 H^2}\\
l^\dagger_{15} &= \tfrac{2(\mu^0_\phi(u^0_y)^2 - \mathcal{D}^0_\phi)}{\phi^0\,dim} - \tfrac{2T^0_y\kappa^0_\phi D}{\phi^0 H^2\,dim} + \tfrac{2\phi^0_y T^0_y\kappa^0_\phi}{(\phi^0 H)^2\,dim}, \quad l^\dagger_{21} = ik_x\phi^0\\
l^\dagger_{22} &= ik_x u^0 - \tfrac{k_x^2(2\mu^0+\lambda^0)+\mu^0 k_z^2}{\phi^0 H^2} + \tfrac{1}{(\phi^0 H)^2}\left[-\mu^0_y\phi^0_y - \mu^0\phi^0_{yy} + \tfrac{2(\phi^0_y)^2\mu^0}{\phi^0} + (\phi^0\mu^0_y - 2\phi^0_y\mu^0)D + \phi^0\mu^0 D^2\right]\\
l^\dagger_{23} &= \tfrac{ik_x\left[(\mu^0+\lambda^0)(\phi^0 D - \phi^0_y) + \phi^0\mu^0_y\right]}{(\phi^0 H)^2}, \quad l^\dagger_{24} = -\tfrac{(\mu^0+\lambda^0)k_x k_z}{\phi^0 H^2}\\
l^\dagger_{25} &= \tfrac{2ik_x p^0}{\phi^0\,dim} - \tfrac{4}{(\phi^0)^2\,dim}\left[\phi^0\left(\mu^0 u^0_y D + \mu^0_y u^0_y + \mu^0 u^0_{yy}\right) - \phi^0_y\mu^0 u^0_y\right]\\
l^\dagger_{31} &= \phi^0 D, \quad l^\dagger_{32} = -u^0_y + \tfrac{ik_x\left[(\mu^0+\lambda^0)(\phi^0 D - \phi^0_y) + \phi^0\lambda^0_y\right]}{(\phi^0 H)^2}\\
l^\dagger_{33} &= ik_x u^0 - \tfrac{\mu^0(k_x^2+k_z^2)}{\phi^0 H^2} + \tfrac{1}{(\phi^0 H)^2}\left[-(2\mu^0_y + \lambda^0_y)\phi^0_y - (2\mu^0+\lambda^0)\phi^0_{yy}\right.\\
&\quad \left. + \phi^0(2\mu^0_y + \lambda^0_y)D - 2(2\mu^0+\lambda^0)\phi^0_y D + \phi^0(2\mu^0+\lambda^0)D^2\right] + \tfrac{2(\phi^0_y)^2(2\mu^0+\lambda^0)}{(\phi^0)^3 H^2}\\
l^\dagger_{34} &= \tfrac{ik_z\left[(\mu^0+\lambda^0)(\phi^0 D - \phi^0_y) + \phi^0\lambda^0_y\right]}{(\phi^0 H)^2}, \quad l^\dagger_{35} = -T^0_y - \tfrac{4ik_x\mu^0 u^0_y}{\phi^0\,dim} + \tfrac{2\left(\phi^0(p^0 D + p^0_y) - \phi^0_y p^0\right)}{(\phi^0)^2\,dim}\\
l^\dagger_{41} &= ik_z\phi^0, \quad l^\dagger_{42} = -\tfrac{(\lambda^0+\mu^0)k_x k_z}{\phi^0 H^2}, \quad l^\dagger_{43} = \tfrac{ik_z\left[(\mu^0+\lambda^0)(\phi^0 D - \phi^0_y) + \phi^0\mu^0_y\right]}{(\phi^0 H)^2}\\
l^\dagger_{44} &= ik_x u^0 - \tfrac{k_x^2(2\mu^0+\lambda^0)+\mu^0 k_z^2}{\phi^0 H^2} + \tfrac{1}{(\phi^0 H)^2}\left[-\mu^0_y\phi^0_y - \mu^0\phi^0_{yy} + \tfrac{2(\phi^0_y)^2\mu^0}{\phi^0} + (\phi^0\mu^0_y - 2\phi^0_y\mu^0)D + \phi^0\mu^0 D^2\right]\\
l^\dagger_{45} &= \tfrac{2ip^0 k_z}{dim\,\phi^0}, \quad l^\dagger_{51} = 0\\
l^\dagger_{52} &= \tfrac{ik_x p^0_T}{\phi^0 H^2} - \tfrac{\left(\phi^0 u^0_y\mu^0_T D - \phi^0_y\mu^0_T u^0_y\right)}{(\phi^0 H)^2}, \quad l^\dagger_{53} = \tfrac{-ik_x u^0_y\mu^0_T}{\phi^0 H^2} + \tfrac{\left(\phi^0 p^0_T D - \phi^0_y p^0_T\right)}{(\phi^0 H)^2}, \quad l^\dagger_{54} = \tfrac{ip^0_T k_z}{\phi^0 H^2}\\
l^\dagger_{55} &= ik_x u^0 + \tfrac{2}{\phi^0\,dim}\left[-\tfrac{1}{H^2}(k_x^2 + k_z^2)\kappa^0 + \mu^0_T(u^0_y)^2 - \mathcal{D}^0_T\right] + \tfrac{4(\phi^0_y)^2\kappa^0}{dim\,H^2(\phi^0)^3}\\
&\quad + \tfrac{2}{dim\,(\phi^0 H)^2}\left[\phi^0_y T^0_y\kappa^0_T - \phi^0_{yy}\kappa^0 - \phi^0_y\kappa^0_y + (\phi^0\kappa^0_y - \phi^0 T^0_y\kappa^0_T - 2\phi^0_y\kappa^0)D + \phi^0\kappa^0 D^2\right]
\end{aligned}\right\}
$$

Appendix 7B. Nonlinear Terms ($\mathcal{N}_2$ and $\mathcal{N}_3$)

The quadratic and cubic nonlinear terms (cf. Eqn. (7.11)) of disturbance equation can be written in vector forms: $\mathcal{N}_2 = (\mathcal{N}_2^1, \mathcal{N}_2^2, \mathcal{N}_2^3, \mathcal{N}_2^4, \mathcal{N}_2^5)$ and $\mathcal{N}_3 = (\mathcal{N}_3^1, \mathcal{N}_3^2, \mathcal{N}_3^3, \mathcal{N}_3^4, \mathcal{N}_3^5)$ where the superscript 1, 2, 3, 4 and 5 correspond to terms from mass, x-momentum, y-momentum, z-momentum and energy equations, respectively.

$$
\begin{aligned}
\mathcal{N}_2^{(1)} &= -\left[\tfrac{\partial(\phi' u')}{\partial x} + \tfrac{\partial(\phi' v')}{\partial y} + \tfrac{\partial(\phi' w')}{\partial z}\right] \\
\mathcal{N}_2^{(2)} &= -H^2\left[\phi^0(\mathbf{u}'.\nabla)u' + \phi'\left(\tfrac{\partial u'}{\partial t} + u^0\tfrac{\partial u'}{\partial x} + u_y^0 v'\right)\right] - \left(\tfrac{1}{2}p_{\phi\phi}^0\tfrac{\partial \phi'^2}{\partial x} + \tfrac{1}{2}p_{TT}^0\tfrac{\partial T'^2}{\partial x} + p_{\phi T}^0\tfrac{\partial \phi' T'}{\partial x}\right) \\
&\quad +2\left(\mu_\phi^0\phi' + \mu_T^0 T'\right)\tfrac{\partial^2 u'}{\partial x^2} + 2\left(\mu_\phi^0\tfrac{\partial \phi'}{\partial x} + \mu_T^0\tfrac{\partial T'}{\partial x}\right)\tfrac{\partial u'}{\partial x} \\
&\quad +(\lambda_\phi^0\phi' + \lambda_T^0 T')\tfrac{\partial(\nabla.\mathbf{u}')}{\partial x} + \left(\lambda_\phi^0\tfrac{\partial \phi'}{\partial x} + +\lambda_T^0\tfrac{\partial T'}{\partial x}\right)(\nabla.\mathbf{u}') \\
&\quad +\left(\tfrac{1}{2}\mu_{\phi\phi}^0\phi'^2 + \tfrac{1}{2}\mu_{TT}^0 T'^2 + \mu_{\phi T}^0\phi' T'\right)u_{yy}^0 + (\mu_\phi^0\phi' + \mu_T^0 T')\tfrac{\partial}{\partial y}\left(\tfrac{\partial u'}{\partial y} + \tfrac{\partial v'}{\partial x}\right) \\
&\quad +u_y^0\left(\tfrac{1}{2}\mu_{\phi\phi y}^0\phi'^2 + \tfrac{1}{2}\mu_{\phi\phi}^0\tfrac{\partial \phi'^2}{\partial y} + \tfrac{1}{2}\mu_{TTy}^0 T'^2 + \tfrac{1}{2}\mu_{TT}^0\tfrac{\partial T'^2}{\partial y} + \mu_{\phi Ty}^0\phi' T' + \mu_{\phi T}^0\tfrac{\partial \phi' T'}{\partial y}\right) \\
&\quad +\left(\tfrac{\partial u'}{\partial y} + \tfrac{\partial v'}{\partial x}\right)\left(\mu_{\phi y}^0\phi' + \mu_\phi^0\tfrac{\partial \phi'}{\partial y} + \mu_{Ty}^0 T' + \mu_T^0\tfrac{\partial T'}{\partial y}\right) \\
&\quad +\left(\mu_\phi^0\tfrac{\partial \phi'}{\partial z} + \mu_T^0\tfrac{\partial T'}{\partial z}\right)\left(\tfrac{\partial u'}{\partial z} + \tfrac{\partial w'}{\partial x}\right) + \left(\mu_\phi^0\phi' + \mu_T^0 T'\right)\tfrac{\partial}{\partial z}\left(\tfrac{\partial u'}{\partial z} + \tfrac{\partial w'}{\partial x}\right) \\
\mathcal{N}_3^{(2)} &= -H^2\phi'(\mathbf{u}'.\nabla)u' - \tfrac{\partial}{\partial x}\left(\tfrac{1}{6}p_{\phi\phi\phi}^0\phi'^3 + \tfrac{1}{6}p_{TTT}^0 T'^3 + \tfrac{1}{2}p_{\phi\phi T}^0\phi'^2 T' + \tfrac{1}{2}p_{\phi TT}^0\phi' T'^2\right) \\
&\quad +2\left(\tfrac{1}{2}\mu_{\phi\phi}^0\phi'^2 + \tfrac{1}{2}\mu_{TT}^0 T'^2 + \mu_{\phi T}^0\phi' T'\right)\tfrac{\partial^2 u'}{\partial x^2} + 2\left(\tfrac{1}{2}\mu_{\phi\phi}^0\tfrac{\partial \phi'^2}{\partial x} + \tfrac{1}{2}\mu_{TT}^0\tfrac{\partial T'^2}{\partial x} + \mu_{\phi T}^0\tfrac{\partial(\phi' T')}{\partial x}\right)\tfrac{\partial u'}{\partial x} \\
&\quad +\left(\tfrac{1}{2}\lambda_{\phi\phi}^0\phi'^2 + \tfrac{1}{2}\lambda_{TT}^0 T'^2 + \lambda_{\phi T}^0\phi' T'\right)\tfrac{\partial(\nabla.\mathbf{u}')}{\partial x} \quad + \left(\tfrac{1}{2}\lambda_{\phi\phi}^0\tfrac{\partial \phi'^2}{\partial x} + +\tfrac{1}{2}\lambda_{TT}^0\tfrac{\partial T'^2}{\partial x} + \lambda_{\phi T}^0\tfrac{\partial(\phi' T')}{\partial x}\right)(\nabla.\mathbf{u}') \\
&\quad +\left(\tfrac{1}{6}\mu_{\phi\phi\phi}^0\phi'^3 + \tfrac{1}{6}\mu_{TTT}^0 T'^3 + \tfrac{1}{2}\mu_{\phi\phi T}^0\phi'^2 T' + \tfrac{1}{2}\mu_{\phi TT}^0\phi' T'^2\right)u_{yy}^0 \\
&\quad +\left(\tfrac{1}{2}\mu_{\phi\phi}^0\phi'^2 + \tfrac{1}{2}\mu_{TT}^0 T'^2 + \mu_{\phi T}^0\phi' T'\right)\tfrac{\partial}{\partial y}\left(\tfrac{\partial u'}{\partial y} + \tfrac{\partial v'}{\partial x}\right) \\
&\quad +u_y^0\left(\tfrac{1}{6}\mu_{\phi\phi\phi y}^0\phi'^3 + \tfrac{1}{6}\mu_{\phi\phi\phi}^0\tfrac{\partial \phi'^3}{\partial y} + \tfrac{1}{6}\mu_{TTTy}^0 T'^3 + \tfrac{1}{6}\mu_{TTT}^0\tfrac{\partial T'^3}{\partial y}\right. \\
&\quad \left. +\tfrac{1}{2}\mu_{\phi\phi Ty}^0\phi'^2 T' + \tfrac{1}{2}\mu_{\phi\phi T}^0\tfrac{\partial \phi'^2 T'}{\partial y} + \tfrac{1}{2}\mu_{\phi TTy}^0\phi' T'^2 + \tfrac{1}{2}\mu_{\phi TT}^0\tfrac{\partial \phi' T'^2}{\partial y}\right) \\
&\quad +\left(\tfrac{\partial u'}{\partial y} + \tfrac{\partial v'}{\partial x}\right)\left(\tfrac{1}{2}\mu_{\phi\phi y}^0\phi'^2 + \tfrac{1}{2}\mu_{\phi\phi}^0\tfrac{\partial \phi'^2}{\partial y} + \tfrac{1}{2}\mu_{TTy}^0 T'^2 + \tfrac{1}{2}\mu_{TT}^0\tfrac{\partial T'^2}{\partial y} + \mu_{\phi Ty}^0\phi' T' + \mu_{\phi T}^0\tfrac{\partial \phi' T'}{\partial y}\right) \\
&\quad +\left(\tfrac{1}{2}\mu_{\phi\phi}^0\phi'^2 + \tfrac{1}{2}\mu_{TT}^0 T'^2 + \mu_{\phi T}^0\phi' T'\right)\tfrac{\partial}{\partial z}\left(\tfrac{\partial u'}{\partial z} + \tfrac{\partial w'}{\partial x}\right) \\
&\quad +\left(\tfrac{1}{2}\mu_{\phi\phi}^0\tfrac{\partial \phi'^2}{\partial z} + \tfrac{1}{2}\mu_{TT}^0\tfrac{\partial T'^2}{\partial z} + \mu_{\phi T}^0\tfrac{\partial(\phi' T')}{\partial z}\right)\left(\tfrac{\partial u'}{\partial z} + \tfrac{\partial w'}{\partial x}\right) \\
\mathcal{N}_2^{(3)} &= -H^2\left[\phi^0(\mathbf{u}'.\nabla)v' + \phi'\left(\tfrac{\partial v'}{\partial t} + u^0\tfrac{\partial v'}{\partial x}\right)\right] \\
&\quad -\left(\tfrac{1}{2}p_{\phi\phi y}^0\phi'^2 + \tfrac{1}{2}p_{\phi\phi}^0\tfrac{\partial \phi'^2}{\partial y} + \tfrac{1}{2}p_{TTy}^0 T'^2 + \tfrac{1}{2}p_{TT}^0\tfrac{\partial T'^2}{\partial y} + p_{\phi Ty}^0\phi' T' + p_{\phi T}^0\tfrac{\partial \phi' T'}{\partial y}\right) \\
&\quad +2\left(\mu_\phi^0\phi' + \mu_T^0 T'\right)\tfrac{\partial^2 v'}{\partial y^2} + 2\left(\mu_{\phi y}^0\phi' + \mu_\phi^0\tfrac{\partial \phi'}{\partial y} + \mu_{Ty}^0 T' + \mu_T^0\tfrac{\partial T'}{\partial y}\right)\tfrac{\partial v'}{\partial y} \\
&\quad +\left(\lambda_\phi^0\phi' + \lambda_T^0 T'\right)\tfrac{\partial(\nabla.\mathbf{u}')}{\partial y} + \left(\lambda_{\phi y}^0\phi' + \lambda_\phi^0\tfrac{\partial \phi'}{\partial y} + \lambda_{Ty}^0 T' + \lambda_T^0\tfrac{\partial T'}{\partial y}\right)(\nabla.\mathbf{u}') \\
&\quad +(\mu_\phi^0\phi' + \mu_T^0 T')\tfrac{\partial}{\partial x}\left(\tfrac{\partial u'}{\partial y} + \tfrac{\partial v'}{\partial x}\right) + u_y^0\left(\mu_{\phi\phi}^0\phi'\tfrac{\partial \phi'}{\partial x} + \mu_{TT}^0 T'\tfrac{\partial T'}{\partial x} + \mu_{\phi T}^0\tfrac{\partial \phi' T'}{\partial x}\right) \\
&\quad +\left(\mu_\phi^0\tfrac{\partial \phi'}{\partial x} + \mu_T^0\tfrac{\partial T'}{\partial x}\right)\left(\tfrac{\partial u'}{\partial y} + \tfrac{\partial v'}{\partial x}\right) \\
&\quad +\left(\mu_\phi^0\phi' + \mu_T^0 T'\right)\tfrac{\partial}{\partial z}\left(\tfrac{\partial v'}{\partial z} + \tfrac{\partial w'}{\partial y}\right) + \left(\mu_\phi^0\tfrac{\partial \phi'}{\partial z} + \mu_T^0\tfrac{\partial T'}{\partial z}\right)\left(\tfrac{\partial v'}{\partial z} + \tfrac{\partial w'}{\partial y}\right)
\end{aligned}
$$

$$
\begin{aligned}
\mathcal{N}_3^{(3)} &= -H^2\phi'(\mathbf{u}'.\nabla)v' - \left(\tfrac{1}{6}p^0_{\phi\phi\phi y}\phi'^3 + \tfrac{1}{6}p^0_{\phi\phi\phi}\tfrac{\partial\phi'^3}{\partial y} + \tfrac{1}{6}p^0_{TTTy}T'^3 + \tfrac{1}{6}p^0_{TTT}\tfrac{\partial T'^3}{\partial y}\right.\\
&\left. + \tfrac{1}{2}p^0_{\phi\phi Ty}\phi'^2T' + \tfrac{1}{2}p^0_{\phi\phi T}\tfrac{\partial\phi'^2T'}{\partial y} + \tfrac{1}{2}p^0_{\phi TTy}\phi'T'^2 + \tfrac{1}{2}p^0_{\phi TT}\tfrac{\partial\phi'T'^2}{\partial y}\right)\\
&+2\left(\tfrac{1}{2}\mu^0_{\phi\phi}\phi'^2 + \tfrac{1}{2}\mu^0_{TT}T'^2 + \mu^0_{\phi T}\phi'T'\right)\tfrac{\partial^2 v'}{\partial y^2}\\
&+2\tfrac{\partial v'}{\partial y}\left(\tfrac{1}{2}\mu^0_{\phi\phi y}\phi'^2 + \tfrac{1}{2}\mu^0_{\phi\phi}\tfrac{\partial\phi'^2}{\partial y} + +\tfrac{1}{2}\mu^0_{TTy}T'^2 + \tfrac{1}{2}\mu^0_{TT}\tfrac{\partial T'^2}{\partial y} + \mu^0_{\phi Ty}\phi'T' + \mu^0_{\phi T}\tfrac{\partial\phi'T'}{\partial y}\right)\\
&+\left(\tfrac{1}{2}\lambda^0_{\phi\phi}\phi'^2 + \tfrac{1}{2}\lambda^0_{TT}T'^2 + \lambda^0_{\phi T}\phi'T'\right)\tfrac{\partial(\nabla.\mathbf{u}')}{\partial y}\\
&+(\nabla.\mathbf{u}')\left(\tfrac{1}{2}\lambda^0_{\phi\phi y}\phi'^2 + \tfrac{1}{2}\lambda^0_{\phi\phi}\tfrac{\partial\phi'^2}{\partial y} + \tfrac{1}{2}\lambda^0_{TTy}T'^2 + \tfrac{1}{2}\lambda^0_{TT}\tfrac{\partial T'^2}{\partial y} + \lambda^0_{\phi Ty}\phi'T' + \lambda^0_{\phi T}\tfrac{\partial\phi'T'}{\partial y}\right)\\
&+\left(\tfrac{1}{2}\mu^0_{\phi\phi}\phi'^2 + \tfrac{1}{2}\mu^0_{TT}T'^2 + \mu^0_{\phi T}\phi'T'\right)\tfrac{\partial}{\partial x}\left(\tfrac{\partial u'}{\partial y} + \tfrac{\partial v'}{\partial x}\right)\\
&+u^0_y\left(\tfrac{1}{6}\mu^0_{\phi\phi\phi}\tfrac{\partial\phi'^3}{\partial x} + \tfrac{1}{6}\mu^0_{TTT}\tfrac{\partial T'^3}{\partial x} + \tfrac{1}{2}\mu^0_{\phi\phi T}\tfrac{\partial(\phi'^2T')}{\partial x} + \tfrac{1}{2}\mu^0_{\phi TT}\tfrac{\partial(\phi'T'^2)}{\partial x}\right)\\
&+\left(\tfrac{1}{2}\mu^0_{\phi\phi}\tfrac{\partial\phi'^2}{\partial x} + \tfrac{1}{2}\mu^0_{TT}\tfrac{\partial T'^2}{\partial x} + \mu^0_{\phi T}\tfrac{\partial(\phi'T')}{\partial x}\right)\left(\tfrac{\partial u'}{\partial y} + \tfrac{\partial v'}{\partial x}\right)\\
&+\left(\tfrac{1}{2}\mu^0_{\phi\phi}\tfrac{\partial\phi'^2}{\partial z} + \tfrac{1}{2}\mu^0_{TT}\tfrac{\partial T'^2}{\partial z} + \mu^0_{\phi T}\tfrac{\partial(\phi'T')}{\partial z}\right)\left(\tfrac{\partial v'}{\partial z} + \tfrac{\partial w'}{\partial y}\right)\\
&+\left(\tfrac{1}{2}\mu^0_{\phi\phi}\phi'^2 + \tfrac{1}{2}\mu^0_{TT}T'^2 + \mu^0_{\phi T}\phi'T'\right)\tfrac{\partial}{\partial z}\left(\tfrac{\partial v'}{\partial z} + \tfrac{\partial w'}{\partial y}\right)
\end{aligned}
$$

$$
\begin{aligned}
\mathcal{N}_2^{(4)} &= -H^2\left[\phi^0(\mathbf{u}'\cdot\nabla)w' + \phi'\left(\tfrac{\partial w'}{\partial t} + u^0\tfrac{\partial w'}{\partial x}\right)\right] - \left(\tfrac{1}{2}p^0_{\phi\phi}\tfrac{\partial\phi'^2}{\partial z} + \tfrac{1}{2}p^0_{TT}\tfrac{\partial T'^2}{\partial z} + p^0_{\phi T}\tfrac{\partial\phi'T'}{\partial z}\right)\\
&+2\left(\mu^0_\phi\phi' + \mu^0_T T'\right)\tfrac{\partial^2 w'}{\partial z^2} + 2\left(\mu^0_\phi\tfrac{\partial\phi'}{\partial z} + \mu^0_T\tfrac{\partial T'}{\partial z}\right)\tfrac{\partial w'}{\partial z}\\
&+\left(\lambda^0_\phi\phi' + \lambda^0_T T'\right)\tfrac{\partial(\nabla\cdot\mathbf{u}')}{\partial z} + \left(\lambda^0_\phi\tfrac{\partial\phi'}{\partial z} + \lambda^0_T\tfrac{\partial T'}{\partial z}\right)(\nabla\cdot\mathbf{u}')\\
&+\left(\mu^0_\phi\phi' + \mu^0_T T'\right)\tfrac{\partial}{\partial x}\left(\tfrac{\partial u'}{\partial z} + \tfrac{\partial w'}{\partial x}\right) + \left(\mu^0_\phi\tfrac{\partial\phi'}{\partial x} + \mu^0_T\tfrac{\partial T'}{\partial x}\right)\left(\tfrac{\partial u'}{\partial z} + \tfrac{\partial w'}{\partial x}\right)\\
&+\left(\mu^0_\phi\phi' + \mu^0_T T'\right)\tfrac{\partial}{\partial y}\left(\tfrac{\partial v'}{\partial z} + \tfrac{\partial w'}{\partial y}\right) + \left(\mu^0_{\phi y}\phi' + \mu^0_\phi\tfrac{\partial\phi'}{\partial y} + +\mu^0_{Ty}T' + \mu^0_T\tfrac{\partial T'}{\partial y}\right)\left(\tfrac{\partial v'}{\partial z} + \tfrac{\partial w'}{\partial y}\right)
\end{aligned}
$$

$$
\begin{aligned}
\mathcal{N}_3^{(4)} &= -H^2\phi'(\mathbf{u}'\cdot\nabla)w' - \left(\tfrac{1}{6}p^0_{\phi\phi\phi}\tfrac{\partial\phi'^3}{\partial z} + \tfrac{1}{6}p^0_{TTT}\tfrac{\partial T'^3}{\partial z} + \tfrac{1}{2}p^0_{\phi\phi T}\tfrac{\partial\phi'^2T'}{\partial z} + \tfrac{1}{2}p^0_{\phi TT}\tfrac{\partial\phi'T'^2}{\partial z}\right)\\
&+2\left(\tfrac{1}{2}\mu^0_{\phi\phi}\phi'^2 + \tfrac{1}{2}\mu^0_{TT}T'^2 + \mu^0_{\phi T}\phi'T'\right)\tfrac{\partial^2 w'}{\partial z^2}\\
&+2\left(\tfrac{1}{2}\mu^0_{\phi\phi}\tfrac{\partial\phi'^2}{\partial z} + \tfrac{1}{2}\mu^0_{TT}\tfrac{\partial T'^2}{\partial z} + \mu^0_{\phi T}\tfrac{\partial\phi'T'}{\partial z}\right)\tfrac{\partial w'}{\partial z}\\
&+\left(\tfrac{1}{2}\lambda^0_{\phi\phi}\phi'^2 + \tfrac{1}{2}\lambda^0_{TT}T'^2 + \lambda^0_{\phi T}\phi'T'\right)\tfrac{\partial(\nabla\cdot\mathbf{u}')}{\partial z}\\
&+\left(\tfrac{1}{2}\lambda^0_{\phi\phi}\tfrac{\partial\phi'^2}{\partial z} + \tfrac{1}{2}\lambda^0_{TT}\tfrac{\partial T'^2}{\partial z} + \lambda^0_{\phi T}\tfrac{\partial\phi'T'}{\partial z}\right)(\nabla\cdot\mathbf{u}')\\
&+\left(\tfrac{1}{2}\mu^0_{\phi\phi}\phi'^2 + \tfrac{1}{2}\mu^0_{TT}T'^2 + \mu^0_{\phi T}\phi'T'\right)\tfrac{\partial}{\partial x}\left(\tfrac{\partial u'}{\partial z} + \tfrac{\partial w'}{\partial x}\right)\\
&+\left(\tfrac{1}{2}\mu^0_{\phi\phi}\tfrac{\partial\phi'^2}{\partial x} + \tfrac{1}{2}\mu^0_{TT}\tfrac{\partial T'^2}{\partial x} + \mu^0_{\phi T}\tfrac{\partial\phi'T'}{\partial x}\right)\left(\tfrac{\partial u'}{\partial z} + \tfrac{\partial w'}{\partial x}\right)\\
&+\left(\tfrac{1}{2}\mu^0_{\phi\phi}\phi'^2 + \tfrac{1}{2}\mu^0_{TT}T'^2 + \mu^0_{\phi T}\phi'T'\right)\tfrac{\partial}{\partial y}\left(\tfrac{\partial v'}{\partial z} + \tfrac{\partial w'}{\partial y}\right)\\
&+\tfrac{\partial}{\partial y}\left(\tfrac{1}{2}\mu^0_{\phi\phi}\phi'^2 + \tfrac{1}{2}\mu^0_{TT}T'^2 + \mu^0_{\phi T}\phi'T'\right)\left(\tfrac{\partial v'}{\partial z} + \tfrac{\partial w'}{\partial y}\right)
\end{aligned}
$$

$$
\begin{aligned}
\mathcal{N}_2^{(5)} &= -\tfrac{dim}{2}\left[\phi^0(\mathbf{u}'.\nabla)T' + \phi'\left(\tfrac{\partial T'}{\partial t} + T^0_y v' + u^0\tfrac{\partial T'}{\partial x}\right)\right]\\
&+\tfrac{1}{H^2}\left[\tfrac{\partial T'}{\partial x}\left(\kappa^0_\phi\tfrac{\partial\phi'}{\partial x} + \kappa^0_T\tfrac{\partial T'}{\partial x}\right) + \tfrac{\partial^2 T'}{\partial x^2}\left(\kappa^0_\phi\phi' + \kappa^0_T T'\right)\right.\\
&+T^0_y\left(\tfrac{1}{2}\kappa^0_{\phi\phi y}\phi'^2 + \tfrac{1}{2}\kappa^0_{\phi\phi}\tfrac{\partial\phi'^2}{\partial y} + \tfrac{1}{2}\kappa^0_{TTy}T'^2 + \tfrac{1}{2}\kappa^0_{TT}\tfrac{\partial T'^2}{\partial y}\right.\\
&\left.+\kappa^0_{\phi Ty}\phi'T' + \kappa^0_{\phi T}\tfrac{\partial\phi'T'}{\partial y}\right) + T^0_{yy}\left(\tfrac{1}{2}\kappa^0_{\phi\phi}\phi'^2 + \tfrac{1}{2}\kappa^0_{TT}T'^2 + \kappa^0_{\phi T}\phi'T'\right)\\
&+\tfrac{\partial T'}{\partial y}\left(\kappa^0_{\phi y}\phi' + \kappa^0_\phi\tfrac{\partial\phi'}{\partial y} + \kappa^0_{Ty}T' + \kappa^0_T\tfrac{\partial T'}{\partial y}\right) + \tfrac{\partial^2 T'}{\partial y^2}\left(\kappa^0_\phi\phi' + \kappa^0_T T'\right)\\
&\left.+\tfrac{\partial T'}{\partial z}\left(\kappa^0_\phi\tfrac{\partial\phi'}{\partial z} + \kappa^0_T\tfrac{\partial T'}{\partial z}\right) + \tfrac{\partial^2 T'}{\partial z^2}\left(\kappa^0_\phi\phi' + \kappa^0_T T'\right)\right]\\
&-(p^0_\phi\phi' + p^0_T T')(\nabla.\mathbf{u}') + 2\mu^0\left[\left(\tfrac{\partial u'}{\partial x}\right)^2 + \left(\tfrac{\partial v'}{\partial y}\right)^2 + \left(\tfrac{\partial w'}{\partial z}\right)^2\right]\\
&+\mu^0\left(\tfrac{\partial u'}{\partial y} + \tfrac{\partial v'}{\partial x}\right)^2 + (u^0_y)^2\left(\tfrac{1}{2}\mu^0_{\phi\phi}\phi'^2 + \tfrac{1}{2}\mu^0_{TT}T'^2 + \mu^0_{\phi T}\phi'T'\right)\\
&+2\,u^0_y\left(\mu^0_\phi\phi' + \mu^0_T T'\right)\left(\tfrac{\partial u'}{\partial y} + \tfrac{\partial v'}{\partial x}\right) + \mu^0\left(\tfrac{\partial v'}{\partial z} + \tfrac{\partial w'}{\partial y}\right)^2 + \mu^0\left(\tfrac{\partial w'}{\partial x} + \tfrac{\partial u'}{\partial z}\right)^2\\
&+\lambda^0(\nabla.\mathbf{u}')^2 - \left(\tfrac{1}{2}\mathcal{D}^0_{\phi\phi}\phi'^2 + \tfrac{1}{2}\mathcal{D}^0_{TT}T'^2 + \mathcal{D}^0_{\phi T}\phi'T'\right)
\end{aligned}
$$

$$
\begin{aligned}
\mathcal{N}_3^{(5)} \;=\; & -\tfrac{dim}{2}\,\phi'(\mathbf{u}'.\nabla)T' + \tfrac{1}{H^2}\left[\frac{\partial T'}{\partial x}\left(\tfrac{1}{2}\kappa^0_{\phi\phi}\frac{\partial \phi'^2}{\partial x} + \tfrac{1}{2}\kappa^0_{TT}\frac{\partial T'^2}{\partial x} + \kappa^0_{\phi T}\frac{\partial \phi' T'}{\partial x}\right)\right. \\
& + \frac{\partial^2 T'}{\partial x^2}\left(\tfrac{1}{2}\kappa^0_{\phi\phi}\phi'^2 + \tfrac{1}{2}\kappa^0_{TT}T'^2 + \kappa^0_{\phi T}\phi' T'\right) \\
& + T^0_y\left(\tfrac{1}{6}\kappa^0_{\phi\phi\phi y}\phi'^3 + \tfrac{1}{6}\kappa^0_{\phi\phi\phi}\frac{\partial \phi'^3}{\partial y} + \tfrac{1}{6}\kappa^0_{TTTy}T'^3 + \tfrac{1}{6}\kappa^0_{TTT}\frac{\partial T'^3}{\partial y}\right. \\
& \left. + \tfrac{1}{2}\kappa^0_{\phi\phi Ty}\phi'^2 T' + \tfrac{1}{2}\kappa^0_{\phi\phi T}\frac{\partial \phi'^2 T'}{\partial y} + \tfrac{1}{2}\kappa^0_{\phi TTy}\phi' T'^2 + \tfrac{1}{2}\kappa^0_{\phi TT}\frac{\partial \phi' T'^2}{\partial y}\right) \\
& + T^0_{yy}\left(\tfrac{1}{6}\kappa^0_{\phi\phi\phi}\phi'^3 + + \tfrac{1}{6}\kappa^0_{\phi TT}T'^3 + \tfrac{1}{2}\kappa^0_{\phi\phi T}\phi'^2 T' + \tfrac{1}{2}\kappa^0_{\phi TT}\phi' T'^2\right) \\
& + \frac{\partial T'}{\partial y}\left(\tfrac{1}{2}\kappa^0_{\phi\phi y}\phi'^2 + \tfrac{1}{2}\kappa^0_{\phi\phi}\frac{\partial \phi'^2}{\partial y} + \tfrac{1}{2}\kappa^0_{TTy}T'^2 + \tfrac{1}{2}\kappa^0_{TT}\frac{\partial T'^2}{\partial y} + \kappa^0_{\phi Ty}\phi' T' + \kappa^0_{\phi T}\frac{\partial \phi' T'}{\partial y}\right) \\
& + \frac{\partial^2 T'}{\partial y^2}\left(\tfrac{1}{2}\kappa^0_{\phi\phi}\phi'^2 + \tfrac{1}{2}\kappa^0_{TT}T'^2 + \kappa^0_{\phi T}\phi' T'\right) + \frac{\partial T'}{\partial z}\left(\tfrac{1}{2}\kappa^0_{\phi\phi}\frac{\partial \phi'^2}{\partial z} + \tfrac{1}{2}\kappa^0_{TT}\frac{\partial T'^2}{\partial z} + \kappa^0_{\phi T}\frac{\partial \phi' T'}{\partial z}\right) \\
& \left. + \frac{\partial^2 T'}{\partial z^2}\left(\tfrac{1}{2}\kappa^0_{\phi\phi}\phi'^2 + \tfrac{1}{2}\kappa^0_{TT}T'^2 + \kappa^0_{\phi T}\phi' T'\right)\right] - \left(\tfrac{1}{2}p^0_{\phi\phi}\phi'^2 + \tfrac{1}{2}p^0_{TT}T'^2 + p^0_{\phi T}\phi' T'\right)(\nabla.\mathbf{u}') \\
& + 2(\mu^0_\phi\phi' + \mu^0_T T')\left[\left(\frac{\partial u'}{\partial x}\right)^2 + \left(\frac{\partial v'}{\partial y}\right)^2 + \left(\frac{\partial w'}{\partial z}\right)^2\right] \\
& + \left(\tfrac{1}{6}\mu^0_{\phi\phi\phi}\phi'^3 + \tfrac{1}{6}\mu^0_{TTT}T'^3 + \tfrac{1}{2}\mu^0_{\phi\phi T}\phi'^2 T' + \tfrac{1}{2}\mu^0_{\phi TT}\phi' T'^2\right)(u^0_y)^2 \\
& + 2u^0_y\left(\tfrac{1}{2}\mu^0_{\phi\phi}\phi'^2 + \tfrac{1}{2}\mu^0_{TT}T'^2 + \mu^0_{\phi T}\phi' T'\right)\left(\frac{\partial u'}{\partial y} + \frac{\partial v'}{\partial x}\right) \\
& + (\mu^0_\phi\phi' + \mu^0_T T')\left[\left(\frac{\partial u'}{\partial y} + \frac{\partial v'}{\partial x}\right)^2 + \left(\frac{\partial v'}{\partial z} + \frac{\partial w'}{\partial y}\right)^2 + \left(\frac{\partial w'}{\partial x} + \frac{\partial u'}{\partial z}\right)^2\right] \\
& + \left(\lambda^0_\phi\phi' + \lambda^0_T T'\right)(\nabla.\mathbf{u}')^2 - \left(\tfrac{1}{6}\mathcal{D}^0_{\phi\phi\phi}\phi'^3 + + \tfrac{1}{6}\mathcal{D}^0_{TTT}T'^3 + \tfrac{1}{2}\mathcal{D}^0_{\phi\phi T}\phi'^2 T' + \tfrac{1}{2}\mathcal{D}^0_{\phi TT}\phi' T'^2\right)
\end{aligned}
$$

Appendix 7C. Nonlinear Terms for Pure Spanwise Flow

$$
\begin{aligned}
\mathcal{N}_2^{(1)} &= -\phi'\frac{\partial w'}{\partial z} - w'\frac{\partial \phi'}{\partial z} \\
\mathcal{N}_2^{(2)} &= -\frac{1}{\phi^0}\left(\phi^0 w'\frac{\partial u'}{\partial z} + \phi'\frac{\partial u'}{\partial t}\right) + \frac{1}{\phi^0 H^2}\left[\left(\mu_\phi^0\phi' + \mu_T^0 T'\right)\frac{\partial^2 u'}{\partial z^2} + \left(\mu_\phi^0\frac{\partial \phi'}{\partial z} + \mu_T^0\frac{\partial T'}{\partial z}\right)\frac{\partial u'}{\partial z}\right] \\
\mathcal{N}_2^{(3)} &= -\frac{1}{\phi^0}\left(\phi^0 w'\frac{\partial v'}{\partial z} + \phi'\frac{\partial v'}{\partial t}\right) + \frac{1}{\phi^0 H^2}\left[\left(\mu_\phi^0\phi' + \mu_T^0 T'\right)\frac{\partial^2 v'}{\partial z^2} + \left(\mu_\phi^0\frac{\partial \phi'}{\partial z} + \mu_T^0\frac{\partial T'}{\partial z}\right)\frac{\partial v'}{\partial z}\right] \\
\mathcal{N}_2^{(4)} &= -\frac{1}{\phi^0}\left(\phi^0 w'\frac{\partial w'}{\partial z} + \phi'\frac{\partial w'}{\partial t}\right) + \frac{1}{\phi^0 H^2}\left[-\left(p_{\phi\phi}^0\phi'\frac{\partial \phi'}{\partial z} + p_{TT}^0 T'\frac{\partial T'}{\partial z} + p_{\phi T}^0\phi'\frac{\partial T'}{\partial z} + p_{\phi T}^0 T'\frac{\partial \phi'}{\partial z}\right)\right. \\
&\quad +2(\mu_\phi^0\phi' + \mu_T^0 T')\frac{\partial^2 w'}{\partial z^2} + 2\left(\mu_\phi^0\frac{\partial \phi'}{\partial z} + \mu_T^0\frac{\partial T'}{\partial z}\right)\frac{\partial w'}{\partial z} \\
&\quad \left.+(\lambda_\phi^0\phi' + \lambda_T^0 T')\frac{\partial^2 w'}{\partial z^2} + \left(\lambda_\phi^0\frac{\partial \phi'}{\partial z} + \lambda_T^0\frac{\partial T'}{\partial z}\right)\frac{\partial w'}{\partial z}\right] \\
\mathcal{N}_2^{(5)} &= -\frac{1}{\phi^0}\left(\phi^0 w'\frac{\partial T'}{\partial z} + \phi'\frac{\partial T'}{\partial t}\right) + \frac{2}{3\phi^0}\left[\frac{1}{H^2}\left(\frac{\partial T'}{\partial z}\left(\kappa_\phi^0\frac{\partial \phi'}{\partial z} + \kappa_T^0\frac{\partial T'}{\partial z}\right) + \frac{\partial^2 T'}{\partial z^2}(\kappa_\phi^0\phi' + \kappa_T^0 T')\right)\right. \\
&\quad -(p_\phi^0\phi' + p_T^0 T')\frac{\partial w'}{\partial z} + \left(\frac{1}{2}\mu_{\phi\phi}^0\phi'^2 + \frac{1}{2}\mu_{TT}^0 T'^2 + \mu_{\phi T}^0\phi' T'\right) + (2\mu^0 + \lambda^0)\left(\frac{\partial w'}{\partial z}\right)^2 \\
&\quad \left.+\mu^0\left(\frac{\partial v'}{\partial z}\right)^2 + \mu^0\left(\frac{\partial u'}{\partial z}\right)^2 - \left(\frac{1}{2}\mathcal{D}_{\phi\phi}^0\phi'^2 + \frac{1}{2}\mathcal{D}_{TT}^0 T'^2 + \mathcal{D}_{\phi T}^0\phi' T'\right)\right] \\
\mathcal{N}_3^{(2)} &= -\frac{1}{\phi^0}\phi' w'\frac{\partial u'}{\partial z} + \frac{1}{\phi^0 H^2}\left[\left(\frac{1}{2}\mu_{\phi\phi}^0\phi'^2 + \frac{1}{2}\mu_{TT}^0 T'^2 + \mu_{\phi T}^0\phi' T'\right)\frac{\partial^2 u'}{\partial z^2}\right. \\
&\quad \left.+\left(\mu_{\phi\phi}^0\phi'\frac{\partial \phi'}{\partial z} + \mu_{TT}^0 T'\frac{\partial T'}{\partial z} + \mu_{\phi T}^0\phi'\frac{\partial T'}{\partial z} + \mu_{\phi T}^0 T'\frac{\partial \phi'}{\partial z}\right)\frac{\partial u'}{\partial z}\right] \\
\mathcal{N}_3^{(3)} &= -\frac{1}{\phi^0}\phi' w'\frac{\partial v'}{\partial z} + \frac{1}{\phi^0 H^2}\left[\left(\frac{1}{2}\mu_{\phi\phi}^0\phi'^2 + \frac{1}{2}\mu_{TT}^0 T'^2 + \mu_{\phi T}^0\phi' T'\right)\frac{\partial^2 v'}{\partial z^2}\right. \\
&\quad \left.+\left(\mu_{\phi\phi}^0\phi'\frac{\partial \phi'}{\partial z} + \mu_{TT}^0 T'\frac{\partial T'}{\partial z} + \mu_{\phi T}^0\phi'\frac{\partial T'}{\partial z} + \mu_{\phi T}^0 T'\frac{\partial \phi'}{\partial z}\right)\frac{\partial v'}{\partial z}\right] \\
\mathcal{N}_3^{(4)} &= -\frac{1}{\phi^0}\phi' w'\frac{\partial w'}{\partial z} + \frac{1}{\phi^0 H^2}\left[-\left\{\frac{1}{2}p_{\phi\phi\phi}^0\phi'^2\frac{\partial \phi'}{\partial z} + \frac{1}{2}p_{TTT}^0 T'^2\frac{\partial T'}{\partial z} + \frac{1}{2}p_{\phi\phi T}^0\left(2\phi'\frac{\partial \phi'}{\partial z}T' + \phi'^2\frac{\partial T'}{\partial z}\right)\right.\right. \\
&\quad \left.\left.+\frac{1}{2}p_{\phi TT}^0\left(\frac{\partial \phi'}{\partial z}T'^2 + 2\phi' T'\frac{\partial T'}{\partial z}\right)\right\} + 2\left(\frac{1}{2}\mu_{\phi\phi}^0\phi'^2 + \frac{1}{2}\mu_{TT}^0 T'^2 + \mu_{\phi T}^0\phi' T'\right)\frac{\partial^2 w'}{\partial z^2}\right. \\
&\quad +2\left(\mu_{\phi\phi}^0\phi'\frac{\partial \phi'}{\partial z} + \mu_{TT}^0 T'\frac{\partial T'}{\partial z} + \mu_{\phi T}^0\phi'\frac{\partial T'}{\partial z} + \mu_{\phi T}^0 T'\frac{\partial \phi'}{\partial z}\right)\frac{\partial w'}{\partial z} \\
&\quad +\left(\frac{1}{2}\lambda_{\phi\phi}^0\phi'^2 + \frac{1}{2}\lambda_{TT}^0 T'^2 + \lambda_{\phi T}^0\phi' T'\right)\frac{\partial^2 w'}{\partial z^2} \\
&\quad \left.+\left(\lambda_{\phi\phi}^0\phi'\frac{\partial \phi'}{\partial z} + \lambda_{TT}^0 T'\frac{\partial T'}{\partial z} + \lambda_{\phi T}^0\phi'\frac{\partial T'}{\partial z} + \lambda_{\phi T}^0 T'\frac{\partial \phi'}{\partial z}\right)\frac{\partial w'}{\partial z}\right] \\
\mathcal{N}_3^{(5)} &= -\frac{1}{\phi^0}\phi' w'\frac{\partial T'}{\partial z} + \frac{2}{3\phi^0}\left[\frac{1}{H^2}\left\{\frac{\partial^2 T'}{\partial z^2}\left(\frac{1}{2}\kappa_{\phi\phi}^0\phi'^2 + \frac{1}{2}\kappa_{TT}^0 T'^2 + \kappa_{\phi T}^0\phi' T'\right)\right.\right. \\
&\quad \left.\left.+\frac{\partial T'}{\partial z}\left(\kappa_{\phi\phi}^0\phi'\frac{\partial \phi'}{\partial z} + \kappa_{TT}^0 T'\frac{\partial T'}{\partial z} + \kappa_{\phi T}^0\phi'\frac{\partial T'}{\partial z} + \kappa_{\phi T}^0 T'\frac{\partial \phi'}{\partial z}\right)\right\}\right. \\
&\quad -\left(\frac{1}{2}p_{\phi\phi}^0\phi'^2 + \frac{1}{2}p_{TT}^0 T'^2 + p_{\phi T}^0\phi' T'\right)\frac{\partial w'}{\partial z} + 2(\mu_\phi^0\phi' + \mu_T^0 T')\left(\frac{\partial w'}{\partial z}\right)^2 + (\lambda_\phi^0\phi' + \lambda_T^0 T')\left(\frac{\partial w'}{\partial z}\right)^2 \\
&\quad +\left(\frac{1}{6}\mu_{\phi\phi\phi}^0\phi'^3 + \frac{1}{6}\mu_{TTT}^0 T'^3 + \frac{1}{2}\mu_{\phi\phi T}^0\phi'^2 T' + \frac{1}{2}\mu_{\phi TT}^0\phi' T'^2\right) + (\mu_\phi^0\phi' + \mu_T^0 T')\left\{\left(\frac{\partial v'}{\partial z}\right)^2 + \left(\frac{\partial u'}{\partial z}\right)^2\right\} \\
&\quad \left.-\left(\frac{1}{6}\mathcal{D}_{\phi\phi\phi}^0\phi'^3 + \frac{1}{6}\mathcal{D}_{TTT}^0 T'^3 + \frac{1}{2}\mathcal{D}_{\phi\phi T}^0\phi'^2 T' + \frac{1}{2}\mathcal{D}_{\phi TT}^0\phi' T'^2\right)\right]
\end{aligned}
$$

Fourth and fifth order nonlinear terms for pure spanwise flow

The nonlinear terms related to x-momentum and y-momentum equations are eventually zero and the continuity equation contains only quadratic nonlinear terms. Thus the nonlinear terms,

at order four and five, related to z-momentum and energy equations are given below. In the following, $F_n(x)$ denotes the n^{th} order term of Taylor series expansion.

$$
\begin{aligned}
\mathcal{N}_4^{(4)} &= \frac{1}{\phi^0 H^2}\left[-\frac{\partial F_4(p)}{\partial z} + 2F_3(\mu)\frac{\partial^2 w'}{\partial z^2} + 2\frac{\partial F_3(\mu)}{\partial z}\frac{\partial w'}{\partial z} + F_3(\lambda)\frac{\partial^2 w'}{\partial z^2} + \frac{\partial F_3(\lambda)}{\partial z}\frac{\partial w'}{\partial z}\right] \\
\mathcal{N}_5^{(4)} &= \frac{1}{\phi^0 H^2}\left[-\frac{\partial F_5(p)}{\partial z} + 2F_4(\mu)\frac{\partial^2 w'}{\partial z^2} + 2\frac{\partial F_4(\mu)}{\partial z}\frac{\partial w'}{\partial z} + F_4(\lambda)\frac{\partial^2 w'}{\partial z^2} + \frac{\partial F_4(\lambda)}{\partial z}\frac{\partial w'}{\partial z}\right] \\
\mathcal{N}_4^{(5)} &= \frac{2}{dim\,\phi^0}\left[\frac{1}{H^2}\left(\frac{\partial^2 T'}{\partial z^2}F_3(\kappa) + \frac{\partial T'}{\partial z}\frac{\partial F_3(\kappa)}{\partial z}\right) - F_3(p)\frac{\partial w'}{\partial z}\right. \\
&\quad \left. + F_4(\mu) + F_2(\mu)\left\{\left(\frac{\partial v'}{\partial z}\right)^2 + \left(\frac{\partial u'}{\partial z}\right)^2\right\} + (2F_2(\mu) + F_2(\lambda))\left(\frac{\partial w'}{\partial z}\right)^2 - F_4(\mathcal{D})\right] \\
\mathcal{N}_5^{(5)} &= \frac{2}{dim\,\phi^0}\left[\frac{1}{H^2}\left(\frac{\partial^2 T'}{\partial z^2}F_4(\kappa) + \frac{\partial T'}{\partial z}\frac{\partial F_4(\kappa)}{\partial z}\right) - F_4(p)\frac{\partial w'}{\partial z}\right. \\
&\quad \left. + F_5(\mu) + F_3(\mu)\left\{\left(\frac{\partial v'}{\partial z}\right)^2 + \left(\frac{\partial u'}{\partial z}\right)^2\right\} + (2F_3(\mu) + F_3(\lambda))\left(\frac{\partial w'}{\partial z}\right)^2 - F_5(\mathcal{D})\right] \\
F_1(x) &= x^0_\phi \phi' + x^0_T T', \quad F_2(x) = 1/2!\left[x^0_{\phi\phi}\phi'^2 + 2x^0_{\phi T}\phi' T' + x^0_{TT}T'^2\right] \\
F_3(x) &= 1/3!\left[x^0_{\phi\phi\phi}\phi'^3 + 3x^0_{\phi\phi T}\phi'^2 T' + 3x^0_{\phi TT}\phi' T'^2 + x^0_{TTT}T'^3\right] \\
F_4(x) &= 1/4!\left[x^0_{\phi\phi\phi\phi}\phi'^4 + 4x^0_{\phi\phi\phi T}\phi'^3 T' + 6x^0_{\phi\phi TT}\phi'^2 T'^2 + 4x^0_{\phi TTT}\phi' T'^3 + x^0_{TTTT}T'^4\right] \\
F_5(x) &= 1/5!\left[x^0_{\phi\phi\phi\phi\phi}\phi'^5 + 5x^0_{\phi\phi\phi\phi T}\phi'^4 T' + 10x^0_{\phi\phi\phi TT}\phi'^3 T'^2 + 10x^0_{\phi\phi TTT}\phi'^2 T'^3\right. \\
&\quad \left. + 5x^0_{\phi TTTT}\phi' T'^4 + x^0_{TTTTT}T'^5\right]
\end{aligned}
$$

Appendix 7D. G_{04}, G_{24} and G_{15}

$$
\begin{aligned}
\mathbf{G}_{04} \;=\;& N_2(X^{[0;2]},X^{[0;2]})+N_2(X^{[2;2]},\tilde{X}^{[2;2]})+N_2(\tilde{X}^{[2;2]},X^{[2;2]})\\
&+N_2(\tilde{X}^{[1;3]},X^{[1;1]})+N_2(X^{[1;1]},\tilde{X}^{[1;3]})+N_2(X^{[1;3]},\tilde{X}^{[1;1]})\\
&+N_2(\tilde{X}^{[1;1]},X^{[1;3]})+N_3(X^{[2;2]},\tilde{X}^{[1;1]},\tilde{X}^{[1;1]})\\
&+N_3(\tilde{X}^{[1;1]},X^{[2;2]},\tilde{X}^{[1;1]})+N_3(\tilde{X}^{[1;1]},\tilde{X}^{[1;1]},X^{[2;2]})\\
&+N_3(\tilde{X}^{[2;2]},X^{[1;1]},X^{[1;1]})+N_3(X^{[1;1]},\tilde{X}^{[2;2]},X^{[1;1]})\\
&+N_3(X^{[1;1]},X^{[1;1]},\tilde{X}^{[2;2]})-\tfrac{c^{[2]}}{\phi^0}\tilde{\phi}^{[1;1]}(0,u^{[1;1]},v^{[1;1]},w^{[1;1]},T^{[1;1]})\\
&-\tfrac{\tilde{c}^{[2]}}{\phi^0}\phi^{[1;1]}(0,\tilde{u}^{[1;1]},\tilde{v}^{[1;1]},\tilde{w}^{[1;1]},\tilde{T}^{[1;1]})\\
&+N_4(\tilde{X}^{[1;1]},\tilde{X}^{[1;1]},X^{[1;1]},X^{[1;1]})+N_4(X^{[1;1]},X^{[1;1]},\tilde{X}^{[1;1]},\tilde{X}^{[1;1]})\\
&+N_4(\tilde{X}^{[1;1]},X^{[1;1]},\tilde{X}^{[1;1]},X^{[1;1]})+N_4(\tilde{X}^{[1;1]},X^{[1;1]},X^{[1;1]},\tilde{X}^{[1;1]})\\
&+N_4(X^{[1;1]},\tilde{X}^{[1;1]},X^{[1;1]},\tilde{X}^{[1;1]})+N_4(X^{[1;1]},\tilde{X}^{[1;1]},\tilde{X}^{[1;1]},X^{[1;1]})
\end{aligned}
$$

$$
\begin{aligned}
\mathbf{G}_{24} \;=\;& +N_2(\tilde{X}^{[1;1]},X^{[3;3]})+N_2(X^{[3;3]},\tilde{X}^{[1;1]})+N_2(X^{[0;2]},X^{[2;2]})\\
&+N_2(X^{[2;2]},X^{[0;2]})+N_2(X^{[1;3]},X^{[1;1]})+N_2(X^{[1;1]},X^{[1;3]})\\
&+N_3(X^{[2;2]},\tilde{X}^{[1;1]},X^{[1;1]})+N_3(X^{[2;2]},X^{[1;1]},\tilde{X}^{[1;1]})\\
&+N_3(X^{[1;1]},X^{[2;2]},\tilde{X}^{[1;1]})+N_3(\tilde{X}^{[1;1]},X^{[2;2]},X^{[1;1]})\\
&+N_3(\tilde{X}^{[1;1]},X^{[1;1]},X^{[2;2]})+N_3(X^{[1;1]},\tilde{X}^{[1;1]},X^{[2;2]})\\
&+N_3(X^{[0;2]},X^{[1;1]},X^{[1;1]})+N_3(X^{[1;1]},X^{[0;2]},X^{[1;1]})\\
&+N_3(X^{[1;1]},X^{[1;1]},X^{[0;2]})-\tfrac{c^{[2]}}{\phi^0}\phi^{[1;1]}(0,u^{[1;1]},v^{[1;1]},w^{[1;1]},T^{[1;1]})\\
&+N_4(X^{[1;1]},X^{[1;1]},X^{[1;1]},\tilde{X}^{[1;1]})+N_4(X^{[1;1]},X^{[1;1]},\tilde{X}^{[1;1]},X^{[1;1]})\\
&+N_4(X^{[1;1]},\tilde{X}^{[1;1]},X^{[1;1]},X^{[1;1]})+N_4(\tilde{X}^{[1;1]},X^{[1;1]},X^{[1;1]},X^{[1;1]})
\end{aligned}
$$

$$
\begin{aligned}
\mathbf{G}_{15} \;=\;& N_2(X^{[0;4]},X^{[1;1]})+N_2(X^{[1;1]},X^{[0;4]})+N_2(X^{[0;2]},X^{[1;3]})+N_2(X^{[1;3]},X^{[0;2]})\\
&+N_2(\tilde{X}^{[1;3]},X^{[2;2]})+N_2(X^{[2;2]},\tilde{X}^{[1;3]})+N_2(\tilde{X}^{[2;2]},X^{[3;3]})+N_2(X^{[3;3]},\tilde{X}^{[2;2]})\\
&+N_2(\tilde{X}^{[1;1]},X^{[2;4]})+N_2(X^{[2;4]},\tilde{X}^{[1;1]})+N_3(X^{[1;1]},X^{[2;2]},\tilde{X}^{[2;2]})\\
&+N_3(X^{[2;2]},X^{[1;1]},\tilde{X}^{[2;2]})+N_3(X^{[2;2]},\tilde{X}^{[2;2]},X^{[1;1]})+N_3(X^{[1;1]},\tilde{X}^{[2;2]},X^{[2;2]})\\
&+N_3(\tilde{X}^{[2;2]},X^{[2;2]},X^{[1;1]})+N_3(\tilde{X}^{[2;2]},X^{[1;1]},X^{[2;2]})+N_3(X^{[1;1]},X^{[0;2]},X^{[0;2]})\\
&+N_3(X^{[0;2]},X^{[1;1]},X^{[0;2]})+N_3(X^{[0;2]},X^{[0;2]},X^{[1;1]})\\
&+N_3(\tilde{X}^{[1;1]},X^{[2;2]},X^{[0;2]})+N_3(\tilde{X}^{[1;1]},X^{[0;2]},X^{[2;2]})+N_3(X^{[2;2]},\tilde{X}^{[1;1]},X^{[0;2]})\\
&+N_3(X^{[0;2]},\tilde{X}^{[1;1]},X^{[2;2]})+N_3(X^{[0;2]},X^{[2;2]},\tilde{X}^{[1;1]})+N_3(X^{[2;2]},X^{[0;2]},\tilde{X}^{[1;1]})\\
&+N_3(X^{[1;1]},X^{[1;3]},\tilde{X}^{[1;1]})+N_3(X^{[1;3]},X^{[1;1]},\tilde{X}^{[1;1]})+N_3(X^{[1;3]},\tilde{X}^{[1;1]},X^{[1;1]})\\
&+N_3(X^{[1;1]},\tilde{X}^{[1;1]},X^{[1;3]})+N_3(\tilde{X}^{[1;1]},X^{[1;3]},X^{[1;1]})+N_3(\tilde{X}^{[1;1]},X^{[1;1]},X^{[1;3]})\\
&+N_3(X^{[1;1]},X^{[1;1]},\tilde{X}^{[1;3]})+N_3(X^{[1;1]},\tilde{X}^{[1;3]},X^{[1;1]})+N_3(\tilde{X}^{[1;3]},X^{[1;1]},X^{[1;1]})\\
&+N_3(X^{[3;3]},\tilde{X}^{[1;1]},\tilde{X}^{[1;1]})+N_3(\tilde{X}^{[1;1]},X^{[3;3]},\tilde{X}^{[1;1]})+N_3(\tilde{X}^{[1;1]},\tilde{X}^{[1;1]},X^{[3;3]})\\
&-\tfrac{c^{(2)}}{\phi^0}\phi^{[0;2]}(0,u^{[1;1]},v^{[1;1]},w^{[1;1]},T^{[1;1]})-\tfrac{\tilde{c}^{(2)}}{\phi^0}\phi^{[2;2]}(0,\tilde{u}^{[1;1]},\tilde{v}^{[1;1]},\tilde{w}^{[1;1]},\tilde{T}^{[1;1]})\\
&-\tfrac{2c^{(2)}}{\phi^0}\tilde{\phi}^{[1;1]}(0,u^{[2;2]},v^{[2;2]},w^{[2;2]},T^{[2;2]})-\tfrac{2a^{(2)}}{\phi^0}\phi^{[1;1]}(0,u^{[0;2]},v^{[0;2]},w^{[2;2]},T^{[0;2]})\\
&-(3a^{(2)}+ib^{(2)})X^{[1;3]}+N_4(\tilde{X}^{[1;1]},\tilde{X}^{[1;1]},X^{[2;2]},X^{[1;1]})+N_4(\tilde{X}^{[1;1]},\tilde{X}^{[1;1]},X^{[1;1]},X^{[2;2]})\\
&+N_4(X^{[2;2]},X^{[1;1]},\tilde{X}^{[1;1]},\tilde{X}^{[1;1]})+N_4(X^{[1;1]},X^{[2;2]},\tilde{X}^{[1;1]},\tilde{X}^{[1;1]})\\
&+N_4(X^{[2;2]},\tilde{X}^{[1;1]},\tilde{X}^{[1;1]},X^{[1;1]})+N_4(X^{[1;1]},\tilde{X}^{[1;1]},\tilde{X}^{[1;1]},X^{[2;2]})\\
&+N_4(\tilde{X}^{[1;1]},X^{[2;2]},\tilde{X}^{[1;1]},X^{[1;1]})+N_4(\tilde{X}^{[1;1]},X^{[2;2]},X^{[1;1]},\tilde{X}^{[1;1]})\\
&+N_4(\tilde{X}^{[1;1]},X^{[1;1]},\tilde{X}^{[1;1]},X^{[2;2]})+N_4(\tilde{X}^{[1;1]},X^{[1;1]},X^{[2;2]},\tilde{X}^{[1;1]})\\
&+N_4(X^{[2;2]},\tilde{X}^{[1;1]},X^{[1;1]},\tilde{X}^{[1;1]})+N_4(X^{[1;1]},\tilde{X}^{[1;1]},X^{[2;2]},\tilde{X}^{[1;1]})\\
&+N_4(X^{[0;2]},\tilde{X}^{[1;1]},X^{[1;1]},X^{[1;1]})+N_4(\tilde{X}^{[1;1]},X^{[0;2]},X^{[1;1]},X^{[1;1]})\\
&+N_4(X^{[0;2]},X^{[1;1]},X^{[1;1]},\tilde{X}^{[1;1]})+N_4(\tilde{X}^{[1;1]},X^{[1;1]},X^{[1;1]},X^{[0;2]})\\
&+N_4(X^{[1;1]},X^{[1;1]},X^{[0;2]},\tilde{X}^{[1;1]})+N_4(X^{[1;1]},X^{[1;1]},\tilde{X}^{[1;1]},X^{[0;2]})\\
&+N_4(X^{[1;1]},X^{[0;2]},X^{[1;1]},\tilde{X}^{[1;1]})+N_4(X^{[1;1]},X^{[0;2]}\tilde{X}^{[1;1]},X^{[1;1]})\\
&+N_4(X^{[1;1]},\tilde{X}^{[1;1]},X^{[1;1]},X^{[0;2]})+N_4(X^{[1;1]},\tilde{X}^{[1;1]},X^{[0;2]},X^{[1;1]})\\
&+N_4(X^{[0;2]},X^{[1;1]},\tilde{X}^{[1;1]},X^{[1;1]})+N_4(\tilde{X}^{[1;1]},X^{[1;1]},X^{[0;2]},X^{[1;1]})\\
&+N_5(X^{[1;1]},X^{[1;1]},X^{[1;1]},\tilde{X}^{[1;1]},\tilde{X}^{[1;1]})+N_5(\tilde{X}^{[1;1]},X^{[1;1]},X^{[1;1]},X^{[1;1]},\tilde{X}^{[1;1]})\\
&+N_5(\tilde{X}^{[1;1]},\tilde{X}^{[1;1]},X^{[1;1]},X^{[1;1]},X^{[1;1]})+N_5(X^{[1;1]},\tilde{X}^{[1;1]},X^{[1;1]},X^{[1;1]},\tilde{X}^{[1;1]})\\
&+N_5(X^{[1;1]},\tilde{X}^{[1;1]},\tilde{X}^{[1;1]},X^{[1;1]},X^{[1;1]})+N_5(X^{[1;1]},X^{[1;1]},\tilde{X}^{[1;1]},\tilde{X}^{[1;1]},X^{[1;1]})\\
&+N_5(\tilde{X}^{[1;1]},X^{[1;1]},X^{[1;1]},\tilde{X}^{[1;1]},X^{[1;1]})+N_5(X^{[1;1]},\tilde{X}^{[1;1]},X^{[1;1]},\tilde{X}^{[1;1]},X^{[1;1]})\\
&+N_5(X^{[1;1]},X^{[1;1]},\tilde{X}^{[1;1]},X^{[1;1]},\tilde{X}^{[1;1]})+N_5(\tilde{X}^{[1;1]},X^{[1;1]},\tilde{X}^{[1;1]},X^{[1;1]},X^{[1;1]})
\end{aligned}
$$

CHAPTER 8

STREAMWISE INDEPENDENT THREE-DIMENSIONAL GRANULAR COUETTE FLOW: PATTERNS AND BIFURCATIONS

In the previous chapter we have studied a special case of banding instability where the disturbances depend only on vorticity direction which lead to vorticity banding in three dimensional granular Couette flow. In this chapter we will discuss about the banding which consists of both gradient and vorticity bandings along the flow gradient and vorticity directions, respectively, in three dimensional granular Couette flow using amplitude expansion method.

The general weakly nonlinear analysis for three dimensional granular Couette flow has been discussed in §7.2-§7.4, thus we will start this chapter by focusing only on streamwise independent flow which leads to banding in gradient as well as vorticity directions.

This chapter is organized as follows. The formulation of linear stability problem for the streamwise independent flow, analytical solution and asymptotic analysis are given in §8.1. The outline of weakly nonlinear analysis is given in §8.2. The symmetries of linear and nonlinear modes, analytical solutions for second harmonic, distortion of mean flow and first Landau coefficient are detailed in §8.2.1, §8.2.2, §8.2.3 and 8.2.4. The results are presented in §8.3. The locus of neutral stability curve is given in §8.3.1; the equilibrium amplitude and bifurcation are given in §8.3.2. The nonlinear results for moderately dense flow regime, dilute flow and dense flow are discussed in §8.3.4, §8.3.3 and §8.3.5. The bifurcation diagrams and finite amplitude patterns are described in §8.3.6 and §8.3.7. The conclusions of this chapter are given in §8.4.

8.1 Linear Stability Analysis: Analytical Solution

The linear and weakly nonlinear analyses for the case of general disturbances ($\frac{\partial}{\partial x}(.) \neq 0$, $\frac{\partial}{\partial y}(.) \neq 0$ and $\frac{\partial}{\partial z}(.) \neq 0$) are given in §7.2-§7.4. In this chapter we focus on perturbations which do not depend on the streamwise direction ($\frac{\partial}{\partial x}(.) = 0$), i.e. $X = X(t, y, z)$. The form of nonlinear disturbance equations for the streamwise independent flow can be written as

$$\left(\frac{\partial}{\partial t} - \mathcal{L}\right) X(t, y, z) = \mathcal{N}_2 + \mathcal{N}_3, \tag{8.1}$$

where $\mathcal{L}$ is the linear operator and, $\mathcal{N}_2$ and $\mathcal{N}_3$ are the quadratic and cubic nonlinear terms, respectively. In the present problem, $\mathcal{L}$, $\mathcal{N}_2$ and $\mathcal{N}_3$ are streamwise independent operators which are given in Appendices 8A and 8B, respectively. The form of general linear eigenvalue problem (7.17) reduces to the streamwise independent problem as

$$c\hat{X}(t, y, z) = \mathbf{L}\hat{X}(t, y, z), \quad \text{with} \quad \mathcal{B}\hat{X}(t, y, z) = 0, \tag{8.2}$$

where the linear stability operator $\mathbf{L}$, (7.18), can be written as

$$\mathbf{L} \equiv \mathcal{L}\left(\frac{\mathrm{d}}{\mathrm{d}y}, \frac{\mathrm{d}^2}{\mathrm{d}y^2}, \frac{\partial}{\partial z} \to ik_z, \frac{\partial^2}{\partial z^2} \to (ik_z)^2\right). \tag{8.3}$$

Similarly the adjoint problem, (7.19), can be written as

$$\tilde{c}X^{\dagger}(t,y,z) = \mathbf{L}^{\dagger}X^{\dagger}(t,y,z), \quad \text{with} \quad \mathcal{B}^{\dagger}X^{\dagger}(t,y,z) = 0, \tag{8.4}$$

where the adjoint operator $\mathbf{L}^{\dagger}$ is obtained from $\mathbf{L}$ by replacing $\frac{\mathrm{d}}{\mathrm{d}y} \to -\frac{\mathrm{d}}{\mathrm{d}y}$ and taking the conjugate transpose of the resultant operator, i.e.,

$$\mathbf{L}^{\dagger} = \left[\mathbf{L}\left(\frac{\mathrm{d}}{\mathrm{d}y} \to -\frac{\mathrm{d}}{\mathrm{d}y}\right)\right]^{H}, \tag{8.5}$$

where the superscript H denotes the conjugate transpose (Hermitian transpose).

It can be verified that the linear eigenvalue problem, (8.2), has analytical solutions,

$$\left.\begin{aligned}\left(\hat{\phi},\hat{T},\hat{w}\right) &= (\phi_1,T_1,w_1)\cos k_\beta(y \pm 1/2)\\ (\hat{u},\hat{v}) &= (u_1,v_1)\sin k_\beta(y \pm 1/2)\end{aligned}\right\}, \tag{8.6}$$

where $k_\beta = \beta\pi$ with $\beta = 1,2,3,\ldots$ being the mode number, which satisfies the following boundary conditions at $y = \pm 1/2$

$$\hat{u} = \hat{v} = 0 \quad \text{and} \quad \frac{\partial \hat{w}}{\partial y} = \frac{\partial \hat{T}}{\partial y} = 0. \tag{8.7}$$

Substituting above solution (8.6) into eigenvalue problem (8.2) we get an algebraic eigenvalue problem

$$cX_1 = \mathcal{A}X_1, \tag{8.8}$$

where $\mathcal{A}$ is given as

$$\mathcal{A} = \begin{pmatrix} 0 & 0 & -k_\beta\phi^0 & -ik_z\phi^0 & 0 \\ \frac{-k_\beta u_y^0 \mu_\phi^0}{H^2\phi^0} & \frac{-\mu^0(k_\beta^2+k_z^2)}{H^2\phi^0} & -u_y^0 & 0 & \frac{-k_\beta u_y^0 \mu_T^0}{H^2\phi^0} \\ \frac{k_\beta p_\phi^0}{H^2\phi^0} & 0 & \frac{-((2\mu^0+\lambda^0)k_\beta^2+\mu^0 k_z^2)}{H^2\phi^0} & \frac{-ik_z k_\beta(\mu^0+\lambda^0)}{H^2\phi^0} & \frac{k_\beta p_T^0}{H^2\phi^0} \\ \frac{-ik_z p_\phi^0}{H^2\phi^0} & 0 & \frac{ik_z k_\beta(\mu^0+\lambda^0)}{H^2\phi^0} & \frac{-(k_\beta^2\mu^0+k_z^2(2\mu^0+\lambda^0))}{H^2\phi^0} & \frac{-ik_z p_T^0}{H^2\phi^0} \\ \frac{2(u_y^{0^2}\mu_\phi^0-\mathcal{D}_\phi^0)}{\dim\phi^0} & \frac{ik_\beta\mu^0 u_y^0}{\dim\phi^0} & \frac{-2p^0 k_\beta}{\dim\phi^0} & \frac{-2ik_z p^0}{\dim\phi^0} & \frac{-2\kappa^0(k_\beta^2+k_z^2)}{\dim H^2\phi^0} + \frac{2(u_y^{0^2}\mu_T^0-\mathcal{D}_T^0)}{\dim\phi^0} \end{pmatrix}.$$

In a similar manner, the adjoint eigenvalue problem, (8.4), satisfies the following solution

$$\left.\begin{aligned}\left(\phi^{\dagger},T^{\dagger},w^{\dagger}\right) &= \left(\phi_1^{\dagger},T_1^{\dagger},w_1^{\dagger}\right)\cos k_\beta(y \pm 1/2)\\ \left(u^{\dagger},v^{\dagger}\right) &= \left(u_1^{\dagger},v_1^{\dagger}\right)\sin k_\beta(y \pm 1/2)\end{aligned}\right\}, \tag{8.9}$$

with boundary conditions

$$u^{\dagger} = 0, \qquad v^{\dagger} = 0, \qquad \frac{\partial w^{\dagger}}{\partial y} = 0, \qquad \frac{\partial T^{\dagger}}{\partial y} = 0, \quad \text{at } y = \pm 1/2. \tag{8.10}$$

The algebraic eigenvalue problem corresponding to the adjoint problem (8.4) is

$$\tilde{c}X_1^{\dagger} = \mathcal{A}^{\dagger}X_1^{\dagger} \quad \text{where} \quad \mathcal{A}^{\dagger} = \mathcal{A}^{H}. \tag{8.11}$$

8.1.1 Asymptotic Analysis: Dispersion Relation

The dispersion relation for (8.8) is a quintic polynomial in c:

$$c^5 + b_4\, c^4 + b_3\, c^3 + b_2\, c^2 + b_1 c + b_0 = 0, \tag{8.12}$$

where b_i's for $0 \leq i \leq 4$ are defined below

$$\begin{aligned} b_0 &= b_{06}/H^6 + b_{08}/H^8, \qquad b_1 = b_{14}/H^4 + b_{16}/H^6 + b_{18}/H^8, \\ b_2 &= b_{22}/H^2 + b_{24}/H^4 + b_{26}/H^6, \quad b_3 = b_{32}/H^2 + b_{34}/H^4, \\ b_4 &= b_{40} + b_{42}/H^2. \end{aligned}$$

In the above, b_{ij}'s are real functions of the base state variables which can be defined as:

$$\begin{aligned}
b_{06} &= -\tfrac{2(k_z^2+k_\beta^2)^2\mu^{0^2}}{3\phi^{0^3}}\left[(k_z^2+k_\beta^2)(\mathcal{D}_\phi^0 p_T^0 - \mathcal{D}_T^0 p_\phi^0) + (k_z^2-k_\beta^2)u_y^{0^2}(p_\phi^0\mu_T^0 - p_T^0\mu_\phi^0)\right] \\
b_{08} &= \tfrac{2}{3\phi^{0^3}}(k_z^2+k_\beta^2)^4\kappa^0\mu^{0^2}p_\phi^0 \\
b_{14} &= \tfrac{4(k_z^2+k_\beta^2)\mu^0}{3\phi^{0^3}}\left[\phi^0(k_z^2+k_\beta^2)(p_\phi^0\mathcal{D}_T^0 - p_T^0\mathcal{D}_\phi^0) - \phi^0 u_y^{0^2}k_z^2(p_\phi^0\mu_T^0 - p_T^0\mu_\phi^0) + u_y^{0^2}k_\beta^2 p_T^0\mu^0\right] \\
b_{16} &= \tfrac{1}{3\phi^{0^4}}(k_z^2+k_\beta^2)^2\mu^0\left[(k_z^2+k_\beta^2)(2\mu^0(\lambda^0+2\mu^0)\mathcal{D}_T^0 + 2p^0\mu^0 p_T^0 + (4\kappa^0+3\mu^0)\phi^{0^2}p_\phi^0)\right. \\
&\quad \left. -2(k_z^2-k_\beta^2)u_y^{0^2}\mu^0(\lambda^0+2\mu^0)\mu_T^0\right] \\
b_{18} &= \tfrac{2}{3\phi^{0^4}}(k_z^2+k_\beta^2)^4\kappa^0\mu^{0^2}(\lambda^0+2\mu^0) \\
b_{22} &= \tfrac{2}{3\phi^{0^2}}\left[(k_z^2+k_\beta^2)\phi^0 p_\phi^0(\mathcal{D}_T^0 - u_y^{0^2}\mu_T^0) + p_T^0(2k_\beta^2 u_y^{0^2}\mu^0 + (k_z^2+k_\beta^2)\phi^0(-\mathcal{D}_\phi^0 + u_y^{0^2}\mu_\phi^0))\right] \\
b_{24} &= \tfrac{2}{3\phi^{0^3}}(k_z^2+k_\beta^2)\left[(k_z^2+k_\beta^2)(\mu^0(2\lambda^0+5\mu^0)\mathcal{D}_T^0 + 2p^0\mu^0 p_T^0 + (\kappa^0+3\mu^0)\phi^{0^2}p_\phi^0)\right. \\
&\quad \left. +u_y^{0^2}\mu^0(k_\beta^2\mu^0 - k_z^2(2\lambda^0+5\mu^0))\mu_T^0\right] \\
b_{26} &= \tfrac{1}{3\phi^{0^3}}(k_z^2+k_\beta^2)^3\mu^0\left[3\mu^0(\lambda^0+2\mu^0) + 2\kappa^0(2\lambda^0+5\mu^0)\right] \\
b_{32} &= \tfrac{1}{3\phi^{0^2}}\left[(k_z^2+k_\beta^2)(2(\lambda^0+4\mu^0)\mathcal{D}_T^0 + 2p^0 p_T^0 + 3\phi^{0^2}p_\phi^0)\right. \\
&\quad \left. -2u_y^{0^2}(k_\beta^2(\lambda^0+2\mu^0) + k_z^2(\lambda^0+4\mu^0))\mu_T^0\right] \\
b_{34} &= \tfrac{1}{3\phi^{0^2}}(k_z^2+k_\beta^2)^2(2\kappa^0(\lambda^0+4\mu^0) + 3\mu^0(2\lambda^0+5\mu^0)) \\
b_{42} &= \tfrac{1}{3\phi^0}(k_z^2+k_\beta^2)\left[2\kappa^0 + 3(\lambda^0+4\mu^0)\right] \\
b_{40} &= \tfrac{2}{3\phi^0}(\mathcal{D}_T^0 - u_y^{0^2}\mu_T^0).
\end{aligned}$$

We have three possibilities for five roots of dispersion relation (8.12): (i) all roots are real, (ii) one root is real and two complex conjugate roots and (iii) three roots are real and a complex conjugate root. From the asymptotic analysis for large H, it can be shown that there are three real roots and a complex conjugate pair. The real roots have the following approximations for large H:

$$\begin{aligned}
c^{(1)} &= c_0^{(1)} - \frac{1}{H^2}\frac{\left(b_{22} + c_0^{(1)}b_{32} + c_0^{(1)^2}b_{42}\right)}{c_0^{(1)}(5c_0^{(1)} + 4b_{40})} + O(H^{-4}), \\
c^{(2,3)} &= \frac{1}{H^2}\frac{\left(-b_{14} \pm \sqrt{b_{14}^2 - 4b_{22}b_{06}}\right)}{2b_{22}} + O(H^{-4}),
\end{aligned} \tag{8.13}$$

where

$$c_0^{(1)} = -\frac{2}{3\phi^0} f_5^0 \sqrt{T^0} < 0.$$

The real and imaginary parts of the complex conjugate pair $c^{(4,5)} = c_r^{(4,5)} \pm ic_i^{(4,5)}$ have the following asymptotic approximations for large H:

$$\left.\begin{aligned} c_r^{(4,5)} &= \frac{1}{H^2}\left[\frac{\left(\frac{b_{22}}{b_{40}}\right)^2 + b_{14} - \frac{b_{22}b_{32}}{b_{40}}}{2b_{22}}\right] + O(H^{-4}), \\ \left(c_i^{(4,5)}\right)^2 &= \frac{1}{H^2}\left[\frac{b_{22}}{b_{40}}\right] + O(H^{-4}) \end{aligned}\right\}. \tag{8.14}$$

In the limit $H \to \infty$, these solutions have the limiting form: $c^{(1)} \to c_0^{(1)}$ and $c^{(2,3,4,5)} \to 0$. A comparison between the eigenvalues calculated from the asymptotic analysis for large H, (8.13)-(8.14), and from the numerical solution of the algebraic eigenvalue problem (8.8) is shown in table 8.1.

H	Asymptotic analysis for large H	From Eqn. (8.8)
100	$-8.719527725 \times 10^{-1}$	$-8.719913447 \times 10^{-1}$
	$-1.114542234 \times 10^{-5}$	$-1.376061879 \times 10^{-5}$
	$-1.089433668 \times 10^{-3}$	$-1.089433668 \times 10^{-3}$
	$-4.454912228 \times 10^{-3} \pm i9.504165561 \times 10^{-2}$	$-4.434318526 \times 10^{-3} \pm i9.52951028 \times 10^{-2}$
1000	$-8.743609636 \times 10^{-1}$	$-8.743609675 \times 10^{-1}$
	$-1.114542234 \times 10^{-7}$	$-1.117169699 \times 10^{-7}$
	$-1.089433668 \times 10^{-5}$	$-1.089433668 \times 10^{-5}$
	$-4.454912228 \times 10^{-5} \pm i9.50416556 \times 10^{-3}$	$-4.454707390 \times 10^{-5} \pm i9.504419713 \times 10^{-3}$
10000	$-8.743850455 \times 10^{-1}$	$-8.743850455 \times 10^{-1}$
	$-1.114542234 \times 10^{-9}$	$-1.114568332 \times 10^{-9}$
	$-1.089433668 \times 10^{-7}$	$-1.089433670 \times 10^{-7}$
	$-4.454912228 \times 10^{-7} \pm i9.504165561 \times 10^{-4}$	$-4.454910180 \times 10^{-7} \pm i9.50416810 \times 10^{-4}$

Table 8.1: Comparison of eigenvalues from asymptotic analysis and exact values for $\phi^0 = 0.2$, $e = 0.8$ and $k_z = 1$.

8.2 Nonlinear Problem for the Streamwise Independent Flow

The general form of weakly nonlinear equations using amplitude expansion method is given by (7.22). Here we are summarizing equations till cubic order in amplitude which we will use in subsequent subsections in order to get the analytical solutions of higher order harmonics as well as an analytical expression of the first Landau coefficient.

Fundamental Mode

At $O(A)$, we get back the linear problem (8.2) by substituting $k = n = 1$ into (7.22):

$$\mathbf{L}_{11}X^{[1;1]} = 0 \;\Rightarrow\; \mathbf{L}_1 X^{[1;1]} = c^{(0)}X^{[1;1]} \;\Rightarrow\; \mathbf{L}\hat{X} = c\hat{X}, \tag{8.15}$$

where $X^{[1;1]} = \hat{X}$ is the linear eigenfunction or fundamental mode and $c^{(0)} = c$ is the corresponding eigenvalue. The flow is linearly stable if $c_r < 0$ (real part of c) and unstable for $c_r > 0$.

Second Harmonic and Distortion of Mean Flow

At $O(A^2)$ we have a second harmonic and distortion to mean flow. Substituting $k = n = 2$

into (7.22) we get the governing equation for second harmonic:

$$\mathbf{L}_{22}X^{[2;2]} = \mathbf{G}_{22} = N_2(X^{[1;1]}, X^{[1;1]}), \tag{8.16}$$

where $\mathbf{L}_{22} = 2c^{(0)}\mathbf{I} - \mathbf{L}_2$, with $\mathbf{L}_2 = \mathbf{L}(k_z \to 2k_z)$, and $\mathbf{G}_{22} = (G^1_{22}, G^2_{22}, G^3_{22}, G^4_{22}, G^5_{22})$ is the vector of nonlinear terms where the superscripts 1, 2, 3, 4 and 5 refer to continuity, x-momentum, y-momentum, z-momentum and energy equations, respectively. Similarly, substituting $k = 0$ and $n = 2$ in (7.22) we have an equation for the distortion of mean flow,

$$\mathbf{L}_{02}X^{[0;2]} = \mathbf{G}_{02} = 0.5(N_2(\tilde{X}^{[1;1]}, X^{[1;1]}) + N_2(X^{[1;1]}, \tilde{X}^{[1;1]})), \tag{8.17}$$

where $\mathbf{L}_{02} = 2a^{(0)}\mathbf{I} - \mathbf{L}_0$ with $\mathbf{L}_0 = \mathbf{L}(k_z \to 0)$. Note that $X^{[0;2]}$ is a real harmonic.

First Landau Coefficient and Distortion to Fundamental

At $O(A^3)$ we get an equation for the distortion to fundamental mode by substituting $k = 1$ and $n = 3$ into (7.22):

$$\mathbf{L}_{13}X^{[1;3]} = \left[(3a^{(0)} + ib^{(0)})\mathbf{I} - \mathbf{L}_1\right] X^{[1;3]} = -c^{(2)}X^{[1;1]} + \mathbf{G}_{13}, \tag{8.18}$$

where the nonlinear terms $\mathbf{G}_{13}$ can be written as

$$\begin{aligned}\mathbf{G}_{13} \;=\; & N_2(X^{[0,2]}, X^{[1;1]}) + N_2(\tilde{X}^{[0,2]}, X^{[1;1]}) + N_2(X^{[1;1]}, X^{[0,2]}) + N_2(X^{[1;1]}, \tilde{X}^{[0,2]}) \\ & + N_2(\tilde{X}^{[1,1]}, X^{[2;2]}) + N_2(X^{[2;2]}, \tilde{X}^{[1,1]}) + N_3(\tilde{X}^{[1,1]}, X^{[1;1]}, X^{[1;1]}) \\ & + N_3(X^{[1;1]}, \tilde{X}^{[1,1]}, X^{[1;1]}) + N_3(X^{[1;1]}, X^{[1;1]}, \tilde{X}^{[1,1]}).\end{aligned} \tag{8.19}$$

The unknown coefficient $c^{(2)}$, the first Landau coefficient, can be obtained from the solvability condition (cf. Eqn. 3.43) which gives:

$$c^{(2)} = a^{(2)} + ib^{(2)} = \frac{\int_{-1/2}^{1/2} \tilde{X}^\dagger \mathbf{G}_{13}\,\mathrm{d}y}{\int_{-1/2}^{1/2} \tilde{X}^\dagger X^{[1;1]}\,\mathrm{d}y}. \tag{8.20}$$

Third Harmonic

At $O(A^3)$ we get an equation for the third harmonic by substituting $k = 3 = n$ into (7.22)

$$\mathbf{L}_{33}X^{[3;3]} = \left[3(a^{(0)} + ib^{(0)})\mathbf{I} - \mathbf{L}_3\right] X^{[3;3]} = \mathbf{G}_{33}, \tag{8.21}$$

where $\mathbf{L}_3 = \mathbf{L}(k_z \to 3k_z)$ is the linear operator and $\mathbf{G}_{33}$ is the vector of nonlinear terms:

$$\mathbf{G}_{33} \;=\; N_2(X^{[2,2]}, X^{[1;1]}) + N_2(X^{[1,1]}, X^{[2;2]}) + N_3(X^{[1,1]}, X^{[1;1]}, X^{[1;1]}). \tag{8.22}$$

8.2.1 Symmetries of Linear and Nonlinear Modes

The symmetries of linear and nonlinear modes of plane Couette flow have been discussed in chapter 5. In order to extend the previous *analytical weakly nonlinear analysis* of 2D plane Couette flow, as described in chapter 5, to the three dimensional case, here we analyze the symmetries of linear and nonlinear modes for three-dimensional disturbances.

Recall that the base state (7.8) has the following symmetry:

$$\phi^0(-y) = \phi^0(y), \quad u^0(-y) = -u^0(y), \quad T^0(-y) = T^0(y), \tag{8.23}$$

because the base state equations are invariant under the above transformation. The fundamental (linear eigenvector) solution satisfies the following symmetry group:

$$\left.\begin{array}{lll} \phi^{[1;1]}(y) = \phi^{[1;1]}(-y), & T^{[1;1]}(y) = T^{[1;1]}(-y) & \\ u^{[1;1]}(y) = -u^{[1;1]}(-y), & v^{[1;1]}(y) = -v^{[1;1]}(-y), & w^{[1;1]}(y) = w^{[1;1]}(-y) \end{array}\right\}, \tag{8.24}$$

and

$$\left.\begin{array}{lll} \phi^{[1;1]}(y) = -\phi^{[1;1]}(-y), & T^{[1;1]}(y) = -T^{[1;1]}(-y) & \\ u^{[1;1]}(y) = u^{[1;1]}(-y), & v^{[1;1]}(y) = v^{[1;1]}(-y), & w^{[1;1]}(y) = -w^{[1;1]}(-y) \end{array}\right\}. \tag{8.25}$$

From the base state (8.23) and fundamental symmetries (8.24)-(8.25), we can observe the symmetry of second harmonic. For example, the second harmonic satisfies the following symmetry:

$$\left.\begin{array}{lll} \phi^{[2;2]}(y) = \phi^{[2;2]}(-y), & T^{[2;2]}(y) = T^{[2;2]}(-y) & \\ u^{[2;2]}(y) = -u^{[2;2]}(-y), & v^{[2;2]}(y) = -v^{[2;2]}(-y), & w^{[2;2]}(y) = w^{[2;2]}(-y) \end{array}\right\}. \tag{8.26}$$

Note that the distortion of mean flow $X^{[0;2]}$ has the same symmetry as the second harmonic. Now using the symmetries (8.23)-(8.26), we get the following symmetries for the distortion of fundamental ($X^{[1;3]}$):

$$\left.\begin{array}{lll} \phi^{[1;3]}(y) = \phi^{[1;3]}(-y), & T^{[1;3]}(y) = T^{[1;3]}(-y) & \\ u^{[1;3]}(y) = -u^{[1;3]}(-y), & v^{[1;3]}(y) = -v^{[1;3]}(-y), & w^{[1;3]}(y) = w^{[1;3]}(-y) \end{array}\right\}, \tag{8.27}$$

and

$$\left.\begin{array}{lll} \phi^{[1;3]}(y) = -\phi^{[1;3]}(-y), & T^{[1;3]}(y) = -T^{[1;3]}(-y) & \\ u^{[1;3]}(y) = u^{[1;3]}(-y), & v^{[1;3]}(y) = v^{[1;3]}(-y), & w^{[1;3]}(y) = -w^{[1;3]}(-y) \end{array}\right\}, \tag{8.28}$$

and for the third harmonic ($X^{[3;3]}$):

$$\left.\begin{array}{lll} \phi^{[3;3]}(y) = \phi^{[3;3]}(-y), & T^{[3;3]}(y) = T^{[3;3]}(-y) & \\ u^{[3;3]}(y) = -u^{[3;3]}(-y), & v^{[3;3]}(y) = -v^{[3;3]}(-y), & w^{[3;3]}(y) = w^{[3;3]}(-y) \end{array}\right\}, \tag{8.29}$$

and

$$\left.\begin{array}{lll} \phi^{[3;3]}(y) = -\phi^{[3;3]}(-y), & T^{[3;3]}(y) = -T^{[3;3]}(-y) & \\ u^{[3;3]}(y) = u^{[3;3]}(-y), & v^{[3;3]}(y) = v^{[3;3]}(-y), & w^{[3;3]}(y) = -w^{[3;3]}(-y) \end{array}\right\}. \tag{8.30}$$

8.2.2 Second Harmonic: Analytical Solution

The analytical solution of fundamental mode (see §8.1) is given in (8.6) where $\hat{X} = X^{[1;1]}$. Substituting the analytical solution (8.6) into the right hand side of (8.16), i.e. $\mathbf{G}_{22}$, and rearranging the terms of *sines* and *cosines* we get

$$\left.\begin{array}{rcl} (G^1_{22}, G^4_{22}, G^5_{22}) & = & (G^{1\beta}_{22}, G^{4\beta}_{22}, G^{5\beta}_{22}) \cos k_{2\beta}(y \pm 1/2) + (f^1_{22}, f^4_{22}, f^5_{22}) \\ (G^2_{22}, G^3_{22}) & = & (G^{2\beta}_{22}, G^{3\beta}_{22}) \sin k_{2\beta}(y \pm 1/2). \end{array}\right\} \tag{8.31}$$

where $k_{2\beta} = 2\beta\pi$, with $\beta = 1, 2, 3, \ldots$, $G^{\beta}_{22} = [G^{1\beta}_{22}, G^{2\beta}_{22}, G^{3\beta}_{22}, G^{4\beta}_{22}, G^{5\beta}_{22}]$, and $Z_{22} = [f^1_{22}, f^4_{22}, f^5_{22}]$ represents nonlinear mean terms corresponding to the continuity, z-momentum and energy equations. The explicit forms of G^{β}_{22} and Z_{22} are given in Appendix 8C. It has been verified that the

second harmonic has the following analytical solution:

$$\left.\begin{array}{rcl}(\phi^{[2;2]}, w^{[2;2]}, T^{[2;2]})(y) &=& (\phi_2, w_2, T_2)\cos k_{2\beta}(y \pm 1/2) + (\phi_m^{22}, w_m^{22}, T_m^{22}) \\ (u^{[2;2]}, v^{[2;2]})(y) &=& (u_2, v_2)\sin k_{2\beta}(y \pm 1/2)\end{array}\right\} \tag{8.32}$$

where

$$X_2 = [\phi_2, u_2, v_2, w_2, T_2]^{Tr} \tag{8.33}$$

is the modal amplitude of the second harmonic and

$$Y_m^{22} = [\phi_m^{22}, w_m^{22}, T_m^{22}]^{Tr} \tag{8.34}$$

is the vector of nonlinear mean terms. Here the density solution contains a mean term ϕ_m^{22} which depends on spanwise coordinate z. For the two dimensional flow $\phi_m^{22} = 0$ and $w = 0$, and thus the above second harmonic solution reduces to the analytical solution for the second harmonic of 2D-plane Couette flow, see chapter 5.

The governing equation for the modal amplitude X_2 can be obtained by substituting the analytical solution (8.32) and the analytical expression of $\mathbf{G}_{22}$ (8.31) into (8.16) and equating the *sine*, *cosine* and constant terms from both sides of (8.16). For *sine* and *cosine* terms we get:

$$L_{22}^{\beta} X_2 = G_{22}^{\beta}, \tag{8.35}$$

where

$$L_{22}^{\beta} = 2(a^{(0)} + ib^{(0)}) - \mathcal{A}(k_\beta \to 2k_\beta, k_z \to 2k_z). \tag{8.36}$$

For the constant terms we get

$$L_{22}^{z} Y_m^{22} = Z_{22}, \tag{8.37}$$

where L_{22}^{z} is a linear operator:

$$L_{22}^{z} = 2c^{(0)} \begin{pmatrix} 1 & 0 & 1 \\ 0 & 1 & 0 \\ 0 & 0 & 1 \end{pmatrix} - \begin{pmatrix} 0 & -ik_{2z}\phi^0 & 0 \\ -\frac{ik_{2z}p_\phi^0}{H^2\phi^0} & -\frac{k_{2z}^2(2\mu^0+\lambda^0)}{H^2\phi^0} & -\frac{ik_{2z}p_T^0}{H^2\phi^0} \\ \frac{2(\mu_\phi^0 - \mathcal{D}_\phi^0)}{\dim\phi^0} & -\frac{2ik_{2z}p^0}{\dim\phi^0} & \frac{2}{\dim\phi^0}\left(\frac{-\kappa^0 k_{2z}^2}{H^2} + \mu_T^0 - \mathcal{D}_T^0\right) \end{pmatrix} \tag{8.38}$$

where $k_{2z} = 2k_z$.

Note that if $2c^{(0)}$ is equal to any of the eigenvalues of the linear operator $\mathcal{A}(k_\beta \to 2k_\beta, k_z \to 2k_z)$, the system (8.35) is not solvable. This is the case of 1:2 wave resonance, and consequently the Landau coefficients cannot be defined at such resonance points.

8.2.3 Distortion of Mean Flow: Analytical Solution

In a similar manner we proceed for the analytical solution for the distortion of mean flow $X^{[0;2]}$. Substituting the analytical solution of the linear problem (8.6) into the right hand side of (8.17) (i.e. $\mathbf{G}_{02}$) and rearranging the terms of *sines* and *cosines* we get

$$\left.\begin{array}{rcl}(G_{02}^1, G_{02}^4, G_{02}^5) &=& (G_{02}^{1\beta}, G_{02}^{4\beta}, G_{02}^{5\beta})\cos k_{2\beta}(y \pm 1/2) + (0, f_{02}^4, f_{02}^5) \\ (G_{02}^2, G_{02}^3) &=& (G_{02}^{2\beta}, G_{02}^{3\beta})\sin k_{2\beta}(y \pm 1/2)\end{array}\right\} \tag{8.39}$$

where $k_{2\beta} = 2k_\beta$, with $\beta = 1, 2, \ldots$, $G_{02}^{\beta} = [G_{02}^{1\beta}, G_{02}^{2\beta}, G_{02}^{3\beta}, G_{02}^{4\beta}, G_{02}^{5\beta}]^{Tr}$, and $Z_{02} = [f_{02}^4, f_{02}^5]^{Tr}$ represents nonlinear mean terms corresponding to the z-momentum and energy equations. The

explicit form of G_{02}^{β} and Z_{02} are given in Appendix 8D. It can be verified that the distortion of mean flow has the following analytical solution:

$$\left.\begin{aligned} \phi^{[0;2]}(y) &= \phi_{02}\cos k_{2\beta}(y \pm 1/2) \\ (u^{[0;2]}, v^{[0;2]})(y) &= (u_{02}, v_{02})\sin k_{2\beta}(y \pm 1/2) \\ (w^{[0;2]}, T^{[0;2]})(y) &= (w_{02}, T_{02})\cos k_{2\beta}(y \pm 1/2) + (w_m^{02}, T_m^{02}) \end{aligned}\right\} \tag{8.40}$$

where

$$X_{02} = [\phi_{02}, u_{02}, v_{02}, w_{02}, T_{02}]^{Tr} \tag{8.41}$$

and

$$Y_m^{02} = [w_m^{02}, T_m^{02}]^{Tr} \tag{8.42}$$

is the vector of nonlinear mean terms. Substituting (8.6) and (8.40) into (8.17) and equating the coefficients of *sine*, *cosine* and constant terms, we get two sets of equations. For *sine* and *cosine* terms we get:

$$L_{02}^{\beta} X_{02} = G_{02}^{\beta} \tag{8.43}$$

where

$$L_{02}^{\beta} = 2a^{(0)} - \mathcal{A}(k_{\beta} \to 2k_{\beta}, k_z \to 0). \tag{8.44}$$

For the constant terms we get:

$$L_{02}^{z} Y_m^{02} = Z_{02} \tag{8.45}$$

where L_{02}^{z} is a matrix operator

$$L_{02}^{z} = 2a^{(0)} \begin{pmatrix} 1 & 0 \\ 0 & 1 \end{pmatrix} - \begin{pmatrix} 0 & 0 \\ 0 & \frac{2}{\dim\phi^0}(\mu_T^0 - \mathcal{D}_T^0) \end{pmatrix}. \tag{8.46}$$

Since the above system (8.45) is decoupled and hence the mean terms w_m^{02} and T_m^{02} are

$$w_m^{02} = \frac{f_{02}^4}{2a^{(0)}} \quad \text{and} \quad T_m^{02} = \frac{f_{02}^5}{2a^{(0)} - \frac{2}{dim\phi^0}(\mu_T^0 - \mathcal{D}_T^0)}. \tag{8.47}$$

If $2a^{(0)}$ is equal to any of the real eigenvalues of linear operator $\mathcal{A}(k_{\beta} \to 2k_{\beta}, k_z \to 0)$, the above system (8.43) is not solvable. This is the case of mean flow resonance and the first Landau coefficient cannot be determined at such resonance points. At such points the pure span-wise modes interact with the streamwise independent mean flow.

8.2.4 First Landau Coefficient

Substituting the analytical solutions of $X^{[1;1]}$, $X^{[2;2]}$ and $X^{[0;2]}$ into (8.19) and equating the coefficients of *sine* and *cosine* terms, we get the following analytical form of G_{13},

$$\left.\begin{aligned} (G_{13}^1, G_{13}^4, G_{13}^5) &= (G_{13}^{1\beta 3}, G_{13}^{4\beta 3}, G_{13}^{5\beta 3})\cos k_{3\beta}(y \pm 1/2) \\ &\quad + (G_{13}^{1\beta 1}, G_{13}^{4\beta 1}, G_{13}^{5\beta 1})\cos k_{\beta}(y \pm 1/2) \\ (G_{13}^2, G_{13}^3) &= (G_{13}^{2\beta 3}, G_{13}^{3\beta 3})\sin k_{3\beta}(y \pm 1/2) + (G_{13}^{2\beta 1}, G_{13}^{3\beta 1})\sin k_{\beta}(y \pm 1/2) \end{aligned}\right\} \tag{8.48}$$

where $G_{13}^{\beta 3} = [G_{13}^{1\beta 3}, G_{13}^{2\beta 3}, G_{13}^{3\beta 3}, G_{13}^{4\beta 3}, G_{13}^{5\beta 3}]^{Tr}$ and $G_{13}^{\beta 1} = [G_{13}^{1\beta 1}, G_{13}^{2\beta 1}, G_{13}^{3\beta 1}, G_{13}^{4\beta 1}, G_{13}^{5\beta 1}]^{Tr}$ are nonlinear terms. From the solvability condition, the analytical expression of the first Landau

coefficient (8.20) can be written as

$$c^{(2)} = a^{(2)} + ib^{(2)} = \frac{\tilde{\phi}_1^\dagger G_{13}^{1\beta 1} + \tilde{u}_1^\dagger G_{13}^{2\beta 1} + \tilde{v}_1^\dagger G_{13}^{3\beta 1} + \tilde{w}_1^\dagger G_{13}^{4\beta 1} + \tilde{T}_1^\dagger G_{13}^{5\beta 1}}{\tilde{\phi}_1^\dagger \phi_1 + \tilde{u}_1^\dagger u_1 + \tilde{v}_1^\dagger v_1 + \tilde{w}_1^\dagger w_1 + \tilde{T}_1^\dagger T_1}, \tag{8.49}$$

where $G_{13}^{1\beta 1}$, $G_{13}^{2\beta 1}$, $G_{13}^{3\beta 1}$, $G_{13}^{4\beta 1}$ and $G_{13}^{5\beta 1}$ are given in Appendix 8E. Since we know the form of $\mathbf{G}_{13}$, the analytical solution for $X^{[1;3]}$ (8.18) is given by:

$$\left.\begin{aligned}(\phi^{[1;3]}, w^{[1;3]}, T^{[1;3]})(y) &= (\phi_{13}^{\beta 3}, w_{13}^{\beta 3}, T_{13}^{\beta 3}) \cos k_{3\beta}(y \pm 1/2) \\ &\quad + (\phi_{13}^{\beta 1}, w_{13}^{\beta 1}, T_{13}^{\beta 1}) \cos k_\beta (y \pm 1/2) \\ (u^{[1;3]}, v^{[1;3]})(y) &= (u_{13}^{\beta 3}, v_{13}^{\beta 3}) \sin k_{3\beta}(y \pm 1/2) + (u_{13}^{\beta 1}, v_{13}^{\beta 1}) \sin k_\beta (y \pm 1/2)\end{aligned}\right\}, \tag{8.50}$$

where $X_{13}^{\beta 3} = [\phi_{13}^{\beta 3}, u_{13}^{\beta 3}, v_{13}^{\beta 3}, w_{13}^{\beta 3}, T_{13}^{\beta 3}]^{Tr}$ and $X_{13}^{\beta 1} = [\phi_{13}^{\beta 1}, u_{13}^{\beta 1}, v_{13}^{\beta 1}, w_{13}^{\beta 1}, T_{13}^{\beta 1}]^{Tr}$ are modal amplitudes which can be obtained by substituting the above solution (8.50) into (8.18) and equating the *sine* and *cosine* terms from both sides. We get two inhomogeneous systems of equations for $X_{13}^{\beta 3}$ and $X_{13}^{\beta 1}$ which in matrix form are:

$$\left.\begin{aligned}L_{13}^{\beta 3} X_{13}^{\beta 3} &= G_{13}^{\beta 3} \\ L_{13}^{\beta 1} X_{13}^{\beta 1} &= -c^{(2)}(\phi_1, u_1, v_1, w_1, T_1) + G_{13}^{\beta 1}\end{aligned}\right\}, \tag{8.51}$$

where

$$\left.\begin{aligned}L_{13}^{\beta 3} &= (3a^{(0)} + ib^{(0)}) - \mathcal{A}(k_\beta \to 3k_\beta, k_z \to k_z) \\ L_{13}^{\beta 1} &= (3a^{(0)} + ib^{(0)}) - \mathcal{A}(k_\beta \to k_\beta, k_z \to k_z)\end{aligned}\right\} \tag{8.52}$$

are linear operators.

8.2.5 Third Harmonic

Substituting the analytical solutions of $X^{[1;1]}$ and $X^{[2;2]}$ into (8.22) and equating the coefficients of *sine* and *cosine* terms we get

$$\left.\begin{aligned}(G_{33}^1, G_{33}^4, G_{33}^5) &= (G_{33}^{1\beta 3}, G_{33}^{4\beta 3}, G_{33}^{5\beta 3}) \cos k_{3\beta}(y \pm 1/2) \\ &\quad + (G_{33}^{1\beta 1}, G_{33}^{4\beta 1}, G_{33}^{5\beta 1}) \cos k_\beta (y \pm 1/2) \\ (G_{33}^2, G_{33}^3) &= (G_{33}^{2\beta 3}, G_{33}^{3\beta 3}) \sin k_{3\beta}(y \pm 1/2) + (G_{33}^{2\beta 1}, G_{33}^{3\beta 1}) \sin k_\beta (y \pm 1/2)\end{aligned}\right\}, \tag{8.53}$$

where $G_{33}^{\beta 3} = [G_{33}^{1\beta 3}, G_{33}^{2\beta 3}, G_{33}^{3\beta 3}, G_{33}^{4\beta 3}, G_{33}^{5\beta 3}]^{Tr}$ and $G_{33}^{\beta 1} = [G_{33}^{1\beta 1}, G_{33}^{2\beta 1}, G_{33}^{3\beta 1}, G_{33}^{4\beta 1}, G_{33}^{5\beta 1}]^{Tr}$ are nonlinear terms.

It has been verified that the analytical solution of $X^{[3;3]}$ is

$$\left.\begin{aligned}(\phi^{[3;3]}, w^{[3;3]}, T^{[3;3]})(y) &= (\phi_{33}^{\beta 3}, w_{33}^{\beta 3}, T_{33}^{\beta 3}) \cos k_{3\beta}(y \pm 1/2) \\ &\quad + (\phi_{33}^{\beta 1}, w_{33}^{\beta 1}, T_{33}^{\beta 1}) \cos k_\beta (y \pm 1/2) \\ (u^{[3;3]}, v^{[3;3]})(y) &= (u_{33}^{\beta 3}, v_{33}^{\beta 3}) \sin k_{3\beta}(y \pm 1/2) + (u_{33}^{\beta 1}, v_{33}^{\beta 1}) \sin k_\beta (y \pm 1/2)\end{aligned}\right\} \tag{8.54}$$

where $X_{33}^{\beta 3} = [\phi_{33}^{\beta 3}, u_{33}^{\beta 3}, v_{33}^{\beta 3}, w_{33}^{\beta 3}, T_{33}^{\beta 3}]$ and $X_{33}^{\beta 1} = [\phi_{33}^{\beta 1}, u_{33}^{\beta 1}, v_{33}^{\beta 1}, w_{33}^{\beta 1}, T_{33}^{\beta 1}]$ are the modal amplitudes of the third harmonic.

The unknown modal amplitudes $X_{33}^{\beta 3}$ and $X_{33}^{\beta 1}$ are obtained by substituting the above solution (8.54) into (8.21) and equating the *sine* and *cosine* terms from both side:

$$L_{33}^{\beta 3} X_{33}^{\beta 3} = G_{33}^{\beta 3} \quad \text{and} \quad L_{33}^{\beta 1} X_{33}^{\beta 1} = G_{33}^{\beta 1},$$

where

$$\left.\begin{aligned} L_{33}^{\beta 3} &= 3(a^{(0)} + ib^{(0)}) - \mathcal{A}(k_\beta \to 3k_\beta, k_z \to 3k_z) \\ L_{33}^{\beta 1} &= 3(a^{(0)} + ib^{(0)}) - \mathcal{A}(k_\beta \to k_\beta, k_z \to 3k_z) \end{aligned}\right\}. \tag{8.55}$$

In the following sections we present numerical results, bifurcation diagrams and patterns using these analytical solutions.

8.3 Results and Discussions

8.3.1 Linear Theory: Locus of Neutral Stability Curve

The locus of the neutral stability curve can be given as $b_0 = 0$, i.e. $H^2 = -b_{08}/b_{06}$ [see (8.12)] which can be simplified to

$$H^2 = \frac{1}{(1-e^2)} \frac{\Psi_4(\phi^0; k_z, k_\beta)}{\Psi_5(\phi^0; k_z, k_\beta)}, \tag{8.56}$$

where

$$\left.\begin{aligned} \Psi_4(\phi^0; k_z, k_\beta) &= (k_z^2 + k_\beta^2) f_{1\phi}^0 f_4^0 \\ \Psi_5(\phi^0; k_z, k_\beta) &= \frac{\chi^0}{\sqrt{\pi}} \left[(k_z^2 + k_\beta^2)(24\phi^0 f_1^0 - 18\phi^{0^2} f_{1\phi}^0) \right. \\ &\quad \left. + \frac{12}{f_2^0}(k_z^2 - k_\beta^2)\phi^{0^2} \left(\frac{1}{2} f_{1\phi}^0 f_2^2 - f_1^0 f_{2\phi}^0 \right) \right] \end{aligned}\right\}.$$

Here $\chi^0 = \chi(\phi^0)$ is the radial distribution as given by (2.12). It can be seen from the above expression (8.56) that $H \to \infty$ for $e \to 1$, i.e. the flow is stable for elastic particles.

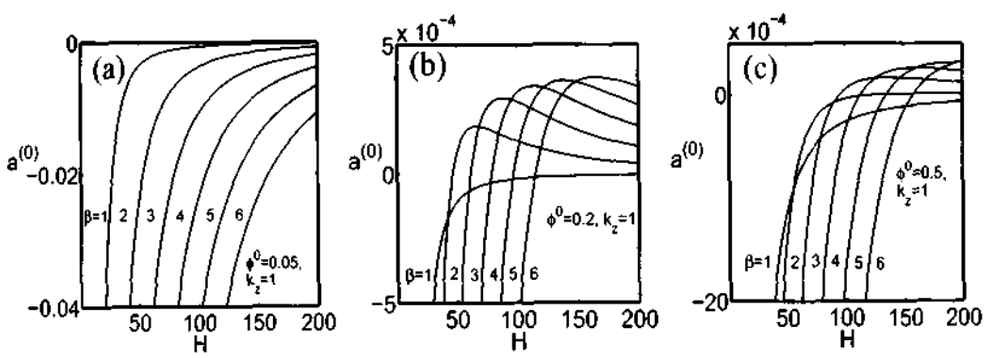

Figure 8.1: Variations of growth rates of modes $\beta = 1$ to 6 for three values of densities (*a*) $\phi^0 = 0.05$, (*b*) $\phi^0 = 0.2$ and (*c*) $\phi^0 = 0.5$ for $k_z = 1$ and $e = 0.8$

Figures 8.1(*a*), 8.1(*b*) and 8.1(*c*) show the variations of the growth rates of first six successive modes ($\beta = 1$ to 6) with the Couette gap for three values of densities $\phi^0 = 0.05$, 0.2 and 0.5, respectively, where the spanwise wavenumber is set to $k_z = 1$ and the restitution coefficient is $e = 0.8$. As seen in figure 8.1(*a*) the growth rates of dilute flow $\phi^0 = 0.05$ are negative for all modes ($\beta = 1$ to 6) at $k_z = 1$ and thus the flow is linearly stable. However for moderately dense ($\phi^0 = 0.2$, see figure 8.1*b*) and dense flows ($\phi^0 = 0.5$, see figure 8.1*c*) the higher order modes become unstable after some critical value of Couette gap. It is seen in figures 8.1(*b*)-(*c*) that for every mode β, the growth rate starts with a negative value, increases with H until some value of H and decreases thereafter. There is a range of Couette gaps between which a particular mode

remains least stable and beyond that the next higher-order mode becomes least stable until the next crossover. Throughout the analysis we are using the maximum growth rate over all mode numbers:

$$a^{(0)} = \max_{\beta} a^{(0)}(\beta).$$

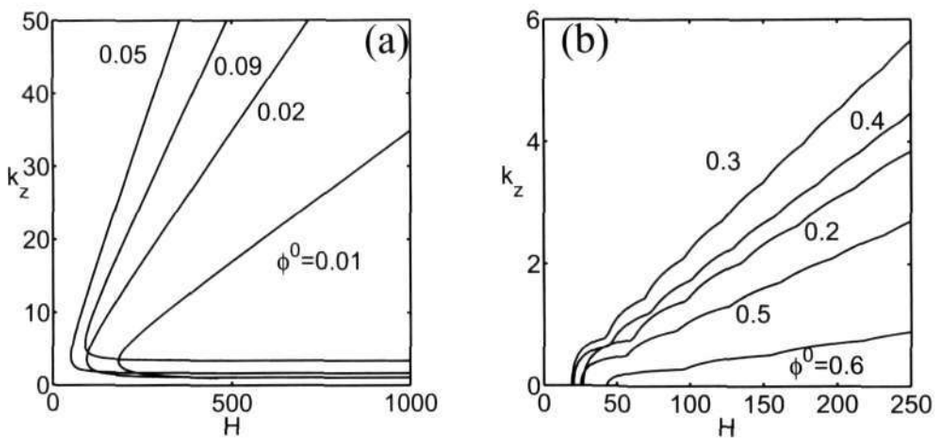

Figure 8.2: Stability diagram for the uniform shear flow in the (H, k_z)-plane for streamwise independent modes $(\partial/\partial x = 0)$: (a) dilute flows for $\phi^0 = 0.01$, 0.02, 0.05 and 0.09; (b) moderate-to-dense flows for $\phi^0 = 0.2$, 0.3, 0.4, 0.5 and 0.6. The coefficient of restitution is set to $e = 0.8$.

Figure 8.2(a) shows four neutral stability contours $(a^{(0)} = 0)$ in the (H, k_z)-plane for dilute flows, $\phi^0 = 0.01$, 0.02, 0.05 and 0.09; the coefficient of restitution is set to $e = 0.8$. Similarly for moderate-to-dense flow regimes, five neutral contours in the (H, k_z)-plane for $\phi^0 = 0.2$, 0.3, 0.4, 0.5 and 0.6 are shown in figure 8.2(b). The growth rate is positive inside each contour and negative outside; thus, the flow is unstable inside each contour and stable outside. For dilute flows, figure 8.2(a), the flow is unstable to a range of k_z, and this range of unstable k_z increases with Couette gap (H). The origin of this instability can be tied to the pure spanwise perturbations (Alam 2006; Gayen & Alam 2006) as discussed in chapter 7. It can be observed from figure 8.2(a) that the growth rate is negative at $k_z = 0$, i.e. the flow is stable for the two-dimensional streamwise perturbations ($k_x = 0$ and $k_z = 0$) in the dilute limit. For a fixed Couette gap (H), the range of unstable wavenumbers increases with increasing density until some critical density. On further increase of density the range of unstable wavenumbers shrinks to zero and this spanwise instability vanishes completely at $\phi^0 > \phi^0_{3d} \approx 0.1$. Consequently, there is a window of mean densities $\phi^0_{3d} < \phi^0 < \phi^0_{2d}$, where $\phi^0_{2d} = \phi^l_c = 0.15$ and $\phi^0_{3d} = 0.1$, for which the flow is always stable (linearly) to streamwise independent perturbations $(k_x = 0)$, [cf. (5.46) and (7.72)].

For densities $\phi^0 > \phi^0_{2d}$ the flow is unstable to two-dimensional streamwise independent perturbations (i.e. pure transverse perturbation: $\partial/\partial y(.) \neq 0$ and $k_x = k_z = 0$) as discussed in chapters 4 and 5. Moreover, the flow remains unstable for a range of spanwise wavenumbers beyond a minimum Couette gap as shown in figure 8.2(b). As seen in this figure, the growth rate of this instability is maximum at $k_z = 0$ and decreases with increasing k_z. Furthermore, the range of unstable wavenumbers first increases with density for a fixed Couette gap until a critical density, beyond which the range of unstable wavenumbers decreases with increasing density. This implies that the flow is more stable in the dense limit.

To see the effect of restitution coefficient, we have shown neutral stability contours for three

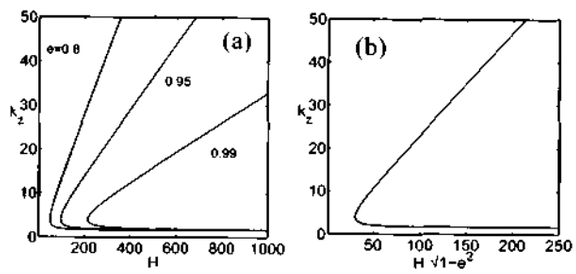

Figure 8.3: Stability diagram for $\phi^0 = 0.05$ in (a) (H, k_z)-plane for $e = 0.8, 0.95, 0.99$, (b) $(H\sqrt{1-e^2}, k_z)$-plane for $e = 0.8, 0.95, 0.99$.

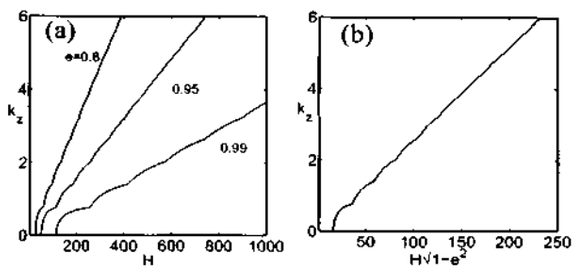

Figure 8.4: Same as figure 8.3 but for $\phi^0 = 0.2$.

values of e (0.8, 0.9 and 0.95) for two mean densities $\phi^0 = 0.05$ and $\phi^0 = 0.2$ in figures 8.3(a) and 8.4(a), respectively. These figures show that the flow becomes more stable with increasing restitution coefficient. From (8.56), we can write the locus of neutral stability as

$$H^{*2} = H^2(1-e^2) = \frac{\Psi_4(\phi^0; k_z, k_\beta)}{\Psi_5(\phi^0; k_z, k_\beta)} = f(\phi^0, k_z, k_\beta). \tag{8.57}$$

Therefore, the Couette gap H can be scaled with e such that $H^* = H\sqrt{1-e^2}$. With this scaling, we replotted figures 8.3(a) and 8.4(a) for all values of e but in the (H^*, k_z)-plane as shown in figures 8.3(b) and 8.4(b), respectively. Clearly we get only one neutral contour inside which the flow is unstable and stable outside.

Figure 8.5 show the neutral stability curve in the (ϕ^0, k_z)-plane for three values of $H = 100$, 500 and 1000. The flow is unstable ($a^{(0)} > 0$) inside each contour and stable ($a^{(0)} < 0$) outside. It is seen from figure 8.5 that the range of unstable spanwise wavenumbers increases with increasing Couette gap and, hence, the flow becomes more unstable for increasing Couette gap. For given H and e, there exists a pair of critical parameters $(\phi^0, k_z) = (\phi^0_c, k_{zc})$ above which the flow is linearly stable.

8.3.2 Equilibrium Amplitude and Bifurcation

The cubic Landau equation can be written as

$$\frac{dA}{dt} = a^{(0)}A + a^{(2)}A^3, \tag{8.58}$$

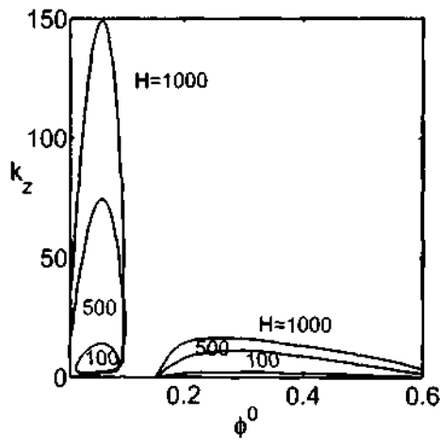

Figure 8.5: Neutral stability curve in (ϕ, k_z)-plane for three values of Couette gaps H = 100, 500 and 1000. The restitution coefficient is e = 0.8.

where $a^{(0)}$ is the growth rate and $a^{(2)}$ is the first Landau coefficient. The equilibrium solution of this equation can be obtained by solving $dA/dt = 0$, which gives a trivial zero solution which represents the uniform shear solution and two non-zero solutions which are finite amplitude solutions at cubic order (see §5.5.2):

$$A_e = \pm\sqrt{-\frac{a^{(0)}}{a^{(2)}}}. \tag{8.59}$$

Depending on the sign of $a^{(0)}$ and $a^{(2)}$ we get subcritical ($a^{(0)} < 0$ and $a^{(2)} > 0$) and supercritical bifurcations ($a^{(0)} > 0$ and $a^{(2)} < 0$).

In the following sections, §8.3.3, §8.3.4 and §8.3.5, we discuss results based on first Landau coefficient and the related bifurcations for three flow regimes: dilute flows ($\phi^0 \sim 0$), moderately dense flow ($\phi^0 << \phi_m$) and dense flow ($\phi^0 \sim \phi_m$) where ϕ_m is the maximum solid fraction at random close packing ($\phi_m = 0.65$).

8.3.3 Dilute Flows

As described in §8.3.1, the instabilities in dilute flows are due to the streamwise independent three-dimensional modes which are originated from the pure spanwise modes. These instabilities are stationary ($b^{(0)} = 0$). In this section we focus on dilute flows and related bifurcations.

For $k_z = 40$, the variations of $a^{(0)}$ (circles) and $a^{(2)}$ (stars) are shown in figure 8.6(a) for a range of Couette gap near the neutral stability curve. It is clear from this figure that $a^{(2)}$ is positive and $a^{(0)}$ changes sign from negative to positive at $H \approx 390$, leading to a subcritical bifurcation. The bifurcation diagram for this subcritical instability is shown in the inset of figure 8.6(a). A sharp jump in $a^{(2)}$, see figure 8.6(a), near the zero growth rate at $H \approx 390$ signals a possibility of resonance.

Since we are dealing with cubic order Landau equation, it is important to check the validity of the second harmonic (8.16) and the distortion of mean flow (8.17). Let us rewrite (8.16) as

$$\mathbf{L}_{22}X^{[2;2]} = \mathbf{G}_{22} = N_2(X^{[1;1]}, X^{[1;1]}), \tag{8.60}$$

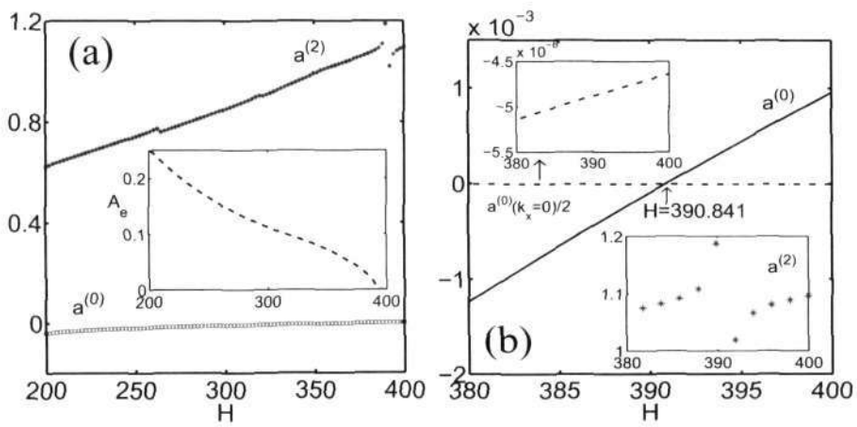

Figure 8.6: Variations with H of (a) $a^{(0)}$ (circles), $a^{(2)}$ (stars) and A_e (inset), (b) $a^{(0)}$ (solid line in main panel), $a^{(2)}$ (lower inset) and $\frac{1}{2}a^{(0)}(k_z = 0)$ (dash-dot line in main panel and in upper inset) where an arrow at $H = 390.841$ indicates a resonance point. Parameters are set to be $\phi^0 = 0.09$, $k_z = 40$ and $e = 0.8$.

where $\mathbf{L}_{22} = 2c^{(0)}\mathbf{I} - \mathbf{L}_2$ (see §8.2 for details). Note that if $2c^{(0)}$ is equal to any of the eigenvalues of $\mathbf{L}_2$, then the left hand side of (8.60) is identically zero, therefore we cannot solve the above equation directly because we have eigensolutions of the associated homogeneous problem of (8.60). From the Fredholm alternatives, the solution of the problem (8.60) exists if and only if the solvability condition is satisfied. This is an unsolvable case of 1:2 wavenumber resonance (Fujimura 1992).

In addition to 1:2 wave resonance, there exists another unsolvable case related to the mean flow distortion (8.17) (Mizushima & Gotoh 1985):

$$\mathbf{L}_{02}X^{[0;2]} = \mathbf{G}_{02} = 0.5(N_2(\tilde{X}^{[1;1]}, X^{[1;1]}) + N_2(X^{[1;1]}, \tilde{X}^{[1;1]})), \tag{8.61}$$

where $\mathbf{L}_{02} = 2a^{(0)}\mathbf{I} - \mathbf{L}_0$. Again if $2a^{(0)}$ is equal to any of the eigenvalues of the operator $\mathbf{L}_0$, we cannot solve this equation. We can summarize the above two resonance conditions:

$$c^{(0)}(k_z) = \frac{1}{2}c_j^{(0)}(\mathbf{L}_2) = \frac{1}{2}c_j^{(0)}(k_z \to 2k_z), \tag{8.62}$$

$$a^{(0)} = \frac{1}{2}c_j^{(0)}(\mathbf{L}_0) = \frac{1}{2}c_j^{(0)}(k_z = 0), \tag{8.63}$$

where $c_j^{(0)}(\mathbf{L}_2)$ and $c_j^{(0)}(\mathbf{L}_0)$ represent the j^{th} eigenvalue of the linear operator $\mathbf{L}_2$ and $\mathbf{L}_0$, respectively, where j denotes a positive integer.

It has been verified that the discontinuity in $a^{(2)}$ in figure 8.6(a) is due to mean flow resonance. To show this resonance graphically, we have plotted $a^{(0)}$ (solid line) at $k_z = 40$ and $\frac{1}{2}a^{(0)}$ associated with $\mathbf{L}_0$ operator at $k_z = 0$ (dash-dot line in main panel and upper inset) in figure 8.6(b). It is clearly seen in the main panel of this figure that the resonance condition (8.63) is exactly satisfied at $H = 390.841$ which leads to a discontinuity in the first Landau coefficient as shown in figure 8.6(a) and the lower inset of figure 8.6(b).

Figures 8.7(a)-(b) and figures 8.7(c)-(d) are same as figures 8.6(a)-(b) but for densities $\phi^0 = 0.05$ and 0.02, respectively. Figures 8.7(a) and 8.7(c) show the variations of $a^{(0)}$ (circles), $a^{(2)}$ (stars) and A_e (inset) for $\phi^0 = 0.05$ and 0.02, respectively. For $\phi^0 = 0.05$, the mean flow resonance

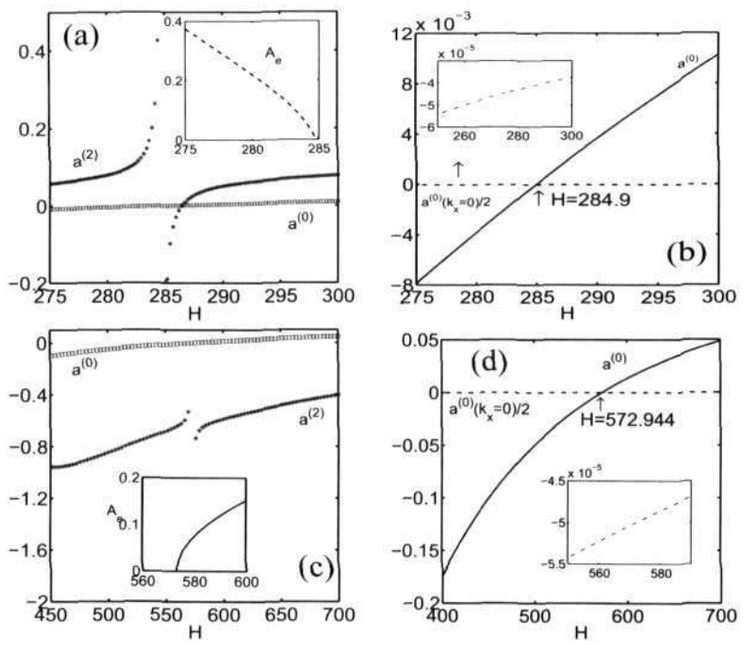

Figure 8.7: Same as figure 8.6(a)-(b) but for (a)-(b) $\phi^0 = 0.05$, (c)-(d) $\phi^0 = 0.02$.

occurs at $H = 284.9$ which is shown by an arrow in figure 8.7(b) where the solid line represents $a^{(0)}$ and the dash-dot line (in main panel and inset) denotes $\frac{1}{2}a^{(0)}$ at $k_z = 0$ (see the description of figure 8.6(b)). Similarly for $\phi^0 = 0.02$, the mean flow resonance occurs at $H = 572.944$ as indicated by an arrow in figure 8.7(d). The bifurcation is subcritical for $\phi^0 = 0.05$ and supercritical for $\phi^0 = 0.02$.

From figures 8.6 and 8.7 we can conclude that for sufficiently large spanwise wavenumbers, there is a transition from supercritical to subcritical bifurcations:

$$\underbrace{\text{Supercritical}}_{\phi^0=0.02} \longrightarrow \underbrace{\text{Subcritical}}_{\phi^0=0.05} \longrightarrow \underbrace{\text{Subcritical}}_{\phi^0=0.09}. \tag{8.64}$$

The variations of $a^{(0)}$ (circles), $a^{(2)}$ (stars) and A_e (inset) for three values of densities $\phi^0 = 0.02$, 0.05 and 0.09 with spanwise wavenumber $k_z = 5$ and $e = 0.8$ are shown in figures 8.8(a), 8.8(b) and 8.8(c), respectively. The flow admits supercritical bifurcations for densities $\phi^0 = 0.02$ and 0.05 and subcritical bifurcation for density 0.09. Therefore, the transition from supercritical to subcritical bifurcation occurs between $\phi^0 = 0.05$ and 0.09,

$$\underbrace{\text{Supercritical}}_{\phi^0=0.02} \longrightarrow \underbrace{\text{Supercritical}}_{\phi^0=0.05} \longrightarrow \underbrace{\text{Subcritical}}_{\phi^0=0.09}. \tag{8.65}$$

Note that the transition from supercritical to subcritical bifurcations for $k_z = 40$ (cf. (8.64)) occurs between $\phi^0 = 0.02$ and 0.05 (see figures 8.6 and 8.7).

In brief, for dilute flows the threshold density for the transition from supercritical to subcritical bifurcations decreases with increasing spanwise wavenumber, or, in other words, the threshold density decreases with decreasing spanwise wavelength.

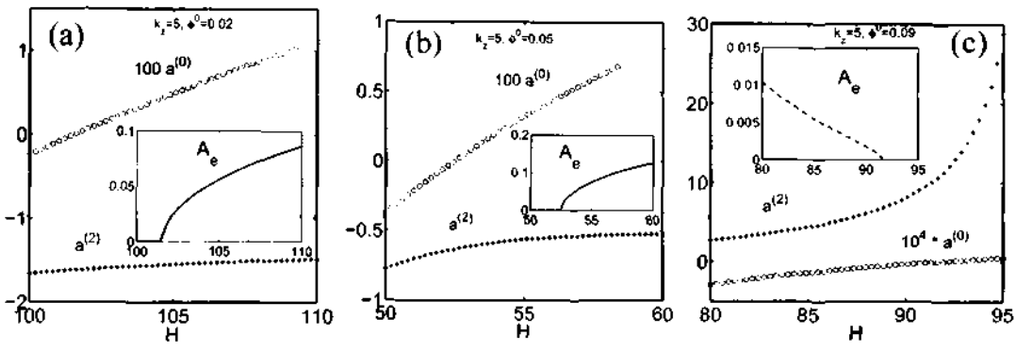

Figure 8.8: Variations of $a^{(0)}$ (circles), $a^{(2)}$ (stars) and A_e (inset) with H for $k_z = 5$, $e = 0.8$ and density (*a*) $\phi^0 = 0.02$, (*b*) $\phi^0 = 0.05$ and (*c*) $\phi^0 = 0.09$.

8.3.4 Moderately Dense Flows

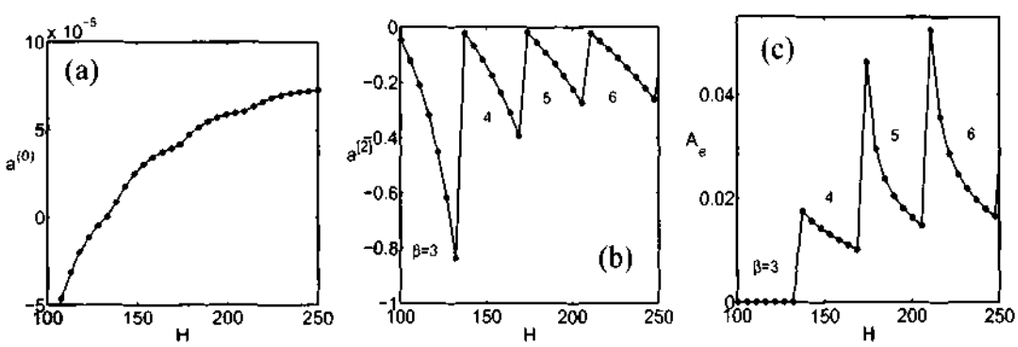

Figure 8.9: Variations of (*a*) $a^{(0)}$, (*b*) $a^{(2)}$ and (*c*) A_e with H. For parameters $\phi^0 = 0.2$, $k_z = 2$ and $e = 0.8$.

In this section we focus on the moderately dense flow regime ($\phi^0 = 0.2$). The stability diagrams for moderate-to-dense flow regimes are shown in figure 8.2(*b*). The instability in this flow regime is originated from the pure transverse mode as explained in §8.3.1. For $\phi^0 = 0.2$ and $k_z = 2$, the variations of $a^{(0)}$, $a^{(2)}$ and A_e with H are shown in figure 8.9(*a*), 8.9(*b*) and 8.9(*c*), respectively. The kinks in $a^{(0)}$, $a^{(2)}$ and A_e correspond to the crossing of modes $\beta = 3$, 4, 5 and 6. (Recall that the mode number β denotes the zero crossings of density or temperature eigenfunctions along the transverse direction y.) It is clear from figures 8.9(*a*) and 8.9(*b*) that $a^{(2)}$ is negative and $a^{(0)}$ varies from negative to positive. Therefore the equilibrium amplitude exists for the range of H for which $a^{(0)} > 0$ and $a^{(2)} < 0$. We have magnified figure 8.9 and replotted $a^{(0)}$ (solid line), $a^{(2)}$ (dashed line) and A_e (inset) in figure 8.10(*a*) for the range of Couette gap $H \in [130, 135]$. In figure 8.10(*a*) an arrow, at $H = 132.6$, indicates the point where $a^{(0)}$ changes sign. Since $a^{(2)}$ is negative, the bifurcation is supercritical (see inset of figure 8.10*a*). Figure 8.10(*b*) is same as 8.10(*a*) but for $e = 0.95$. Note that in both cases the bifurcation is supercritical.

To see the scaling of Couette gap with restitution coefficient we have plotted bifurcation diagram in the (A_e, H^*)-plane for three values of restitution coefficient $e = 0.6$, 0.8 and 0.95 in figure 8.10(*c*). It can be seen from figure 8.10(*c*) that the Couette gap scaling with restitution

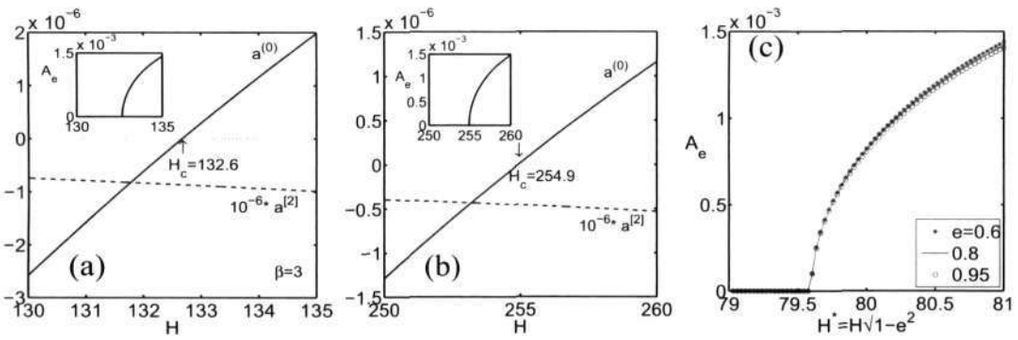

Figure 8.10: For $\phi^0 = 0.2$ and $k_z = 2$, variations of $a^{(0)}$ (solid line), $a^{(2)}$ (dashed line) and A_e (inset) with H: (a) $e = 0.8$ and (b) $e = 0.95$. (c) Bifurcation diagram in $(A_e, H\sqrt{1-e^2})$-plane for three values of restitution coefficient: $e = 0.6$ (stars), 0.8 (solid line) and 0.95 (circles).

coefficient, $H^* = H\sqrt{1-e^2}$, for the equilibrium amplitude agrees well near the critical point ($H \sim 79.5$).

8.3.5 Dense Flows

For $\phi^0 = 0.5$, $k_z = 2$ and $e = 0.8$, the variations of $a^{(0)}$, $a^{(2)}$ and A_e are shown in figures 8.11(a)-(c). The bifurcation is subcritical for the range of H where $a^{(0)} < 0$ and $a^{(2)} > 0$. Similar plots for $e = 0.95$ are shown in figures 8.12(a)-(c). The bifurcation remains subcritical for $e = 0.95$ too.

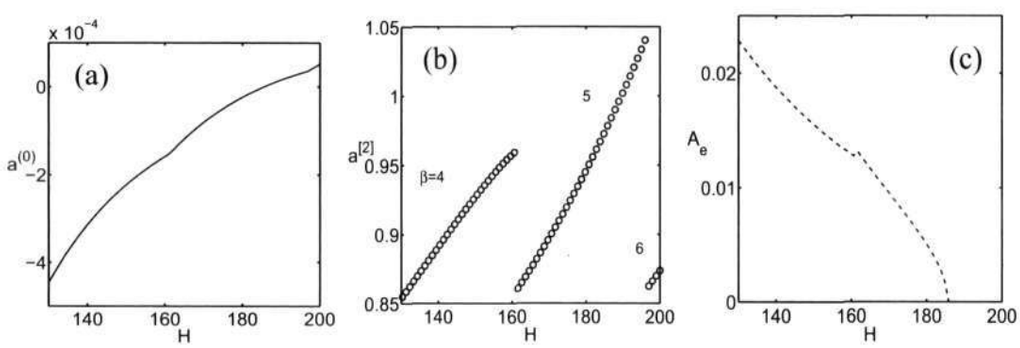

Figure 8.11: Same as figure 8.9 but for $\phi^0 = 0.5$.

The variations of $a^{(0)}$, $a^{(2)}$, A_e and β with H^* for three values of restitution coefficients $e = 0.8$ (circles), 0.95 (stars) and 0.99 (squares) are shown in figure 8.13$(a$-$c)$. It is seen from figure 8.13(a) that the scaling holds for the zero crossing of the growth rate and for the mode numbers (see inset of figure 8.13a). Figure 8.13(c) shows that the Couette gap scaling agrees well for equilibrium amplitude.

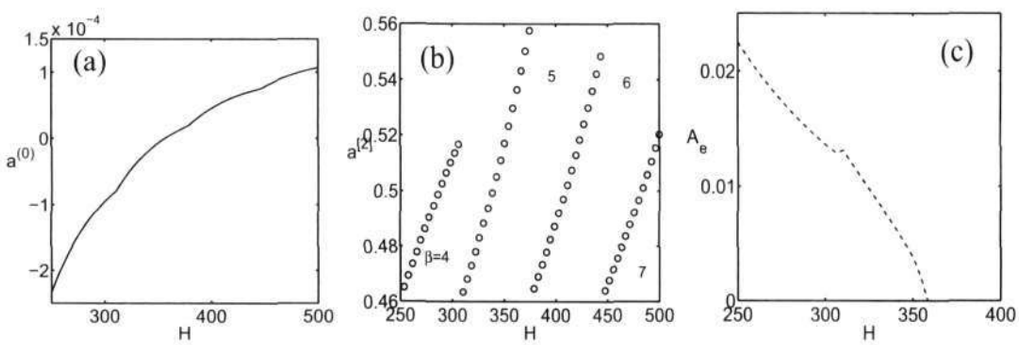

Figure 8.12: Same as figure 8.11 but for $e = 0.95$.

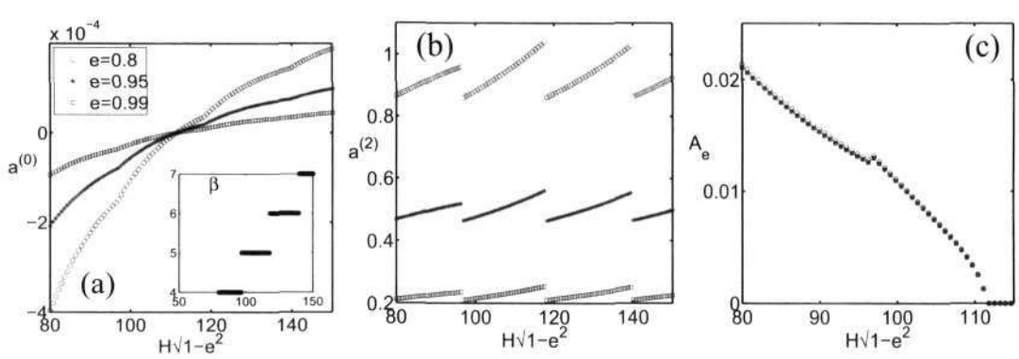

Figure 8.13: Variations with H^* for three values of restitution coefficient $e = 0.8$, 0.95 and 0.99; other parameters are same as figure 8.11: (a) $a^{(0)}$ (main panel) and β (inset), (b) $a^{(2)}$ and (c) A_e.

8.3.6 Bifurcation Diagrams

Figure 8.14(a) shows the bifurcation diagrams in the $(A_e, H - H_c)$-plane for a series of densities $\phi^0 = 0.1, 0.2, 0.24, 0.25, 0.3, 0.4$ and with $k_z = 2$ and $e = 0.8$. The solid and dash lines represent the stable and unstable equilibrium solutions, respectively. This figure shows that there is a transition from subcritical to supercritical between $\phi^0 \in (0.1, 0.2)$ and supercritical to subcritical between $\phi^0 \in (0.24, 0.25)$. The abscissas are scaled with the critical Couette gap, H_c, to shift the

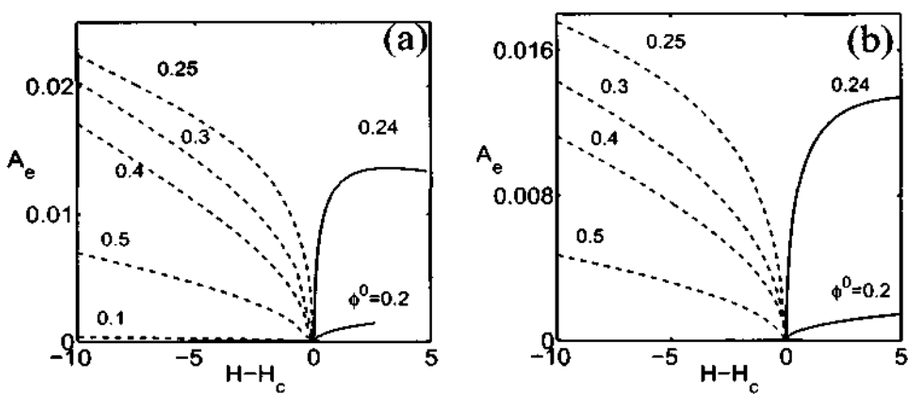

Figure 8.14: Bifurcation diagrams in the $(A_e, H - H_c)$-plane for moderate-to-dense regime where $k_z = 2$. (a) $e = 0.8$ and (b) $e = 0.95$. Solid and dash lines represent stable and unstable solutions, respectively.

origin of bifurcation diagrams for each density to zero.

Similar bifurcation diagrams are shown in figure 8.14(b) for densities $\phi^0 = 0.2, 0.24, 0.25, 0.3, 0.4$ and 0.5 where the restitution coefficient is set to $e = 0.95$. The transition from supercritical to subcritical for $e = 0.95$ is same as that for $e = 0.8$, i.e. between $H \in (0.24, 0.25)$ but there is no transition for subcritical to supercritical between $\phi^0 \in (0.1, 0.2)$ because the flow is non-linearly stable ($a^{(0)} < 0$ and $a^{(2)} < 0$) for $\phi^0 < 0.2$ with $k_z = 2$.

Next we show the bifurcation diagrams for subcritical bifurcations in the $(A_e, H - H_c)$-plane in dilute flow regime for two densities $\phi^0 = 0.02$ and 0.05. From figure 8.15, it is observed that the threshold for the subcritical instabilities, above which the uniform shear flow is unstable and below which it is stable, is higher at lower densities.

So far we have seen the bifurcation diagrams in the $(A_e, H - H_c)$-plane; now we will show the bifurcation diagrams in the $(A_e, k_z - k_{zc})$-plane, where k_{zc} is the critical spanwise wavenumber. A series of bifurcation diagrams in the $(A_e, k_z - k_{zc})$-plane for $H = 200$ is shown in figure 8.16(a) for densities $\phi^0 = 0.2, 0.23, 0.24, 0.3, 0.4$ and 0.5. The transition density from supercritical to subcritical lies between $\phi = (0.23, 0.24)$. Figure 8.16(b) shows the variation of $a^{(2)}$ with wave number k_z for $\phi^0 = 0.1$. It is seen in this figure that the $a^{(2)}$ is positive and decreasing with increasing wavenumber. For this range of wavenumber, $a^{(0)}$ is negative as shown in the lower inset of figure 8.16(b); thus the bifurcation is subcritical. The corresponding variation of equilibrium amplitude is shown in the upper inset of figure 8.16(b).

Figures 8.17(a) and 8.17(b) show the bifurcation diagrams for a series of densities as marked in the panel and for a Couette gap $H = 400$ in the $(A_e, k_z - k_{zc})$-plane for the dilute and moderate-to-dense flows, respectively, It can be seen from figures 8.17(a) and 8.17(b) that there is a transition from subcritical to supercritical between $\phi^0 = (0.06, 0.65)$ for dilute flows and again supercritical to subcritical between $\phi^0 = (0.22, 0.23)$ for moderate-to-dense flows.

The effect of density at $H = 500$ and $k_z = 50$ is shown in figure 8.18 where we have plotted the variation of $a^{(2)}$ with densities $\phi^0 \in (0.01, 0.6)$ in the main panel and the growth rate in the

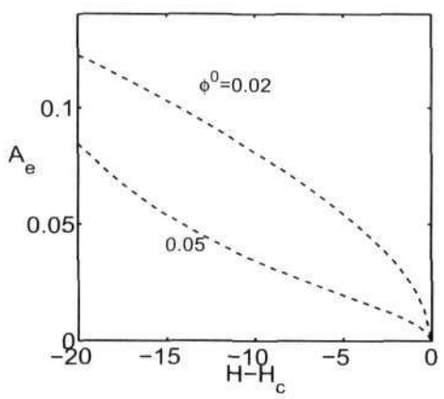

Figure 8.15: Bifurcation diagrams for dilute flows for densities $\phi^0 = 0.02$ and 0.05. Other parameters are same as figure 8.14(a).

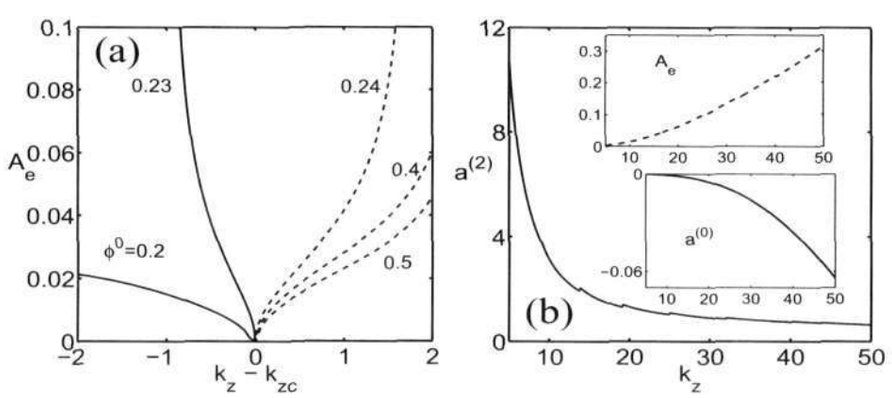

Figure 8.16: (a) Bifurcation diagram in the $(k_z - k_{zc})$-plane for $e = 0.8$ and $H = 200$ (b) Variation of $a^{[2]}$ (main panel), $a^{(0)}$ (lower inset) and amplitude (inset) with k_z for $\phi^0 = 0.1$, $e = 0.8$ and $H = 200$.

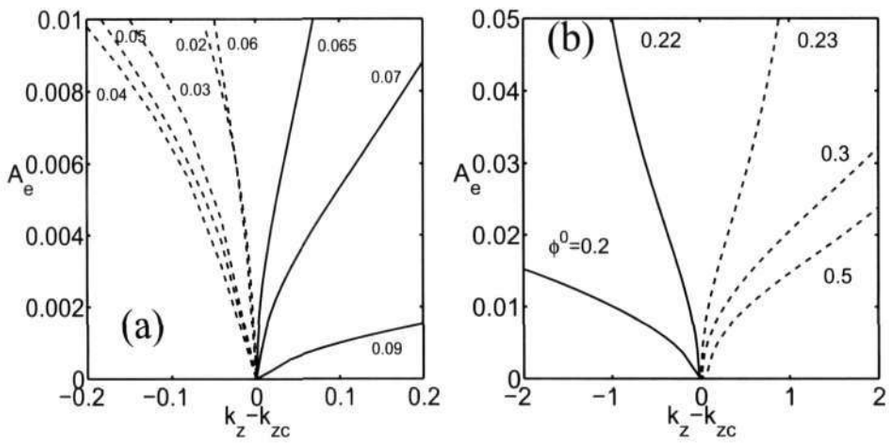

Figure 8.17: (a, b) Bifurcation diagram for $H = 400$ in the $(k_z - k_{zc})$-plane for various densities as marked in the panel. The coefficient of restitution is $e = 0.8$.

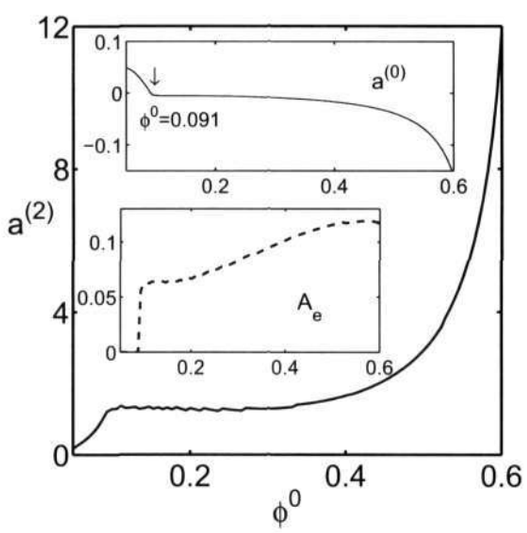

Figure 8.18: Variation of $a^{(2)}$, $a^{(0)}$ (inset) and A_e (inset) with density for $H = 500$, $k_z = 50$. The coefficient of restitution is $e = 0.8$.

upper inset. Since $a^{(2)}$ is positive for all densities and $a^{(0)}$ changes sign from positive to negative near $\phi^0 \approx 0.15$ (see upper inset), there is a subcritical bifurcation. The equilibrium amplitude is shown in the lower inset of figure 8.17(b).

8.3.7 Finite Amplitude Patterns

The disturbance fields up-to cubic order in amplitude can be written as

$$\begin{aligned} X(y,z,t) &= A^2 X^{[0;2]} + \Big[\Big(AX^{[1;1]}e^{i\theta} + A^2X^{[2;2]}e^{2i\theta} + A^3X^{[1;3]}e^{i\theta} \\ &\quad + A^3X^{[3;3]}e^{3i\theta}\Big) + \text{c.c.}\Big], \end{aligned} \tag{8.66}$$

where $X = (\phi', u', v', w', T')$ is the disturbance field, A is the amplitude and $\theta = k_z z + \omega t$, with ω being the real frequency (cf. Eqn.(3.11)). At equilibrium ($dA/dt = 0$), $A(t) = A_e$ (i.e. amplitude is independent of time) and $\omega = b^{(0)} + b^{(2)}t$.

In the present problem (streamwise independent flow) the instability is stationary, i.e. $b^{(0)} = b^{(2)} = 0$, and hence $\omega = 0$. Therefore, at equilibrium the disturbance vector (8.66) is written as:

$$\begin{aligned} X(y,z) \equiv X(y,z,t) &= A_e^2 X^{[0;2]} + 2A_e\left[X_r^{[1;1]}\cos(2\pi z/\lambda_z) - X_i^{[1;1]}\sin(2\pi z/\lambda_z)\right] \\ &\quad + 2A_e^2\left[X_r^{[2;2]}\cos(4\pi z/\lambda_z) - X_i^{[2;2]}\sin(4\pi z/\lambda_z)\right] \\ &\quad + 2A_e\left[X_r^{[1;3]}\cos(2\pi z/\lambda_z) - X_i^{[1;3]}\sin(2\pi z/\lambda_z)\right] \\ &\quad + 2A_e^3\left[X_r^{[3;3]}\cos(6\pi z/\lambda_z) - X_i^{[3;3]}\sin(6\pi z/\lambda_z)\right], \end{aligned} \tag{8.67}$$

where $\lambda_z = 2\pi/k_z$ is the spanwise wavelength and the subscripts r and i refer to the real and imaginary parts of a quantity, respectively. The streamwise vorticity component is defined as

$$\Omega_x = \frac{\partial w'}{\partial y} - \frac{\partial v'}{\partial z}. \tag{8.68}$$

Using (8.66) we can write the derivatives of w' and v' with respect to y and z as given below

$$\begin{aligned} \frac{\partial w'}{\partial y} &= A^2 w_y^{[0;2]} + 2A\ \text{Real}\left[w_y^{[1;1]}e^{i\theta} + A^2 w_y^{[1;3]}e^{i\theta} + Aw_y^{[2;2]}e^{2i\theta} + A^2 w_y^{[3;3]}e^{3i\theta}\right], \\ \frac{\partial v'}{\partial z} &= 2A\,k_z\ \text{Real}\left[i\left(X^{[1;1]}e^{i\theta} + A^2X^{[1;3]}e^{i\theta} + 2AX^{[2;2]}e^{2i\theta} + 3A^2X^{[3;3]}e^{3i\theta}\right)\right]. \end{aligned}$$

Figures 8.19 - 8.22 show the comparison between the linear and nonlinear disturbance patterns in (z, y)-plane. In following figures, the z-coordinate is normalized with the spanwise wavelength (λ_z) and therefore each figure has to be stretched by a factor $2\pi/k_z$ in the spanwise direction to get the true aspect ratio of each pattern. In each figure, 8.19 - 8.22, the patterns in the first column (panel (a)-(e)) are linear and those in the second column (panel (f)-(j)) are nonlinear. The first (a and f), second (b and g), third (c and h), fourth (d and i) and fifth (e and j) rows of each figure represent the disturbance patterns of density (ϕ'), vector plot of perturbation velocity (v', w'), streamwise velocity (u'), temperature (T') and streamwise vorticity (Ω_x), respectively. On the gray scale, the white and black represent maximum and minimum values, respectively.

The unstable disturbance patterns for two values of Couette gap $H = 140$ and 180 with $\phi^0 = 0.5$, $k_z = 2$ and $e = 0.8$ corresponding to figure 8.11 are shown in figures 8.19 and 8.20, respectively. Figure 8.19(a) shows four rows of density clusters along the transverse (y) direction since the associated linear eigenfunction corresponds to mode $\beta = 4$. Figure 8.19(e) shows the

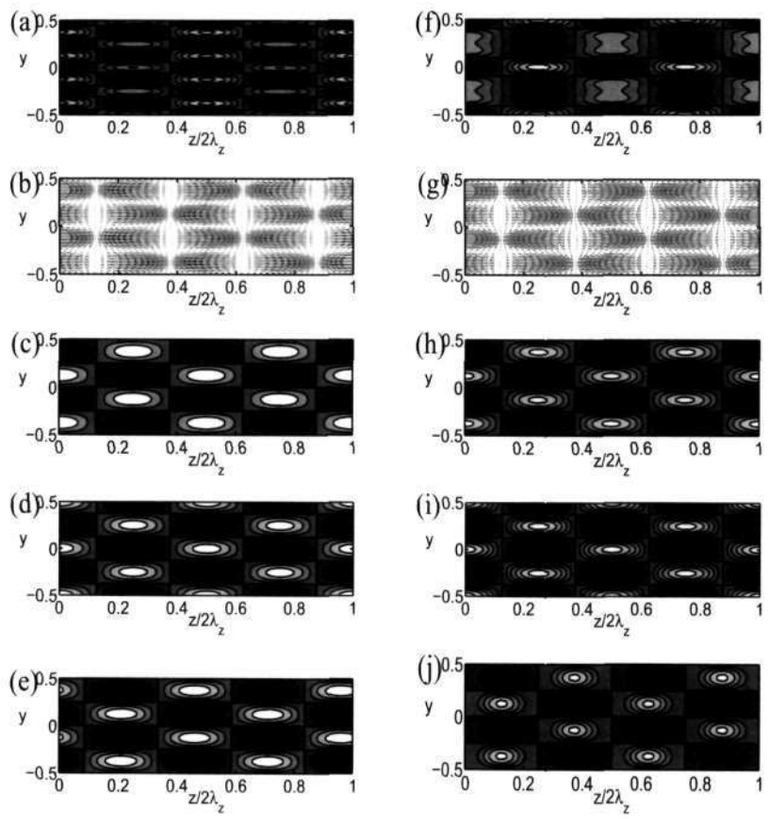

Figure 8.19: *Linear approximation of disturbed flow* (a)-(e) *and cubic approximation* (f)-(j). (a) and (f): contours of density; (b) and (g): (v, w) velocity field, (c) and (h): contours of streamwise velocity; (d) and (i): contours of temperature; (e) and (j): streamwise vorticity contours (Ω_x) in (z, y) plane. For $H = 140$, $\phi^0 = 0.5$, $e = 0.8$, $k_z = 2$ and $\beta = 4$ (cf. figure 8.11(c)) In gray scale white denotes maximum and black denotes minimum. for these parameters flow has subcritical instability.

four counter-rotating vortical structures. The contours of streamwise velocity, figure 8.19(c),

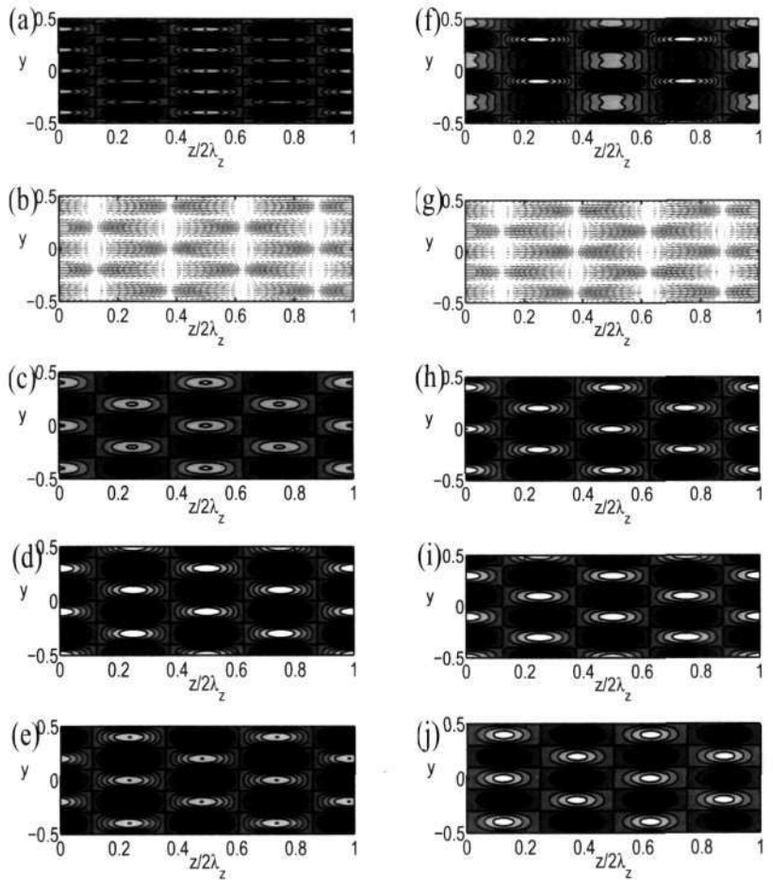

Figure 8.20: Same as figure 8.19 but for $H = 180$ and $\beta = 5$. See figure 8.11(c)

look similar to streamwise vorticity contours, figure 8.19(e), which show that the streamwise velocity is maximum at the location of minimum vorticity. The (v, w) velocity vector plot, see figures 8.19(b), shows that the magnitude of velocity is low at dense clusters and the velocity field changes its direction at the region of density maxima. The corresponding granular temperature pattern in figure 8.19(d) depicts that the granular temperature is maximum at the region of low density.

The subcritically unstable nonlinear patterns corresponding to figure 8.19(a)-(e) are shown in figure 8.19(f)-(j). While the distorted nonlinear velocity (v, w), streamwise velocity (u), temperature (T) and vorticity (Ω_x) look similar to the its linear analogue, the density field is distorted significantly. As seen in figure 8.19(f), there are three dense clusters, one appears at the center of the domain and two near the two walls, along the transverse direction; note that the linear density pattern has four dense clusters, see figure 8.19(a).

The overall structure of these patterns remains similar if we increase the Couette gap to $H = 180$ as shown in figure 8.20. We observe that the density pattern in figure 8.20(a) has five dense clusters along the transverse (y) direction which corresponds to mode $\beta = 5$, whereas the

density pattern for $H = 140$ in figure 8.19(a) has four dense clusters which corresponds to mode $\beta = 4$. For the description of other patterns see the related text of figure 8.19.

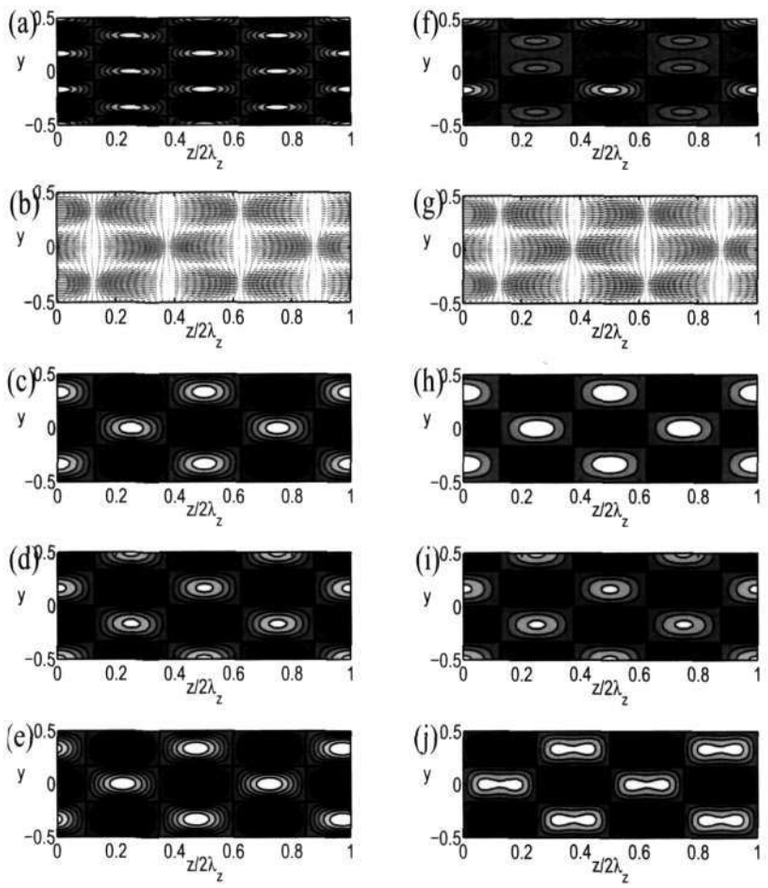

Figure 8.21: Same as figure 8.19 but for $H = 135$, $\phi^0 = 0.2$ and $\beta = 3$. These patterns are stable and the supercritical equilibrium amplitude is $A_e = 0.001416$.

For $\phi^0 = 0.2$, $H = 135$ and $e = 0.8$, the linear and nonlinear patterns are shown in figure 8.21. For this parameter values the flow admits supercritical bifurcation, see the inset of figure 8.10. The nonlinear supercritical density pattern in figure 8.21(f) show two dense clusters along the transverse direction, one at the top wall and other near the lower wall. However, the linear density patterns in figure 8.21(a) contains three dense clusters (since $\beta = 3$) along the transverse direction. The linear and nonlinear velocity and temperature fields are look similar. The temperature is maximum at low density region. The supercritical vorticity contours, as shown in figure 8.21(j), are stretched along the streamwise direction as compared to its linear analogue.

The linear and nonlinear patterns in dilute limit for $\phi^0 = 0.05$, $H = 90$ and $e = 0.8$ are shown in figure 8.22. The density and vorticity patterns are seen to be highly distorted from their linear counterparts, see figures 8.22(a, f) and 8.22(e, j), while the nonlinear velocity and temperature patterns look similar to its linear analogue.

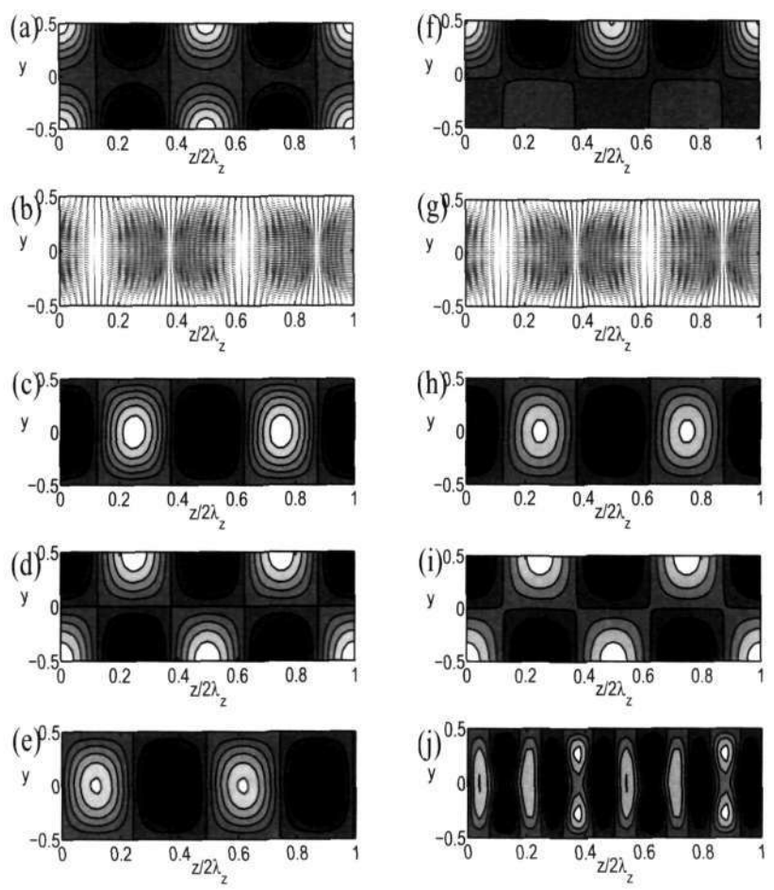

Figure 8.22: Same as figure 8.19 but for $H = 90$, $\phi = 0.05$ and $\beta = 1$. These are unstable patterns (originated from the subcritical bifurcation).

8.4 Conclusion

In this chapter we have analyzed the nonlinear stability of streamwise independent three-dimensional granular plane Couette flow. The streamwise instabilities in three-dimensional granular plane Couette flow lead to banding in the transverse and spanwise directions. Due to this banding the uniform shear flow breaks into bands of different rheological properties (different shear stresses and shear rates) along the transverse and mean vorticity directions. We have used the amplitude expansion method for reducing the nonlinear problem into a sequence of linear problems. The analytical solutions of these problems have been derived using *sine* and *cosine* functions. The results for all flow regimes have been shown in this chapter.

Our analysis shows that the transitions from supercritical-to-subcritical and subcritical-to-supercritical bifurcations occur for varying density and spanwise wavenumber. In the dilute flow regime we have found the presence of mean flow resonance. The equilibrium amplitude follows the Couette gap scaling with restitution coefficient. The comparison of linear and nonlinear subcritical and supercritical patterns has been discussed in this chapter. The density and vorticity patterns are seen to be more distorted from their linear counterparts than the corresponding velocity and temperature patterns.

Appendix 8A. Elements of Linear Stability Matrix $\mathcal{L} = [l_{ij}]$ for $\partial/\partial x = 0$

$$
\left.\begin{array}{rcl}
l_{11} &=& 0, \quad l_{12} = 0, \quad l_{13} = -\phi^0 \frac{\partial}{\partial y}, \quad l_{14} = -\phi^0 \frac{\partial}{\partial z}, \quad l_{15} = 0 \\
l_{21} &=& \frac{u_y^0 \mu_\phi^0}{H^2 \phi^0} \frac{\partial}{\partial y}, \quad l_{22} = \frac{\mu^0}{H^2 \phi^0} \left(\frac{\partial^2}{\partial y^2} + \frac{\partial^2}{\partial z^2} \right), \quad l_{23} = -u_y^0, \quad l_{24} = 0, \quad l_{25} = \frac{u_y^0 \mu_T^0}{H^2 \phi^0} \frac{\partial}{\partial y} \\
l_{31} &=& \frac{-p_\phi^0}{H^2 \phi^0} \frac{\partial}{\partial y}, \quad l_{32} = 0, \quad l_{33} = \frac{1}{H^2 \phi^0} \left((2\mu^0 + \lambda^0) \frac{\partial^2}{\partial y^2} + \mu^0 \frac{\partial^2}{\partial z^2} \right) \\
l_{34} &=& \frac{(\lambda^0 + \mu^0)}{H^2 \phi^0} \frac{\partial^2}{\partial y \partial z}, \quad l_{35} = \frac{-p_T^0}{H^2 \phi^0} \frac{\partial}{\partial y} \\
l_{41} &=& \frac{-p_\phi^0}{H^2 \phi^0} \frac{\partial}{\partial z}, \quad l_{42} = 0, \quad l_{43} = \frac{(\mu^0 + \lambda^0)}{H^2 \phi^0} \frac{\partial^2}{\partial y \partial z} \\
l_{44} &=& \frac{1}{H^2 \phi^0} \left((2\mu^0 + \lambda^0) \frac{\partial^2}{\partial z^2} + \mu^0 \frac{\partial^2}{\partial y^2} \right), \quad l_{45} = \frac{-p_T^0}{H^2 \phi^0} \frac{\partial}{\partial z} \\
l_{51} &=& \frac{2}{dim\, \phi^0} \left(u_y^{0^2} \mu_\phi^0 - \mathcal{D}_\phi^0 \right), \quad l_{52} = \frac{4\mu^0 u_y^0}{dim\, \phi^0} \frac{\partial}{\partial y}, \quad l_{53} = \frac{-2p^0}{dim\, \phi^0} \frac{\partial}{\partial y} \\
l_{54} &=& \frac{-2p^0}{dim\, \phi^0} \frac{\partial}{\partial z}, \quad l_{55} = \frac{2}{dim\, \phi^0} \left(\frac{\kappa^0}{H^2} \left(\frac{\partial^2}{\partial y^2} + \frac{\partial^2}{\partial z^2} \right) + (\mu_T^0 u_y^{0^2} - \mathcal{D}_T^0) \right)
\end{array}\right\}
$$

Note that the elements of $\mathbf{L}$ (cf. (8.2) can be obtain by replacing $\frac{\partial}{\partial y} = \frac{d}{dy}$ and $\frac{\partial}{\partial z} = ik_z$.

Appendix 8B. Nonlinear Terms

$$
\left.\begin{array}{rcl}
\mathcal{N}_2^1 &=& -\phi' \frac{\partial v'}{\partial y} - v' \frac{\partial \phi'}{\partial y} - \phi' \frac{\partial w'}{\partial z} - w' \frac{\partial \phi'}{\partial z} \\
\mathcal{N}_2^2 &=& -\frac{1}{\phi^0} \left[\phi^0 \left(v' \frac{\partial u'}{\partial y} + w' \frac{\partial u'}{\partial z} \right) + \phi' \frac{\partial u'}{\partial t} + u_y^0 \phi' v' \right] \\
&& + \frac{1}{\phi^0 H^2} \left[(\mu_\phi^0 \phi' + \mu_T^0 T') \frac{\partial^2 u'}{\partial y^2} + u_y^0 \left(\mu_{\phi\phi}^0 \phi' \frac{\partial \phi'}{\partial y} + \mu_{TT}^0 T' \frac{\partial T'}{\partial y} + \mu_{\phi T}^0 \phi' \frac{\partial T'}{\partial y} + \mu_{\phi T}^0 T' \frac{\partial \phi'}{\partial y} \right) \right. \\
&& \left. + \frac{\partial u'}{\partial y} \left(\mu_\phi^0 \frac{\partial \phi'}{\partial y} + \mu_T^0 \frac{\partial T'}{\partial y} \right) + \left(\mu_\phi^0 \frac{\partial \phi}{\partial z} + \mu_T^0 \frac{\partial T'}{\partial z} \right) \frac{\partial u'}{\partial z} + \left(\mu_\phi^0 \phi' + \mu_T^0 T' \right) \frac{\partial^2 u'}{\partial z^2} \right] \\
\mathcal{N}_2^3 &=& -\frac{1}{\phi^0} \left[\phi^0 \left(v' \frac{\partial v'}{\partial y} + w' \frac{\partial v'}{\partial z} \right) + \phi' \frac{\partial v'}{\partial t} \right] \\
&& + \frac{1}{\phi^0 H^2} \left[- \left(p_{\phi\phi}^0 \phi' \frac{\partial \phi'}{\partial y} + p_{TT}^0 T' \frac{\partial T'}{\partial y} + p_{\phi T}^0 \phi' \frac{\partial T'}{\partial y} + p_{\phi T}^0 T' \frac{\partial \phi'}{\partial y} \right) + 2 \frac{\partial^2 v'}{\partial y^2} \left(\mu_\phi^0 \phi' + \mu_T^0 T' \right) \right. \\
&& + 2 \frac{\partial v'}{\partial y} \left(\mu_\phi^0 \frac{\partial \phi'}{\partial y} + \mu_T^0 \frac{\partial T'}{\partial y} \right) + \frac{\partial}{\partial y} \left(\frac{\partial v'}{\partial y} + \frac{\partial w'}{\partial z} \right) \left(\lambda_\phi^0 \phi' + \lambda_T^0 T' \right) \\
&& + \left(\frac{\partial v'}{\partial y} + \frac{\partial w'}{\partial z} \right) \left(\lambda_\phi^0 \frac{\partial \phi'}{\partial y} + \lambda_T^0 \frac{\partial T'}{\partial y} \right) + (\mu_\phi^0 \phi' + \mu_T^0 T') \frac{\partial}{\partial z} \left(\frac{\partial v'}{\partial z} + \frac{\partial w'}{\partial y} \right) \\
&& \left. + \left(\mu_\phi^0 \frac{\partial \phi'}{\partial z} + \mu_T^0 \frac{\partial T'}{\partial z} \right) \left(\frac{\partial v'}{\partial z} + \frac{\partial w'}{\partial y} \right) \right] \\
\mathcal{N}_2^4 &=& -\frac{1}{\phi^0} \left[\phi^0 \left(v' \frac{\partial w'}{\partial y} + w' \frac{\partial w'}{\partial z} \right) + \phi' \frac{\partial w'}{\partial t} \right] \\
&& + \frac{1}{\phi^0 H^2} \left[- \left(p_{\phi\phi}^0 \phi' \frac{\partial \phi'}{\partial z} + p_{TT}^0 T' \frac{\partial T'}{\partial z} + p_{\phi T}^0 \phi' \frac{\partial T'}{\partial z} + p_{\phi T}^0 T' \frac{\partial \phi'}{\partial z} \right) + 2(\mu_\phi^0 \phi' + \mu_T^0 T') \frac{\partial^2 w'}{\partial z^2} \right. \\
&& + 2 \left(\mu_\phi^0 \frac{\partial \phi'}{\partial z} + \mu_T^0 \frac{\partial T'}{\partial z} \right) \frac{\partial w'}{\partial z} + (\lambda_\phi^0 \phi' + \lambda_T^0 T') \frac{\partial}{\partial z} \left(\frac{\partial v'}{\partial y} + \frac{\partial w'}{\partial z} \right) \\
&& + \left(\lambda_\phi^0 \frac{\partial \phi'}{\partial z} + \lambda_T^0 \frac{\partial T'}{\partial z} \right) \left(\frac{\partial v'}{\partial y} + \frac{\partial w'}{\partial z} \right) + (\mu_\phi^0 \phi' + \mu_T^0 T') \frac{\partial}{\partial y} \left(\frac{\partial v'}{\partial z} + \frac{\partial w'}{\partial y} \right) \\
&& \left. + \left(\mu_\phi^0 \frac{\partial \phi'}{\partial y} + \mu_T^0 \frac{\partial T'}{\partial y} \right) \left(\frac{\partial v'}{\partial z} + \frac{\partial w'}{\partial y} \right) \right] \\
\mathcal{N}_2^5 &=& -\frac{1}{\phi^0} \left[\phi^0 \left(v' \frac{\partial T'}{\partial y} + w' \frac{\partial T'}{\partial z} \right) + \phi' \frac{\partial T'}{\partial t} \right] \\
&& + \frac{2}{dim \phi^0} \left[\frac{1}{H^2} \left\{ \frac{\partial T'}{\partial y} \left(\kappa_\phi^0 \frac{\partial \phi'}{\partial y} + \kappa_T^0 \frac{\partial T'}{\partial y} \right) + \frac{\partial^2 T'}{\partial y^2} \left(\kappa_\phi^0 \phi' + \kappa_T^0 T' \right) \right. \right. \\
&& \left. \left. + \frac{\partial T'}{\partial z} \left(\kappa_\phi^0 \frac{\partial \phi'}{\partial z} + \kappa_T^0 \frac{\partial T'}{\partial z} \right) + \frac{\partial^2 T'}{\partial z^2} \left(\kappa_\phi^0 \phi' + \kappa_T^0 T' \right) \right\} \right. \\
&& - (p_\phi^0 \phi' + p_T^0 T') \left(\frac{\partial v'}{\partial y} + \frac{\partial w'}{\partial z} \right) + 2\mu^0 \left[\left(\frac{\partial v'}{\partial y} \right)^2 + \left(\frac{\partial w'}{\partial z} \right)^2 + \frac{1}{2} \left(\frac{\partial u'}{\partial y} \right)^2 + \frac{1}{2} \left(\frac{\partial u'}{\partial z} \right)^2 \right] \\
&& + u_y^{0^2} \left(\frac{1}{2} \mu_{\phi\phi}^0 \phi'^2 + \frac{1}{2} \mu_{TT}^0 T'^2 + \mu_{\phi T}^0 \phi' T' \right) + 2 u_y^0 \left(\mu_\phi^0 \phi' + \mu_T^0 T' \right) \frac{\partial u'}{\partial y} \\
&& \left. + \mu^0 \left(\frac{\partial v'}{\partial z} + \frac{\partial w'}{\partial y} \right)^2 + \lambda^0 \left(\frac{\partial v'}{\partial y} + \frac{\partial w'}{\partial z} \right)^2 - \left(\frac{1}{2} \mathcal{D}_{\phi\phi}^0 \phi'^2 + \frac{1}{2} \mathcal{D}_{TT}^0 T'^2 + \mathcal{D}_{\phi T}^0 \phi' T' \right) \right]
\end{array}\right\}
$$

$$
\begin{aligned}
\mathcal{N}_3^2 &= -\frac{\phi'}{\phi^0}\left(v'\frac{\partial u'}{\partial y}+w'\frac{\partial u'}{\partial z}\right)+\frac{1}{\phi^0 H^2}\left[\left(\tfrac{1}{2}\mu^0_{\phi\phi}\phi'^2+\tfrac{1}{2}\mu^0_{TT}T'^2+\mu^0_{\phi T}\phi'T'\right)\left(\frac{\partial^2 u'}{\partial y^2}+\frac{\partial^2 u'}{\partial z^2}\right)\right.\\
&+\left(\tfrac{1}{2}\mu^0_{\phi\phi\phi}\phi'^2\frac{\partial\phi'}{\partial y}+\tfrac{1}{2}\mu^0_{TTT}T'^2\frac{\partial T'}{\partial y}+\mu^0_{\phi\phi T}\phi'\frac{\partial\phi'}{\partial y}T'+\tfrac{1}{2}\mu^0_{\phi TT}\phi'^2\frac{\partial T'}{\partial y}+\mu^0_{\phi TT}T'\frac{\partial T'}{\partial y}\phi'\right.\\
&\left.+\tfrac{1}{2}\mu^0_{\phi TT}T'^2\frac{\partial\phi'}{\partial y}\right)+\frac{\partial u'}{\partial y}\left(\mu^0_{\phi\phi}\phi'\frac{\partial\phi'}{\partial y}+\mu^0_{TT}T'\frac{\partial T'}{\partial y}+\mu^0_{\phi T}\phi'\frac{\partial T'}{\partial y}+\mu^0_{\phi T}T'\frac{\partial\phi'}{\partial y}\right)\\
&\left.+\frac{\partial u'}{\partial z}\left(\mu^0_{\phi\phi}\phi'\frac{\partial\phi'}{\partial z}+\mu^0_{TT}T'\frac{\partial T'}{\partial z}+\mu^0_{\phi T}\phi'\frac{\partial T'}{\partial z}+\mu^0_{\phi T}T'\frac{\partial\phi'}{\partial z}\right)\right]\\
\mathcal{N}_3^3 &= -\frac{\phi'}{\phi^0}\left(v'\frac{\partial v'}{\partial y}+w'\frac{\partial v'}{\partial z}\right)+\frac{1}{\phi^0 H^2}\left[-\left(\tfrac{1}{2}p^0_{\phi\phi\phi}\phi'^2\frac{\partial\phi'}{\partial y}+\tfrac{1}{2}p^0_{TTT}T'^2\frac{\partial T'}{\partial y}+p^0_{\phi\phi T}\phi'\frac{\partial\phi'}{\partial y}T'\right.\right.\\
&+\tfrac{1}{2}p^0_{\phi\phi T}\phi'^2\frac{\partial T'}{\partial y}+p^0_{\phi TT}T'\frac{\partial T'}{\partial y}\phi'+\tfrac{1}{2}p^0_{\phi TT}T'^2\frac{\partial\phi'}{\partial y}\Big)+2\frac{\partial^2 v'}{\partial y^2}\left(\tfrac{1}{2}\mu^0_{\phi\phi}\phi'^2+\tfrac{1}{2}\mu^0_{TT}T'^2+\mu^0_{\phi T}\phi'T'\right)\\
&+2\frac{\partial v'}{\partial y}\left(\mu^0_{\phi\phi}\phi'\frac{\partial\phi'}{\partial y}+\mu^0_{TT}T'\frac{\partial T'}{\partial y}+\mu^0_{\phi T}\phi'\frac{\partial T'}{\partial y}+\mu^0_{\phi T}T'\frac{\partial\phi'}{\partial y}\right)\\
&+\frac{\partial}{\partial y}\left(\frac{\partial v'}{\partial y}+\frac{\partial w'}{\partial z}\right)\left(\tfrac{1}{2}\lambda^0_{\phi\phi}\phi'^2+\tfrac{1}{2}\lambda^0_{TT}T'^2+\lambda^0_{\phi T}\phi'T'\right)\\
&+\left(\frac{\partial v'}{\partial y}+\frac{\partial w'}{\partial z}\right)\left(\lambda^0_{\phi\phi}\phi'\frac{\partial\phi'}{\partial y}+\lambda^0_{TT}T'\frac{\partial T'}{\partial y}+\lambda^0_{\phi T}\phi'\frac{\partial T'}{\partial y}+\lambda^0_{\phi T}T'\frac{\partial\phi'}{\partial y}\right)\\
&+\frac{\partial}{\partial z}\left(\frac{\partial v'}{\partial z}+\frac{\partial w'}{\partial y}\right)\left(\tfrac{1}{2}\mu^0_{\phi\phi}\phi'^2+\tfrac{1}{2}\mu^0_{TT}T'^2+\mu^0_{\phi T}\phi'T'\right)\\
&\left.+\left(\frac{\partial v'}{\partial z}+\frac{\partial w'}{\partial y}\right)\left(\mu^0_{\phi\phi}\phi'\frac{\partial\phi'}{\partial z}+\mu^0_{TT}T'\frac{\partial T'}{\partial z}+\mu^0_{\phi T}\phi'\frac{\partial T'}{\partial z}+\mu^0_{\phi T}T'\frac{\partial\phi'}{\partial z}\right)\right]\\
\mathcal{N}_3^4 &= -\frac{\phi'}{\phi^0}\left(v'\frac{\partial w'}{\partial y}+w'\frac{\partial w'}{\partial z}\right)+\frac{1}{\phi^0 H^2}\left[-\left(\tfrac{1}{2}p^0_{\phi\phi\phi}\phi'^2\frac{\partial\phi'}{\partial z}+\tfrac{1}{2}p^0_{TTT}T'^2\frac{\partial T'}{\partial z}+p^0_{\phi\phi T}\phi'T'\frac{\partial\phi'}{\partial z}\right.\right.\\
&+\tfrac{1}{2}p^0_{\phi\phi T}\phi'^2\frac{\partial T'}{\partial z}+p^0_{\phi TT}\phi'T'\frac{\partial T'}{\partial z}+\tfrac{1}{2}p^0_{\phi TT}T'^2\frac{\partial\phi'}{\partial z}\Big)+2\frac{\partial^2 w'}{\partial z^2}\left(\tfrac{1}{2}\mu^0_{\phi\phi}\phi'^2+\tfrac{1}{2}\mu^0_{TT}T'^2+\mu^0_{\phi T}\phi'T'\right)\\
&+2\frac{\partial w'}{\partial z}\left(\mu^0_{\phi\phi}\phi'\frac{\partial\phi'}{\partial z}+\mu^0_{TT}T'\frac{\partial T'}{\partial z}+\mu^0_{\phi T}\phi'\frac{\partial T'}{\partial z}+\mu^0_{\phi T}T'\frac{\partial\phi'}{\partial z}\right)\\
&+\frac{\partial}{\partial z}\left(\frac{\partial v'}{\partial y}+\frac{\partial w'}{\partial z}\right)\left(\tfrac{1}{2}\lambda^0_{\phi\phi}\phi'^2+\tfrac{1}{2}\lambda^0_{TT}T'^2+\lambda^0_{\phi T}\phi'T'\right)\\
&+\left(\frac{\partial v'}{\partial y}+\frac{\partial w'}{\partial z}\right)\left(\lambda^0_{\phi\phi}\phi'\frac{\partial\phi'}{\partial z}+\lambda^0_{TT}T'\frac{\partial T'}{\partial z}+\lambda^0_{\phi T}\phi'\frac{\partial T'}{\partial z}+\lambda^0_{\phi T}T'\frac{\partial\phi'}{\partial z}\right)\\
&+\frac{\partial}{\partial y}\left(\frac{\partial v'}{\partial z}+\frac{\partial w'}{\partial y}\right)\left(\tfrac{1}{2}\mu^0_{\phi\phi}\phi'^2+\tfrac{1}{2}\mu^0_{TT}T'^2+\mu^0_{\phi T}\phi'T'\right)\\
&\left.+\left(\frac{\partial v'}{\partial z}+\frac{\partial w'}{\partial y}\right)\left(\mu^0_{\phi\phi}\phi'\frac{\partial\phi'}{\partial y}+\mu^0_{TT}T'\frac{\partial T'}{\partial y}+\mu^0_{\phi T}\phi'\frac{\partial T'}{\partial y}+\mu^0_{\phi T}T'\frac{\partial\phi'}{\partial y}\right)\right]\\
\mathcal{N}_3^5 &= -\frac{\phi'}{\phi^0}\left(v'\frac{\partial T'}{\partial y}+w'\frac{\partial T'}{\partial z}\right)\\
&+\frac{2}{dim\phi^0}\left[\frac{1}{H^2}\left\{\frac{\partial T'}{\partial y}\left(\kappa^0_{\phi\phi}\phi'\frac{\partial\phi'}{\partial y}+\kappa^0_{TT}T'\frac{\partial T'}{\partial y}+\kappa^0_{\phi T}\phi'\frac{\partial T'}{\partial y}+\kappa^0_{\phi T}T'\frac{\partial\phi'}{\partial y}\right)\right.\right.\\
&+\left(\frac{\partial^2 T'}{\partial y^2}+\frac{\partial^2 T'}{\partial z^2}\right)\left(\tfrac{1}{2}\kappa^0_{\phi\phi}\phi'^2+\tfrac{1}{2}\kappa^0_{TT}T'^2+\kappa^0_{\phi T}\phi'T'\right)\\
&\left.\left.+\frac{\partial T'}{\partial z}\left(\kappa^0_{\phi\phi}\phi'\frac{\partial\phi'}{\partial z}+\kappa^0_{TT}T'\frac{\partial T'}{\partial z}+\kappa^0_{\phi T}\phi'\frac{\partial T'}{\partial z}+\kappa^0_{\phi T}T'\frac{\partial\phi'}{\partial z}\right)\right\}\right.\\
&-\left(\tfrac{1}{2}p^0_{\phi\phi}\phi'^2+\tfrac{1}{2}p^0_{TT}T'^2+p^0_{\phi T}\phi'T'\right)\left(\frac{\partial v'}{\partial y}+\frac{\partial w'}{\partial z}\right)\\
&+(\mu^0_\phi\phi'+\mu^0_T T')\left\{2\left(\frac{\partial v'}{\partial y}\right)^2+2\left(\frac{\partial w'}{\partial z}\right)^2+\left(\frac{\partial u'}{\partial y}\right)^2+\left(\frac{\partial v'}{\partial z}+\frac{\partial w'}{\partial y}\right)^2+\left(\frac{\partial u'}{\partial z}\right)^2\right\}\\
&+u_y^{0^2}\left(\tfrac{1}{6}\mu^0_{\phi\phi\phi}\phi'^3+\tfrac{1}{6}\mu^0_{TTT}T'^3+\tfrac{1}{2}\mu^0_{\phi\phi T}\phi'^2T'+\tfrac{1}{2}\mu^0_{\phi TT}\phi'T'^2\right)\\
&+2u_y^0\left(\tfrac{1}{2}\mu^0_{\phi\phi}\phi'^2+\tfrac{1}{2}\mu^0_{TT}T'^2+\mu^0_{\phi T}\phi'T'\right)\frac{\partial u'}{\partial y}+\left(\lambda^0_\phi\phi'+\lambda^0_T T'\right)\left(\frac{\partial v'}{\partial y}+\frac{\partial w'}{\partial z}\right)^2\\
&\left.-\left(\tfrac{1}{6}\mathcal{D}^0_{\phi\phi\phi}\phi'^3+\tfrac{1}{6}\mathcal{D}^0_{TTT}T'^3+\tfrac{1}{2}\mathcal{D}^0_{\phi\phi T}\phi'^2T'+\tfrac{1}{2}\mathcal{D}^0_{\phi TT}\phi'T'^2\right)\right]
\end{aligned}
$$

Appendix 8C. Analytical Expressions for Second Harmonic

$$
\begin{aligned}
G_{22}^{1\beta} &= -k_\beta \phi_1 v_1, \quad f_{22}^{1} = -ik_z \phi_1 w_1 \\
G_{22}^{2\beta} &= \tfrac{1}{2}\Big[-\tfrac{1}{\phi^0}\left\{\phi^0(k_\beta v_1 u_1 + ik_z w_1 u_1) + \phi_1 v_1 + c^{(0)}\phi_1 u_1\right\} \\
&\quad -\tfrac{1}{\phi^0 H^2}\left\{(2k_\beta^2 + 2k_z^2)(\mu_\phi^0 \phi_1 + \mu_T^0 T_1)u_1 + k_\beta(\mu_{\phi\phi}^0 \phi_1^2 + \mu_{TT}^0 T_1^2 + 2\mu_{\phi T}^0 \phi_1 T_1)\right\}\Big] \\
G_{22}^{3\beta} &= \tfrac{1}{2}\Big[-\tfrac{1}{\phi^0}\left\{\phi^0(k_\beta v_1^2 + ik_z w_1 v_1) + c^{(0)}\phi_1 v_1\right\} \\
&\quad +\tfrac{1}{\phi^0 H^2}\left\{k_\beta\left(p_{\phi\phi}^0 \phi_1^2 + p_{TT}^0 T_1^2 + 2p_{\phi T}^0 \phi_1 T_1\right) - 4k_\beta^2(\mu_\phi^0 \phi_1 + \mu_T^0 T_1)v_1\right. \\
&\quad \left.-2k_\beta(\lambda_\phi^0 \phi_1 + \lambda_T^0 T_1)(k_\beta v_1 + ik_z w_1) - 2k_z(\mu_\phi^0 \phi_1 + \mu_T^0 T_1)(k_z v_1 + ik_\beta w_1)\right\}\Big] \\
G_{22}^{4\beta} &= \tfrac{1}{2}\Big[-\tfrac{1}{\phi^0}\left\{\phi^0(k_\beta w_1 v_1 + ik_z w_1^2) + c^{(0)}\phi_1 w_1\right\} \\
&\quad +\tfrac{1}{\phi^0 H^2}\left\{-ik_z(p_{\phi\phi}^0 \phi_1^2 + p_{TT}^0 T_1^2 + 2p_{\phi T}^0 \phi_1 T_1) - 4k_z^2(\mu_\phi^0 \phi_1 + \mu_T^0 T_1)w_1\right. \\
&\quad \left.+2ik_z(\lambda_\phi^0 \phi_1 + \lambda_T^0 T_1)(k_\beta v_1 + ik_z w_1) + 2ik_\beta(\mu_\phi^0 \phi_1 + \mu_T^0 T_1)(k_z v_1 + ik_\beta w_1)\right\}\Big] \\
f_{22}^{4} &= \tfrac{1}{2}\Big[-\tfrac{1}{\phi^0}\left\{-\phi^0(k_\beta w_1 v_1 + ik_z w_1^2) + c^{(0)}\phi_1 w_1\right\} \\
&\quad +\tfrac{1}{\phi^0 H^2}\left\{-ik_z(p_{\phi\phi}^0 \phi_1^2 + p_{TT}^0 T_1^2 + 2p_{\phi T}^0 \phi_1 T_1) - 4k_z^2(\mu_\phi^0 \phi_1 + \mu_T^0 T_1)w_1\right. \\
&\quad \left.+2ik_z(\lambda_\phi^0 \phi_1 + \lambda_T^0 T_1)(k_\beta v_1 + ik_z w_1)\right\}\Big] \\
G_{22}^{5\beta} &= \tfrac{1}{2}\Big[-\tfrac{1}{\phi^0}\left\{\phi^0(k_\beta v_1 T_1 + ik_z w_1 T_1) + c^{(0)}\phi_1 T_1\right\} \\
&\quad +\tfrac{2}{dim\phi^0}\left\{-\tfrac{2}{H^2}(k_\beta^2 + k_z^2)(\kappa_\phi^0 \phi_1 + \kappa_T^0 T_1)T_1 - (p_\phi^0 \phi_1 + p_T^0 T_1)(k_\beta v_1 + ik_z w_1)\right. \\
&\quad +2\mu^0(k_\beta^2 v_1^2 - k_z^2 w_1^2) + \left(\tfrac{1}{2}\mu_{\phi\phi}^0 \phi_1^2 + \tfrac{1}{2}\mu_{TT}^0 T_1^2 + \mu_{\phi T}^0 \phi_1 T_1\right) \\
&\quad +2k_\beta(\mu_\phi^0 \phi_1 + \mu_T^0 T_1)u_1 - \mu^0(-k_z^2 v_1^2 + k_\beta^2 w_1^2 - 2ik_z k_\beta v_1 w_1) + \mu^0(k_z^2 + k_\beta^2)u_1^2 \\
&\quad \left.+\lambda^0\left(k_\beta^2 v_1^2 - k_z^2 w_1^2 + 2ik_z k_\beta v_1 w_1\right) - \left(\tfrac{1}{2}\mathcal{D}_{\phi\phi}^0 \phi_1^2 + \tfrac{1}{2}\mathcal{D}_{TT}^0 T_1^2 + \mathcal{D}_{\phi T}^0 \phi_1 T_1\right)\right\}\Big] \\
f_{22}^{5} &= \tfrac{1}{2}\Big[-\tfrac{1}{\phi^0}\left\{\phi^0(-k_\beta v_1 T_1 + ik_z w_1 T_1) + c^{(0)}\phi_1 T_1\right\} \\
&\quad +\tfrac{2}{dim\phi^0}\left\{-\tfrac{2}{H^2}k_z^2(\kappa_\phi^0 \phi_1 + \kappa_T^0 T_1)T_1 - (p_\phi^0 \phi_1 + p_T^0 T_1)(k_\beta v_1 + ik_z w_1)\right. \\
&\quad +2\mu^0(k_\beta^2 v_1^2 - k_z^2 w_1^2) + \left(\tfrac{1}{2}\mu_{\phi\phi}^0 \phi_1^2 + \tfrac{1}{2}\mu_{TT}^0 T_1^2 + \mu_{\phi T}^0 \phi_1 T_1\right) \\
&\quad +2k_\beta(\mu_\phi^0 \phi_1 + \mu_T^0 T_1)u_1 + \mu^0(-k_z^2 v_1^2 + k_\beta^2 w_1^2 - 2ik_z k_\beta v_1 w_1) + \mu^0(-k_z^2 + k_\beta^2)u_1^2 \\
&\quad \left.+\lambda^0\left(k_\beta^2 v_1^2 - k_z^2 w_1^2 + 2ik_z k_\beta v_1 w_1\right) - \left(\tfrac{1}{2}\mathcal{D}_{\phi\phi}^0 \phi_1^2 + \tfrac{1}{2}\mathcal{D}_{TT}^0 T_1^2 + \mathcal{D}_{\phi T}^0 \phi_1 T_1\right)\right\}\Big]
\end{aligned}
$$

If we substitute $k_z = 0$ and $w = 0$ in the above expression we get the inhomogeneous terms of second harmonic for stream-wise plane Couette flow problem which are given in §5.4.1,

$$
\underbrace{(G_{22}^{1\beta}, G_{22}^{2\beta}, G_{22}^{3\beta}, G_{22}^{4\beta}, G_{22}^{4\beta})}_{3D} \overset{k_z=0, w=0}{\longrightarrow} \underbrace{(G_{22}^{1\beta}, G_{22}^{2\beta}, G_{22}^{3\beta}, 0, G_{22}^{4\beta})}_{2D}.
$$

Similarly

$$
\underbrace{(f_{22}^{1}, f_{22}^{4}, f_{22}^{5})}_{3D} \overset{k_z=0, w=0}{\longrightarrow} \underbrace{(0, 0, f_{nl})}_{2D}.
$$

Appendix 8D. Analytical Expressions for Distortion of Mean Flow

$$
\begin{aligned}
G_{02}^{1\beta} &= -k_\beta \phi_1 \tilde{v}_1 + c.c \\
G_{02}^{2\beta} &= \tfrac{1}{2}\Big[-\tfrac{1}{\phi^0}\left\{\phi^0(k_\beta v_1 \tilde{u}_1 - ik_z w_1 \tilde{u}_1) + \phi_1 \tilde{v}_1 + \tilde{c}^{(0)}\phi_1 \tilde{u}_1\right\} \\
&\quad -\tfrac{1}{\phi^0 H^2}\left\{2k_\beta^2(\mu_\phi^0 \phi_1 + \mu_T^0 T_1)\tilde{u}_1 + k_\beta(\mu_{\phi\phi}^0 \phi_1 \tilde{\phi}_1 + \mu_{TT}^0 T_1 \tilde{T}_1 + \mu_{\phi T}^0 \phi_1 \tilde{T}_1 + \mu_{\phi T}^0 T_1 \tilde{\phi}_1)\right\}\Big] + c.c \\
G_{02}^{3\beta} &= \tfrac{1}{2}\Big[-\tfrac{1}{\phi^0}\left\{\phi^0(k_\beta v_1 \tilde{v}_1 - ik_z w_1 \tilde{v}_1) + \tilde{c}^{(0)}\phi_1 \tilde{v}_1\right\} \\
&\quad +\tfrac{1}{\phi^0 H^2}\left\{k_\beta\left(p_{\phi\phi}^0 \phi_1 \tilde{\phi}_1 + p_{TT}^0 T_1 \tilde{T}_1 + 2p_{\phi T}^0 \phi_1 \tilde{T}_1\right) - 4k_\beta^2 v_1(\mu_\phi^0 \tilde{\phi}_1 + \mu_T^0 \tilde{T}_1)\right. \\
&\quad \left.-2k_\beta(k_\beta v_1 + ik_z w_1)(\lambda_\phi^0 \tilde{\phi}_1 + \lambda_T^0 \tilde{T}_1)\right\}\Big] + c.c \\
G_{02}^{4\beta} &= \tfrac{1}{2}\Big[-\tfrac{1}{\phi^0}\left\{\phi^0(k_\beta v_1 \tilde{w}_1 - ik_z w_1 \tilde{w}_1) + \tilde{c}^{(0)}\phi_1 \tilde{w}_1\right\} - \tfrac{1}{\phi^0 H^2}(\mu_\phi^0 \phi_1 + \mu_T^0 T_1)(ik_z k_\beta \tilde{v}_1 + k_\beta^2 \tilde{w}_1)\Big] + c.c \\
G_{02}^{5\beta} &= \tfrac{1}{2}\Big[-\tfrac{1}{\phi^0}\left\{\phi^0(k_\beta v_1 \tilde{T}_1 - ik_z w_1 \tilde{T}_1) + \tilde{c}^{(0)}\phi_1 \tilde{T}_1\right\} \\
&\quad +\tfrac{2}{dim\phi^0}\left\{-\tfrac{2}{H^2}k_\beta^2 T_1(\kappa_\phi^0 \tilde{\phi}_1 + \kappa_T^0 \tilde{T}_1) - (p_\phi^0 \phi_1 + p_T^0 T_1)(k_\beta \tilde{v}_1 - ik_z \tilde{w}_1)\right. \\
&\quad +2\mu^0\left(v_1 \tilde{v}_1 k_\beta^2 + k_z^2 w_1 \tilde{w}_1\right) + \mu^0 u_1 \tilde{u}_1 k_\beta^2 + \left(\tfrac{1}{2}\mu_{\phi\phi}^0 \phi_1 \tilde{\phi}_1 + \tfrac{1}{2}\mu_{TT}^0 T_1 \tilde{T}_1 + \mu_{\phi T}^0 \phi_1 \tilde{T}_1\right) \\
&\quad +2(\mu_\phi^0 \phi_1 + \mu_T^0 T_1)k_\beta \tilde{u}_1 - \mu^0(k_z^2 v_1 \tilde{v}_1 + k_\beta^2 w_1 \tilde{w}_1 - 2ik_z k_\beta v_1 \tilde{w}_1) - k_z^2 \mu^0 u_1 \tilde{u}_1 \\
&\quad \left.+\lambda^0(k_\beta^2 v_1 \tilde{v}_1 + k_z^2 w_1 \tilde{w}_1 - 2ik_z k_\beta v_1 \tilde{w}_1) - \left(\tfrac{1}{2}\mathcal{D}_{\phi\phi}^0 \phi_1 \tilde{\phi}_1 + \tfrac{1}{2}\mathcal{D}_{TT}^0 T_1 \tilde{T}_1 + \mathcal{D}_{\phi T}^0 \phi_1 \tilde{T}_1\right)\right\}\Big] + c.c \\
f_{02}^4 &= -\tfrac{1}{2\phi^0}\left[\phi^0(-k_\beta v_1 \tilde{w}_1 - ik_z w_1 \tilde{w}_1) + \tilde{c}^{(0)}\phi_1 \tilde{w}_1\right] + c.c \\
f_{02}^5 &= \tfrac{1}{2}\Big[-\tfrac{1}{\phi^0}\left\{\phi^0(-k_\beta v_1 \tilde{T}_1 - ik_z w_1 \tilde{T}_1) + \tilde{c}^{(0)}\phi_1 \tilde{T}_1\right\} + \tfrac{2}{dim\phi^0}\left\{-(p_\phi^0 \phi_1 + p_T^0 T_1)(k_\beta \tilde{v}_1 - ik_z \tilde{w}_1)\right. \\
&\quad +2\mu^0\left(v_1 \tilde{v}_1 k_\beta^2 + k_z^2 w_1 \tilde{w}_1\right) + \mu^0 u_1 \tilde{u}_1 k_\beta^2 + \left(\tfrac{1}{2}\mu_{\phi\phi}^0 \phi_1 \tilde{\phi}_1 + \tfrac{1}{2}\mu_{TT}^0 T_1 \tilde{T}_1 + \mu_{\phi T}^0 \phi_1 \tilde{T}_1\right) \\
&\quad +2(\mu_\phi^0 \phi_1 + \mu_T^0 T_1)k_\beta \tilde{u}_1 + \mu^0(k_z^2 v_1 \tilde{v}_1 + k_\beta^2 w_1 \tilde{w}_1 - 2ik_z k_\beta v_1 \tilde{w}_1) + k_z^2 \mu^0 u_1 \tilde{u}_1 \\
&\quad \left.+\lambda^0(k_\beta^2 v_1 \tilde{v}_1 + k_z^2 w_1 \tilde{w}_1 - 2ik_z k_\beta v_1 \tilde{w}_1) - \left(\tfrac{1}{2}\mathcal{D}_{\phi\phi}^0 \phi_1 \tilde{\phi}_1 + \tfrac{1}{2}\mathcal{D}_{TT}^0 T_1 \tilde{T}_1 + \mathcal{D}_{\phi T}^0 \phi_1 \tilde{T}_1\right)\right\}\Big] + c.c
\end{aligned}
$$

In two-dimensional limit

$$
\underbrace{(G_{02}^{1\beta}, G_{02}^{2\beta}, G_{02}^{3\beta}, G_{02}^{4\beta}, G_{02}^{4\beta})}_{3D} \xrightarrow{k_z=0, w=0, X^{[1:1]} \in \mathrm{Re}} \underbrace{2(G_{22}^{1\beta}, G_{22}^{2\beta}, G_{22}^{3\beta}, 0, G_{22}^{4\beta})}_{2D}.
$$

Similarly $\underbrace{(f_{02}^4, f_{02}^5)}_{3D} \xrightarrow{k_z=0, w=0, X^{[1:1]} \in \mathrm{Re}} \underbrace{2(0, f_{nl})}_{2D}$.

Appendix 8E. Analytical Expression for $\mathbf{G}_{13}$

Consider $\mathbf{G}_{13}$ as follows

$$\begin{aligned}\mathbf{G}_{13} &= N_2(X^{[2;2]},\tilde{X}^{[1;1]})+N_2(\tilde{X}^{[1;1]},X^{[2;2]})+N_2(X^{[0;2]},X^{[1;1]})+N_2(X^{[1;1]},X^{[0;2]})\\ &\quad +N_3(\tilde{X}^{[1;1]},X^{[1;1]},X^{[1;1]})+N_3(X^{[1;1]},\tilde{X}^{[1;1]},X^{[1;1]})+N_3(X^{[1;1]},X^{[1;1]},\tilde{X}^{[1;1]})\end{aligned}$$

where $\mathbf{G}_{13}=(G^1_{13},G^2_{13},G^3_{13},G^4_{13},G^5_{13})$ which has an analytical expression in terms of sine and cosine function

$$\left.\begin{array}{rcl}(G^1_{13},G^4_{13},G^5_{13}) &=& (G^{1\beta 3}_{13},G^{4\beta 3}_{13},G^{5\beta 3}_{13})cos\,k_{3\beta}\theta+(G^{1\beta 1}_{13},G^{4\beta 1}_{13},G^{5\beta 1}_{13})cos\,k_\beta\theta\\ (G^2_{13},G^3_{13}) &=& (G^{2\beta 3}_{13},G^{3\beta 3}_{13})sin\,k_{3\beta}\theta+(G^{2\beta 1}_{13},G^{3\beta 1}_{13})sin\,k_\beta\theta\end{array}\right\}$$

where $\theta=y\pm 1/2$ and $k_{3\beta}=3k_\beta$ with $\beta=1,2,\ldots$ being the mode number. In vector notation

$$\begin{aligned}\mathbf{G}_{13} &= G^{\beta 3}_{13}(cos\,k_{3\beta}\theta,sin\,k_{3\beta}\theta,sin\,k_{3\beta}\theta,cos\,k_{3\beta}\theta,cos\,k_{3\beta}\theta)\\ &\quad +G^{\beta 1}_{13}(cos\,k_\beta\theta,sin\,k_\beta\theta,sin\,k_\beta\theta,cos\,k_\beta\theta,cos\,k_\beta\theta)\end{aligned}$$

where $G^{\beta 3}_{13}=(G^{1\beta 3}_{13},G^{2\beta 3}_{13},G^{3\beta 3}_{13},G^{4\beta 3}_{13},G^{5\beta 3}_{13})$ and $G^{\beta 1}_{13}=(G^{1\beta 1}_{13},G^{2\beta 1}_{13},G^{3\beta 1}_{13},G^{4\beta 1}_{13},G^{5\beta 1}_{13})$ are functions which do not dependent of y,

$$\begin{aligned}(G^{\beta 1}_{13},G^{\beta 3}_{13}) &= \underbrace{N_2(X_2,\tilde{X}_1)+N_2(\tilde{X}_1,X_2)}_{(1)}+\underbrace{N_2(X_{02},X_1)+N_2(X_1,X_{02})}_{(2)}\\ &\quad +\underbrace{N_3(\tilde{X}_1,X_1,X_1)+N_3(X_1,\tilde{X}_1,X_1)+N_3(X_1,X_1,\tilde{X}_1)}_{(3)}\\ &= \underbrace{(N^{\beta 1}_{13},N^{\beta 3}_{13})}_{(1)}+\underbrace{(M^{\beta 1}_{13},M^{\beta 3}_{13})}_{(2)}+\underbrace{(C^{\beta 1}_{13},C^{\beta 3}_{13})}_{(3)}\end{aligned}$$

or we can write $(G^{\beta 1}_{13},G^{\beta 3}_{13})=(N^{\beta 1}_{13}+M^{\beta 1}_{13}+C^{\beta 1}_{13},N^{\beta 3}_{13}+M^{\beta 3}_{13}+C^{\beta 3}_{13})$. In $2D$ case, X_1 is real and $X_{02}=2X_2$, this simplify expressions of $\mathbf{G}_{13}$ as $(G^{\beta 1}_{13},G^{\beta 3}_{13})=3[N_2(X_2,X_1)+N_2(X_1,X_2)++N_3(X_1,X_1,X_1)]$.

Continuity equation

$$(G^{1\beta 1}_{13},G^{1\beta 3}_{13}) = (N^{1\beta 1}_{13}+M^{1\beta 1}_{13}+C^{1\beta 1}_{13},N^{1\beta 3}_{13}+M^{1\beta 3}_{13}+C^{1\beta 3}_{13})$$

$$\left.\begin{array}{rcl}N^{1\beta 3}_{13} &=& -\frac{1}{2}\left[k_{3\beta}(\tilde{\phi}_1 v_2+\tilde{v}_1\phi_2)+ik_z(\tilde{\phi}_1 w_2+\tilde{w}_1\phi_2)\right]\\ N^{1\beta 1}_{13} &=& -\frac{1}{2}\left[k_\beta(\tilde{\phi}_1 v_2-\phi_2\tilde{v}_1)+ik_z(\tilde{\phi}_1 w_2+\tilde{w}_1\phi_2)\right]-ik_z(\tilde{\phi}w^{22}_m+\tilde{w}_1\phi^{22}_m)-k_\beta\phi^{22}_m\tilde{v}_1\\ M^{1\beta 3}_{13} &=& -\frac{1}{2}\left[k_{3\beta}(\phi_1 v_{02}+v_1\phi_{02})+ik_z(\phi_1 w_{02}+w_1\phi_{02})\right]\\ M^{1\beta 1}_{13} &=& -\frac{1}{2}\left[k_\beta(\phi_1 v_{02}-\phi_{02}v_1)+ik_z(\phi_1 w_{02}+w_1\phi_{02})\right]-ik_z\phi_1 w^{22}_m\\ C^{1\beta 3}_{13} &=& 0\\ C^{1\beta 1}_{13} &=& 0\end{array}\right\}$$

x-momentum equation

$$
\begin{aligned}
N_{13}^{2\beta 3} &= \tfrac{1}{2}\Big[-\tfrac{1}{\tilde{\phi}}\Big\{2c^{(0)}\tilde{\phi}_1 u_2 + \tilde{c}^{(0)}\phi_2\tilde{u}_1 + \tilde{\phi}_1 v_2 + \phi_2\tilde{v}_1 \\
&\quad +\phi^0(k_{2\beta}\tilde{v}_1 u_2 + k_\beta v_2\tilde{u}_1 + 2ik_z\tilde{w}_1 u_2 - ik_z w_2\tilde{u}_1)\Big\} \\
&\quad +\tfrac{1}{\phi^0 H^2}\Big\{(k_z^2 - k_\beta^2 - k_\beta k_{2\beta})(\mu_\phi^0\phi_2 + \mu_T^0 T_2)\tilde{u}_1 \\
&\quad -(2k_z^2 + k_{2\beta} + k_\beta k_{2\beta})(\mu_\phi^0\tilde{\phi}_1 + \mu_T^0\tilde{T}_1)u_2 \\
&\quad -k_{3\beta}(\mu_{\phi\phi}^0\tilde{\phi}_1\phi_2 + \mu_{TT}^0\tilde{T}_1 T_2 + \mu_{\phi T}^0\tilde{\phi}_1 T_2 + \mu_{\phi T}^0\tilde{T}_1\phi_2)\Big\}\Big] \\
N_{13}^{2\beta 1} &= \tfrac{1}{2}\Big[-\tfrac{1}{\tilde{\phi}}\Big\{2c^{(0)}\tilde{\phi}_1 u_2 - \tilde{c}^{(0)}\phi_2\tilde{u}_1 + \tilde{\phi}_1 v_2 - \phi_2\tilde{v}_1 \\
&\quad +\phi^0(-k_{2\beta}\tilde{v}_1 u_2 + k_\beta v_2\tilde{u}_1 + 2ik_z\tilde{w}_1 u_2 - ik_z w_2\tilde{u}_1)\Big\} \\
&\quad +\tfrac{1}{\phi^0 H^2}\Big\{(k_\beta^2 - k_z^2 - k_\beta k_{2\beta})(\mu_\phi^0\phi_2 + \mu_T^0 T_2)\tilde{u}_1 \\
&\quad -(k_{2\beta}^2 + 2k_z^2 - k_\beta k_{2\beta})(\mu_\phi^0\tilde{\phi}_1 + \mu_T^0\tilde{T}_1)u_2 \\
&\quad -k_\beta(\mu_{\phi\phi}^0\tilde{\phi}_1\phi_2 + \mu_{TT}^0\tilde{T}_1 T_2 + \mu_{\phi T}^0\tilde{\phi}_1 T_2 + \mu_{\phi T}^0\tilde{T}_1\phi_2)\Big\}\Big] \\
&\quad -\tfrac{1}{\phi^0}\left(\tilde{c}^{(0)}\phi_m^{22}\tilde{u}_1 + \phi_m^{22}\tilde{v}_1 - ik_z\phi^0 w_m^{22}\tilde{u}_1\right) \\
&\quad +\tfrac{1}{\phi^0 H^2}\Big[(-k_\beta^2 + k_z^2)(\mu_\phi^0\phi_m^{22} + \mu_T^0 T_m^{22})\tilde{u}_1 \\
&\quad -k_\beta\left(\mu_{\phi\phi}^0\phi_m^{22}\tilde{\phi}_1 + \mu_{TT}^0 T_m^{22}\tilde{T}_1 + \mu_{\phi T}^0\phi_m^{22}\tilde{T}_1 + \mu_{\phi T}^0 T_m^{22}\tilde{\phi}_1\right)\Big] \\
M_{13}^{2\beta 3} &= \tfrac{1}{2}\Big[-\tfrac{1}{\phi^0}\left\{2a^{(0)}\phi_1 u_{02} + \phi_1 v_{02} + c^{(0)}u_1\phi_{02} + v_1\phi_{02}\right. \\
&\quad \left.+\phi^0(k_{2\beta}v_1 u_{02} + k_\beta u_1 v_{02} + ik_z u_1 w_{02})\right\} \\
&\quad +\tfrac{1}{\phi^0 H^2}\Big\{-(k_{2\beta}^2 + k_\beta k_{2\beta})u_{02}(\mu_\phi^0\phi_1 + \mu_T^0 T_1) \\
&\quad -(k_\beta k_{2\beta} + k_\beta^2 + k_z^2)u_1(\mu_\phi^0\phi_{02} + \mu_T^0 T_{02}) \\
&\quad -k_{3\beta}(\mu_{\phi\phi}^0\phi_{02}\phi_1 + \mu_{TT}^0 T_{02}T_1 + \mu_{\phi T}^0\phi_{02}T_1 + \mu_{\phi T}^0 T_{02}\phi_1)\Big\}\Big] \\
M_{13}^{2\beta 1} &= \tfrac{1}{2}\Big[-\tfrac{1}{\phi^0}\left\{2a^{(0)}\phi_1 u_{02} + \phi_1 v_{02} - c^{(0)}u_1\phi_{02} - v_1\phi_{02}\right. \\
&\quad \left.+\phi^0(-k_{2\beta}v_1 u_{02} + k_\beta u_1 v_{02} - ik_z u_1 w_{02})\right\} \\
&\quad +\tfrac{1}{\phi^0 H^2}\Big\{(-k_{2\beta}^2 + k_\beta k_{2\beta})u_{02}(\mu_\phi^0\phi_1 + \mu_T^0 T_1) \\
&\quad +(-k_\beta k_{2\beta} + k_\beta^2 + k_z^2)u_1(\mu_\phi^0\phi_{02} + \mu_T^0 T_{02}) \\
&\quad -k_\beta(\mu_{\phi\phi}^0\phi_{02}\phi_1 + \mu_{TT}^0 T_{02}T_1 + \mu_{\phi T}^0\phi_{02}T_1 + \mu_{\phi T}^0 T_{02}\phi_1)\Big\}\Big] \\
&\quad -ik_z w_m^{02}u_1 - \tfrac{T_m^{02}}{\phi^0 H^2}\left[\mu_T^0 k_\beta^2 u_1 + k_\beta(\mu_{TT}^0 T_1 + \mu_{\phi T}^0\phi_1) + k_z^2\mu_T^0 u_1\right] \\
C_{13}^{2\beta 3} &= -\tfrac{1}{4\phi^0}\left[k_\beta(\tilde{\phi}v_1 u_1 + \phi_1\tilde{v}_1 u_1 + \phi_1 v_1\tilde{u}_1) + ik_z(\tilde{\phi}w_1 u_1 + \phi_1\tilde{w}_1 u_1 - \phi_1 w_1\tilde{u}_1)\right] \\
&\quad +\tfrac{1}{4\phi^0 H^2}\Big[-(k_\beta^2 + k_z^2)\left(\tfrac{1}{2}\mu_{\phi\phi}^0\phi_1(2\tilde{\phi}_1 u_1 + \phi_1\tilde{u}_1) + \tfrac{1}{2}\mu_{TT}^0 T_1(2\tilde{T}_1 u_1 + T_1\tilde{u}_1)\right. \\
&\quad \left.+\mu_{\phi T}^0(\tilde{\phi}_1 T_1 u_1 + \phi_1\tilde{T}_1 u_1 + \phi_1 T_1\tilde{u}_1)\right) \\
&\quad -\tfrac{3k_\beta}{2}\left(\mu_{\phi\phi\phi}^0\phi_1^2\tilde{\phi}_1 + \mu_{TTT}^0 T_1^2\tilde{T}_1 + \mu_{\phi\phi T}^0\phi_1(2\tilde{\phi}_1 T_1 + \phi_1\tilde{T}_1) + \mu_{\phi TT}^0 T_1(2\phi_1\tilde{T}_1 + T_1\tilde{\phi}_1)\right) \\
&\quad -k_\beta^2\left(\mu_{\phi\phi}^0\phi_1(\tilde{u}_1\phi_1 + 2u_1\tilde{\phi}_1) + \mu_{TT}^0 T_1(\tilde{u}_1 T_1 + 2u_1\tilde{T}_1)\right. \\
&\quad \left.+2\mu_{\phi T}^0(\tilde{u}_1\phi_1 T_1 + u_1\tilde{\phi}_1 T_1 + u_1\phi_1\tilde{T}_1)\right) + k_z^2\tilde{u}_1(\mu_{\phi\phi}^0\phi_1^2 + \mu_{TT}^0 T_1^2 + 2\mu_{\phi T}^0\phi_1 T_1)\Big] \\
C_{13}^{2\beta 3} &= C_{13}^{2\beta 1}
\end{aligned}
$$

y-momentum equation

$$
\begin{aligned}
N_{13}^{3\beta 3} &= \tfrac{1}{2}\Big[-\tfrac{1}{\phi^0}\Big\{2c^{(0)}\tilde{\phi}_1 v_2+\tilde{c}^{(0)}\phi_2\tilde{v}_1+\phi^0(k_{3\beta}\tilde{v}_1 v_2+2ik_z\tilde{w}_1 v_2-ik_z w_2\tilde{v}_1)\Big\}\\
&+\tfrac{1}{\phi^0 H^2}\Big\{k_{3\beta}(p^0_{\phi\phi}\tilde{\phi}_1\phi_2+p^0_{TT}\tilde{T}_1T_2+p^0_{\phi T}\tilde{\phi}_1T_2+p^0_{\phi T}\tilde{T}_1\phi_2)\\
&-2k_\beta k_{3\beta}\tilde{v}_1(\mu^0_\phi\phi_2+\mu^0_T T_2)-2k_{2\beta}k_{3\beta}v_2(\mu^0_\phi\tilde{\phi}_1+\mu^0_T\tilde{T}_1)\\
&-k_{3\beta}(\lambda^0_\phi\phi_2+\lambda^0_T T_2)(k_\beta\tilde{v}_1-ik_z\tilde{w}_1)-k_{3\beta}(\lambda^0_\phi\tilde{\phi}_1+\lambda^0_T\tilde{T}_1)(k_{2\beta}v_2+2ik_z w_2)\\
&+ik_z(\mu^0_\phi\tilde{\phi}_1+\mu^0_T\tilde{T}_1)(2ik_z v_2-k_{2\beta}w_2)-ik_z(\mu^0_\phi\phi_2+\mu^0_T T_2)(ik_z\tilde{v}_1+k_\beta w_1)\Big\}\Big]\\
N_{13}^{3\beta 1} &= \tfrac{1}{2}\Big[-\tfrac{1}{\phi^0}\Big\{2c^{(0)}\tilde{\phi}_1 v_2-\tilde{c}^{(0)}\phi_2\tilde{v}_1+\phi^0(-k_\beta\tilde{v}_1 v_2+2ik_z\tilde{w}_1 v_2+ik_z w_2\tilde{v}_1)\Big\}\\
&+\tfrac{1}{\phi^0 H^2}\Big\{k_\beta(p^0_{\phi\phi}\tilde{\phi}_1\phi_2+p^0_{TT}\tilde{T}_1T_2+p^0_{\phi T}\tilde{\phi}_1T_2+p^0_{\phi T}\tilde{T}_1\phi_2)\\
&-2k_\beta^2\tilde{v}_1(\mu^0_\phi\phi_2+\mu^0_T T_2)-2k_{2\beta}k_\beta v_2(\mu^0_\phi\tilde{\phi}_1+\mu^0_T\tilde{T}_1)\\
&-k_\beta(\lambda^0_\phi\phi_2+\lambda^0_T T_2)(k_\beta\tilde{v}_1-ik_z\tilde{w}_1)-k_\beta(\lambda^0_\phi\tilde{\phi}_1+\lambda^0_T\tilde{T}_1)(k_{2\beta}v_2+2ik_z w_2)\\
&+ik_z(\mu^0_\phi\tilde{\phi}_1+\mu^0_T\tilde{T}_1)(2ik_z v_2-k_{2\beta}w_2)+ik_z(\mu^0_\phi\phi_2+\mu^0_T T_2)(ik_z\tilde{v}_1+k_\beta w_1)\Big\}\Big]\\
&-\tfrac{1}{\phi^0}\left(-ik_z\phi^0 w^{22}_m\tilde{v}_1+\tilde{c}^{(0)}\phi^{22}_m\tilde{v}_1\right)\\
&+\tfrac{1}{\phi^0 H^2}\Big[k_\beta(p^0_{\phi\phi}\phi^{22}_m\tilde{\phi}_1+p^0_{TT}T^{22}_m\tilde{T}_1+p^0_{\phi T}\phi^{22}_m\tilde{T}_1+p^0_{\phi T}T^{22}_m\tilde{\phi}_1)\\
&-2ik_z k_\beta w^{22}_m(\lambda^0_\phi\tilde{\phi}_1+\lambda^0_T\tilde{T}_1)+ik_z(\mu^0_\phi\phi^{22}_m+\mu^0_T T^{22}_m)(-ik_z\tilde{v}_1-k_\beta\tilde{w}_1)\\
&-2k_\beta^2\tilde{v}_1\left(\mu^0_\phi\phi^{22}_m+\mu^0_T T^{22}_m\right)+\left(-k_\beta^2\tilde{v}_1+ik_z k_\beta\tilde{w}_1\right)\left(\lambda^0_\phi\phi^{22}_m+\lambda^0_T T^{22}_m\right)\Big]\\
M_{13}^{3\beta 3} &= \tfrac{1}{2}\Big[-\tfrac{1}{\phi^0}\left\{2a^{(0)}\phi_1 v_{02}+c^{(0)}\phi_{02}v_1+\phi^0(k_{3\beta}v_1 v_{02}+ik_z w_{02}v_1)\right\}\\
&+\tfrac{1}{\phi^0 H^2}\Big\{k_{3\beta}\left(p^0_{\phi\phi}\phi_1\phi_{02}+p^0_{TT}T_1T_{02}+p^0_{\phi T}\phi_1T_{02}+p^0_{\phi T}T_1\phi_{02}\right)\\
&-2k_\beta k_{3\beta}v_1\left(\mu^0_\phi\phi_{02}+\mu^0_T T_{02}\right)-2k_{2\beta}k_{3\beta}v_{02}\left(\mu^0_\phi\phi_1+\mu^0_T T_1\right)\\
&-k_{3\beta}(k_\beta v_1+ik_z w_1)\left(\lambda^0_\phi\phi_{02}+\lambda^0_T T_{02}\right)-k_{2\beta}k_{3\beta}v_{02}\left(\lambda^0_\phi\phi_1+\lambda^0_T T_1\right)\\
&-ik_z k_{2\beta}(\mu^0_\phi\phi_1+\mu^0_T T_1)w_{02}+ik_z(\mu^0_\phi\phi_{02}+\mu^0_T T_{02})(ik_z v_1-k_\beta w_1)\Big\}\Big]\\
M_{13}^{3\beta 1} &= \tfrac{1}{2}\Big[-\tfrac{1}{\phi^0}\left\{2a^{(0)}\phi_1 v_{02}-c^{(0)}\phi_{02}v_1+\phi^0\left(-k_\beta v_1 v_{02}-ik_z w_{02}v_1\right)\right\}\\
&+\tfrac{1}{\phi^0 H^2}\Big\{k_\beta\left(p^0_{\phi\phi}\phi_1\phi_{02}+p^0_{TT}T_1T_{02}+p^0_{\phi T}\phi_1T_{02}+p^0_{\phi T}T_1\phi_{02}\right)\\
&-2k_\beta^2 v_1\left(\mu^0_\phi\phi_{02}+\mu^0_T T_{02}\right)-2k_\beta k_{2\beta}v_{02}\left(\mu^0_\phi\phi_1+\mu^0_T T_1\right)\\
&-k_\beta(k_\beta v_1+ik_z w_1)(\lambda^0_\phi\phi_{02}+\lambda^0_T T_{02})-k_\beta k_{2\beta}v_{02}(\lambda^0_\phi\phi_1+\lambda^0_T T_1)\\
&-ik_z k_{2\beta}(\mu^0_\phi\phi_1+\mu^0_T T_1)w_{02}-ik_z(\mu^0_\phi\phi_{02}+\mu^0_T T_{02})(ik_z v_1-k_\beta w_1)\Big\}\Big]\\
&-ik_z w^{02}_m v_1+\tfrac{T^{02}_m}{\phi^0 H^2}\Big[-2k_\beta^2\mu^0_T v_1-(k_\beta^2 v_1+ik_z k_\beta w_1)\lambda^0_T\\
&+k_\beta(p^0_{\phi\phi}T_1+p^0_{\phi T}\phi_1)+ik_z\mu^0_T(ik_z v_1-k_\beta w_1)\Big]\\
C_{13}^{3\beta 3} &= -\tfrac{1}{4\phi^0}\Big[k_\beta v_1(\tilde{\phi}_1 v_1+2\phi_1\tilde{v}_1)+ik_z(\tilde{\phi}_1 w_1 v_1+\phi_1\tilde{w}_1 v_1-\phi_1 w_1\tilde{v}_1)\Big]+\tfrac{1}{4\phi^0 H^2}\Big[\\
&\tfrac{3k_\beta}{2}\left(p^0_{\phi\phi\phi}\phi_1^2\tilde{\phi}_1+p^0_{TTT}T_1^2\tilde{T}_1+p^0_{\phi\phi T}\phi_1(2\tilde{\phi}_1T_1+\phi_1\tilde{T}_1)+p^0_{\phi TT}T_1(2\phi_1\tilde{T}_1+\tilde{\phi}_1T_1)\right)\\
&-6k_\beta^2\left(\tfrac{1}{2}\mu^0_{\phi\phi}\phi_1(\tilde{v}_1\phi_1+2v_1\tilde{\phi}_1)+\tfrac{1}{2}\mu^0_{TT}T_1(\tilde{v}_1T_1+2v_1\tilde{T}_1)+\mu^0_{\phi T}(\tilde{v}_1\phi_1T_1+v_1\tilde{\phi}_1T_1+v_1\phi_1\tilde{T}_1)\right)\\
&-3k_\beta^2\left(\tfrac{1}{2}\lambda^0_{\phi\phi}\phi_1(\tilde{v}_1\phi_1+2v_1\tilde{\phi}_1)+\tfrac{1}{2}\lambda^0_{TT}T_1(\tilde{v}_1T_1+2v_1\tilde{T}_1)+\lambda^0_{\phi T}(\tilde{v}_1\phi_1T_1+v_1\tilde{\phi}_1T_1+v_1\phi_1\tilde{T}_1)\right)\\
&+3ik_z k_\beta\tilde{w}_1\left(\tfrac{1}{2}\lambda^0_{\phi\phi}\phi_1^2+\tfrac{1}{2}\lambda^0_{TT}T_1^2+\lambda^0_{\phi T}\phi_1T_1\right)+ik_z k_\beta w_1\lambda^0_{\phi T}(\tilde{\phi}_1T_1-\phi_1\tilde{T}_1)\\
&-ik_z(ik_z\tilde{v}_1+k_\beta\tilde{w}_1)\left(\tfrac{1}{2}\mu^0_{\phi\phi}\phi_1^2+\tfrac{1}{2}\mu^0_{TT}T_1^2+\mu^0_{\phi T}\phi_1T_1\right)\\
&+ik_z(ik_z v_1-k_\beta w_1)\left(\tfrac{1}{2}\mu^0_{\phi\phi}\phi_1\tilde{\phi}_1+\tfrac{1}{2}\mu^0_{TT}T_1\tilde{T}_1+\mu^0_{\phi T}\tilde{\phi}_1T_1+\mu^0_{\phi T}\tilde{T}_1\phi_1\right)\Big]\\
C_{13}^{3\beta 3} &= C_{13}^{3\beta 1}
\end{aligned}
$$

z-momentum equation

$$
\begin{aligned}
N_{13}^{4\beta 3} &= \tfrac{1}{2}\Big[-\tfrac{1}{\phi^0}\Big\{2c^{(0)}\tilde{\phi}_1 w_2+\tilde{c}^{(0)}\phi_2\tilde{w}_1+\phi^0(k_{2\beta}\tilde{v}_1 w_2+k_\beta v_2\tilde{w}_1+ik_z\tilde{w}_1 w_2)\Big\}\\
&+\tfrac{1}{\phi^0 H^2}\Big\{-ik_z(p^0_{\phi\phi}\tilde{\phi}_1\phi_2+p^0_{TT}\tilde{T}_1T_2+p^0_{\phi T}\tilde{\phi}_1T_2+p^0_{\phi T}\tilde{T}_1\phi_2)\\
&-2k_z^2\Big(2(\mu^0_\phi\tilde{\phi}_1+\mu^0_T\tilde{T}_1)w_2-(\mu^0_\phi\phi_2+\mu^0_T T_2)\tilde{w}_1\Big)\\
&+ik_z\Big((\lambda^0_\phi\tilde{\phi}_1+\lambda^0_T\tilde{T}_1)(k_{2\beta}v_2+2ik_z w_2)+(\lambda^0_\phi\phi_2+\lambda^0_T T_2)(k_\beta\tilde{v}_1-ik_z\tilde{w}_1)\Big)\\
&+k_{3\beta}\Big((\mu^0_\phi\tilde{\phi}_1+\mu^0_T\tilde{T}_1)(2ik_z v_2-k_{2\beta}w_2)+(\mu^0_\phi\phi_2+\mu^0_T T_2)(-ik_z\tilde{v}_1-k_\beta\tilde{w}_1)\Big)\Big\}\Big]\\
N_{13}^{4\beta 1} &= \tfrac{1}{2}\Big[-\tfrac{1}{\phi^0}\Big\{2c^{(0)}\tilde{\phi}_1 w_2+\tilde{c}^{(0)}\phi_2\tilde{w}_1+\phi^0(-k_{2\beta}\tilde{v}_1 w_2-k_\beta v_2\tilde{w}_1+ik_z\tilde{w}_1 w_2)\Big\}\\
&+\tfrac{1}{\phi^0 H^2}\Big\{-ik_z(p^0_{\phi\phi}\tilde{\phi}_1\phi_2+p^0_{TT}\tilde{T}_1T_2+p^0_{\phi T}\tilde{\phi}_1T_2+p^0_{\phi T}\tilde{T}_1\phi_2)\\
&-2k_z^2\Big(2(\mu^0_\phi\tilde{\phi}_1+\mu^0_T\tilde{T}_1)w_2-(\mu^0_\phi\phi_2+\mu^0_T T_2)\tilde{w}_1\Big)\\
&+ik_z\Big((\lambda^0_\phi\tilde{\phi}_1+\lambda^0_T\tilde{T}_1)(k_{2\beta}v_2+2ik_z w_2)+(\lambda^0_\phi\phi_2+\lambda^0_T T_2)(k_\beta\tilde{v}_1-ik_z\tilde{w}_1)\Big)\\
&+k_\beta\Big((\mu^0_\phi\tilde{\phi}_1+\mu^0_T\tilde{T}_1)(2ik_z v_2-k_{2\beta}w_2)-(\mu^0_\phi\phi_2+\mu^0_T T_2)(-ik_z\tilde{v}_1-k_\beta\tilde{w}_1)\Big)\Big\}\Big]\\
&-\tfrac{1}{\phi^0}\Big[ik_z\phi^0\tilde{w}_1 w_m^{22}+2c^{(0)}\tilde{\phi}_1 w_m^{22}+\tilde{c}^{(0)}\phi_m^{22}\tilde{w}_1\Big]\\
&+\tfrac{1}{\phi^0 H^2}\Big[-ik_z\Big(p_{\phi\phi}\tilde{\phi}_1\phi_m^{22}+p^0_{TT}\tilde{T}_1T_m^{22}+p^0_{\phi T}\tilde{\phi}_1T_m^{22}+p^0_{\phi T}\tilde{T}_1\phi_m^{22}\Big)\\
&-2k_z^2 w_m^{22}\Big\{2\Big(\mu^0_\phi\tilde{\phi}_1+\mu^0_T\tilde{T}_1\Big)+\Big(\lambda^0_\phi\tilde{\phi}_1+\lambda^0_T\tilde{T}_1\Big)\Big\}\\
&+2k_z^2\Big(\mu^0_\phi\phi_m^{22}+\mu^0_T T_m^{22}\Big)\tilde{w}_1+ik_z\Big(\lambda^0_\phi\phi_m^{22}+\lambda^0_T T_m^{22}\Big)\left(k_\beta\tilde{v}_1-ik_z\tilde{w}_1\right)\\
&+\Big(\mu^0_\phi\phi_m^{22}+\mu^0_T T_m^{22}\Big)\Big(-ik_z k_\beta\tilde{v}_1-k_\beta^2\tilde{w}_1\Big)\Big]\\
M_{13}^{4\beta 3} &= \tfrac{1}{2}\Big[-\tfrac{1}{\phi^0}\left\{2a^{(0)}\phi_1 w_{02}+c^{(0)}\phi_{02}w_1+\phi^0(k_{2\beta}v_1 w_{02}+k_\beta v_{02}w_1+ik_z w_{02}w_1)\right\}\\
&+\tfrac{1}{\phi^0 H^2}\Big\{-ik_z(p^0_{\phi\phi}\phi_{02}\phi_1+p^0_{TT}T_{02}T_1+p^0_{\phi T}\phi_{02}T_1+p^0_{\phi T}T_{02}\phi_1)\\
&ik_z k_{2\beta}\Big(\lambda^0_\phi\phi_1+\lambda^0_T T_1\Big)v_{02}-k_{3\beta}k_{2\beta}\Big(\mu^0_\phi\phi_1+\mu^0_T T_1\Big)w_{02}\\
&-2k_z^2(\mu^0_\phi\phi_{02}+\mu^0_T T_{02})w_1+ik_z(\lambda^0_\phi\phi_{02}+\lambda^0_T T_{02})(k_\beta v_1+ik_z w_1)\\
&+k_{3\beta}(\mu^0_\phi\phi_{02}+\mu^0_T T_{02})(ik_z v_1-k_\beta w_1)\Big\}\Big]\\
M_{13}^{4\beta 1} &= \tfrac{1}{2}\Big[-\tfrac{1}{\phi^0}\left\{2a^{(0)}\phi_1 w_{02}+c^{(0)}\phi_{02}w_1+\phi^0(-k_{2\beta}v_1 w_{02}-k_\beta v_{02}w_1+ik_z w_{02}w_1)\right\}\\
&+\tfrac{1}{\phi^0 H^2}\Big\{ik_z k_{2\beta}(\lambda^0_\phi\phi_1+\lambda^0_T T_1)v_{02}-k_\beta k_{2\beta}(\mu^0_\phi\phi_1+\mu^0_T T_1)w_{02}\\
&-ik_z(p^0_{\phi\phi}\phi_{02}\phi_1+p^0_{TT}T_{02}T_1+p^0_{\phi T}\phi_{02}T_1+p^0_{\phi T}T_{02}\phi_1)\\
&-2k_z^2(\mu^0_\phi\phi_{02}+\mu^0_T T_{02})w_1+ik_z(\lambda^0_\phi\phi_{02}+\lambda^0_T T_{02})(k_\beta v_1+ik_z w_1)\\
&-k_\beta(\mu^0_\phi\phi_{02}+\mu^0_T T_{02})(ik_z v_1-k_\beta w_1)\Big\}\Big]-\tfrac{w_m^{02}}{\phi^0}\left(2a^{(0)}\phi_1+ik_z\phi^0 w_1\right)\\
&+\tfrac{T_m^{02}}{\phi^0 H^2}\Big[-ik_z(p^0_{TT}T_1+p^0_{\phi T}\phi_1)-2k_z^2\mu^0_T w_1+ik_z\lambda^0_T(k_\beta v_1+ik_z w_1)\\
&+\mu^0_T k_\beta(ik_z v_1-k_\beta w_1)\Big]
\end{aligned}
$$

$$
\begin{aligned}
C_{13}^{4\beta 3} \;=\; & -\tfrac{1}{4\phi^0}\left[ik_z\tilde{\phi}_1 w_1^2 + k_\beta\left(\tilde{\phi}_1 v_1 w_1 + \phi_1\tilde{v}_1 w_1 + \phi_1 v_1\tilde{w}_1\right)\right] + \tfrac{1}{4\phi^0 H^2}\,[\\
& -ik_z\left\{\tfrac{1}{2}p^0_{\phi\phi\phi}\phi_1^2\tilde{\phi}_1 + \tfrac{1}{2}p^0_{TTT}T_1^2\tilde{T}_1 + p^0_{\phi\phi T}\phi_1\left(T_1\tilde{\phi}_1 + \tfrac{1}{2}\phi_1\tilde{T}_1\right) + p^0_{\phi TT}T_1\left(\phi_1\tilde{T}_1 + \tfrac{1}{2}T_1\tilde{\phi}_1\right)\right\}\\
& +2k_z^2\left\{\mu^0_{\phi\phi}\phi_1\left(\tfrac{1}{2}\tilde{w}_1\phi_1 - w_1\tilde{\phi}_1\right) + \mu^0_{TT}T_1\left(\tfrac{1}{2}\tilde{w}_1T_1 - w_1\tilde{T}_1\right)\right.\\
& \left.+\mu^0_{\phi T}\left(\tilde{w}_1\phi_1T_1 - w_1\tilde{\phi}_1T_1 - w_1\phi_1\tilde{T}_1\right)\right\} + ik_zk_\beta\left\{\lambda^0_{\phi\phi}\phi_1\left(\tfrac{1}{2}\tilde{v}_1\phi_1 + v_1\tilde{\phi}_1\right)\right.\\
& \left.+\lambda^0_{TT}T_1\left(\tfrac{1}{2}\tilde{v}_1T_1 + v_1\tilde{T}_1\right) + \lambda^0_{\phi T}\left(\tilde{v}_1\phi_1T_1 + v_1\tilde{\phi}_1T_1 + v_1\tilde{T}_1\phi_1\right)\right\}\\
& +k_z^2\left\{\lambda^0_{\phi\phi}\phi_1\left(\tfrac{1}{2}\tilde{w}_1\phi_1 - w_1\tilde{\phi}_1\right) + \lambda^0_{TT}T_1\left(\tfrac{1}{2}\tilde{w}_1T_1 - w_1\tilde{T}_1\right)\right.\\
& \left.+\lambda^0_{\phi T}\left(\tilde{w}_1\phi_1T_1 - w_1\tilde{\phi}_1T_1 - w_1\phi_1\tilde{T}_1\right)\right\}\\
& -3ik_\beta k_z\left\{\mu^0_{\phi\phi}\phi_1\left(\tfrac{1}{2}\tilde{v}_1\phi_1 - v_1\tilde{\phi}_1\right) + \mu^0_{TT}T_1\left(\tfrac{1}{2}\tilde{v}_1T_1 - v_1\tilde{T}_1\right)\right.\\
& \left.+\mu^0_{\phi T}\left(\tilde{v}_1\phi_1T_1 - v_1\tilde{\phi}_1T_1 - v_1\phi_1\tilde{T}_1\right)\right\}\\
& -3k_\beta^2\left\{\mu^0_{\phi\phi}\phi_1\left(\tfrac{1}{2}\tilde{w}_1\phi_1 + w_1\tilde{\phi}_1\right) + \mu^0_{TT}T_1\left(\tfrac{1}{2}\tilde{w}_1T_1 + w_1\tilde{T}_1\right)\right\}\\
& +\mu^0_{\phi T}\left(\tilde{w}_1\phi_1T_1 + w_1\tilde{\phi}_1T_1 + w_1\phi_1\tilde{T}_1\right)\Big\}\Big]\\
C_{13}^{4\beta 1} \;=\; & -\tfrac{1}{4\phi^0}\left[3ik_z\tilde{\phi}_1 w_1^2 - k_\beta\left(\tilde{\phi}_1 v_1 w_1 + \phi_1\tilde{v}_1 w_1 + \phi_1 v_1\tilde{w}_1\right)\right] + \tfrac{1}{4\phi^0 H^2}\,[\\
& -3ik_z\left\{\tfrac{1}{2}p^0_{\phi\phi\phi}\phi_1^2\tilde{\phi}_1 + \tfrac{1}{2}p^0_{TTT}T_1^2\tilde{T}_1 + p^0_{\phi\phi T}\left(\phi_1T_1\tilde{\phi}_1 + \tfrac{1}{2}\phi_1^2\tilde{T}_1\right) + p^0_{\phi TT}\left(\phi_1T_1\tilde{T}_1 + \tfrac{1}{2}T_1^2\tilde{\phi}_1\right)\right\}\\
& +6k_z^2\left\{\mu^0_{\phi\phi}\phi_1\left(\tfrac{1}{2}\tilde{w}_1\phi_1 - w_1\tilde{\phi}_1\right) + \mu^0_{TT}T_1\left(\tfrac{1}{2}\tilde{w}_1T_1 - w_1\tilde{T}_1\right)\right.\\
& \left.+\mu^0_{\phi T}\left(\tilde{w}_1\phi_1T_1 - w_1\tilde{\phi}_1T_1 - w_1\phi_1\tilde{T}_1\right)\right\} + 3ik_zk_\beta\left\{\lambda^0_{\phi\phi}\left(\tfrac{1}{2}\tilde{v}_1\phi_1^2 + v_1\phi_1\tilde{\phi}_1\right)\right.\\
& \left.+\lambda^0_{TT}\left(\tfrac{1}{2}\tilde{v}_1T_1^2 + v_1T_1\tilde{T}_1\right) + \lambda^0_{\phi T}\left(\tilde{v}_1\phi_1T_1 + v_1\tilde{\phi}_1T_1 + v_1\tilde{T}_1\phi_1\right)\right\}\\
& +3k_z^2\left\{\lambda^0_{\phi\phi}\left(\tfrac{1}{2}\tilde{w}_1\phi_1^2 - w_1\tilde{\phi}_1\phi_1\right) + \lambda^0_{TT}\left(\tfrac{1}{2}\tilde{w}_1T_1^2 - w_1\tilde{T}_1T_1\right)\right.\\
& \left.+\lambda^0_{\phi T}\left(\tilde{w}_1\phi_1T_1 - w_1\tilde{\phi}_1T_1 - w_1\phi_1\tilde{T}_1\right)\right\} - ik_zk_\beta\tilde{v}_1\left(\tfrac{1}{2}\mu^0_{\phi\phi}\phi_1^2 + \tfrac{1}{2}\mu^0_{TT}T_1^2 + \mu^0_{\phi T}\phi_1T_1\right)\\
& +ik_zk_\beta v_1\left(\mu^0_{\phi\phi}\phi_1\tilde{\phi}_1 + \mu^0_{TT}T_1\tilde{T}_1 + \mu^0_{\phi T}(\tilde{\phi}_1T_1 + \phi_1\tilde{T}_1)\right)\\
& -k_\beta^2\tilde{w}_1\left(\tfrac{1}{2}\mu^0_{\phi\phi}\phi_1^2 + \tfrac{1}{2}\mu^0_{TT}T_1^2 + \mu^0_{\phi T}\phi_1T_1\right)\\
& -k_\beta^2 w_1\left(\mu^0_{\phi\phi}\phi_1\tilde{\phi}_1 + \mu^0_{TT}T_1\tilde{T}_1 + \mu^0_{\phi T}(\tilde{\phi}_1T_1 + \phi_1\tilde{T}_1)\right)\Big]
\end{aligned}
$$

Energy equation

$$
\begin{aligned}
N_{13}^{5\beta 3} \;=\; & -\tfrac{1}{2\phi^0}\left[\tilde{c}^{(0)}\phi_2\tilde{T}_1 + 2c^{(0)}\tilde{\phi}_1T_2 + \phi^0\left(k_\beta v_2\tilde{T}_1 + k_{2\beta}\tilde{v}_1T_2 - ik_zw_2\tilde{T}_1 + 2ik_z\tilde{w}_1T_2\right)\right]\\
& +\tfrac{1}{\phi^0 dim}\left[\tfrac{1}{H^2}\left\{-T_2(\kappa^0_\phi\tilde{\phi}_1 + \kappa^0_T\tilde{T}_1)(k_\beta k_{2\beta} + k_{2\beta}^2 + 2k_z^2)\right.\right.\\
& \left.+\tilde{T}_1(\kappa^0_\phi\phi_2 + \kappa^0_TT_2)(-k_\beta k_{2\beta} - k_\beta^2 + k_z^2)\right\}\\
& -(p^0_\phi\phi_2 + p^0_TT_2)(k_\beta\tilde{v}_1 - ik_z\tilde{w}_1) - (p^0_\phi\tilde{\phi}_1 + p^0_T\tilde{T}_1)(k_{2\beta}v_2 + 2ik_zw_2)\\
& +4\mu^0(k_\beta k_{2\beta}v_2\tilde{v}_1 + 2k_z^2w_2\tilde{w}_1) + 2\mu^0u_2\tilde{u}_1(k_\beta k_{2\beta} - 2k_z^2)\\
& +(\mu^0_{\phi\phi}\phi_2\tilde{\phi}_1 + \mu^0_{TT}T_2\tilde{T}_1 + \mu^0_{\phi T}\phi_2\tilde{T}_1 + \mu^0_{\phi T}\phi_1T_2)\\
& +2k_\beta(\mu^0_\phi\phi_2 + \mu^0_TT_2)\tilde{u}_1 + 2k_{2\beta}(\mu^0_\phi\tilde{\phi}_1 + \mu^0_T\tilde{T}_1)u_2\\
& -\mu^0(4k_z^2v_2\tilde{v}_1 - 4ik_zk_\beta v_2\tilde{w}_1 + 2k_\beta k_{2\beta}w_2\tilde{w}_1 + 2ik_zk_{2\beta}\tilde{v}_1w_2)\\
& +\lambda^0(2k_\beta k_{2\beta}v_2\tilde{v}_1 + 4k_z^2w_2\tilde{w}_1 - 2ik_zk_{2\beta}v_2\tilde{w}_1 + 4ik_zk_\beta\tilde{v}_1w_2)\\
& -(\mathcal{D}^0_{\phi\phi}\phi_2\tilde{\phi}_1 + \mathcal{D}^0_{TT}T_2\tilde{T}_1 + \mathcal{D}^0_{\phi T}\phi_2\tilde{T}_1 + \mathcal{D}^0_{\phi T}\tilde{\phi}_1T_2)\Big]
\end{aligned}
$$

$$
\begin{aligned}
N_{13}^{5\beta 1} &= -\tfrac{1}{2\phi^0}\left[\tilde{c}^{(0)}\phi_2\tilde{T}_1 + 2c^{(0)}\tilde{\phi}_1 T_2 + \phi^0\left(-k_\beta v_2\tilde{T}_1 - k_{2\beta}\tilde{v}_1 T_2 - ik_z w_2\tilde{T}_1 + 2ik_z\tilde{w}_1 T_2\right)\right] \\
&+\tfrac{1}{\phi^0 dim}\left[\tfrac{1}{H^2}\left\{T_2(\kappa_\phi^0\tilde{\phi}_1 + \kappa_T^0\tilde{T}_1)(k_\beta k_{2\beta} - k_{2\beta}^2 - 2k_z^2)\right.\right. \\
&\left.\left.+\tilde{T}_1(\kappa_\phi^0\phi_2 + \kappa_T^0 T_2)(k_\beta k_{2\beta} - k_\beta^2 + k_z^2)\right\}\right. \\
&-(p_\phi^0\phi_2 + p_T^0 T_2)(k_\beta\tilde{v}_1 - ik_z\tilde{w}_1) - (p_\phi^0\tilde{\phi}_1 + p_T^0\tilde{T}_1)(k_{2\beta}v_2 + 2ik_z w_2) \\
&+4\mu^0(k_\beta k_{2\beta}v_2\tilde{v}_1 + 2k_z^2 w_2\tilde{w}_1) + 2\mu^0 u_2\tilde{u}_1(k_\beta k_{2\beta} + 2k_z^2) \\
&+(\mu_{\phi\phi}^0\phi_2\tilde{\phi}_1 + \mu_{TT}^0 T_2\tilde{T}_1 + \mu_{\phi T}^0\phi_2\tilde{T}_1 + \mu_{\phi T}^0\tilde{\phi}_1 T_2) \\
&+2k_\beta(\mu_\phi^0\phi_2 + \mu_T^0 T_2)\tilde{u}_1 + 2k_{2\beta}(\mu_\phi^0\tilde{\phi}_1 + \mu_T^0\tilde{T}_1)u_2 \\
&+\mu^0(4k_z^2 v_2\tilde{v}_1 - 4ik_z k_\beta v_2\tilde{w}_1 + 2k_\beta k_{2\beta}w_2\tilde{w}_1 + 2ik_z k_{2\beta}\tilde{v}_1 w_2) \\
&+\lambda^0(2k_\beta k_{2\beta}v_2\tilde{v}_1 + 4k_z^2 w_2\tilde{w}_1 - 2ik_z k_{2\beta}v_2\tilde{w}_1 + 4ik_z k_\beta\tilde{v}_1 w_2) \\
&\left.-(\mathcal{D}_{\phi\phi}^0\phi_2\tilde{\phi}_1 + \mathcal{D}_{TT}^0 T_2\tilde{T}_1 + \mathcal{D}_{\phi T}^0\phi_2\tilde{T}_1 + \mathcal{D}_{\phi T}^0\tilde{\phi}_1 T_2)\right] \\
&-\tfrac{1}{\phi^0}\left[2ik_z\phi^0\tilde{w}_1 T_m^{22} + 2c^{(0)}\tilde{\phi}_1 T_m^{22} - ik_z\phi^0\tilde{T}_1 w_m^{22} + \tilde{c}^{(0)}\tilde{T}_1\phi_m^{22}\right] \\
&+\tfrac{2}{\phi^0 d}\left[\tfrac{1}{H^2}\left\{\tilde{T}_1(\kappa_\phi^0\phi_m^{22} + \kappa_T^0 T_m^{22})(-k_\beta^2 + k_z^2) - 2k_z^2 T_m^{22}(\kappa_\phi^0\tilde{\phi}_1 + \kappa_T^0\tilde{T}_1)\right\}\right. \\
&-2ik_z w_m^{22}(p_\phi^0\tilde{\phi}_1 + p_T^0\tilde{T}_1) - (p_\phi^0\phi_m^{22} + p_T^0 T_m^{22})(\tilde{v}_1 k_\beta - ik_z\tilde{w}_1) \\
&+8\mu^0 k_z^2\tilde{w}_1 w_m^{22} + (\mu_{\phi\phi}^0\tilde{\phi}_1\phi_m^{22} + \mu_{TT}^0\tilde{T}_1 T_m^{22} + \mu_{\phi T}^0\tilde{\phi}_1 T_m^{22} + \mu_{\phi T}^0\tilde{T}_1\phi_m^{22}) \\
&\left.+\lambda^0(4k_z^2\tilde{w}_1 w_m^{22} + 4ik_z k_\beta\tilde{v}_1 w_m^{22}) - (\mathcal{D}_{\phi\phi}^0\tilde{\phi}_1\phi_m^{22} + \mathcal{D}_{TT}^0\tilde{T}_1 T_m^{22} + \mathcal{D}_{\phi T}^0\tilde{\phi}_1 T_m^{22} + \mathcal{D}_{\phi T}^0\tilde{T}_1\phi_m^{22})\right] \\
M_{13}^{5\beta 3} &= -\tfrac{1}{2\phi^0}\left[2a^{(0)}\phi_1 T_{02} + c^{(0)}\phi_{02}T_1 + \phi^0\left(k_{2\beta}v_1 T_{02} + k_\beta v_{02}T_1 + ik_z w_{02}T_1\right)\right] \\
&+\tfrac{1}{dim\phi^0}\left[\tfrac{1}{H^2}\left\{-T_1(\kappa_\phi^0\phi_{02} + \kappa_T^0 T_{02})(k_\beta k_{2\beta} + k_\beta^2 + k_z^2) - T_{02}(\kappa_\phi^0\phi_1 + \kappa_T^0 T_1)(k_\beta k_{2\beta} + k_{2\beta}^2)\right\}\right. \\
&-k_{2\beta}(p_\phi^0\phi_1 + p_T^0 T_1)v_{02} - (p_\phi^0\phi_{02} + p_T^0 T_{02})(k_\beta v_1 + ik_z w_1) \\
&+4\mu^0 k_\beta k_{2\beta}(v_1 v_{02} + \tfrac{1}{2}u_1 u_{02}) + (\mu_{\phi\phi}^0\phi_1\phi_{02} + \mu_{TT}^0 T_1 T_{02} + \mu_{\phi T}^0\phi_1 T_{02} + \mu_{\phi T}^0\phi_{02}T_1) \\
&+2k_{2\beta}(\mu_\phi^0\phi_1 + \mu_T^0 T_1)u_{02} + 2k_\beta u_1(\mu_\phi^0\phi_{02} + \mu_T^0 T_{02}) \\
&-\mu^0 k_{2\beta}(k_\beta w_1 - 2ik_z v_1)w_{02} - k_{2\beta}k_\beta\mu^0 w_{02}w_1 + \lambda^0 k_{2\beta}(2k_\beta v_1 v_{02} + 2ik_z v_{02}w_1) \\
&\left.-(\mathcal{D}_{\phi\phi}^0\phi_1\phi_{02} + \mathcal{D}_{TT}^0 T_1 T_{02} + \mathcal{D}_{\phi T}^0\phi_1 T_{02} + \mathcal{D}_{\phi T}^0\phi_{02}T_1)\right] \\
M_{13}^{5\beta 1} &= -\tfrac{1}{2\phi^0}\left[2a^{(0)}\phi_1 T_{02} + c^{(0)}\phi_{02}T_1 + \phi^0\left(-k_{2\beta}v_1 T_{02} - k_\beta v_{02}T_1 + ik_z w_{02}T_1\right)\right] \\
&+\tfrac{1}{dim\,\phi^0}\left[\tfrac{1}{H^2}\left\{T_1\left(\kappa_\phi^0\phi_{02} + \kappa_T^0 T_{02}\right)\left(k_\beta k_{2\beta} - k_\beta^2 - k_z^2\right)\right.\right. \\
&\left.\left.+T_{02}\left(\kappa_\phi^0\phi_1 + \kappa_T^0 T_1\right)\left(k_\beta k_{2\beta} - k_{2\beta}^2\right)\right\}\right. \\
&-k_{2\beta}\left(p_\phi^0\phi_1 + p_T^0 T_1\right)v_{02} - \left(p_\phi^0\phi_{02} + p_T^0 T_{02}\right)\left(k_\beta v_1 + ik_z w_1\right) \\
&+4\mu^0 k_\beta k_{2\beta}\left(v_1 v_{02} + \tfrac{1}{2}u_1 u_{02}\right) + \left(\mu_{\phi\phi}^0\phi_1\phi_{02} + \mu_{TT}^0 T_1 T_{02} + \mu_{\phi T}^0\phi_1 T_{02} + \mu_{\phi T}^0\phi_{02}T_1\right) \\
&+2k_{2\beta}\left(\mu_\phi^0\phi_1 + \mu_T^0 T_1\right)u_{02} + 2k_\beta u_1\left(\mu_\phi^0\phi_{02} + \mu_T^0 T_{02}\right) \\
&+\mu^0 k_{2\beta}\left(k_\beta w_1 - 2ik_z v_1\right)w_{02} + k_{2\beta}k_\beta\mu^0 w_{02}w_1 + \lambda^0 k_{2\beta}\left(2k_\beta v_1 v_{02} + 2ik_z v_{02}w_1\right) \\
&\left.-\left(\mathcal{D}_{\phi\phi}^0\phi_1\phi_{02} + \mathcal{D}_{TT}^0 T_1 T_{02} + \mathcal{D}_{\phi T}^0\phi_1 T_{02} + \mathcal{D}_{\phi T}^0\phi_{02}T_1\right)\right] \\
&+\tfrac{2T_m^{02}}{dim\phi^0}\left[-\tfrac{1}{H^2}\left(k_\beta^2 + k_z^2\right)T_1\kappa_T^0 + \left(\mu_{TT}^0 T_1 + \mu_{\phi T}^0\phi_1\right) - \left(\mathcal{D}_{TT}^0 T_1 + \mathcal{D}_{\phi T}^0\phi_1\right)\right. \\
&\left.-p_T^0\left(k_\beta v_1 + ik_z w_1\right) + 2\mu_T^0 k_\beta u_1\right] - \tfrac{1}{\phi^0}\left(2a^{(0)}\phi_1 T_m^{02} + ik_z\phi^0 T_1 w_m^{02}\right)
\end{aligned}
$$

$$
\begin{aligned}
C_{13}^{5\beta 3} \;=\;& -\tfrac{1}{4}\Big[\tfrac{k_\beta}{\phi^0}(\phi_1 v_1 \tilde{T}_1 + \tilde{\phi}_1 v_1 T_1 + \phi_1 \tilde{v}_1 T_1) \\
& + \tfrac{2}{dim\phi^0}\Big\{\tfrac{k_\beta^2}{H^2}\Big(2T_1(\kappa^0_{\phi\phi}\tilde{\phi}_1\phi_1 + \kappa^0_{TT}\tilde{T}_1 T_1 + \kappa^0_{\phi T}\tilde{\phi}_1 T_1 + \kappa^0_{\phi T}\tilde{T}_1\phi_1) \\
& + \tilde{T}_1(\kappa_{\phi\phi}\phi_1^2 + \kappa^0_{TT}T_1^2 + 2\kappa^0_{\phi T}\phi_1 T_1)\Big)\Big\} \\
& + (\mu^0_\phi\phi_1 + \mu^0_T T_1)\Big(2k_z^2(u_1\tilde{u}_1 + v_1\tilde{v}_1) + 2k_\beta^2 w_1\tilde{w}_1 - 2ik_z k_\beta(v_1\tilde{w}_1 - \tilde{v}_1 w_1)\Big) \\
& + (\mu^0_\phi\tilde{\phi}_1 + \mu^0_T\tilde{T}_1)(-k_z^2(v_1^2 + u_1^2) + k_\beta^2 w_1^2 - 2ik_z k_\beta v_1 w_1)\Big] \\
& + \tfrac{1}{2dim\phi^0}\Big[\tfrac{1}{H^2}\Big\{-k_z^2\Big(\kappa^0_{\phi\phi}\phi_1\Big(3\tilde{\phi}_1 T_1 - \tfrac{1}{2}\tilde{T}_1\phi_1\Big) \\
& + \kappa^0_{TT}T_1\Big(3\tilde{T}_1 T_1 - \tfrac{1}{2}\tilde{T}_1 T_1\Big) + \kappa^0_{\phi T}\Big(2T_1\phi_1\tilde{T}_1 + 3T_1^2\tilde{\phi}_1\Big)\Big) \\
& - k_\beta^2\Big(\kappa^0_{\phi\phi}\phi_1(T_1\tilde{\phi}_1 + \tfrac{1}{2}\tilde{T}_1\phi_1) + \tfrac{3}{2}\kappa^0_{TT}\tilde{T}_1 T_1^2 + \kappa^0_{\phi T}T_1(2\phi_1\tilde{T}_1 + T_1\tilde{\phi}_1)\Big)\Big\} \\
& - \Big(\tfrac{1}{2}p^0_{\phi\phi}\phi_1^2 + \tfrac{1}{2}T_1^2 + p^0_{\phi T}\phi_1 T_1\Big)(k_\beta\tilde{v}_1 - ik_z\tilde{w}_1) \\
& - (p^0_{\phi\phi}\tilde{\phi}\phi_1 + p^0_{TT}\tilde{T}_1 T_1 + p^0_{\phi T}\tilde{\phi}T_1 + p^0_{\phi T}\phi_1\tilde{T}_1)(k_\beta v_1 + ik_z w_1) \\
& + 2(\mu^0_\phi\phi_1 + \mu^0_T T_1)(2k_\beta^2 v_1\tilde{v}_1 + 2k_z^2 w_1\tilde{w}_1 + k_\beta u_1\tilde{u}_1) \\
& + (\mu^0_\phi\tilde{\phi}_1 + \mu^0_T\tilde{T}_1)(2k_\beta^2 v_1^2 - 2k_z^2 w_1^2 + k_\beta^2 u_1^2) \\
& + \tfrac{1}{2}\Big(\mu^0_{\phi\phi\phi}\phi_1^2\tilde{\phi}_1 + \mu^0_{TTT}T_1^2\tilde{T}_1 + \mu^0_{\phi\phi T}(\phi_1^2\tilde{T}_1 + 2\tilde{\phi}_1\phi_1 T_1) + \mu^0_{\phi TT}(T_1^2\tilde{\phi}_1 + 2\phi_1\tilde{T}_1 T_1)\Big) \\
& + 2k_\beta\Big(\tfrac{1}{2}\mu^0_{\phi\phi}\phi_1^2 + \tfrac{1}{2}\mu^0_{TT}T_1^2 + \mu^0_{\phi T}\phi_1 T_1\Big)\tilde{u}_1 \\
& + 2k_\beta\Big(\mu^0_{\phi\phi}\phi_1\tilde{\phi}_1 + \mu^0_{TT}T_1\tilde{T}_1 + \mu^0_{\phi T}\tilde{\phi}_1 T_1 + \mu^0_{\phi T}\phi_1\tilde{T}_1\Big)u_1 \\
& + \Big(\lambda^0_\phi\phi_1 + \lambda^0_T T_1\Big)\Big(2k_\beta^2 v_1\tilde{v}_1 + 2k_z^2 w_1\tilde{w}_1 - 2ik_z k_\beta(v_1\tilde{w}_1 - \tilde{v}_1 w_1)\Big) \\
& + (\lambda^0_\phi\tilde{\phi}_1 + \lambda^0_T\tilde{T}_1)(k_\beta^2 v_1^2 - k_z^2 w_1^2 + 2ik_z k_\beta v_1 w_1) \\
& - \tfrac{1}{2}\Big(\mathcal{D}^0_{\phi\phi\phi}\phi_1^2\tilde{\phi}_1 + \mathcal{D}^0_{TTT}T_1^2\tilde{T}_1 + \mathcal{D}^0_{\phi\phi T}(\phi_1^2\tilde{T}_1 + 2\tilde{\phi}_1\phi_1 T_1) + \mathcal{D}^0_{\phi TT}(T_1^2\tilde{\phi}_1 + 2\phi_1\tilde{T}_1 T_1)\Big)\Big] \\
C_{13}^{5\beta 1} \;=\;& \tfrac{1}{4}\Big[\tfrac{k_\beta}{\phi^0}(\phi_1 v_1\tilde{T}_1 + \tilde{\phi}_1 v_1 T_1 + \phi_1\tilde{v}_1 T_1) \\
& + \tfrac{2}{dim\phi^0}\Big\{\tfrac{k_\beta^2}{H^2}\Big(2T_1(\kappa^0_{\phi\phi}\tilde{\phi}_1\phi_1 + \kappa^0_{TT}\tilde{T}_1 T_1 + \kappa^0_{\phi T}\tilde{\phi}_1 T_1 + \kappa^0_{\phi T}\tilde{T}_1\phi_1) \\
& + \tilde{T}_1(\kappa_{\phi\phi}\phi_1^2 + \kappa^0_{TT}T_1^2 + 2\kappa^0_{\phi T}\phi_1 T_1)\Big)\Big\} \\
& + (\mu^0_\phi\phi_1 + \mu^0_T T_1)\Big(2k_z^2(u_1\tilde{u}_1 + v_1\tilde{v}_1) + 2k_\beta^2 w_1\tilde{w}_1 - 2ik_z k_\beta(v_1\tilde{w}_1 - \tilde{v}_1 w_1)\Big) \\
& + (\mu^0_\phi\tilde{\phi}_1 + \mu^0_T\tilde{T}_1)(-k_z^2(v_1^2 + u_1^2) + k_\beta^2 w_1^2 - 2ik_z k_\beta v_1 w_1)\Big] \\
& + \tfrac{3}{2dim\phi^0}\Big[\tfrac{1}{H^2}\Big\{-k_z^2\Big(\kappa^0_{\phi\phi}\phi_1\Big(3\tilde{\phi}_1 T_1 - \tfrac{1}{2}\tilde{T}_1\phi_1\Big) \\
& + \kappa^0_{TT}T_1\Big(3\tilde{T}_1 T_1 - \tfrac{1}{2}\tilde{T}_1 T_1\Big) + \kappa^0_{\phi T}\Big(2T_1\phi_1\tilde{T}_1 + 3T_1^2\tilde{\phi}_1\Big)\Big) \\
& - k_\beta^2\Big(\kappa^0_{\phi\phi}\phi_1(T_1\tilde{\phi}_1 + \tfrac{1}{2}\tilde{T}_1\phi_1) + \tfrac{3}{2}\kappa^0_{TT}\tilde{T}_1 T_1^2 + \kappa^0_{\phi T}T_1(2\phi_1\tilde{T}_1 + T_1\tilde{\phi}_1)\Big)\Big\} \\
& - \Big(\tfrac{1}{2}p^0_{\phi\phi}\phi_1^2 + \tfrac{1}{2}T_1^2 + p^0_{\phi T}\phi_1 T_1\Big)(k_\beta\tilde{v}_1 - ik_z\tilde{w}_1) \\
& - (p^0_{\phi\phi}\tilde{\phi}\phi_1 + p^0_{TT}\tilde{T}_1 T_1 + p^0_{\phi T}\tilde{\phi}T_1 + p^0_{\phi T}\phi_1\tilde{T}_1)(k_\beta v_1 + ik_z w_1) \\
& + 2(\mu^0_\phi\phi_1 + \mu^0_T T_1)(2k_\beta^2 v_1\tilde{v}_1 + 2k_z^2 w_1\tilde{w}_1 + k_\beta u_1\tilde{u}_1) \\
& + (\mu^0_\phi\tilde{\phi}_1 + \mu^0_T\tilde{T}_1)(2k_\beta^2 v_1^2 - 2k_z^2 w_1^2 + k_\beta^2 u_1^2) \\
& + \tfrac{1}{2}\Big(\mu^0_{\phi\phi\phi}\phi_1^2\tilde{\phi}_1 + \mu^0_{TTT}T_1^2\tilde{T}_1 + \mu^0_{\phi\phi T}(\phi_1^2\tilde{T}_1 + 2\tilde{\phi}_1\phi_1 T_1) + \mu^0_{\phi TT}(T_1^2\tilde{\phi}_1 + 2\phi_1\tilde{T}_1 T_1)\Big) \\
& + 2k_\beta\Big(\tfrac{1}{2}\mu^0_{\phi\phi}\phi_1^2 + \tfrac{1}{2}\mu^0_{TT}T_1^2 + \mu^0_{\phi T}\phi_1 T_1\Big)\tilde{u}_1 \\
& + 2k_\beta\Big(\mu^0_{\phi\phi}\phi_1\tilde{\phi}_1 + \mu^0_{TT}T_1\tilde{T}_1 + \mu^0_{\phi T}\tilde{\phi}_1 T_1 + \mu^0_{\phi T}\phi_1\tilde{T}_1\Big)u_1 \\
& + \Big(\lambda^0_\phi\phi_1 + \lambda^0_T T_1\Big)\Big(2k_\beta^2 v_1\tilde{v}_1 + 2k_z^2 w_1\tilde{w}_1 - 2ik_z k_\beta(v_1\tilde{w}_1 - \tilde{v}_1 w_1)\Big) \\
& + (\lambda^0_\phi\tilde{\phi}_1 + \lambda^0_T\tilde{T}_1)(k_\beta^2 v_1^2 - k_z^2 w_1^2 + 2ik_z k_\beta v_1 w_1) \\
& - \tfrac{1}{2}\Big(\mathcal{D}^0_{\phi\phi\phi}\phi_1^2\tilde{\phi}_1 + \mathcal{D}^0_{TTT}T_1^2\tilde{T}_1 + \mathcal{D}^0_{\phi\phi T}(\phi_1^2\tilde{T}_1 + 2\tilde{\phi}_1\phi_1 T_1) + \mathcal{D}^0_{\phi TT}(T_1^2\tilde{\phi}_1 + 2\phi_1\tilde{T}_1 T_1)\Big)\Big]
\end{aligned}
$$

CHAPTER 9

THEORY FOR MODE INTERACTION: COUPLED LANDAU EQUATIONS

9.1 Introduction

Examples of mode interactions due to linear resonance are shown in figure 9.1. The variation of growth rate with Couette gap H is shown in figure 9.1 for mode numbers $\beta = 1$, 2, 3 and 4. The circles represent points where two modes cross each other and beyond that a higher mode becomes least stable mode until next crossing. For parameters denoted by circles, the single

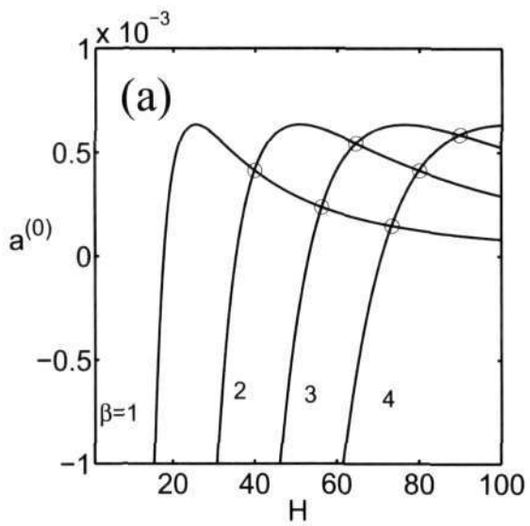

Figure 9.1: Variation of growth rate with scaled Couette gap for $\beta = 1, 2, 3$ and 4 with $\phi^0 = 0.3$ and $e = 0.8$. The mode crossing are shown by circles. The Carnahan-Starling radial distribution function (2.13) for $\phi_{max} = 0.65$ are used.

Landau equation description is not valid. Near such resonance points we need a theory for mode interactions leading to coupled Landau equations.

Davey & Nguyen (1971) have shown that the Watson's method encounters mean flow resonance in subcritical conditions. Later Mizushima & Gotoh (1985) resolved this problem by considering coupled Landau equations using the amplitudes of the fundamental mode and the mean flow distortion. Another kind of resonance, e.g. $1:2$ wave number resonance, between waves of different wave numbers are also possible as discussed by Fujimura & Mizushima (1985), Proctor & Jones (1988) and Fujimura (1992).

This chapter begins with a general derivation of coupled Landau equations, §9.2.1, related to two non-resonating waves having growth rates of two modes close to zero. It was shown in chapters 5 and 6 that the granular Couette flow admits various types of resonances, namely, 1:2

wave resonance and mean flow resonance. Sections §9.3 and §9.4 cover the topics of 1:2 and mean flow resonances in detail (Knobloch & Guckenheimer 1983; Coullet & Spiegel 1983; Guckenheimer & Holmes 1983; Mizushima & Gotoh 1985; Dangelmayr 1986; Proctor & Jones 1988; Fujimura 1992; Dawes & Proctor 2008; Guba & Worster 2010).

The weakly nonlinear theory for the streamwise independent flow using the analytical solution of linear problem has been discussed in chapter 5 (Shukla & Alam 2011). In the framework of previously derived analytical solutions for streamwise independent flow, we derive the analytical expressions for the coefficients of coupled Landau equations in §9.5 for non-resonating modes.

This chapter is organized as follows. The expansion formalism and derivations of coupled Landau equations for interactions of non-resonating waves are given §9.2. The derivation of coupled Landau equations for interactions of resonating modes having the wavenumbers ratio 1:2 is given in §9.3. The mean flow resonance interaction and the corresponding coupled Landau equations are derived in §9.4. Analytical solutions for mode interactions (non-resonating) of the streamwise independent 2D granular plane Couette flow are developed in §9.5. The conclusions are given in 9.6.

9.2 Interaction of Non-resonating Waves

9.2.1 Expansion Formalism

The nonlinear disturbance equations can be written as (cf. Eqns. (3.6) and (4.14)):

$$\left(\frac{\partial}{\partial t} - \mathcal{L}\right) X = \mathcal{N}_2 + \mathcal{N}_3 + \mathcal{N}_4 + \mathcal{N}_5. \tag{9.1}$$

The disturbances can be decomposed as a linear combination of the critical modes, Φ, corresponding to two interacting modes (for example, interactions of pure spanwise disturbances with the one dimensional shearbanding modes) and infinitely many noncritical modes, Ψ, as defined below:

$$X(x,y,t) \;=\; \Phi(x,y,t) + \Psi(x,y,t). \tag{9.2}$$

From the linear stability theory we can define Φ as (cf. Eqn. (4.26))

$$\Phi \;=\; \mathscr{A}_1(t)E_1X^{[1;1]}(y) + \mathscr{A}_2(t)E_2Y^{[1;1]}(y) + \text{c.c}, \tag{9.3}$$

where $X^{[1;1]}$ and $Y^{[1;1]}$ are the eigenfunctions (fundamental modes) of the linear problems associated with two interacting modes which satisfy the following eigenvalue problems:

$$L_{10}X^{[1;1]} \;=\; c_1X^{[1;1]} \qquad \text{and} \qquad L_{01}Y^{[1;1]} = c_2Y^{[1;1]}, \tag{9.4}$$

respectively, with c_1 and c_2 being the corresponding eigenvalues. Here $E_1 = e^{ik_{x_1}+c_1t}$ and $E_2 = e^{ik_{x_1}+c_1t}$ (Eqn. 9.3) are the exponential contributions of the critical modes. Recall from §4.3 that the fundamental mode is the eigenfunction associated with the least stable eigenvalue.

Similar to the single mode analysis as discussed in chapter 4, (§4.3), we can express solution X in terms of generalized Fourier series:

$$X(x,y,t) = \sum_{k=-\infty}^{\infty}\left(X^{(k)}E_1^k + Y^{(k)}E_2^k\right) + \left[\sum_{i,j\geq 0, i=j\neq 0}^{\infty} Z^{(ij)}E_1^iE_2^j + c.c.\right], \tag{9.5}$$

where $X^{(k)} \equiv X^{(k)}(y)$, $Y^{(k)} \equiv Y^{(k)}(y)$ and $Z^{(ij)} \equiv Z^{(ij)}(y)$ represent complex valued functions

originated from the interactions of fundamentals of interacting modes. The pure interactions of first mode with amplitude $\mathscr{A}_1$ and the second mode with amplitude $\mathscr{A}_2$ are represented by series $X^{(k)}$ and $Y^{(k)}$, respectively. The interactions of fundamentals of $X^{(k)}$ and $Y^{(k)}$ generate mixed type modes which are represented by a series $Z^{(ij)}$. Hereafter we refer modes related to $X^{(k)}$, $Y^{(k)}$ and $Z^{(ij)}$ by X, Y and Z modes, respectively.

Substituting above ansatz (9.5) into equation (9.1) and equating the like-order, E^n, terms, we get:

$$\begin{aligned}
\left(\frac{d}{dt}-c_1\right)\mathscr{A}_1 X^{[1;1]} &= \mathcal{N}_2(X^{(1)},X^{(0)})+\mathcal{N}_2(X^{(0)},X^{(1)})+\mathcal{N}_2(\tilde{X}^{(1)},X^{(2)})\\
&\quad +\mathcal{N}_2(X^{(2)},\tilde{X}^{(1)})+\mathcal{N}_2(X^{(1)},Y^{(0)})+\mathcal{N}_2(Y^{(0)},X^{(1)})\\
&\quad +\mathcal{N}_2(Z^{(11)},\tilde{Y}^{(1)})+\mathcal{N}_2(\tilde{Y}^{(1)},Z^{(11)})+\mathcal{N}_2(Y^{(1)},Z^{(1-1)})\\
&\quad +\mathcal{N}_2(Z^{(1-1)},Z^{(1)})+\mathcal{N}_3(\tilde{X}^{(1)},X^{(1)},X^{(1)})\\
&\quad +\mathcal{N}_3(X^{(1)},\tilde{X}^{(1)},X^{(1)})+\mathcal{N}_3(X^{(1)},X^{(1)},\tilde{X}^{(1)})+\ldots, \qquad (9.6)\\
\left(\frac{d}{dt}-c_2\right)\mathscr{A}_2 Y^{[1;1]} &= \mathcal{N}_2(Y^{(1)},Y^{(0)})+\mathcal{N}_2(Y^{(0)},Y^{(1)})+\mathcal{N}_2(\tilde{Y}^{(1)},Y^{(2)})\\
&\quad +\mathcal{N}_2(Y^{(2)},\tilde{Y}^{(1)})+\mathcal{N}_2(Y^{(1)},X^{(0)})+\mathcal{N}_2(X^{(0)},Y^{(1)})\\
&\quad +\mathcal{N}_2(Z^{(11)},\tilde{X}^{(1)})+\mathcal{N}_2(\tilde{X}^{(1)},Z^{(11)})+\mathcal{N}_2(X^{(1)},Z^{(-11)})\\
&\quad +\mathcal{N}_2(Z^{(-11)},X^{(1)})+\mathcal{N}_3(\tilde{Y}^{(1)},Y^{(1)},Y^{(1)})\\
&\quad +\mathcal{N}_3(Y^{(1)},\tilde{Y}^{(1)},Y^{(1)})+\mathcal{N}_3(Y^{(1)},Y^{(1)},\tilde{Y}^{(1)})+\ldots, \qquad (9.7)\\
\left(\frac{d}{dt}-\mathcal{L}\right)\Psi(y,t) &= \text{nonlinear terms.} \qquad (9.8)
\end{aligned}$$

The first two equations (9.6)-(9.7) are the evolution equations for the critical mode Φ, and the last equation (9.8) for the noncritical/passive modes, Ψ, is called enslaved or passive equation [cf. (4.30), (4.31)] (Carr 1981; Shukla & Alam 2009).

In order to reduce the above set of equations, (9.6)-(9.8), into ordinary differential equations and subsequently to reduce the dimensionality of the system, we use center manifold theorem (Carr 1981; Wiggins 1990) which states that the dynamics in the neighborhood of the critical conditions is governed by a low dimensional system which can be obtained by projecting the infinite dimensional non-critical modes onto critical modes. Therefore all noncritical modes, which are represented by Ψ, can be written as a function of critical modes, i.e. $\Psi = \Psi(\Phi)$. Following theorem 3 of Carr (1981), we can approximate noncritical modes as Taylor series as given below:

$$\left.\begin{aligned}
X^{(0)}(y,t) &= |\mathscr{A}_1|^2\left(X^{[0;2]}(y)+|\mathscr{A}_1|^2 X^{[0;4]}(y)+\ldots\right)\\
X^{(1)}(y,t) &= \mathscr{A}_1\left(X^{[1;1]}(y)+|\mathscr{A}_1|^2 X^{[1;3]}(y)+\ldots\right)\\
X^{(2)}(y,t) &= \mathscr{A}_1^2\left(X^{[2;2]}(y)+|\mathscr{A}_1|^2 X^{[2;4]}(y)+\ldots\right)\\
Y^{(0)}(y,t) &= |\mathscr{A}_2|^2\left(Y^{[0;2]}(y)+|\mathscr{A}_2(t)|^2 Y^{[0;4]}(y)+\ldots\right)\\
Y^{(1)}(y,t) &= \mathscr{A}_2\left(Y^{[1;1]}(y)+|\mathscr{A}_2|^2 Y^{[1;3]}(y)+\ldots\right)\\
Y^{(2)}(y,t) &= \mathscr{A}_2^2\left(Y^{[2;2]}(y)+|\mathscr{A}_2|^2 Y^{[2;4]}(y)+\ldots\right)\\
Z^{(1-1)}(y,t) &= \mathscr{A}_1\tilde{\mathscr{A}}_2\left(Z_{1-1}^{[0;2]}(y)+|\mathscr{A}_1|^2 Z_{1-1X}^{[0;4]}(y)+|\mathscr{A}_2|^2 Z_{1-1Y}^{[0;4]}(y)+\ldots\right)\\
Z^{(-11)}(y,t) &= \tilde{\mathscr{A}}_1\mathscr{A}_2\left(Z_{-11}^{[0;2]}(y)+|\mathscr{A}_1|^2 Z_{-11X}^{[0;4]}(y)+|\mathscr{A}_2|^2 Z_{-11Y}^{[0;4]}(y)+\ldots\right)\\
Z^{(10)}(y,t) &= \mathscr{A}_1\left(|\mathscr{A}_2|^2 Z_{10Y}^{[1;3]}(y)+|\mathscr{A}_2|^4 Z_{10Y}^{[1;5]}(y)+\ldots\right)\\
Z^{(01)}(y,t) &= \mathscr{A}_2\left(|\mathscr{A}_1|^2 Z_{01X}^{[1;3]}(y)+|\mathscr{A}_1|^4 Z_{01X}^{[1;5]}(y)+\ldots\right)\\
Z^{(11)}(y,t) &= \mathscr{A}_1\mathscr{A}_2\left(Z_{11}^{[2;2]}(y)+|\mathscr{A}_1|^2 Z_{11X}^{[2;4]}(y)+|\mathscr{A}_2|^2 Z_{11Y}^{[2;4]}(y)+\ldots\right)
\end{aligned}\right\}, \qquad (9.9)$$

where the subscripts X and Y refer to mean flow contributions from X and Y modes, respectively. In the notation $Z_{ij}^{[i+j;m]}$ the subscripts i and j denote the powers of E_1 or $\mathscr{A}_1$ and E_2 or $\mathscr{A}_2$, and the superscript m represents the sum of the powers of amplitudes of X and Y modes. The definitions of pure and mixed modes are given in figure 9.2.

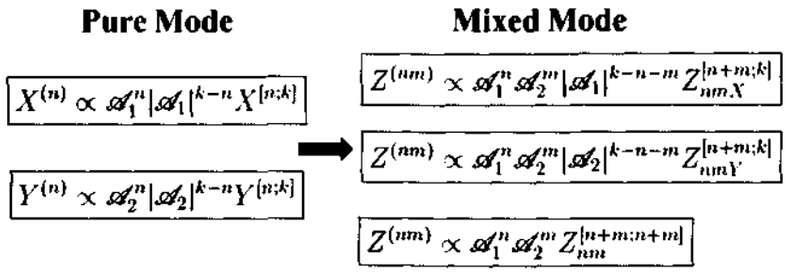

Figure 9.2: Definition of Fourier modes $X^{(k)}$, $Y^{(k)}$ and $Z^{(nm)}$.

Now substituting (9.9) into (9.6) and (9.7) and simplifying the resulting expression in terms of like amplitudes, we get:

$$\left.\begin{array}{rcl} \left(\frac{d}{dt} - c_1\right)\mathscr{A}_1 X^{[1;1]} &=& G_{13}^{11}\mathscr{A}_1|\mathscr{A}_1|^2 + G_{13}^{12}\mathscr{A}_1|\mathscr{A}_2|^2 + \ldots \\ \left(\frac{d}{dt} - c_2\right)\mathscr{A}_2 Y^{[1;1]} &=& G_{13}^{21}\mathscr{A}_2|\mathscr{A}_1|^2 + G_{13}^{22}\mathscr{A}_2|\mathscr{A}_2|^2 + \ldots \end{array}\right\}, \tag{9.10}$$

where

$$\left.\begin{array}{rcl} G_{13}^{11} &=& \Big[N_2(X^{[0;2]}, X^{[1;1]}) + N_2(X^{[1;1]}, X^{[0;2]}) + N_2(\tilde{X}^{[1;1]}, X^{[2;2]}) \\ && +N_2(X^{[2;2]}, \tilde{X}^{[1;1]}) + N_3(\tilde{X}^{[1;1]}, X^{[1;1]}, X^{[1;1]}) \\ && +N_3(X^{[1;1]}, \tilde{X}^{[1;1]}, X^{[1;1]}) + N_3(X^{[1;1]}, X^{[1;1]}, \tilde{X}^{[1;1]})\Big] \\ G_{13}^{12} &=& \Big[N_2(X^{[1;1]}, Y^{[0;2]}) + N_2(Y^{[0;2]}, X^{[1;1]}) + N_2(Z_{11}^{[2;2]}, \tilde{Y}^{[1;1]}) \\ && +N_2(\tilde{Y}^{[1;1]}, Z_{11}^{[2;2]}) + N_2(Z_{1-1}^{[0;2]}, Y^{[1;1]}) + N_2(Y^{[1;1]}, Z_{1-1}^{[0;2]}) \\ && +N_3(X^{[1;1]}, Y^{[1;1]}, \tilde{Y}^{[1;1]}) + N_3(X^{[1;1]}, \tilde{Y}^{[1;1]}, Y^{[1;1]}) \\ && +N_3(Y^{[1;1]}, X^{[1;1]}, \tilde{Y}^{[1;1]}) + N_3(Y^{[1;1]}, \tilde{Y}^{[1;1]}, X^{[1;1]}) \\ && +N_3(\tilde{Y}^{[1;1]}, X^{[1;1]}, Y^{[1;1]}) + N_3(\tilde{Y}^{[1;1]}, Y^{[1;1]}, X^{[1;1]})\Big] \\ G_{13}^{21} &=& \Big[N_2(Y^{[1;1]}, X^{[0;2]}) + N_2(X^{[0;2]}, Y^{[1;1]}) + N_2(Z_{11}^{[2;2]}, \tilde{X}^{[1;1]}) \\ && +N_2(\tilde{X}^{[1;1]}, Z_{11}^{[2;2]}) + N_2(Z_{-11}^{[0;2]}, X^{[1;1]}) + N_2(X^{[1;1]}, Z_{-11}^{[0;2]}) \\ && +N_3(Y^{[1;1]}, X^{[1;1]}, \tilde{X}^{[1;1]}) + N_3(Y^{[1;1]}, \tilde{X}^{[1;1]}, X^{[1;1]}) \\ && +N_3(X^{[1;1]}, Y^{[1;1]}, \tilde{X}^{[1;1]}) + N_3(X^{[1;1]}, \tilde{X}^{[1;1]}, Y^{[1;1]}) \\ && +N_3(\tilde{X}^{[1;1]}, X^{[1;1]}, Y^{[1;1]}) + N_3(\tilde{X}^{[1;1]}, Y^{[1;1]}, X^{[1;1]})\Big] \\ G_{13}^{22} &=& \Big[N_2(Y^{[0;2]}, Y^{[1;1]}) + N_2(Y^{[1;1]}, Y^{[0;2]}) + N_2(\tilde{Y}^{[1;1]}, Y^{[2;2]}) \\ && +N_2(Y^{[2;2]}, \tilde{Y}^{[1;1]}) + N_3(\tilde{Y}^{[1;1]}, Y^{[1;1]}, Y^{[1;1]}) \\ && +N_3(Y^{[1;1]}, \tilde{Y}^{[1;1]}, Y^{[1;1]}) + N_3(Y^{[1;1]}, Y^{[1;1]}, \tilde{Y}^{[1;1]})\Big] \end{array}\right\} \tag{9.11}$$

9.2.2 Coupled Landau Equations

The coupled Landau equations can be derived by taking the inner product of Eqn. (9.10) with the adjoint linear eigenfunctions related to X mode and Y mode:

$$\frac{d\mathscr{A}_1}{dt} = c_1\mathscr{A}_1 + \lambda_{11}\mathscr{A}_1|\mathscr{A}_1|^2 + \lambda_{12}\mathscr{A}_1|\mathscr{A}_2|^2, \tag{9.12}$$

$$\frac{d\mathscr{A}_2}{dt} = c_2\mathscr{A}_2 + \lambda_{21}\mathscr{A}_2|\mathscr{A}_1|^2 + \lambda_{22}\mathscr{A}_2|\mathscr{A}_2|^2, \tag{9.13}$$

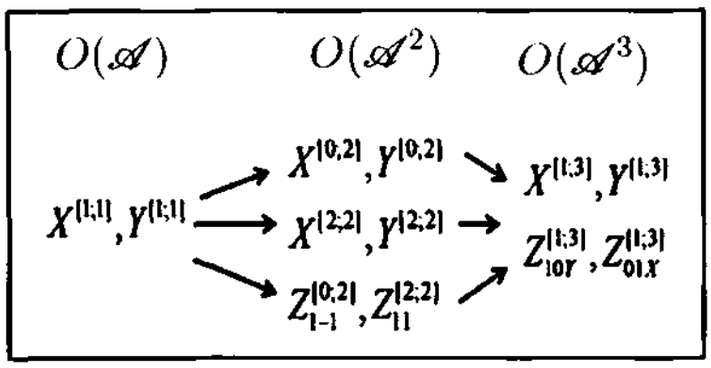

Figure 9.3: Sketch of nonzero functions for coupled Landau equations at different orders where arrows indicate the dependence of these functions on other functions.

where

$$\lambda_{11} = \langle \tilde{X}^\dagger, G^{11}_{13}\rangle / \langle \tilde{X}^\dagger, X^{[1;1]}\rangle, \quad \lambda_{12} = \langle \tilde{X}^\dagger, G^{12}_{13}\rangle / \langle \tilde{X}^\dagger, X^{[1;1]}\rangle \tag{9.14}$$

$$\lambda_{21} = \langle \tilde{Y}^\dagger, G^{21}_{13}\rangle / \langle \tilde{Y}^\dagger, Y^{[1;1]}\rangle, \quad \lambda_{22} = \langle \tilde{Y}^\dagger, G^{22}_{13}\rangle / \langle \tilde{Y}^\dagger, Y^{[1;1]}\rangle. \tag{9.15}$$

Here $X^\dagger$ and $Y^\dagger$ denote the adjoint eigenfunctions corresponding to $X^{[1;1]}$ and $Y^{[1;1]}$, respectively. From equation (9.11) we see that G^{11}_{13}, G^{12}_{13}, G^{21}_{13} and G^{22}_{13} are functions of higher order harmonics ($X^{[0;2]}$, $X^{[2;2]}$, $Y^{[0;2]}$, $Y^{[2;2]}$, $Z^{[2;2]}_{11}$ and $Z^{[2;2]}_{1-1}$) of interacting modes (enslaved modes) which can be obtained by substituting (9.9) into (9.8) and equating different order equations:

$$\left.\begin{array}{lll}
O(|\mathscr{A}_1|^2): & (2c_{1r} - L_{00})X^{[0;2]} = & N_2(X^{[1;1]}, \tilde{X}^{[1;1]}) + N_2(\tilde{X}^{[1;1]}, X^{[1;1]}) \\
O(\mathscr{A}_1^2): & (2c_1 - L_{20})X^{[2;2]} = & N_2(X^{[1;1]}, X^{[1;1]}) \\
O(|\mathscr{A}_2|^2): & (2c_{2r} - L_{00})Y^{[0;2]} = & N_2(Y^{[1;1]}, \tilde{Y}^{[1;1]}) + N_2(\tilde{Y}^{[1;1]}, Y^{[1;1]}) \\
O(\mathscr{A}_2^2): & (2c_2 - L_{02})Y^{[2;2]} = & N_2(Y^{[1;1]}, Y^{[1;1]}) \\
O(\mathscr{A}_1\bar{\mathscr{A}}_2): & ((\bar{c}_1 + c_2) - L_{-11})Z^{[0;2]}_{-11} = & N_2(Y^{[1;1]}, \tilde{X}^{[1;1]}) + N_2(\tilde{X}^{[1;1]}, Y^{[1;1]}) \\
O(\mathscr{A}_1\bar{\mathscr{A}}_2): & ((c_1 + \bar{c}_2) - L_{1-1})Z^{[0;2]}_{1-1} = & N_2(\tilde{Y}^{[1;1]}, X^{[1;1]}) + N_2(X^{[1;1]}, \tilde{Y}^{[1;1]}) \\
O(\mathscr{A}_1\mathscr{A}_2): & ((c_1 + c_2) - L_{11})Z^{[2;2]}_{11} = & N_2(X^{[1;1]}, Y^{[1;1]}) + N_2(Y^{[1;1]}, X^{[1;1]}) \\
O(\mathscr{A}_1|\mathscr{A}_1|^2): & ((c_1 + 2c_{1r}) - L_{10})X^{[1;3]} = & -\lambda_{11}X^{[1;1]} + G^{11}_{13} \\
O(\mathscr{A}_2|\mathscr{A}_2|^2): & ((c_2 + 2c_{2r}) - L_{01})Y^{[1;3]} = & -\lambda_{22}Y^{[1;1]} + G^{22}_{13} \\
O(\mathscr{A}_1|\mathscr{A}_2|^2): & ((c_1 + 2c_{2r}) - L_{10})Z^{[1;3]}_{10Y} = & -\lambda_{12}X^{[1;1]} + G^{12}_{13} \\
O(\mathscr{A}_2|\mathscr{A}_1|^2): & ((c_2 + 2c_{1r}) - L_{01})Z^{[1;3]}_{01X} = & -\lambda_{21}Y^{[1;1]} + G^{21}_{13}
\end{array}\right\} \tag{9.16}$$

where $L_{mn} = \mathcal{L}(\partial_x \to i(mk_{x_1} + nk_{x_2}), \partial/\partial y \to d/dy)$. We have used (9.12) and (9.13) to derive the above equations. The non-zero harmonics and distortions, which are needed to calculate the coefficients of coupled Landau equations (9.12)-(9.13), are shown in figure 9.3 where the arrows direct to the higher order harmonics and distortions.

9.3 Theory for 1:2 Wave Resonance

In §9.2 we considered the interactions of two non-resonating modes. Let us now consider the case where 1:2 wave number resonance occurs.

9.3.1 Resonance Condition for 1:2 Resonance

We consider two modes at wavenumbers k_{x_1} and k_{x_2} and proportional to $e^{ik_{x_1}x+c_1t}$ and $e^{ik_{x_2}x+c_2t}$, where $k_{x_2} > k_{x_1}$; c_1 and c_2 are complex eigenvalues whose real parts represent growth rates. The condition for $1:2$ resonance is:

$$\frac{k_{x_1}}{k_{x_2}} = \frac{1}{2} \quad \text{and} \quad \frac{c_1}{c_2} = \frac{1}{2}. \tag{9.17}$$

9.3.2 Derivation of Amplitude Equation for 1:2 Resonance

We follow the same procedure as described in the last section for non-resonating modes. Eqns. (9.1)-(9.5) are common for both cases (resonating and non resonating). Substituting (9.5) into (9.1) and equating the like powers of E_1 and E_2 we get:

$$\begin{aligned}
\left(\frac{d}{dt} - c_1\right)\mathscr{A}_1 X^{[1;1]} &= \mathcal{N}_2(X^{(1)}, X^{(0)}) + \mathcal{N}_2(X^{(0)}, X^{(1)}) + \mathcal{N}_2(\tilde{X}^{(1)}, X^{(2)}) \\
&\quad + \mathcal{N}_2(X^{(2)}, \tilde{X}^{(1)}) + \mathcal{N}_2(X^{(1)}, Y^{(0)}) + \mathcal{N}_2(Y^{(0)}, X^{(1)}) \\
&\quad + \mathcal{N}_2(Z^{(11)}, \tilde{Y}^{(1)}) + \mathcal{N}_2(\tilde{Y}^{(1)}, Z^{(11)}) + \mathcal{N}_2(Y^{(1)}, Z^{(1-1)}) \\
&\quad + \mathcal{N}_2(Z^{(1-1)}, Y^{(1)}) + \underline{\mathcal{N}_2(\tilde{X}^{(1)}, Y^{(1)}) + \mathcal{N}_2(Y^{(1)}, \tilde{X}^{(1)})} \\
&\quad + \ldots, \qquad (9.18) \\
\left(\frac{d}{dt} - c_2\right)\mathscr{A}_2 Y^{[1;1]} &= \mathcal{N}_2(Y^{(1)}, Y^{(0)}) + N_2(Y^{(0)}, Y^{(1)}) + \mathcal{N}_2(\tilde{Y}^{(1)}, Y^{(2)}) \\
&\quad + \mathcal{N}_2(Y^{(2)}, \tilde{Y}^{(1)}) + \mathcal{N}_2(Y^{(1)}, X^{(0)}) + \mathcal{N}_2(X^{(0)}, Y^{(1)}) \\
&\quad + \mathcal{N}_2(Z^{(11)}, \tilde{X}^{(1)}) + \mathcal{N}_2(\tilde{X}^{(1)}, Z^{(11)}) + \mathcal{N}_2(X^{(1)}, Z^{(-11)}) \\
&\quad + \mathcal{N}_2(Z^{(-11)}, X^{(1)}) + \underline{\mathcal{N}_2(X^{(1)}, X^{(1)})} + \ldots, \qquad (9.19) \\
\left(\frac{d}{dt} - \mathcal{L}\right)\Psi(y,t) &= \text{nonlinear terms.} \qquad (9.20)
\end{aligned}$$

The underlined terms of (9.18) and (9.19) are due to the resonance (1:2). Owing to these extra terms, the amplitude equation has additional nonlinear terms at quadratic order. The Fourier coefficients $X^{(i)}$, $Y^{(i)}$ and $Z^{(ij)}$ are given in terms of Taylor series as given by (9.9).

Now substituting equation (9.9) into (9.18) and (9.19) and simplifying the resulting expression in terms of amplitude up to cubic order, we get

$$\left(\frac{d}{dt} - c_1\right)\mathscr{A}_1 X^{[1;1]} = G_{13}^{11}\mathscr{A}_1|\mathscr{A}_1|^2 + G_{13}^{12}\mathscr{A}_1|\mathscr{A}_2|^2 + G_{13}^{13}\tilde{\mathscr{A}_1}\mathscr{A}_2, \tag{9.21}$$

$$\left(\frac{d}{dt} - c_2\right)\mathscr{A}_2 Y^{[1;1]} = G_{13}^{21}\mathscr{A}_2|\mathscr{A}_1|^2 + G_{13}^{22}\mathscr{A}_2|\mathscr{A}_2|^2 + G_{13}^{23}\mathscr{A}_1^2. \tag{9.22}$$

The explicit expressions for G_{13}^{11}, G_{13}^{12}, G_{13}^{21} and G_{13}^{22} are given in (9.11) and the nonlinear terms related to quadratic terms in Eqn. (9.21)-(9.22), i.e. G_{13}^{13} and G_{13}^{22}, are given below:

$$G_{13}^{13} = N_2(\tilde{X}^{[1;1]}, Y^{[1;1]}) \quad \text{and} \quad G_{13}^{23} = N_2(X^{[1;1]}, X^{[1;1]}). \tag{9.23}$$

Taking the inner product of above Eqns. (9.21)-(9.22) with adjoint eigenfunctions $X^\dagger$ and $Y^\dagger$, respectively, we get coupled amplitude equations (cf. Eqns. (9.12), (9.13)):

$$\frac{d\mathscr{A}_1}{dt} = c_1\mathscr{A}_1 + \lambda_{11}\mathscr{A}_1|\mathscr{A}_1|^2 + \lambda_{12}\mathscr{A}_1|\mathscr{A}_2|^2 + \lambda_{13}\tilde{\mathscr{A}_1}\mathscr{A}_2, \tag{9.24}$$

$$\frac{d\mathscr{A}_2}{dt} = c_2\mathscr{A}_2 + \lambda_{21}\mathscr{A}_2|\mathscr{A}_1|^2 + \lambda_{22}\mathscr{A}_2|\mathscr{A}_2|^2 + \lambda_{23}\mathscr{A}_1^2, \tag{9.25}$$

where λ_{13} and λ_{23} are additional coefficients at quadratic order due to 1:2 wave number resonance

as defined below:

$$\lambda_{13} = \langle \tilde{X}^\dagger, G_{13}^{13} \rangle / \langle \tilde{X}^\dagger, X^{[1;1]} \rangle, \quad \lambda_{23} = \langle \tilde{Y}^\dagger, G_{13}^{23} \rangle / \langle \tilde{X}^\dagger, Y^{[1;1]} \rangle. \tag{9.26}$$

Here $X^\dagger$ and $Y^\dagger$ are adjoint eigenfunctions of two interacting modes corresponding to $X^{[1;1]}$ and $Y^{[1;1]}$, respectively; the other coefficients are given by equations (9.14) and (9.15). The equations for higher order harmonics can be obtained by substituting (9.9) into (9.20) and equating the coefficients of like powers of amplitude:

$$\left.\begin{array}{rcl} O(\mathscr{A}_1^2) : (2c_1 - L_{20})X^{[2;2]} & = & -\lambda_{13}X^{[1;1]} + N_2(X^{[1;1]}, X^{[1;1]}) \\ O(\mathscr{A}_1\mathscr{A}_2) : ((\tilde{c}_1 + c_2) - L_{-11})Z_{-11}^{[0;2]} & = & -\lambda_{23}Y^{[1;1]} + N_2(Y^{[1;1]}, \tilde{X}^{[1;1]}) \\ & & +N_2(\tilde{X}^{[1;1]}, Y^{[1;1]}) \end{array}\right\}. \tag{9.27}$$

We make use of Eqns. (9.24)-(9.25) to derive Eqn. (9.27). In the case of 1:2 resonance, we have to solve solvability condition at order two (see Eqn. (9.27)). On the other hand, for the non-resonant interaction, the solvability condition appears only at cubic order. In the absence of resonance, $\lambda_{13} \to 0$ and $\lambda_{23} \to 0$ and therefore all the governing equations of the previous section can be attained.

In a similar manner we can derive coupled amplitude equations for 1:3 resonance case. In this case the extra terms appears at cubic order:

$$\frac{d\mathscr{A}_1}{dt} = c_1\mathscr{A}_1 + \lambda_{11}\mathscr{A}_1|\mathscr{A}_1|^2 + \lambda_{12}\mathscr{A}_1|\mathscr{A}_2|^2 + \lambda_{13}\tilde{\mathscr{A}}_1^2\mathscr{A}_2, \tag{9.28}$$

$$\frac{d\mathscr{A}_2}{dt} = c_2\mathscr{A}_2 + \lambda_{21}\mathscr{A}_2|\mathscr{A}_1|^2 + \lambda_{22}\mathscr{A}_2|\mathscr{A}_2|^2 + \lambda_{23}\mathscr{A}_1^3. \tag{9.29}$$

In general, if 1:n resonance occurs for $n = 2, 3, 4, \ldots$, the coupled amplitude equations contain some extra terms at order n (in addition to standard nonlinearities for non-resonant interactions). For a general theory of 1:n resonance, see Dangelmayr (1986), Proctor & Jones (1988) and Dawes & Proctor (2008).

9.4 Theory for Mean Flow Resonance

9.4.1 Resonance Condition

Let us consider two modes at wave numbers k_{x_1} and $k_{x_2} = 0$ and proportional to $e^{ik_{x_1}x + c_1 t}$ and $e^{c_2 t}$; c_1 and c_2 are the complex eigenvalues whose real parts represent growth rates. The condition for the mean flow resonance is

$$2c_{1r} = c_2. \tag{9.30}$$

Here c_2 is real that corresponds to shearbanding mode ($k_{x_2} = 0$). For instance, in a single mode analysis using a mode with wave number k_{x_1}, the governing equation for the second order mean flow distortion can be obtained by substituting $k = 0$ and $n = 2$ into Eqn. (3.39):

$$\left[2a^{(0)} - \mathbf{L}_0\right] X^{[0;2]} = N_2(\tilde{X}^{[1;1]}, X^{[1;1]}) + N_2(X^{[1;1]}, \tilde{X}^{[1;1]}), \tag{9.31}$$

where $\mathbf{L}_0$ is the linear operator at $k_x = 0$ and $a^{(0)} = c_{1r}$. If c_2 is one of the real eigenvalues of operator $\mathbf{L}_0$, the homogeneous problem associated with the above equation has eigensolutions and therefore we need to solve solvability condition (cf. Eqn. (3.44)). This is called mean flow resonance because the fundamental mode with nonzero wave number k_{x_1} interacts with the mean flow distortion mode.

9.4.2 Derivation of Amplitude Equation

In contrast to Eqn. (9.5), the only change for the mean flow resonance is that the amplitude related to second interacting mode A_2 is real. The expansion in this case simplifies to

$$X(x,y,t) = \sum_{k=-\infty}^{\infty} X^{(k)} E_1^k + \sum_{k=-\infty, k\neq 0}^{\infty} Y^{(k)} + \left[\sum_{i,j\geq 0, i=j\neq 0}^{\infty} Z^{(ij)} E_1^i + c.c. \right]. \tag{9.32}$$

Substituting (9.32) into equation (9.1) and separating the equations at each order in amplitude we get:

$$\begin{aligned}
\left(\frac{d}{dt} - c_1\right) \mathscr{A}_1 X^{[1;1]} &= \mathcal{N}_2(X^{(1)}, X^{(0)}) + \mathcal{N}_2(X^{(0)}, X^{(1)}) + \mathcal{N}_2(\tilde{X}^{(1)}, X^{(2)}) + \mathcal{N}_2(X^{(2)}, \tilde{X}^{(1)}) \\
&\quad + \mathcal{N}_2(X^{(1)}, Y^{(2)}) + \mathcal{N}_2(Y^{(2)}, X^{(1)}) + \mathcal{N}_2(Z^{(11)}, Y^{(1)}) \\
&\quad + \mathcal{N}_2(Y^{(1)}, Z^{(11)}) + \mathcal{N}_3(\tilde{X}^{(1)}, X^{(1)}, X^{(1)}) + \mathcal{N}_3(X^{(1)}, \tilde{X}^{(1)}, X^{(1)}) \\
&\quad + \mathcal{N}_3(X^{(1)}, X^{(1)}, \tilde{X}^{(1)}) + \underline{\mathcal{N}_2(X^{(1)}, Y^{(1)}) + \mathcal{N}_2(Y^{(1)}, X^{(1)})} \ldots, \qquad (9.33) \\
\left(\frac{d}{dt} - c_2\right) \mathscr{A}_2 Y^{[1;1]} &= \mathcal{N}_2(Y^{(1)}, Y^{(2)}) + N_2(Y^{(2)}, Y^{(1)}) + \mathcal{N}_2(Y^{(1)}, X^{(0)}) + \mathcal{N}_2(X^{(0)}, Y^{(1)}) \\
&\quad + \mathcal{N}_2(Z^{(11)}, \tilde{X}^{(1)}) + \mathcal{N}_2(\tilde{X}^{(1)}, Z^{(11)}) + \mathcal{N}_2(X^{(1)}, Z^{(-11)}) + \mathcal{N}_2(Z^{(-11)}, X^{(1)}) \\
&\quad + \mathcal{N}_3(Y^{(1)}, Y^{(1)}, Y^{(1)}) + \underline{\mathcal{N}_2(Y^{(1)}, Y^{(1)}) + \mathcal{N}_2(\tilde{X}^{(1)}, X^{(1)})}, \qquad (9.34) \\
\left(\frac{\partial}{\partial t} - \mathcal{L}\right) \Psi &= \text{nonlinear term.} \qquad (9.35)
\end{aligned}$$

The underlined terms of Eqns. (9.33) and (9.34) are due to the mean flow resonance. The complex coefficients of series (9.32) can be written as

$$\left.\begin{aligned}
X^{(0)}(y,t) &= |\mathscr{A}_1|^2 \left(X^{[0;2]} + |\mathscr{A}_1|^2 X^{[0;4]} + \ldots \right) \\
X^{(1)}(y,t) &= \mathscr{A}_1 \left(X^{[1;1]} + |\mathscr{A}_1|^2 X^{[1;3]} + \ldots \right) \\
X^{(2)}(y,t) &= \mathscr{A}_1^2 \left(X^{[2;2]} + |\mathscr{A}_1|^2 X^{[2;4]} + \ldots \right) \\
Y^{(1)}(y,t) &= \mathscr{A}_2 \left(Y^{[1;1]} + \mathscr{A}_2^2 Y^{[1;3]}(y) + \ldots \right) \\
Y^{(2)}(y,t) &= \mathscr{A}_2^2 \left(Y^{[2;2]} + \mathscr{A}_2^2 Y^{[2;4]}(y) + \ldots \right) \\
Z^{(10)}(y,t) &= \mathscr{A}_1 \left(\mathscr{A}_2^2 Z_{10Y}^{[1;3]} + \mathscr{A}_2^4 Z_{10Y}^{[1;5]} + \ldots \right) \\
Z^{(01)}(y,t) &= \mathscr{A}_2 \left(|\mathscr{A}_1|^2 Z_{01X}^{[1;3]} + |\mathscr{A}_1|^4 Z_{01X}^{[1;5]} + \ldots \right) \\
Z^{(11)}(y,t) &= \mathscr{A}_1 \mathscr{A}_2 \left(Z_{11}^{[2;2]} + |\mathscr{A}_1|^2 Z_{11X}^{[2;4]} + \mathscr{A}_2^2 Z_{11Y}^{[2;4]} + \ldots \right) \\
Z^{(-11)}(y,t) &= \tilde{\mathscr{A}_1} \mathscr{A}_2 \left(Z_{-11}^{[0;2]} + |\mathscr{A}_1|^2 Z_{-11X}^{[0;4]} + \mathscr{A}_2^2 Z_{-11Y}^{[0;4]} + \ldots \right)
\end{aligned}\right\}. \tag{9.36}$$

Substituting (9.36) into (9.33)-(9.34) and after rearrangement we get:

$$\left(\frac{d}{dt} - c_1\right) \mathscr{A}_1 X^{[1;1]} = G_{13}^{11} \mathscr{A}_1 |\mathscr{A}_1|^2 + G_{13}^{12} \mathscr{A}_1 \mathscr{A}_2^2 + G_{13}^{13} \mathscr{A}_1 \mathscr{A}_2, \tag{9.37}$$

$$\left(\frac{d}{dt} - c_2\right) \mathscr{A}_2 Y^{[1;1]} = G_{13}^{21} \mathscr{A}_2 |\mathscr{A}_1|^2 + G_{13}^{22} \mathscr{A}_2^3 + G_{13}^{23} |\mathscr{A}_1|^2 + G_{13}^{24} \mathscr{A}_2^2, \tag{9.38}$$

where the nonlinear functions are

$$\left.\begin{array}{rcl}
G_{13}^{11} &=& \Big[N_2(\tilde{X}^{[1;1]}, X^{[2;2]}) + N_2(X^{[2;2]}, \tilde{X}^{[1;1]}) + N_3(\tilde{X}^{[1;1]}, X^{[1;1]}, X^{[1;1]}) \\
&& +N_3(X^{[1;1]}, \tilde{X}^{[1;1]}, X^{[1;1]}) + N_3(X^{[1;1]}, X^{[1;1]}, \tilde{X}^{[1;1]})\Big] \\
G_{13}^{12} &=& \Big[N_2(Z_{11}^{[2;2]}, Y^{[1;1]}) + N_2(Y^{[1;1]}, Z_{11}^{[2;2]}) \\
&& +N_2(Z_{11}^{[2;2]}, Y^{[1;1]}) + N_2(Y^{[1;1]}, Z_{11}^{[2;2]}) + N_3(X^{[1;1]}, Y^{[1;1]}, Y^{[1;1]}) \\
&& +N_3(Y^{[1;1]}, X^{[1;1]}, Y^{[1;1]}) + N_3(Y^{[1;1]}, Y^{[1;1]}, X^{[1;1]})\Big] \\
G_{13}^{13} &=& N_2(X^{[1;1]}, Y^{[1;1]}) \\
G_{13}^{21} &=& \Big[N_2(Y^{[1;1]}, X^{[2;2]}) + N_2(X^{[2;2]}, Y^{[1;1]}) + N_2(Z_{11}^{[2;2]}, \tilde{X}^{[1;1]}) \\
&& +N_2(\tilde{X}^{[1;1]}, Z_{11}^{[2;2]}) + N_2(Z_{-11}^{[0;2]}, X^{[1;1]}) + N_2(X^{[1;1]}, Z_{-11}^{[0;2]}) \\
&& +N_3(Y^{[1;1]}, X^{[1;1]}, \tilde{X}^{[1;1]}) + N_3(Y^{[1;1]}, \tilde{X}^{[1;1]}, X^{[1;1]}) \\
&& +N_3(X^{[1;1]}, Y^{[1;1]}, \tilde{X}^{[1;1]}) + N_3(X^{[1;1]}, \tilde{X}^{[1;1]}, Y^{[1;1]}) \\
&& +N_3(\tilde{X}^{[1;1]}, X^{[1;1]}, Y^{[1;1]}) + N_3(\tilde{X}^{[1;1]}, Y^{[1;1]}, X^{[1;1]})\Big] \\
G_{13}^{22} &=& \big[N_2(Y^{[2;2]}, Y^{[1;1]}) + N_2(Y^{[1;1]}, Y^{[2;2]}) + N_3(Y^{[1;1]}, Y^{[1;1]}, Y^{[1;1]})\big] \\
G_{13}^{23} &=& N_2(X^{[1;1]}, \tilde{X}^{[1;1]}) + N_2(\tilde{X}^{[1;1]}, X^{[1;1]}) \quad G_{13}^{24} = N_2(Y^{[1;1]}, Y^{[1;1]})
\end{array}\right\}. \tag{9.39}$$

In order to get coupled Landau equations we take the inner product of (9.37) and (9.38) with the adjoint eigenfunctions $X^\dagger$ and $Y^\dagger$ corresponding to $X^{[1;1]}$ and $Y^{[1;1]}$, respectively. We get

$$\frac{d\mathscr{A}_1}{dt} = c_1\mathscr{A}_1 + \lambda_{11}\mathscr{A}_1|\mathscr{A}_1|^2 + \lambda_{12}\mathscr{A}_1\mathscr{A}_2^2 + \lambda_{13}\mathscr{A}_1\mathscr{A}_2, \tag{9.40}$$

$$\frac{d\mathscr{A}_2}{dt} = c_2\mathscr{A}_2 + \lambda_{21}\mathscr{A}_2|\mathscr{A}_1|^2 + \lambda_{22}\mathscr{A}_2^3 + \lambda_{23}|\mathscr{A}_1|^2 + \lambda_{24}\mathscr{A}_2^2, \tag{9.41}$$

where the λ_{ij}'s are:

$$\lambda_{11} = \frac{\langle\tilde{X}^\dagger, G_{13}^{11}\rangle}{\langle\tilde{X}^\dagger, X^{[1;1]}\rangle}, \quad \lambda_{12} = \frac{\langle\tilde{X}^\dagger, G_{13}^{12}\rangle}{\langle\tilde{X}^\dagger, X^{[1;1]}\rangle}, \quad \lambda_{13} = \frac{\langle\tilde{X}^\dagger, G_{13}^{13}\rangle}{\langle\tilde{X}^\dagger, X^{[1;1]}\rangle},$$

$$\lambda_{21} = \frac{\langle\tilde{Y}^\dagger, G_{13}^{21}\rangle}{\langle\tilde{Y}^\dagger, Y^{[1;1]}\rangle}, \quad \lambda_{22} = \frac{\langle\tilde{Y}^\dagger, G_{13}^{22}\rangle}{\langle\tilde{Y}^\dagger, Y^{[1;1]}\rangle}, \quad \lambda_{23} = \frac{\langle\tilde{Y}^\dagger, G_{13}^{23}\rangle}{\langle\tilde{Y}^\dagger, Y^{[1;1]}\rangle}, \quad \lambda_{24} = \frac{\langle\tilde{Y}^\dagger, G_{13}^{24}\rangle}{\langle\tilde{Y}^\dagger, Y^{[1;1]}\rangle}.$$

Substituting (9.36) into (9.35) and equating the equations at each order we get:

$$\left.\begin{array}{lll}
O(|\mathscr{A}_1|^2): & (2c_{1r} - L_{00})X^{[0;2]} &= -\lambda_{23}Y^{[1;1]} + G_{13}^{23} \\
O(\mathscr{A}_1^2): & (2c_1 - L_{20})X^{[2;2]} &= N_2(X^{[1;1]}, X^{[1;1]}) \\
O(\mathscr{A}_2^2): & (2c_2 - L_{02})Y^{[2;2]} &= -\lambda_{24}Y^{[1;1]} + G_{13}^{24} \\
O(\mathscr{A}_1\mathscr{A}_2): & ((\tilde{c}_1 + c_2) - L_{-11})Z_{-11}^{[0;2]} &= N_2(Y^{[1;1]}, \tilde{X}^{[1;1]}) + N_2(\tilde{X}^{[1;1]}, Y^{[1;1]}) \\
O(\mathscr{A}_1\mathscr{A}_2): & ((c_1 + c_2) - L_{11})Z_{11}^{[2;2]} &= -\lambda_{13}X^{[1;1]} + G_{13}^{13} \\
O(\mathscr{A}_1|\mathscr{A}_1|^2): & ((c_1 + 2c_{1r}) - L_{10})X^{[1;3]} &= -\lambda_{11}X^{[1;1]} + G_{13}^{11} \\
O(\mathscr{A}_2^3): & (3c_2 - L_{01})Y^{[1;3]} &= -\lambda_{22}Y^{[1;1]} + G_{13}^{22} \\
O(\mathscr{A}_1\mathscr{A}_2^2): & ((c_1 + 2c_2) - L_{10})Z_{10Y}^{[1;3]} &= -\lambda_{12}X^{[1;1]} + G_{13}^{12} \\
O(\mathscr{A}_2|\mathscr{A}_1|^2): & ((c_2 + 2c_{1r}) - L_{01})Z_{01X}^{[1;3]} &= -\lambda_{21}Y^{[1;1]} + G_{13}^{21}
\end{array}\right\} \tag{9.42}$$

These inhomogeneous equations are solved to obtain higher harmonics.

9.5 Analytical Solution for Non-resonating Mode Interactions: $k_x = 0$

For the case of streamwise independent ($\frac{\partial}{\partial x}(.) = 0$) 2D granular Couette flow, we have found analytical solutions for "non-resonating" mode interactions. These solutions are described in this section.

9.5.1 Linear Problems: $O(\mathscr{A}_1)$ and $O(\mathscr{A}_2)$

The linear eigenvalue problems for two interacting modes (cf. §9.2.1, viz (9.4)) are:

$$L_{10}X^{[1;1]} = c_1 X^{[1;1]} \quad \text{and} \quad L_{01}Y^{[1;1]} = c_2 Y^{[1;1]}, \tag{9.43}$$

where L_{10} and L_{01} are the streamwise independent linear operators, and $X^{[1;1]} = (\phi_x^{[1;1]}, u_x^{[1;1]}, v_x^{[1;1]}, T_x^{[1;1]})$ and $Y^{[1;1]} = (\phi_y^{[1;1]}, u_y^{[1;1]}, v_y^{[1;1]}, T_y^{[1;1]})^{Tr}$ are the eigenvectors corresponding to eigenvalues c_1 and c_2, respectively. Note that for the streamwise independent flow $L = L_{mn} = \mathcal{L}(\partial_x(.) = 0, \partial/\partial y \rightarrow d/dy)$ which is given by Eqn. (4.15). Recall that the eigenvalue problems Eqn. (9.43) can be solved analytically in terms of *sine* and *cosine* functions (Alam & Nott 1998):

$$\left.\begin{array}{rcl} (\phi_x^{[1;1]}, T_x^{[1;1]}) & = & (\phi_1^{(\beta)}, T_1^{(\beta)})\cos k_\beta\theta, \\ (u_x^{[1;1]}, v_x^{[1;1]}) & = & (u_1^{(\beta)}, v_1^{(\beta)})\sin k_\beta\theta, \end{array}\right\} \tag{9.44}$$

where $k_\beta = \beta\pi$, $\beta = 1, 2, \ldots$ and $\theta = y \pm 1/2$ and

$$\left.\begin{array}{rcl} (\phi_y^{[1;1]}, T_y^{[1;1]}) & = & (\phi_1^{(\alpha)}, T_1^{(\alpha)})\cos k_\alpha\theta, \\ (u_y^{[1;1]}, v_y^{[1;1]}) & = & (u_1^{(\alpha)}, v_1^{(\alpha)})\sin k_\alpha\theta, \end{array}\right\} \tag{9.45}$$

where $k_\alpha = \alpha\pi$, $\alpha = 1, 2, \ldots$. We use the superscript '(β)' and '(α)' for representing the modal amplitudes of $X^{[1;1]}$ and $Y^{[1;1]}$ modes, respectively.

9.5.2 Second Harmonic: $O(\mathscr{A}_1^2)$, $O(\mathscr{A}_2^2)$ and $O(\mathscr{A}_1\mathscr{A}_2)$

The governing equation for the mixed second harmonic at $O(\mathscr{A}_1\mathscr{A}_2)$ (see 7th equation of (9.16)) is

$$[(c_1 + c_2)I - L]\, Z_{11}^{[2;2]} = N_2(X^{[1;1]}, Y^{[1;1]}) + N_2(Y^{[1;1]}, X^{[1;1]}) = G_{22z}, \tag{9.46}$$

where $Z_{11}^{[2;2]} = (\phi_z^{[2;2]}, u_z^{[2;2]}, v_z^{[2;2]}, T_z^{[2;2]})^{Tr}$ is the second harmonic at $O(\mathscr{A}_1\mathscr{A}_2)$ and $G_{22z} = (G_{22z}^1, G_{22z}^2, G_{22z}^3, G_{22z}^4)^{Tr}$ represents the nonlinear terms as given below:

$$\left.\begin{array}{rcl} (G_{22z}^1, G_{22z}^4) & = & (G_{22z}^{1(\alpha+\beta)}, G_{22z}^{4(\alpha+\beta)})\cos k_{\alpha+\beta}\theta + (G_{22z}^{1(\alpha-\beta)}, G_{22z}^{4(\alpha-\beta)})\cos k_{\alpha-\beta}\theta \\ (G_{22z}^2, G_{22z}^3) & = & (G_{22z}^{2(\alpha+\beta)}, G_{22z}^{3(\alpha+\beta)})\sin k_{\alpha+\beta}\theta + (G_{22z}^{2(\alpha-\beta)}, G_{22z}^{3(\alpha-\beta)})\sin k_{\alpha-\beta}\theta \end{array}\right\}, \tag{9.47}$$

where the analytical forms of $G_{22z}^{j(\alpha\pm\beta)}$ for $j = 1, 2, 3, 4$ are given in Appendix 9A.

The form of $G_{22z}^{j(\alpha\pm\beta)}$ for $j = 1$ to 4 are functions of modal amplitudes of fundamentals of interacting modes, $(\phi_1^{(\beta)}, u_1^{(\beta)}, v_1^{(\beta)}, T_1^{(\beta)})$ and $(\phi_1^{(\alpha)}, u_1^{(\alpha)}, v_1^{(\alpha)}, T_1^{(\alpha)})$. This suggests an analytical solution for $Z_{11}^{[2;2]} = (\phi_z^{[2;2]}, u_z^{[2;2]}, v_z^{[2;2]}, T_z^{[2;2]})^{Tr}$ as

$$\left.\begin{array}{rcl} (\phi_z^{[2;2]}, T_z^{[2;2]}) & = & (\phi_2^{(\alpha+\beta)}, T_2^{(\alpha+\beta)})\cos k_{\alpha+\beta}\theta + (\phi_2^{(\alpha-\beta)}, T_2^{(\alpha-\beta)})\cos k_{\alpha-\beta}\theta \\ (u_z^{[2;2]}, v_z^{[2;2]}) & = & (u_2^{(\alpha+\beta)}, v_2^{(\alpha+\beta)})\sin k_{\alpha+\beta}\theta + (u_2^{(\alpha-\beta)}, v_2^{(\alpha-\beta)})\sin k_{\alpha-\beta}\theta \end{array}\right\}. \tag{9.48}$$

Substituting Eqn. (9.48) and the inhomogeneous terms Eqn. (9.47) into Eqn. (9.46) and separating the coefficients of *sine* and *cosine* we get following equations associated with the unknown modal amplitudes of the mixed second harmonic mode:

$$\left.\begin{array}{rcl} \left[(c_1 + c_2)I - L_2^{\alpha+\beta}\right] X_2^{\alpha+\beta} & = & [G_{22z}^{1(\alpha+\beta)}, G_{22z}^{2(\alpha+\beta)}, G_{22z}^{3(\alpha+\beta)}, G_{22z}^{4(\alpha+\beta)}]^{Tr} \\ \left[(c_1 + c_2)I - L_2^{\alpha-\beta}\right] X_2^{\alpha-\beta} & = & [G_{22z}^{1(\alpha-\beta)}, G_{22z}^{2(\alpha-\beta)}, G_{22z}^{3(\alpha-\beta)}, G_{22z}^{4(\alpha-\beta)}]^{Tr} \end{array}\right\} \tag{9.49}$$

where $X_2^{\alpha+\beta} = (\phi_2^{\alpha+\beta}, u_2^{\alpha+\beta}, v_2^{\alpha+\beta}, T_2^{\alpha+\beta})^{Tr}$ and $X_2^{\alpha-\beta} = (\phi_2^{\alpha-\beta}, u_2^{\alpha-\beta}, v_2^{\alpha-\beta}, T_2^{\alpha-\beta})^{Tr}$ are modal amplitudes related to the mixed mode $Z_{11}^{[2;2]}$.

The governing equations for second harmonic at $O(\mathscr{A}_1^2)$ and $O(\mathscr{A}_2^2)$ (see 2nd and 4th equations of (9.16)) can be written as:

$$\text{X mode}: \quad [2c_1 I - L]\, X^{[2;2]} = N_2(X^{[1;1]}, X^{[1;1]}), \tag{9.50}$$

$$\text{Y mode}: \quad [2c_2 I - L]\, Y^{[2;2]} = N_2(Y^{[1;1]}, Y^{[1;1]}), \tag{9.51}$$

where

$$X^{[2;2]} = (\phi_x^{[2;2]}, u_x^{[2;2]}, v_x^{[2;2]}, T_x^{[2;2]}) \quad \text{and} \quad Y^{[2;2]} = (\phi_y^{[2;2]}, u_y^{[2;2]}, v_y^{[2;2]}, T_y^{[2;2]}). \tag{9.52}$$

The analytical solution of second harmonic has been detailed in chapter 5. In short, the explicit forms of second harmonics (see chapter 5) are:

$$\left.\begin{aligned} (\phi_x^{[2;2]}, T_x^{[2;2]}) &= (\phi_2^{(\beta)}, T_2^{(\beta)})\cos k_{2\beta}\theta + (0, T_{mean}^{(\beta)}) \\ (u_x^{[2;2]}, v_x^{[2;2]}) &= (u_2^{(\beta)}, v_2^{(\beta)})\sin k_{2\beta}\theta \end{aligned}\right\}, \tag{9.53}$$

$$\left.\begin{aligned} (\phi_y^{[2;2]}, T_y^{[2;2]}) &= (\phi_2^{(\alpha)}, T_2^{(\alpha)})\cos k_{2\alpha}\theta + (0, T_{mean}^{(\alpha)}) \\ (u_y^{[2;2]}, v_y^{[2;2]}) &= (u_2^{(\alpha)}, v_2^{(\alpha)})\sin k_{2\alpha}\theta \end{aligned}\right\}, \tag{9.54}$$

where $k_{2\beta} = 2k_\beta$ and $k_{2\alpha} = 2k_\alpha$. The distortion of mean flow is related to second harmonic (Shukla & Alam 2011): $X^{[0;2]} = 2X^{[2;2]}$ and $Y^{[0;2]} = 2Y^{[2;2]}$. Recall from chapters 4 and 5 that the least stable eigenvalue and associated eigenfunction are real (shear-banding mode) and therefore the second harmonic of fundamental and the distortion of mean flow are real functions.

9.5.3 First Landau Coefficients: $O(\mathscr{A}_1|\mathscr{A}_2|^2)$ and $O(\mathscr{A}_2|\mathscr{A}_1|^2)$

At cubic order, we have two coupled equations (see 10th and 11th equation of (9.16)):

$$((c_1 + 2c_{2r}) - L_{10})Z_{10Y}^{[1;3]} = -\lambda_{12}X^{[1;1]} + G_{13}^{12}, \tag{9.55}$$

$$((c_2 + 2c_{1r}) - L_{01})Z_{01X}^{[1;3]} = -\lambda_{21}Y^{[1;1]} + G_{13}^{21}, \tag{9.56}$$

where G_{13}^{12} and G_{13}^{21} are the nonlinear terms. For simplicity we are using the notation H_{12} for G_{13}^{12} and H_{21} for G_{13}^{21} now onwards.

From the analytical solutions of fundamentals and second harmonics of pure and mixed modes, it can be easily verified that the nonlinear terms H_{12} and H_{21} are:

$$\left.\begin{aligned} (H_{12}^1, H_{12}^4) &= (H_{12}^{1(2\alpha+\beta)}, H_{12}^{4(2\alpha+\beta)})\cos k_{2\alpha+\beta}\theta + (H_{12}^{1(2\alpha-\beta)}, H_{12}^{4(2\alpha-\beta)})\cos k_{|2\alpha-\beta|}\theta \\ &\quad +(H_{12}^{1(\beta)}, H_{12}^{4(\beta)})\cos k_\beta\theta \\ (H_{12}^2, H_{12}^3) &= (H_{12}^{2(2\alpha+\beta)}, H_{12}^{3(2\alpha+\beta)})\cos k_{2\alpha+\beta}\theta + (H_{12}^{2(2\alpha-\beta)}, H_{12}^{3(2\alpha-\beta)})\cos k_{|2\alpha-\beta|}\theta \\ &\quad +(H_{12}^{2(\beta)}, H_{12}^{3(\beta)})\cos k_\beta\theta \end{aligned}\right\}, \tag{9.57}$$

$$\left.\begin{aligned} (H_{21}^1, H_{21}^4) &= (H_{21}^{1(2\alpha+\beta)}, H_{21}^{4(2\alpha+\beta)})\cos k_{2\alpha+\beta}\theta + (H_{21}^{1(2\alpha-\beta)}, H_{21}^{4(2\alpha-\beta)})\cos k_{|2\alpha-\beta|}\theta \\ &\quad +(H_{21}^{1(\beta)}, H_{21}^{4(\beta)})\cos k_\beta\theta \\ (H_{21}^2, H_{21}^3) &= (H_{21}^{2(2\alpha+\beta)}, H_{21}^{3(2\alpha+\beta)})\cos k_{2\alpha+\beta}\theta + (H_{21}^{2(2\alpha-\beta)}, H_{21}^{3(2\alpha-\beta)})\cos k_{|2\alpha-\beta|}\theta \\ &\quad +(H_{21}^{2(\beta)}, H_{21}^{3(\beta)})\cos k_\beta\theta \end{aligned}\right\}. \tag{9.58}$$

From (9.14)-(9.15), the expressions for the first Landau coefficients are:

$$\lambda_{12} = \frac{\langle \tilde{X}^\dagger, G_{13}^{12} \rangle}{\langle \tilde{X}^\dagger, X^{[1:1]} \rangle} = \frac{\langle \tilde{X}^\dagger, H_{12} \rangle}{\langle \tilde{X}^\dagger, X^{[1:1]} \rangle} \quad \text{and} \quad \lambda_{21} = \frac{\langle \tilde{Y}^\dagger, G_{13}^{21} \rangle}{\langle \tilde{Y}^\dagger, Y^{[1:1]} \rangle} = \frac{\langle \tilde{Y}^\dagger, H_{21} \rangle}{\langle \tilde{Y}^\dagger, Y^{[1:1]} \rangle}, \tag{9.59}$$

where the inner product is defined as

$$\langle a, b \rangle = \int_{-1/2}^{1/2} \tilde{a}\, b\, dy. \tag{9.60}$$

Substituting (9.57)-(9.58) into (9.59) and using (9.60) we get analytical expressions for the coupled Landau coefficients as given below:

$$\lambda_{12} = = \frac{\left(\tilde{\phi}_1^{(\beta)\dagger} H_{12}^{1(\beta)} + \tilde{u}_1^{(\beta)^\dagger} H_{12}^{2(\beta)} + \tilde{v}_1^{(\beta)\dagger} H_{12}^{3(\beta)} + \tilde{T}_1^{(\beta)\dagger} H_{12}^{4(\beta)} \right)}{\tilde{\phi}_1^{(\beta)\dagger} \phi_1^{(\beta)} + \tilde{u}_1^{(\beta)^\dagger} u_1^{(\beta)} + \tilde{v}_1^{(\beta)\dagger} v_1^{(\beta)} + \tilde{T}_1^{(\beta)\dagger} T_1^{(\beta)}}, \tag{9.61}$$

$$\lambda_{21} = \frac{\left(\tilde{\phi}_1^{(\alpha)\dagger} H_{21}^{1(\alpha)} + \tilde{u}_1^{(\alpha)^\dagger} H_{21}^{2(\alpha)} + \tilde{v}_1^{(\alpha)\dagger} H_{21}^{3(\alpha)} + \tilde{T}_1^{(\alpha)\dagger} H_{21}^{4(\alpha)} \right)}{\tilde{\phi}_1^{(\alpha)\dagger} \phi_1^{(\alpha)} + \tilde{u}_1^{(\alpha)^\dagger} u_1^{(\alpha)} + \tilde{v}_1^{(\alpha)\dagger} v_1^{(\alpha)} + \tilde{T}_1^{(\alpha)\dagger} T_1^{(\alpha)}}. \tag{9.62}$$

9.5.4 Bifurcation Analysis

Coupled Landau equations can be written as

$$\frac{d\mathscr{A}_1}{dt} = c_1 \mathscr{A}_1 + \lambda_{11} \mathscr{A}_1 |\mathscr{A}_1|^2 + \lambda_{12} \mathscr{A}_1 |\mathscr{A}_2|^2, \tag{9.63}$$

$$\frac{d\mathscr{A}_2}{dt} = c_2 \mathscr{A}_2 + \lambda_{21} \mathscr{A}_2 |\mathscr{A}_1|^2 + \lambda_{22} A_2 |A_2|^2. \tag{9.64}$$

Substituting $\mathscr{A}_j = |\mathscr{A}_j| e^{i\theta_j t}$ into above equations and separating the real and imaginary parts we get

$$\frac{d|\mathscr{A}_1|}{dt} = |\mathscr{A}_1| \left(c_{1r} + \lambda_{11r} |\mathscr{A}_1|^2 + \lambda_{12r} |\mathscr{A}_2|^2 \right), \tag{9.65}$$

$$\frac{d|\mathscr{A}_2|}{dt} = |\mathscr{A}_2| \left(c_{2r} + \lambda_{21r} |\mathscr{A}_1|^2 + \lambda_{22r} |\mathscr{A}_2|^2 \right). \tag{9.66}$$

In the present case (streamwise independent flow), both the least stable eigenvalue and corresponding eigenfunction are real and it can be verified that the Landau coefficients are also real (Shukla & Alam 2011) (i.e. λ_{11}, λ_{12}, λ_{21} and λ_{22} are real). The equilibrium solutions of (9.65) and (9.66) are discussed below:
(*i*) trivial solution (base flow), $|\mathscr{A}_1| = |\mathscr{A}_2| = 0$,
(*ii*) pure mode X, $|\mathscr{A}_2| = 0$ and $|\mathscr{A}_1|^2 = -c_{1r}/\lambda_{11r} > 0$,
(*iii*) pure mode Y, $|\mathscr{A}_1| = 0$ and $|\mathscr{A}_2|^2 = -c_{2r}/\lambda_{22r} > 0$,
(*iv*) coupled modes,

$$|\mathscr{A}_1|^2 = \frac{c_{2r}\lambda_{12r} - c_{1r}\lambda_{22r}}{\lambda_{11r}\lambda_{22r} - \lambda_{12r}\lambda_{21r}} > 0 \quad \text{and} \quad |\mathscr{A}_2|^2 = \frac{c_{1r}\lambda_{21r} - c_{2r}\lambda_{11r}}{\lambda_{11r}\lambda_{22r} - \lambda_{12r}\lambda_{21r}} > 0 \tag{9.67}$$

To find the stability of equilibrium solutions (9.67) we linearize the system (9.65-9.66) around this solution and find the Jacobian matrix as given below:

$$J = \begin{vmatrix} c_{1r} + 2\lambda_{11r}|\mathscr{A}_1|^2 + \lambda_{12r}|\mathscr{A}_2|^2 & \lambda_{12r}\mathscr{A}_1\tilde{A}_2 \\ \lambda_{21r}\mathscr{A}_2\tilde{\mathscr{A}}_1 & c_{2r} + \lambda_{21r}|\mathscr{A}_1|^2 + 2\lambda_{22r}|\mathscr{A}_2|^2 \end{vmatrix} \tag{9.68}$$

The eigenvalues of the above matrix can be obtained by solving equation,

$$\Lambda^2 - (J_{11} + J_{22})\Lambda + (J_{11}J_{22} - J_{12}J_{21}) = 0. \tag{9.69}$$

The explicit expressions of two eigenvalues can be written as:

$$\Lambda = \frac{1}{2}\left[J_{11} + J_{22} \pm \sqrt{(J_{11} + J_{22})^2 - 4(J_{11}J_{22} - J_{12}J_{21})}\right],$$

where J_{ij} is the ijth element of matrix J. The negative (/positive) real part of Λ implies that the mixed mode is stable (/unstable).

9.5.5 Limit of Single Landau Equation

In the limit of single mode analysis, i.e. $\lambda_{12}, \lambda_{21} \to 0$, equations (9.63)-(9.64) reduce to the following equations,

$$\frac{d\mathscr{A}_1}{dt} = c_1\mathscr{A}_1 + \lambda_{11}\mathscr{A}_1|\mathscr{A}_1|^2, \tag{9.70}$$

$$\frac{d\mathscr{A}_2}{dt} = c_2\mathscr{A}_2 + \lambda_{21}\mathscr{A}_2|\mathscr{A}_1|^2. \tag{9.71}$$

Similarly, the amplitudes reduce to

$$|\mathscr{A}_1| = \sqrt{\frac{-c_{1r}}{\lambda_{11r}}} \quad \text{and} \quad |\mathscr{A}_2| = \sqrt{\frac{-c_{2r}}{\lambda_{22r}}}. \tag{9.72}$$

Therefore we get back the single cubic order Landau equation and its equilibrium solutions as discussed in chapters 4 and 5.

9.5.6 Preliminary Numerical Results

H	c_1	c_2
40.0841683	1.89492×10^{-4}	-1.86532×10^{-4}
20	-1.92286×10^{-4}	-1.20865×10^{-2}
50	1.41351×10^{-4}	1.58747×10^{-4}

Table 9.1: Numerical values of growth rate at various values of Couette gap. Other parameters are same as in figure 9.4.

H	λ_{11}	λ_{12}	λ_{21}	λ_{22}
40.0841683	-2.12943×10^{-3}	7.89940×10^{-4}	2.83102×10^{-3}	-1.31451×10^{-4}
20	-2.10300×10^{-3}	-3.09284×10^{-4}	1.43298×10^{-3}	-2.17263×10^{-2}
50	1.58327×10^{-4}	6.24264×10^{-4}	2.65205×10^{-3}	-1.03568×10^{-3}

Table 9.2: Numerical values of coefficients of coupled Landau equation. Other parameters are same as in figure 9.4.

The variation of second harmonic across the channel, related to mixed mode, i.e. $Z_{11}^{[2;2]}$, is

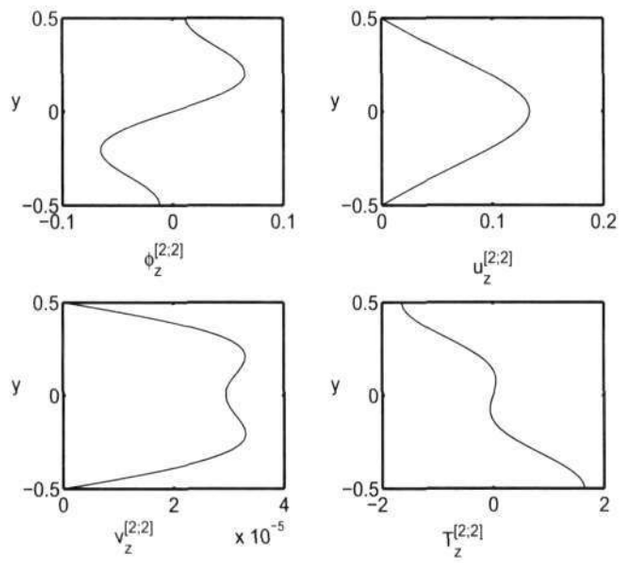

Figure 9.4: Variation for $Z_{11}^{[2;2]}$ for $e = 0.8$, $\phi^0 = 0.3$, $H = 40.08416833$ and $(\beta, \alpha) = (1, 2)$.

shown in figure 9.4 for modes $\beta = 1$ and $\alpha = 2$ near the zero crossing. Sample numerical values of growth rate and coefficients of coupled Landau equations are given in tables 9.1 and 9.2, respectively, for three values of Couette gap. A detailed numerical analysis will be carried out in future.

9.6 Summary

Two types of resonances are possible in the present case of granular Couette flow which should be dealt with coupled Landau equations. The coupled Landau equations have been derived for two cases: the mean flow resonance and 1:2 resonance. Similar analysis has also been carried out for two non-resonating mode interactions.

The analytical solutions for the coefficients of coupled Landau equations have been derived for non-resonating mode interactions in two-dimensional granular plane Couette flow ($k_x = 0$). The detailed numerical results are deferred to a future work.

Appendix 9A. Nonlinear Terms of Eqn. (9.47)

$$
\begin{aligned}
G_{22z}^{1(\alpha+\beta)} &= -\frac{(k_\alpha + k_\beta)}{2}\left(v_1^{(1)}\phi_1^{(2)} + v_1^{(2)}\phi_1^{(1)}\right) \\
G_{22z}^{1(\alpha-\beta)} &= \frac{(k_\alpha - k_\beta)}{2}\left(v_1^{(1)}\phi_1^{(2)} - v_1^{(2)}\phi_1^{(1)}\right) \\
G_{22z}^{2(\alpha+\beta)} &= \frac{1}{2}\Big[-k_\alpha v_1^{(1)}u_1^{(2)} - \frac{k_\alpha k_\beta}{\phi^0 H^2}(\mu_\phi^0\phi_1^{(1)} + \mu_T^0 T_1^{(1)})u_1^{(2)} \\
&\quad -\frac{1}{\phi^0}\left(\omega_2\phi_1^{(1)}u_1^{(2)} + u_y^0\phi_1^{(1)}v_1^{(2)}\right) + \frac{1}{\phi^0 H^2}\Big[-k_\alpha^2(\mu_\phi^0\phi_1^{(1)} + \mu_T^0 T_1^{(1)})u_1^{(2)} \\
&\quad -k_\alpha\left(\mu_{\phi\phi}^0\phi_1^{(1)}\phi_1^{(2)} + \mu_{TT}^0 T_1^{(1)}T_1^{(2)} + \mu_{\phi T}^0\phi_1^{(1)}T_1^{(2)} + \mu_{\phi T}^0 T_1^{(1)}\phi_1^{(2)}\right)\Big]\Big] \\
&\quad +\frac{1}{2}\Big[-k_\beta v_1^{(2)}u_1^{(1)} - \frac{k_\alpha k_\beta}{\phi^0 H^2}(\mu_\phi^0\phi_1^{(2)} + \mu_T^0 T_1^{(2)})u_1^{(1)} \\
&\quad -\frac{1}{\phi^0}\left(\omega_1\phi_1^{(2)}u_1^{(1)} + u_y^0\phi_1^{(2)}v_1^{(1)}\right) + \frac{1}{\phi^0 H^2}\Big[-k_\beta^2(\mu_\phi^0\phi_1^{(2)} + \mu_T^0 T_1^{(2)})u_1^{(1)} \\
&\quad -k_\beta\left(\mu_{\phi\phi}^0\phi_1^{(2)}\phi_1^{(1)} + \mu_{TT}^0 T_1^{(2)}T_1^{(1)} + \mu_{\phi T}^0\phi_1^{(2)}T_1^{(1)} + \mu_{\phi T}^0 T_1^{(2)}\phi_1^{(1)}\right)\Big]\Big] \\
G_{22z}^{2(\alpha-\beta)} &= \frac{1}{2}\Big[k_\alpha v_1^{(1)}u_1^{(2)} + \frac{k_\alpha k_\beta}{\phi^0 H^2}(\mu_\phi^0\phi_1^{(1)} + \mu_T^0 T_1^{(1)})u_1^{(2)} \\
&\quad -\frac{1}{\phi^0}\left(\omega_2\phi_1^{(1)}u_1^{(2)} + u_y^0\phi_1^{(1)}v_1^{(2)}\right) + \frac{1}{\phi^0 H^2}\Big[-k_\alpha^2(\mu_\phi^0\phi_1^{(1)} + \mu_T^0 T_1^{(1)})u_1^{(2)} \\
&\quad -k_\alpha\left(\mu_{\phi\phi}^0\phi_1^{(1)}\phi_1^{(2)} + \mu_{TT}^0 T_1^{(1)}T_1^{(2)} + \mu_{\phi T}^0\phi_1^{(1)}T_1^{(2)} + \mu_{\phi T}^0 T_1^{(1)}\phi_1^{(2)}\right)\Big]\Big] \\
&\quad +\frac{1}{2}\Big[k_\beta v_1^{(2)}u_1^{(1)} + \frac{k_\alpha k_\beta}{\phi^0 H^2}(\mu_\phi^0\phi_1^{(2)} + \mu_T^0 T_1^{(2)})u_1^{(1)} \\
&\quad -\frac{1}{\phi^0}\left(\omega_1\phi_1^{(2)}u_1^{(1)} + u_y^0\phi_1^{(2)}v_1^{(1)}\right) + \frac{1}{\phi^0 H^2}\Big[-k_\beta^2(\mu_\phi^0\phi_1^{(2)} + \mu_T^0 T_1^{(2)})u_1^{(1)} \\
&\quad -k_\beta\left(\mu_{\phi\phi}^0\phi_1^{(2)}\phi_1^{(1)} + \mu_{TT}^0 T_1^{(2)}T_1^{(1)} + \mu_{\phi T}^0\phi_1^{(2)}T_1^{(1)} + \mu_{\phi T}^0 T_1^{(2)}\phi_1^{(1)}\right)\Big]\Big] \\
G_{22z}^{3(\alpha+\beta)} &= \frac{1}{2}\Big[-k_\alpha v_1^{(1)}v_1^{(2)} - \frac{k_\alpha k_\beta}{\phi^0 H^2}\left(2\mu_\phi^0\phi_1^{(1)} + 2\mu_T^0 T_1^{(1)} + \lambda_\phi^0\phi_1^{(1)} + \lambda_T^0 T_1^{(1)}\right)v_1^{(2)} \\
&\quad -\frac{1}{\phi^0}\omega_2\phi_1^{(1)}v_1^{(2)} + \frac{1}{\phi^0 H^2}\Big(k_\alpha(p_{\phi\phi}^0\phi_1^{(1)}\phi_1^{(2)} + p_{TT}^0 T_1^{(1)}T_1^{(2)} + p_{\phi T}^0\phi_1^{(1)}T_1^{(2)} + p_{\phi T}^0 T_1^{(1)}\phi_1^{(2)}) \\
&\quad -k_\alpha^2(2\mu_\phi^0\phi_1^{(1)} + 2\mu_T^0 T_1^{(1)} + \lambda_\phi^0\phi_1^{(1)} + \lambda_T^0 T_1^{(1)})v_1^{(2)}\Big)\Big] \\
&\quad +\frac{1}{2}\Big[-k_\beta v_1^{(2)}v_1^{(1)} - \frac{k_\alpha k_\beta}{\phi^0 H^2}\left(2\mu_\phi^0\phi_1^{(2)} + 2\mu_T^0 T_1^{(2)} + \lambda_\phi^0\phi_1^{(2)} + \lambda_T^0 T_1^{(2)}\right)v_1^{(1)} \\
&\quad -\frac{1}{\phi^0}\omega_1\phi_1^{(2)}v_1^{(1)} + \frac{1}{\phi^0 H^2}\Big(k_\beta(p_{\phi\phi}^0\phi_1^{(2)}\phi_1^{(1)} + p_{TT}^0 T_1^{(2)}T_1^{(1)} + p_{\phi T}^0\phi_1^{(2)}T_1^{(1)} + p_{\phi T}^0 T_1^{(2)}\phi_1^{(1)}) \\
&\quad -k_\beta^2(2\mu_\phi^0\phi_1^{(2)} + 2\mu_T^0 T_1^{(2)} + \lambda_\phi^0\phi_1^{(2)} + \lambda_T^0 T_1^{(2)})v_1^{(1)}\Big)\Big]
\end{aligned}
$$

$$
\begin{aligned}
G_{22z}^{3(\alpha-\beta)} &= \frac{1}{2}\Big[k_\alpha v_1^{(1)}v_1^{(2)} + \frac{k_\alpha k_\beta}{\phi^0 H^2}\left(2\mu_\phi^0\phi_1^{(1)} + 2\mu_T^0 T_1^{(1)} + \lambda_\phi^0\phi_1^{(1)} + \lambda_T^0 T_1^{(1)}\right)v_1^{(2)} \\
&\quad -\frac{1}{\phi^0}\omega_2\phi_1^{(1)}v_1^{(2)} + \frac{1}{\phi^0 H^2}\Big(k_\alpha(p_{\phi\phi}^0\phi_1^{(1)}\phi_1^{(2)} + p_{TT}^0 T_1^{(1)}T_1^{(2)} + p_{\phi T}^0\phi_1^{(1)}T_1^{(2)} + p_{\phi T}^0 T_1^{(1)}\phi_1^{(2)}) \\
&\quad -k_\alpha^2(2\mu_\phi^0\phi_1^{(1)} + 2\mu_T^0 T_1^{(1)} + \lambda_\phi^0\phi_1^{(1)} + \lambda_T^0 T_1^{(1)})v_1^{(2)}\Big)\Big] \\
&\quad +\frac{1}{2}\Big[-k_\beta v_1^{(2)}v_1^{(3)} - \frac{k_\alpha k_\beta}{\phi^0 H^2}\left(2\mu_\phi^0\phi_1^{(2)} + 2\mu_T^0 T_1^{(2)} + \lambda_\phi^0\phi_1^{(2)} + \lambda_T^0 T_1^{(2)}\right)v_1^{(1)} \\
&\quad +\frac{1}{\phi^0}\omega_1\phi_1^{(2)}v_1^{(1)} - \frac{1}{\phi^0 H^2}\Big(k_\beta(p_{\phi\phi}^0\phi_1^{(2)}\phi_1^{(1)} + p_{TT}^0 T_1^{(2)}T_1^{(1)} + p_{\phi T}^0\phi_1^{(2)}T_1^{(1)} + p_{\phi T}^0 T_1^{(2)}\phi_1^{(1)}) \\
&\quad -k_\beta^2(2\mu_\phi^0\phi_1^{(2)} + 2\mu_T^0 T_1^{(2)} + \lambda_\phi^0\phi_1^{(2)} + \lambda_T^0 T_1^{(2)})v_1^{(1)}\Big)\Big] \\
G_{22z}^{4(\alpha+\beta)} &= \frac{1}{2}\Big[-k_\alpha v_1^{(1)}T_1^{(2)} - \frac{2k_\alpha k_\beta}{\phi^0 H^2\, dim}T_1^{(1)}(\kappa_\phi^0\phi_1^{(2)} + \kappa_T^0 T_1^{(2)}) - \frac{1}{\phi^0}\omega_2\phi_1^{(1)}T_1^{(2)} \\
&\quad +\frac{2}{\phi^0\, dim}\Big\{-\frac{k_\beta^2}{H^2}T_1^{(1)}(\kappa_\phi^0\phi_1^{(2)} + \kappa_T^0 T_1^{(2)}) - k_\alpha(p_\phi^0\phi_1^{(1)} + p_T^0 T_1^{(1)})v_1^{(2)} + 2\mu^0 k_\alpha k_\beta(v_1^{(1)}v_1^{(2)} + \frac{1}{2}u_1^{(1)}u_1^{(2)}) \\
&\quad +\left(\frac{1}{2}\mu_{\phi\phi}^0\phi_1^{(1)}\phi_1^{(2)} + \frac{1}{2}\mu_{TT}^0 T_1^{(1)}T_1^{(2)} + \mu_{\phi T}^0\phi_1^{(1)}T_1^{(2)}\right) + 2k_\alpha(\mu_\phi^0\phi_1^{(1)} + \mu_T^0 T_1^{(1)})u_1^{(2)} \\
&\quad +k_\alpha k_\beta\lambda^0 v_1^{(1)}v_1^{(2)} + \left(\frac{1}{2}\mathcal{D}_{\phi\phi}^0\phi_1^{(1)}\phi_1^{(2)} + \frac{1}{2}\mathcal{D}_{TT}^0 T_1^{(1)}T_1^{(2)} + \mathcal{D}_{\phi T}^0\phi_1^{(1)}T_1^{(2)}\right)\Big\}\Big] \\
&\quad +\frac{1}{2}\Big[-k_\beta v_1^{(2)}T_1^{(1)} - \frac{2k_\alpha k_\beta}{\phi^0 H^2\, dim}T_1^{(2)}(\kappa_\phi^0\phi_1^{(1)} + \kappa_T^0 T_1^{(1)}) - \frac{1}{\phi^0}\omega_1\phi_1^{(2)}T_1^{(1)} \\
&\quad +\frac{2}{\phi^0\, dim}\Big\{-\frac{k_\alpha^2}{H^2}T_1^{(2)}(\kappa_\phi^0\phi_1^{(1)} + \kappa_T^0 T_1^{(1)}) - k_\beta(p_\phi^0\phi_1^{(2)} + p_T^0 T_1^{(2)})v_1^{(1)} + 2\mu^0 k_\alpha k_\beta(v_1^{(2)}v_1^{(1)} + \frac{1}{2}u_1^{(2)}u_1^{(1)}) \\
&\quad +\left(\frac{1}{2}\mu_{\phi\phi}^0\phi_1^{(2)}\phi_1^{(1)} + \frac{1}{2}\mu_{TT}^0 T_1^{(2)}T_1^{(1)} + \mu_{\phi T}^0\phi_1^{(2)}T_1^{(1)}\right) + 2k_\beta(\mu_\phi^0\phi_1^{(2)} + \mu_T^0 T_1^{(2)})u_1^{(1)} \\
&\quad +k_\alpha k_\beta\lambda^0 v_1^{(2)}v_1^{(1)} + \left(\frac{1}{2}\mathcal{D}_{\phi\phi}^0\phi_1^{(2)}\phi_1^{(1)} + \frac{1}{2}\mathcal{D}_{TT}^0 T_1^{(2)}T_1^{(1)} + \mathcal{D}_{\phi T}^0\phi_1^{(2)}T_1^{(1)}\right)\Big\}\Big] \\
G_{22z}^{4(\alpha-\beta)} &= \frac{1}{2}\Big[k_\alpha v_1^{(1)}T_1^{(2)} + \frac{2k_\alpha k_\beta}{\phi^0 H^2\, dim}T_1^{(1)}(\kappa_\phi^0\phi_1^{(2)} + \kappa_T^0 T_1^{(2)}) - \frac{1}{\phi^0}\omega_2\phi_1^{(1)}T_1^{(2)} \\
&\quad +\frac{2}{\phi^0\, dim}\Big\{-\frac{k_\beta^2}{H^2}T_1^{(1)}(\kappa_\phi^0\phi_1^{(2)} + \kappa_T^0 T_1^{(2)}) - k_\alpha(p_\phi^0\phi_1^{(1)} + p_T^0 T_1^{(1)})v_1^{(2)} + 2\mu^0 k_\alpha k_\beta(v_1^{(1)}v_1^{(2)} + \frac{1}{2}u_1^{(1)}u_1^{(2)}) \\
&\quad +\left(\frac{1}{2}\mu_{\phi\phi}^0\phi_1^{(1)}\phi_1^{(2)} + \frac{1}{2}\mu_{TT}^0 T_1^{(1)}T_1^{(2)} + \mu_{\phi T}^0\phi_1^{(1)}T_1^{(2)}\right) + 2k_\alpha(\mu_\phi^0\phi_1^{(1)} + \mu_T^0 T_1^{(1)})u_1^{(2)} \\
&\quad +k_\alpha k_\beta\lambda^0 v_1^{(1)}v_1^{(2)} + \left(\frac{1}{2}\mathcal{D}_{\phi\phi}^0\phi_1^{(1)}\phi_1^{(2)} + \frac{1}{2}\mathcal{D}_{TT}^0 T_1^{(1)}T_1^{(2)} + \mathcal{D}_{\phi T}^0\phi_1^{(1)}T_1^{(2)}\right)\Big\}\Big] \\
&\quad +\frac{1}{2}\Big[k_\beta v_1^{(2)}T_1^{(1)} + \frac{2k_\alpha k_\beta}{\phi^0 H^2\, dim}T_1^{(2)}(\kappa_\phi^0\phi_1^{(1)} + \kappa_T^0 T_1^{(1)}) - \frac{1}{\phi^0}\omega_1\phi_1^{(2)}T_1^{(1)} \\
&\quad +\frac{2}{\phi^0\, dim}\Big\{-\frac{k_\alpha^2}{H^2}T_1^{(2)}(\kappa_\phi^0\phi_1^{(1)} + \kappa_T^0 T_1^{(1)}) - k_\beta(p_\phi^0\phi_1^{(2)} + p_T^0 T_1^{(2)})v_1^{(1)} + 2\mu^0 k_\alpha k_\beta(v_1^{(2)}v_1^{(1)} + \frac{1}{2}u_1^{(2)}u_1^{(1)}) \\
&\quad +\left(\frac{1}{2}\mu_{\phi\phi}^0\phi_1^{(2)}\phi_1^{(1)} + \frac{1}{2}\mu_{TT}^0 T_1^{(2)}T_1^{(1)} + \mu_{\phi T}^0\phi_1^{(2)}T_1^{(1)}\right) + 2k_\beta(\mu_\phi^0\phi_1^{(2)} + \mu_T^0 T_1^{(2)})u_1^{(1)} \\
&\quad +k_\alpha k_\beta\lambda^0 v_1^{(2)}v_1^{(1)} + \left(\frac{1}{2}\mathcal{D}_{\phi\phi}^0\phi_1^{(2)}\phi_1^{(1)} + \frac{1}{2}\mathcal{D}_{TT}^0 T_1^{(2)}T_1^{(1)} + \mathcal{D}_{\phi T}^0\phi_1^{(2)}T_1^{(1)}\right)\Big\}\Big]
\end{aligned}
$$

CHAPTER 10

COMPLEX GINZBURG LANDAU EQUATION FOR GRANULAR COUETTE FLOW

The granular Couette flow is unstable to disturbances of finite wavelengths in the form of traveling and stationary waves (cf. chapter 6). The wave numbers corresponding to the most unstable modes, where the growth rates are positive for a small band of wave numbers, form an envelop of waves which moves with a group velocity. The analysis of aperiodic/disordered patterns is typically carried out via Ginzburg-Landau equation (Eckhaus 1965; Newell & Whitehead 1969; Stewartson & Stuart 1971; Benney & Maslowe 1975; Benney 1984; Craik 1985; Deissler 1987; Manneville 1990; Guba & Worster 2010).

In this chapter, a cubic complex Ginzburg Landau equation (CGLE) has been derived for the nonlinear stability of plane Couette flow of granular material for non-periodic waves. It was shown by Stewartson & Stuart (1971) that the slow variation in the amplitude of a non-periodic disturbance wave satisfies a Ginzburg-Landau equation. Following Stewartson & Stuart (1971), we have employed the multiple scale analysis to derive CGLE for the most unstable mode of the linear theory near criticality. The present derivation is a generalization of the previous derivation of Landau equation using amplitude expansion method (cf. chapter 3) as it considers both time and space dependence of order parameter.

This chapter is organized as follows. The temporal and spatial development of wave system is given in §10.1. The derivation of Ginzburg Landau equation using multiple scale analysis is detailed in §10.2. The summary is given in §10.3.

10.1 Temporal and Spatial Development of a Linear Wave System

In the linear stability analysis, we seek a normal mode solution in which we study only a single mode, the least stable mode. The positive growth rate of this mode predicts an instability in the flow. The amplitude of the disturbance is an exponential function of time. This theory is restricted to a monochromatic wave and does not hold for the development of a wave system (packet) moving with a group velocity. From the weakly nonlinear analysis we will derive an amplitude equation (*Ginzburg-Landau equation*) using multiple scale analysis that holds for a wave system in two-dimensional granular plane Couette flow.

10.1.1 Linear Problem for Wave Systems

We start with the linearized disturbance equations of the following form

$$\left(\mathcal{M}\frac{\partial}{\partial t} - \mathcal{L}\right) X(x, y, t) = 0, \tag{10.1}$$

where $X = (\phi', u', v', T')$ is a disturbance vector, $\mathcal{L} = \mathcal{L}(\partial_x, \partial_x^2, \partial_y, \partial_y^2, \ldots)$ is a linear operator and $\mathcal{M}$ is a positive definite operator. The boundary conditions are

$$\mathcal{B}X = 0 \,\text{at}\, y = \pm 1/2, \tag{10.2}$$

where $\mathcal{B}$ is the boundary operator (for example no-slip and zero heat flux boundary conditions). The disturbance X is a smooth function of x and y at $t = 0$ (initial condition) and X vanishes at $|x| \to \infty$ at all time.

The solution of above linear system can be obtained by using Fourier-Laplace transform:

$$\hat{X}(y; k_x, \omega; H) = \int_0^\infty e^{-\omega t} dt \int_{-\infty}^\infty e^{-ik_x x} X(t, x, y; H) dx, \tag{10.3}$$

where H is the control parameter (e.g. the gap between two walls). The inverse transform of $\hat{X}$ is

$$X(t, x, y; H) = \frac{1}{4\pi^2 i} \int_{-\infty}^\infty e^{ik_x x} dk_x \int_{\gamma - i\infty}^{\gamma + i\infty} \hat{X}(y; k_x, \omega; H) e^{\omega t} d\omega, \tag{10.4}$$

where the line $\omega_r = \gamma$ lies to the right of any singularity of $\hat{X}$. The solution X depends on the branch points of outer integrand of (10.4) and poles of inner integrand. Now substituting (10.4) into (10.1), we get an eigenvalue problem with eigenvalue ω:

$$\mathbf{L}(k_x, H)\hat{X} \equiv (\omega M_{k_x} - L_{k_x})\, \hat{X} = 0, \tag{10.5}$$

where M_{k_x} and L_{k_x} can be obtained by replacing $\partial/\partial x$ by ik_x in matrix operators $\mathcal{M}$ and $\mathcal{L}$.

For subcritical parameters $H < H_c$, the real part ω_r of eigenvalue $\omega = \omega_r + i\omega_i$ is negative for each k_x. When $H > H_c$, ω_r becomes positive and the maximum value of the real part of ω occurs at $k_x = k_{xm}$ (see figure 10.1) where $k_x \to k_{xc}$ as $H \to H_c$. For $H > H_c$ and $k_x \sim k_{xm}$, we can write

$$\omega(k_x) = -ik_{xm}c_m + i\bar{a}_{1r}(k_x - k_{xm}) - \bar{a}_2(k_x - k_{xm})^2 + \ldots, \tag{10.6}$$

where $c_m = c_{mr} + ic_{mi}$ and $\bar{a}_2$ are complex numbers and $\bar{a}_{1r}$ is a real number. It has been verified

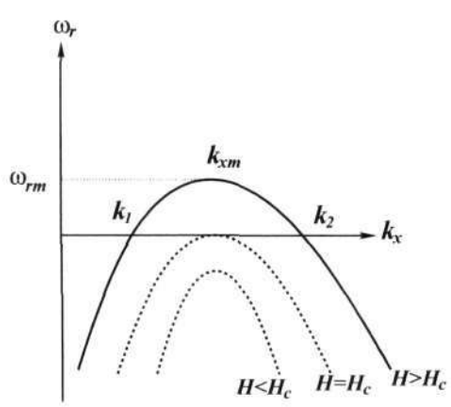

Figure 10.1: Schematic diagram for the variation of linear growth rate with wavenumber for three values of control parameter H. ω_{rm} is the maximum growth rate at k_{xm}. At $H = H_c$, $\omega_{rm} = 0$ and for $H < H_c$, $\omega_{rm} < 0$. The dynamics of system is dominated by the modes between (k_1, k_2) for $H > H_c$. These modes form a wave packet which moves with group velocity rather than the phase velocity.

that c_{mi} is proportional to $(H - H_c)$ as $H \to H_c$ as shown in figures 10.3(c, f, i), and the real part of a_2 is positive as $H \sim H_c$, i.e. $\bar{a}_{2r} > 0$ as $H \sim H_c$. We assume that the residue of integral (10.4) is a regular function and hence can be expanded as a power series around maximum wave number k_{xm}.

The residue of $\hat{X}$ at a pole gives the eigenfunction as defined below:

$$\mathrm{Res}(\hat{X}) = F = \frac{1}{2\pi i}\int_{\gamma-i\alpha}^{\gamma+i\alpha} \hat{X}(y;k_x,\omega;H)\mathrm{d}\omega. \tag{10.7}$$

Similar to (10.6) we can assume the form of eigenfunction $F = \mathrm{Res}(\hat{X})$ as

$$\mathrm{Res}(\hat{X}) = F(y;k_x,H) = \Gamma_0(y;H) + (k_x - k_{xm})\Gamma_1(y;H) + (k_x - k_{xm})^2\Gamma_2(y;H) + \ldots, \tag{10.8}$$

where Γ_n's with $n = 0, 1, 2, \ldots$ are complex functions of y which are independent of wave number k_x. We can write X in terms of residue F as:

$$X = \frac{1}{2\pi}\int_{-\infty}^{\infty} e^{[ik_x x + \omega(k_x)t]}F(y;k_x,H)dk_x. \tag{10.9}$$

At (H_c, k_{xc}), $\omega_r = 0$ and the eigenfunction $X_1(y)$ is $X_1 = \lim_{H\to H_c}\Gamma_0(y)$ which satisfies (cf. Eqn. 10.5)

$$\mathbf{L}(k_{xc},H_c)X_1 \equiv [i\omega_i M_{k_{xc}} - L_{k_{xc}}]\,X_1 = 0, \tag{10.10}$$

where $L_{k_{xc}} \equiv \mathcal{L}(\partial_x \to ik_{xc}, \partial_x^2 \to -k_{xc}^2, \partial_y, \partial_y^2, H_c)$.

We assume that $(k_x - k_{xc})$ and $(H - H_c)$ are small and double power series expansion is valid near the critical condition for both eigenvalue ω and eigenfunction F. Thus we can write

$$\omega(k_x,H) = -ic_r k_{xc} + ia_{1r}(k_x - k_{xc}) - a_2(k_x - k_{xc})^2 + \ldots + d_1(H - H_c) + \ldots, \tag{10.11}$$

$$F = X_1(y) + (k - k_{xc})X_{10}(y) + (H - H_c)X_{11}(y) + (k_x - k_{xc})^2 X_{12}(y) + \ldots, \tag{10.12}$$

where X_{10}, X_{11} and X_{12} are complex functions and independent of $(k_x - k_{xc})$ and $(H - H_c)$ and a_2 and d_1 are complex numbers. Note that F satisfies (10.10). From the definition of Taylor series we can write

$$X_{10} = \left.\frac{\partial F}{\partial k_x}\right|_c, \quad X_{11} = \left.\frac{\partial F}{\partial H}\right|_c \quad \text{and} \quad X_{12} = \left.\frac{1}{2}\frac{\partial^2 F}{\partial k_x^2}\right|_c, \tag{10.13}$$

where the subscript 'c' refers to the fact that the quantity is being evaluated at the critical point. Now using $\mathbf{L}(k_{xc},H_c)F = 0$ and (10.13), we get

$$\mathbf{L}\left.\frac{\partial F}{\partial k_x}\right|_c = -\left.\frac{\partial \mathbf{L}}{\partial k_x}F\right|_c \Rightarrow \mathbf{L}X_{10} = -\mathbf{L}_{10}X_1, \tag{10.14}$$

$$\mathbf{L}\left.\frac{\partial F}{\partial H}\right|_c = -\left.\frac{\partial \mathbf{L}}{\partial H}F\right|_c \Rightarrow \mathbf{L}X_{11} = -\mathbf{L}_{11}X_1, \tag{10.15}$$

$$\mathbf{L}\left.\frac{\partial^2 F}{\partial k_x^2}\right|_c = -2\frac{\partial \mathbf{L}}{\partial k_x}\frac{\partial F}{\partial k_x} + \left.\frac{\partial^2 \mathbf{L}}{\partial k_x^2}F\right|_c \Rightarrow \mathbf{L}X_{12} = \frac{1}{2}[-2\mathbf{L}_{10}X_{10} - \mathbf{L}_{12}X_1], \tag{10.16}$$

where

$$\mathbf{L}_{10} = \left.\frac{\partial \omega}{\partial k_x}M_{k_x} + \omega\frac{\partial M_{k_x}}{\partial k_x} - \frac{\partial L_{k_x}}{\partial k_x}\right|_c, \tag{10.17}$$

$$\mathbf{L}_{11} = \left.\frac{\partial \omega}{\partial H}M_{k_x} + \omega\frac{\partial M_{k_x}}{\partial H} - \frac{\partial L_{k_x}}{\partial H}\right|_c, \tag{10.18}$$

$$\mathbf{L}_{12} = \left.\frac{\partial^2 \omega}{\partial k_x^2}M_{k_x} + 2\frac{\partial s}{\partial k_x}\frac{\partial M_{k_x}}{\partial k_x} + \omega\frac{\partial^2 M_{k_x}}{\partial k_x^2} - \frac{\partial^2 L_{k_x}}{\partial k_x^2}\right|_c. \tag{10.19}$$

From equation (10.11) we can write

$$\left.\frac{\partial\omega}{\partial k_x}\right|_c = ia_{1r} = -ic_g, \qquad \left.\frac{1}{2}\frac{\partial^2\omega}{\partial k_x^2}\right|_c = -a_2, \qquad \left.\frac{\partial\omega}{\partial H}\right|_c = d_1, \tag{10.20}$$

where c_g is defined as group velocity. This is the velocity of propagation of slow modulation (envelop of waves) of a wave system. At the critical condition ($k_x = k_{xc}, H = H_c$) the growth rate is zero which gives a real group velocity. In general the group velocity is complex.

Substituting (10.20) into (10.17), (10.18) and (10.19), we get

$$\mathbf{L}_{10} = -ic_g M_{k_x} + \omega\frac{\partial M_{k_x}}{\partial k_x} - \left.\frac{\partial L_{k_x}}{\partial k_x}\right|_c, \tag{10.21}$$

$$\mathbf{L}_{11} = d_1 M_{k_x} + \omega\frac{\partial M_{k_x}}{\partial H} - \left.\frac{\partial L_{k_x}}{\partial H}\right|_c, \tag{10.22}$$

$$\mathbf{L}_{12} = -2a_2 M_{k_x} - 2ic_g\frac{\partial M_{k_x}}{\partial k_x} + \omega\frac{\partial^2 M_{k_x}}{\partial k_x^2} - \left.\frac{\partial^2 L_{k_x}}{\partial k_x^2}\right|_c. \tag{10.23}$$

For the present case $M = M_{k_x} = I$ is an identity operator. Substituting $M_{k_x} = I$ into (10.21), (10.22) and (10.23), we get

$$\mathbf{L}_{10} = -ic_g I - \left.\frac{\partial L_{k_x}}{\partial k_x}\right|_c, \quad \mathbf{L}_{11} = d_1 I - \left.\frac{\partial L_{k_x}}{\partial H}\right|_c, \quad \mathbf{L}_{12} = -2a_2 I - \left.\frac{\partial^2 L_{k_x}}{\partial k_x^2}\right|_c. \tag{10.24}$$

The inhomogeneous equations (10.14)-(10.16) contain the same operator $\mathbf{L}$ as in linear stability (10.10) and hence the solvability condition has to be satisfied. This implies that the solutions of (10.14)-(10.16) exist if and only if the inhomogeneous parts of (10.14)-(10.16) are orthogonal to adjoint eigenfunctions corresponding to linear stability operator $\mathbf{L}$.

The solvability condition yields expressions for c_g, d_1 and a_2 as given below:

$$c_g = i\frac{\left\langle X_1^\dagger, \left[\frac{\partial L_{k_x}}{\partial k_x}\right]_{(H_c,k_{xc})} X_1\right\rangle}{\langle X_1^\dagger, X_1\rangle}, \qquad d_1 = \frac{\left\langle X_1^\dagger, \left[\frac{\partial L_{k_x}}{\partial H}\right]_{(H_c,k_{xc})} X_1\right\rangle}{\langle X_1^\dagger, X_1\rangle}, \tag{10.25}$$

$$a_2 = \frac{\left\langle X_1^\dagger, \left(\mathbf{L}_{10}X_{10} - \frac{1}{2}\left[\frac{\partial^2 L_{k_x}}{\partial k_x^2}\right]_{(H_c,k_{xc})} X_1\right)\right\rangle}{\langle X_1^\dagger, X_1\rangle}. \tag{10.26}$$

where $X_1^\dagger$ is the adjoint eigenfunction which satisfies

$$\mathbf{L}^\dagger(k_{xc}, H_c)X_1^\dagger = 0, \tag{10.27}$$

with adjoint boundary conditions (no-slip and zero heat flux at the walls). The elements of $\mathbf{L}^\dagger$ are given in Appendix 10B. The system of adjoint equations can be derived via integration by parts using an inner product as defined below:

$$\langle f, g\rangle = \int_{-1/2}^{1/2} \tilde{f} g dy, \tag{10.28}$$

where tilde denotes a complex conjugate.

10.1.2 Preliminary Linear Results

Figure 10.2 shows the neutral stability curve in (H, k_x)-plane for $\phi^0 = 0.2$ and $e = 0.8$. In the panel SW denotes stationary wave instability, and $TW1$ and $TW2$ represent travelling waves instabilities. The flow is unstable inside the neutral stability curve and stable outside. It is seen from this figure that there are ranges of wavenumbers between which the flow is unstable due to stationary and travelling waves.

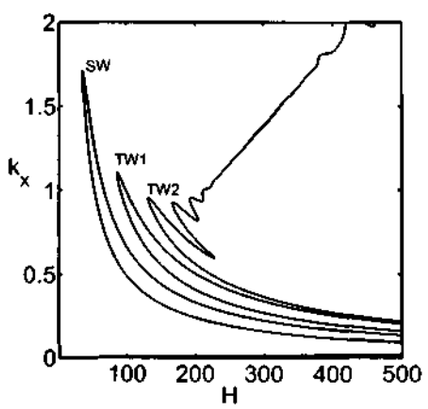

Figure 10.2: Neutral stability contour in (H, k_x)-plane for $\phi^0 = 0.2$ and $e = 0.8$. SW, $TW1$ and $TW2$ are the contours representing standing waves (SW) and travelling waves ($TW1$ and $TW2$). Flow is unstable inside this contour and stable outside.

We have magnified three loops at the onset of three instabilities, SW, $TW1$ and $TW2$, and replotted them in figures 10.3(a), 10.3(d) and 10.3(g), respectively. The stable and unstable regions are shown in each panel. In figure 10.3, the first, second and third rows correspond to SW, $TW1$ and $TW2$ wave instabilities, respectively. Figures 10.3(b), 10.3(e) and 10.3(h) show the variation of growth rate with wavenumber for three values of Couette gap: $H < H_c$, $H = H_c$ and $H > H_c$. It is seen from figures 10.3(b), 10.3(e) and 10.3(h) that at (i) $H < H_c$ all modes are stable, (ii) $H = H_c$ one mode becomes neutrally stable, and (iii) $H > H_c$ there exists a band of unstable modes. These modes, corresponding to the unstable band of wavenumbers, lead to spatio-temporal patterns in the flow. The assumption of monochromatic perturbation waves is no-longer valid for simultaneously growing modes. Therefore, we need to consider aperiodic perturbations in the flow in order to study natural development of a wave system from some initial conditions.

The variations of growth rate of the least stable eigenvalue with $|H - H_c|$ with H_c being the critical Couette gap (for SW, $TW1$ and $TW2$, the critical Couette gap H_c is equal to $\sim$ 35, 84 and 131, respectively), for $H > H_c$ (circles) and $H < H_c$ (stars) are shown in figures 10.3(c), 10.3(f) and 10.3(i) It clearly seen in these figures that the maximum growth rate is proportional to $H - H_c$ near the critical condition. The inset in each panel is the log-log plot of the main panel.

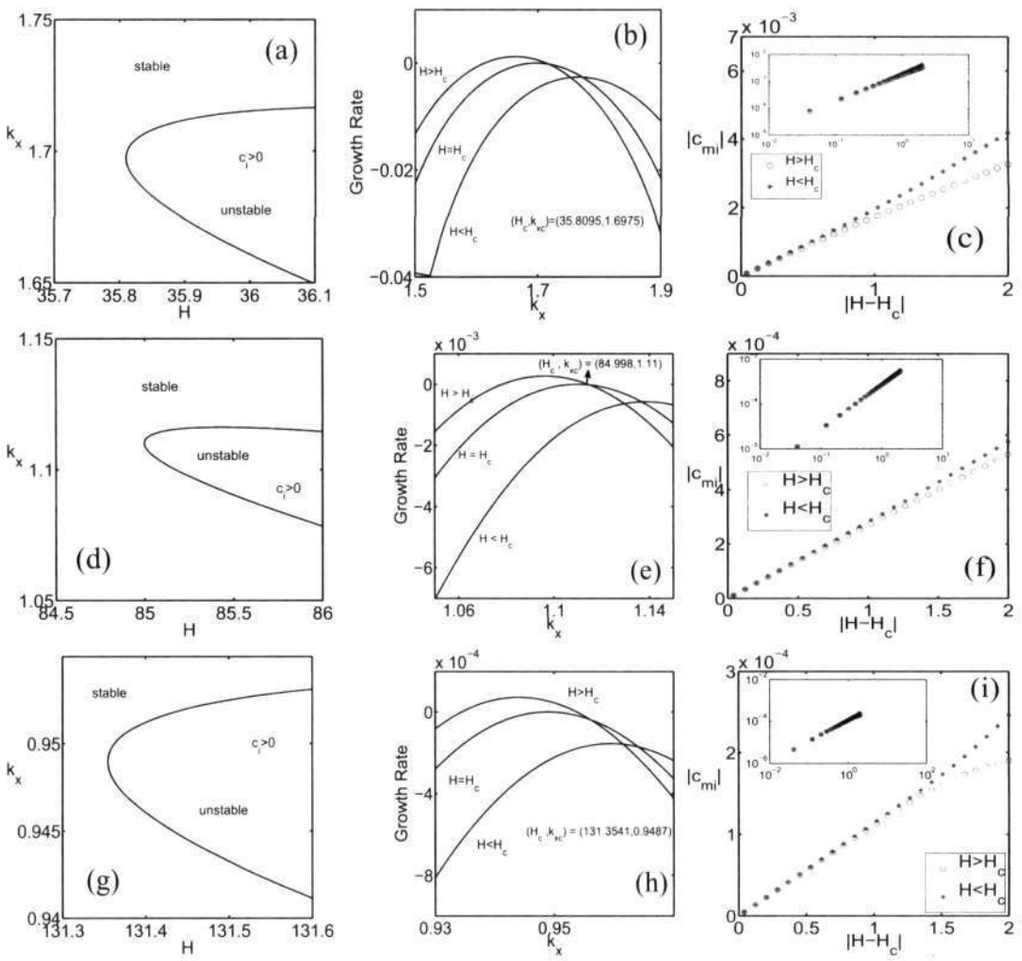

Figure 10.3: Panels: (a), (b), (c) correspond to SW; (d), (e), (f) correspond to $TW1$, and (g), (h), (i) correspond to $TW2$, of figure 10.2. (a, d, g) Neutral stability contour in (H, k_x) plane. (b, e, h) Variation of growth rate for $H = H_c$, $H < H_c$ and $H > H_c$. (c, f, i) The maximum of growth rate $\omega_{rm} = c_m^i$ vs $H - H_c$ for $H > H$ (circles) and $H < H_c$ (stars), where the inset in each panel shows the log-log plot. Other parameters are same as in figure 10.2.

10.2 Nonlinear Problem: Complex Ginzburg Landau Equation

We use the method of multiple scales as described in Stewartson & Stuart (1971) and Fujimura (1989). The nonlinear disturbance equations (3.6) can be written in operator form:

$$\left(\mathbf{I}\frac{\partial}{\partial t} - \mathcal{L}\right) X = \sum_{j=2}^{\infty} \mathcal{N}_j, \tag{10.29}$$

where $\mathcal{N}_j = (\mathcal{N}_j^{(1)}, \mathcal{N}_j^{(2)}, \mathcal{N}_j^{(3)}, \mathcal{N}_j^{(4)})$ are the nonlinear terms at jth order. The superscripts 1, 2, 3 and 4 in $\mathcal{N}_j$ refer to continuity, x-momentum, y-momentum and energy equations, respectively.

Consider a perturbation from a linear neutral state $(k_x, H) = (k_{xc}, H_c)$, where $|H - H_c| << 1$ holds for a slightly supercritical or a subcritical state. Let us consider the case of slightly supercritical, i.e., $H > H_c$ and define ϵ^2, a small parameter, as

$$\epsilon^2 = d_{1r}|H - H_c|, \qquad H = H_c + \frac{\epsilon^2}{d_{1r}}. \tag{10.30}$$

Stewartson & Stuart (1971) considered that the timescale at which nonlinear interactions affect the evolution of fundamental mode is of order (linear growth rate)$^{-1}$ (slow time scale) and the linear growth rate is of order ϵ^2. We are using two time scales (τ, t) such that

$$\tau = \epsilon^2 t. \tag{10.31}$$

The slow length scale is defined as

$$\xi = \epsilon(x - c_g t), \tag{10.32}$$

where c_g is the group velocity. Using above transformations, the derivatives with respect to time and streamwise direction can be written as

$$\frac{\partial}{\partial t} \rightarrow \frac{\partial}{\partial t} - \epsilon c_g \frac{\partial}{\partial \xi} + \epsilon^2 \frac{\partial}{\partial \tau}, \tag{10.33}$$

$$\frac{\partial}{\partial x} \rightarrow \frac{\partial}{\partial x} + \epsilon \frac{\partial}{\partial \xi}. \tag{10.34}$$

Now we write the solution in terms of perturbation series around the base state:

$$X(x, y, t) = \epsilon X^{(1)}(x, y, \xi, \tau, t) + \epsilon^2 X^{(2)}(x, y, \xi, \tau, t) + \epsilon^3 X^{(3)}(x, y, \xi, \tau, t) + \ldots \tag{10.35}$$

We substitute (10.30), (10.33), (10.34) and (10.35) into (10.29) and equate the coefficients of like powers of ϵ in order to extract equations of different order.

10.2.1 $O(\epsilon)$: Linear Problem

At $O(\epsilon)$, we get a linear problem:

$$\left(\mathbf{I}\frac{\partial}{\partial t} - \mathcal{L}\right) X^{(1)} = 0. \tag{10.36}$$

The solution $X^{(1)}$ of above equation can be written as

$$X^{(1)}(x,y,t,\xi,\tau) = \mathscr{A}(\xi,\tau)X_1(y)e^{ik_{xc}x+\omega t} + \text{c.c}, \tag{10.37}$$

where ω is a complex frequency (i.e. eigenvalue from the linear theory), $\mathscr{A}(\xi,\tau)$ is a slowly varying complex amplitude of the disturbance which depends on both time and space, and X_1 is the eigenvector from the linear problem. The exponential term of (10.37) corresponds to fast length and time scales.

10.2.2 $O(\epsilon^2)$: Second Harmonic and Mean Flow Distortion

At $o(\epsilon^2)$ we get:

$$\left(\mathbf{I}\frac{\partial}{\partial t} - \mathcal{L}\right) X^{(2)} = c_g\mathbf{I}\frac{\partial X^{(1)}}{\partial \xi} + L_{\xi xy}X^{(1)} + \mathcal{N}_2(X^{(1)}, X^{(1)}), \tag{10.38}$$

where $L_{\xi xy}$ is a linear operator which consists of partial derivatives of slow (ξ) and fast (x and y) variables. The solution of above equation is

$$X^{(2)}(x,y,t,\xi,\tau) = \mathscr{A}^2E^2X^{[2;2]}(y) + |\mathscr{A}|^2X^{[0;2]}(y) + \frac{\partial \mathscr{A}}{\partial \xi}EX^{[1;2]}(y) + \text{c.c.}, \tag{10.39}$$

where $E = e^{ik_{xc}+\omega t}$. The first and second index of superscript in the notation $X^{[i;j]}$ correspond to powers of exponential and ϵ, respectively. Substituting (10.39) into (10.38) and equating the coefficient of $\mathscr{A}^2E^2$, $|\mathscr{A}|^2$ and $\mathscr{A}_\xi E$, we get equations for $X^{[2;2]}$, $X^{[0;2]}$ and $X^{[1;2]}$. The explicit forms of these equations in matrix notation are

$$(2\omega\mathbf{I} - L_{2k_{xc}})X^{[2;2]} = N_2(X_1, X_1) \tag{10.40}$$

$$(2\omega_r\mathbf{I} - L_0)X^{[0;2]} = N_2(X_1, \tilde{X}_1) + N_2(\tilde{X}_1, X_1) \tag{10.41}$$

$$(\omega\mathbf{I} - L_{k_{xc}})X^{[1;2]} = c_gIX_1 + \frac{1}{i}\left[\frac{\partial L_{k_x}}{\partial k_x}\right]X_1 \tag{10.42}$$

The derivation of above three equations (10.40)-(10.42) is given in Appendix 10A.

Comparing equation (10.42) with (10.14) we get

$$i(\omega\mathbf{I} - L_{k_{xc}})X^{[1;2]} = -\mathbf{L}_{10}X_1. \tag{10.43}$$

This implies that $X_{10} = iX^{[1;2]}$. This shows the relation between the nonlinear analysis of this section with the linear analysis for wave system described in the previous section. Note that $X^{[2;2]}$ and $X^{[0;2]}$ are the second harmonic and the distortion to mean flow, respectively. $X^{[1;2]}$ represents the term due to slow spatial variation in flow direction. The left hand side of (10.42) has the same operator as in the linear eigenvalue problem; the solution $X^{[1;2]}$ is possible if the inhomogeneous part is orthogonal to adjoint eigenfunction which gives c_g (see §10.1.1).

10.2.3 $O(\epsilon^3)$: Solvability Condition and Complex Ginzburg Landau Equation

At $o(\epsilon^3)$ we get:

$$\begin{aligned}\left(\mathbf{I}\frac{\partial}{\partial t}-\mathcal{L}\right)X^{(3)} &= \left(c_g I\frac{\partial X^{(2)}}{\partial\xi}+L_{\xi xy}\right)X^{(2)}-\frac{\partial X^{(1)}}{\partial\tau}+\frac{1}{d_{1r}}\frac{\partial L_{k_x}}{\partial H}X^{(1)}+f(X^1)\\ &\quad+\mathcal{N}_2(X^{(1)},X^{(2)})+\mathcal{N}_2(X^{(2)},X^{(1)})+\mathcal{N}_3(X^{(1)},X^{(1)},X^{(1)})\\ &\quad+\mathcal{N}_2^{\text{slow}}(X^{(1)},X^{(1)}),\end{aligned}\tag{10.44}$$

where $f(X^{(1)})$ is a function of $X^{(1)}$. Now we expand $X^{(3)}$ as

$$X^{(3)}(x,y,t,\xi,\tau) = EX_{13}(y,\xi,\tau)+E^3X_{33}(y,\xi,\tau)+\ldots.\tag{10.45}$$

Note that X_{13} depends on y and the slow variables. Substituting expressions (10.45), (10.37) and (10.39) into (10.44) and equating powers of E from both sides, we get

$$\begin{aligned}(\omega I-L_{k_{xc}})X_{13} &= \frac{1}{d_{1r}}\frac{\partial L_{k_x}}{\partial H}\mathscr{A}X_1-\frac{\partial\mathscr{A}}{\partial\tau}X_1+G_{13}|\mathscr{A}|^2\mathscr{A}\\ &\quad+\frac{\partial^2\mathscr{A}}{\partial\xi^2}\left[\left(c_g+\frac{1}{i}\left[\frac{\partial L_{k_x}}{\partial k_x}\right]\right)X^{[1;2]}-\frac{1}{2}\left[\frac{\partial^2 L_{k_x}}{\partial k_x^2}\right]X_1\right],\end{aligned}\tag{10.46}$$

where G_{13} is the vector of nonlinear terms,

$$\begin{aligned}G_{13} &= N_2(\tilde{X}_1,X^{[2;2]})+N_2(X^{[2;2]},\tilde{X}_1)+N_2(X_1,X^{[0;2]})+N_2(X^{[0;2]},X_1)\\ &\quad+N_3(\tilde{X}_1,X_1,X_1)+N_3(X_1,\tilde{X}_1,X_1)+N_3(X_1,X_1,\tilde{X}_1).\end{aligned}\tag{10.47}$$

Note that

$$\left(c_g+\frac{1}{i}\left[\frac{\partial L_{k_x}}{\partial k_x}\right]\right)X^{[1;2]}=-\frac{1}{i}L_{10}X^{[1;2]}.\tag{10.48}$$

It is obvious from the right hand side of (10.46) that X_{13} contains terms which depend on $\mathscr{A}$, $\mathscr{A}|\mathscr{A}|^2$, $\frac{\partial\mathscr{A}}{\partial\tau}$ and $\frac{\partial^2\mathscr{A}}{\partial\xi^2}$.

The *Ginzburg-Landau equation* can be derived from the solvability condition of equation (10.46):

$$\frac{\partial\mathscr{A}(\xi,\tau)}{\partial\tau} = \frac{d_1}{d_{1r}}\mathscr{A}+a_2\frac{\partial^2\mathscr{A}}{\partial\xi^2}+c^{(2)}|\mathscr{A}|^2\mathscr{A},\tag{10.49}$$

where

$$d_1=\frac{\left\langle X_1^\dagger,\frac{\partial L_{k_x}}{\partial H}\right\rangle}{\left\langle X_1^\dagger,X_1\right\rangle},\qquad c^{(2)}=\frac{\langle X_1^\dagger,G_{13}\rangle}{\langle X_1^\dagger,X_1\rangle},\tag{10.50}$$

and

$$a_2=\frac{\left\langle X_1^\dagger,\left(c_gX^{[1;2]}+\frac{1}{i}\left[\frac{\partial L_{k_x}}{\partial k_x}\right]X^{[1;2]}-\frac{1}{2}\left[\frac{\partial^2 L_{k_x}}{\partial k_x^2}\right]X_1\right)\right\rangle}{\left\langle X_1^\dagger,X_1\right\rangle}.\tag{10.51}$$

Here $c^{(2)}$ is the first Landau coefficient. The form of a_2, (10.51), is same as given by (10.26). This can be verified by substituting $X^{[1;2]}=-iX_{10}$ into (10.51).

Let us define new variables $X=(x-c_gt)$ and $\mathscr{A}=\epsilon^{-1}\mathscr{A}_1e^{id_{1i}\epsilon t/d_{1r}}$. Substituting the above

transformation into (10.49) and eliminating the wave speed part of d_1/d_{1r},

$$\frac{d_1}{d_{1r}} = 1 + i\frac{d_{1i}}{d_{1r}}, \tag{10.52}$$

we get another form of CGLE:

$$\frac{\partial \mathscr{A}_1}{\partial t} = \epsilon^2 \mathscr{A}_1 + a_2 \frac{\partial^2 \mathscr{A}_1}{\partial X^2} + c^{(2)} \mathscr{A}_1 |\mathscr{A}_1|^2. \tag{10.53}$$

10.3 Summary

Using the multiple scale analysis the complex Ginzburg Landau equation has been derived for aperiodic patterns in two-dimensional granular Couette flow. The linear stability problem for the development of a wave system has been detailed in §10.1. The integral expressions of the group velocity (c_g) and other coefficients (d_1 and a_1) have been derived from the linear theory of wave systems which are the coefficients of linear terms in CGLE. Furthermore we have rederived integral expressions c_g, d_1 and a_1 from the nonlinear analysis of wave systems. We have shown that expressions of c_g, d_1 and a_1 derived from the linear and nonlinear theories are exactly same. The first Landau coefficient is derived using solvability condition. The above derivation is a generalization of Stewartson & Stuart's (1971) work since we are considering four balance equations rather than a single equation. The detailed numerical results are deferred to a future work.

Appendix 10A. Outline of Derivation

In this appendix, we will derive eqns. (10.40), (10.41), (10.42) and (10.46). We will start with x-momentum equation and will give all necessary details of the weakly nonlinear analysis using multiple scales as described in the previous section. The other disturbance equations, continuity, y-momentum and energy, can be derived in a similar manner.

Step 1

We substitute (10.33)-(10.34) into (10.29). The resulting x-momentum equation is given by

$$\left(\frac{\partial}{\partial t}-\epsilon c_g\frac{\partial}{\partial \xi}+\epsilon^2\frac{\partial}{\partial \tau}\right)u'+u^0\left(\frac{\partial}{\partial x}+\epsilon\frac{\partial}{\partial \xi}\right)u'+u^0_y v'$$
$$-\frac{1}{\phi^0}\left(\frac{1}{H_c^2}-\frac{2\epsilon^2}{H_c^3 d_{1r}}\right)\left[-p^0_\phi\left(\frac{\partial}{\partial x}+\epsilon\frac{\partial}{\partial \xi}\right)+u^0_y\mu^0_{\phi y}+u^0_{yy}\mu^0_\phi+\mu^0_\phi u^0_y\frac{\partial}{\partial y}\right]\phi'$$
$$-\frac{1}{\phi^0}\left(\frac{1}{H_c^2}-\frac{2\epsilon^2}{H_c^3 d_{1r}}\right)\left[(2\mu^0+\lambda^0)\left(\frac{\partial^2}{\partial x^2}+\epsilon^2\frac{\partial^2}{\partial \xi^2}+2\epsilon\frac{\partial^2}{\partial x\partial \xi}\right)+\mu^0_y\frac{\partial}{\partial y}+\mu^0\frac{\partial^2}{\partial y^2}\right]u'$$
$$-\frac{1}{\phi^0}\left(\frac{1}{H_c^2}-\frac{2\epsilon^2}{H_c^3 d_{1r}}\right)\left[\mu^0_y\left(\frac{\partial}{\partial x}+\epsilon\frac{\partial}{\partial \xi}\right)+(\mu^0+\lambda^0)\left(\frac{\partial}{\partial x}+\epsilon\frac{\partial}{\partial \xi}\right)\frac{\partial}{\partial y}\right]v'$$
$$-\frac{1}{\phi^0}\left(\frac{1}{H_c^2}-\frac{2\epsilon^2}{H_c^3 d_{1r}}\right)\left[-p^0_T\left(\frac{\partial}{\partial x}+\epsilon\frac{\partial}{\partial \xi}\right)+u^0_y\mu^0_{Ty}+u^0_{yy}\mu^0_T+\mu^0_T u^0_y\frac{\partial}{\partial y}\right]T'=\mathcal{N}_2^{(2)}+\mathcal{N}_3^{(2)}.$$

Step 2

We substitute (10.35) into disturbance equations obtained from step 1 and equate like order terms. At $O(\epsilon^2)$ the form of x-momentum equation is

$$\frac{\partial u^{(2)}}{\partial t}+u^{(0)}\frac{\partial u^{(2)}}{\partial x}+u^0_y v^{(2)}-\frac{1}{\phi^0 H_c^2}\left(-p^0_\phi\frac{\partial}{\partial x}+u^0_y\mu^0_{\phi y}+u^0_{yy}\mu^0_\phi+\mu^0_\phi u^0_y\frac{\partial}{\partial y}\right)\phi^{(2)}$$
$$-\frac{1}{\phi^0 H_c^2}\left[(2\mu^0+\lambda^0)\frac{\partial^2}{\partial x^2}+\mu^0_y\frac{\partial}{\partial y}+\mu^0\frac{\partial^2}{\partial y^2}\right]u^{(2)}-\frac{1}{\phi^0 H_c^2}\left[\mu^0_y\frac{\partial}{\partial x}+(\mu^0+\lambda^0)\frac{\partial^2}{\partial x\partial y}\right]v^{(2)}$$
$$-\frac{1}{\phi^0 H_c^2}\left[-p^0_T\frac{\partial}{\partial x}+u^0_y\mu^0_{Ty}+u^0_{yy}\mu^0_T+\mu^0_T u^0_y\frac{\partial}{\partial y}\right]T^{(2)}+u^0\frac{\partial u^{(1)}}{\partial \xi}-c_g\frac{\partial u^{(1)}}{\partial \xi}$$
$$-\frac{1}{\phi^0 H_c^2}\left[-p^0_\phi\frac{\partial \phi^{(1)}}{\partial \xi}\right]-\frac{1}{\phi^0 H_c^2}\left[2(2\mu^0+\lambda^0)\frac{\partial^2 u^{(1)}}{\partial x\partial \xi}\right]-\frac{1}{\phi^0 H_c^2}\left[\mu^0_y\frac{\partial v^{(1)}}{\partial \xi}+(\mu^0+\lambda^0)\frac{\partial^2 v^{(1)}}{\partial y\partial \xi}\right]$$
$$-\frac{1}{\phi^0 H_c^2}\left[-p^0_T\frac{\partial T^{(1)}}{\partial \xi}\right]=\mathcal{N}_2^{(2)}(X^{(1)},X^{(1)}).$$

Next we separate the terms related to fast and slow variables:

$$\begin{aligned}\frac{\partial u^{(2)}}{\partial t}-R_2\cdot X^{(2)} &= c_g\frac{\partial u^{(1)}}{\partial \xi}-u^0\frac{\partial u^{(1)}}{\partial \xi}+\frac{1}{\phi^0 H_c^2}\left[-p^0_\phi\frac{\partial \phi^{(1)}}{\partial \xi}\right]\\ &\quad+\frac{1}{\phi^0 H_c^2}\left[2(2\mu^0+\lambda^0)\frac{\partial^2 u^{(1)}}{\partial x\partial \xi}\right]+\frac{1}{\phi^0 H_c^2}\left[\mu^0_y\frac{\partial v^{(1)}}{\partial \xi}+(\mu^0+\lambda^0)\frac{\partial^2 v^{(1)}}{\partial y\partial \xi}\right]\\ &\quad+\frac{1}{\phi^0 H_c^2}\left[-p^0_T\frac{\partial T^{(1)}}{\partial \xi}\right]+\mathcal{N}_2^{(2)}(X^{(1)},X^{(1)})\end{aligned}$$

where $R_2\cdot X^{(2)}$ is the inner product of the second row of linear matrix $\mathcal{L}$ with $X^{(2)}$.

Step 3

We substitute (10.37) and (10.39) into equations which are obtained from the step 2 and equate the coefficient of $\mathscr{A}^2E^2$, $|\mathscr{A}|^2$ and $\mathscr{A}_\xi E$.

$$\left.\begin{aligned}O(\mathscr{A}^2E^2):\quad 2\omega u^{[2;2]}-R_2|_{\frac{\partial}{\partial x}\to 2ik_x}\cdot X^{[2;2]} &= N_2^{(2)}(X_1,X_1)\\ O(|\mathscr{A}|^2):\quad 2\omega_r u^{[0;2]}-R_2|_{\frac{\partial}{\partial x}\to 0}\cdot X^{[0;2]} &= N_2^{(2)}(X_1,\tilde{X}_1)+N_2^{(2)}(\tilde{X}_1,X_1)\\ O(\mathscr{A}_\xi E):\quad \omega u^{[1;2]}-R_2|_{\frac{\partial}{\partial x}\to ik_x}\cdot X^{[1;2]} &= c_g u_1-u^0u_1+\tfrac{1}{\phi^0H_c^2}\left(-p^0_\phi\phi_1\right)+\tfrac{1}{\phi^0H_c^2}2(2\mu^0+\lambda^0)ik_xu_1\\ &\quad+\tfrac{1}{\phi^0H_c^2}\left(\mu^0_y v_1+(\mu^0+\lambda^0)\tfrac{\mathrm{d}v_1}{\mathrm{d}y}\right)+\tfrac{1}{\phi^0H_c^2}\left(-p^0_T T_1\right)\\ &= c_g u_1+\tfrac{1}{i}\left[da_{21},da_{22},da_{23},da_{24}\right]\cdot X_1\end{aligned}\right\}$$

where da_{ij} are the elements of matrix $\left[\frac{\partial L_{k_x}}{\partial k_x}\right]$ as given in Appendix 10C. The full matrix form of above equations can be written as

$$\left.\begin{array}{lcl}(2\omega\mathbf{I}-L_{2k_x})\,X^{[2;2]} & = & N_2(X_1,X_1)\\ (2\omega_r\mathbf{I}-L_0)X^{[0;2]} & = & N_2(X_1,\tilde{X}_1)+N_2(\tilde{X}_1,X_1)\\ (\omega\mathbf{I}-L_{k_x})X^{[1;2]} & = & c_g I X_1+\frac{1}{i}\left[\frac{\partial L_{k_x}}{\partial k_x}\right]X_1\end{array}\right\}.$$

Note that, $\mathcal{N}_j$ and N_j for $j=1,2,\ldots,\infty$ are the vector form of nonlinear terms containing partial and ordinary derivatives, respectively. Thus, equations (10.40), (10.41) and (10.42) have been derived.

In order to derive (10.46), we repeat step 2 for $O(\epsilon^3)$ to get

$$\left.\begin{array}{l}\frac{\partial u^{(3)}}{\partial t}-R_2\cdot X^{(3)}=c_g\frac{\partial u^{(2)}}{\partial\xi}-\frac{\partial u^{(1)}}{\partial\tau}-u^0\frac{\partial u^{(2)}}{\partial\xi}-\frac{2}{\phi^0H_c^3d_{1r}}\left[-p_\phi^0\frac{\partial}{\partial x}+u_y^0\left(\mu_{\phi y}^0+\mu_\phi^0\frac{\partial}{\partial y}\right)\right]\phi^{(1)}\\ -\frac{2}{\phi^0H_c^3d_{1r}}\left[(2\mu^0+\lambda^0)\frac{\partial^2}{\partial x^2}+\mu_y^0\frac{\partial}{\partial y}+\mu^0\frac{\partial^2}{\partial y^2}\right]u^{(1)}-\frac{2}{\phi^0H_c^3d_{1r}}\left[\mu_y^0\frac{\partial}{\partial x}+(\mu^0+\lambda^0)\frac{\partial^2}{\partial x\partial y}\right]v^{(1)}\\ -\frac{2}{\phi^0H_c^3d_{1r}}\left[-p_T^0\frac{\partial}{\partial x}+u_y^0\left(\mu_{Ty}^0+\mu_T^0\frac{\partial}{\partial y}\right)\right]T^{(1)}+\frac{1}{\phi^0H_c^2}\left[-p_\phi^0\frac{\partial\phi^{(2)}}{\partial\xi}\right]\\ +\frac{1}{\phi^0H_c^2}\left[2(2\mu^0+\lambda^0)\frac{\partial^2u^{(2)}}{\partial x\partial\xi}+(2\mu^0+\lambda^0)\frac{\partial^2u^{(1)}}{\partial\xi^2}\right]+\frac{1}{\phi^0H_c^2}\left[\mu_y^0\frac{\partial v^{(2)}}{\partial\xi}+(\mu^0+\lambda^0)\frac{\partial^2v^{(2)}}{\partial y\partial\xi}\right]\\ +\frac{1}{\phi^0H_c^2}\left[-p_T^0\frac{\partial T^{(2)}}{\partial\xi}\right]+\mathcal{N}_2^{(2)}(X^{(1)},X^{(2)})+\mathcal{N}_2^{(2)}(X^{(2)},X^{(1)})+\mathcal{N}_3^{(2)}(X^{(1)},X^{(1)},X^{(1)})\end{array}\right\}.$$

Substituting (10.37), (10.39) and (10.45) into above equation and equating the coefficient of E we get:

$$\left.\begin{array}{l}\omega u_{13}-R_2|_{\frac{\partial}{\partial x}\to ik_x}\cdot X_{13}=\\ c_gu^{[1;2]}\frac{\partial^2\mathscr{A}}{\partial\xi^2}-\frac{\partial\mathscr{A}}{\partial\tau}u_1-u^0u^{[1;2]}\frac{\partial^2\mathscr{A}}{\partial\xi^2}-\frac{2}{\phi^0H_c^3d_{1r}}\left[-p_\phi^0ik_x+u_y^0\left(\mu_{\phi y}^0+\mu_\phi^0\frac{\partial}{\partial y}\right)\right]\mathscr{A}\phi_1\\ -\frac{2}{\phi^0H_c^3d_{1r}}\left[-(2\mu^0+\lambda^0)k_x^2+\mu_y^0\frac{\partial}{\partial y}+\mu^0\frac{\partial^2}{\partial y^2}\right]\mathscr{A}u_1-\frac{2ik_x}{\phi^0H_c^3d_{1r}}\left[\mu_y^0+(\mu^0+\lambda^0)\frac{\partial}{\partial y}\right]\mathscr{A}v_1\\ -\frac{2}{\phi^0H_c^3d_{1r}}\left[-p_T^0ik_x+u_y^0\left(\mu_{Ty}^0+\mu_T^0\frac{\partial}{\partial y}\right)\right]\mathscr{A}T_1+\frac{1}{\phi^0H_c^2}\left(-p_\phi^0\phi^{[1;2]}\right)\frac{\partial^2\mathscr{A}}{\partial\xi^2}\\ +\frac{1}{\phi^0H_c^2}\left[2ik_x(2\mu^0+\lambda^0)u^{[1;2]}+(2\mu^0+\lambda^0)u_1\right]\frac{\partial^2\mathscr{A}}{\partial\xi^2}\\ +\frac{1}{\phi^0H_c^2}\left[\mu_y^0v^{[1;2]}+(\mu^0+\lambda^0)\frac{\partial v^{[1;2]}}{\partial y}\right]\frac{\partial^2\mathscr{A}}{\partial\xi^2}+\frac{1}{\phi^0H_c^2}\left(-p_T^0T^{[1;2]}\right)\frac{\partial^2\mathscr{A}}{\partial\xi^2}\\ +\left[N_2^{(2)}(X^{[2;2]},\tilde{X}_1)+N_2^{(2)}(\tilde{X}_1,X^{[2;2]})+N_2^{(2)}(X^{[0;2]},X_1)+N_2^{(2)}(X_1,X^{[0;2]})\right.\\ \left.+N_3^{(2)}(\tilde{X}_1,X_1,X_1)+N_3^{(2)}(X_1,\tilde{X}_1,X_1)+N_3^{(2)}(X_1,X_1,\tilde{X}_1)\right]\mathscr{A}|\mathscr{A}|^2\end{array}\right\}.$$

The above expression, in the matrix notation, can be written as

$$\begin{array}{rcl}\omega u_{13}-R_2|_{\frac{\partial}{\partial x}\to ik_x}\cdot X_{13} & = & \frac{1}{d_{1r}}[db_{21},db_{22},db_{23},db_{24}]\cdot\mathscr{A}X_1-\frac{\partial\mathscr{A}}{\partial\tau}u_1\\ & & +\frac{\partial^2\mathscr{A}}{\partial\xi^2}\left[c_gu^{[1;2]}+\frac{1}{i}[da_{21},da_{22},da_{23},da_{24}]\cdot X^{[1;2]}\right.\\ & & \left.-\frac{1}{2}[0,da'_{22},0,0]\cdot X_1\right]+G_{13}\mathscr{A}|\mathscr{A}|^2\end{array}$$

where da_{ij}, da'_{ij} and db_{ij} are the elements of matrices $\left[\frac{\partial L_{k_x}}{\partial k_x}\right]$, $\left[\frac{\partial^2 L_{k_x}}{\partial k_x^2}\right]$ and $\left[\frac{\partial L_{k_x}}{\partial H}\right]$ and given in Appendix 10C. The complete matrix form including continuity, y-momentum and energy equations can be written as

$$\begin{array}{rcl}(\omega I-L_{k_{xc}})\,X_{13} & = & \frac{1}{d_{1r}}\frac{\partial L_{k_x}}{\partial H}\mathscr{A}X_1-\frac{\partial\mathscr{A}}{\partial\tau}X_1\\ & & +\frac{\partial^2\mathscr{A}}{\partial\xi^2}\left(c_gX^{[1;2]}+\frac{1}{i}\left[\frac{\partial L_{k_x}}{\partial k_x}\right]X^{[1;2]}-\frac{1}{2}\left[\frac{\partial^2L_{k_x}}{\partial k_x^2}\right]X_1\right)+G_{13}|\mathscr{A}|^2\mathscr{A}\end{array}$$

which is same as equation (10.46).

Appendix 10B. Adjoint Matrix Elements $\mathbf{L}^\dagger = [l_{ij}^\dagger]$

$$
\left.
\begin{aligned}
l_{11}^\dagger &= ik_x u^0 \qquad l_{12}^\dagger = \tfrac{ik_x p_\phi^0}{\phi^0 H^2} + \tfrac{\mu_\phi^0 u_y^0}{(\phi^0 H)^2}\left(\phi_y^0 - \phi^0 D\right)\\
l_{13}^\dagger &= -\tfrac{ik_x u_y^0 \mu_\phi^0}{\phi^0 H^2} + \tfrac{p_\phi^0}{(\phi^0 H)^2}\left(\phi^0 D - \phi_y^0\right)\\
l_{14}^\dagger &= \tfrac{2(\mu_\phi^0 u_y^{0^2} - \mathcal{D}_\phi^0)}{\phi^0\, dim} + \tfrac{2\kappa_\phi^0 T_y^0}{(\phi^0 H)^2\, dim}(\phi_y^0 - \phi^0 D)\\
l_{21}^\dagger &= ik_x \phi^0\\
l_{22}^\dagger &= ik_x u^0 - \tfrac{k_x^2(2\mu^0+\lambda^0)}{\phi^0 H^2} + \tfrac{1}{(\phi^0 H)^2}\left[-\mu_y^0\phi_y^0 - \mu^0\phi_{yy}^0\right.\\
&\quad \left. +(\phi^0\mu_y^0 - 2\phi_y^0\mu^0)D + \phi^0\mu^0 D^2 + \tfrac{2\phi_y^{0^2}\mu^0}{\phi^0}\right]\\
l_{23}^\dagger &= \tfrac{ik_x}{(\phi^0 H)^2}\left[(\mu^0+\lambda^0)(\phi^0 D - \phi_y^0) + \phi^0\mu_y^0\right]\\
l_{24}^\dagger &= \tfrac{2ik_x p^0}{\phi^0\, dim} - \tfrac{4}{(\phi^0)^2\, dim}\left[\phi^0\left(\mu^0 u_y^0 D + \mu_y^0 u_y^0 + \mu^0 u_{yy}^0\right) - \phi_y^0\mu^0 u_y^0\right]\\
l_{31}^\dagger &= \phi^0 D\\
l_{32}^\dagger &= -u_y^0 + \tfrac{ik_x}{(\phi^0 H)^2}\left[(\mu^0+\lambda^0)(\phi^0 D - \phi_y^0) + \phi^0\lambda_y^0\right]\\
l_{33}^\dagger &= ik_x u^0 - \tfrac{k_x^2\mu^0}{\phi^0 H^2} + \tfrac{1}{(\phi^0)^2 H^2}\left[-(2\mu_y^0+\lambda_y^0)\phi_y^0 - (2\mu^0+\lambda^0)\phi_{yy}^0\right.\\
&\quad \left. +\left(\phi^0(2\mu_y^0+\lambda_y^0) - 2\phi_y^0(2\mu^0+\lambda^0)\right)D + \phi^0(2\mu^0+\lambda^0)D^2 + \tfrac{2\phi_y^{0^2}(2\mu^0+\lambda^0)}{\phi^0}\right]\\
l_{34}^\dagger &= -T_y^0 - \tfrac{4ik_x\mu^0 u_y^0}{\phi^0\, dim} + \tfrac{2}{(\phi^0)^2\, dim}\left[p^0(\phi^0 D - \phi_y^0) + \phi^0 p_y^0\right]\\
l_{41}^\dagger &= 0, \qquad l_{42}^\dagger = \tfrac{ik_x p_T^0}{\phi^0 H^2} + \tfrac{\mu_T^0 u_y^0}{(\phi^0 H)^2}\left(\phi_y^0 - \phi^0 D\right)\\
l_{43}^\dagger &= \tfrac{-ik_x u_y^0 \mu_T^0}{\phi^0 H^2} + \tfrac{p_T^0}{(\phi^0 H)^2}\left(\phi^0 D - \phi_y^0\right)\\
l_{44}^\dagger &= ik_x u^0 + \tfrac{2}{\phi^0\, dim}\left[-\tfrac{k_x^2\kappa^0}{H^2} + \mu_T^0(u_y^0)^2 - \mathcal{D}_T^0\right] + \tfrac{2}{(\phi^0 H)^2 dim}\left[\phi^0\kappa_y D\right.\\
&\quad \left. -\phi^0 T_y^0\kappa_T^0 D + \phi_y^0 T_y^0\kappa_T^0 + \phi^0\kappa^0 D^2 - 2\phi_y^0\kappa^0 D - \phi_{yy}^0\kappa^0 - \phi_y^0\kappa_y^0 + \tfrac{2(\phi_y^0)^2\kappa^0}{\phi^0}\right]
\end{aligned}
\right\}
$$

Here $D = \mathrm{d}/\mathrm{d}y$.

Appendix 10C. Elements of Matrices

$L_{k_x} = [a_{ij}]$, $\frac{\partial L_{k_x}}{\partial k_x} = [da_{ij}]$, $\frac{\partial^2 L_{k_x}}{\partial k_x^2} = [da'_{ij}]$ and $\frac{\partial L_{k_x}}{\partial H} = [db_{ij}]$

$$
\left.\begin{array}{rcl}
a_{11} &=& -ik_x u^0, \\
a_{12} &=& -ik_x \phi^0, \\
a_{13} &=& -\left(\phi^0_y + \phi^0 D\right), \\
a_{14} &=& 0, \\
a_{21} &=& \frac{1}{\phi^0 H^2}\left(-ik_x p^0_\phi + u^0_y \mu^0_{\phi y} + u^0_{yy}\mu^0_\phi + \mu^0_\phi u^0_y D\right), \\
a_{22} &=& -ik_x u^0 + \frac{1}{\phi^0 H^2}\left((2\mu^0+\lambda^0)(ik_x)^2 + \mu^0_y D + \mu^0 D^2\right), \\
a_{23} &=& -u^0_y + \frac{1}{\phi^0 H^2}\left(ik_x \mu^0_y + ik_x(\mu^0+\lambda^0)D\right), \\
a_{24} &=& \frac{1}{\phi^0 H^2}\left(-ik_x p^0_T + u^0_y \mu^0_{Ty} + u^0_{yy}\mu^0_T + \mu^0_T u^0_y D\right), \\
a_{31} &=& \frac{1}{\phi^0 H^2}\left(ik_x u^0_y \mu^0_\phi - p^0_{\phi y} - p^0_\phi D\right), \\
a_{32} &=& \frac{1}{\phi^0 H^2}\left(ik_x \lambda^0_y + ikk_x(\lambda^0+\mu^0)D\right), \\
a_{33} &=& -ik_x u^0 + \frac{1}{\phi^0 H^2}\left((ik_x)^2\mu^0 + (2\mu^0_y + \lambda^0_y)D + (2\mu^0+\lambda^0)D^2\right), \\
a_{34} &=& \frac{1}{\phi^0 H^2}\left(ik_x u^0_y \mu^0_T - p^0_{Ty} - p^0_T D\right), \\
a_{41} &=& \frac{2}{\phi^0 d}\left(\frac{1}{H^2}\left(T^0_y \kappa^0_{\phi y} + T^0_y \kappa^0_\phi D + \kappa^0_\phi T^0_{yy}\right) + \mu^0_\phi (u^0_y)^2 - \mathcal{D}^0_\phi\right), \\
a_{42} &=& \frac{2}{\phi^0 d}\left(-ik_x p^0 + 2\mu^0 u^0_y D\right), \\
a_{43} &=& -T^0_y + \frac{2}{\phi^0 d}\left(-p^0 D + 2ik_x \mu^0 u^0_y\right), \\
a_{44} &=& -ik_x u^0 + \frac{2}{\phi^0 d}\left[\frac{1}{H^2}\left((ik_x)^2\kappa^0 + \left(T^0_y \kappa^0_{Ty} + \kappa^0_T T^0_{yy}\right)\right.\right. \\
&& \left.\left. + \left(\kappa^0_y + T^0_y \kappa^0_T\right) D + \kappa^0 D^2\right) + \mu^0_T (u^0_y)^2 - \mathcal{D}^0_T\right]
\end{array}\right\}
$$

$$
\frac{\partial L_{k_x}}{\partial k_x} = \begin{pmatrix}
-iu^0 & -i\phi^0 & 0 & 0 \\
\frac{-ip^0_\phi}{H^2\phi^0} & -iu^0 - \frac{2(2\mu^0+\lambda^0)k_x}{H^2\phi^0} & \frac{i(\mu^0_y+(\mu^0+\lambda^0)D)}{H^2\phi^0} & \frac{-ip^0_T}{H^2\phi^0} \\
\frac{iu^0_y\mu^0_\phi}{H^2\phi^0} & \frac{i(\lambda^0_y+(\mu^0+\lambda^0)D)}{H^2\phi^0} & -iu^0 - \frac{2k_x\mu^0}{H^2\phi^0} & \frac{iu^0_y\mu^0_T}{H^2\phi^0} \\
0 & \frac{-2ip^0}{\phi^0 dim} & \frac{4i\mu^0 u^0_y}{\phi^0 dim} & -iu^0 - \frac{4k_x\kappa^0}{\phi^0 H^2 dim}
\end{pmatrix}
$$

$(da'_{11}, da'_{22}, da'_{33}, da'_{44}) = \left(0, -\frac{2(2\mu^0+\lambda^0)}{H^2\phi^0}, -\frac{2\mu^0}{H^2\phi^0}, -\frac{4\kappa^0}{\phi^0 H^2 dim}\right)$ $da'_{ij} = 0$ for $i \neq j$.

$$
\left.\begin{array}{rcl}
db_{11} &=& db_{12} = db_{13} = db_{14} = 0, \\
db_{21} &=& \frac{-2}{\phi^0 H^3}\left(-ik_x p^0_\phi + u^0_y \mu^0_{\phi y} + u^0_{yy}\mu^0_\phi + \mu^0_\phi u^0_y D\right), \\
db_{22} &=& \frac{-2}{\phi^0 H^3}\left(-(2\mu^0+\lambda^0)k^2_x + \mu^0_y D + \mu^0 D^2\right), \\
db_{23} &=& \frac{-2}{\phi^0 H^3}\left(ik_x \mu^0_y + ik_x(\mu^0+\lambda^0)D\right), \\
db_{24} &=& \frac{-2}{\phi^0 H^3}\left(-ik_x p^0_T + u^0_y \mu^0_{Ty} + u^0_{yy}\mu^0_T + \mu^0_T u^0_y D\right), \\
db_{31} &=& \frac{-2}{\phi^0 H^3}\left(ik_x u^0_y \mu^0_\phi - p^0_{\phi y} - p^0_\phi D\right), \\
db_{32} &=& \frac{-2}{\phi^0 H^3}\left(ik_x \lambda^0_y + ik_x(\lambda^0+\mu^0)D\right), \\
db_{33} &=& \frac{-2}{\phi^0 H^3}\left(-k^2_x \mu^0 + (2\mu^0_y + \lambda^0_y)D + (2\mu^0+\lambda^0)D^2\right), \\
db_{34} &=& \frac{-2}{\phi^0 H^3}\left(ik_x u^0_y \mu^0_T - p^0_{Ty} - p^0_T D\right), \\
db_{41} &=& \frac{-4}{\phi^0 dim H^3}\left(T^0_y \kappa^0_{\phi y} + T^0_y \kappa^0_\phi D + \kappa^0_\phi T^0_{yy}\right), \\
db_{42} &=& db_{43} = 0, \\
db_{44} &=& \frac{-4}{\phi^0 dim H^3}\left(-k^2_x \kappa^0 + \left(T^0_y \kappa^0_{Ty} + \kappa^0_T T^0_{yy}\right) + \left(\kappa^0_y + T^0_y \kappa^0_T\right) D + \kappa^0 D^2\right)
\end{array}\right\}
$$

CHAPTER 11

SUMMARY AND OUTLOOK

11.1 Introduction

In this thesis, we have studied the nonlinear stability of granular plane Couette flow, focussing on various instabilities induced by shearing (Alam & Nott 1998; Alam 2005, 2006; Alam *et al.* 2008) which lead to spatially heterogeneous structures of macroscopic dimensions. The main objective of the present thesis is to describe shearbanding (gradient and vorticity bandings), stationary wave and traveling wave patterns of granular plane Couette flow using an order parameter theory via Landau equation and Ginzburg-Landau equation.

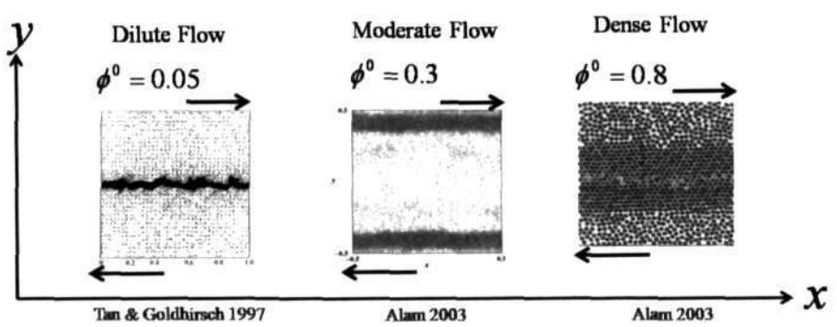

Figure 11.1: Three snap-shots from MD-simulations for $\phi^0 = 0.05$, 0.3 and 0.8 showing the gradient banding in granular plane Couette flow. Taken from Tan & Goldhirsch (1997) and Alam (2003).

One typical instability in granular shear flows is shearbanding instability which leads to banding of particles. The banding transitions have been observed in molecular dynamic simulations of granular plane Couette flow. The MD-simulation results of granular plane Couette flow of Tan & Goldhirsch (1997) showed the existence of gradient bands even in dilute flows. Figure 11.1 shows three snap-shots from MD-simulations for three values of densities in dilute ($\phi^0 = 0.05$), moderate (0.3) and dense (0.8) flow regimes. In this figure x- and y-coordinates refer to streamwise and gradient directions, respectively. The gradient banding can be seen in all flow regimes. Depending on the banding directions, the banding transition can be classified as "gradient banding" or "vorticity banding". If the bands of different shear-rates extend along the gradient direction, the banding is known as gradient banding, and if the bands of different shear-stresses accumulate along the vorticity direction it is referred to as vorticity banding. In other words, gradient and vorticity bandings represent shear-localization and stress-localization in the flow, respectively.

Apart from the shearbanding transition, the granular plane Couette flow supports various types of stationary and traveling wave instabilities (Alam & Nott 1998). The earliest MD-simulations of Hopkins & Louge (1991) identified travelling-wave patterns in the form of oblique bands, aligned along the compressional axis of the shear flow for a range of densities.

This thesis started with a brief introduction of patterns in rapid granular flows driven by vibration, gravity and shear, e.g., standing wave patterns and convection rolls in a vibrated granular

system, density waves in gravity driven granular Poiseuille flow, fingering in chute flow, shearbanding in shear flow, etc. We then reviewed the pattern forming order parameter models such as coupled complex Ginzburg-Landau model, Swift-Hohenberg model and continuous coupled map model, etc. in §1.3. The MD-simulation and experimental observations of shearbanding patterns in granular plane Couette flow has been discussed in §1.4. The basic hydrodynamic equations along with few widely used constitutive models for the inelastic hard-sphere and hard-disk fluids have been described in chapter 2.

11.2 Development of Nonlinear Theory

The overview of existing nonlinear stability theories is given in §3.1. In the first part of chapter 3, a general weakly nonlinear stability analysis using amplitude expansion method of Stuart and others (Stuart 1960; Watson 1960; Reynolds & Potter 1967) has been described in detail. Using this perturbation method, the nonlinear stability problem has been reduced to a sequence of linear inhomogeneous differential equations for the fundamental mode (linear eigenfunction) and its harmonics and the related distortions of the base flow and the fundamental at various order. The amplitude expansion method constitutes an *indirect* method to arrive at the Landau equation, and the related nonlinear corrections, the Landau coefficients, are determined from the Fredholm alternative or the solvability condition at the cubic/higher order in the perturbation amplitude. We have adapted this amplitude expansion method for the present nonlinear stability analysis of granular plane Couette flow.

Concurrently, we have developed a numerical method in chapter 3, based on Chebyshev spectral collocation technique and Gauss-Chebyshev quadrature (Canuto *et al.* 1988), to solve the inhomogeneous differential equations at each order in perturbation amplitude.

While the amplitude expansion method is physically appealing and easy to adapt the present method differs from several *direct* methods of nonlinear stability analysis, for example the center manifold reduction (Carr 1981; Shukla & Alam 2009) and multiple scale analysis (Newell *et al.* 1993) wherein the Landau equation is derived directly from the nonlinear perturbation equations which is in contrast to the *amplitude expansion method* where the order parameter equation is postulated based on physical arguments about possible time evolution of the linear mode.

In the case of the center manifold reduction, the nonlinear analysis is carried out via a spectral decomposition of fast and slow modes (Shukla & Alam 2009); the relevant order parameter equation is derived by taking inner product of the evolution equation of the slow mode with its adjoint eigenfunction and the Landau coefficients are subsequently picked up from the coefficients of nonlinear terms of various order. We have shown that both direct and indirect methods lead to the same expression for the first Landau coefficient which is the first nonlinear correction to the well-studied linear theory. Therefore, up-to the first Landau coefficient, both the amplitude expansion method and the center manifold reduction are *equivalent* for the present problem of granular plane Couette flow.

11.3 Gradient Banding in Granular Couette Flow

Figure 11.2 shows the neutral stability curve (left plot) along with density eigenfunctions in its inset; the flow is unstable inside the neutral contour and stable outside. Therefore, according to linear theory, the non-uniform solutions are not possible in dilute limit because the uniform shear flow is stable there. This is in contrast to MD-simulations of Tan & Goldhirsch (1997) who found non-uniform solutions in dilute limit as shown in the right picture of figure 11.2. Thus the linear stability analysis is not capable to explain shearbanding patterns in dilute granular plane Couette flow.

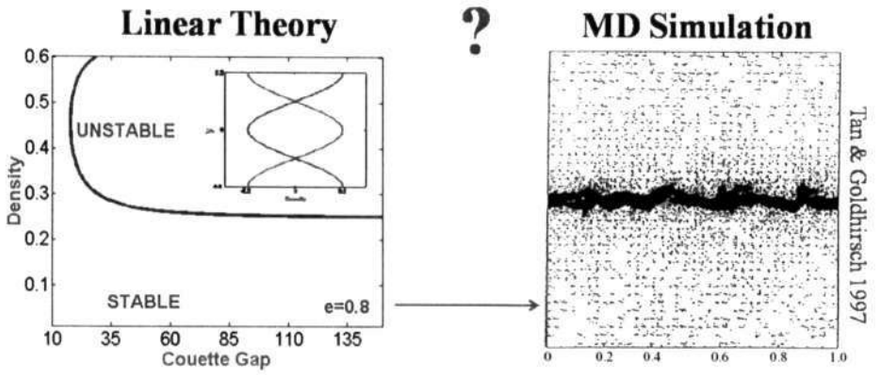

Figure 11.2: Comparison of linear theory and MD-simulation.

In the first problem of present thesis, a weakly nonlinear theory, in terms of the well-known Landau equation, has been developed to describe the nonlinear saturation of shear-banding instability in rapid granular plane Couette flow. The shear-banding instability corresponds to streamwise-independent perturbations ($\partial/\partial x(\cdot) = 0$ and $\partial/\partial y(\cdot) \neq 0$, where x and y refer to flow and gradient directions, respectively) of the underlying steady uniform shear flow which degenerates into alternate layers of dense and dilute regions of low and high shear-rates, respectively, along the gradient direction. The nonlinear stability of this shear-banding instability is analyzed using two perturbation methods, the *center manifold reduction method* (chapter 4) and the *amplitude expansion method* (chapter 5)

In chapter 4, we have derived Landau equation using *center manifold reduction method*. The first Landau coefficient has been calculated using an spectral-based numerical method. Our results on the first Landau coefficient suggest that there is a subcritical finite-amplitude instability for dilute flows even though the dilute flow is stable according to the linear stability theory. We have shown the equivalence between amplitude expansion method and center manifold reduction method in chapter 4.

An order-parameter theory for the same shear-banding instability in the granular plane Couette flow using the amplitude expansion method has been developed in chapter 5. For the shear-banding instability, the nonlinear modes are found to follow certain symmetries of the fundamental mode and the base state solution which have helped us to discover analytical solutions for the second harmonic and the distortion to the fundamental mode. It is shown that the second harmonic and the base state distortion at the quadratic order are equal to each other for this instability. The present analytical solutions for nonlinear modes have been used to evaluate the first Landau coefficient exactly which complements and verifies our previous numerical solution of the same problem in chapter 4 (Shukla & Alam 2009). These analytical solutions further helped to identify universal scalings for the first Landau coefficient, the equilibrium amplitude, and the phase diagram in the (H, ϕ^0)-plane in terms of the mode number β and the inelasticity $(1 - e^2)^{1/2}$ as detailed in §5.5.5. Uncovering the analytical solution for the nonlinear shear-banding instability in granular plane Couette flown constitutes one outcome of the present thesis.

The quantitative agreement in figures (5.3)-(5.3) between our *analytical* and the *spectral* solutions for the fundamental mode and its harmonics (of various order) as well as for the first Landau coefficient ascertains the accuracy of our spectral-based numerical method which has been developed in chapter 4. This constitutes another outcome of this thesis: the validation of a numerical scheme for nonlinear stability calculations, via its comparison with our analytical

solutions, which can now be adapted to other types of granular shear flows.

Analyzing the zero contour of the first Landau coefficient in the (H, ϕ^0)-plane, where $H = \overline{h}/\overline{d}$ is the ratio between the Couette gap and the particle diameter and ϕ^0 is the mean volume fraction of particles, we have reestablished our previous prediction which is documented in chapter 4 and (Shukla & Alam 2009) that the lower branch of the neutral stability curve (i.e. the 'zero' growth-rate contour) in the (H, ϕ^0)-plane is *subcritically* unstable. The related threshold-amplitude for nonlinear stability has been determined, leading to the possibility of shear-banding-type solutions in dilute flows via subcritical bifurcations. In contrast to the predictions of nonlinear theory, the dilute flows are known to be stable according to the linear stability theory. Irrespective of the nature of bifurcation, the predicted nonlinear solutions indicate that the uniform shear-flow undergoes an ordering transition into alternate layers of dense and dilute regions of low and high shear rates, respectively, parallel to the flow-direction.

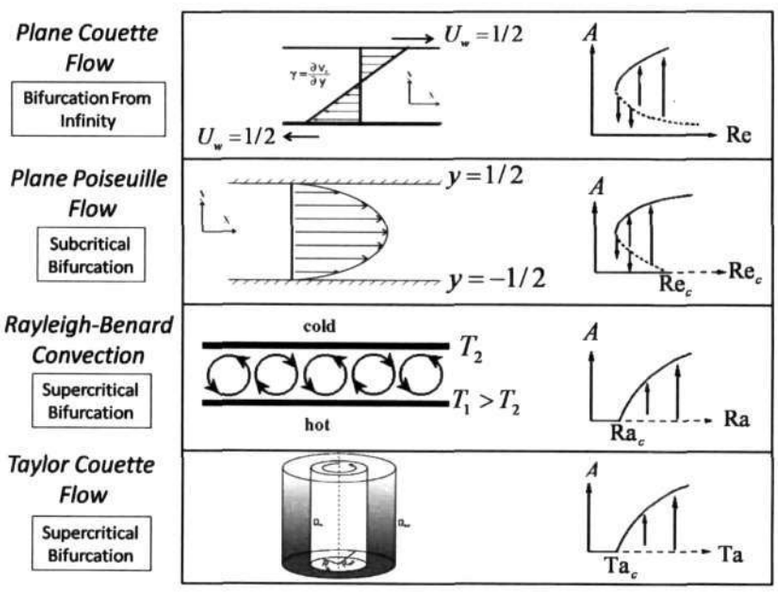

Figure 11.3: Various Newtonian flow configurations and associated bifurcations: plane Couette flow, plane Poiseuille flow, Rayleigh-Bénard convection and Taylor Couette flow.

Our order-parameter theory predicts that the nonlinear shear-banding instability leads to different types of pitchfork bifurcations (see Figure 5.38) as we increase the mean density (ϕ^0) from the Boltzmann limit: (i) bifurcation from infinity in the Boltzmann limit ($\phi^0 < \phi_c^l$), (ii) subcritical bifurcations over a small window of moderate densities ($\phi_c^l < \phi^0 < \phi_c^s$), (iii) supercritical bifurcations at moderate densities ($\phi_c^s < \phi^0 > \phi_c^{s1}$), (iv) subcritical bifurcations in the dense limit ($\phi_c^{s1} < \phi^0 > \phi_c^{s2}$), and finally again to (v) supercritical bifurcations near the close packing limit ($\phi^0 > \phi_c^{s2} \sim \phi_m$), Note that the 'bifurcation from infinity' can be considered as a generalized subcritical bifurcation wherein the bifurcation point originates from infinity ($H = \infty$). The critical density at which a transition occurs from one bifurcation-type to another (ϕ_c^l, ϕ_c^s, ϕ_c^{s1} and ϕ_c^{s2}) depends on the detailed forms of constitutive relations as well as on the choice of the contact radial distribution function. We have found that while the first three sequences of bifurcations (i–iii) appear to be independent of the choice of constitutive relations, the last two bifurcation sequences (iv–v), especially the appearance of subcritical bifurcations in the dense limit, depend on the choice of the contact radial distribution function. Since all three possible types of pitchfork

bifurcations can be realized in this flow by just varying the mean density, we conclude that the granular plane Couette flow truly serves as a *microcosm* of pitchfork bifurcations.

Let us have a quick glance at various prototypical problems of Newtonian fluids and their related bifurcations in figure 11.3. A similar type of bifurcation from infinity occurs in the plane Couette flow (Nagata 1990) but there is no subcritical or supercritical pitchfork bifurcations because the plane Couette flow of Newtonian fluids is stable according to linear theory (Romanov 1973). Another example is the plane Poiseuille flow of Newtonian fluids which admits subcritical bifurcations (Stuart 1960; Reynolds & Potter 1967). Note that this bifurcation is not stationary and this is a case of subcritical-Hopf bifurcation rather than pitchfork. The Rayleigh-Bénard convection (Busse 1978) and Taylor Couette flow are examples of supercritical pitchfork bifurcations. As per our knowledge no other flow admits all types of pitchfork bifurcations, and therefore the granular plane Couette flow is truly a *paradigm* for pitchfork bifurcations.

11.4 Two-dimensional Patterns in Granular Couette Flow

We have developed an order-parameter theory to describe the nonlinear periodic patterns in a two-dimensional granular plane Couette flow which is known to linearly unstable to a variety of stationary and travelling instabilities, having modulations in both streamwise (x) and gradient (y) directions in chapter 6. This is the first nonlinear study of its kind in the literature of granular fluids for spatially inhomogeneous two-dimensional patterns. The related order-parameter equation, the Landau-Stuart equation, has been derived using the amplitude expansion method (Stuart 1960; Watson 1960) of nonlinear stability theory, extending our previous work (chapters 4, 5, and Shukla & Alam 2009, 2011) on one-dimensional shear-banding instability. The nonlinear stability of two classes of modes (in different regimes of streamwise wavenumber k_x) in granular plane Couette flow has been studied in detail using the present order-parameter theory. The numerical results, obtained by employing a spectral-based numerical method, are presented on the first Landau coefficient, the equilibrium amplitude, the equilibrium phase velocity, the limit cycle and the nonlinear perturbation fields. The supercritical and subcritical regimes of both pitchfork/static and Hopf/oscillatory bifurcations have been identified, and the first evidence of two-dimensional nonlinear equilibrium states for stationary and travelling waves has been found in granular plane Couette flow.

In addition to the well-known shear-banding instability ($k_x = 0$) whose nonlinear saturation has been studied recently by us (Shukla & Alam 2009, 2011), there are long-wave ($k_x \sim 0$) stationary and travelling instabilities in granular plane Couette flow. For such long-wave modes, we have uncovered nonlinear equilibrium states of stationary waves in the dilute limit (where the flow is known to be stable to the shear-banding mode) and of both stationary and travelling waves at moderate-to-large densities. While the nonlinear solutions in the dilute limit appear via a subcritical pitchfork bifurcation, those at larger densities via supercritical pitchfork and Hopf bifurcations. From a comparison between linear and nonlinear perturbation fields, we found that the origin of nonlinear states at $k_x \sim 0$ is tied to the corresponding 'subcritical'/'supercritical' nonlinear shear-banding solutions ($k_x = 0$).

There are stationary and travelling instabilities at moderate values of wavenumber $k_x \sim O(1)$ whose growth rates are larger than those at long-waves by an order-of-magnitude or more – these are referred to as 'dominant' instabilities (see, for example, two dominant peaks at $k_x \sim 0.6$ and $k_x \sim 0.95$ in figure 6.3) in granular plane Couette flow. For the dominant stationary instability, we found that the nonlinear solutions appear via supercritical pitchfork bifurcations (figures 6.20 and 6.25) over a range of mean densities (ϕ^0) at sufficiently large Couette gaps ($H > H_c^{SW}$) and this range of unstable ϕ^0 increases with increasing H; in the linearly stable regime ($H < H_c^{SW}$) there could be subcritical bifurcations (figure 6.25). The nonlinear stationary patterns have density

bands that are located at some oblique angle to the streamwise direction (figure 6.21) – similar oblique density bands have been observed in particle simulations (Hopkins & Louge 1991; Tan & Goldhirsch 1997). The structural features of supercritical stationary solutions look similar at any value of ϕ^0 and H, but the related unstable subcritical solutions are markedly different (having density bands parallel to the streamwise direction) from their supercritical counterparts, even though the linear eigenfunctions are similar for both cases.

For the dominant travelling instability, the flow is linearly unstable for a range of mean densities if the Couette gap is sufficiently large ($H > H_c^{TW} > H_c^{SW}$), and there are subcritical nonlinear travelling waves at $H < H_c^{TW}$ at a given ϕ^0. For $H > H_c^{TW}$, there are supercritical and subcritical Hopf bifurcations at small and large values of ϕ^0 (figure 6.22), respectively – the latter finding of subcritical travelling solutions at moderate-to-large densities is in contrast to supercritical solutions for dominant stationary mode. The supercritical and subcritical solutions look structurally different for the dominant travelling waves too. In addition to dominant travelling wave instability, there are linearly stable travelling waves at $k_x \sim O(1)$ which could also be unstable with respect to finite-amplitude disturbances (figure 6.14).

The effect of restitution coefficient on the nonlinear saturation of dominant instabilities was studied. We found that the structural features of the nonlinear stationary and travelling wave solutions remain unaffected by the level of inelastic dissipation as long as the underlying linear eigenfunctions are similar. We have uncovered a new stationary instability in a very wide Couette cell ($H = 500$) which seems to persist at any restitution coefficient ($e \neq 1$), and the equilibrium amplitude A_e required to attain this mode is much smaller than the corresponding 'dominant' stationary instability. Apart from providing the first evidence of a variety of two-dimensional nonlinear patterns in granular plane Couette flow, we hope that the present work will inspire large-scale particle simulations to detect such stable and unstable nonlinear states in plane Couette flow.

By analysing the modal equations at quadratic order in perturbation amplitude, we have identified two types of nonlinear resonances: (1) the 'mean-flow' resonance and (2) the '$1:2$' resonance. The former occurs due to the interaction of least-stable mode at some $k_x \neq 0$ with a shear-banding mode ($k_x = 0$) mode, obeying the following condition on growth rate $[a^{(0)}]$ and frequency $[b^{(0)}]$: $2a_\alpha^{(0)}(k_x) = a_\beta^{(0)}(k_x = 0)$ and $b_\beta^{(0)}(k_x = 0) = 0$, where α and β refer to two interacting modes. The $1:2$ resonance occurs due to the interaction of two modes α and β, obeying $2a_\alpha^{(0)}(k_x) = a_\beta^{(0)}(2k_x)$ and $2b_\alpha^{(0)}(k_x) = b_\beta^{(0)}(2k_x)$, with their wave-number ratio being $1:2$. The signature of either type of resonances is implicated by the divergence of the first Landau coefficient at specific values of wave-number k_x where the resonance takes place. Our numerical results in §6.7.3 have clearly demonstrated the existence of mean-flow resonance in granular plane Couette flow, however, the existence of $1:2$ resonance remained illusive in the present flow. Note that the $1:2$ resonance points, being codimension-3 bifurcation points, require an exhaustive search in the parameter space to locate them which was not pursued in this thesis.

11.5 Nonlinear Stability of 3D Granular Couette Flow

11.5.1 Vorticity Banding in Granular Couette Flow

The vorticity banding in three-dimensional granular plane Couette flow has been investigated via nonlinear stability analysis in chapter 7 of this thesis. We have started this chapter with a preamble containing a review on gradient and vorticity bandings and then we have written down all necessary theoretical background for the nonlinear stability analysis of three dimensional granular plane Couette flow.

We mainly focussed on pure spanwise instability in this chapter. Due to the pure spanwise ($\partial/\partial x(.) = 0, \partial/\partial y(.) = 0, \partial/\partial z(.) \neq 0$) instability, the uniform shear flow breaks into regions of

high and low shear stresses along the mean vorticity direction - this is known as vorticity banding. For such pure spanwise instabilities, an *analytical* order parameter theory has been developed. The general solutions of the nonlinear equations (distortions of mean flow and fundamental, and harmonics of fundamental) and Landau coefficients (§7.6.5) have been derived at any arbitrary order in amplitude. We have calculated first (7.57) and second (7.69) Landau coefficients analytically. The bifurcation analysis has been carried out for all flow regimes. Our analysis suggests that the vorticity banding appears via supercritical pitchfork bifurcation for density $\phi^0 < \phi^d$ and via subcritical pitchfork bifurcation for density $\phi^0 > \phi^d$, where ϕ^0 is the mean density and ϕ^d is the critical mean density for the transition from supercritical to subcritical bifurcations as shown in figure 7.10. The first (see figures 7.12 and 7.15) and second (see figure 7.13) order transitions at the onset of pure spanwise instabilities have been investigated using cubic and quintic order Landau equations. Our analysis shows that the cubic and quintic order amplitudes are almost equal near the critical point, but they deviate from each other away from the critical point. The subcritical Hopf bifurcation has been found for large spanwise wavenumbers in moderate-to-dense flows which has been shown in figure 7.25.

The present analysis suggests that for parameters far away from the neutral stability curve there exist both Hopf and pitchfork bifurcations (see schematic figure 7.29). The crucial effect of higher order nonlinear terms while calculating higher order Landau coefficients has been demonstrated in figures 7.23-7.24. It has been concluded that the n^{th} order nonlinearities must be retained while calculating n^{th} order Landau coefficient. The variations of perturbation fields, pressure and shear viscosity have been shown which verified shear-stress localization in the flow due to vorticity banding

11.5.2 Gradient and Vorticity Bandings

In chapter 8, the gradient and vorticity bandings in three-dimensional streamwise-independent granular plane Couette flow have been probed via analytical solutions of weakly nonlinear analysis. Such streamwise independent instabilities lead to bands along gradient and vorticity directions. The analytical expressions for the distortion of mean flow, second harmonic and first Landau coefficient have been derived in terms of trigonometric functions. The bifurcation analysis for these instabilities has been carried out. The comparison between linear and nonlinear finite amplitude patterns for density, temperature, velocity and vorticity has been made.

The bifurcation analysis shows that the transition can occur from subcritical-to-supercritical and supercritical-to-subcritical bifurcations in different flow regimes. The streamwise and transverse 3D-structures have been observed from the disturbance patterns. The subcritical and supercritical density and vorticity patterns have been found to be more distorted than their linear patterns. The corresponding velocity and temperature fields are found to be relatively unaffected by nonlinearities.

11.6 Order-parameter Theory using Coupled Landau Equations

One limitation of a 'single' Landau equation is that it cannot deal with situations that involve possible *interactions* among different modes which might occur either (i) due to a linear resonance among two or more modes or (ii) due to two or more non-resonating modes having growth-rates that are arbitrarily close to each other.

In chapter 9, we have developed a general theory of mode interactions for both non-resonant and resonant interactions. We have used center manifold reduction method to derive Coupled Landau equations. The analytical weakly nonlinear solutions for the streamwise independent 2D-granular plane Couette flow has been extended and the coupled Landau equations for situations

of mode crossing (without resonance, see figure 9.1) have been derived. Preliminary numerical results for the interaction of modes $\beta = 1$ and 2 have been discussed. The detailed numerical analysis for all densities and other cases of mode interactions are left for future work.

11.7 Complex Ginzburg-Landau Equation

Tsimring & Aranson (1997) proposed a phenomenological order parameter model, the Ginzburg-Landau equation coupled with an effective mass conservation equation, to theoretically study the patterns in a vibrated granular bed (squares, stripes, hexagons, oscillons, etc, see figure 1.5). Note that their model is "phenomenological" in the sense that it has not been derived from the governing equations of granular fluid and the coefficients of this model have to be found from either experiments or simulations.

In chapter 10, following Stewartson & Stuart (1971), we have been derived a complex Ginzburg Landau equation for two dimensional granular plane Couette flow. We have used multiple scale analysis to derive complex Ginzburg Landau equation. The detailed numerical analysis for aperiodic spatio-temporal patterns is left to future work.

11.8 Future Work

In weakly nonlinear stability studies, one important issue is the convergence of the Stuart-Landau series (3.32)-(3.33) which can be checked by determining its radius of convergence provided we know higher-order (second, third, etc.) Landau coefficients. Such works have been carried out for incompressible shear flows of Newtonian fluids (Herbert 1980; Newell *et al.* 1993) by calculating the first ten or more Landau coefficients, and then finding the nearest singularity from Domb-Sykes plots (Hinch 1991) to estimate the radius of convergence. It should be noted that the procedure to calculate the higher-order Landau coefficients seems to non-unique (Herbert 1980) in shear flows of Newtonian fluids.

For the present problem of granular plane Couette flow, we have calculated only the first Landau coefficient, except for the pure spanwise granular plane Couette flow problem (in chapter 7 for which we have calculated both first and second Landau coefficients) and therefore we are unable to make any conclusion about the range of validity of our nonlinear solutions in the parameter space (away from the neutral contour). It is necessary to calculate at least the second Landau coefficient to determine the stable solution branches for subcritical bifurcations for all cases. It has been shown in chapter 7 that the n^{th} order Landau coefficient requires n^{th} order nonlinear terms to be retained in the nonlinear perturbation equations in order to get correct bifurcations. In principle the higher-order Landau coefficients can be calculated, however, the related analysis and algebra becomes messy and tedious due to the nonlinearities inherent in the transport coefficients of granular fluids. Such an exercise would further help to establish a detailed term-by-term equivalence between the amplitude expansion method and the center manifold reduction for granular plane Couette flow. These issues should be looked into in future.

Although we have focussed on granular plane Couette flow in this thesis, our analysis is in no way limited but can be easily extended to analyze patterns in various other granular flow configurations. Our spectral-based numerical code can be adapted to such cases to analyze the nonlinear stability in a host of granular flow problems: granular Faraday waves (Umbanhower *et al.* 1996; Tsimring & Aranson 1997), granular Rayleigh-Bénard convection (Hayakawa *et al.* 1995; Khain & Meerson 2003; Eshuis *et al.* 2010), granular Poiseuille flow (Liss *et al.* 2002; Alam *et al.* 2010), inclined chute flow (Forterre & Pouliquen 2002; Mitarai & Nakanishi 2004), etc., see figure 11.4. To investigate these flows using the present order parameter theory, first we need to incorporate realistic boundary conditions (for example, slip velocity and non-adiabatic walls, etc.) instead of our choice of no-slip and zero heat flux conditions. Even though this

issue of realistic boundary conditions was not addressed in this thesis, this can, in principle, be incorporated to derive the relevant order-parameter equation and the resulting problem has to be solved numerically to determine the Landau coefficients. This work is left for future.

Various nonlinear resonances and spatially-extended patterns in rapid granular flows can be studied using coupled Landau equations and Ginzburg-Landau equation. Such theoretical studies are needed to uncover various pattern forming phenomena as observed in the experiments and particle simulations of rapid granular flows.

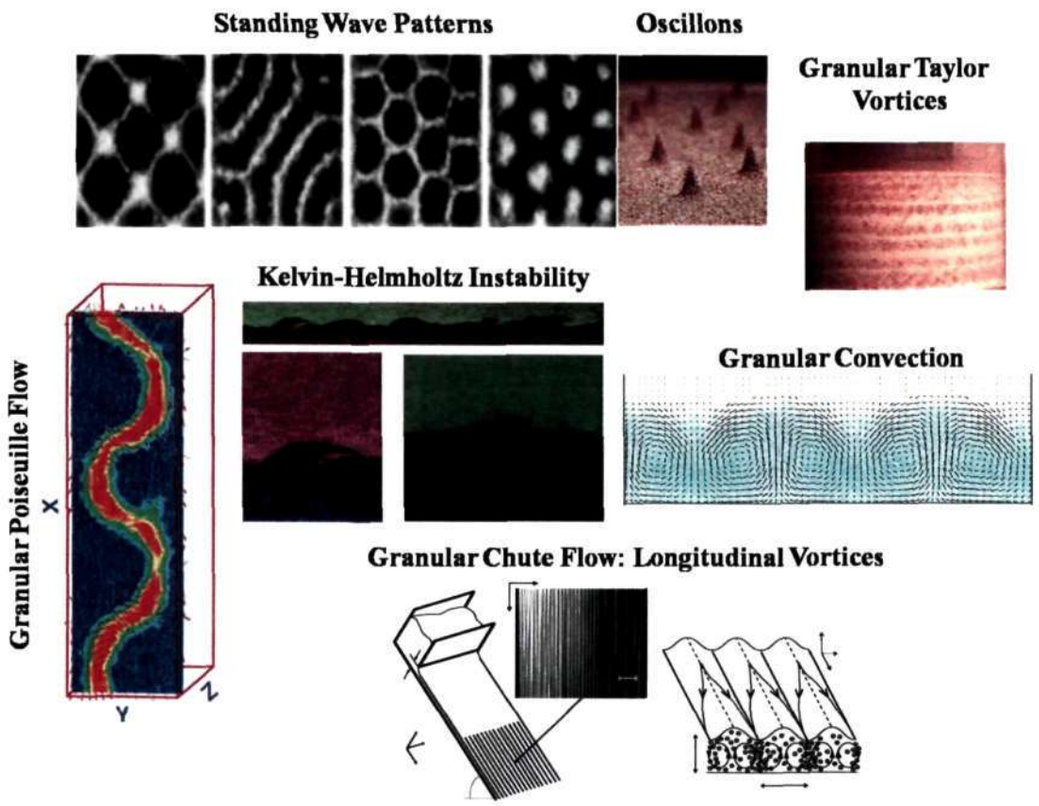

Figure 11.4: Various patterns in granular flows.

References

Alam, M. 2005 Universal unfolding of pitchfork bifurcations and the shear-band formation in rapid granular Couette flow. In *Trends in Applications of Mathematics to Mechanics* (ed. Y. Wang & K. Hutter), pp. 11–20. Shaker-Verlag, Aachen.

Alam, M. 2006 Streamwise structures and density patterns in rapid granular couette flow: a linear stability analysis. *J. Fluid Mech.* **553**, 1.

Alam, M., Arakeri, V., Goddard, J., Nott, P. & Herrmann, H. 2005 Instability-induced ordering, universal unfolding and the role of gravity in granular couette flow. *J. Fluid Mech.* **523**, 277.

Alam, M., Chikkadi, V. K. & Gupta, V. K. 2010 Density waves and the effect of wall roughness in granular poiseuille flow: simulation and linear stability. *Euro. Phys. Jour. ST* **179**, 69.

Alam, M. & Luding, S. 2003*a* First normal stress difference and crystallization in a dense sheared granular fluid. *Phys. Fluids* **15**, 2298.

Alam, M. & Luding, S. 2003*b* Rheology of bidisperse granular mixtures via event-driven simulations. *J. Fluid Mech.* **476**, 69.

Alam, M. & Nott, P. R. 1997 The influence of friction on the stability of unbounded granular shear flow. *J. Fluid Mech.* **343**, 267.

Alam, M. & Nott, P. R. 1998 Stability of plane couette flow of a granular material. *J. Fluid Mech.* **377**, 99.

Alam, M., Shukla, P. & Luding, S. 2008 Universality of shearbanding instability adn crystallization in sheared granular fluid. *J. Fluid Mech.* **615**, 293.

Alam, M., Willits, J., Aranson, B. & Luding, S. 2002 Kinetic theory of a binary mixture of nearly elastic disks with size and mass disparity. *Phys. Fluids* **14**, 4085.

Aranson, I. S. & Kramer, L. 2002 The world of the complex ginzburg-landau equation. *Rev. Mod. Phys.* **74**, 99.

Aranson, I. S. & Tsimring, L. S. 2006 Patterns and collective behaviour in granular media: theoretical concepts. *Rev. Mod. Phys.* **78**, 641.

Aranson, I. S., Tsimring, L. S. & Vinokur, V. M. 1999 Hexagons and interfaces in a vibrated granular layer. *Phys. Rev. E* **59**, R1327.

Babic, M. 1993 On the stability of rapid granular flows. *J. Fluid Mech.* **254**, 127.

Bagnold, R. A. 1954 Experiments on a gravity-free dispersion of large solid spheres in a newtonian fluid under shear. *Proc. R. Soc. Lond. A* **225**, 49.

Becherer, P., Morozov, A. N. & van Saarloos, W. 2009 Probing a subcritical instability with an amplitude expansion: an exploration of how far can one get. *Physica D* **238**, 1827.

Beijeren, H. V. & Ernst, M. H. 1973 The modified enskog equation. *Physica* **68**, 437.

Benney, D. J. 1984 The evolution of disturbances in shear flows at high reynolds numbers. *Stud. Appl. Math* **70**, 1–19.

Benney, D. J. & Maslowe, S. A. 1975 The evolution in space and time of nonlinear waves in parallel shear flows. *Stud. Appl. Math* **LIV No. 3**, 181.

Berret, J.-F., Porte, G. & Decruppe, J.-P. 1997 Inhomogeneous shear flows of wormlike micelles: a master dynamic phase diagram. *Phys. Rev. E* **55**, 1668.

Bizon, C., Shattuck, M. D., de Bruyn, J. R., Swift, J. B., Cormick, W. D. M. & Swinney, H. L. 1998 Convection and diffusion in patterns in oscillated granular media. *J. Stat. Phys.* **93**, 7210.

Blair, D. L., Neicu, T. & Kudrolli, A. 2003 Vortices in vibrated granular rods. *Phys. Rev. E* **67**, 031303.

Bonn, D., Meunier, J., Greffier, O., Al-Kahwaji, A. & Kellay, H. 1998 Bistability in non-newtonian flow: rheology and lyotropic liquid crystals. *Phys. Rev. E* **58**, 2115.

Bourzutschky, M. & Miller, J. 1995 Granular convection in a vibrated fluid. *Phys. Rev. Lett.* **74**, 2216.

Breu, A. P. J., Ensner, H.-M., Kruelle, C. A. & Rehberg, I. 2003 Reversing the brazil-nut effect: Competition between percolation and condensation. *Phys. Rev. Lett.* **90**, 014302.

Brey, J. J. & Cubero, D. 2000 . In *Granular Gases* (ed. T. Poschel & S. Luding), , vol. 564. Springer.

Brey, J. J., Dufty, J. W., Kim, C.-S. & Santos, A. 1998 Hydrodynamics for granular flow at low density. *Phys. Rev. E* **58**, 4638.

Brilliantov, N. & Pöschel, T. 2004 *Kinetic Theory of Granular Gases*. Oxford University Press.

Britton, M. M. & Callaghan, P. T. 1997 Two-phase shear band structures at uniform stress. *Phys. Rev. Lett.* **78** (26), 4930.

de Bruyn, J. R., Bizon, C., Shattuck, M. D., Goldman, D., Swift, J. B. & Swinney, H. L. 1998 Continuum-type stability balloon in oscillated granular layers. *Phys. Rev. Lett.* **81**, 1421.

Busse, F. H. 1978 Nonlinear properties of thermal convection. *Rep. Prog. Phys.* **41**, 1929.

Campbell, C. S. 1990 Rapid granular flow. *Annu. Rev. Fluid Mech.* **22**, 57.

Campbell, C. S. & Brennen, C. E. 1985 Computer simulation of granular shear flows. *J. Fluid Mech.* **151**, 167.

Canuto, C., Hussani, M. Y., Quarteroni, A. & Zang, T. A. 1988 *Spectral Methods in Fluid Dynamics*. Springer.

Carnahan & Starling, K. E. 1969 Equation of state of nonattracting rigid spheres. *J.Chem.Phys.* **51**, 635.

Carr, J. 1981 *Applications of Center Manifold Theory*. Springer.

Caserta, S., Simeon, M. & Guido, S. 2008 Shearbanding in biphasic liquid-liquid systems. *Phys. Rev. Lett.* **100**, 137801.

Conway, S. & Glasser, B. J. 2004 Density waves and coherent structures in granular couette flow. *Phys. Fluids* **16**, 509.

Conway, S., Liu, X. & Glasser, B. J. 2006 Instability-induced clustering and segregation in high-shear couette flows of model granular materials. *Chem. Engg. Sci.* **61**, 6404.

Coullet, P. H. & Spiegel, E. A. 1983 Amplitude equations for systems with competing instabilities. *SIAM J Appl. Math* **43**, 776.

Coussot, P., Raynaud, J. S., Bertrand, F., Moucheront, P., Guilbaud, J. P., Huynh, H. T., Jarny, S. & Lesueur, D. 2002 Coexistence of liquid and solid phases in flowing soft-glassy materials. *Phys. Rev. Lett.* **88**, 218301.

Craik, A. D. D. 1985 *Wave interactions and fluid flows*. Cambridge.

Crawford, C. & Riecke, H. 1999 Oscillon-type structures and their interaction in a swift-hohenberg model. *Physica D* **129**, 83.

Cross, M. C. & Hohenberg, I. 1993 Pattern formation outside of equilibrium. *Rev. Mod. Phys* **65**, 851.

Dangelmayr, G. 1986 Steady state mode interactions in the presence of o(2)-symmetry. *Dyn. Stab. Systems* **1**, 159.

Davey, A. 1962 The growth of taylor vortices in flow between rotating cylinders. *J. Fluid Mech.* **14**, 336.

Davey, A. & Nguyen, H. P. F. 1971 Finite-amplitude stability of pipe flow. *J. Fluid Mech.* **45**, 701.

Davey, A., Prime, D. & Stuart, J. T. 1968 On the instability of taylor vortices. *J. Fluid Mech.* **31**, 17.

Davies, S. J. & White, C. M. 1928 An experimental study of the flow of water in pipes of rectangular section. *Proc. R. Soc. Lond. A* **119**, 92.

Dawes, J. H. P. & Proctor, M. R. E. 2008 Secondary turing-type instabilities due to strong spatial resonance. *Proc. R. Soc. Lond. A* **464**, 923.

Deissler, R. J. 1987 Spatially growing waves, intermittency and convective chaos in an open-flow system. *Physica* **25D**, 233.

Dhont, J. K. G. & Briels, W. J. 2008 Gradient and vorticity banding. *Rheol Acta* **47**, 257.

Eagles, P. M. 1971 On stability of taylor vortices by fifth-order amplitude expansions. *J. Fluid Mech.* **49**, 529.

Eckhaus, W. 1965 *Studies in non-linear stability theory*. Springer-Verlag.

Eshuis, P., van der Meer, D., Alam, M., van Gerner, H. J., van der Welle, K. & Lohse, D. 2010 Onset convection in strongly shaken granular matter. *Phys. Rev. Lett.* **104**, 038001.

Eshuis, P., van der Weele, K., van der Meer, D. & Lohse, D. 2005 Granular leidenfrost effect: Experiment and theory of floating particle clusters. *Phys. Rev. Lett.* **95**, 258001.

FARADAY, M. 1831 On the forms and states assumed by fluids in contact with vibrating elastic surface. *Phil. Trans. Roy. Soc. London* **52**, 299.

FIELDING, S. M. 2007 Complex dynamics of shear banded flows. *Soft Matter* **3**, 1262.

FORTERRE, F. & POULIQUEN, O. 2002 Stability analysis of rapid granular chute flows: formation of longitudinal vortices. *J. Fluid Mech.* **467**, 361.

FORTERRE, Y. & POULIQUEN, O. 2001 Longitudinal vortices in granular flows. *Phys. Rev. Lett.* **86**, 5886.

FUJIMURA, K. 1989 The equivalence between two perturbation method in weakly nonlinear stability theory for parallel flows. *Proc. R. Soc. Lond. A* **424**, 373.

FUJIMURA, K. 1991 Methods of centre manifold and multiple scales in the theory of weakly nonlinear stability for fluid motions. *Proc. R. Soc. Lond. A* **434**, 179.

FUJIMURA, K. 1992 Higher harmonic resonances in free convection between vertical parallel plates. *Proc. R. Soc. Lond. A* **349**, 95.

FUJIMURA, K. & KELLY, R. E. 1997 Degenerate bifurcation in stably stratified plane poiseuille flow. *J. Fluid Mech.* **331**, 261.

FUJIMURA, K. & MIZUSHIMA, J. 1985 Nonlinear interaction of disturbances in free convection between vertical parallel plates. In *Nonlinear wave interactions in fluid* (ed. R. W. Miksad, T. Akylas & T. Herbert), , vol. 87, p. 123. Springer.

GARZÓ, V. & DUFTY, J. W. 1999 Dense fluid transport for inelastic hard spheres. *Phys. Rev. E* **59**, 5895.

GARZÓ, V. & MONTANERO, J. M. 2002 Transport coefficients of a heated granular gas. *Physica A* **313**, 336.

GASS, D. M. 1971 Enskog theory for a rigid disk fluid. *J. Chem. Phys.* **54**, 1898.

GAYEN, B. & ALAM, M. 2006 Algebraic and exponential instabilities in a sheared micropolar granular fluid. *J. Fluid Mech.* **567**, 195.

GOLDFARB, D. J., GLASSER, B. J. & SHINBROT, T. 2002 Shear instabilities in granular flows. *Nature* **415**, 302.

GOLDHIRSCH, I. 2003 Rapid granular flows. *Annu. Rev. Fluid Mech.* **35**, 267.

GOLDHIRSCH, I. & ZANETTI, G. 1993 Clustering instability in dissipative gases. *Phys. Rev. Lett.* **70**, 1619.

GOLUB, G. H. & VAN-LOAN, C. F. 1983 *Matrix computations*. The Johns Hopkins University Press.

GOLUBITSKY, M. & SCHAEFFER, D. 1985 *Singularities and Groups in Bifurcation Theory I*. New York: Springer.

GUBA, P. & WORSTER, G. 2010 Interactions between steady and oscillatory convection in mushy layers. *J Fluid Mech.* **645**, 411.

GUCKENHEIMER, J. & HOLMES, P. J. 1983 *Nonlinear Oscillations, Dynamical Systems, and Bifurcations of Vector Fields*. Springer.

HAFF, P. K. 1983 Grain flow as a fluid-mechanical phenomenon. *J. Fluid Mech.* **134**, 401.

HANES, D. M. & INMAN, D. L. 1985 Observations of rapidly flowing granular fluid flow. *J. Fluid Mech.* **150**, 357.

HANIFI, A., SCHMID, P. J. & HENNINGSON, D. S. 1996 Transient growth in compressible boundary layer flow. *Phys. Fluids* **8**, 826.

HAYAKAWA, H., YUE, S. & HONG, D. C. 1995 Hydrodynamic description of granular convection. *Phys. Rev. Lett.* **75**, 2328.

HERBERT, T. 1980 Nonlinear stability of parallel flows by high-order amplitude expansions. *AIAA J.* **18**, 243.

HERBERT, T. 1983 On the perturbation methods in nonlinear stability theory. *J. Fluid Mech.* **126**, 167.

HINCH, E. J. 1991 *Perturbation Methods*. Cambridge University Press.

HOFFMAN, R. L. 1972 Discontinuous and dilatant viscosity behaviour in concentrated suspensions. *Trans. Soc. Rheol.* **16**, 155.

HOLMES, W. M., CALLAGHAN, P. T., VLASSOPOULOS, D. & ROOVERS, J. 2004 Shear banding phenomena in ultrasoft colloidal glasses. *J. Rheol* **48**, 1085.

HOPKINS, M. A., JENKINS, J. T. & LOUGE, M. Y. 1992 On the structure of three-dimensional shear flows. In *Advances in Micromechanics of Granular Materials* (ed. H. H. Shen, M. Satake, M. Mehrabadi, C. S. Chang & C. S. Campbell), pp. 271–279. Elsevier Science, New York.

HOPKINS, M. A. & LOUGE, M. Y. 1991 Inelastic microstructure in rapid granular flows of smooth disks. *Physics of Fluids A: Fluid Dynamics* **3**, 47.

HUI, K., HAFF, P. K., UNGAR, J. E. & JACKSON, R. 1984 Boundary conditions for high-shear grain flows. *J. Fluid Mech.* **145**, 223.

Jackson, R. 1983 Some mathematical and physical aspects of continuum models for the motion of the granular materials. In *In Theory of Dispersed Multiphase Flow* (ed. R. E. Meyer), pp. 291–337. New York: Academic Press.

Jaeger, H. M., Nagel, S. R. & Behringer, R. P. 1996 Granular solids, liquids, and gases. *Rev. Mod. Phys.* **68**, 1259.

Jenkins, J. T. 1992 Boundary conditions for rapid granular flows: flat, frictional walls. *J. Appl. Mech.* **59**, 120.

Jenkins, J. T. & Richman, M. W. 1985 Kinetic theory for plane flows of a dense gas of identical, rough, inelastic, circular disks. *Phys. Fluids* **28**, 3485.

Jenkins, J. T. & Richman, M. W. 1986 Boundary conditions for plane flows of smooth, nearly elastic, circular disks. *J. Fluid Mech.* **171**, 53.

Johnson, P. C. & Jackson, R. 1987 Frictional-collisional constitutive relations for granular materials, with application to plane shearing. *J. Fluid Mech.* **176**, 67.

Kadanoff, L. 1999 Built upon sand: Theoretical ideas inspired by granular flows. *Rev. Mod. Phys.* **64**, 111.

Khain, E. 2007 Hydrodynamics of fluid-solid coexistence in dense shear granular flow. *Phys. Rev. E* **75**, 051310.

Khain, E. & Meerson, B. 2003 Onset of thermal convection in a horizontal layer of granular gas. *Phys. Rev. E* **67**, 021306.

Khain, E. & Meerson, B. 2006 Shear-induced crystallization of a dense rapid granular flow: Hydrodynamics beyond the melting point. *Phys. Rev. E* **73**, 061301.

Khorrami, M. R., Malik, M. R. & Ash, R. L. 1989 Numerical methods for hypersonic boundary layer stability. *J. Comput. Phys.* **81**, 206.

Knobloch, E. & Guckenheimer, J. 1983 Convective transitions induced by a varying aspect ratio. *Phys. Rev. A* **27**, 408.

Kreyszig, E. 1978 *Introductory Functional Analysis with applications*. John Wiley & Sons.

Kudrolli, A., Wolpert, M. & Gollub, J. P. 1997 Cluster formation due to collisions in granular material. *Phys. Rev. Lett.* **78**, 1383.

Kumaran, V. 2004 Constitutive relations and linear stability of a sheares granular flow. *J. Fluid Mech.* **506**, 1.

Lettinga, M. P. & Dhont, J. K. G. 2004 Non-equilibrium phase behaviour of rodlike viruses under shear flow. *J. Phys. Cond. Matter* **16**, S3929.

Lin-Gibson, S., Pathak, J. A., Grulke, E. A., Wang, H. & Hobbie, E. K. 2004 Elastic flow instability in nanotube suspensions. *Phys. Rev. Lett.* **92**, 048302.

Liss, E. D., Conway, S. L. & Glasser, B. J. 2002 Density waves in gravity-driven granular flow through a channel. *Phys. Fluids* **14**, 3309.

Luding, S. 2009 Towards dense, realistic granular media in 2d. *Nonlinearity* **22**, R101.

Lun, C. K. K., Savage, S. B., Jeffrey, D. J. & Chepurniy, N. 1984 Kinetic theories for granular flow: inelastic particles in couette flow and slightly inelastic particles in a general flow field. *J. Fluid Mech.* **140**, 223.

Lutsko, J. F. 2005 Transport properties of dense dissipative hard-sphere fluids for arbitrary energy loss models. *Phys. Rev. E* **72**, 021306.

Malik, A. 2008 Density waves and fluctuations in three-dimensional granular poiseuille flow. *MS Engg. Thesis, JNCASR, Bangalore* .

Malik, M. R. 1990 Numerical methods for hypersonic boundary layer stability. *J. Comput. Phys.* **86**, 376.

Manneville, P. 1990 *Dissipative Structures and Weak Turbulence*. Academic Press.

Mason, J. C. & Handscomb, D. 2003 *Chebyshev polynomials*. Baltimore and London: Chapman and Hall/CRC.

McLennan, J. A. 1989 *Introduction to nonequilibrium statsitical mechanics*. Englewood Cliffs, NJ: Prentice-Hall.

McNamara, S. & Falcon, E. 2005 Simulations of vibrated granular medium with impact-velocity-dependent restitution coefficient. *Phys. Rev. E* **71**, 031302.

Melo, F., Umbanhowar, P. B. & Swinney, H. L. 1994 Transition to parametric wave patterns in a vertically oscillated granular layer. *Phys. Rev. Lett.* **72**, 172.

Melo, F., Umbanhowar, P. B. & Swinney, H. L. 1995 Hexagons, kinks, and disorder in oscillated granular layers. *Phys. Rev. Lett.* **75**, 3838.

Mitarai, N. & Nakanishi, H. 2004 Linear stability analysis of rapid granular flow down a slope and density wave formation. *J. Fluid Mech.* **507**, 309.

Mizushima, J. & Gotoh, K. 1985 Nonlinear stability of parallel flows. *J. Phys. Soc. Japan* **54**, 2061.

Morozov, A. & Saarloos, W. 2007 An introductory essay on subcritical instabilities and the transition to turbulence in visco-elastic parallel shear flows. *Phys. Rep.* **447**, 112.

Morozov, A. N. & van Saarloos, W. 2005 Subcritical finite-amplitude solutions for plane couette flow of viscoelastic fluids. *Phys. Rev. Lett.* **95**, 024501.

Mueth, D. M., Debregeas, G. F., Karczmar, G. S., Eng, P. J., Nagel, S. & Jaeger, H. J. 2000 Signatures of granular microstructure in dense shear flows. *Nature* **406**, 385.

Mullin, T. 2000 Coarsening of self-organized clusters in binary mixtures of particles. *Phys. Rev. Lett.* **84**, 4741.

Nagata, M. 1990 Three-dimensional finite-amplitude solutions in plane couette flow: bifurcation from infinity. *J. Fluid Mech.* **217**, 519.

Newell, A. C., Passot, T. & Lega, J. 1993 Order parameter equations for patterns. *Annu. Fluid Mech.* **25**, 399.

Newell, A. C. & Whitehead, J. A. 1969 Finite bandwidth, finite amplitude convection. *J. Fluid Mech.* **279**, 38.

Nishioka, M., Iid, S. & Ichikawa, Y. 1975 An experimental investigation of the stability of plane poiseuille flow. *J. Fluid Mech.* **72**, 731.

Nott, P. R., Alam, M., Agrawal, K., Jackson, R. & Sundaresan, S. 1999 The effect of boundaries on the plane couette flow of granular materials: a bifurcation analysis. *J. Fluid Mech.* **397**, 203.

Ogawa, S., Umemura, A. & Oshima, N. 1980 On the equations of fully granular materials. *ZAMP* **31**, 483.

Olafsen, J. S. & Urbach, J. S. 1998 Clustering, order, and collapse in a driven granular monolayer. *Phys. Rev. Lett.* **81**, 4369.

Olmsted, P. D. 2008 Perspective on shear banding in complex fluids. *Rheol. Acta* **47**, 283.

Orpe, A. V. & Khakhar, D. V. 2007 Rheology of surface granular flows. *Journal of Fluid Mechanics* **571**, 1.

Ottino, J. M. & Khakhar, D. V. 2000 Mixing and segregation of granular materials. *Annu. Rev. Fluid Mech.* **32**, 55.

Pak, H. K., Van Doorn, E. & Behringer, R. P. 1995 Effects of ambient gases on granular materials under vertical vibration. *Phys. Rev. Lett.* **74**, 4643.

Paolotti, D., Barrat, A., Marini Bettolo Marconi, U. & Puglisi, A. 2004 Thermal convection in monodisperse and bidisperse granular gases: A simulation study. *Phys. Rev. E* **69**, 061304.

Pöschel, T. & Brilliantov, N. V. 2001 Extremal collision sequences of particles on a line: Optimal transmission of kinetic energy. *Phys. Rev. E* **63**, 021505.

Pouliquen, O., Delour, J. & Savage, S. B. 1997 Fingering in granular flows. *Nature* **386**, 816.

Press, W. H., Teukolsky, S. A., Vellerling, W. T. & Flannery, B. P. 1992 *Numerical Recipes*. Cambridge University Press.

Proctor, M. R. E. & Jones, C. A. 1988 The interaction of two spatially resonant patterns in thermal convection. part 1. exact 1:2 resonance. *J. Fluid Mech.* **188**, 301.

Ramirez, R., Pöschel, T., Brilliantov, N. V. & Schwager, T. 1999 Coefficient of restitution of colliding viscoelastic spheres. *Phys. Rev. E* **60**, 4465.

Ramirez, R., Risso, D. & Cordero, P. 2000 Thermal convection in fluidized granular systems. *Phys. Rev. Lett.* **85**, 1230.

Rao, K. K. & Nott, P. R. 2008 *An introduction to granular flow*. Cambridge.

Reynolds, W. C. & Potter, M. C. 1967 Finite amplitude instability of parallel shear flows. *J. Fluid Mech.* **27**, 465.

Richman, M. W. 1988 Boundary conditions based upon a modified maxwellian velocity distribution for flows of identical, smooth, nearly elastic spheres. *Acta Mechanica* **75**, 227.

Romanov, J. 1973 Stability of incompressible plane couette flow. *J. Funct. Anal.* **37**, 1.

Rosenblat, S. & Davis, S. H. 1979 Bifurcation from infinity. *SIAM J. Appl. Maths.* **37**, 1.

Saitoh, K. & Hayakawa, H. 2007 Rheology of a granular gas under a plane shear. *Phys. Rev. E* **75**, 021302.

Salmon, J.-B., Manneville, S. & Colin, A. 2003 Shear banding in a lyotropic lamellar phase. i. time-averaged velocity profiles. *Phys. Rev. E* **68**, 051503.

Sapozhnikov, M. V., Tolmachev, Y. V., Aranson, I. S. & Kwok, W.-K. 2003 Dynamic self-assembly and patterns in electrostatically driven granular media. *Phys. Rev. Lett.* **90**, 114301.

Sasvári, M., Kertész, J. & Wolf, D. E. 2000 Instability of symmetric couette flow in a granular gas: Hydrodynamic field profiles and transport. *Phys. Rev. E* **62**, 3817.

SAVAGE, S. B. 1984 The mechanics of rapid granular flows, Advances in Applied Mechanics. In *Advances in Applied Mechanics* (ed. J. Hutchinson & T. Wu), , vol. 24, pp. 289–366. Academic.

SAVAGE, S. B. 1992 Instability of unbounded uniform granular shear flow. *J. Fluid Mech.* **241**, 109.

SAVAGE, S. B. & SAYED, S. 1984 Stresses developed by dry cohesionless granular materials sheared in an annular shear cell. *J. Fluid Mech.* **142**, 391.

SCHALL, P. & VAN HECKE, M. 2010 Shear bands in matter with granularity. *Annu. Rev. Fluid Mech.* **42**, 67.

SCHMID, P. J. & HENNINGSON, D. S. 2001 *Stability and Transition in shear flows*. Springer-Verlag.

SCHMID, P. J. & KYTOMAA, H. K. 1994 Transient and asymptotic stability of granular shear flow. *Journal of Fluid Mechanics* **264**, 255.

SELA, N. & GOLDHIRSCH, I. 1998 Hydrodynamic equations for rapid shear flows of smooth, inelastic spheres, to burnett order. *J. Fluid Mech.* **41**, 361.

SHUKLA, P. & ALAM, M. 2008 Nonlinear stability of granular shear flow: Landau equation, shearbanding and universality. In *Proc. of International Conference on Theoretical and Applied Mechanics*. (ISBN 978-0-9805142-0-9), 24–29 August, Adelaide, Australia.

SHUKLA, P. & ALAM, M. 2009 Landau-type order parameter equation for shearbanding in granular couette flow. *Phys. Rev. Lett.* **103**, 068001.

SHUKLA, P. & ALAM, M. 2011 Weakly nonlinear theory of shear-banding instability in granular plane couette flow: analytical solution, comparison with numerics and bifurcation. *J. Fluid Mech.* **666**, 204.

SNEZHKO, A., ARANSON, I. S. & KWOK, W.-K. 2005 Structure formation in electromagnetically driven granular media. *Phys. Rev. Lett.* **94**, 108002.

STEWARTSON, K. & STUART, J. T. 1971 A non-linear instability theory for a wave system in plane poiseuille flow. *J. Fluid Mech.* **48**, 529.

STROGATZ, S. H. 1994 *Nonlinear dynamics and chaos*. Reading, Massachusetts: Perseus Books.

STUART, J. T. 1960 On the nonlinear mechanics of wave disturbances in stable and unstable parallel flows. *J. Fluid Mech.* **9**, 353.

STUART, J. T. 1971 Nonlinear stability theory. *Annu. Rev. Fluid Mech.* **3**, 347.

SUSLOV, S. A. & PAOLUCCI, S. 1997 Nonlinear analysis of convection flow in a tall vertical enclosure under non-boussinesq conditions. *J. Fluid Mech.* **344**, 1.

TAN, M.-L. 1995 Microstructure and macrostructure in ripid granular flows. PhD thesis, Princeton University, USA.

TAN, M.-L. & GOLDHIRSCH, I. 1997 Intercluster interactions in rapid granular shear flows. *Phys. Fluids* **9**, 856.

TREFETHEN, L. N. & BAU, D. 1997 *Numerical linear algebra*. Philadelphia: SIAM.

TSIMRING, L. S. & ARANSON, I. S. 1997 Localized and cellular patterns in a vibrated granular layer. *Phys. Rev. Lett.* **79**, 213.

UMBANHOWER, P., MELO, F. & SWINNEY, H. L. 1996 Localized excitation in a vertically vibrated granular layer. *Nature* **382**, 793.

VENKATARAMANI, S. C. & OTT, E. 1998 Spatiotemporal bifurcation phenomena with temporal period doubling: Patterns in vibrated sand. *Phys. Rev. Lett.* **80**, 3495.

VOLFSON, D., TSIMRING, L. S. & ARANSON, I. S. 2003 Order parameter description of stationary partially fluidized shear granular flows. *Phys. Rev. Lett.* **90**, 254301.

VOTH, G. A., BIGGER, B., BUCKLEY, M. R., LOSERT, W., BRENNER, M. P., STONE, H. A. & GOLLUB, J. P. 2002 Ordered clusters and dynamical states of particles in a vibrated fluid. *Phys. Rev. Lett.* **88**, 234301.

WATSON, J. 1960 On the nonlinear mechanics of wave disturbances in stable and unstable parallel flows. *J. Fluid Mech.* **9**, 371.

WEINSTEIN, M. 1981 Nonlinear instability in plane poiseuille flow: a quantitative comparison between the methods of amplitude expansions and the method of multiple scales. *Proc. R. Soc. Lond. A* **375**, 155.

WIGGINS, S. 1990 *Inroduction to Applied Nonlinear Dynamical Systems and Chaos*. Springer.

WILLITS, J. T. & ARNARSON, B. O. 1999 Kinetic theory of a binary mixture of nearly elastic disks. *Physics of Fluids* **11** (10), 3116.

WILSON, H. J. & FIELDING, S. M. 2006 Linear instability of planar shear banded flow of both diffusive and non-diffusive johnson-segalman fluids. *Journal of Non-Newtonian Fluid Mechanics* **138**, 181.

ZHANG, W. & VIÑALS, J. 1995 Secondary instabilities and spatiotemporal chaos in parametric surface waves. *Phys. Rev. Lett.* **74**, 690.

Publications

Journal Publication

1. Nonlinear stability and patterns in granular plane Couette flow: Hopf and pitchfork bifurcations, and evidence for resonance.
   Priyanka Shukla & Meheboob Alam,
   Journal of Fluid Mechanics, In Press, 2011.

2. Weakly nonlinear theory of shear-banding instability in granular plane Couette flow: analytical solution, comparison with numerics and bifurcation,
   Priyanka Shukla & Meheboob Alam,
   Journal of Fluid Mechanics **666**, p. 204-253, 2011.

3. Landau-type order parameter equation for shear banding in granular Couette flow,
   Priyanka Shukla & Meheboob Alam,
   Physical Review Letters, **103**, 2009.

4. Universality of shear-banding instability and crystallization in sheared granular fluid,
   Meheboob Alam, Priyanka Shukla & Stefan Luding,
   Journal of Fluid Mechanics **615**, p. 293-321, 2008.

5. Vorticity banding as Hopf and pitchfork bifurcations in granular Couette flow,
   Priyanka Shukla & Meheboob Alam, 2010 (submitted)

6. Nonlinear stability of three-dimensional granular plane Couette flow: analytical solution for gradient and vorticity bandings,
   Priyanka Shukla & Meheboob Alam. 2010 (preprint)

Conference Publication

1. Shearbanding instability and patterns in granular shear flows,
   Priyanka Shukla & Meheboob Alam,
   APS March Meeting 2011, 21-25 March 2011, Dallas, Texas, USA.

2. Nonlinear stability of granular plane Couette flow: Shear banding,
   Priyanka Shukla & Meheboob Alam,
   63rd Annual Meeting of the APS Divison of Fluid Dynamics, (21-23 November 2010, Long Beach, California, USA).

3. Nonlinear stability, bifurcation and resonance in granular plane Couette flow,
   Priyanka Shukla & Meheboob Alam,
   63rd Annual Meeting of the APS Divison of Fluid Dynamics, (21-23 November 2010, Long Beach, California, USA).

4. Nonlinear stability, bifurcation and patterns in granular plane Couette flow,
8th EUROMECH Fluid Mechanics Conference (EFMC-8), (13-16 September 2010, Altes Koenigliches Kurhaus, Bad Reichenhall, Germany).

5. Nonlinear Stability of Granular Shear Flow: Landau Equation, Shearbanding and Universality,
Meheboob Alam & Priyanka Shukla,
22nd International Congress of Theoretical and Applied Mechanics (ICTAM2008), p. 1-2 (24-30 August 2008, Adelaide, Australia; ISBN 978-0-9805142-0-9).

6. Nonlinear stability of granular shear flow: Landau equation and shearbanding,
Priyanka Shukla & Meheboob Alam,
Proc. of 12th Asian Congress of Fluid Mechanics (ACFM-12), p. 1-4 (18-21 August 2008, Daejeon, Korea).

7. Weakly Nonlinear Stability of Granular Couette Flow,
Priyanka Shukla & Meheboob Alam,
EUROMECH 492: Shearbanding Phenomena in Entangled Systems, 3-5 September 2007, University College London (UCL), London, England.

8. An exact order-parameter description of granular plane Couette flow from nonlinear stability analysis: Landau equation,
Meheboob Alam & Priyanka Shukla,
Traffic and Granular Flow 2007 (TGF07), 20-22 June 2007, Paris Sud University, Orsay, France.

Nothing puzzles me more than time and space; and yet nothing troubles me less, as I never think about them.

*Charles Lamb

I don't consider this algebra, but this doesn't mean that algebraists can't do it.

**Garrett Birkhoff

*taken from Turbulence an introduction for scientists and engineers by P.A.Davidson.
** taken from Artin Algebra.

Recd on 24/2/2011

DD. 12/9/11